Microstructural Analysis of Ni-WC Metal Matrix Composites Deposited Using Plasma Transferred Arc Additive Manufacturing

by

Dylan Rose

A thesis submitted in partial fulfillment of the requirements for the degree of

Doctor of Philosophy
in
Materials Engineering

Department of Chemical and Materials Engineering

University of Alberta

Abstract

The objective of this thesis is to examine how the composition and solidification rate influences the thermal degradation of WC and the resulting microstructure of WC-Ni metal matrix composites (MMCs) deposited using plasma transferred arc additive manufacturing (PTA-AM). Scanning electron microscopy (SEM) and electron dispersive spectroscopy (EDX) were used to gather semi-quantitative compositional data. The thesis explores the effect of the composition of the metal matrix composite on the microstructure by altering the WC content, WC type, and metal matrix composition. The WC type and Cr content in the matrix played a significant role in the amount of dissolution-diffusion damage to the WC, resulting in the formation of complex carbides. The matrix microstructure consisted of γ-Ni dendrites, a Ni halo around the primary dendrites, and a γ-Ni/Ni_3B eutectic.

Convolutional neural networks (CNN) were used to quantify the distribution of the WC in the PTA-AM samples by determining the carbide volume percent and mean free path. The final model could segment the WC particles with above 90% accuracy for the intersection over union (IOU), dice coefficient, and area under the receiver operating characteristic curve across the entire test dataset. Compared to the ground truth, the model calculated statistically similar values for the carbide volume percent and slightly more conservative values for the mean free path. It was found that the mean free path between carbides tended to increase with the height of the sample, which suggests more carbide degradation.

Electromagnetic levitation was used to estimate a relationship between the secondary dendrite arm spacing (SDAS) and the solidification cooling rate for 70wt% angular monocrystalline WC in a NiBSi matrix. The relationship between SDAS and cooling rate was then used to determine the cooling rate at different heights throughout a PTA-AM build of the same composition. The composition of the phases present in the microstructure was determined for the different cooling rates that are experienced during the complex thermal cycling of PTA-AM. The phase and composition data are compared to Scheil solidification conditions using Thermo-calc software. The culmination of this data provides a microstructural analysis of 70wt% WC - NiBSi of cooling rates up to 1000°C/s.

Preface

I, Dylan Kenneth Rose, declare that this thesis titled, 'Microstructural Analysis of Ni-WC Metal Matrix Composites Deposited Using Plasma Transferred Arc Additive Manufacturing' and the work presented in it are my own. Furthermore, permission is hereby granted to the University of Alberta Libraries to reproduce single copies of this thesis and to lend or sell such copies for private, scholarly or scientific research purposes only. Where the thesis is converted to, or otherwise made available in digital form, the University of Alberta will advise potential users of the thesis of these terms.

The author reserves all other publication and other rights in association with the copyright in the thesis and, except as herein before provided, neither the thesis nor any substantial portion thereof may be printed or otherwise reproduced in any material form whatsoever without the author's prior written permission.

Signed:

_____

Date:

_____

"When nothing seems to help, I go and look at a stonecutter hammering away at his rock perhaps a hundred times without as much as a crack showing in it. Yet at the hundred-and-first blow it will split in two, and I know it was not that blow that did it—but all that had gone before."

- Jacob A. Riis

Acknowledgements

I would like the dedicate this thesis to my wife Skye. You were my rock through the hard times, and you gave the strength to keep moving forward. I could not have done this without you in my corner.

I would like thank my parents, Ken and Cindy, for your unconditional love and support through my decade of school. I am forever indebted to you.

To my doggo Teddy, thanks for always having a smiling face and wagging tail waiting for me when I got home.

I would like the thank Innotech Alberta for allowing me to have access to their PTA, and supplying the consumables for my work. A special thanks to Mike Danych for always giving a helping hand when needed, and sharing his knowledge of overlaying with me.

A huge thank you to Thomas Volkmann, Stefan Burggraf, and Ahmed Manawa from DLR in Köln, Germany for running my EML experiments for me and helping with my analysis. Additionally, would like to thank the TEMPUS parabolic flight crew for allowing me to be a passenger on a parabolic flight. To this day it is still the coolest thing I have ever experienced.

To the members of the AMPL and AM2G group, thank you for your all of your support through this journey - Ry, Tamara, Marcelino, Jonas, Akki, Geoffrey, Quentin, Anne, Anqi, Thomas, Shiyu, and Pepe. Special thanks to AMPL alumni Kim Meszaros for your guidance and support. I would also like to thank Dr. Ahmed Qureshi for always providing a mechanical engineers perspective, and helping me figure out what to do post graduation.

To Syncrude - Stefano Chiovelli, and Dr. Hugh Roth, thank you for your support, and giving me access to your facilities. I always felt like you had my back regardless of the outcomes of my work were positive or negative.

Lastly, a heartfelt thank you to my supervisors Dr. Hani Henein, and Dr. Tonya Wolfe. You were there through the good times, and the bad, and your mentorship is something I will cherish for the rest of my days.

Contents

List of Figures

List of Tables

Abbreviations

ALC	Arc length controller
AM	Additive Manufacturing
ANN	Artificial neural network
AUC-ROC	Area under the receiver characteristic curve
BCE	Binary cross entropy
BPNN	Back propagation neural network
CAD	Computer-aided design
CAM	Computer-aided machining
CBP	Counting the black pixels
CCD	Charge-coupled device
CMOS	Complementary metal-oxide semiconductor
CMT	Cold metal transfer
CNN	Convolutional neural network
DBTT	Ductile-to-brittle transition temperature
DC	Mean dice coefficient
DED	Direct energy deposition
DL	Dice coefficient loss
DOF	Degrees of freedom
DSC	Differential scanning calorimetry
EBM	Electron beam melting
EBSD	Electron backscatter diffraction

EDX	Energy-dispersive X-ray spectroscopy
EML	Electromagnetic levitation
FESEM	Field emission scanning electron microscopy
GMAW	Gas metal arc welding
GTAW	Gas tungsten arc welding
HIP	Hot isostatic pressing
ILC	Iterative learning controller
IOU	Intersection over union
IR	Infrared
LDED	Laser direct energy deposition
MAT	Medial axis transformation
MC	Monocrystalline
MFP	Mean free path
MISO	Multiple-input single-output
ML	Machine learning
MMC	Metal matrix composite
PBF	Powder bed fusion
PID	Proportional-integral-derivative
PM	Powder metallurgy
PPA	Pulse plasma arc
PSD	Proportional summational differential
PTA	Plasma transferred arc
PTA-AM	Plasma transferred arc additive manufacturing
RBFN	Radial basis function network
ReLU	Rectified linear unit
ROC	Receiver characteristic curve
ROS	Robot operating system
SDAS	Secondary dendrite arm spacing
SDF	Shape diameter function

SE	Spherical eutectic
SEM	Scanning electron microscopy
SGD	Stochastic gradient decent
TCS	Temperature control system
WAAM	Wire and arc additive manufacturing
XRD	X-ray diffraction

List of Symbols

The following list describes the symbols used throughout this work.

α	Value of ELU saturation for negative values
β	Weights for a given layer
$\hat{p}$	The models probability that a pixel belongs to a particular class.
λ	L2 regularization term
λ_o	Material constant
λ_S	Secondary dendrite arm spacing (μm)
λ_{MFP}	Mean free path (μm)
σ	Standard deviation of the noise
B	Kernel of pixels
C	Nominal composition (atomic fraction)
C_s	Concentration in the solid (atomic fraction)
d	Euclidean distance
f	Volume fraction of reinforcement particles (vol%)

FN Type II error (false negative)

FP Type I error (false positive)

FPR False positive rate is the ratio of type I errors over the total number of pixels belonging to another class.

h Filtering parameter

i Color channels of the image

j Number of pixels away from the center of the kernel

k Partition coefficient

n Material constant

N_L Number of particles per unit length

p Center of kernel being adjusted

q Center of kernel being used for comparison

R Cooling rate (°C/s)

r Radius of the kernel

T Temperature (°C)

T_e^{DSC} Eutectic temperature from DSC (°C)

T_e^{pyr} Eutectic temperature from pyrometer (°C)

T_{pyr} Pyrometer temperature (°C)

TP True positive (correctly labelled pixels)

TPR True positive rate is the models ability to correctly classify pixels.

u Pixel intensity

V_s Volume fraction of solid (volume fraction)

w The weight (value) the pixel is multiplied by

y Class value of the ground truth

Chapter 1

Introduction

1.1 Motivation

Abrasive wear-provoking environments are found across a spectrum of industries, including agriculture [1–3], pipelines [4–6], and mining [7–9]. Replacing damaged components that have failed due to abrasive wear costs the Canadian Energy Sector billions of dollars a year [10]. Traditional mitigation methods include material substitution, surface treatments, and overlaying the equipment with a hard metal or some form of metal matrix composite (MMC). The MMC consists of a tough metal matrix with a homogenous distribution of a hard reinforcement phase, typically in the form of a chrome or tungsten carbide (WC). For metal matrix composites, interfacial bonding is essential for transferring force from the matrix to the ceramic and ensuring that the reinforcement particles are not removed from the matrix during service. Currently, the MMC most commonly selected in mining applications with severe abrasion and impact wear is a NiCrBSi with 65wt% WC, overlayed using plasma transfer arc (PTA) [11].

PTA is a welding process where an arc is struck between a tungsten electrode housed in a nozzle and a substrate, with co-axially fed powder melting within the plasma. The nozzle moves over the surface, and the powder is deposited onto the substrate. In a typical overlaying process, a part must first be produced through traditional manufacturing methods such as casting, forging, or welded assembly. It is then transported to a separate facility, and the overlay is applied using PTA. The multi-step process of applying current wear-resistant

technology requires significant lead time or inventory. The deposition of PTA overlays has limitations. The part's surface must be relatively flat and horizontal to ensure mechanical consistency throughout the overlay. The large amount of current required to have good adherence to the substrate and to deposit a 3-5mm thick overlay, causes dilution of the MMC overlay with the base material and distortion of the part due to thermal residual stress, which can drastically reduce the wear resistance of the coating [12]. For MMCs with solid ceramic additions, reactions between the metal matrix and the reinforcement particles also become apparent at higher temperatures [10, 13–20]. Large currents also result in large matrix superheat, thus giving a longer time for solidification resulting in settling of WC, leaving the surface depleted of carbides. This increases the wear rate of the overlay [11].

Additive manufacturing (AM) creates objects layer by layer from a computer-aided design (CAD) model. Many traditional manufacturing methods rely on machining to remove unwanted material from an ingot. In contrast, additive manufacturing is a relatively new field with immense potential to transform manufacturing processes. One of the primary advantages of AM over conventional manufacturing is its ability to construct complex geometries without shape constraints. This eliminates the need to combine multiple pieces, which is often required in traditional manufacturing processes. As a result, AM can potentially reduce component lead time, cost, material waste, energy consumption, carbon footprint, and the need for post-processing. Although still in its infancy, AM is expected to revolutionize the manufacturing industry. [21–23]

Direct energy deposition (DED) is a subset of AM, where the material feedstock is fed directly into the plasma, laser, or electron beam heat source. Multi-axis manipulators allow for conventional welding techniques like gas metal arc welding (GMAW) [24, 25], and PTAW [26, 27] to be used as an AM process without the need for support structures. Increasing the degrees of freedom (DOF) of these systems can potentially eliminate size limitations for parts produced through additive manufacturing. This technology has sparked interest in various industries, including energy, shipping, and mining, which require large-scale parts. Plasma transferred arc additive manufacturing (PTA-AM) has been used to deposit various steels [26, 28–31], Ti alloys [32, 33], and Ni alloys [34]. During PTA-AM, powder or wire is fed while the welding torch continuously moves along a programmed tool path to construct the part layer by layer. There is limited research on PTA-AM of WC-Ni MMCs [35, 36]. WC-Ni MMC parts made possible by AM's geometrical freedom can replace simple parts that are prone to

severe abrasive wear but cannot be overlaid. This replacement can significantly improve the component's service life and reduce the processing downtime required for part replacements.

The layer-by-layer nature of the PTA-AM process results in the parts being subject to repeated solid and liquid state phase transformations, rapid solidification, and directional cooling. This causes each discrete volume to undergo different thermal cycling, resulting in a different microstructure than the adjacent volume [37]. Thus, many microstructural complexities arise, such as columnar grain growth from directional heat flow, minimal elemental partitioning, reduced grain size, increased solid solubility, metastable phases, and supersaturation of solute in the matrix due to rapid solidification. Furthermore, parts can be subject to mechanical anisotropy that are absent in traditional manufacturing [38]. Post-processing heat treatments can alleviate the non-equilibrium microstructures and thermal stresses formed during thermal cycling [39].

For metal matrix composites, the carbide distribution is an essential factor for understanding the overall microstructure of the MMC, as it plays a significant role in the abrasive wear resistance. Conventional PTA's high heat input leads to the convective mass transfer of W and C from the WC particles [40–42]. Convective mass transfer of W and C reduces the overall WC content and increases the mean free path between particles. Incorporating W and C into the matrix results in the formation of brittle high W-containing intermetallics dispersed throughout the Ni matrix. These intermetallics include Cr_3C_2, Cr_7C_3, Ni_2W_4C, W_2C (β) polymorphs, and α-WC [10, 11, 42, 43]. The reduced WC content, larger mean free path between WC particles, and introduction of brittle intermetallics all contribute to the reduction of the abrasive wear resistance of the metal matrix composite. Understanding how the degree of WC convective mass transfer in PTA-AM deposits changes with differing thermal conditions (i.e. the height of the build) is imperative for optimizing the PTA-AM process for WC-Ni MMCs.

1.2 Thesis Objectives

This thesis aims to understand the effects of MMC composition and solidification rate on the thermal degradation of WC, and the corresponding microstructure of WC-Ni MMCs, deposited using PTA-AM. The thermal degradation of WC is assessed by quantifying the

carbide distribution (carbide volume percent and mean free path), secondary carbide fraction, and analyzing the W content contained in the Ni matrix. For the context of this thesis, the composition of the MMC refers to the carbide content (wt%), the matrix chemical composition, and the carbide type and morphology (angular monocrystalline WC and spherical eutectic WC/W_2C). The main thesis objective is dissociated into the following minor objectives:

1 Establish a method to automate the quantification of carbide volume fraction and mean free path for WC - NiCrBSi MMCs, and determine how carbide percent and mean free path differ at varying heights of a PTA-AM build of 60wt% WC - NiCrBSi. A robust and automated method of measuring carbide volume fraction and mean free path will reduce the processing time required to quantify the carbide distribution of a PTA-AM deposit. Understanding how the carbide distribution changes with height will allow for the PTA-AM deposition process to be optimized to maximize the retention of WC.

2 Determine how increasing the addition of WC from 60 to 70, and 80wt% WC changes the carbide distribution, complex carbide formation, matrix solidification structure, and abrasive wear resistance of WC-Ni MMCs. It is crucial to comprehend the feasibility of augmenting the WC content in PTA-AM deposits and its impact on WC retention and abrasive wear resistance. Moreover, it is essential to comprehend how the WC content amplifies the thermal degradation of WC and how the W content influences the solidification structure of the Ni matrix.

3 Create a correlation between solidification cooling rate, deposition height, amount of thermal degradation of the WC particles, and corresponding microstructure of 70wt% WC - NiBSi MMCs during the PTA-AM process. By understanding how the thermal history affects the degradation of WC, and the microstructure of the MMC modalities to control the heat accumulation, and solidification cooling rate of the PTA-AM deposition process can be implemented to reduce the thermal degradation of the WC particles. This project will establish the boundaries of processing conditions and material compositions that can be utilized with PTA-AM of WC-NiBSi.

4 Determine the effects of adding different ratios of angular monocrystalline WC and spherical eutectic WC/W_2C on the amount of WC thermal degradation and how that changes the resulting microstructure of 70wt% WC - NiCrBSi deposited using PTA-AM. The different morphology of WC/W_2C will offer particle packing that cannot be achieved with

just an angular morphology particle. Additionally, understanding how the degree of thermal degradation of WC/W_2C changes throughout the build will allow for the PTA-AM process to be optimized for WC/W_2C, and achieve carbide distributions that may not be possible in conventional PTA overlays.

1.3 Thesis Structure

This thesis is a blend of research published as journal manuscripts presented as individual chapters, and unpublished work. The information entailed in each chapter is as follows:

- Chapter 2: "Literature Review". The published manuscript is "Large-scale metal additive manufacturing: a holistic review of the state of the art and challenges" published in the journal *International Materials Reviews* as Thomas Lehmann, Dylan Rose, Ehsan Ranjbar, Morteza Ghasri-Khouzani, Mahdi Tavakoli, Hani Henein, Tonya Wolfe, and Ahmed Jawad Qureshi, 2022. My roles in the publication were: conceptualization, investigation, writing - original draft, writing - review and editing, and visualization.
- Chapter 3: “Automated semantic segmentation of NiCrBSi-WC optical microscopy images using convolutional neural networks." Published in the journal *Computational Materials Science* as Dylan Rose, Justin Forth, Hani Henein, Tonya Wolfe, and Ahmed Jawad Qureshi, 2022. My roles in the publication were: Conceptualization, methodology, software, validation, formal analysis, investigation, data curation, writing - original draft, writing - review and editing, and visualization. This chapter addressed thesis objective 1 by creating an automated pipeline to quantify the carbide volume percent and mean free path from WC-Ni optical microscopy images.
- Chapter 4: “Microstructural Characterization and Wear Resistance of 60 and 70wt% WC - NiCrBSi Thin Walls Deposited Using Plasma Transferred Arc Additive Manufacturing.” to be submitted to *JOM* as Dylan Rose, Tonya Wolfe, and Hani Henein, 2023. My roles in the publication were: Conceptualization, methodology, software, validation, formal analysis, investigation, data curation, writing - original draft, writing - review and editing, and visualization. The goal of this chapter is to address thesis objective 2 by changing the WC content from 60wt% to 70 and 80wt% WC in a NiCrBSi matrix.

- Chapter 5: “Microstructural Characterization of 70wt% WC-NiBSi Deposited by PTA-AM”. to be submitted to the journal *Additive Manufacturing* as Dylan Rose, Tonya Wolfe, and Hani Henein, 2023. My roles in the publication were: Conceptualization, methodology, software, validation, formal analysis, investigation, data curation, writing - original draft, writing - review and editing, and visualization. This chapter established a relationship among the cooling rate during solidification, deposition height, degree of thermal degradation experienced by WC particles, and the resulting microstructure of 70wt% WC-NiBSi MMCs produced through the PTA-AM method to satisfy thesis objective 3.

- Chapter 6 "Adding Spherical Eutectic WC/W_2C". This chapter aims to fulfill the fourth (4) objective of the thesis, which involves the incorporation of different quantities of monocrystalline (MC) WC and spherical eutectic (SE) WC/W_2C into a NiCrBSi matrix to achieve a total of 70wt% WC. PTA-AM was used to deposit thin walls of (35wt% MC, 35wt% SE)WC -, (52.5 wt% MC, 17.5wt%SE)WC -, and (17.5 wt% MC, 52.5wt% SE) in a NiCrBSi matrix.

- Chapter 7: “Conclusion and Future Work” summarizes the contributions from this work and provides an outline for future work.

Chapter 2

Literature Review

Published as Lehmann,T; **Rose, D**; Ranjbar, E; Ghasri-Khouzani, M; Tavakoli, M; Henein, H; Wolfe, T; and Qureshi, AJ. *Large-scale metal additive manufacturing: a holistic review of the state of the art and challenges*, International Materials Reviews. Vol. 67(4), 2022. Both Thomas Lehmann, and Dylan Rose contributed equally to this manuscript. The contribution of the following paper to the thesis is to provide a systematic review of the as-built and post-processed microstructures across multiple material systems using the available direct energy deposition modalities. The presented literature review provides evidence of the minimal research that has been conducted on Ni-WC metal matrix composites and highlights the need for an in-depth microstructural analysis of this system under different solidification conditions.

2.1 Abstract

Additive Manufacturing (AM) has the potential to completely reshape the manufacturing space by removing the geometrical constraints of commercial manufacturing and reducing component lead time, especially for large-scale parts. Coupling robotic systems with direct energy deposition (DED) additive manufacturing techniques allow for support-free printing of parts where part sizes are scalable from sub-meter to multi-meter sizes. This paper offers a holistic review of large-scale robotic additive manufacturing, beginning with an introduction to AM, followed by the different DED techniques, the compatible materials, and their typical

as-built microstructures. Next, the multitude of robotic build platforms that extend the deposition from the standard 2.5 degrees of freedom (DOF) to 6 and 8 DOF are discussed. With this context, the decomposition and slicing of the computerized model will be described, and the challenges of planning the deposition trajectory with be discussed. The different modalities to monitor and control the deposition in an attempt to meet the geometrical and performance specifications are outlined and discussed. A wide range of metals and alloys have been reported and evaluated for large-scale AM parts. These include steels, Ti, Al, Mg, Cu, Ni, Co-Cr, and W alloys. Different post-processing steps, including heat treatments, are discussed, along with their microstructures. The paper finally addresses the authors' perspective on the future of the field and the largest knowledge gaps that need to be filled before the commercial implementation of robotic AM.

2.2 Introduction

Additive Manufacturing (AM), also known as 3D printing, uses computer-aided design (CAD) to build objects layer by layer [44]. This contrasts a significant portion of traditional manufacturing, which uses casting, sintering, or removing unwanted material from an ingot using machining [21]. AM is still in its infancy, but the projected possibilities will drastically change the manufacturing space. One of the proven advantages of AM compared to conventional manufacturing is the lack of shape constraints on components. This allows for complex geometries to be constructed, where conventional manufacturing would require the joining of multiple pieces to create the same part [22]. Geometrical freedom has the potential to reduce component lead time, cost (fabrication of cast not needed, lower energy consumption, material cost), material waste, energy usage, carbon footprint, and drastically reduce the need for post-processing [23].

The industrial applications of AM range from aerospace to the energy sector to healthcare. The ultimate goal is to have on-site access to this technology, eliminating the need for stockpiles of replacement parts. Although AM research is currently also conducted in the construction sector [45], the focus of this paper is on metal AM. According to ISO standard 17296-2, 7 process categories currently exist, including vat photopolymerization, material jetting, binder jetting, powder bed fusion, material extrusion, direct energy deposition, and sheet lamination [46]. A large portion of the research and commercial development of metal

AM systems has been on powder bed fusion (PBF) [47–49]. In these machines, a laser is scanned over a fine layer of powder, fusing it together. The build substrate drops down according to the layer thickness, and the powder is redistributed using a roller or scraper, and the laser fuses the newly distributed powder to the previously deposited material. This process repeats until the part is complete. These platforms are intrinsically limited to 2.5 Degrees of Freedom (DOF), where each layer is printed on a 2-dimensional plane [50, 51]. A limitation of 2.5 DOF is the need for support structures on overhanging features of more than 30-40°, where 0° is perpendicular to the build plate. It should be noted that the degree of overhang before manufacturing defects begin to form is a function of the thermophysical properties of the molten material being printed [52–55]. This introduces complex designing, planning, and post-processing to remove the supports, adding significant material cost due to added support material (waste material) and labour cost caused by the required removal of the support material.

There is garnering interest in expanding the DOF of AM systems to allow for the manipulation of the part in-situ.. This would eliminate the need for support structures [56–59]. The increase in DOF is achieved via the integration of robotic manipulators and positioners (see Figure 2.1). The manipulators can then house various direct energy deposition (DED) modalities such as: gas metal arc welding (GMAW), gas tungsten arc welding (GTAW), laser-based direct energy deposition (LDED), and plasma arc transfer welding(PTAW), enabling multi-directional deposition [24, 25, 60, 61]. A depiction of this is shown in Figure 2.1, where the part's orientation has changed to compensate for the overhanging angle. Combining these systems can theoretically eliminate the size restrictions of the parts that can be built using AM. This sparks considerable interest from not only the energy sector but shipping, mining, and any industry that requires large-scale parts. The complexity of these parts is not due to stringent geometrical tolerances but is restricted by the sheer size of the components [62]. One rendition of this is the combination of additive and subtractive manufacturing, which takes the free formability of AM and combines it with the surface finish capabilities of machining. This is known as hybrid manufacturing [63, 64]. Researchers have been developing path planning programs for these types of systems, but the combination of the two processes drastically increases cost compared to pure AM processes because of longer fabrication times, and would not be suitable for large scale applications in the current state [65–71].

The current objective of large-scale additive manufacturing is to use 7- and 8-axis robotic

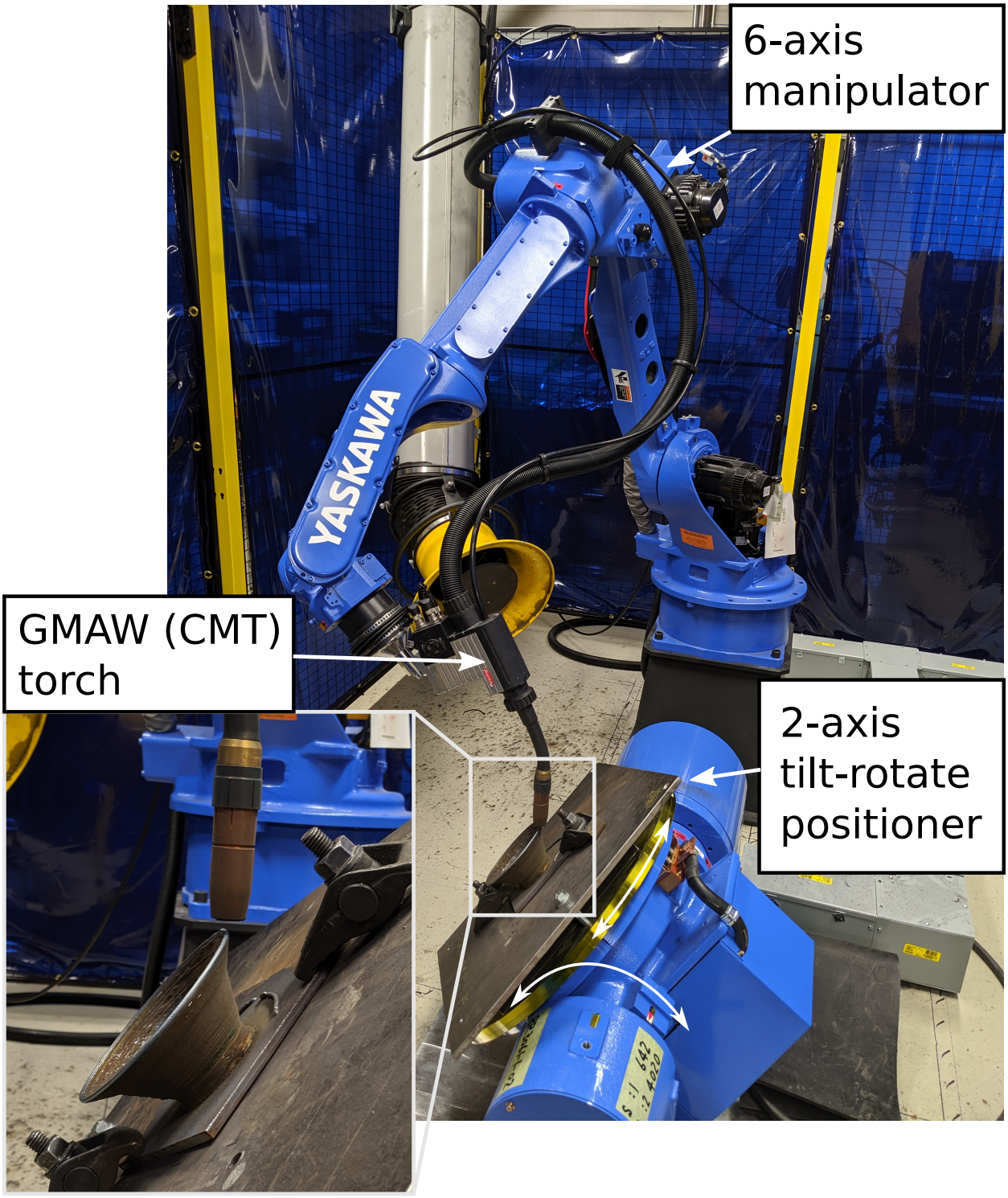

FIGURE 2.1: An example of a large-scale robotic AM fabrication platform using a wire and arc welding system for metal deposition.

serial manipulator systems, and in-situ monitoring and control systems, to eliminate the need for subtractive measures and supporting structures [56, 58, 74–77]. The different technologies to achieve this have been implemented in various other applications but have not yet been integrated into a holistic process. Various companies have implemented commercial large-scale robotic AM, including: Relativity Space [78], MX3D [79], MER corporation, AML3D [80], and AMFG [81]. Two examples of large-scale components fabricated via robotic AM are shown in Figure 2.2. However, their methodologies have not been published and will not be considered in this work.

With the increase in commercialization of additive manufacturing systems, and the implementation of additively manufactured parts into various industrial applications, it is critical to developing standards to qualify and certify the entirety of the process, from feedstock to finished part. This ensures the same repeatable quality and performance of additive manufactured parts, as those seen in the commercial manufacturing space. Furthermore, it is important that the development of these systems conform to the strict environmental, health, and safety regulations currently in place. As engineers, it is imperative that the

A B

FIGURE 2.2: Examples of companies adopting the large-scale robotic AM technology with (a) a rocket nozzle fabricated by Relativity Space, Inc. [72] and (b) a component of a serial manipulator fabricated by MX3D [73].

safety of the public is the top priority. The codes and standards pertaining to the qualification and certification of DED AM are shown in Table 2.1. It should be noted that many of these standards are still under development, highlighting the challenges the various standard committees have with developing strict qualifications for DED AM.

This paper aims to identify the state-of-the-art technologies and how they relate to large-scale additive manufacturing and the interdisciplinary engineering challenges that this process encompasses. For this work, large-scale AM constitutes the ability to fabricate a part with a volume of 1 m^3. The current state of research highlights the lack of collaboration between engineering disciplines and the connections that lie between different research bodies. The majority of other published literature reviews only review a sub-set of the various research bodies and sub-topics of large-scale robotic AM, whereas this work reviews these independent research findings and attempts to highlight the relationships between them. Most of the research discussed herein encompasses laboratory-scale coupons and not specifically large-scale parts. However, it is speculated that many of the contributions made will be transferable beyond the lab.

The structure of this paper is as follows. The first sections will discuss the various DED technologies to provide context to the complexity of the manufacturing systems. This will transition to the different stages of the AM workflow, shown in Figure 2.3, where stage 1 is pre-process planning, stage 2 is printing/deposition, and stage 3 is post-processing. Stage 1 encompasses the decomposition of the part into sub-volumes, the cross-sectional slicing of said subvolumes, and the conversion of the sliced layers to a tool path and deposition strategy based on the deposition system being used. Although not directly addressed by the publications, the thermo-physical properties, and the thermal properties will dictate the optimal deposition strategy to reduce residual stresses, deposition defects, and microstructural anisotropy. This will vary depending on the material being deposited. Stage 2 corresponds to the monitoring and control of the deposition and extracting the valuable information from the various sensors, which are used to adjust the operating parameters of the system in-situ. The development of this stage is critical to automating large-scale AM, making it commercially viable for on-site manufacturing by non-specialized personnel and potentially eliminating the need for stage 3. An important consideration is optimizing the thermal cycles to achieve the microstructure and corresponding mechanical properties required for the parts application. Stage 3 deals with the post-processing required for the part to meet metallurgical, geometrical, and performance specifications required for in-service use. Each

TABLE 2.1: Some of the existing and under development codes and standards pertaining to additive manufacturing. It should be noted that this is not an exhaustive list, but provides insight on the magnitude and breadth of standards being developed for DED AM.

Identifier	Description
ISO 17296-(1-4)	Additive manufacturing – General principles (Active standard)
ISO/ASTM 52901:2017	Additive manufacturing – General principles – Requirements for purchased AM parts (active standard)
ISO/ASTM 52907:2019	Additive manufacturing – Feedstock materials – Methods to characterize metal powders (active standard)
ISO/ASTM 52902 - 19	Additive manufacturing – Test artifacts – Geometric capability assessment of additive manufacturing systems (active standard)
ASTM F3413 - 19	Guide for Additive Manufacturing – Design – Directed Energy Deposition (active standard)
ASTM F3049 - 14	Standard Guide for Characterizing Properties of Metal Powders Used for Additive Manufacturing Processes (active standard)
ASTM F3187 - 16	Standard Guide for Directed Energy Deposition of Metals (active standard)
AMS7027	Electron Beam Directed Energy Deposition-Wire Additive Manufacturing Process (EB-DED-Wire) (active standard)
AMS7010	Wire Fed Laser Directed Energy Deposition Additive Manufacturing Process (L-DED-wire) (active standard)
AMS7005	Wire Fed Plasma Arc Directed Energy Deposition Additive Manufacturing Process (active standard)
AMS7004	Titanium Alloy Preforms from Plasma Arc Directed Energy Deposition Additive Manufacturing on Substrate Ti-6Al-4V Stress Relieved (active standard)
ASTM F3187-16	Standard Guide for Directed Energy Deposition of Metals, 2016 (active standard)
ASTM WK69730	New Specification for Additive Manufacturing – Wire for Directed Energy Deposition (DED) Processes in Additive Manufacturing (under development)
ISO/ASTM AWI TR 52905	Additive manufacturing of metals – Non-destructive testing and evaluation – Defect detection in parts (under development)
ISO/ASTM CD 52926-4	Additive manufacturing of metals – Qualification principles – Part 4: Qualification of machine operators for DED-LB (under development)
ISO/ASTM CD 52926-5	Additive manufacturing of metals – Qualification principles – Part 5: Qualification of machine operators for DED-Arc (under development)
AMS7037	Steel, Corrosion and Heat-Resistant, Powder for Additive Manufacturing 17Cr - 13Ni - 2.5Mo (316L) (under development)

stage corresponds to separate chronological sections of this paper, where each constituent of that stage and its current state in regards to large-scale additive manufacturing will be discussed. The paper will conclude with the author's perspectives on the challenges that must be overcome to make large-scale AM a commercially viable manufacturing option.

2.3 Metal deposition technologies

The main metal deposition technologies found in large-scale AM are: Gas Metal Arc Welding (GMAW), Gas Tungsten Arc Welding (GTAW), Plasma Transferred Arc Welding (PTAW), and Laser-based direct energy deposition (LDED). A detailed illustration of these deposition technologies can be seen in Figure 2.4. These systems are most readily used due to the ease of integration with the current multi-axis systems or have previously been used on robotic systems in industries such as automotive manufacturing. One advantageous characteristic with these modalities is higher heat inputs, which enables higher deposition rates, accelerating the printing process. This is an essential factor for large-scale AM to reduce the lead time for part production. However, one caveat to higher heat input is higher thermal stresses and heat accumulation, resulting in large amounts of material undergoing complex thermal cycling and anisotropic microstructures [82–84]. Furthermore, the material feedstock for DED is typically wire, or powder-based, which offers the ability to alter both deposition rate and composition based on the mechanical specifications of that localized area [85–87]. Changing the composition could range from going from one material to another or changing the volume loading of reinforcement particles in a metal matrix composite. This functional gradient could allow for customized spatial mechanical properties of areas that require them while also reducing the material cost of manufacturing. In this section, the following technologies will be discussed: GMAW, PTAW, and LDED. This will include the fundamentals of the operation and the mechanisms of deposition. This will be followed by the common material feedstocks and the as-deposited microstructures that are typically found. The range of processing parameters for each deposition technology based on whether the feedstock is powder (Table 2.2) or wire (Table 2.3 and Table 2.4). The values listed in the tables are the minima and maxima for each parameter recorded in the literature. Additionally, authors whose parameters fall within the range are given. It should be noted that lamination AM and cold-spray AM are also capable of creating large-scale parts. Lamination AM is currently not compatible with multi-axis robotic systems, eliminating it from consideration.

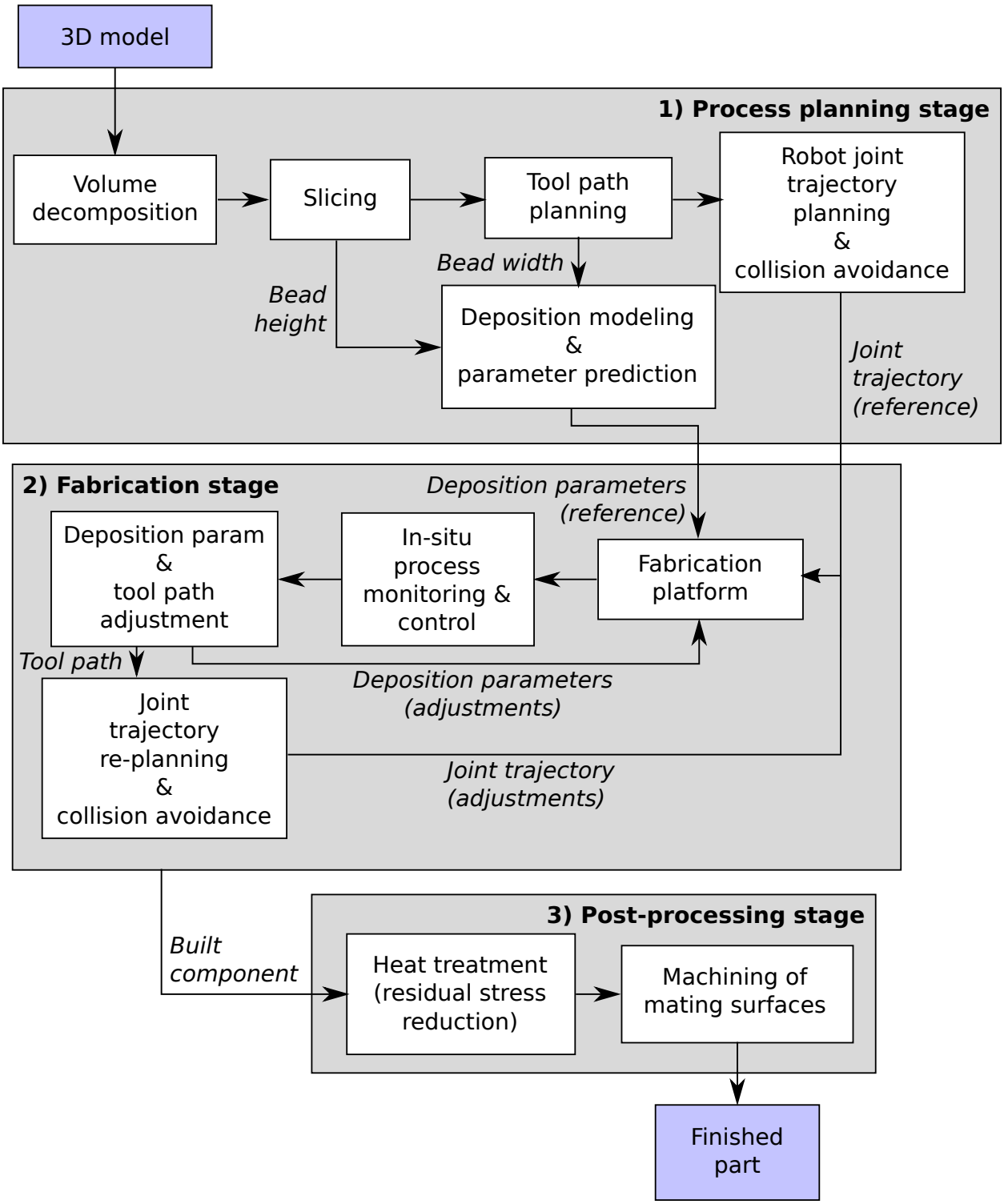

FIGURE 2.3: The robotic large-scale metal AM process workflow.

TABLE 2.2: A listing of various powder fed deposition technologies and associated parameter based on the material being deposited. The values listed provide the maximum and minimum for each parameter and the authors who's parameters fall within those ranges.

Process	Material	Travel Speed (mm/s)	Heat Input (W)	Spot Size (mm)	Layer height (mm)	Material feed rate (g/min)
laser DED	Steels	2.5 [91] - 20 [92] Within range: [91, 93–97]	360 [96] - 2600 [92] Within range: [93–95, 97]	1.2 [97] - 2 [92]	0.25 [96] - 0.5 [97]	2 [97] - 20.4 [91] Within range: [91–95]
	Ti-6Al-4V	2 [98] - 17 [99] Within range: [100–108]	330 [106] - 7000 [102] Within range: [98–101, 103–105, 107, 108]	0.3 [106] - 8.6 [103] Within range: [98, 100–102, 105, 107, 108]	0.3 [98] - 3 [102] Within range: [99, 103, 104]	1 [101] - 59 [108] Within range: [98–107]
	Aluminium	6 [109] - 16 [110] Within range: [111–115]	120 [113] - 3600 [109] Within range: [110–112, 114, 115]	0.6 [114] - 3.5 [109] Within range: [112]	0.5 [109]	0.66 [113] - 23.2 [112] Within range: [111, 114, 115]
	Nickel (Inconel 625)	6.7 [116] - 25 [117] Within range: [118]	1500 [118] - 3000 [116] Within range: [117]	0.4 [118] - 3 [116] Within range: [117]		6 [116] - 33.3 [117] Within range: [118]
	Nickel (Inconel 718)	2 [119] - 26.6 [120] Within range: [107, 117, 121–125]	250 [119] - 4000 [120] Within range: [107, 117, 121–125]	0.8 [121] - 5 [120] Within range: [107, 117, 122, 123]	0.1 [119] - 0.5 [121]	1.2 [107] - 36.6 [120] Within range: [117, 122–125]
	Co-Cr	5.5 [126] - 20 [127] Within range: [128, 129]	200 [128] - 410 [126] Within range: [127, 129]	0.25 [129] - 0.7 [128]	0.25 [128] - 0.5 [126]	0.57 [129] - 5 [127] Within range: [128]
	W	2 [15] - 5 [130]	200 [15] - 2000 [130]	0.6 [15] - 3 [130]	0.8 - 0.9 [15]	7 [15] - 8 [130]
PTA	Steels	1.3 - 1.7 [30]				25 - 35 [30]
	NiCrBSi	10 [35]	1100 [35]	4.7 [35]	0.75 [35]	20 [35]

Cold-spray AM is compatible with robotic systems but lacks the ability to create complex parts without special equipment, and significant post-processing [88–90]. Thus, it was not considered in this work.

2.3.1 Gas metal/tungsten arc welding

In gas metal arc welding, an arc is struck between a substrate and a consumable wire electrode that is fed through the welding torch, where it is melted and deposited onto the substrate. The molten material is protected from moisture and oxidation through the use

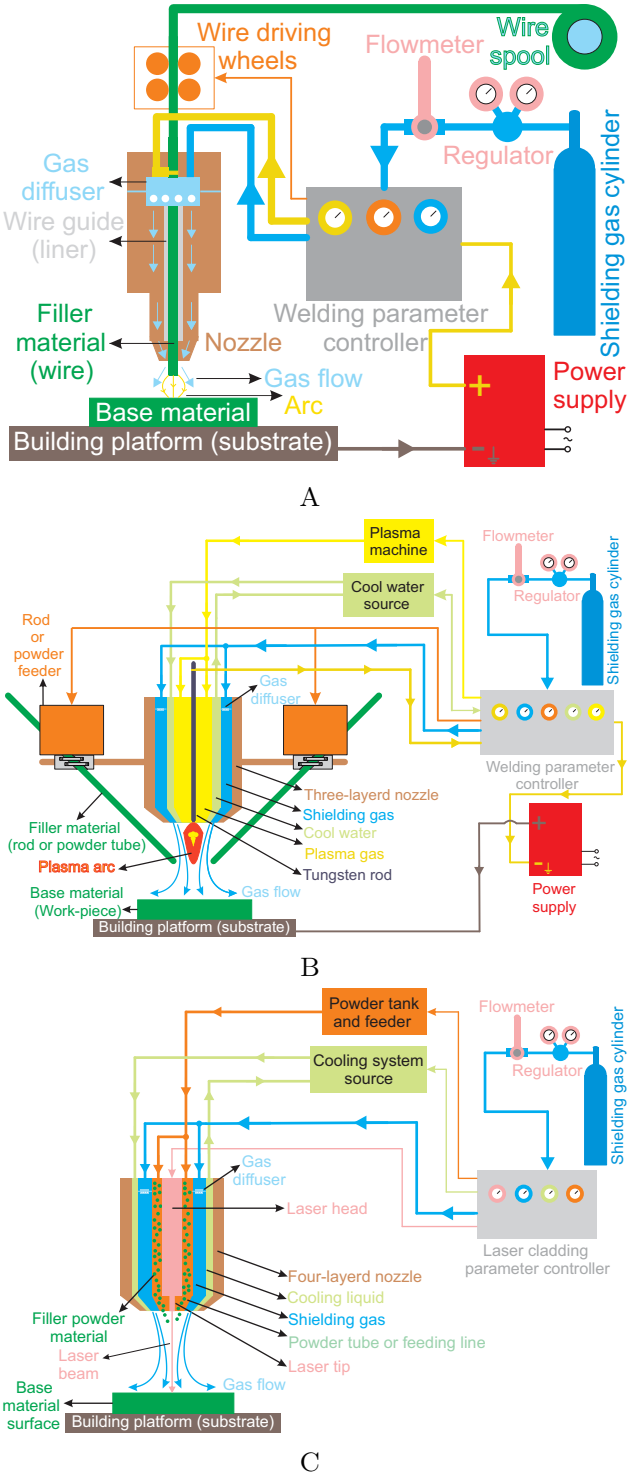

FIGURE 2.4: Various AM DED technologies; (A) GMAW, (B) PTAW, and (C) LDED.

TABLE 2.3: A listing of various wire fed deposition technologies and associated parameter based on the material being deposited. The values listed provide the maximum and minimum for each parameter and the authors who's parameters fall within those ranges.

Process	Material	Travel Speed (mm/s)	Heat Input (W)	Spot Size (mm)	Layer height (mm)	Wire feed Speed (mm/s)
laser DED	Ti-6Al-4V	1.4 [131] - 10 [132] Within range: [133, 134]	1000 [134] - 3500 [132] Within range: [131, 133]	2.5 [131] - 5 [132] Within range: [133]	1 [132] - 1.28 [133]	30 [133] - 40 [132]
	Nickel (Inconel 718)		5000 [135]	1 [135]		
GMAW	Steels	2.5 [136] - 30 [137] Within range: [138–145]	3500 [146] - 8400 [147]		0.5 - 2 [137]	28 [139] - 166 [147] Within range: [136–139, 141–145]
	Ti-6Al-4V	1.5 [148] - 9.4 [149] Within range: [150–152]	1430 [148] - 12500 [151] Within range: [149]	6 [150] - 10 [148]	14 - 16 [148]	7.2 [148] - 142 [149] Within range: [151]
	Aluminium	6.13 [153] - 22 [154] Within range: [155]	3360 - 7360 [154]			100 [153] - 250 [154] Within range: [155]
	Nickel (Inconel 718)	6 [156] - 10 [157] Within range: 6.5 [158]		12.8 [157]	1.7 [157] - 2.8 [156]	10 [157] - 116.6 [156] Within range: 33.3 [158]
	Nickel (Inconel 625)	6.3 [159] - 10 [160]	2160 [160]			108 [160]
	Magnesium	3.3 - 16.6 [161] Within range: [162, 163]	400 - 1400 [161] Within range: 541 - 857 [162]	5 [162]	3 [162]	30 [162] - 200 [163]
	Copper alloys	6.6 [164] - 8.3 [165]	4620 [165] - 7424 [164]			117 [165]
	Co-Cr	2.1 [166]	1454 [166]		3.5 [166]	75 [166]
GTAW	Steels	2.92 [167] - 7 [168] Within range: [169]	1920 [169]			16.67 [167] - 58 [168] Within range: [169]
	Ti-6Al-4V	0.27 [170] - 6.7 [171] Within range: [132, 168, 172–174]	1320 [173] - 2200 [132]	5 [171] - 9.1 [132] Within range: [172, 173]	1 [132]	10 [171] - 128 [171] Within range: [132, 148, 168, 170, 172–174]
	Aluminum	3.3 [175] - 100 [176]				17 [175] - 160 [176]
	Nickel (Inconel 718)	5 [177]		10 [177] -16 [178]		25 [177]
	Magnesium	3.3 [179] - 5 [180, 181]			1.25 - 2.5 [179]	19.2 [180, 181] - 33.3 [179]
	Copper Alloys	1.6 [182]				21.6 [182]
	Co-Cr				1.1 [183]	16.6 [183]
	W	2 [184]				35 [184]

TABLE 2.4: A listing of various wire fed deposition technologies and associated parameter based on the material being deposited. The values listed provide the maximum and minimum for each parameter and the authors who's parameters fall within those ranges.

Process	Material	Travel Speed (mm/s)	Heat Input (W)	Spot Size (mm)	Layer height (mm)	Wire feed Speed (mm/s)
PTA	Steels	0.6 [185] - 2 [186]	350 [185] - 3510 [187]			9 [186] - 28 [185]
	Ti-6Al-4V	4 [32, 33]	2700 - 5400 [33]		1.5 [32, 33]	58 [32, 33]
	Nickel (Inconel 625)	21.6 [34]			1.2 [34]	3 [34]
EB	Ti-6Al-4V	2.4 [188] - 18 [188] Within range: [189–199]	690 [195] - 8500 [199] Within range: [188–194, 196–198]	1.2 [189]	1 [200]	14 [193] - 141 [188] Within range: [189, 192, 194, 196–198]
	Inconel 718	5 [201]	600 - 960 [201]			5.4 [201]

of shielding gases, which are typically a combination of inert (Ar) and active (CO_2). The shielding gas varies things like the stability of the arc, metal transfer, and penetration of the weld and is tailored to the material being deposited. The wire is continuously fed as the welding torch is translated in the geometry of the weld or AM part. The consumable electrode is either a solid wire or a cored wire, with a powdered interior in various ferrous and non-ferrous compositions. The current is directly proportional to the deposition rate but inversely proportional to the electrode extension, which is the distance between the end of the wire guide and the tip of the electrode, shown in Figure 2.4A. The arc voltage is a means of electrically quantifying the physical length of the arc and can be affected by many factors, including: electrode composition and size, shielding gas composition, electrode extension, and the length of the welding cable [202]. The deposition rate for GMAW in terms of AM is material dependent, but is in the range of 15-160 g/min [164, 203, 204].

Three traditional transfer modes are commonly used with the GMAW process, which are: spray, globular, and short circuiting [205]. Cold metal transfer (CMT) is a modified subsidiary of short circuiting, where the mechanical movement of the wire electrode is synchronized with the electrical control parameters [149]. Instead of increasing the current during the short circuit phase, the current is dropped, extinguishing the arc and limiting the amount of thermal energy transferred to the deposit [206]. The electrode is then retracted, pinching the molten material, depositing it into the melt pool. The current is then increased to reignite the arc, and the process repeats [207]. The decrease in thermal energy transfer reduces the heat accumulation in multi-layer deposits, which can be characterized by the finer grain structures when compared to continuous welding techniques [149, 208]. This can be

seen in Figure 2.5 [209], where the lower heat input and heat accumulation is characterized by the finer grain structure. Furthermore, the pulsing of the arc has been shown to sever dendrite arms, increasing the heterogeneous nucleation sites, further refining the microstructure [153, 170]. It also drastically reduces the dilution of previously deposited material, reducing the amount of material being melted with each pass and possibly reducing the number of thermal cycles [207, 210]. Thus, these reasons make CMT the most viable option for wire and arc additive manufacturing (WAAM). It should be noted that although there is a reduction in heat input and thermal cycles compared to continuous welding, WAAM deposits still suffer from heat accumulation, cracking, porosity, delamination, and anisotropic microstructures. [211] The first study of using GMAW for AM was conducted by Dickens *et al.*, who tried to expand the realm of 3D welding from large pressure vessels, to more complex geometries [212].

Gas Tungsten Arc Welding is similar to the GMAW process, but the arc is struck between a non-consumable tungsten electrode and the workpiece. A filler metal can be fed manually or mechanically into the arc, where it melts and is deposited onto the substrate. Multiple filler metals can be fed simultaneously to increase the deposition rate and allow for the customization of the material being deposited. Inert shielding gasses (typically Ar or He) protect the melt from oxidation while also affecting weld bead geometry. The polarity of the system can be altered from DC to AC if the material being deposited is prone to forming passive films [213]. The microstructure and mechanical properties of AM deposits are highly dependent on the material feeding orientation [214, 215]. Some of the materials that have been deposited include: TiAl [216], Fe-FeAl functionally graded material [217], FeAl [218], Ti64 [132, 171, 219, 220], Al [221], and Ni alloys [222].

GMAW and GTAW offer a cost-effective means of AM, with techniques that are already common industrial practice. The ease of integration with robotic control and gantry systems, coupled with the high deposition rates, makes these technologies enticing for large-scale additive manufacturing [223]. However, some complications reside when using a welding heat source for AM. Distortion and residual stresses are common side effects of the concentrated heat flux generated from an arc [224]. Inconsistent bead geometries can lead to poor surface finish, and dimensional accuracy [225]. Research has predominately been on GMAW, which is speculated to be due to the added complexity of integrating a wire feeding system with the robotic system. Ensuring the feeding angle is constant during deposition would increase the difficulty of path planning and building strategies. The continuous heat input experienced

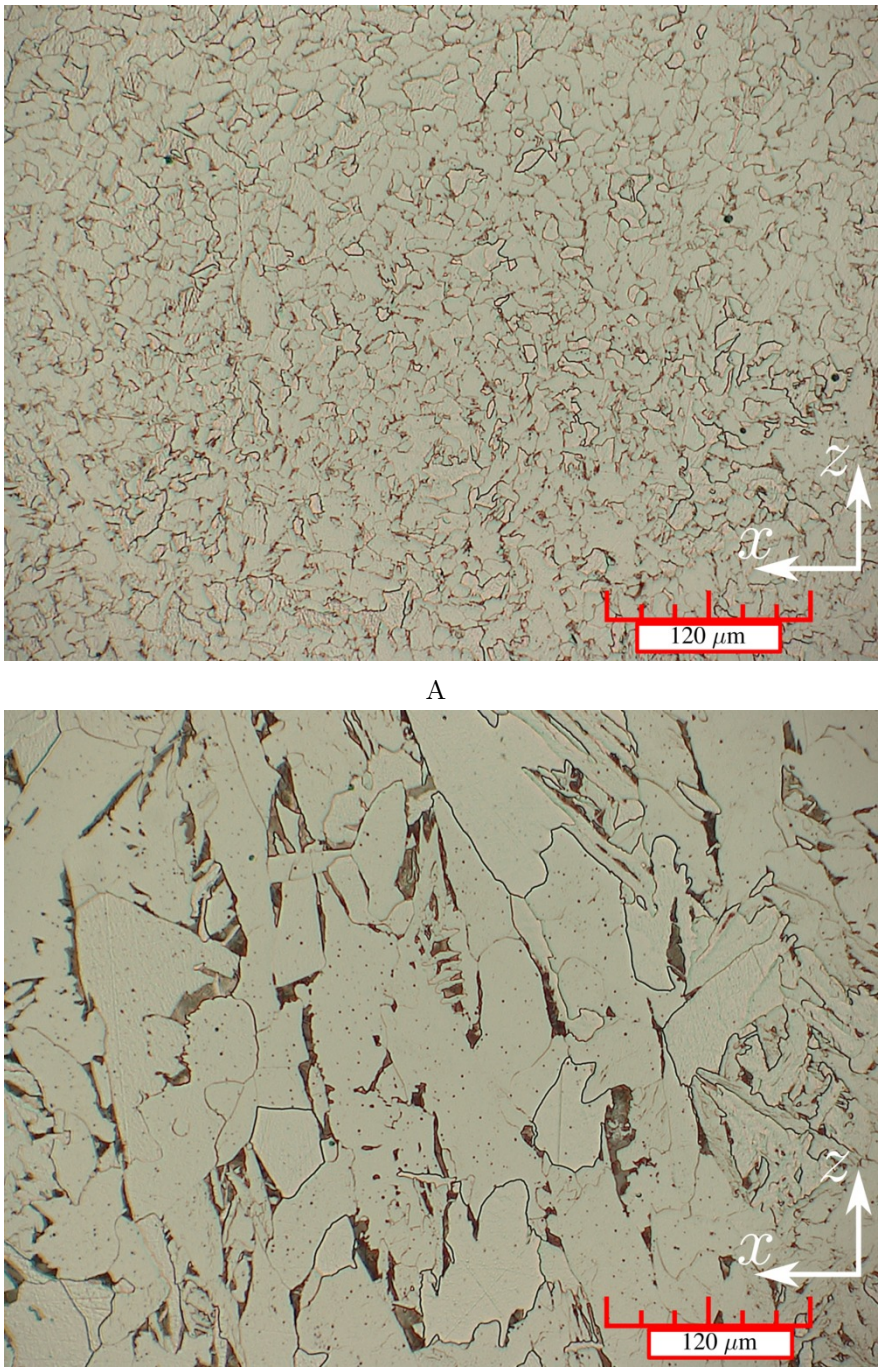

FIGURE 2.5: Microstructure variations from the WAAM deposition of AWS ER70S-6 where A shows the finer grain structure of a deposit with low heat input and low amounts of heat accumulation, and B show the grain structure with high heat input and large amount of heat accumulation [209].

during GTAW could cause increased heat accumulation, resulting in manufacturing defects such as the slumping of different features. Furthermore, GMAW's ability to easily strike and extinguish an arc increase the thermal control during the build by extinguishing the arc after each pass to allow for the part to cool. The tungsten electrode in GTAW also requires frequent sharpening to maintain arc characteristics, decreasing the production rate of large-scale parts.

2.3.2 Plasma Transferred Arc

Plasma transferred arc utilizes a non-consumable tungsten electrode, similar to that seen in GTAW; however, there are some stark differences between the processes as can be viewed in Figure 2.4B. Generally, there are two inert gas inlets: the plasma and shielding gas. The gasses used in this process (such as Ar) are chosen due to their low ionization potential, making it easier to strike an arc between the electrode and the substrate. The flow of the plasma gas allows the arc to be self-sustaining, while the shielding gas protects the melt from the surrounding environment [11]. The plasma is constricted by a nozzle, changing the arc shape from the traditional bell shape to columnar, increasing the energy density [226]. The feeding material can either be wire, or powdered materials, allowing for a large degree of compositions and functionally graded parts. The deposition rate is the highest of the welding techniques are 33-166g/min [11]. Some of the materials that are being explored with PTA for additive manufacturing are: Ni alloys [26, 227–229], Ni-WC [35], Ti [28], functionally graded Fe-Ni [230, 231], and stainless steel alloys [29, 232].

2.3.3 Laser-based direct energy deposition

Laser-based DED techniques share the basic principles with the aforementioned plasma-based methods, where the main difference lies in the energy source. For laser systems, a series of lenses are used to focus a laser beam to melt the desired material [233]. The laser source can vary depending on the particular application. CO_2 lasers are better suited for low precision, simpler geometries, where an Nd-YAG laser is better suited for finer, complex geometries [234]. The feed material for laser DED can be powder, wire, or a combination of the two, depending on the application. A schematic of a typical laser system is shown in Figure 2.4C. The deposition rate can be up to 25 g/min with varying deposition efficiencies

depending on the components geometry [235]. Both heat sources share a Gaussian energy distribution, with the highest temperatures in the center of the melt. However, the heat flux provided by a laser source is upwards of 1kW/mm^2 with a 2mm diameter spot size [236–238], while a plasma provides upwards of 60W/mm^2 over 16mm diameter spot size [11, 239]. Another critical distinction is the safety precautions that workers must abide by during laser DED. To strike an arc, the workpiece must be electrically grounded and can only be sustained within a certain stand-off distance. Commercial lasers do not have any of these pre-requisites, meaning they can theoretically be directed at any surface. Additionally, a laser can be reflected by certain metallic surfaces that can damage facilities or personnel. Thus, proper control measures must be implemented to ensure the safety of anyone working with this equipment.

2.3.4 Materials

In all AM techniques, the feedstock metals can be in the form of wire or micron-size powder. Powder metals are typically much more expensive than their wire counterparts, but offers material compositions that are not able to be drawn into a wire. An example of this are higher reinforcement loaded MMC's and intermetallics, where the inherent brittle nature of these materials make it un-suitable for wire applications [240]. However, the deposition efficiency of wire fed systems are beyond what is possible with powder [241]. Moreover, storage of metal powders requires significantly more safety precaution than that of metal wires and the higher surface area to volume ratio makes them more susceptible to oxidation [242]. The quality of the feedstock is of utmost importance, as porosity in the feedstock stock powders has been shown to drastically increase the porosity of the printed part[30]. Poor surface quality and diameter variances of wire feedstock can trap moisture and hydrocarbon residue during the deposition process, resulting in porosity in the final deposit [243–246]. This section of the report will outline the common materials and the as-built microstructures found in the above mentioned AM techniques, as shown in Table 2.2 and Table 2.3. The variation in mechanical properties of AM deposits will be compared to conventional manufacturing where applicable, and the microstructural justification for differences will be discussed. The order of materials is as follows: first steels will be discussed, followed by titanium, aluminum, nickel, magnesium, copper, cobalt-chrome, and tungsten alloys. It should be noted that there has been work done on energetic materials, typically in the form of metal-polymer composites.

However, the printing modalities for these materials are currently limited to those suited for polymer materials and were deemed out of the scope of this paper. The topics discussed in Section 2.4 and Section 2.5 can be applied to the deposition of energetic materials, specifically those that utilize a deposition nozzle like direct writing, fused deposition modelling and photopolymerization [247].

2.3.4.1 Steels

Steels are extensively used in various industrial sectors due to their high strength, good toughness, and low cost. There has been extensive work on the AM of steels, especially with WAAM. Some honourable mentions include: ER70S-6 [136, 138, 139, 248], 304 SS [136, 137, 167, 249], 308L SS [140, 141, 168, 186], and AISI 420 SS [142].

In the case of 316L austenitic stainless steel, LDED fabricated parts were reported to exhibit a higher hardness, yield stress, and tensile strength with lower elongation than their wrought counterparts [94]. These differences in mechanical properties were attributed to the finer cellular arm spacing of the LDED manufactured steel compared with the wrought one [94]. The grain structure of LDED fabricated 316L stainless steel is highly dependent on process parameters, where grains become coarser by increasing power density and decreasing scan speed [91]. The 316L stainless steel fabricated by GMAW-AM was reported to have greater hardness and UTS, but a lower elongation than the wrought steel [143]. Microstructure and mechanical properties of the GMAW-AM fabricated 316L stainless steel depend on arc mode. A finer grain size (and consequently a higher strength and hardness) is achieved when spray transfer mode is replaced with short-circuiting transfer mode [143]. This is explained by the lower heat input of the short-circuiting than the spray transfer more, which leads to a faster cooling rate [143].

Another common steel grade in AM is 17-4 PH martensitic stainless steel. However, the majority of the work has been on powder bed methods [250–255], as opposed to DED [30, 92, 144, 204, 256, 257]. High cooling rates associated with the selected AM processes limit transformation of δ-ferrite to γ-austenite at high temperatures so that some amounts of δ-ferrite remain at room temperature. AM fabricated 17-4 PH stainless steels commonly exhibit a dendritic microstructure with interdendritic δ-ferrite in a lath martensitic matrix

[92, 144, 204]. It has been shown that proper shielding must be implemented with PTA-AM of 17-4 to prevent interlayer oxidation during fabrication[30]. Caballero *et al.* [144] fabricated 17-4 PH stainless steel from a wire feedstock using a GMAW-AM technique. They reported that decreasing the heat input to the system increased the solidification rate and subsequently the amount of retained austenite in the as-built microstructure. Moreover, the as-built parts had lower yield stress and UTS than wrought 17-4 PH stainless steel. However, exposure to a solution and aging heat treatment increased their yield stress and UTS significantly to be comparable with those of the wrought alloy [144]. Adeyemi *et al.* [92] investigated the influence of laser power on the microstructure of LDED fabricated 17-4 PH stainless steel. They observed a coarse microstructure at a high laser power due to high laser intensity and consequently slower cooling rate [92]. In another study, Martina *et al.* [204] fabricated walls from 17-4 PH stainless steel wires using a GMAW-AM technique, a tandem torch. They reported a drop in strength and hardness of the deposited walls with an increase in wire feed speed, which was attributed to an increase in grain size [204].

Anisotropy of both microstructure and mechanical properties is significant in DED fabricated steel parts. The microstructural grains and dendrites are preferentially oriented along the build direction with the highest thermal gradient [95]. Thus, for the vertical orientation parts in which the build direction is parallel to the deformation direction, fewer grain boundaries exist compared to the horizontal orientation parts in which the tensile direction is perpendicular to the build direction. Since grain boundaries act as barriers to dislocation motion during the deformation, less dislocation accumulation occurs in the vertical orientation parts than horizontal orientation parts. Consequently, the vertical orientation parts exhibit a lower tensile strength but a higher elongation than the horizontal orientation parts. This anisotropy of the mechanical properties has been reported for the LDED fabricated 304L stainless steel [96], WAAM fabricated 304L stainless steel [167] LDED fabricated 316L stainless steels [95–97], WAAM fabricated 316L stainless steel [145], WAAM fabricated H13 tool steel [146], and WAAM fabricated 17-4 PH stainless steel [144].

For example, the influence of part orientation on the tensile behavior of WAAM fabricated 304L stainless steel is depicted in Figure 2.6 [167]. The vertical orientation parts (L1, L2, and L3) exhibited an average yield stress, UTS, and elongation of 231 MPa, 622 MPa, and 88.1%, respectively [167]. Horizontal orientation parts (T1, T2, and T3), however, were reported to have an average yield stress, UTS, and elongation of 235 MPa, 678 MPa, and 55.6%, respectively [167]. For most industrial applications, fabricated parts need to exhibit

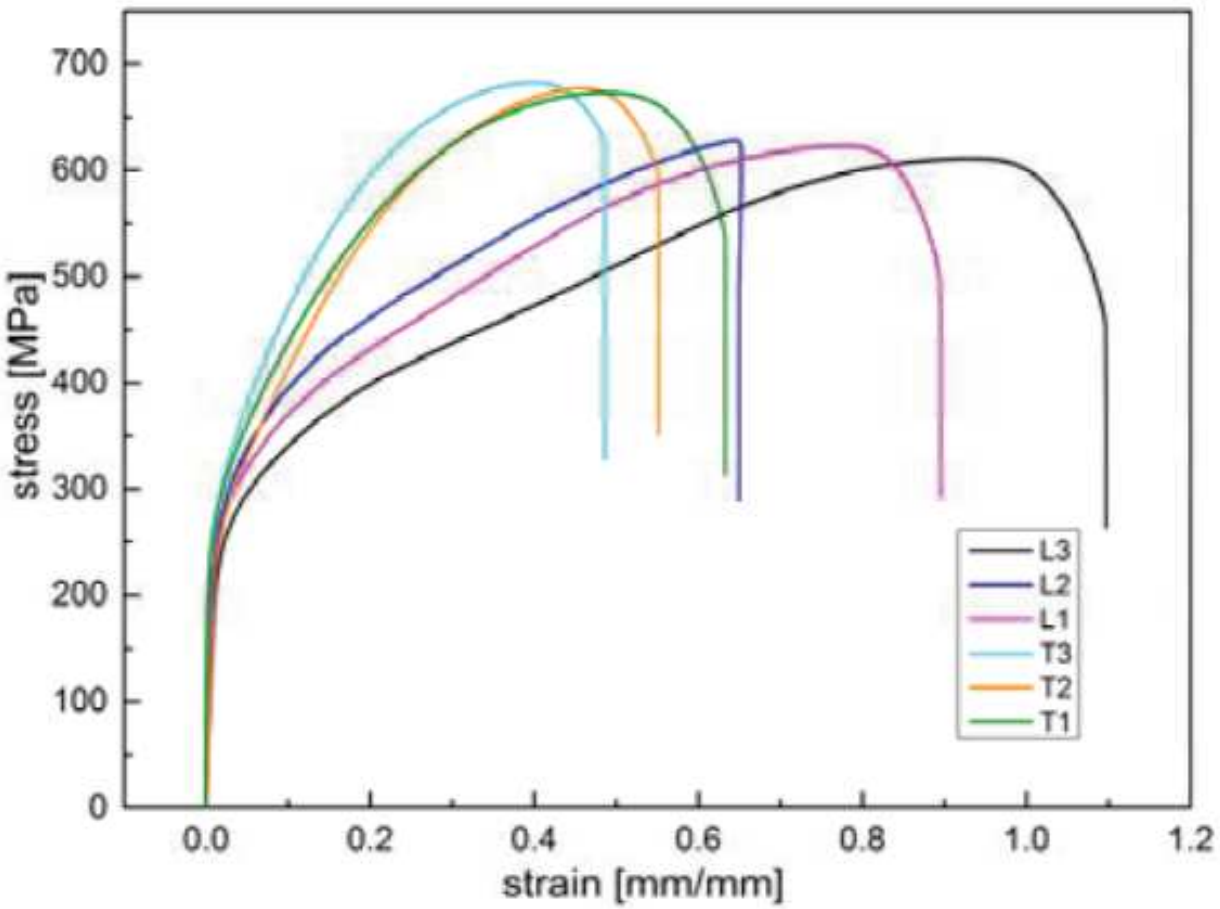

FIGURE 2.6: Tensile plots of WAAM fabricated 304L stainless steel for vertical orientation (L1, L2, and L3) and horizontal orientation (T1, T2, and T3) [167].

uniform mechanical properties. Thus, the anisotropy of the mechanical properties in the AM steel parts is a challenge. Several studies were conducted to solve this issue. Wu et al. [145] investigated the anisotropy of the mechanical properties in 316L stainless steel components fabricated by speed cold welding AM. They observed a pronounced reduction in the anisotropy by decreasing scan speed and increasing cooling time. This was attributed to the cooling rate reduction [145]. Wang et al. [146] reported that the mechanical properties of the WAAM fabricated H13 steel became isotropic as a consequence of annealing at 830 C for 4 hours. In another study, Fu et al. [258] eliminated anisotropy of mechanical properties in a bainitic steel using a combination of WAAM and micro-rolling. This hybrid technique's fully equiaxed grain structure resulted in the isotropic mechanical properties [258].

2.3.4.2 Titanium Alloys

Titanium alloys are widely used in the aerospace industry due to their high strength-to-weight ratio [259]. The allotropic nature of titanium alloys, in addition to high-temperature thermal cycles associated with AM techniques, allows for various microstructures, and consequently, mechanical properties [260]. Moreover, titanium components with complex geometries cannot be easily fabricated using conventional manufacturing techniques due to titanium alloys' poor machinability. The low thermal conductivity of Ti results in poor thermal dissipation during machining, leading to poor surface quality, accuracy and reduces machining tool life [261]. These factors make titanium alloys an attractive candidate for AM. Ti-6Al-4V (Ti64) alloy contains an allotropic microstructure of hcp α- and bcc β-phases, and is the most widely AM-fabricated alloy among all metallic alloys [103, 104, 132, 172–174, 199]. AM-fabricated Ti-6Al-4V alloys exhibit higher strength but lower ductility than conventional manufacturing techniques such as casting and forging [33, 105]. This can be explained by the formation of α'-martensite due to the high cooling rates associated with the selected AM techniques. The ductility of AM-fabricated Ti-6Al-4V components can be enhanced by applying heat treatments at the cost of reducing the overall strength of the material [106, 151]. Zhai *et al.* used a high-power laser to fabricate Ti-6Al-4V components, resulting in an as-built UTS and elongation of 1042 MPa and 7%, respectively [106]. Similar mechanical properties were reported for the Ti-6Al-4V alloy fabricated by GMAW [151] and pulsed plasma arc AM [33]. These findings can be explained by the similarity in their microstructures, where fine acicular α'-martensite with a small amount of $\alpha + \beta$ lamellae was observed [33, 106, 151]. In the case of LDED, when the laser power decreased from 780 W to 330 W, the mixed microstructure of α'-martensite and $\alpha + \beta$ lamellae was replaced with a fully martensitic microstructure [106]. This was attributed to the acceleration of the cooling rate as a consequence of the decreased laser power. The microstructure change led to a UTS enhancement from 1042 MPa to 1103 MPa, but an elongation drop from 7% to 4% [106].

Columnar grains and strong crystallographic texture of β <001> along the build direction in DED fabricated titanium alloys lead to an anisotropic microstructure [262, 263]. The anisotropy of the microstructure causes anisotropy of mechanical properties. In general, horizontally built parts exhibit higher yield stress and UTS but lower elongation than vertically built parts. This behavior has been observed for LDED fabricated Ti-6Al-4V alloy [264], LDED fabricated TC21 alloy [265], LDED fabricated TA15 alloy [266] and WAAM fabricated

Ti-6Al-4V alloy [219]. Anisotropic mechanical properties can be eliminated by obtaining an equiaxed grain structure with a random crystallographic orientation. Such a microstructure can be achieved by using interpass rolling between deposited layers [174], adding grain refining elements during AM [267], changing process parameters (for example, increasing powder feed rate and lowering laser energy density) [268], and applying post-process heat treatments [269]. These procedures can extend the application of DED fabricated titanium alloys into components that are required to exhibit uniform mechanical properties in all directions.

2.3.4.3 Aluminum Alloys

Aluminum alloys are the most extensively used non-ferrous metallic alloys in engineering components due to their high strength, low density, good ductility, and high corrosion resistance. Additive manufacturing of aluminum alloys is more challenging than steels and titanium alloys due to their high thermal conductivity. Therefore, the power of the different heat sources needs to be increased during AM to prevent quick heat dissipation [153, 270]. This is especially prevalent when the heat source is a laser beam because aluminum alloys have a high reflectivity [111]. The optics train can be damaged from the reflected laser, which can be counteracted by introducing a minor z-axis tilt to the laser head [270]. The increased power of heat sources can lead to the evaporation of some alloying elements such as zinc and magnesium during manufacturing, resulting in porosity due to gas entrapment [271, 272]. This limits the range of aluminum alloys that can be fabricated by AM. Aluminum also forms a strong passive oxide layer on the feedstock material, reducing the wettability of the melt during fabrication [273]. The presence of a large solidification range is another factor limiting AM of aluminum alloys. The segregation of alloying elements during solidification decreases the melting temperature of the grain boundaries, creating a liquid film. The thermal stresses induced by the high thermal expansion of Al can cause intergranular rupture of the grain boundaries, resulting in hot cracking [154, 176, 274]. The addition of silicon has been shown to reduce the susceptibility of hot cracking by reducing the solidification range, enhancing fluidity, and decreasing the thermal expansion coefficient [272, 275]. Moreover, it forms a fine low melting eutectic structure that can backfill cracks and increase the grain boundary area, preventing crack growth [272]. Among aluminum alloys, AlSi10Mg is the most extensively AM-fabricated alloy [109, 112, 114, 276, 277], although others like Al 5356 [278–281] and Al 4043 [282–285] have also been studied. The alloy is a hypoeutectic Al-Si alloy with a

composition close to eutectic. The presence of a small amount of magnesium ($\approx$ 1 wt. %) makes this alloy age-hardenable through Mg_2Si precipitation. The mechanical properties of AlSi10Mg alloy mainly depend on the morphology and size of the eutectic phase. The slower cooling rate in casting results in a larger cell structure with large intercellular Si particles. The larger Si particles act as crack initiation sites that can propagate easily through larger celled structures leading to low strength, and poor ductility [286–288]. However, AM techniques with high solidification rates can refine the eutectic phase and consequently enhance the alloy mechanical properties [110, 277].

2.3.4.4 Nickel Alloys

Nickel alloys are extensively applied in gas turbine engines, nuclear reactors, rocket engines, submarines, and space vehicles owing to their high strength and oxidation resistance at elevated temperatures [158]. Various nickel alloys have been used in the selected AM techniques including Inconel 625 (In625) [117, 289, 290], NiCrBSi alloy [35], Inconel 718 (In718) [135, 291] and Ni-Fe-V [292, 293] alloy. AM-fabricated Inconel 718 typically yields a dendritic structure of FCC γ, with the segregation of Nb and Mo to the interdendritic regions, characterized by the formation of Laves phase ($(Ni,Cr,Fe)_2(Nb,Mo,Ti)$) [157, 158, 178]. The presence of the Laves phase suppresses the formation of γ" (Ni_3Nb), the main contributor to In 718 superior mechanical performance, by depleting the matrix of Nb [121]. The fast cooling rates associated with AM, lead to a finer microstructure and less segregation than that of cast Inconel 718, resulting in comparable or slightly superior mechanical properties [119, 177]. The lack of precipitation strengthening and the defect accumulation during deposition leaves as-built AM deposits with inferior properties compared to wrought Inconel 718. This is remedied through heat treatment or hot isostatic pressing (HIP) [122, 123, 156]. Inconel 625 superalloys fabricated by a pulsed plasma arc (PPA) AM exhibited a yield stress, UTS, and elongation of 438 MPa, 721 MPa, and 49%, respectively [34]. Similar mechanical properties were reported for the same superalloy manufactured by a GMAW-AM technique [159]. These mechanical properties are greater than those of the as-cast Inconel 625 superalloy. This can be explained by finer dendrites and precipitates observed in the microstructure of AM built Inconel 625 superalloy [34, 159]. However, yield stress and UTS of Inconel 625 fabricated by PTA-AM or GMAW-AM are not as high as those of the wrought Inconel 625. This can be attributed to the fine equiaxed grain structure of the wrought superalloy. The

LDED built Inconel 625 superalloy was reported to have higher yield stress (540 MPa) but a lower UTS (690 MPa) and elongation (36%) than the wrought superalloy [116].

2.3.4.5 Magnesium Alloys

Magnesium alloys are the lightest engineering metal available with an approximate density of 1.74 g/cm3, which is significantly lower than that of steels, titanium alloys, and aluminum alloys[294]. Although the application of magnesium alloys has been limited owing to their low corrosion resistance and poor mechanical properties, their biocompatibility and elastic modulus comparable with human bones make these alloys an attractive candidate for biomedical applications [295]. Moreover, magnesium alloys are widely used to fabricate dissolvable downhole tools, where a high specific strength and corrosion rate are required [296]. Fabrication of magnesium alloys through forming processes such as forging and extrusion has been limited due to their limited active slip systems at room temperature, and high oxidation rate at elevated temperatures [297]. Furthermore, the casting of magnesium alloys does not allow for the fabrication of parts with complex geometries or the fine microstructures required to achieve good mechanical properties. Thus, AM techniques are being explored to target unique microstructures and high performance in magnesium alloys. Guo et al. [180] fabricated single pass multi-layer walls from AZ80M alloy wires using a GTAW-AM method. The as-built microstructure mainly comprised α-Mg and β-Mg17Al12 with small amounts of Al2Y phase [180]. This phase assemblage is typical for wrought AZ80M magnesium alloys. Mechanical properties of the GTAW-AM fabricated AZ80M alloy [180] were insignificantly different from those of a wrought sample. In another study, Guo et al. [179] fabricated full-dense components from AZ31 alloy wires using the GTAW-AM technique, where various pulse frequencies (from 1 Hz to 500 Hz) were employed. The finest grain structure and consequently greatest mechanical properties were achieved when the pulse frequency was either 5 Hz or 10 Hz [179]. A GMAW-AM process has also been used to manufacture components from AZ31B alloy wires [161]. Both size and volume fraction of pores in the as-built parts [161] were reported to be dramatically lower than those of pores in die-cast magnesium alloys. The GMAW-AM fabricated AZ31B alloy exhibited a higher elongation but lower yield stress than its wrought counterpart [161]. However, the UTS of the GMAW-AM fabricated AZ31B alloy was comparable to that of the wrought one [161].

2.3.4.6 Copper Alloys

Copper and copper alloys are widely used for manufacturing heat sinks, electrical wires, tooling inserts, busbars, cooling components, and electric motors due to their high electrical and thermal conductivity. Additive manufacturing allows the fabrication of complex geometries made from copper, such as internal cooling channels, while reducing the required material and shortening the manufacturing cycle. However, poor dimensional accuracy and significant porosity were observed in the AM-fabricated copper parts [298]. These problems are attributed to the rapid heat dissipation during AM resulting from the high thermal conductivity of copper. Thus, limited research has been conducted using the selected AM techniques to fabricate Cu components [164, 165, 182]. Dong et al. [182] fabricated a Cu-9 at. % Al parts using GTAW-AM, where separate pure Cu and Al wires were fed into a melt pool. The rapid solidification associated with GTAW-AM resulted in a microstructure predominately consisting of Cu_9Al_4 and $CuAl_2$ intermetallics in the as-built condition [182]. Homogenization heat treatment of the as-built parts reduced the amount of the intermetallic phases and enhanced yield stress, UTS, and elongation [182]. In another study, Shen et al. fabricated a Cu-Ni-Al part using a multi-axis GMAW-AM technique and compared it with the same part made from conventional casting. The AM-fabricated microstructure contained a lower volume fraction of K-phase precipitates but higher amounts of intermetallic phases than the as-cast one. This was attributed to the suppression of the eutectoid reaction by the high cooling rate associated with the GMAW-AM process [165].

2.3.4.7 Cobalt-Chrome Alloys

Cobalt-chromium alloys exhibit excellent wear resistance, high-temperature hardness, corrosion resistance, and biocompatibility. They are extensively used in cutting tools, gas turbines, combustion engines, surgical prosthesis, and machine gun barrels. However, their high hardness and low thermal conductivity quickly increase their temperature during cutting, making these alloys very difficult to machine. Thus, AM can be a good candidate for manufacturing Co-Cr parts. The AM-fabricated microstructure is mainly composed of Co-matrix dendrites and inter-dendritic eutectic, similar to the as-cast microstructure. However, both the dendritic branches and eutectic structure of the AM components are significantly finer than those of cast ones [126, 129, 183]. This can be explained by the significantly

higher cooling rates of the selected AM techniques compared to casting. As a result of the finer solidification structure of the AM parts, the inter-dendritic eutectic carbides mostly have a lamellar morphology [126, 129, 183]. This contrasts the coarse blocky eutectic carbides typically observed in the cast microstructure [183]. This explains the higher hardness, yield stress, and UTS of the AM parts compared to their cast counterparts [183]. However, compared with wrought Co-Cr alloys, the AM-fabricated Co-Cr alloys exhibit a comparable volume fraction of carbides and hardness value [129]. Moreover, the wear resistance of AM parts under dry sand/rubber wheel test conditions was reported to be less than that of the wrought ones [129]. This is attributed to the lamellar carbides of the AM deposit creating a continuous network that is easily removed during the wear test [129]. Mechanical properties and corrosion resistance of as-deposited AM Co-Cr alloys can be enhanced by performing post-processing heat treatments. The best combination of hardness, wear resistance, and corrosion resistance was reported to be achieved when the as-fabricated component is subjected to solutionizing heat treatment without being aged [127].

2.3.4.8 Tungsten Alloys

Tungsten and its alloys are widely used in many high-temperature applications such as collimators, arc welding electrodes, rocket nozzles, and heating elements in high-temperature furnaces owing to their high melting point, low thermal expansion coefficient, high tensile strength, and good creep resistance. However, their low ductility at room temperature and high ductile-to-brittle transition temperature (DBTT) limit their ability to be fabricated. Powder metallurgy (PM) techniques are commonly used to fabricate W components. However, parts with complex geometries are challenging to manufacture by PM techniques due to the limitation in mold/die geometry. Moreover, porosity is a common defect in PM-fabricated parts due to the high melting point of tungsten alloys. Thus, AM can be considered a promising candidate for the fabrication of fully dense W components with complex geometries. Marinelli et al. [184] fabricated defect-free parts from pure W wires by a GTAW-AM technique using a front wire feeding approach. Both the grain structure and the number of structural defects (such as gas-trapped pores, keyholes, and lack of fusion) were reported to be highly dependent on the orientation of the wire feeding [184]. In another study, Zhong et al. [130] used an LDED technique to fabricate a collimation component from pure W and W-Ni powder. No cracks or pores were observed in the microstructure of

the as-deposited parts [130]. Both tensile strength and elongation of LDED W-Ni alloys are enhanced by the addition of Fe, and Co [15].

2.3.4.9 Defects

This section will focus on the defects found in Ti-6Al-4V deposits across the different deposition technologies due to the lack of correlation between defects and the material or deposition system. The defects found are typically anisotropic microstructure [100, 102, 132, 189], porosity [99, 196, 264], thermal residual stress [100, 150, 200], lack of fusion [98, 192] and cracking [152]. These defects were found in LDED [98–100, 102, 131–133, 264], GMAW [148, 150, 152], GTAW [132], PTA [32, 33], and EB [189, 191–193, 196, 198, 200] deposits. Eliminating these defects is a challenge that will need to be overcome before the full commercialization of AM, especially for large-scale parts. Some of the remedies being explored are HIPing [104, 123, 189, 192, 299–301], hot rolling [173, 174], shot peening [124, 302], and cold working [303].

2.4 Fabrication platforms

This section introduces various considered fabrication platforms for the AM techniques discussed in Section 2.3, that were commonly found in the literature. For the context of this paper, an AM fabrication platform was considered as any actuated mechanical platform capable of carrying, translating, and potentially re-orienting a deposition system–such as a laser cladding head or a GMAW torch–with the desired accuracy. Alternatively, the system can be designed to translate and re-orient the substrate plate onto which components are printed or a combination of both re-orientation of the substrate plate and translation of the deposition system. The platform can be programmed to carry out deposition trajectories, including the complete integration of the deposition system, where parameters can be adjusted, and deposition can be activated and deactivated.

Various system types are reviewed in this section, and their suitability towards scalable, support-less, large-scale metal AM are assessed. Table 2.5 lists the platform types covered in this section and the advantages and disadvantages. Support-less printing is the aforementioned ability of a platform to re-orient a component during fabrication sufficiently to enable

TABLE 2.5: A summary and comparison of various fabrication platform types.

Platform type	DOF (dep. head)	DOF (build plate)	Advantages	Disadvantages	References
5-axis CNC	3 trans.	2 orient.	- Existing process planning methods - Good transitional technology - High component mass	- Limited scaleability - Deposition system limited to translation - Relatively expensive	[60, 61, 304–307]
Parallel mechanism	0	3 trans., 2 orient.	- Cost-effective	- Limited scaleability - Limited build plate orientation angles - Limited component mass	[308–310]
Serial manipulator carrying build plate	0	3 trans., 3 orient.	- High-DOF build plate	- Limited scaleability - Deposition system limited to translation - Limited component mass	[311, 312]
6-axis ser. manip. and 2-axis positioner	3 trans., 3 orient.	2 orient.	- Deposition system orientation can be changed - Scaleable - High component mass	- Relatively expensive	[56, 58, 74–76]

multi-directional deposition, which allows for support-less printing through re-alignment of the print direction with the gravity vector. The scope of the reviewed systems in this section is limited to systems capable of multi-directional deposition. It should be noted that the materials for each referenced publication are listed in Table 2.6. However, Mg, Cu, Co-Cr, and tungsten alloys were not mentioned in any of the referenced works and will not be included.

Multiple groups of researchers–Anzalone *et al.* [308], Nilsiam *et al.* [309], and Lu *et al.* [310]–introduced open-source fabrication platforms where the substrate plate is actuated by

TABLE 2.6: Sample of materials used in the various pieces of work discussed in Section 2.4

Steel	Ti	Al	Ni	Non-metals	Not Mentioned
[56, 60, 61, 74, 75] [304–306, 308, 310]	[306]	[306, 309, 313]	[306]	[311, 312, 314]	[58, 77, 307]

a parallel mechanism, which allows for 5 degrees of freedom (DOF) motion enabling multi-directional deposition. The substrate plate can be translated in all three directions (x,y, and z planes) and rotated about the two horizontal coordinates. The rotational capabilities are, however, not utilized when fabricating sample components with the proposed systems. In each system, the deposition system (a GMAW torch) is rigidly mounted above the actuated substrate plate. The system proposed by Anzalone *et al.* is shown in Figure 2.7B. Each of the systems is highly cost-effective at the proposed scale and type of hardware used. However, these systems have a limited build volume and re-orientation angles, making them ill-suited for larger parts. Another limitation is the limit of payload scaleability as the build plate's actuation system carries the full weight of the build.

Another system found in the literature capable of 5-axis AM is standard CNC milling systems retrofitted with a deposition system such as a GMAW or an LDED cladding head, introduced in Section 2.3.1 and Section 2.3.3 respectively. CNC milling machines have existing process planning and computer-aided manufacturing (CAM) infrastructure that can be integrated with these deposition systems, making them a popular industrial choice. This established pipeline of technology will be important in streamlining commercial 5-axis AM systems, especially for components of a limited size. Panchagnula *et al.* mounted a GMAW torch on the side of their CNC milling system's tool spindle, allowing the torch to be moved in three translational dimensions. Furthermore, the CNC milling system is equipped with a 2-axis positioner (see Section 2.7A), enabling the substrate plate to be tilted and rotated. The combined total of 5 DOF allows for multi-directional deposition and, therefore, the fabrication of support-less components [60, 61]. A further 5-axis metal AM platform, where a CNC milling system was retrofitted with a laser cladding system was introduced by Tabernero *et al.* and Calleja *et al.* [304, 305], with similar capabilities as Panchagnula *et al.*

In addition to the above-listed 5-axis platforms, there are also commercialized 5-axis hybrid platforms for metal AM available such as the Mazak INTEGREX i-400 AM [306] and the DMG Mori LASERTEC 65 3D hybrid [307]. Each of these two platforms is equipped with an LDED deposition system and a tool spindle. A component is first fabricated, or a feature is added to an existing component through AM. The finished component or feature is then finalized by milling the surfaces to an accurate size. This combination of additive and subtractive manufacturing is gaining popularity in the industry due to the lack of geometrical constraints of AM coupled with the surface tolerances offered by subtractive manufacturing. This offers unique capabilities that are currently not achievable with either technology alone.

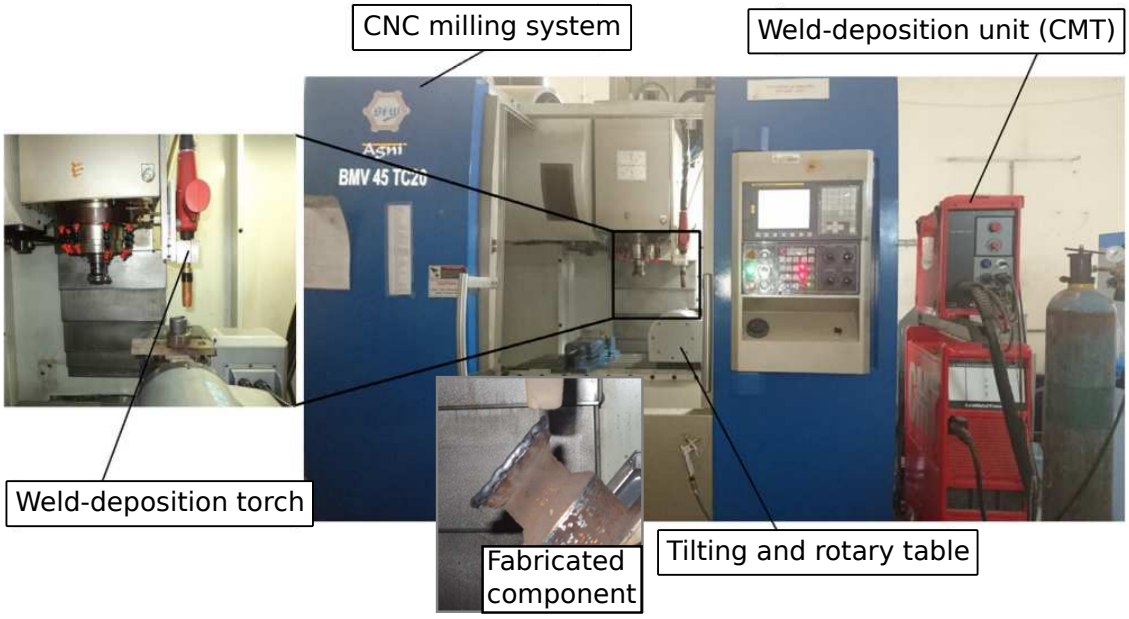
CNC milling system
Weld-deposition unit (CMT)
Weld-deposition torch
Fabricated component
Tilting and rotary table

A

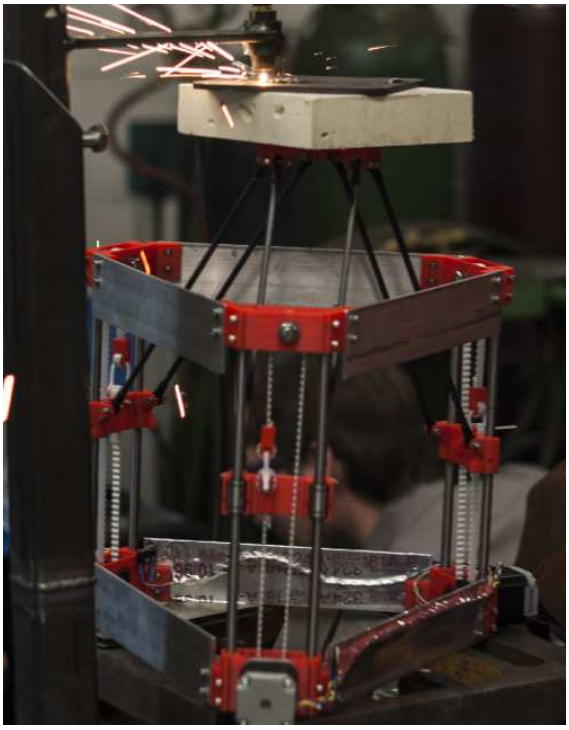

B

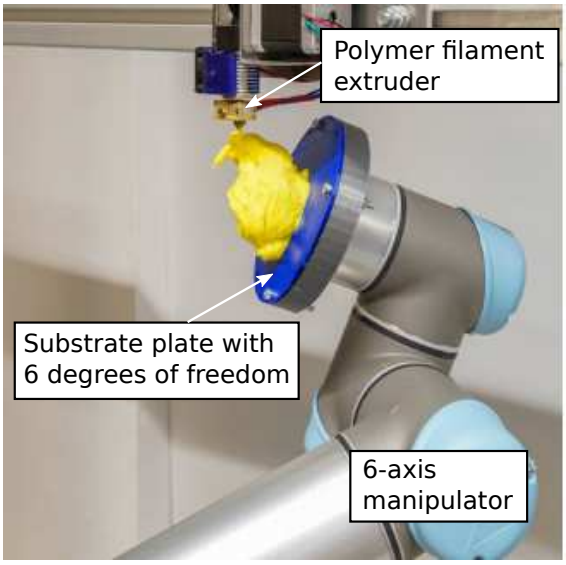
Polymer filament extruder
Substrate plate with 6 degrees of freedom
6-axis manipulator

C

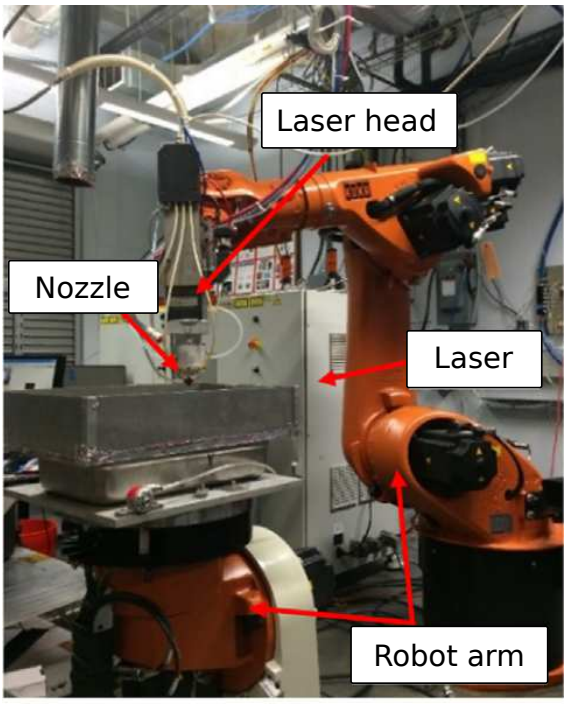

D

E

FIGURE 2.7: Examples of AM platforms with multi-directional deposition capabilities. (a) A 5-axis WAAM platform [61], (b) a parallel-mechanism-based WAAM system [308], (c) a 6-axis robotic polymer AM platform [312], (d) an 8-axis robotic LDED platform [56], (e) a collaborative multi-manipulator platform [314].

Another platform that can potentially be utilized for metal AM was first introduced by Wu *et al.* and Dai *et al.* and is shown in Figure 2.7C. The platform consists of a 6-axis serial manipulator and a rigidly mounted deposition system above the manipulator. The substrate plate is mounted on the tool flange of the manipulator and can be moved in 6 DOF, allowing for multi-directional deposition [311, 312]. While both Wu and Dai *et al.* utilized polymer extruders as a deposition system, simple modifications could render it to be compatible with the metal deposition systems introduced in Section 2.3. One inherent limitation of this proposition is that the size of the component is constrained to the maximum payload of the manipulator, possibly limiting the scalability to large metallic parts. [56, 58, 74–77]

A better-suited metal AM fabrication platform uses a large-scale serial manipulator to carry the deposition system (6 DOF), while the components are fabricated on a two-axis positioner (2 DOF) such that the overall systems offers 8 DOF. These systems have various advantages over the reviewed parallel, 5-axis gantry-based, and 6-axis manipulator-based platforms. An advantage compared to 5-axis systems is that the deposition head's orientation can be changed in all three rotational directions when a 6-axis manipulator carries the deposition system. This capability to change the orientation also facilitates tangential continuity, allowing for smoother surface finishes and optimizing the feeding angle of material into the melt pool while maintaining alignment with the gravity vector for multi-directional deposition. During GMAW-based deposition, for example, specific drag or pull angles can help achieve the desired bead geometry. Another significant advantage, which has been appreciated since the 1980s for welding complex, curved contours is the redundancy of the 8-axis manipulator and positioner combination. Redundancy in the context of a kinematic system is when more degrees of freedom are available than are required to complete the desired task. Thus, redundancy implies kinematic advantages such as enhanced relative reachability and dexterity between fabricated components and deposition systems.

The coordinated motion between manipulator and positioner offers the following advantages: reduction of execution time, added flexibility in motion optimization and collision avoidance, maximization of the manipulator workspace, and the ability to track smooth corners using smooth paths [315]. Generally speaking, manipulator/positioner combinations have been used for welding applications for over 30 years. Therefore, using these platforms for DED deposition is a natural extension of robotics research, where prior research can be utilized seamlessly.

The first example of using an 8 DOF system for DED was proposed by Dwivedi *et al.*, where radial components were fabricated using multi-directional deposition. The authors used a powder-based LDED system for metal deposition [58] mounted on the manipulator's tool flange. Ding *et al.* [56, 74, 75] (see Figure 2.7D) and Zheng *et al.* [76] proposed equivalent platforms also using powder-based LDED as deposition systems. Ding *et al.* explored the augmentation of a 6-axis manipulator with a 2-axis positioner, totaling 8 DOF for multi-directional deposition, as shown in Figure 2.7D. The author eliminated the need for support structures while fabricating a propeller, which consisted of a core volume (a shaft) and radially overhanging features (propeller blades). Such a component is difficult to manufacture using conventional subtractive manufacturing [56]. Platforms utilizing arc-welding-based deposition technologies have been less explored in combination with 8-axis motion platforms than LDED-based deposition. Such a platform was used by Ma *et al.* for experimental trials with Aluminium [77]. Moreover, in a collaborative effort between the University of Alberta and InnoTech Alberta in Edmonton, Canada, a robotic large-scale WAAM platform–as shown in Figure 2.1–has been put in use by the authors of this work and initial research on parameter identification towards the optimization of deposition parameters is currently being conducted [209]. An interesting extension for robotic large-scale metal AM is the use of multiple mobilized manipulators, each carrying a deposition system. Research on such a platform in the area of civil engineering for fabrication of concrete components using AM has been conducted by Zhang *et al.* The researchers propose a platform consisting of two 6-axis manipulators, each mobilized by a holonomic mobile platform where a concrete deposition nozzle is mounted on each manipulator's tool flange (see Figure 2.7E).

A holonomic mobile platform can translate in any direction (sideways or forward) without the need to change the orientation of the platform, which means that the manipulators can reach any location within the fabrication space at an optimum duration and trajectory. Zhang *et al.* identified that the most significant advantage of this platform is the ability to fabricate components larger than the reach of one manipulator. The mobility aspect of the platform extends the reach of each manipulator, significantly enhancing the scalability and duration of fabrication. The extent of the scalability can be enhanced by increasing the number of mobile manipulators to the system. Some of the associated research challenges are robot localization, multi-robot coordination (e.g., swarm intelligence) and collision-free motion planning, and robot placement accuracy and optimization [314]. While Zhang *et al.*'s proposed platform is not capable of multi-directional deposition, a multi-manipulator

platform can also be augmented with a large-scale multi-axis positioning system in order to facilitate multi-directional deposition.

2.5 Process planning

Process planning refers to converting a 3D model of a component to an optimal manufacturing strategy prior to fabrication. An integral part of this strategy for multi-directional large-scale AM is avoiding support structures as commonly required for 2.5 DOF AM. Depending on the geometric complexity of the overhanging features, the 3D model is decomposed into sub-volumes typically consisting of a core volume and multiple overhanging features. These are then sliced into cross-sectional layers, followed by the generation of an optimized deposition tool path for each layer. An example of such a process planning sequence is shown in Figure 2.8 [56]. This example shows the decomposition of a propeller where a clear separation between core volume (shaft) and the overhanging features (propeller blades) can be found. For many other components, however, this separation is less obvious or nonexistent (see Figure 2.9).

After slicing is complete, a deposition tool path is computed that fills the required areas of each layer with material. Using a numerical model, the bead geometry (bead width and height) required to fill the layer to a predetermined height is correlated to a set of deposition system parameters, including the material feed rate, deposition system speed, and dwell times. The magnitudes of these parameter values depend on the material and deposition technology being used. This information is then provided to the fabrication platform, theoretically allowing for unsupervised deposition.

In order to fully exploit the possible advantages of large-scale robotic AM, the systems and algorithms for the automated process planning of near net shape components need to be capable of decomposing complex volumes into sub-volumes. Additionally, the algorithm must account for the multi-directional and non-planar slicing of these volumes, and the tool path and robot joint trajectory planning, including collision avoidance [316]. The substantial work that has been done towards this objective will be discussed herein. First, state of the art in volume decomposition and slicing will be reviewed (Section 2.5.1), followed by the established tool path generation methods for planar layers, as many of these tool path

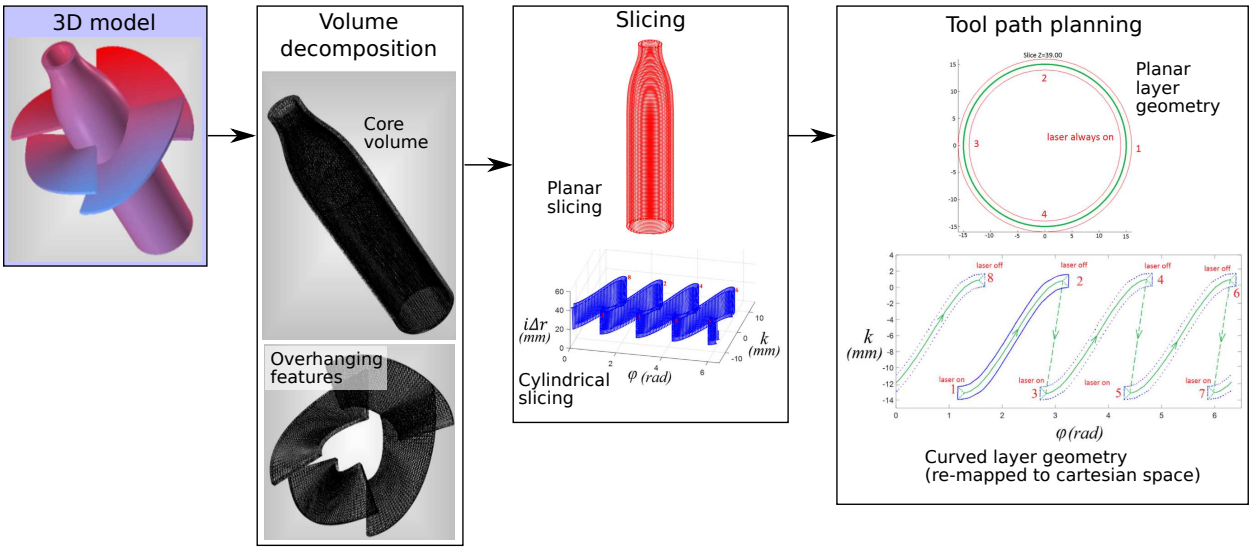

FIGURE 2.8: An example of a process planning sequence on a 3D model of a propeller including volume decomposition, slicing and path planning of each sub-volume. (Image source: [56])

generation strategies constitute a basis for further research on tool path planning for non-planar layers. Finally, some open-source software frameworks for robot joint trajectory planning and collision avoidance are reviewed in Section 2.5.3. It should be noted that all of the materials that were used in the reviewed studies have been summarized in Table 2.7; however, Co-Cr and W were not included.

2.5.1 Volume decomposition & slicing for multi-directional deposition

Some of the first researchers to recognize the need for an advanced process planning framework capable of decomposition and multi-directional slicing of complex 3D models with overhangs were Sing, and Dutta [57]. The objective of their proposed method was to improve

TABLE 2.7: Materials used in the various pieces of work discussed in Section 2.5

Steel	Ti	Al	Ni	Mg	Non-metals	Not Mentioned
[56, 85, 87, 317–320] [59, 77, 86, 321–323]	[321]	[321]	[321]	[321]	[62, 311, 312, 316, 324] [325–328]	[57, 57, 58, 77, 317, 329–332] [333–338]

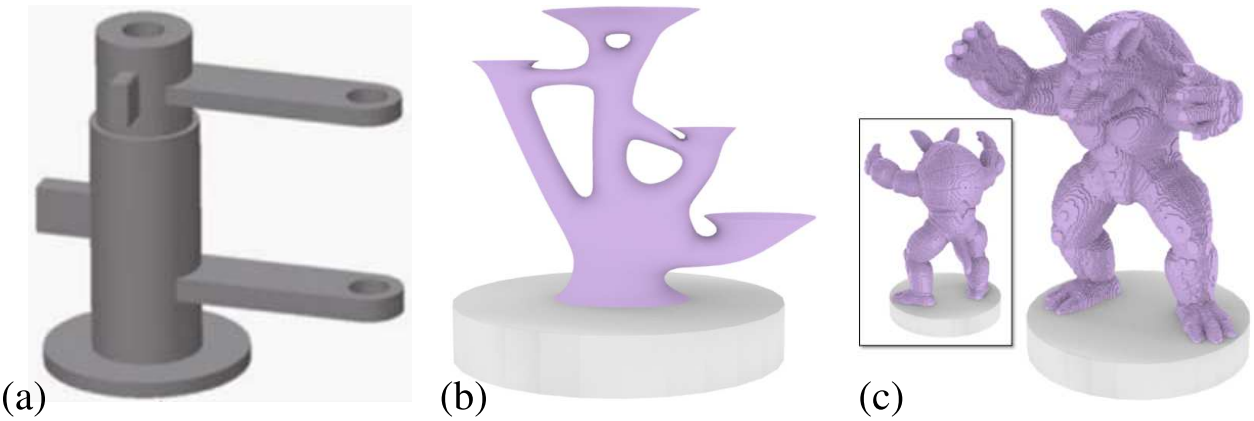

FIGURE 2.9: Examples of 3D models of varying complexity with a) a radial component with easily separable overhangs [317], b) and c) more complex components with less clearly separable overhangs [312].

the surface accuracy and reduce the support volume through multi-directional deposition. The decomposition sequence is as follows:

1. choose a build direction; by default along the component's Z direction to avoid collision of the deposition head with the table,
2. identify and decompose overhanging features (often referred to as "unbuildable structures" in the literature) in build direction,
3. determine the build direction for each sub-volume, and
4. sequence and slice each sub-volume along its computed build direction.

At the core of the approach is a recursive volume decomposition scheme meaning that overhanging features within sub-volumes are also identified. The performance of the proposed process planning framework was shown on two example 3D models, but no components were fabricated. Dwivedi *et al.* proposed a framework for automated process planning for LDED [58]. The process planning framework is based on first-order logic and a knowledge base consisting of rule and fact attributes represented by a semantic tree structure. The authors of the study successfully verified their framework on a radial component consisting of 5 helical blades. Ruan *et al.* proposed a method using the centroid axis of a component to compute the deposition direction to produce collision-free slicing directions for multi-directional deposition [319]. The basic tasks are defined as

1. centroid axis computation and formation, and

2. collision-free multi-axis slicing based on the centroid axis.

The detection of change in build direction–and therefore slicing direction–is based on the degree of shift from the centroid axis. The slicing algorithm can produce layers of non-uniform thickness, thus requiring the deposition system to be capable of producing beads of varying geometry. The algorithm was verified on a 3D model of a hinge with overhangs on a multi-axis LDED fabrication platform.

Ren *et al.* identified limitations with the previous centroid-axis-based decomposition algorithms for certain corner cases of axis-symmetric overhanging structures where no shift in the centroid axis occurs. Thus, an algorithm combining the centroid axis-based and boundary-based decomposition methods–where concave edges and loops marking the interface between core volume and overhanging feature (see Figure 2.10)–of the type as previously proposed by Singh and Dutta [57] was introduced [318]. Furthermore, the authors proposed a method for representing layers of non-uniform thickness by further decomposing the non-uniform layer into uniform sub-layers of a smaller cross-section than the parent layer. The algorithm was verified by fabricating a turbine wheel with a conical shaft and winged blades on an LDED platform.

In order to further improve non-planar interfaces between a core volume and overhanging feature, Singh and Dutta further extended their previous work on multi-directional deposition

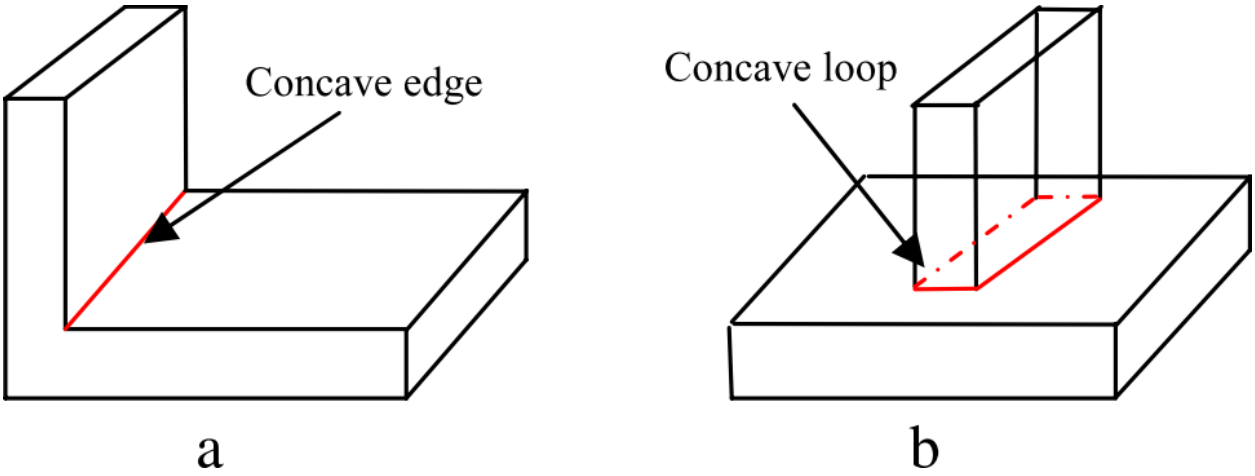

FIGURE 2.10: Schematic representations of a) a concave edge and b) a concave loop as defined in [318]. (Image source: [318])

[57], by introducing so-called offset slices, which are essentially non-planar layers [329]. The concept of offset slices is illustrated in Figure 2.11. If the base surface is non-planar, which is frequently the case for radial components with overhanging features, the build quality of the overhanging features can be significantly improved when each layer follows the same contour as the core volume and subsequently the previous layer.

In order to simplify process planning and fabrication of special cases of components with overhanging features containing holes (see Figure 2.9a), Ding *et al.* proposed a framework that fills all holes and protrusions within the 3D model prior to decomposition [317]. The volume decomposition itself is boundary-based, whereas, with previous algorithms, concave loops and edges are detected. After decomposition, each sub-volume is sliced into planar layers according to the identified build direction. The framework was not verified experimentally. Furthermore, due to the hole-filling operation prior to decomposition, additional post-processing is required to drill the holes.

Ding *et al.* introduced a process planning framework for radial components such as propellers or impellers [56], shown in Figure 2.12. The decomposition algorithm is based on silhouette edges, as first introduced by Singh and Dutta [57], and Dwivedi *et al.* [320]. The algorithm is similar to previously proposed boundary-based algorithms as it looks for concave edges and loops on the core volume. Slicing is divided into two steps (see Figure 2.8):

1. planar slicing of the core volume, typically a cylindrical volume for radial components and

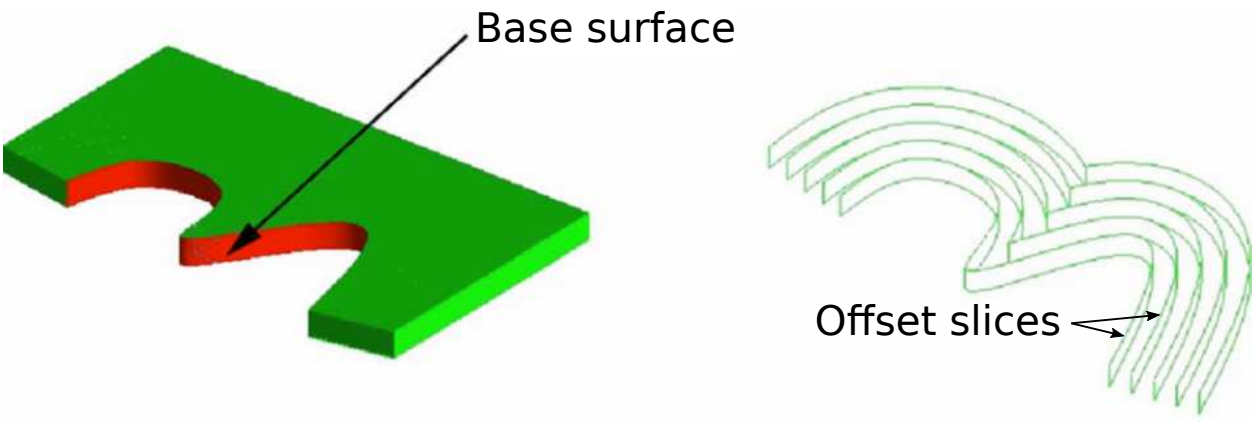

FIGURE 2.11: The concept of offset slices as introduced by Singh and Dutta [329]. The offset slices follow the contour of the non-planar base surface where each offset slice is equidistant to the previous one. (Image source: [329])

2. mapping of the overhanging feature's curved geometry from a cylindrical to a cartesian coordinate system to allow for a planar representation of each curved layer, similar to the principles proposed by Singh and Dutta [329].

The process planning framework was verified on a 8-DOF robot LDED platform (see Figure 2.7D) by fabricating the propeller model shown in Figure 2.8.

It should be noted that all of the frameworks for process planning reviewed up to this point can only process components where the overhanging features are sharp concave edges or concave loops (see Figure 2.10), meaning that they are distinguishable from the core volume. The works reviewed in the following, however, propose process planning algorithms and frameworks designed for volumes with non-sharp edges that are more difficult to decompose (see Figure 2.9b and Figure 2.9c). Wu *et al.* introduced an advanced volume decomposition algorithm capable of processing volumes that are not composed of a distinguishable core and overhanging volumes (see Figure 2.13a) [311]. The decomposition algorithm consists of 3 major steps as illustrated in Figure 2.13:

1. *Coarse decomposition*: A skeleton is generated based on a mean-curvature flow algorithm (see Figure 2.13b) followed by the computation of a distance metric–the shape diameter function (SDF)–between volume boundary and skeleton (see Figure 2.13c) and partitioning the mesh using the distance metric based on [330]. The partitioning algorithm identifies significant differences in the SDF and creates a boundary plane where the change occurs. When considering the bunny model, a significant change in SDF can be found at the bunny's neck, ears, and tail.

2. *Sequence planning*: A graph is constructed that defines the preliminary build sequence–nodes are the sub-volumes–and the print orientation for each sub-volume is determined (see Figure 2.13d). The preliminary build sequence is $A \rightarrow B \rightarrow C \rightarrow D \rightarrow E$

3. *Constrained fine tuning*: The decomposition is refined and re-configured to satisfy manufacturing constraints (see Figure 2.13e and Figure 2.13f). For example, the bunny tail as labelled B in Figure 2.13d can not be manufactured with the platform shown in Figure 2.7C due to inaccessibility. It, therefore, needs to be merged with A. In addition, $A*$ needs to be separated into H and K since the belly of the rabbit is an overhanging feature.

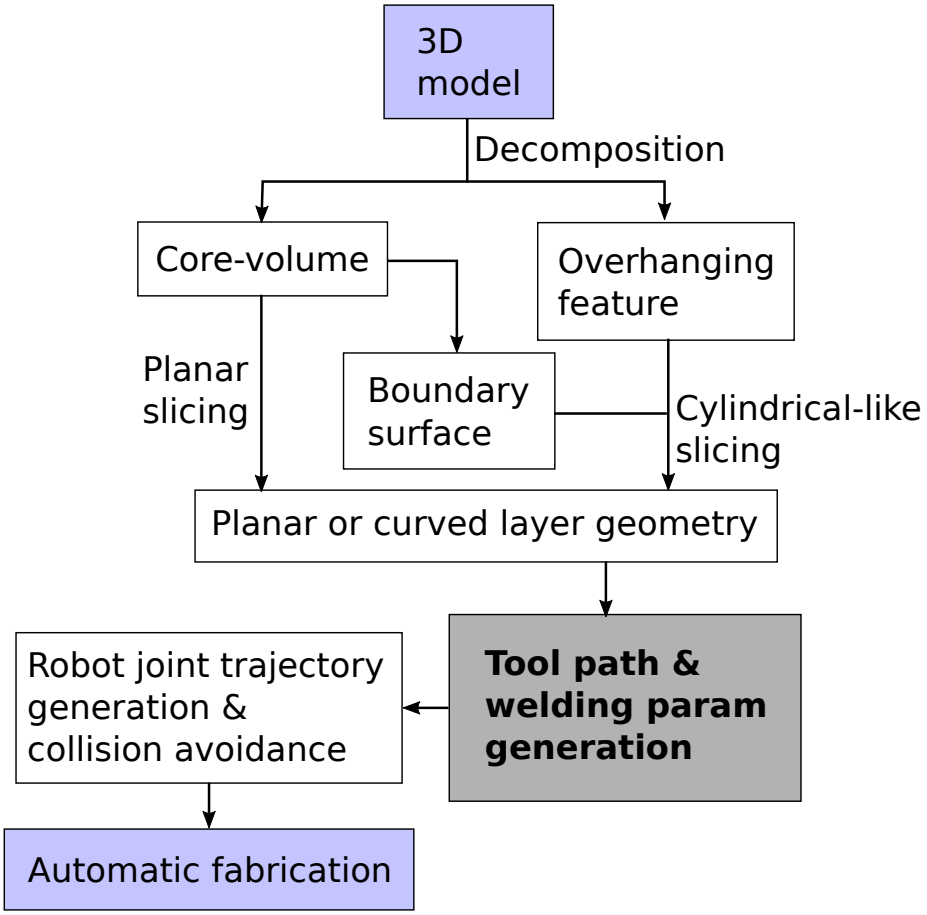

FIGURE 2.12: Flowchart of an example process plan similar to the one devised by Ding *et al.* for propeller fabrication [56].

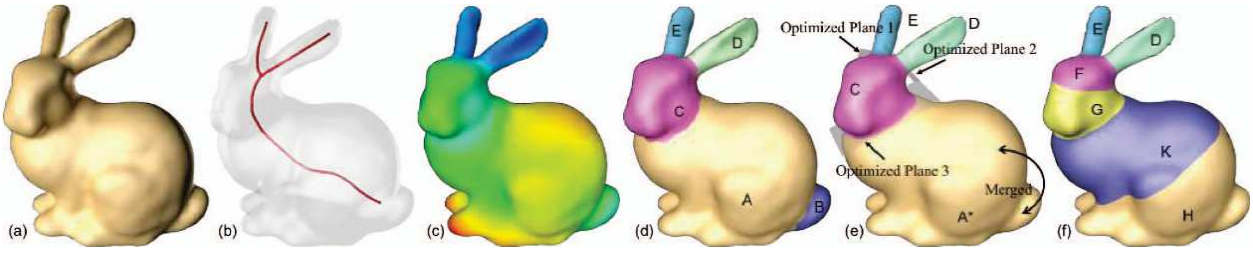

FIGURE 2.13: The volume decomposition algorithm proposed by Wu *et al.* [311] with a) the input 3D model, b) the extracted skeleton, c) the shape diameter metric (distance of every point to skeleton), d) the result of initial decomposition and sequence planning, e) after merging (B into A), and f) the final result after fine decomposition to ensure manufacturability. (Image source: [311])

The decomposition algorithm was verified experimentally on a robotic AM platform equivalent to the one shown in Figure 2.7C.

One limitation of Wu *et al.*s work is that it relies on planar layers, which imposes constraints on the manufacturability of more complex components (see Figure 2.9c). Dai *et al.* proposed a novel method utilizing curved layer decomposition relying on dimensionality reduction [312]. The algorithm is separated into the following steps as illustrated in Figure 2.14:

1. Discretization of the input model into a voxel grid–a discretization into small cubes–where the voxel dimensions are determined by the deposition system's resolution (Figure 2.14b). This is done to reduce the computational load on the following steps since the volume decomposition of the input model is posed as a global search problem.
2. Sequencing of the voxels to obtain a sequence of voxel accumulation representing the flow of fabrication. By iterating over all voxels, satisfying manufacturing constraints can be significantly simplified. The color scheme shown in Figure 2.14b represents the voxel sequencing by layer.
3. Computation of each curved layer while avoiding voxel aliasing (see Figure 2.14c).
4. Computation of a tool path for each layer using the method introduced by Zhao *et al.* and based on Fermat spirals [324] (see Figure 2.14d).

This algorithm was also verified experimentally on a robotic AM platform equivalent to the one shown in Figure 2.7C. The limitations of the algorithm identified by the authors include

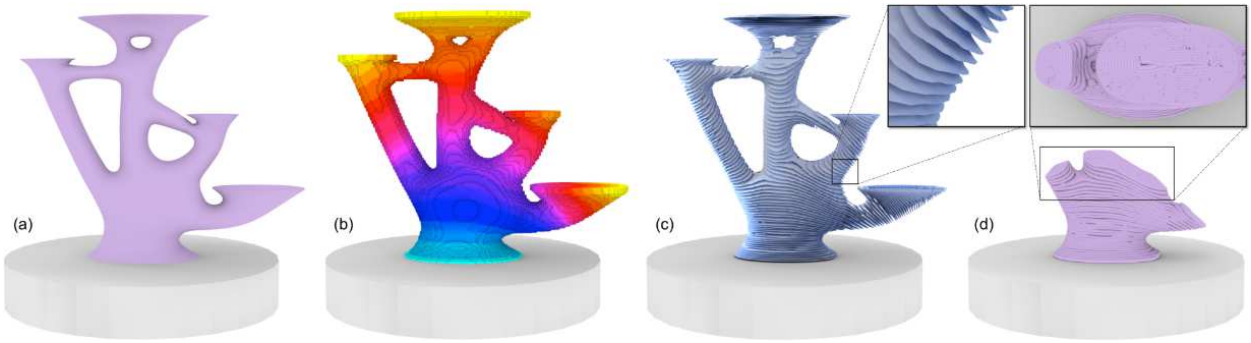

FIGURE 2.14: The volume decomposition algorithm proposed by Dai *et al.* [312] with a) the input 3D model, b) after voxel discretization and voxel sequencing where the color scheme represents the fabrication sequence by layer, c) generated curved layers based on (b), and d) a detailed view on a computed tool path. (Image source: [312])

the reliability of thin-feature deposition, fabrication errors due to the used hardware, and voids in the filling patterns of the tool path planning algorithm.

Despite the limitations of the frameworks and algorithms proposed by Wu *et al.* and Dai *et al.*, their works contain important contributions to process planning of complex models with significant adoption potential to metal AM.

2.5.2 Tool path planning

Once the component has been decomposed and sliced into cross-sectional layers, the optimal path to accurately deposit the material within the boundaries of the cross-section is computed. This process is known as tool path planning. An optimized deposition path planning strategy results in dense parts with minimized residual stress, free of any porosity, better control of anisotropic microstructures, mitigation and minimization of heat accumulation, geometrical accuracy, and a smooth surface finish [62]. In order to develop an optimal deposition path planning strategy, features that are unique to the various kinematic systems and deposition technologies (consistency of deposition, motion delay, dynamics, lag) need to be considered. Notably, the varying delays and inaccuracies in deposition system motion (especially for larger systems with increased mass) and material deposition (material feeding, melting) that are difficult to predict can cause unwanted variations on the rate of deposition and therefore complicate path planning significantly [85]. Inter-layer dwell time, start-stop minimization, smooth directional changes, as well as minimization of weld path cross-overs, are some of the commonly adopted strategies to mitigate these complications [85, 87, 321]. Towards the development of an optimized path planning strategy, Ding *et al.* identified various requirements for WAAM such as geometrical accuracy, minimization of start-stop points, minimization of rapid directional changes caused by sharp corners in every tool-path pass, and simplicity allowing for fast implementation [85].

Ding *et al.* reviewed various path planning methods with respect to their suitability for WAAM, using the above-mentioned evaluation criteria. Among the reviewed path planning algorithms are: Raster [331], Zigzag [332, 333], Contour [334–336], Spiral [325, 337], Fractal Space Filling Curve [326, 338], Continuous [327, 328, 338] and Hybrid (Combination of contour and zig-zag) [59, 322]. However, Raster (see 2.15A), Zig-zag (see 2.15B), Contour (see 2.15C), Fractal (see 2.15E) and Spiral (see 2.15F) should be entirely avoided for metal

AM due to the many issues listed by Ding *et al.* [85]. Raster and Zig-zag suffer from poor outline accuracy due to discretization errors on non-parallel edges. Contour generates many disconnected closed curves, therefore violating the requirement to minimize start-stop points. Fractal Space Filling Curve involves many path direction change motions, violating the requirement to minimize rapid directional changes. Finally, the Spiral method is only suitable for unique geometrical models that are convex [85]. Hence, these methods will not be reviewed in detail in this section.

The Hybrid method (see Figure 2.15H) is a combination of the Contour and Zig-zag methods in that first, the contour of the layer boundary is traversed followed by filling the interior of the layer with the Zig-zag and Contour method (see 2.15D). As this method combines the advantages of the Zig-zag and Contour methods, it is particularly promising for WAAM as it meets both the geometrical accuracy and surface quality. According to Ding *et al.*, the Hybrid method is still insufficient due to the increased amount of tool-path passes and tool-path elements [85].

Ding *et al.* therefore proposed a novel tool path planning method intended to address the limitations of the previously proposed methods [85] and to conform with the aforementioned requirements: geometrical accuracy, minimization of start-stop points, minimization of rapid directional changes, and simplicity of implementation. The method is henceforth referred to as Convex Polygon Generation (CPG, see Figure 2.15I). In order to generate a set of simpler convex or monotone sub-polygons, and to simplify the implementation of path generation for each sub-polygon, a polygon decomposition algorithm first decomposes each 2D slice via a *divide-and-conquer* strategy. Then the Hybrid path planning method is used for tool path generation due to the aforementioned advantages of this planning method. After tool paths are generated for each sub-polygon, the sub-paths from each sub-polygon are connected into a closed curve that spans the entire layer, thus minimizing start-stop points [85]. This algorithm extends the Hybrid path planning method to polygons with an arbitrary complexity through convex polygon decomposition. As this method, however, also utilizes the Zig-zag method for space-filling, voids can still occur [85, 87].

To address the issue of voids while retaining geometrical accuracy, Ding *et al.* proposed a method based on Medial Axis Transformation (MAT), or also referred to as skeletonization, as depicted in Figure 2.15J [86]. MAT was first proposed by Blum to describe shapes [339] by generating tool paths in a contour-like fashion from the center outwards along a skeleton to

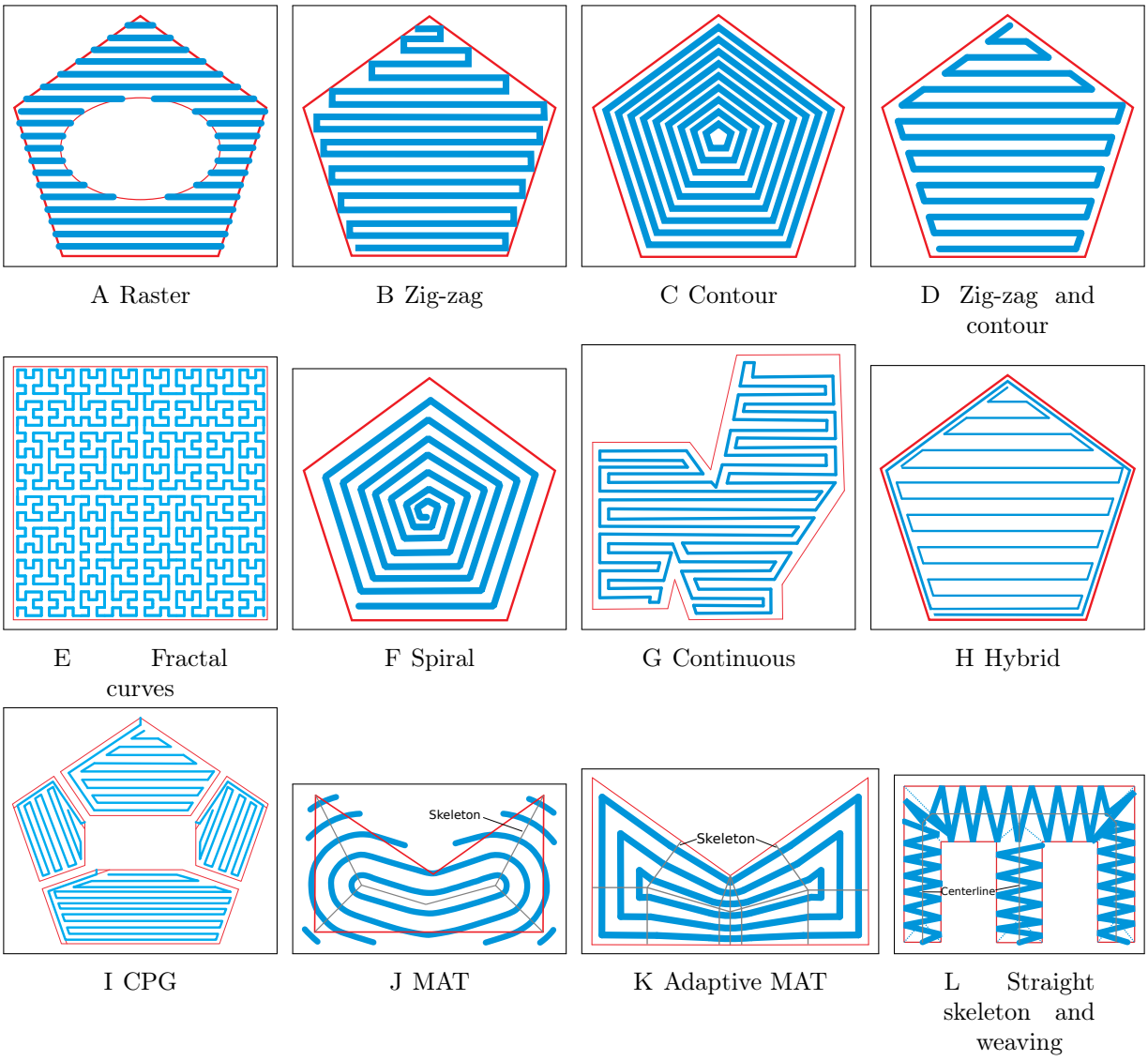

FIGURE 2.15: Different path planning methods: A Raster, B Zig-zag, C Contour, D Zig-zag and contour, E Fractal curves, F Spiral, G Continuous, H Hybrid, I CPG, J MAT, K Adaptive MAT, and L Straight skeleton and weaving deposition strategy.

the boundary of the geometry. First, the skeleton or the branch lines are generated, followed by the generation of loops representing the tool paths at a given step-over distance, which is the distance between passes representing the resolution of the deposition system [86]. With this method, the occurrence of voids is minimized. However, there are some disadvantages, such as start- and stop points and discontinuities at the geometry boundaries and deposition beyond the geometry boundaries [87]. While these deficits can be mitigated by post-process milling, they essentially limit the MAT path planning method to hybrid manufacturing.

Further iterating on their previous work with the objective of addressing the deficits raised with MAT, Ding *et al.* proposed adaptive MAT [87]. The difference being that the tool-path elements are designed so that the contour of the geometry boundary is followed and discontinuous path segments are minimized (see Figure 2.15K). Benefits of adaptive MAT include the capability of generating continuous tool-path elements and following the geometry contour, void-free layers, good geometrical accuracy, and thus minimal post-milling, and suitability for thin-wall structures. For adaptive MAT to produce void-free deposition, the bead geometry must be able to be varied in-situ. To facilitate bead geometry adjustment, Ding *et al.* developed a Neural-network-based model that takes the desired bead geometry as an input and outputs welding parameters that significantly influence the bead geometry. Moreover, the adaptive MAT algorithm is experimentally validated using the proposed deposition model [323].

In summary, some of the variants of Contour-based algorithms such as Hybrid, CPG, and adaptive MAT are preferred over raster or pure Zig-zag algorithms since they are more suitable for thin wall structures and allow for improved geometric accuracy, void-free deposition, and minimization of start-stop discontinuities in tool paths. Among the more suitable tool path planning methods, adaptive MAT is preferable from the aspects of void-freeness and accuracy if in-situ bead geometry adjustments are possible or feasible for a given deposition system.

A further tool path planning method specifically designed for the particular case of thin-walled structures with varying thickness was proposed by Ma *et al.* [77]. Adjustment of the wall width is achieved through a weaving trajectory where the weaving amplitude is the same as the width of the thin wall. After computing the skeleton of the polygon, the centerline is then obtained (see Figure 2.15L), which constitutes an approximation of the polygon's median axis. During deposition, the torch weaves about the centerline in a triangular way, as illustrated in Figure 2.15L. The authors of the study successfully fabricated multiple thin-walled components with gradually varying wall thickness through this weaving technique.

2.5.3 Software frameworks for robotics hardware interfacing & trajectory planning

As can be seen from this section, process planning is an integral part of robotic metal AM and involves many algorithms and software components. The cascade of complex software needs to interface and exchange information efficiently to provide robust performance while simultaneously providing flexibility, modularity, and reusability to integrate new algorithms and software in a research environment. For robotic research platforms, the used software frameworks facilitating novel research need to be as open as possible. This enables maximum flexibility and customization for each software component across research groups within the toolchain and facilitates the integration of custom hardware (HW).

A popular open-source software framework and middleware providing such a software ecosystem for advanced robotics research is the Robot Operating System (ROS). ROS is leveraged for wide varieties of robotics research and provides structured messaging between software components, robot-specific tools and libraries, various visualization and convenience tools, HW abstraction, low-level device control, and tools and libraries for obtaining, building, writing, and executing code (see [340]). ROS, therefore, simplifies and facilitates robotics research and software development significantly. The ROS software package MoveIt!, for example, provides interfaces to sophisticated path planners for free-space motion and inverse kinematics solvers for industrial robot arms such as the one shown in Figure 2.1.

In recent years, multiple open-source software frameworks have been developed within the ROS ecosystem for the planning of complex cartesian trajectories with an emphasis on industrial robotics applications such as welding, routing, milling, deburring, and grinding. In 2015, Edwards *et al.* introduced a path planning software package called *Descartes* for semi-constrainted cartesian trajectory planning [341]. The software takes a 6-DOF cartesian trajectory that can be under-defined and is generated for any industrial application. Under-defined means, for example, that there is no rotational constraint on the rotation about the vertical axis of a welding torch. This enlarges the inverse kinematics solution space such that there are more options for the joint trajectory planner to avoid collisions.

Armstrong introduced a further cartesian path planning stack (collection of packages) called *Tesseract* for complex industrial motion planning applications with flexibility and modularity in mind [342]. The stack offers features such as fully and semi-constraint cartesian

motion planning and free space planning. A significant advantage of this package, particularly towards multi-directional deposition, is its capability to plan collision-free trajectories between two moving coordinate frames, therefore enabling planning of coordinated motion between a positioner and manipulator (see Figure 2.1).

While there is currently an open-source robotic AM software framework available (ROS AM) [343], providing limited 2.5-DOF slicing capabilities, tool path visualization, and AM-specific message definitions, significant limitations exist. Besides being limited to 2.5-DOF AM, there is no generalized, hardware-agnostic, and computer-integrated interfacing with the hardware available since post-processors generate instructions written in a hardware-specific language that only allows for open-loop execution.

2.6 In-situ process monitoring, modeling and control

Commercializing large-scale AM systems will require a high degree of self-regulation and automation to eliminate the need for highly skilled personnel to operate and monitor the fabrication process. To maintain compliance to mechanical, metallurgical, and geometrical specifications and design constraints, the bead geometry, layer geometry, weld pool temperature, and cooling rate need to be controlled in real-time as the component is fabricated (in-situ). A significant proponent of this is dictated through the optimization of the operating parameters based on the material system and the proposed tool path. Changes to the systems heat input (welding current/voltage, laser power), material feed rate, and deposition system travel speed can drastically alter the geometry of the bead of deposited material and ultimately the success of the manufacturing process. During the fabrication stage, sensors and optical systems can be used to monitor measurable aspects of the deposition and use this information as feedback to control the operating parameters of the fabrication platform. This allows for better adherence to the desired tool path generated during process planning while detecting and mitigating any defects created by non-ideal tool path planning (voids, gaps).

A basic control scheme for in-situ control of metal AM processes is shown in Figure 2.16. Process monitoring and control of the AM fabrication platform can be divided into three categories: condition monitoring, build monitoring, and environmental condition monitoring. The first category impacts the outcome of deposition and includes the power source (arc

voltage and current, laser power, etc.) for heat input assessment, material feed rate and deposition head motion speed for deposition rate estimation and evaluation, and shielding gas flow for oxidation level determination. This is achieved using electrical sensors to monitor instantaneous voltage and current, mechanical sensors for positional and feed rate estimation, and flow sensors for various fluid flow rates. The second category includes observation of the following conditions: geometric shape, build temperature, cooling rate, heat accumulation, melt pool state, and inferred metallurgical considerations. The typical sensing modalities include:

1. Optical sensors for evaluation of bead and layer geometry (profilometer, 3D scanner, charged-coupled device (CCD) & complementary metal-oxide-semiconductor (CMOS) cameras),

2. thermal sensors (infrared (IR) camera, pyrometers & thermo-couples) for molten pool condition and temperature monitoring, and overall build temperature monitoring.

Calibration and validation experiments are imperative to ensuring the functionality of the various in-situ monitoring methods. This is especially important for thermal sensors like IR cameras, where electrical sensors measure the thermal energy emitted from an object and convert it to a temperature. The emissivity, which is the efficiency at which natural objects radiate heat, must be determined to ensure that the temperature measured by the IR sensor is correct [344]. This can be done in situ using an emissivity probe or post mortem by measuring the temperature with a different calibrated thermal sensor, and adjusting the emissivity value until the temperatures match. With emissivity being a function of both temperature and surface roughness, unless extreme care is taken to validate the temperatures measured by infrared sensors, these results should be taken as qualitative [344].

Structural defects (absence of fusion, porosity, and cracks) can be evaluated by acoustic signal propagation measurement inside the part or even radio-graphic reflections. The third category can entail arc image, O_2 concentration, and acoustic propagation in the working area [85, 87, 321]. It should be noted that only optical and thermal sensors will be discussed explicitly in this paper. One of the main problems with monitoring and control of automated arc welding is the fusion of all the data in association with machine, component, and environment, which are time-variant and nonlinear transduction quantities [86, 214, 215].

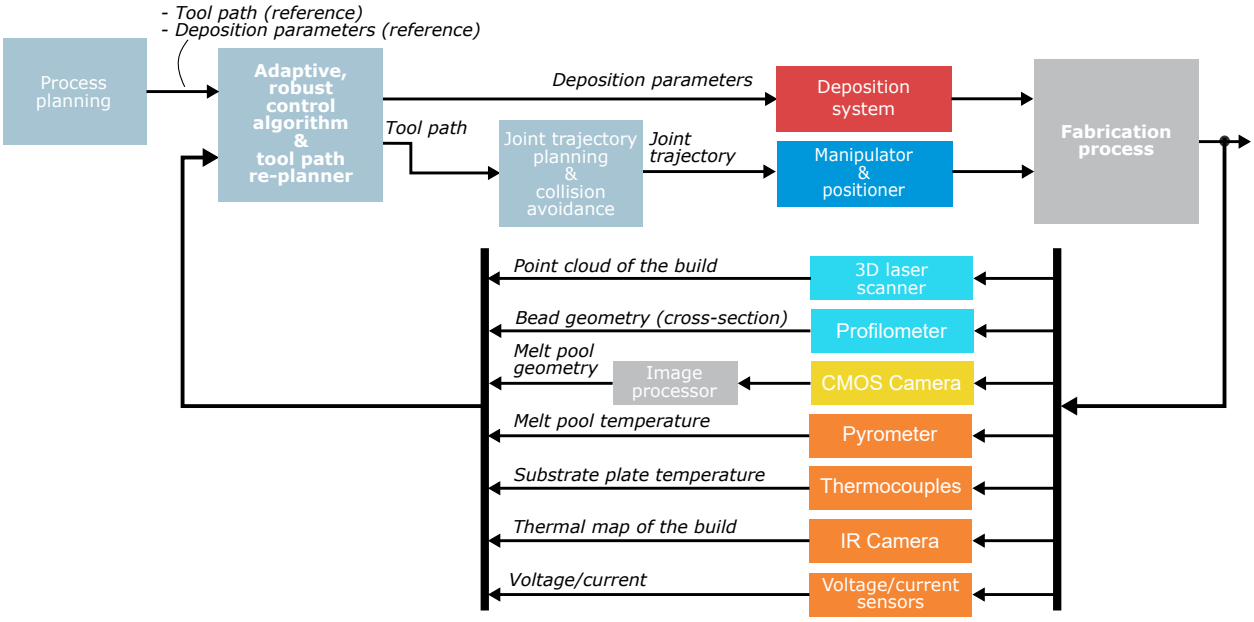

FIGURE 2.16: A basic monitoring and control schematic for robotic metal AM processes.

Some literature review works on in-situ sensing and control have previously been published. Tapia and Elwany reviewed multiple sensors primarily utilized to conduct studies on monitoring of metal-based AM [345]. Purtonen *et al.* also presented an overview of monitoring and control techniques used laser-based metal AM [346]. Everton *et al.* reviewed AM in-situ monitoring methods, research in the field of in-situ analysis for AM processes, and state-of-the-art for major process control technologies of metal AM [347]. They remarked that monitoring has been done mostly for process understanding rather than identifying defects and part discontinuities. This highlights the lack of holistic understanding of the implications that various processing conditions have on the metallurgical quality of the deposit, on both the macro and micro scale. Although process understanding is a step in the right direction, the collaboration between the different engineering disciplines involved in AM can extend the capabilities of process monitoring and control modalities to correlate the quantifiable manufacturing conditions to optimize metallurgical and mechanical properties.

This section will review how monitoring technologies are used in AM to provide feedback to the control algorithms that adjust bead geometry, melt pool temperature, and the layer surface geometry. More specifically, the physical monitoring systems and control algorithms proposed for wire-and-arc-based, plasma-based, and laser-based deposition technologies will be outlined and discussed. This will be followed by the work that has been done on the mathematical and physical models of these systems and how the two fields are coupled. The

materials that were used are shown in Table 2.8 It should be noted that due to differences in the physical nature of the different heat sources, not all of the sensor and optical systems are compatible with both laser and arc deposition systems.

2.6.1 Bead geometry

When joining two components using welding, the need for in-situ inspection of the welding bead geometry arises from the need to detect weld defects, as these typically lead to topological variations on the surface of the bead. This need to monitor and control the shape of the weld bead also extends to metal AM as an important means to ensure the quality of an additively manufactured component during fabrication. Observing and controlling the bead's adherence to the desired geometry (width, height, and curvature) determined during process planning is essential to avoiding voids, porosity, and geometrical inaccuracy of the final build. Bead height is also important to maintain a constant distance between the deposition head nozzle and the melt pool, known as the stand-off distance. For welding techniques, the stand-off distance dictates the voltage of the system.

One of the most common sensing methods used for detecting weld defects is based on laser line scanners (also referred to as profilometers) that are mounted on the deposition head and observe the cross-section of the bead's geometry (height, width, curvature) almost directly after deposition [374, 375]. Profilometers are now standard equipment in the manufacturing industry for various inspection tasks due to their high accuracy (∼0.02 mm), high sampling rate (∼1kHz), and ability to obtain the complete geometry of the bead cross-section, thus giving direct feedback on deviations from the desired bead geometry. Moreover, as the profilometer is moved along the bead while continuously measuring the cross-section, a 3D profile of the bead can be reconstructed to analyze surface defects, voids, and gaps. The working principle of a commercially available profilometer is illustrated in Figure 2.17. In

TABLE 2.8: Materials used in the various pieces of work discussed in Section 2.6

Steel	Ti	Al	Ni	Mg	Cu	Co-Cr	W	Non-metals	Not Mentioned
[85–87, 215, 321, 345, 346] [347–353] [354–360] [361–367]	[214, 321] [345–347] [368–370]	[321] [345–347] [365, 371]	[321, 345–347]	[321, 345, 346]	[345, 346]	[345, 346]	[345, 346]	[372, 373]	[374–377]

the following paragraphs, contributions to weld bead inspections using laser line scanning systems are reviewed.

Early work on a method for in-situ measurement of bead geometry during wire-and-arc welding using a profilometer with multiple deposited layers was introduced by Doumanidis and Kwak [348]. The bead profile obtained from the profilometer is used to validate a real-time analytical deposition model and provide feedback to a closed-loop control system for bead surface geometry control. Li *et al.* designed a scanning system and algorithms for feature extraction and dimension measurements to measure the dimensional properties of the weld, including groove width, bead width, filling depth, and reinforcement height, in root- pass and cap welding [374]. Flaws such as plate displacement, weld bead misalignment, and undercut were detected via the proposed feature extraction method. Huang and Kovacevic also

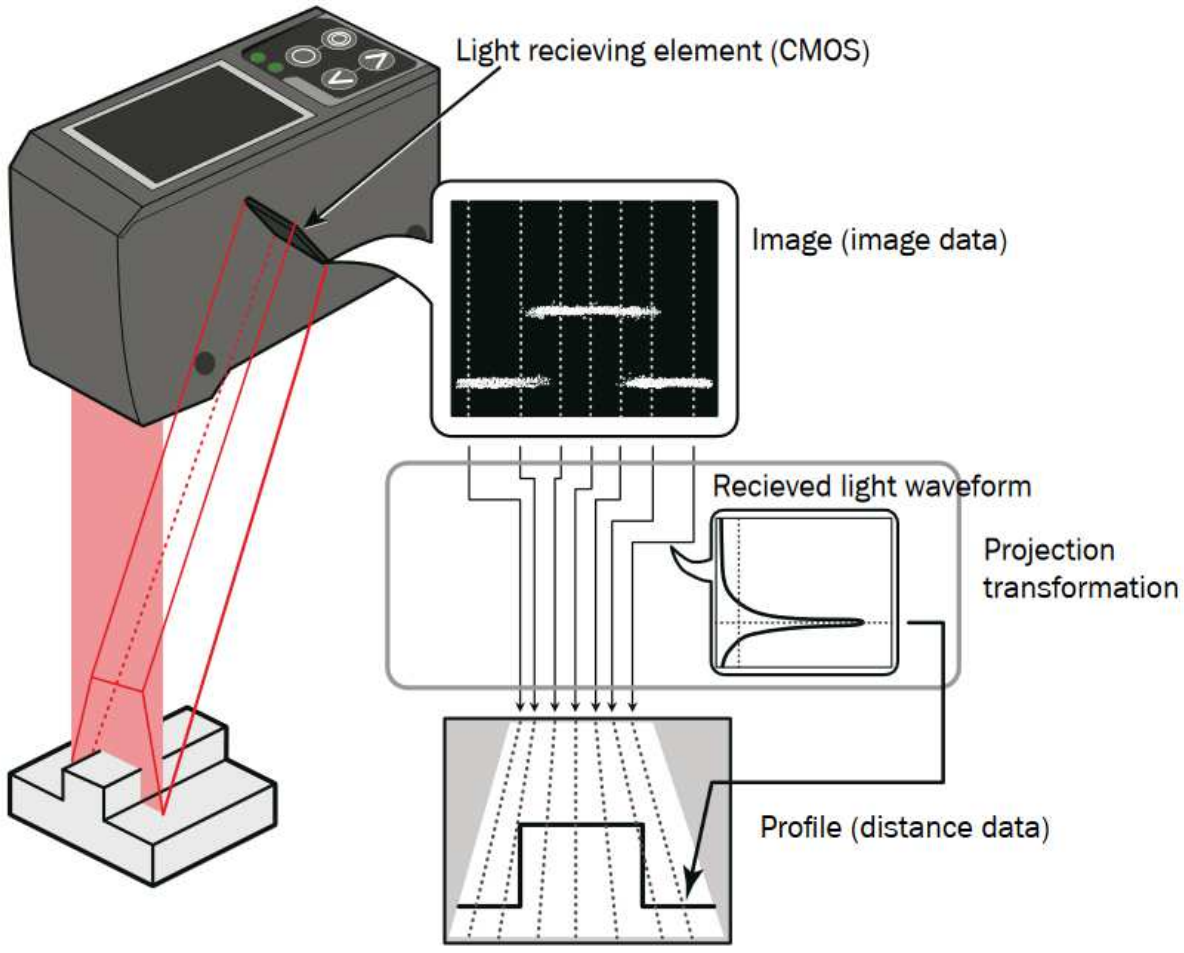

FIGURE 2.17: The operating principle of a laser line scanner (profilometer). (Image source: [378])

designed a scanning system for monitoring the weld joint [375]. Furthermore, a computer-vision-based seam tracking controller and a feature tracking algorithm were developed for tracking weld bead features such as the width and height of the bead.

Many methods for bead geometry control utilize the above-introduced monitoring modality. However, there are also camera-based monitoring methods used for control feedback. In the following paragraphs, the literature on bead geometry modeling and control methods and algorithms is reviewed. It should be noted that the optical vision system required some neural and narrow-band filtering to remove the intensity of the arc and allow for the observation of the weld pool [376].

Iravani-Tabrizipour and Toyserkani proposed a vision-based system for in-situ measurement of clad height during LDED [349]. A trinocular arrangement of three cameras pointed at the melt pool at an angle of 120° allows for a measurement of the melt pool from all directions. In order to infer the clad height, the melt pool shape is extracted from the raw image, followed by a perspective transformation. Then, detected elliptical features are provided as inputs to a neural network, which maps the shape of the elliptical features to the clad height. Experimental results show that the authors can obtain in-situ measurements at a rate of 10 Hz and with an accuracy of ±0.15 mm.

Xiong and Zhang developed a passive-vision-based method for measuring the bead geometry in-situ during multi-layer, single-track GMAW-deposition of a thin wall [376]. A schematic of the experimental setup is shown in Figure 2.18A. The vision system captures a side and top view of the weld pool and the solidification area after the weld pool. Basic image processing techniques such as edge detection combined with Hough transform are used to find the bead width and height. Images with overlaid bead geometry detection are shown in Figure 2.18B and Figure 2.18C. Validation experiments indicate a relative error of 5.7% between the ground truth and the vision-based measurement, which would be an error of 0.171 mm for a bead height of 3 mm. The passive-vision-based bead geometry measurement method proposed in [376] is then used by Xiong *et al.* for in-situ feedback control of the bead width [350]. The control algorithm–a segmented neuron self-learning Proportional Summational Differential (PSD) controller–takes the measured bead width as feedback and adjusts the torch travel speed to keep the bead width constant across layers. Disturbances in the bead width are due to variations in the shape of the previous bead and the slumping of

subsequent layers caused by accumulating heat. The experimental results show that better consistency in the bead width can be achieved across layers.

In a further application of the vision-based bead geometry measurement method introduced in [376], Xiong and Zhang propose a controller for layer height control [351]. This control algorithm–an adaptive, model-based controller–takes the measured bead height as feedback and adjusts the deposition rate to achieve a constant nozzle standoff distance and, by extension, a constant bead height. The adaptive component of the controller is based on a delayed first-order model and a controlled autoregressive moving average model to describe the relationship between deposition rate as input and nozzle standoff distance as output. The control system is comprised of two loops: an inner loop for conventional feedback control of the nozzle standoff distance and an outer loop for online identification of the process parameters and adjustment of the inner loop controller parameters. Noted bead height disturbances result from inter-layer temperature and shape fluctuations of previous layers due to heat accumulation. It is shown experimentally that the control algorithm maintains an accuracy of ± 0.5 mm.

In a further study, Xiong *et al.* used their previously developed vision-based bead geometry sensing system combined with their previously proposed segmented neuron self-learning PSD controller for adjusting the layer width [352]. The control variable in their scheme is the torch travel speed, and a first-order process model is considered. The experimentally verified range of layer width was 6 to 9 mm and a mean absolute error of 0.5 mm.

In order to address the issue of poor accuracy when depositing beads with sharp corners, Li *et al.* also proposed an adaptive process control scheme capable of guaranteeing a uniform bead morphology during WAAM. In their scheme, the tool path is divided into several segments at sharp corners [313]. For each segment, a permissible travel speed, subjected to the dynamic constraint, is selected, and the wire-feed speed is set beforehand according to a process model. In this method, matching the travel speed and the wire-feed rate leads to a uniform bead morphology among different segments.

Many of the above-reviewed control schemes use models for adaptive control of the various geometric features of the bead. Models that can be used in real-time to predict the bead geometry and related factors are important for adaptive and robust control schemes. As a requirement, these models must supply prediction updates at high sampling rates. Some suitable modeling methods for real-time control are reviewed next. Pal *et al.* developed

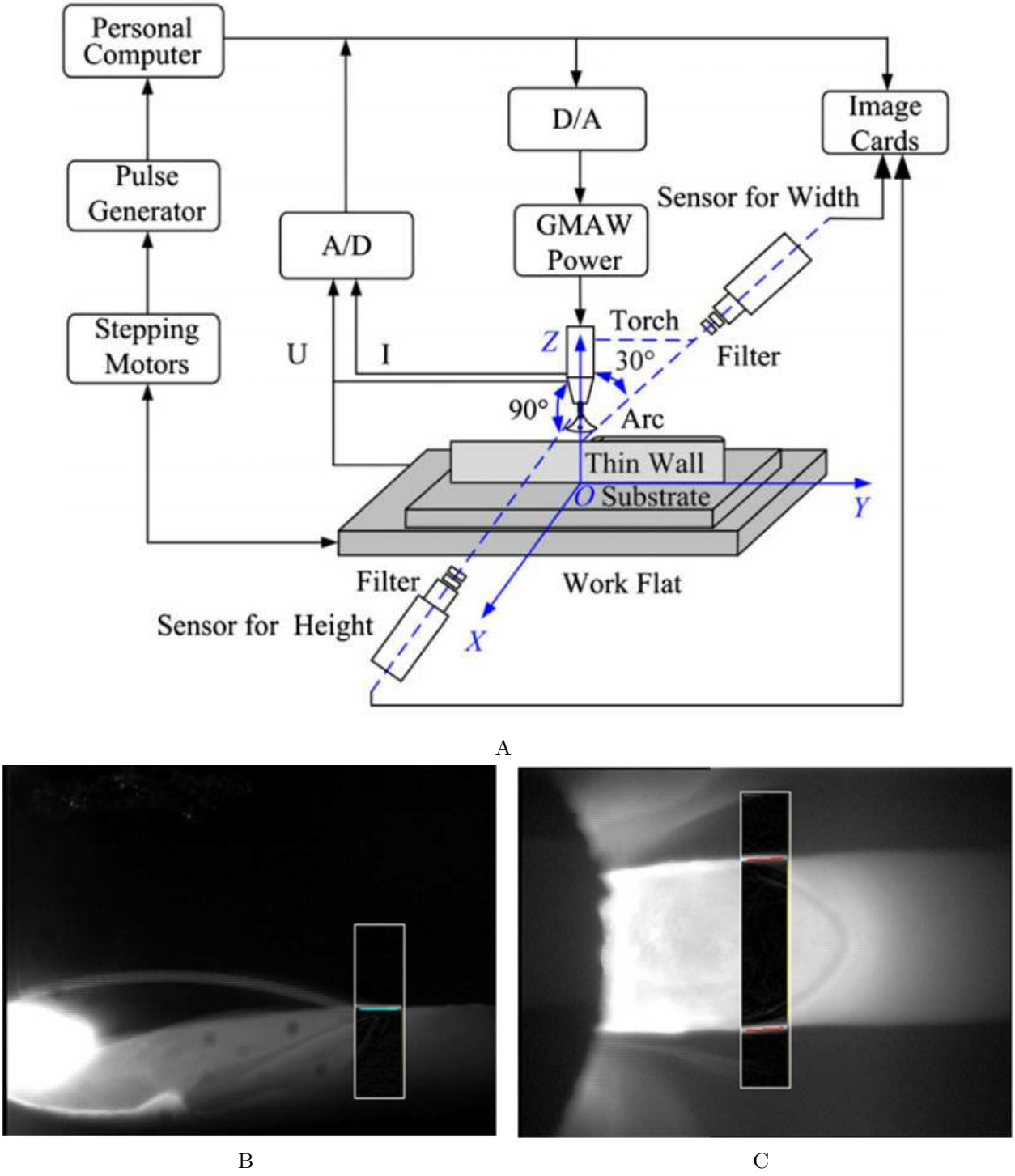

FIGURE 2.18: The vision-based method of bead width and height measurement as proposed by Xiong *et al.* [376] with a) a schematic representation of the experimental setup, b) detected bead height and c) detected bead width. (Image source: [376])

models for the prediction of the bead geometry using a Back Propagation Neural Network (BPNN) model, a Radial Basis Function Network (RBFN) model, as well as a regression model [353]. The bead width and height were predicted as a function of process parameters, including pulse voltage, back-ground voltage, pulse duration, pulse frequency, wire feed rate, and RMS welding voltage and current. Akkas *et al.* designed an Artificial Neural Network (ANN) and neuro-fuzzy system for predicting the bead thickness and penetration area while providing the three welding parameters of voltage, current, and speed [354]. Ding *et al.* trained an ANN model to specify welding parameters according to the bead width and height during WAAM applications [371]. Li *et al.* proposed a predictive ANN for specifying the offset distance of the beads in order to control the real center distance of the side-by-side beads according to the desired values of bead width, height, and the center distance between the beads for the WAAM process [355]. Ríos *et al.* presented an analytical process model which correlates layer width and height with the WAAM process parameters [368].

The limitation of camera systems such as the one introduced in [376] is that the measurements are obtained at a low sampling rate due to the need for computationally intensive image data processing. A further drawback caused by the increased processing time is a significant measurement time delay, which is not feasible for fast-response control algorithms. Profilometers are much more suitable for bead geometry measurement since the bead geometry is detected directly and does not have to be extracted from the pixel data of an image, thus increasing the sampling rate. They can also provide a 3D profile of the bead at higher resolution, which improves the accuracy of prediction algorithms that use historical data to make predictions. Many of the reviewed control algorithms that use cameras for feedback (e.g., [350, 351]) could obtain the same feedback information from profilometers at a higher sampling rate, possibly resulting in a more responsive and accurate controller design.

2.6.2 Layer surface geometry

As each layer is typically comprised of deposited beads, defects can be caused by inadequate process planning, such as inaccuracies in the overlapping model, voids caused by the path planning algorithm, parameter uncertainty, and deviations in deposition caused by the dynamics of the robotic system. Therefore, besides measuring and controlling the bead geometry, it is important to monitor the adherence of each printed layer surface geometry to the desired geometry determined during process planning and to ensure that voids and other

defects are mitigated by modification of the subsequent layer's tool path. A 3D laser scanner can obtain a point cloud of the surface geometry of a deposited layer.

In order to mitigate accumulating deviations of layer surface geometry during a print using a wire-fed LDED system, Heralic *et al.* developed a method for obtaining a 3D point-cloud of the layer surface geometry by moving a profilometer across the part after the completion of each layer [369]. 3D point cloud data was used to control the layer height during the print using an iterative learning controller (ILC). A comparison between an open-loop (without deviation feedback) and closed-loop (with deviation feedback) part print shows that the ILC can suppress deviations that would lead to a failed print during open-loop printing. The authors acknowledge that some issues exist with their used profilometer model as it was not designed for welding applications.

Also, to detect deviations from a desired layer surface geometry, Preissler *et al.* devised a stereoscopic camera system using the pattern projection method for polymer AM to obtain a 3D point cloud from a top-down perspective of the layer surface geometry after the completion of each layer [372]. Although the system is developed for polymer AM, the same proposed method is also fundamentally suitable for metal AM. Preissler *et al.* then used their developed 3D scanner to compare the desired surface geometry of the current layer to the measured layer surface geometry [373]. The 3D point cloud data is sufficiently accurate to detect deviations of 0.5% that can lead to a manufacturing failure.

2.6.3 Melt pool temperature and geometry

The primary devices used for monitoring the melt pool temperature and geometry are pyrometers, IR, CCD, and CMOS cameras. The temperature and geometrical features of the melt pool could be used as inputs to a predictive system, such as an artificial neural network, to specify bead width and height, providing predictions for model-based predictive controllers. In addition, thermal maps obtained from IR cameras may be used for monitoring thermal dissipation, temperature gradients, and thermal cycles throughout the build and the melt pool geometry [86, 214, 215]. In this section, various proposed measurement systems and control methods that use thermal and geometrical measurements for feedback are reviewed for the various deposition technologies. First, the literature on LDED is reviewed, followed by the literature on arc-based deposition methods (e.g., GMAW, GTAW).

A method for the temperature-based measurement of the melt pool size in powder-fed LDED using a CCD camera equipped with a narrow-band IR filter was introduced by Hu, and Kovacevic [356]. The laser power and, therefore, the melt pool temperature was controlled in order to control the bead width by adjusting the size of the melt pool. Experimental results showed that it is possible to effectively control the temperature of the processing zone by adjusting the width of the melt pool by controlling the heat input and metal powder feed.

Bi *et al.* proposed in 2006 the first thorough study on the feasibility of various in-situ measurement systems for LDED, such as a photodiode and quotient pyrometer temperature control system (TCS) to measure the temperature [357]. The deposition head is shown in Figure 2.19. Moreover, a CCD camera, which was coaxially aligned with the laser beam through mirrors, measured the size of the melt pool during powder-fed LDED. The introduced methods were verified experimentally to be suitable for temperature control. Furthermore, the influence of process parameters such as laser power on the temperature signal was investigated. Through adjusting multiple process parameters such as deposition head travel speed, material (powder) feed rate, and laser power, it was found that the laser power shows the strongest influence on the IR temperature signal. Based on the results obtained in the previous work, Bi *et al.* then proposed a closed-loop proportional-integral-derivative (PID) controller taking temperature feedback from a pyrometer to control the melt pool temperature [358]. The proposed controller was able to increase the dimensional accuracy of single-track, multi-layered walls. Bi *et al.* then further proposed a compact laser cladding head with integrated temperature sensors as previously proposed in [357] including a Germanium (Ge) photodiode for measuring the melt pool temperature and a CCD camera for monitoring the melt pool geometry [359]. A PID controller was used to keep the melt pool temperature constant by adjusting the laser power. The authors were able to significantly improve the quality of an additively manufactured airfoil by minimizing the accumulated temperature through their temperature control system. Tang and Landers proposed a melt pool model based on a first-order transfer function for LDED [360]. It was found that previously proposed models were not suitable for online temperature control due to their complexity. A digital tracking controller was designed to control the process quality via a *Kalman-filtered* feedback of a temperature sensor. However, it was concluded that the controller might not perform well with multi-layer depositions due to heat transfer issues. To further improve the laser cladding process to facilitate adoption in the industry, Bi *et*

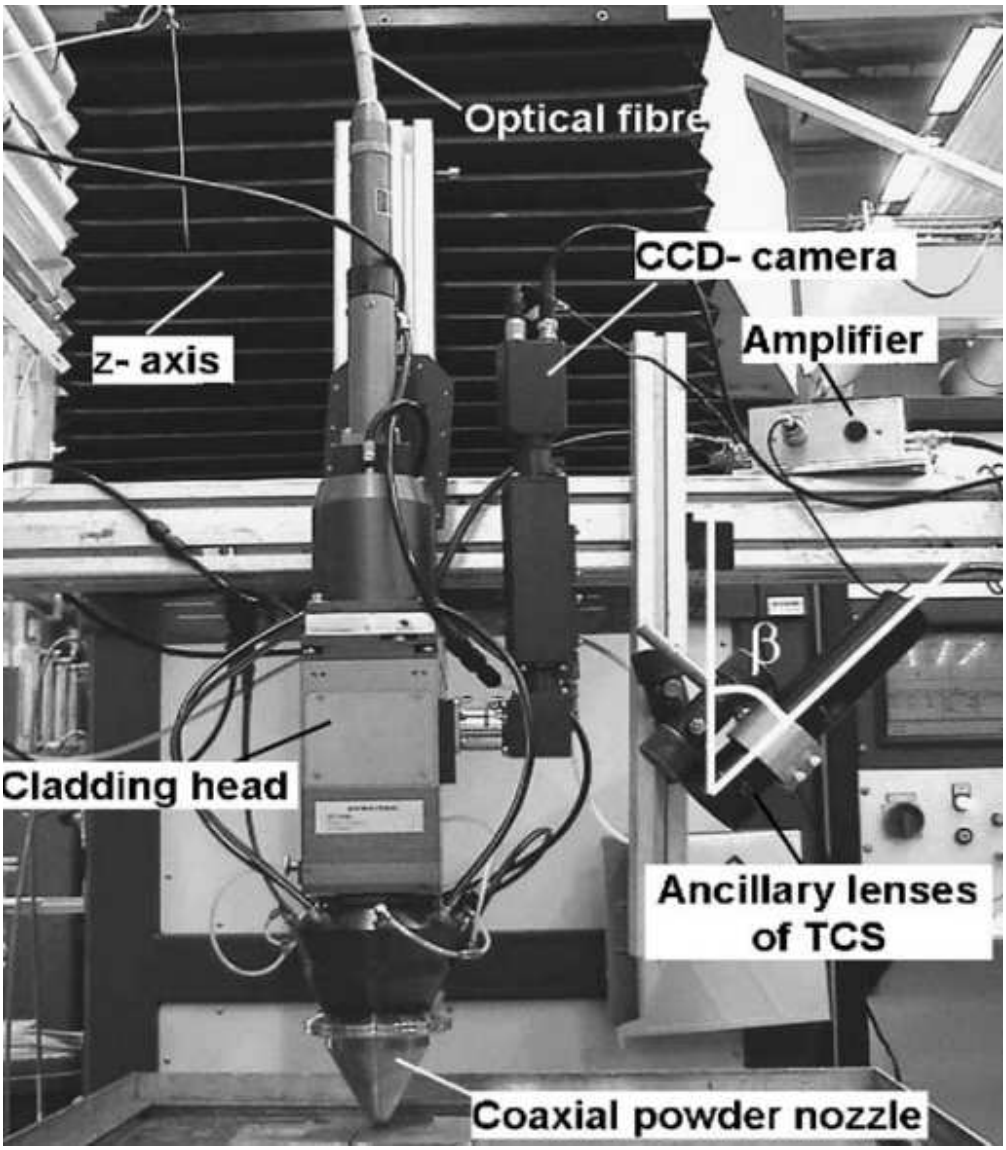

FIGURE 2.19: The experimental setup for temperature monitoring as proposed by Bi *et al.* [357]. (Image source: [357])

al. identified key factors influencing process monitoring and control in laser-based DED [361]. A single-color pyrometer was integrated with a powder feeding nozzle to monitor melt pool temperature to identify influencing factors. Geometry, power density, and oxidation were identified as affecting the process control performance. Nassar *et al.* presented a closed-loop control architecture for controlling the path plan during LDED to optimize the build microstructure. A temperature-based controller was implemented [370]. An application of in-situ temperature sensing for control of the solidification rate and, therefore, the microstructure during powder-fed LDED was proposed by Farshidianfar *et al.* [362]. Using

a CCD camera equipped with an IR filter to observe the melt pool and solidification area, the temperature gradient of the solidification area after the melt pool was obtained. The authors then proposed a PID-based controller for regulating the cooling rate, and therefore the microstructure, via adjustment of the deposition head travel speed. It was shown experimentally that the microstructure remained consistent due to the controlled cooling rate.

Doumanidis and Hardt proposed a multi-variable adaptive closed-loop controller using temperature feedback of heat affected zone in arc welding [363]. They considered a structured heat model with uncertain parameters. In addition to the layer geometry sensing via profilometer described in Section 2.6.1 for wire-and-arc welding, Doumanidis and Kwak also used an infrared camera to measure the temperature and geometry of the melt pool [348]. The in-situ melt pool measurements were then used to identify the parameters of a lumped-parameter model for the melt pool that models the relationship between its geometrical and thermal properties and the process parameters, including torch power, material feed, torch angle, and motion. This model was then utilized for real-time bead geometry control. In order to overcome sensory delay, a Smith predictor was used. The overall RMS error between the desired and achieved layer geometry was 0.23 mm. Wu et al. also utilized a CCD camera in combination with a narrow-band IR filter to construct a passive vision sensing system for imaging the weld pool during constant-current GTAW [364]. The images were then processed to obtain the melt pool size. Lü *et al.* proposed a multiple-input single-output (MISO) adaptive controller for adjusting the width of the weld pool during GTAW utilizing feedback of wire feed rate, welding current, and topside image of the weld pool [377]. A backpropagation neural network (BPNN) model was used to estimate the backside pool width and compared it with the desired value. Xu *et al.* focused on two issues in their study on GTAW and GMAW: capturing a clear weld image and developing an image processing technique for feature extraction [365]. For the former, a novel passive vision system taking advantage of a CCD camera with a moveable motorized filter, which could cross out disturbances of the arc light during seam tracking, was proposed. For the latter, image processing algorithms encompassing restoration, smoothing, edge detection, false edge removal, and edge scan were developed. Babkin and Gladkov introduced a new graphical method for GMAW welding parameter determination [366]. The influence of the workpiece temperature control over the geometrical preciseness of the deposited layer was highlighted. Feng *et al.* used a CCD camera to monitor the weld pool surface in GTAW [367]. The contribution was

to compute the height of the mirror-like bead surface via processing of the reflection image of the reversed electrode on the bead surface, knowing its constant tip-to-workpiece distance.

2.7 Post-processing

As mentioned above, the microstructure is highly dependent on the local cooling rate the part experiences during deposition. Processing parameters, such as travel speed, dwell time, material feed rate, and travel direction, affect the solidification velocity and the resulting crystalline morphology [379]. The layer-by-layer variance in processing conditions results in non-uniform and transient temperature gradients throughout the build, leading to an anisotropic microstructure [99]. Thus, the mechanical properties have a directional dependency, which is undesirable for many applications. Heat treatment is used to manipulate and control the final microstructure, ensuring optimum performance when the final part is placed in service.

One of the more important heat-treating processes for AM is annealing, where the material is held at elevated temperatures for extended periods of time and then cooled at various rates. The different annealing treatments for AM deposits are shown in Figure 2.20. Residual stresses result from the unique thermal cycling that occurs during the AM deposition process [380]. Low-temperature annealing (T1 in Figure 2.20) improves atomic diffusion, allowing for dislocation motion and annihilation, relieving some of the induced thermal stresses. The significant strain induced by residual stresses can provide the driving force for the nucleation and growth of stress-free equiaxed grains, further reducing the internal stress. This phenomenon is known as recrystallization and has also been observed when stress relieving AM deposits [381]. Increasing the annealing temperature (T2 in Figure 2.20) to a point where all elemental constituents are dissolved in a single solid phase is known as a solution annealing heat treatment. The deposit is then quenched to prevent any diffusion or phase formation, resulting in a supersaturated solid phase. This is followed by a precipitation heat treatment, also referred to as aging, where the deposit is heated to a temperature (T3 in Figure 2.20) where diffusion is energetically favorable. This results in the nucleation of finely dispersed precipitates, or the formation of desirable secondary phases, improving the mechanical performance [382]. This section will outline the different heat treatments that are common for the materials discussed in 2.3.4. First, the conventional heat treatments

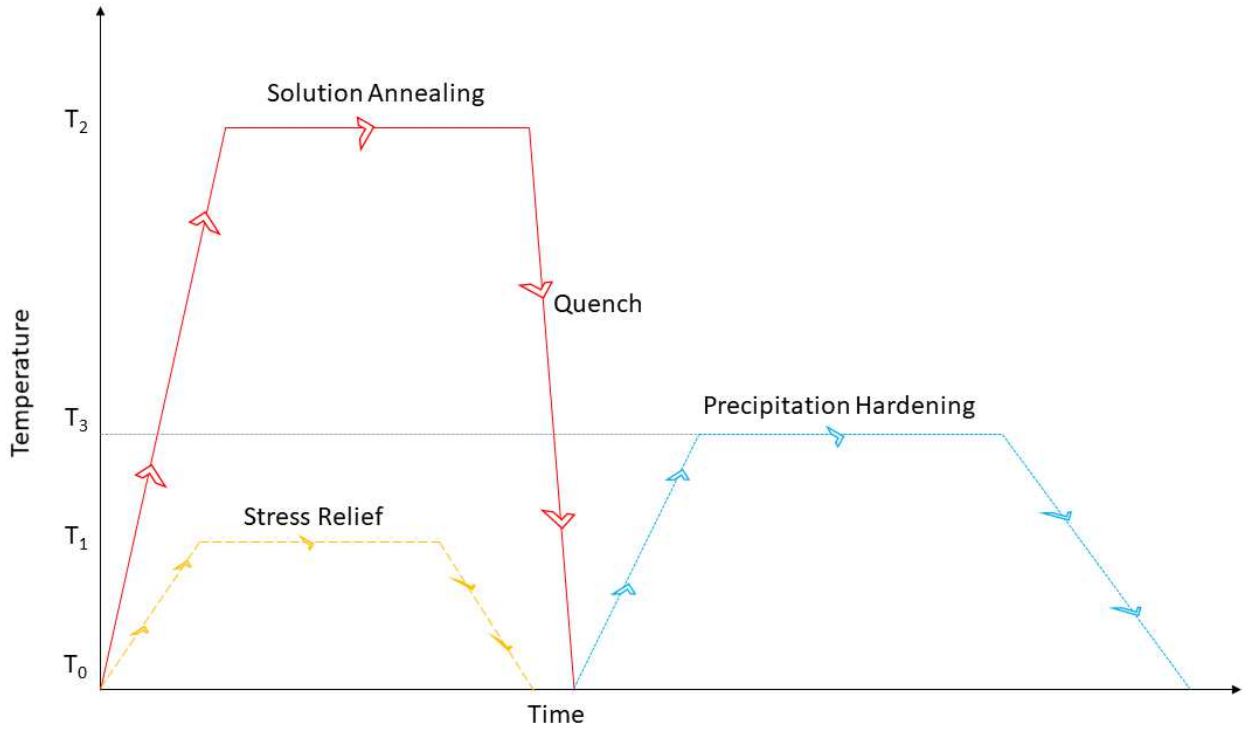

FIGURE 2.20: A re-imagining from [382]. The different thermal cycles for the heat treatments typically conducted on AM deposits, where the red solid line represents the solution annealing, the blue dotted line represents precipitation hardening, and the yellow dashed line represents stress relieving heat treatments. Note that T1, T2, and T3, as well as the hold times, heating and cooling rates are material specific, and the depicted plots are not accurate representations.

will be discussed where applicable to outline each heat treatment step's purpose and give insights on how heat-treating AM parts may result in different microstructures with the same heat treatment. This will lead to the as-built microstructure for each material when using different heat sources. Then a general overview on what heat treatments have been done by other researchers, and how it changes the as-built microstructure and corresponding performance will be discussed. It should be noted that the scope of this section is limited to studies on DED. The materials that require further investigation will be identified. Furthermore, the heat treatments presented are generalized to highlight the effects the different heat treatments have on microstructure and mechanical performance. Thus, details including temperature, hold times, and cooling rates may not be mentioned. Finally, any mention of an aging process is done post solutionizing and not to the as-built structure due to the limited researchers utilizing a direct aging process directly after printing. This is thought to be attributed to the anisotropic microstructure of the as-built parts. Although there is an

extended solid solution due to the rapid solidification, the nucleation of precipitates would not be homogeneously distributed throughout the part. Therefore, the mechanical properties would still be directionally dependent.

2.7.1 Titanium Alloys

The scope of this section is limited to Ti-6Al-4V (Ti64) due to the abundance of studies conducted on this material system. There are other Ti alloys that are being studied, such as TC21 [100, 263, 265, 383–385], near β Ti alloys [386–389] and near α Ti alloys [390], but they will not specifically be mentioned.

The heat treatment of Ti64 typically includes solution annealing and aging at a range of temperatures depending on the desired mechanical properties. Typically, the solution temperature is below the β transus temperature [391]. Lower annealing temperatures result in mostly α, with some β at the grain boundaries. The higher the annealing temperature, the higher the fraction of β that will form upon cooling. However, there is a decrease in solubility of V as the temperature increases, causing the β phase to turn to α' with quenching. If any β is retained after solution treatment at higher temperatures, a martensitic transformation to α' will be induced when plastically deformed [392]. Higher cooling rates are more desirable for Ti64 to maximize the amount of supersaturated β or α', which can be decomposed to α precipitates during aging [391, 393].

Laser-based AM techniques result in a mix of columnar and equiaxed grain morphologies, depending on the thermal history of the part. Equiaxed grains tend to form closer to the edges due to the higher thermal gradient achieved at these locations [98–100, 264]. The microstructure consists of primary β with α lamellae, which form in colonies, Widmanstätten or basketweave morphology. These colonies are more prevalent along prior β grain boundaries and close to the β transus lines from the interlayer passes.This microstructure has been seen for both powder and wire fed processes [98, 100–102, 131–134, 171]. Electron beam and plasma techniques have also shown to have similar microstructures, with martensitic α' and α laths in a Widmanstätten or basketweave morphology, and a small amount of acicular α [32, 33, 148, 150, 152, 192, 193]. Defects such as pores are also prevalent in the as-built parts that cannot be removed with standard heat treatment methods [102, 394–396]. Lower annealing temperatures tend to lead to coarsening of the α laths to more plate-like

morphology, with interplate transformed β [131, 134]. The α plates transform into "crab-like" morphology closer to the β transus temperature [100]. Furthermore, recrystallization of β grains begins at higher solution temperatures, while the primary α laths increase in aspect ratio and decrease in volume percent. The formation of β with solution treatment has been shown to increase the corrosion resistance of AM Ti64 parts. The coarsening of the α laths decreases strength while increasing the elongation [101, 397]. Increasing the annealing time decreases the aspect ratio of the α phase while also inducing a higher amount of precipitation of secondary α in the retained β phase [98, 193]. This causes an initial spike in strength, but this decreases as the secondary α coarsens. Increasing aging times decreases the volume fraction and aspect ratios of primary α laths while increasing the volume fraction of fine secondary α. Increasing aging time slightly coarsens the secondary α but decreases the width of the primary α, causing slight increases in the strength and ductility. Aging times over 8h will result in the globularization of the α laths. These precipitates tend to coarsen with higher subsequent aging temperatures [101]. Heat treatment has shown to reduce hardness due to grain coarsening and dislocation annihilation [100]. Under dynamic loading, heat treatment may reduce strain rate sensitivity while increasing the risks of adiabatic shear localization [98].

2.7.2 Ni Alloys

This section will discuss the heat treatment protocols of both Inconel 718 and Inconel 625. A summary of the standard heat treatment and corresponding microstructure will be presented for each material, followed by a tabular summary of the effects of heat treatment on mechanical performance.

2.7.2.1 Inconel 718

Heat treatments for industrial casting and forging operations of In718 follow solution treatment and age protocol outlined in AMS-5383D [398], and a solution treatment and aging protocol discussed in AMS-5662M [399], respectively. The high-temperature mechanical properties of In718 are attributed to the precipitation of the γ"(Ni_3Nb) and γ' (Ni_3(Al,Ti)), which forms in the γ matrix [400, 401]. The elements with large atomic radius are rejected from the γ phase during solidification. This causes the formation of a Nb-rich laves phase

($(Ni,Cr,Fe)_2(Nb,Mo,Ti)$) that depletes the γ matrix of Nb, preventing the formation of γ" and γ' [402]. This diminishes the ductility, fracture toughness, fatigue, and creep-rupture properties of the alloy [403]. Thus a proper heat treatment protocol must be followed to redistribute the Nb and control the cooling rate to maximize the formation of γ" and γ'. Preforming solid solutionizing alone at 980°C does not alleviate the Nb segregation in AM deposits, like that of wrought In718 alloys [158]. The partial dissolution of the laves phase promotes the formation of acicular δ phase, reducing the formation of γ" and γ'[158].

There are limited publications discussing the effects of different heat treatment protocols on the microstructure and corresponding mechanical properties of DED additive manufactured In718. Thus, this is an area of research that requires more investigation. Some of the heat treatment steps being utilized are homogenization, solutionizing, and aging [158]. Homogenization alleviates residual stress, increases grain boundary strengthening, and eliminates segregation of Nb [119, 122, 404–407]. Solutionizing results in needle-shaped δ precipitation, which pins the grain boundaries impeding grain growth [158], while aging is done to precipitation harden In718 by forming γ" precipitates [407, 408]. A summary of the mechanical properties comparing conventional manufacturing methods to AM was presented by Hosseini *et al.* and is shown below in Figure 2.21 [409].

2.7.2.2 Inconel 625

The macrostructure of as-built In625 produced by AM is a range between cellular and columnar dendrites, depending on the specific thermal history of that region [160, 410]. The

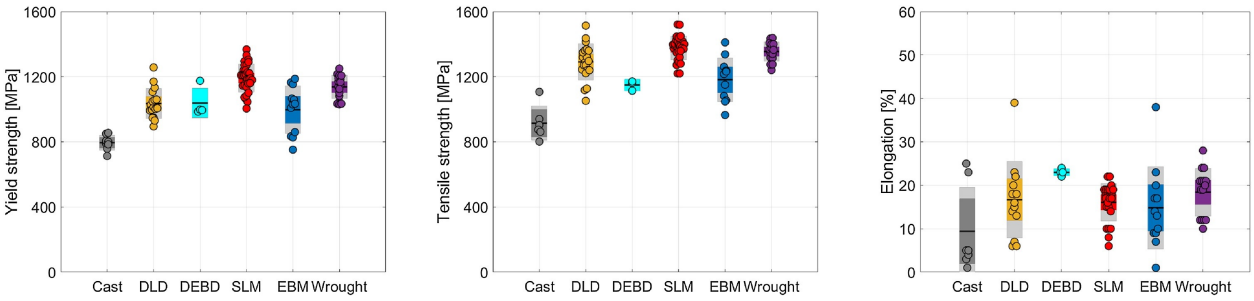

FIGURE 2.21: A comparison of the mechanical properties (a) yield strength, b) Ultimate tensitle strength and c) elongation) of heat treated In718 alloys produced by conventional manufacturing methods (wrought and cast) and AM methods (DLD, DEBD, SLM, and EBM) [409]

columnar dendritic structure has been seen to be stable up in heat treatments up to 1000°C, which becomes fully equiaxed at 1200°C [411, 412]. The high solidification rate and temperature gradient achieved during additive manufacturing are problematic for In625 due to the segregation of Nb and Mo in the interdendritic regions [413]. This causes the formation of M_6C, $M_{23}C_6$, and eutectic γ + Laves phases forming between the primary γ dendrites. There are also trace amounts of FCC γ' (Ni_3(Nb,Al,Ti)), BCT γ" (Ni_3(Nb,Al,Ti)), and orthorhombic δ (Ni_3(Nb,Mo)) when subject to the rapid solidification conditions experienced during laser-based AM techniques [414]. Plasma-based techniques have been shown to lead to course pockets of Laves phases, MC, and larger needle-like δ precipitates in the as-built condition [34, 222, 415]. Dinda *et al* found that solutionizing at temperatures above 1000°C cause the precipitation of γ" (Ni_3Nb) in the γ matrix, increasing the microhardness [411]. Xu *et al.* found that a solution treatment followed by aging results in partial dissolution of the Laves eutectic, resulting in the redistribution of Nb for the precipitation of the γ" and γ' precipitation improving the tensile and yield properties [415]. Hu *et al.* found that the dissolution of the Laves phase is proportional to the solutionizing temperature, causing an increase in ductility but a decrease in the tensile strength of the alloy [412].

2.7.3 Steels

This section will discuss the post-processing of 316L and 17-4 stainless steel. This will include the microstructural changes from the as-built condition with heat treatment and the corresponding changes to the mechanical properties.

2.7.3.1 316L Stainless Steel

AM of 316L typically results in an ultra-fine and cellular columnar dendritic grain structure due to the rapid cooling rates experienced during the building process [416, 417]. There have also been reports of large amounts of anisotropic crystal orientations and grain sizes in 316L deposits from the complex thermal cycling seen in all AM techniques [418, 419]. A common defect is silicide, and oxide inclusions, which is attributed to possible oxygen contamination in the feedstock, or during the building process [416, 418, 420]. Pores are also a common defect found in AM deposits of 316L, which are detrimental to the mechanical properties and corrosion resistance [417, 421]. Saeidi *et al.* found when using a laser-based

AM technique that the single-phase FCC austenitic structure seen in the powdered feedstock is mostly conserved in the as-built condition, with varying amounts of BCC ferrite. Sub-grain boundaries were found to be enriched in alloying elements such as Ni and Mo [418, 419, 421, 422]. Plasma AM methods typically resulted in columnar structures of austenite (γ) of varying coarseness depending upon the location with respect to the fusion line. The inter-columnar area consisted of vermicular δ ferrite and σ (FeCr)intermetallic at the γ/δ interface [143, 147, 423]. The formation of the σ phase has also been reported in EBM, and LMD of 316L [422, 424]. The brittle σ phase acts as a crack nucleation site that could lead to decreased ductility, while both the δ and σ drastically reduce the corrosion resistance of the part [423, 425, 426]. Thus, heat treatment is typically used to increase the ductility and decrease the susceptibility to corrosion [427]. The effects of heat treatment of additively manufactured 316L using DED have not been thoroughly investigated and is an area that requires further research. It has been seen that heat treatments up to 800°C provide no apparent changes in the microstructure, but mechanical properties, such as tensile strength and hardness, tend to decrease when compared to the as-built deposit [417, 421]. This has been attributed to dislocation annihilation at the sub-grain boundaries post-heat treatment [417, 418]. Performing a homogenization heat treatment has been shown to decrease the amount of BCC δ ferrite and helps eliminate the anisotropic grain structure seen in the as-built condition [417]. However, exposure to high temperature for a prolonged period increases the average grain size, which decreases the strength while increasing the elongation of the deposit [419]. Chen *et al.* found that the σ phase can be eliminated with heat treatment of 1100°C for 1h, while the delta phase can be eliminated at 1200°C for 4h, resulting in a decrease in strength and increase in ductility and corrosion resistance [423].

2.7.3.2 17-4 PH Stainless Steel

The industrial standard heat treatment of 17-4 PH hot-rolled and cold-finished bars and shapes follows ASTM A564/A564M. This standard outlines a solution treatment of 1040± 15°C for 30min, followed by several different options for age-hardening treatments [428]. The goal of the solution treatment is to control the amount of retained austenite due to its higher solubility of Cu, decreasing the amount of precipitation during the aging process [429, 430]. The solution treatment results in a martensitic phase with a lath-like morphology that is supersaturated with Cu and Cr [431]. There is also a trace amount of δ ferrite that contains

some Cu precipitates [432]. The steel is then quenched and aged to cause the precipitation of Cu in the supersaturated martensitic laths [431]. The peaked age condition (H900 in ASTM A564/A564M) yields the highest hardness after aging at 480°C for 1hour, due to the coherency of the Cu particles and the retention of the large amounts of dislocations found in the martensite [428, 431, 433]. However, peak age condition is not suitable for all applications, thus implementing an overaged microstructure (H1100 in ASTM A564/A564M), with courser copper precipitates and slightly tempered martensite, is more desirable [434, 435]. The as-built structure of 17-4 produced using laser-based AM results in a fine martensitic lath microstructure, with some retained austenite in the inter-lath regions, due to the re-heating of previously deposited material during the deposition process [30, 436, 437]. Arc heat sources result in dendritic martensite, with δ ferrite in the inter-dendritic regions and small amounts of retained austenite [144, 204]. Solution treatment has been shown to convert the retained austenite to nearly 100% lath martensite [144]. Any retained austenite is attributed to the ultrafine austenite grains suppressing the transformation of austenite to martensite [437, 438]. Peak aging following the solution treatment allows for the formation of fine Cu precipitates with small amounts of retained austenite, while over aging results in an increase in the retained austenite concentration. The diffusion of austenite stabilizing elements like Cu and Ni to form precipitates decreases the martensitic transformation temperature below room temperature, resulting in an increase in retained austenite [431, 439]. Furthermore, dissolved nitrogen from the building atmosphere can drastically increase retained austenite, requiring longer aging times to achieve peak performance [254]. Many researchers have also found Mn, Si, and O inclusions that form at the grain boundaries [436, 437]. The mechanical properties after solution and aging treatment typically increase in all facets compared to the as-deposited conditions. It is also found to eliminate the anisotropic properties, typically seen in the AM deposits [30, 144]. The mechanical properties after solution and aging heat treatment have been shown to be comparable to conventional manufacturing techniques [144]. However, there is a need for further investigation on whether this is true for all DED technologies and whether this statement holds true for fatigue and corrosion properties for 17-4 PH.

2.7.4 Al Alloys

The post-fabrication heat treatment discussed in this section will be limited to the hypo-eutectic alloy AlSi10Mg, as it is the most studied of the Al alloys. An outline of the standard heat treatment will be reviewed, followed by the as-built and post heat treatment microstructure, and the corresponding effect on mechanical properties.

The typical heat treatment for Al-Si alloys is a T6 treatment, which is a solution heat treatment at 535°C, quench and artificial age hardening protocol at 158°C for 10h, outlined in the ASM Metal Handbook vol. 2 [440]. The solution treatment is done close to the eutectic temperature of the alloy to ensure the dissolution of Mg-containing phases, homogenize the alloying elements, and create spherical eutectic Si particles. The quench is done to preserve the vacancy and solute concentration, while aging is done to form a uniform distribution of particles, increasing the strength [441, 442]. The microstructure of as-built AlSi10Mg can consist of a columnar or a rod-like dendritic structure, depending on the heat input of the energy source [114]. However, the cellular structures can vary in coarseness depending on the spatial thermal history of the sample [112]. LMD of AlSi10Mg has also shown to form cellular and divergent dendrites [109, 277]. The dendrites are α-Al, while the interdendritic regions are eutectic Si [109, 110, 114]. There are also cases of Mg_2Si precipitates in the interdendritic regions [110, 112, 114, 443]. Laser-based techniques have shown to result in deposits that are not fully dense [109, 110, 115] and heat treatment has not been shown to alleviate this issue [114]. Heat treatment of AlSi10Mg has shown to decrease the solubility of Si in the primary α dendrites, suggesting that Si is rejected from the primary dendrites to form Mg_2Si [109]. This is due to the supersaturation of α-Al resulting from the rapid solidification and undercooling of Mg_2Si. Increasing the solution temperature or time tends to coarsen the Si particles while also decreasing the number of particles due to particle coalescence and Oswald ripening [109, 444]. Lv *et al.* studied heat treatment of LMD AlSi10Mg and found that the tensile properties increase with a T6 heat treatment[109]. The formation of a fine cellular α-Al dendrites supersaturated with Si, and the localization of Mg at the grain boundaries of the as-built samples, increase the hardness of the primary dendrites. However, the T6 heat treatment allows for the diffusion of Si, which causes a slight reduction in hardness [109]. Most publications on DED AM of AlSi10Mg use L-DED; thus, more investigation using other DED methods with AlSi10Mg needs to be done. Furthermore, additional work

is required to determine the optimal heat treatment protocol for AlSi10Mg using all types of DED technologies.

2.7.5 Co-Cr Alloys

This section will discuss the heat treatment of AM deposited Co-Cr alloys. The focus will be on Stellite 21, and Stellite 6 Co-Cr-Mo alloys, as they are the most studied. An outline of the standard heat treatment will be reviewed, followed by the as-built and post heat treatment microstructure, and the corresponding effect on mechanical properties.

For cast Co-Cr-Mo alloys complying with ASTM F75, no standard heat treatment is included [445]. The as-cast condition of this composition typically consists of FCC γ Co, a σ intermetallic, and M_26C_6 interdendritic carbides [446]. The goal of heat treatment is to homogenize the microstructure, remove cast defects and improve mechanical properties through precipitation dissolution [447–449]. The most common treatment consists of a solution treatment at temperatures of approximately 1200°C for a range of times from 1-4 hours [448, 450, 451]. However, for pin-on-disk and hardness tests, increased performance has been shown when aging is included in the heat treatment [452, 453]. Laser deposited Stellite 21 typically consists of a range between columnar and equiaxed dendrites, with a σ intermetallic, and $M_{26}C_6$ in the interdendritic regions [129]. WAAM of Stellite 6 results in a dendritic structure with Co-rich FCC γ primary dendrites, and eutectic γ-Co with M_yC_3 carbides [183]. Porosity has also been found in laser deposited Co-Cr-Mo deposits [454]. For LENS of Co-Cr-Mo, increasing the solution treatment time leads to decreases in size and amount of carbides due to improved kinetics for carbide dissolution at higher temperatures. This is opposite to increasing the aging time, which increases the precipitation concentration, due to decreases in solid solubility of carbide forming elements at higher temperatures [127]. Depending on the particular application of the part, the resulting microstructure from the heat treatment will yield different performance results. Longer solutionizing times with no aging may increase corrosion resistance due to high Cr contents in the matrix [453]. Variations in temperature and hold times will result in different carbide sizes, morphologies, and distributions, which will result in a range of properties [127, 455].

2.7.6 Mg Alloys

The use of Mg alloys for AM has not been explored in as much depth as the other alloys presented in this work. Thus, no work has been published on the effects of heat treatment on the microstructure and corresponding properties of Mg deposits.

2.7.7 Copper Alloys

The majority of the work on Cu alloys for DED technologies has been on WAAM of nickel aluminum bronze. Shen *et al.* deposited nickel aluminum bronze using WAAM and found that the as-built microstructure mainly consisted of Widmanstätten α phase and martensitic β phase [164, 165, 456]. Dharmendra *et al* found no retained β, but instead found κ_{II-IV} precipitates in the interdendritic regions[457, 458]. Homogenization at 900°C and quenching transformed the microstructure to equiaxed and columnar α with some retained β' and κ phases. This tends to decrease the strength and hardness but increases the elongation to failure, which is attributed to the absorption of some of the previously formed κ phases [458]. With post quench tempering, it was found that the equiaxed grains disintegrated to columnar grains, while the already formed columnar grains coarsened. Increasing the tempering temperature resulted in the elimination of the retained β and κ lamellae, and particles begin to form [164, 165]. This causes the mechanical properties to increase closer to the as-built condition. However, the distribution of κ phases becomes more uniform, decreasing the spatial variation in properties [458]. However, further increasing the tempering temperature results in significant coarsening of the κ phase, causing a decrease in performance [165].

2.7.8 Tungsten Alloys

As mentioned previously, some work has been done on DED of pure W [459], W-Ni alloys [130], W-Fe alloys [460], and tungsten heavy alloys [15]. However, no work has been conducted on how post-processing affects the microstructure and the corresponding properties.

2.8 Challenges & future perspectives

This work provides a holistic overview of the current state of the art in large scale robotic AM, from process planning to the microstructure and performance of the final component. Although the contributions made by the many researchers in progressing this field have been substantial in the last few decades, the technology is still in its infancy. Dr. Hannes Gostner compared AM to celestial observation at the 2019 Holistic Innovation in Additive Manufacturing (HI-AM) conference in Vancouver. He stated that AM is currently in the technological stage of Galileo's telescope and that the capabilities have the potential to be as revolutionary as the Hubble telescope. However, the boulder has a long way to be pushed before the innovative pinnacle can be crested. The lack of the field's maturity is also evident from the lack of finalized qualification and certification standards (see Table 2.1). The majority of the standards listed in Table 2.1 are currently still in draft status. Robotic large-scale AM as a sub-category within AM as a whole is highly interdisciplinary–like any other groundbreaking and paradigm-shifting endeavor. The major engineering and science disciplines involved in large-scale robotic metal AM include computer science, electrical engineering (mechatronics-, control- and systems engineering), materials engineering, and mechanical engineering. In addition, each of the process workflow stages as outlined in Figure 2.3 are also highly coupled. For example, a process plan consisting of a deposition system motion sequence and parameters generated by the process planning stage will affect the thermal distribution, which will affect the amount of residual stress and heat accumulation, and microstructure and corresponding mechanical properties.

Naturally, computer scientists, mechatronics-, control- and systems engineers are predominantly concerned with issues relating to their particular domains and can not necessarily appreciate the coupled challenges faced by materials-, and mechanical engineers. Therefore, a close and direct collaboration between diverse research groups is required to progress this technology further. Extensive collaboration and sharing of information will result in more holistic studies on, for example, how different path planning strategies affect the surface roughness and microstructure of an as-built component. This will give rise to new information on the different strategies that can be implemented to solve the current challenges, such as residual stress, porosity, and anisotropic microstructures. This need for collaboration has already been recognized, which has resulted in the creation of networks such as the NSERC Holistic Innovation in Additive Manufacturing (HI-AM), America Makes, and

others. However, the lack of research-level fabrication of large-scale parts makes it hard to fully understand the challenges that will need to be overcome to make this a viable commercial process. It is currently speculated that overcoming the current challenges of fabricating lab-scale coupons will translate to large-scale parts. The true challenges that lie ahead for large-scale AM will not be revealed until more researchers begin to fabricate parts outside of a lab setting.

This section summarizes and discusses the largest knowledge gaps in the topics outlined in Section 2.3 to Section 2.7, followed by a holistic view of the challenges that must be overcome to commercialize large scale AM. The subsections will be structured where the challenges of each topic will be addressed, followed by the authors' suggestions on the future of research areas pertaining to the topic.

2.8.1 Process planning

Current path planning methods are generally limited to 2.5 DOF, with few systems available for 3-5 DOF path planning. 2.5 DOF systems are inherently inefficient due to support structures, requiring post-processing as well as design limitations. For large-scale parts, this entails additional manufacturing costs (such as labor and delivery time). 5 DOF path planning overcomes these challenges to a large extent but has limited industrial integration. A number of algorithms have been reviewed in this paper. While the algorithms are fundamentally suitable for metal AM, work is still required on non-planar tool path planning for metal AM where the generated tool path must satisfy the requirements identified in Section 2.5.2. Adaptive slicing offers an advantage in terms of reducing both the layer height and variation in material properties. This necessitates a fundamental understanding of bead deposition geometry, microstructure, and solidification modeling. Combining this knowledge with adaptive slicing will allow efficient manufacturing of high-quality parts, but this requires a significant multidisciplinary effort in material science and mechanical and manufacturing engineering. Path planning, which is a function of part geometry, directly affects heat transfer and conduction through the part being made. This results in varying amounts of additional heat in the part at any given time and build location, resulting in varying solidification rates, thereby affecting the geometry of the build and the resultant microstructure. Therefore, it is necessary to include heat transfer modeling at an earlier stage concurrent to the path planning. Current models suffer from long simulation times, inherent

assumptions to reduce computational time, and a limited set of manufacturing systems and material system availability which need to be improved through further research.

Incorporation of multi-degree of freedom path planning along with considerations of the aspects mentioned above will enable in-situ modification of material metallurgy and its mechanical and geometric properties during deposition. This will truly unleash the potential freedom of design and complexity that AM processes have to offer.

Prior to fabrication, it is also necessary in many cases to calibrate the workpiece with the fabrication platform. This is especially important when the build requires coordinated motion between the workpiece and deposition system–as is always the case during multi-directional deposition. Workpiece calibration can be automated by using a 3D or line scanner mounted on the deposition head.

2.8.2 Deposition Technologies

An area where considerable research potential can be found in the powder delivery during multi-axis DED (e.g., using an 8 DOF robotic LDED platform). Currently, the LDED deposition head must always remain vertical and thus align with the gravity vector to provide ideal powder delivery. Developing methods to loosen these constraints on the deposition head orientation is necessary to utilize the full potential of an 8 DOF robotic LDED platform. Several challenges need to be overcome to enable this, including, but not limited to, modeling of powder flow at different angles to the build surface and the effect of shielding gas dispersion in the build area at non-vertical angles.

While in contrast to LDED, deposition at varying orientations is intrinsically possible with fewer limitations using GMAW-based deposition technologies. However, they are at a stage of lower maturity regarding monitoring the melt pool temperature and geometry and energy input. Sensing the melt pool in a GMAW-based deposition system is also challenging due to the rapidly and drastically changing lighting conditions due to the presence of the arc.

Work is also ongoing on the minimization of the energy input during GMAW-based deposition, where CMT technology plays a significant role. Owing to the highly controlled CMT process where it is possible to fine-tune the deposition process, significant potential for the optimization and adaptation to particular material considerations is possible. For

example, in recent years, Fronius International GmbH has been developing custom synergic lines to further reduce the heat input during WAAM using CMT technology [L. Hudson and M. Zablocki, personal email and oral communications, March 2020]. Further potential for advanced research on optimizing the deposition process exists and should be considered. This necessitates in-situ and high-speed sensing of the welding current and voltage, providing important insight into the energy input into the build during fabrication. It can also provide valuable insight into the process, and the measurements themselves can be used as feedback for temperature control systems. Moreover, tremendous potential for robust sensor-fusion-based technologies exists.

2.8.3 In-situ monitoring, modeling, and control

The control algorithms reviewed in Section 2.6.1 for bead geometry control are relatively basic and have only been developed for and tested with single-track walls. Significant research is required to advance process monitoring and control towards the objective of robust, adaptive, and intelligent control methods that provide a sufficient degree of autonomy and robustness to unanticipated conditions during fabrication. Moreover, bead profile sensing and feature extraction have only been done for simple beads. The sensing and feature extraction capabilities need to be expanded and combined with modeling to provide accurate predictions of single beads and overlapping regions of multi-track deposition.

Substantial research potential is also apparent for advancing the area of layer geometry sensing and tool path re-planning during fabrication. The fact that during fabrication, a component is built layer by layer provides a unique insight into the current state of the build through the methods reviewed in Section 2.6.2. Impending catastrophic build failures can be detected, and the tool path for the following layer can be re-planned to mitigate and correct potential build failures.

Most work on temperature monitoring, and control has been done for LDED, as is apparent from Section 2.6.3. Particularly melt pool temperature sensing needs substantial work for arc-based deposition technologies. Heat accumulation is coupled with the deposition system travel speed and the material feed rate, which influence the bead and layer geometry. This means that if the bead geometry is adjusted (which is necessary), the heat input changes, which can modify the material composition.

Similarly, as for the layer geometry monitoring, IR cameras can also monitor the overall surface temperature of the component during the build to adjust dwell times and cooling rate of the substrate plate. This is especially important for maintaining consistent metallurgical properties.

2.8.4 Materials

Many challenges still need to be addressed in regards to materials for AM. One of the more apparent areas of exploration is expanding the number of materials available in AM. This is clearly highlighted by the chart presented in Figure 2.22 [461]. Although many of the materials used in conventional manufacturing are ill-suited for AM, there are still important contributions that can be made through failed experimentation. Increasing the amount of data on what materials may or may not be compatible with AM, allows for significant deductions to be made on the essential material properties a material must have to be used in AM.

Another future avenue of interest is using AM to achieve manufacturing feats that are outside the realm of possibility with conventional manufacturing. Although metals toughness far exceeds any other type of material, this comes with a poor strength to weight ratio. However, with AM, the internal structure can be altered to a lattice type, drastically increasing the strength to weight ratio. Additionally, polymer-based AM techniques could be used to fabricate these structures, which can be converted to a mold, and then cast, known as hybrid investment casting. This allows for the use of well-understood material systems in the way they were originally designed.

One of the challenges that is starting to be addressed is the current material selection for AM [462]. The current materials landscape for AM is dominated by materials that were successful with conventional manufacturing techniques. These materials were not designed for the complex thermal cycling inherent to AM, which result in material defects and anisotropic microstructures. Thus, the development of new materials created explicitly for AM could allow for more control over phase transformations, elemental segregation, and the resulting microstructure. This is especially crucial for large components, where heat treatment procedures incur a financial cost that make them unfeasible compared to conventional manufacturing. Furthermore, microstructural control will allow for predictions in how the part

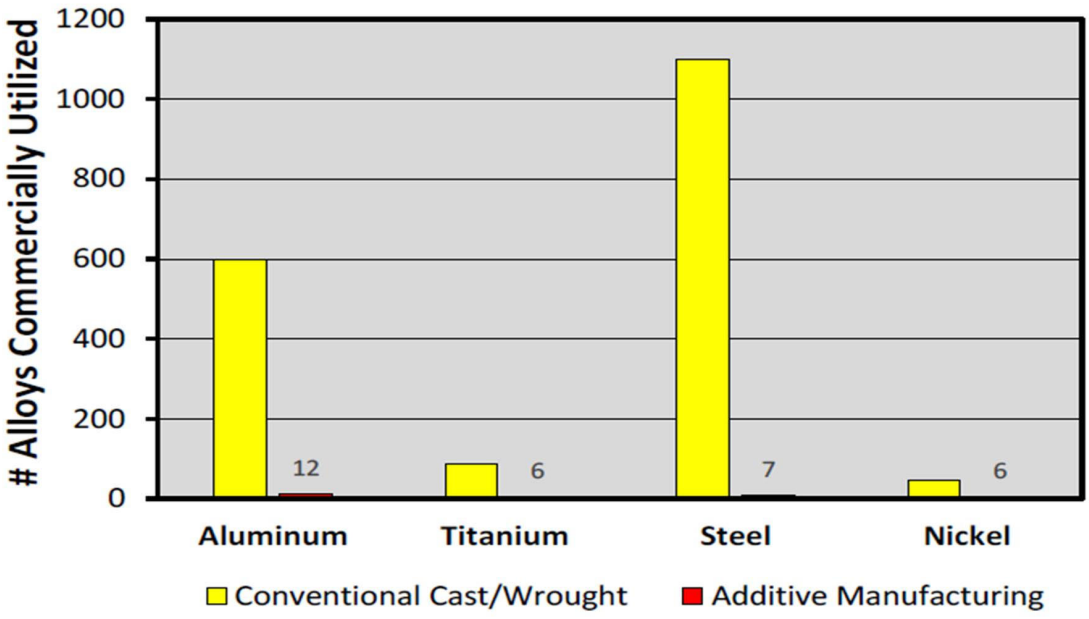

FIGURE 2.22: The comparison of materials used in conventional manufacturing to the materials used in AM [461]. (Image source: [461])

will perform when in service, which is imperative for on-site fabrication. Some promising alternative methodologies are being explored to prevent the epitaxial growth of large columnar grains. The addition of inoculants to aid in the nucleation of equiaxed grains would eliminate anisotropic mechanical properties prevalent in a lot of AM deposits [463]. The addition of boron to Ti64 has been shown to form TiB, which allows for the nucleation of α-grains, resulting in an isotropic grain structure [464]. A similar phenomenon has been reported with the addition of Ti to 5356 Al [281]. Furthermore, the addition of carbon to Ti64's hypoeutectic composition decreases the solidification temperature, causing grain growth restriction through constitutional supercooling. Although a different mechanism, a similar isotropic grain structure occurred[465]. These studies highlight that the development of materials better suited for AM is going to involve understanding the fundamental material paradigms involved in grain growth and solidification, and how these can be used to manipulate the thermodynamics of the system, to mitigate some of the microstructural challenges that researchers are currently faced with. Large amounts of data can be compiled by completing the aforementioned experiments on increasing the materials being trialed for AM, trying completely new material compositions, and in-situ grain control, which can then be used as input for artificial neural networks, to synthesize new materials specifically for AM. This

would also incorporate all the data from the published process planning and monitoring and control strategies, allowing the network to develop the appropriate deposition strategy for the new material. The seed to the network would be a material of known composition, as-built microstructure, and mechanical properties. The network would have the ability to simulate the deposition of the material and then predict its as-built microstructure and mechanical properties. The model would employ reinforcement learning strategies to iterate over various compositions of the material, based on the data acquired from the research, to optimize the microstructure and mechanical properties based on the part's specifications. This could completely reinvent how material selection is done and produce materials specifically tailored to the additive manufacturing of that specific part.

The materials available for large-scale robotic AM are currently limited to current alloys in either the welding or coating processes. Material development for various processes used in AM is in its infancy and will yield significant opportunities as the processes mature.

2.8.5 Post Processing

The complex thermal cycling of AM leads to microstructures that are not found in conventional casting and forging operations. Using design guidelines of traditional heat treatment protocols can result in poorer mechanical properties in some materials. This is attributed to the varying degrees of segregation or the novel grain structure that occurs during deposition [466]. Furthermore, many post-processing operations rely on HIPing to reduce internal porosity. This is problematic for large-scale AM due to the inherent cost of this procedure and the size of the processing chamber needed to contain the large part. Thus, developing techniques to reduce porosity in situ will be an essential future contribution to AM. Furthermore, the poor geometric tolerance obtained from parts manufactured using particular metal DED systems will need to be improved to reduce the manufacturing costs. This problem currently necessitates hybrid manufacturing systems or some combination of additive and subtractive technologies. This requires developing frameworks that unify positioning, referencing, and planning software to negate the need to detach the part from the build plate and any post-processing. The framework would also need to include localized heat treatment and a means to control the whole part's thermal cycle to ensure the promised mechanical performance. Thus, it is speculated that the next generation of large-scale AM systems will appear more similar to traditional manufacturing approaches than powder bed fusion

systems. There will be some modularity, where the part will be fabricated and machined in one module and then transferred automatically to a separate heat treatment module, similar to what is seen in traditional manufacturing. It is clear that an integrated automation system will increase productivity for this type of manufacturing. However, this manufacturing system would offer the geometrical freedom and the multi-meter scalability that both traditional and PBF are unable to provide.

The challenge remains to identify the raw materials, process conditions, and process control to maximize product quality using the AM processes and minimize subsequent post-processing requirements. The novel solutions will only be met through multidisciplinary and cross-functional teams closely collaborating. For example, this paper could not have been written without the close collaboration between mechanical, process control, mechatronics, electrical, and materials engineers. The future young engineers trained in AM will require a holistic knowledge base and the ability to work cooperatively with other disciplines in engineering, sciences, design, and visual arts. This paper has intentionally not addressed the redesign of components from both an engineering or artistic design approach. However, the possibilities using AM technologies will reveal new opportunities that are currently not imaginable.

Chapter 3

Automated semantic segmentation of NiCrBSi-WC optical microscopy images using convolutional neural networks

Published as **Rose, D**; Forth, J; Henein, H; Wolfe, T; and Qureshi, AJ. *Automated semantic segmentation of NiCrBSi-WC optical microscopy images using convolutional neural networks*, Computational Materials Science. Vol. 210 (2022). The goal of this chapter is to provide an automated methodolgy to quantify the carbide distribution in NiCrBSi - WC MMCs that were deposited using PTA-AM (thesis objective 1). The carbide distribution is the microstructural feature that is responsible for the abrasive wear resistance of MMCs. Garnering an understanding of how the carbide distribution changes with thermal history is imperative to predicting how the MMC will perform in abrasive wear conditions.

3.1 Abstract

Convolutional neural networks (CNNs) were used for the semantic segmentation of angular monocrystalline WC from NiCrBSi-WC optical microscopy images. This deep learning approach was able to emulate the laborious task of manual segmentation effectively, with a mean intersection over union (IOU) and a mean dice coefficient (DC) of 0.911 and 0.953, respectively, across the entire test dataset. From the model output, the carbide percent can

be determined by dividing the area of positively labelled pixels by the total area of the image. Additionally, the mean free path can be quantified using the method described in ASTM STP 839, and by physically counting the black pixels (CPB) between the particles in the image. Comparing the models predictions to the ground truth, the carbide percent had an average difference of 1.2 area %, while the mean free path differed by 15.7 μm for the ASTM method, and 24.8 μm for the CPB method. The robustness of the model was tested on images containing both spherical eutectic WC and angular monocrystalline WC to determine whether the model was capable of accurately predicting the location of objects that were not part of the training dataset. The U-Net CNN was able to segment the spherical and angular WC with considerable accuracy. These results show that the application of computer vision models for microstructural characterization is not limited to complex imaging modalities, and can be applied to readily available methods such as optical microscopy.

3.2 Introduction

Materials used in the mining and processing of natural resources require the ability to resist high levels of abrasive and erosive wear caused by direct exposure to various sands, ores, and rocks. A typical mitigation strategy is the application of a NiCrBSi-WC metal matrix composite (MMC) overlay, using plasma transferred arc welding (PTAW), to prolong the service life of the base part[10, 42]. With the estimated cost of wear in the Canadian industry being $2.5 billion per year[467], there is a constant push to reduce the downtime of operation by increasing the wear resistance of Ni-WC MMCs. In the conventional manufacturing space, some of the ongoing research to extend overlay lifetime involves altering the: matrix chemistry [10, 13], carbide crystallinity and shape [10, 42], reinforcement/matrix ratio [468], and coating method [12, 469–471]. Advances in additive manufacturing have extended the capabilities of well-known welding techniques to become fully automated manufacturing processes, where the layer by layer deposition is based on the cross-sectional geometry of a digitally rendered product. Plasma transferred arc-additive manufacturing (PTA-AM) offers the ability to build parts using composite materials (NiCrBSi-WC), removing the requirement for wear-resistant overlays while theoretically enhancing the service life [35, 36].

The underlying philosophy regarding the use of composite materials is combining the benefits of two individual constituents so they may compensate for their individually poor material

properties [472]. In abrasive wear applications, the hardness of the WC reduces material loss due to micro-cutting [468] while the ductility and toughness of the NiCrBSi matrix allow for adequate force transfer to the WC particles and significant plastic deformation, adding resistance to brittle fracture [473–475]. The wear performance of composite materials is also greatly affected by the distribution of the reinforcement particles within the metal matrix. Lack of homogeneity in the distribution of the carbide particles can lead to non-uniform wear rates and premature failure of the coating[11]. Thus, it is imperative to quantify the distribution of the reinforcement phase to optimize the wear resistance of MMCs. The mean free path of the matrix phase has shown a strong inverse correlation to the abrasive wear resistance of the composite material[10, 13, 476, 477]. The mean free path (MFP) can be determined using equation 3.1[478].

$$\lambda_{MFP} = \frac{1 - f}{N_L} \tag{3.1}$$

The size of the reinforcement particles has also been shown to alter the tribological behavior of the MMC[3, 479], though particle size is unable to be quantified from 2-D projections, as were gathered for this work.

The carbide characteristics (mean free path, and volume fraction) can be determined using quantitative metallography on optical microscopy images [478]. This can be achieved by manually segmenting each carbide particle or semi-autonomously with various image processing techniques to threshold out the carbide particles from the image. Image processing modalities to segment desirable features from an image range from common approaches such as Otsu's method [480] and Canny edge detection [481], to more complex unsupervised learning algorithms like K-means clustering[482]. Image processing methods generally require the areas of interest to have distinct, non-overlapping pixel distributions, and distinct edges; However, the nature of optical microscopy induces significant user variance in the quality of the image attempting to be segmented. Some common technician sources of noise in the pixel distribution include poor metallographic preparation, and sub-optimal focus and contrast. There are also features beyond the equipment's resolution limits (∼0.2 μm [483]), which can contribute further to noise in the pixel distribution. During image processing, noise in the pixel distribution leads to type I (false positive) errors, type II (false negative) errors, and poor edge definition. [484–486]. Figure 3.1a displays a 512x512 pixel optical image of Ni-WC, and Figure 3.1b shows the ground truth image for the segmentation of the WC particles,

where the location of the WC particles are highlighted by the white pixels. The segmentation of Figure 3.1a using Otsu's method [480], Canny edge detection [481], and k-means clustering [482] can be found in Figure 3.1 c, d, and e, respectively. For Otsu's method [480] the scikit-image [487] algorithm selected 170 as the optimal threshold value. Using Canny edge detection [481] with OpenCV [488], a minimum and maximum gradient value was set to 15 and 63, respectively, with a sobel kernel size of 3. The k-means clustering was done in OpenCV [488] using 3 clusters, max iterations of 100, ϵ of 0.1, and the centroids were initialized using the k-means++ method [489]. The parameters for the image processing methods found in Figure 3.1 were selected through trial and error, and were analyzed visually for the capability to segment the WC particles. It can be seen that due to the pixel luminance overlap of the features contained within the WC particles, and the surrounding matrix, poor segmentation is achieved when compared to the ground truth (Figure 3.1b). Although optimization of the image processing algorithms shown in Figure 3.1 could increase the accuracy

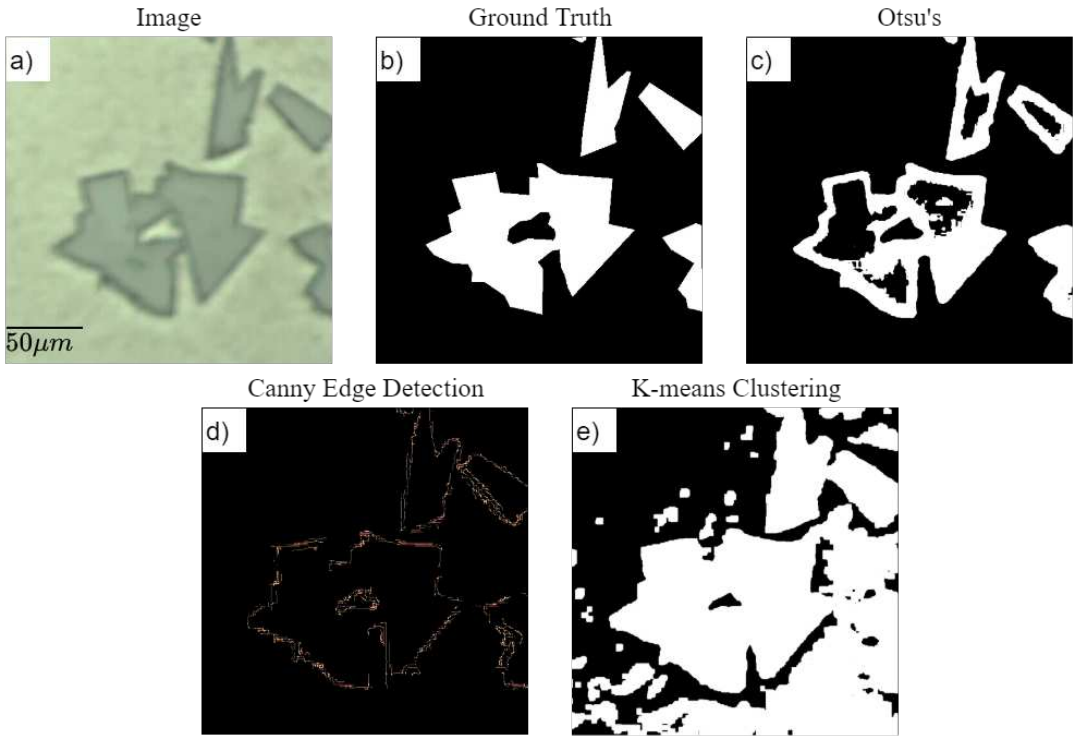

FIGURE 3.1: a) NiCrBSi-WC optical image, where the dark green particles represent the WC and the surrounding lighter portion is the Ni matrix, b) the ground truth corresponding to image a), where the location of the WC particle is shown in white; c) thresholding of image a) using Otsu's method [480]; d) thresholding of detectable edges in image a) using Canny edge detection [481]; e) segmentation of image a) using K-means clustering [482].

of the segmentation, one set of parameters would not work for all images, making it difficult to automate without some degree of manual intervention. The aforementioned shortcomings in traditional image processing, highlighted by Figure 3.1, show these techniques may not be the best approach for an automated pipeline to segment Ni-WC optical images.

Semantic segmentation is a branch of computer vision that uses machine learning (ML) models to assign a class label to each pixel in an image with an accuracy that can out perform humans in some contexts [490]. Convolutional neural networks (CNNs) use filters that are rastered (scanned) over an image to create a feature map [491, 492]. A feature map is a tensor representing the multiplication of the features in the image, or input feature maps, by the weights in the kernel of a given layer; this can give insight into the signal that the network has learned to be important to the task at hand. Each filter represents a single layer in the network, and are organized in blocks of multiple layers that have similar spatial dimensions. After each filter passes over the image, the feature activation values are passed through an activation function to account for the nonlinearity of the image pixel data[493]. The last stage of a convolution block is downsampling, which decreases the (x,y) dimensionality of the output by reducing a rectangular kernel of pixels to a single value (typically the max value of the kernel[494]). The number of convolutional blocks is based on the depth and architecture of the model being used. For image classification, the final layer from the encoder is flattened to a feature vector, which is then used for the classification stage [179, 495]. On the other hand, for semantic segmentation, the activations from the final layers of the encoder must be restored to the original size of the image, using a decoder network, to perform pixel-wise classification while replicating the original dimensionality of the image[496]. Typically these models are developed to classify: people [497, 498], natural objects [491, 492, 497, 499], and biomedical phenomena[500]. Semantic segmentation models' ability to extract features in an image extends beyond their original intent and can be used for more abstract concepts such as phase segmentation in microstructural images [501–506]. The development of easy-to-use APIs [507, 508], makes the application of computer vision models far easier for researchers outside the immediate industry.

The present study aims to test state-of-the-art CNNs for the semantic segmentation of Ni-WC MMCs deposited using PTA-AM. The effect of varying the hyperparameters, as well as the encoder architecture, will be discussed. Following the segmentation of the carbides, the quantification of the carbide volume percent, and mean free path (MFP) can be determined.

The computational uncertainty associated with the quantification of the microstructure and the carbide characteristics will be disclosed, and the ability for the trained CNN to be able to segment more complex optical microscopy images is shown.

3.3 Materials and Methods

The framework for the experimental work conducted in this study can be found in Figure 3.2. Each step in the framework corresponds to a chronological sub-section of Materials and Methods, where the details of each step will be discussed. A high-level overview of the section is as follows. The first step was image acquisition which included the PTA-AM deposition of Ni-WC MMC deposits, the sample preparation, and dataset generation through optical microscopy. The images were pre-processed with non-local means denoising and pixel mean shift algorithms prior to being passed through the CNN. The CNNs had to be optimized for the task of semantic segmentation of Ni-WC optical microscopy images. This included a hyperparameter search, k-fold cross-validation, and receiver operating characteristic curve analysis. Finally, the predictions from the CNN are subject to various post-processing methods before the final evaluation.

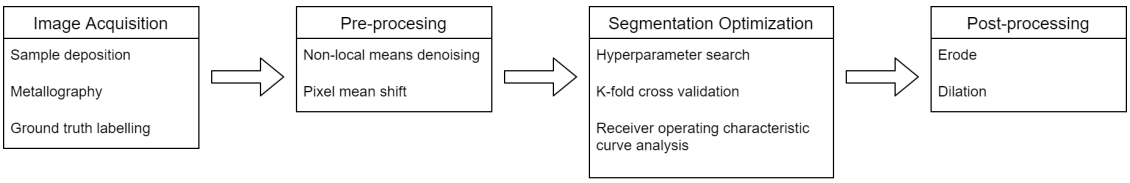

FIGURE 3.2: Framework for segmentation pipeline used for this study.

3.3.1 Image Acquisition

The Ni-WC samples were deposited using the PTA-AM system developed by Rojas *et al.*, consisting of a Kennametal Stellite ™ STARWELD 400A PTA and a positioning table capable of moving 365mm x 170mm x 300mm in the X, Y, and Z plane, respectively [35, 36]. The powdered feedstock used for the samples contained in the training data was 60wt% (45 vol.%) angular monocrystalline WC, with the remaining 40wt% (55 vol.%) being a NiCrBSi

matrix with a hardness of 30 HRC. Additional samples were deposited to test the transferability of the trained CNN using a powdered feedstock of 35wt% (∼26 vol.%) angular monocrystalline WC, 35wt% (∼26 vol.%) spherical eutectic WC, and 30wt% (48 vol. %) NiBSi. The size distribution for the angular and spherical WC were (-180, +63µm), and (-180, +125 µm), respectively. The single track multi-layer deposits consisted of 40x0.75mm layers resulting in sample dimensions of 100mm x 7mm x 30mm for the length, thickness, and height, respectively. The metallurgical samples were mounted, and polished using 6 and 1 µm diamond, and 0.05 µm colloidal silica suspensions. There was no etching step required for any of the samples. Following metallographic preparation, the samples were observed under an Olympus PMG3 optical microscope, and images were captured using an Olympus Q color 5 camera with Quartz PCI V5 software. The optical microscope used for this work captured the images with a green hue. Therefore, the model was only trained on images with a green color distribution, and further normalization may need to be done prior to using the model. An example of a larger sample image taken at 50x magnification can be seen in Figure 3.3. From the larger images, 256x256 pixel crops were taken to increase the size of the dataset to a total of 229 images. The difference in density between Ni (8.9 gcm^{-3}) and WC (15.6 gcm^{-3}) caused there to be settling of the WC particles, which is evident in Figure 3.3. The settling of the WC caused the class balance of the images to vary depending on where the cropped image originated in the sample. When the images were split into training and test sets, it was ensured that the class balance was as close to the same as possible. The images were all taken at the same magnification, as the magnification would effect the resolution of features in the images, impacting the final results.

The ground truth for each image was made by manually tracing each carbide in the images using the labelme [509] python package and exporting the recorded vertices to a binary image. An example of a cropped image and its corresponding ground truth can be seen in Figure 3.1a and Figure 3.1b, respectively. Pores, cracks, and defects were counted as being part of the background class to simplify the problem, constraining it to binary segmentation. During the initial experimentation, it was evident that the increased computational complexity of a multi-class system was too much of an out-of-discipline leap. The end goal was to quantify the WC distribution in the composite, providing a metallurgical justification for the improved wear resistance, with an automated pipeline with base level complexity, that can be built upon with future iterations. Including the defects as part of the background made the labelling of ground truth images more challenging, since the labelme [509] exports the

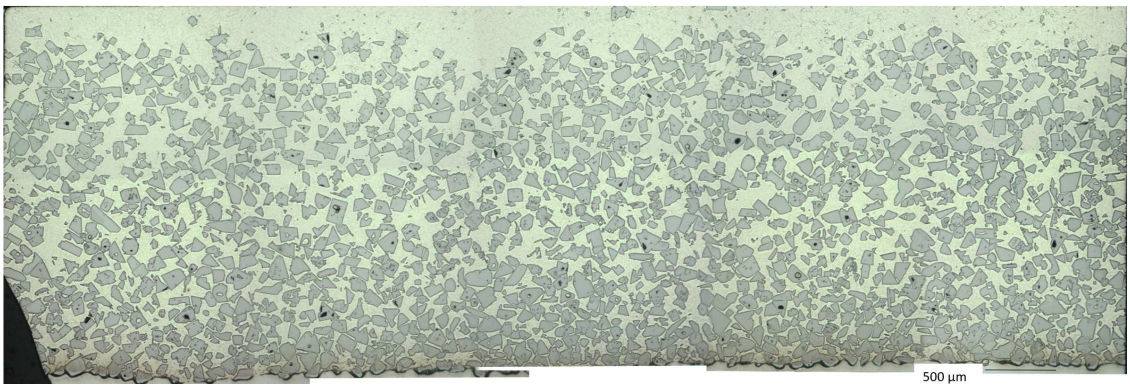

FIGURE 3.3: An example of a large optical microscopy image used to compile the training and test datasets. The above image is 9138W x 3322H pixels, meaning that 468 256x256 pixel crops can be taken from one image.

edge coordinates of the object, and internal structures cannot be removed from the object. To remove the defects from the WC, the particles had to be broken up into multiple parts; this reduced the pixel wise accuracy of the defects, adding some user error. Additionally, the complex morphology of the WC made it difficult to perfectly trace the outside of the particles, resulting in shadowing around the WC to be included in the mask, further contributing to user error. From a metallurgical standpoint, the error of including the boundary or defect is insignificant and the occasional inclusion makes little difference to the overall quantification of the WC distribution; however, the effects of this decision from a machine learning perspective were unknown at the time. The lessons learned from the above ground truth decisions are important part of out-of-discipline experimentation.

3.3.2 Pre-processing

A pixel-wise non-local means filter [510] was the first pre-processing step that was done to reduce the noise induced by the phase structure of the Ni matrix material, and reduce the variability in the pixel intensities belonging to the WC. This has been shown to decrease the generalization error, and may allow the user to reduce the depth of the model required to perform the task [511]. A pixel-wise non-local means filter attempts to reduce the variance between similar rectangular kernels found throughout the image. An example of the results of the non-local means filter on a Ni-WC optical micrscopy image is shown in Figure 3.4, where the black square represents the kernel containing the pixel p being adjusted, and the red and purple squares are examples of kernels that would be used to adjust p. The pixel

values provided in Figure 3.4 are samples of the pixel intensities from the green color channel for each region, and the red pixel represents the pixel p, while the green pixel is the pixel q. The first step is determining the squared Euclidean distance between the like patches, shown in equation 3.2. An exponential kernel, shown in equation 3.3, is then used to calculate the per pixel weight factor. Due to the exponential nature of the weight, distance values less than $2\sigma^2$ result in a value of 1, while more significant variances between the patches are adjusted exponentially[510]. The weights are then used in equation 3.4 to adjust the value of the pixel p. Referring back to Figure 3.4a the euclidean distance between the pixels belonging to the black kernel and purple kernel, will be smaller than the red kernel, which agrees with the metallurgical context of them being the same phase; this means the purple kernel will have a larger influence on the pixel value of p. Following the adjustment, the center of the kernel is moved the adjacent pixel, and the process is repeated until the entire image has been analyzed. Figure 3.4b shows Figure 3.4a after being processed with a non-local means filter, and the black kernel reflects the reduced variance in pixel intensity. The decision to use the non-local means filter coincided with the use of image augmentation in the early stages of the model development, preventing the isolation of the contribution from the non-local means pre-processing. However, convergence was unable to be achieved prior to the implementation of these pre-processing methods.

$$d^2(B(p,r),B(q,r)) = \frac{1}{3(2r+1)^2}\sum_{i=1}^{3}\sum_{j\in B(0,r)}(u_i(p+j)-u_i(q+j))^2 \tag{3.2}$$

$$w(p,q) = e^{-\frac{max(d^2-2\sigma^2,0.0)}{h^2}} \tag{3.3}$$

$$\hat{u_i}(p) = \frac{1}{\sum_{q\in B(p,r)} w(p,q)}\sum_{q\in B(p,r)} u_i(q)w(p,q) \tag{3.4}$$

Following the denoising, the mean and standard deviation of any outlier input image was adjusted to match the pixel distribution of the training data. If the mean of any of the color channels of the input image were greater than 20 away from the mean of the same channel in the training set, all channels of the input image were normalized to match the distribution of the training data. The model only has the capability to generalize features based on the data available during training. The small dataset used during training limited the variability

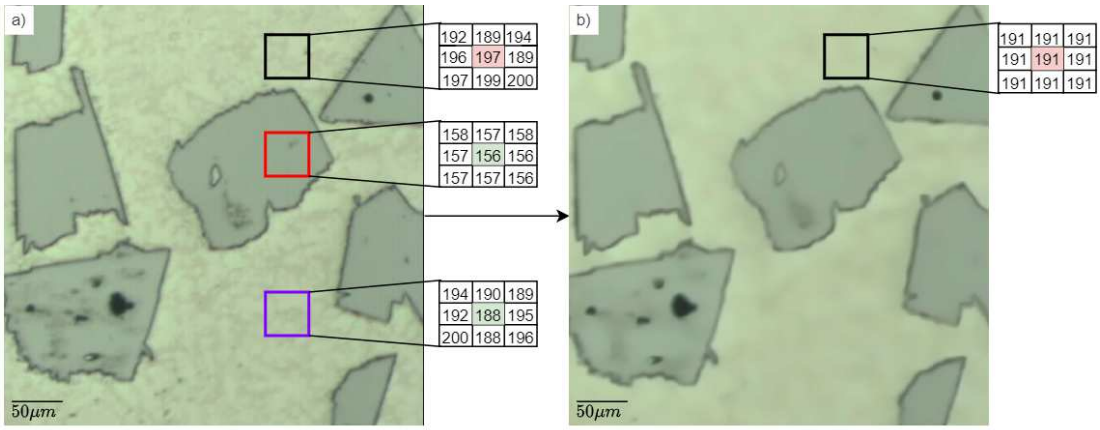

FIGURE 3.4: a) The input image before non-local means filtering and b) post non-local means filtering. The black square is the kernel surrounding the pixel p that is being adjusted, which is shown in red. The red and purple kernels are used to calculate the weight by which p will be adjusted, with the green pixel denoting the center q. The euclidean distance between the pixels belonging to the purple kernel is lower than that of the red kernel, causing the purple kernel to have a larger weight than that of the red kernel.

of the features belonging to the carbide class. Normalizing the outlying images increased the mean IOU by 5%.

Image augmentation was employed to expand the size of the dataset used during training in order to increase the model's ability to generalize across the range of features that belong to the carbide class, and reduce the chances of overfitting to the training data[512]. Prior to be fed into the CNN, the images were randomly augmented with either a horizontal or vertical shift by 51 pixels, a horizontal or vertical shearing of the image by 5°, a rotation by 25° both clockwise and counterclockwise, a brightness shift by 0.8-1.2, and a shift in the intensity of one of the three color channels by 10 (4%). Augmentations were chosen to account for user errors that occur during the procurement of images using an optical microscope.

3.3.3 Optimization

This section of the paper will outline the process taken to optimize the CNN for the semantic segmentation of WC particles in Ni-WC optical images, which includes: Neural network selection, hyperparameter search, and k-fold cross-validation.

3.3.3.1 Neural Network Selection

The primary convolutional neural network architecture used for this work is the U-net developed by Ronneberger *et al.* [500], which was originally developed for the segmentation of cell structure images for biomedical applications. A visual depiction of the U-Net is shown in Figure 3.5. The selection of this architecture was primarily due to the similarity in the features between cell structures and microstructural images, since both contain areas of interest surrounded by background pixels with a similar pixel distribution. Additionally, the U-Net was developed for optimal performance with limited data (30 training images [500]) available for training. Architecturally, the U-net has a symmetrical encoder and decoder. In the context of CNNs, the encoder creates low resolution feature maps from the input image, and the decoder increases the resolution of the feature maps to perform pixelwise classification [513]; both the encoder and decoder use trained parameters. The encoder consists of a repeated sequence of two 3x3 unpadded convolutions rastered across images and their derived feature maps, each followed by an activation function (eg. ReLU[514]), and then downsampled using a 2x2 max pooling with a stride of 2. The convolutional and pooling layers are illustrated in Figure 3.5 by the purple, and blue rectangles, respectively. Following each downsampling step, the amount of feature maps is doubled to increase the models' ability to learn complex structures. The increase in depth and decrease in the size of the output increases the model's ability to extract features from the image but sacrifices the spatial context of these features. Thus, to expand the dimensionality of the output to contain precise pixel-wise predictions, the model requires a symmetric decoder path. Each upsampling block begins with a transpose convolution, causing a reduction in the depth of the output while increasing the size, shown by the red rectangles in Figure 3.5. The upsampled feature map is concatenated with the feature maps from the encoder block of the same depth, increasing the spatial precision of the predictions. Similar to the encoder, the combined feature maps and transposed convolution is passed through two 3x3 convolutional layers, each followed by a ReLU. The final layer contains a 1x1 convolutional layer, which maps the final feature vector to the corresponding number of classes [500], shown in green in Figure 3.5.

LinkNet, developed by Chaurasia *et al.*[515] and shown in Figure 3.6, was also used for the segmentation of WC particles from Ni-WC optical images and compared with the results from the U-net. Convolutional layers used in this architecture are all followed by batch normalization, where the activations are rescaled to have a mean of 0 and a standard deviation

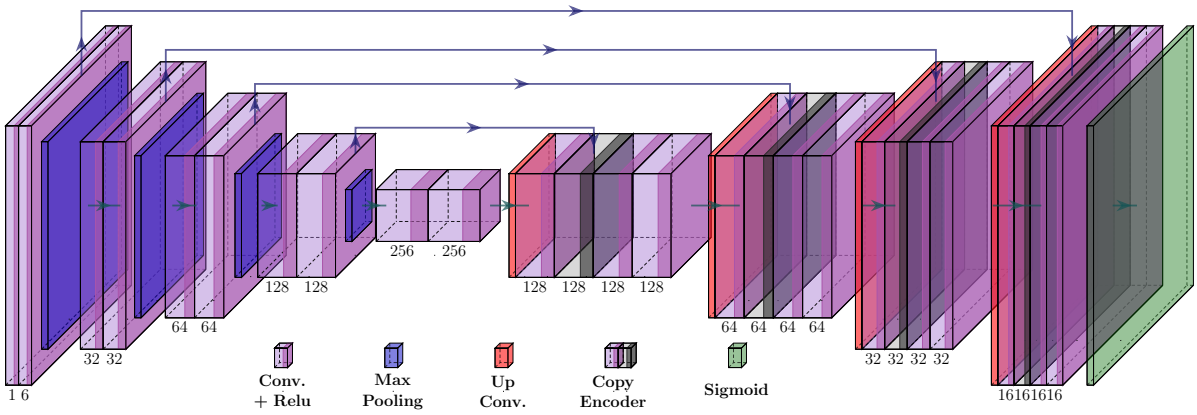

FIGURE 3.5: The U-Net CNN architecture proposed by Ronneberger *et al.* [500]. The depth of the output for each layer is shown at the bottom; However, magnitude of these values reflect the current study. The blue arrows indicate where the feature maps from the encoder are added to the decoder.

of 1 [516], and a ReLU activation function. The convolutional layers are shown in green, and the ReLU is shown in purple in Figure 3.6. The encoder begins with a 7x7 convolutional layer, followed by a 3x3 max pooling with a stride of 2. This output enters four consecutive residual blocks [517], each containing two sets of 3x3 convolutional layers. Every two convolutional layers are followed by a skip-connection, where the input and output of the two convolutional layers are combined to reduce the likelihood of a vanishing gradient without impacting the model's performance. The residual connections are highlighted by the combination of the blue arrows, and purple spheres in Figure 3.6. Furthermore, the depth of the model can be increased without sacrificing its ability to learn identity-like mappings [517]. The decoder path includes four blocks containing two 1x1 convolutional layers, with a 3x3 transpose convolutional layer in between. The output of each decoder block is combined with the input from the corresponding encoder block to recover the spatial knowledge that was lost during feature extraction; these are illustrated by the red arrows in Figure 3.6. Before localization, the output of the decoder is passed through two more transpose convolutional layers, with a 3x3 convolutional layer in between [515].

Along with the original architectures the encoders from VGG16[492], resnet50[517], and mobilenet[518] were also tested. The corresponding decoders were designed to conserve the original U-net and LinkNet structure. The final layer activation was achieved using the sigmoid activation function, which outputs the class probabilities between 0 and 1, shown in

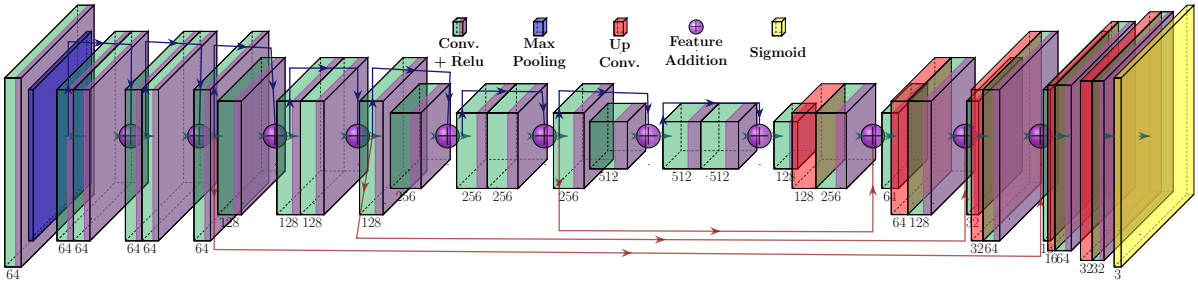

FIGURE 3.6: The LinkNet CNN architecture created by Chaurasia *et al.*[515]. The depth of the output from each layer are shown at the bottom, and these values are the same as the original architecture. The blue arrows indicate the residual connections in the encoder, and the red arrows indicate where the feature maps from the encoder and decoder are added.

equation 3.5 [519]. The sigmoid activation was used for all models analyzed in this work.

$$f(x) = \left(\frac{1}{1 + exp^{-x}} \right) \tag{3.5}$$

Keras[520], and Tensorflow [508] were used as the machine learning API for all the models in this work. The python/Keras version of the models was written by Yakubovskiy *et al.*, and provided in the Segmentation Models Github repository [521]. Computing resources were provided by Industry Sandbox and AI Computing (ISAIC) at the University of Alberta, which included 2 16GB NVidia Tesla V100 GPUs.

3.3.3.2 Performance Metrics

The two performance metrics used in this work were the Jaccard index [522], also known as intersection over union (IOU), and the dice coefficient[523](DC), shown in equations 3.6 and 3.7, respectively.

$$IOU = \frac{TP}{TP + FP + FN} \tag{3.6}$$

$$DC = \frac{2TP}{2TP + FP + FN} \tag{3.7}$$

Although their formulation is similar and the metrics are positively correlated, there are some differences when the evaluation is across many instances. Though both the IOU and dice coefficient metrics are positively correlated, it is of note that the IOU is more sensitive to poorly performing outliers than the dice coefficient and, therefore, their relative values

will differ depending on the dataset. One disadvantage both the IOU and the dice coefficient share is that the lower the percentage of true positive pixels compared to background pixels, the higher the penalty for having any type I or type II errors; though as discussed previously it will likely be exacerbated for the IOU. Thus, it is essential to consider the imbalances in the dataset during the evaluation[524].

The receiver operating characteristic (ROC) curve measures the model's ability to correctly predict the features belonging to a particular class. The use of the sigmoid activation function causes the output of the CNN to be pixel-wise probabilities of that pixel belonging to the carbide class. Thus, the ROC curve allows for the selection of the optimal probability threshold to maximize the predictive ability of the model. This is done by plotting the true positive rate (TPR a.k.a. sensitivity) against the false positive rate (FPR), which are shown in equations 3.8, and 3.9, respectively.

$$TPR(Sensitivity) = \frac{TP}{TP + FN} \tag{3.8}$$

$$FPR = 1 - Specificity = \frac{FP}{TN + FP} \tag{3.9}$$

The closer the area under the ROC curve (AUC-ROC) is to unity, the higher the probability that the model will correctly classify each pixel to the correct class. Since different probability thresholds will give rise to varying TPRs and FPRs, it is important to determine the area under the ROC curve for a range of values. This can be seen in Figure 3.7, where the ROC curve for fold 1 of the U-net is plotted for various threshold values. For this particular model, the optimal threshold value was 0.77, where values higher and lower had reduced area under the ROC curve. During the training of the models in this work, 50 threshold values between 0 and 1 were tested to find the best possible threshold value. For the hyperparameter search, predictions were based on the validation set, and for k-fold cross-validation, the predictions were from the test set.

3.3.3.3 Hyperparameter Optimization

Machine learning models attempt to define the features in a given dataset using a non-linear function. This is achieved by using affine transformations that are dictated using learned parameters and non-linear activation functions, such as the ReLU. The model parameters

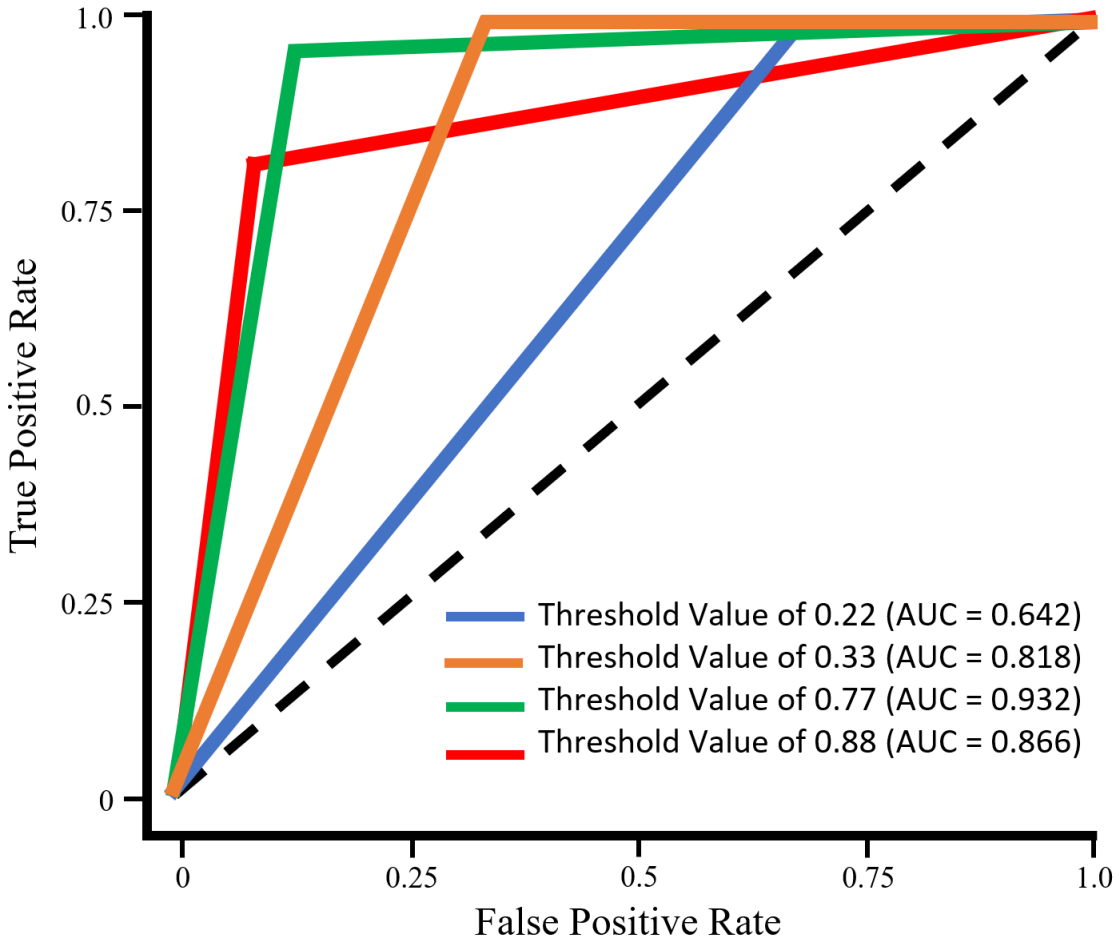

FIGURE 3.7: The ROC curve for fold 1 of the U-net used in this work at varying thresholds. The threshold value for each line is given in the legend, along with the corresponding area under the ROC curve. The dashed line represents the lowest possible denomination of the ROC curve.

are internal coefficients that are updated using a gradient-based optimization algorithm to produce the smallest possible error on the dataset. Hyperparameters are configurational arguments that are specified by the user to help facilitate the training process and tailor a model's performance to a particular dataset. Typically, the general effect each hyperparameter has on the models functionality is known. However, the various hyperparameters may have non-linear interactions, resulting in drastic differences in performance.

The hyperparameters tested and their range of values for the U-net are shown in Table 3.1, and the alternative backbones for the U-net and LinkNet are shown in Table 3.2. As mentioned above, batch normalization refers to rescaling all of the activations from the hidden layers to be between 0 and 1 [516]. Batch size is the number of training images that are

TABLE 3.1: The hyperparameters and their corresponding value ranges used for the hyperparameter optimization of the U-net. Note that for SGD, momentum was set to the default of 0 and for Adam β_1 and β_2 were set to the recommended values of 0.9 and 0.999 respectively [525]. Larger incremental ranges are shown in brackets (start,finish,increment)

Hyperparameter	Value Range
Batch Normalization	True, False
Batch Size	2, 4, 6, 8
Learning Rate	0.00001, 0.0001, 0.001, 0.01, 0.1
Learning Rate Decay	0, 0.25, 0.5, 0.75, 0.99
Dropout Rate	(0, 1, 0.1)
L2 Regularization term	0, 0.0001, 0.001, 0.01, 0.1
Kernel Size	2, 3, 4, 5
Number of Filters	16, 32
Activation	ReLU [514], ELU [526]
Loss Function	binary cross entropy (BCE)[527], dice coefficient loss (DL)[528], BCE plus dice coefficient loss (BCE+DL)[529]
Optimizer	stochastic gradient decent (SGD)[530][531], RMSprop[532], Adam[525]

used to estimate the expected value of the gradient for a particular loss function over the entire dataset[533]. Smaller batch sizes have been shown to improve the model's ability to generalize features [534–536], while reducing the memory footprint during training. The learning rate controls the magnitude the weight parameters of the model are updated per epoch [537]. Decaying the value of the learning rate during training has been shown to improve the model's ability to learn complex patterns and reduces the chance of the model being stuck in a local minima[538]. The decay patience is the number of epochs, with no improvement to the validation loss, it takes for the learning rate to decrease by the specified decay rate. The value for the learning rate decay refers to the amount in which the learning

TABLE 3.2: The hyperparameters and their corresponding value ranges used for the hyperparameter optimization of the U-net and LinkNet for the different backbones. These ranges are the same for all of the different backbones trialed. Note that for SGD, momentum was set to the default of 0 and for Adam β_1 and β_2 were set to the recommended values 0.9 and 0.999 respectively. [525]

Hyperparameter	Value Range
Batch Normalization	True, False
Batch Size	2, 4, 6, 8
Learning Rate	0.00001, 0.0001, 0.001, 0.01, 0.1
Learning Rate Decay	0, 0.25, 0.5, 0.75, 0.99
Decay Patience	5, 10, 20, 30
Decoder Block Type	nearest-neighbor (nn) upsampling, transpose convolution
Encoder Weights	he normal, ImageNet
Freeze Encoder	True, False
Loss Function	binary cross entropy (BCE)[527], dice coefficient loss[528], BCE plus dice coefficient loss[529]
Optimizer	stochastic gradient decent (SGD)[530][531], RMSprop[532], Adam[525]

rate drops after there has been no improvement in validation loss after the epochs specified by the patience. Dropout is a regularization technique that temporarily removes neurons and their connections from the network based on the probability defined by the dropout rate to help reduce overfitting[539]. L2 regularization adds a $\lambda \sum_{j=1}^{p} \beta_j^2$ to the objective function to reduce the value of the weights to be closer to zero. Kernel size is the size of the convolution window that is used during the convolutional layers, while the number of filters increases the depth of the convolutional layers. Kernel weights were initialized from a truncated normal distribution, with a mean of 0 and a standard deviation of $\sqrt{2/n}$, where n is the number of input units in the weight tensor [540]. ReLU [514] and ELU [526], shown in equations 3.10

and 3.11, are non-linear activation functions that follow each convolutional layer, to account for the complex nature of the pixel data.

$$R(z) = \begin{cases} z & z > 0 \\ 0 & z <= 0 \end{cases} \tag{3.10}$$

$$R(z) = \begin{cases} z & z > 0 \\ \alpha(e^z - 1) & z <= 0 \end{cases} \tag{3.11}$$

In deep learning, the objective function that is used to quantify the model's ability to perform a particular task is called the loss function. The cumulative error associated with the entirety of the model is distilled down to a single value, where a reduction in this value indicates improvement in the model's performance. The loss functions tested in this work are pixelwise binary cross entropy[527], the dice coefficient loss[528], and a combination of the two[529], shown in equations 3.12, 3.13, and 3.14 respectively.

$$L_{BCE}(y, \hat{p}) = -(ylog(\hat{p}) + (1 - y)log(1 - \hat{p})) \tag{3.12}$$

$$L_{DL}(y, \hat{p}) = 1 - \frac{2y\hat{p} + 1}{y + \hat{p} + 1} \tag{3.13}$$

$$L_{BCE,DL} = \beta L_{BCE} - (1 - \beta)L_{DL} \tag{3.14}$$

Parameters of the model are updated after each batch through gradient descent using an optimization algorithm. The optimizers trialed were stochastic gradient decent (SGD)[530], RMSprop[532], and Adam [525].

Different hyperparameters were able to be analyzed for the different backbones based on the input arguments specified by Yakubovskiy's Github repo [521], which include changing the encoder weights, freezing the encoder weights, and altering the decoder block type. Transfer learning [541] using an encoder that was pre-trained on the ImageNet dataset[542] was used to take advantage of the model's ability to generalize and extract features. Otherwise, the weights were initialized from a truncated normal distribution [540]. These weights from ImageNet could be frozen and prevented from being adjusted during training, resulting in only the decoder parameters being updated. The decision to include freezing the weights was made so the large gradient from the new dataset doesn't override the ImageNet weights,

eliminating the feature extraction benefits of the pre-trained encoder, potentially causing the entire model to be trained from scratch. The decoder block type was also altered between nearest-neighbor upsampling, which does not use learned parameters, or a transpose convolution.

Hyperparameter optimization was done using the Talos python package [543], using a random search method. The training was stopped after 50 epochs with no improvement to the validation loss, with a max of 500 epochs, and only the top-performing model was evaluated. The dataset was manually split into training (80%) and validation (20%) to conserve class balance between the datasets and to ensure comparable results across the experiments. The metrics used to evaluate the raw output were IOU (equation 3.6) and the dice coefficient (equation 3.7), averaged across the entire validation set.

3.3.3.4 K-fold Cross Validation

Once the optimal hyperparameters were determined for each model, the evaluation was done using k-fold cross-validation. This is a widely used technique for model evaluation since it improves the models ability to generalize by using all of the available data for training and validation [544]. A value of k=5 was selected to reduce the computational load, while being large enough to reduce the bias and variance of the model's performance[545]. The total 229 training images were split into a training set (192 images) and a test set (37 images), where the test set was selected to closely match the class distribution of the training set. During training, the training set is split into five folds, one fold being used as the validation set and four folds being used for training, as shown in Figure 3.8. The model is trained for 500 epochs, with the goal being to minimize the loss associated with the validation set as a representation of how the model performs on new data. Following training, the test set is passed through the model, and the mean IOU and dice coefficient are determined across the entire test set. This process is repeated five times, and the ultimate performance of the model is the averaged performance across the folds.

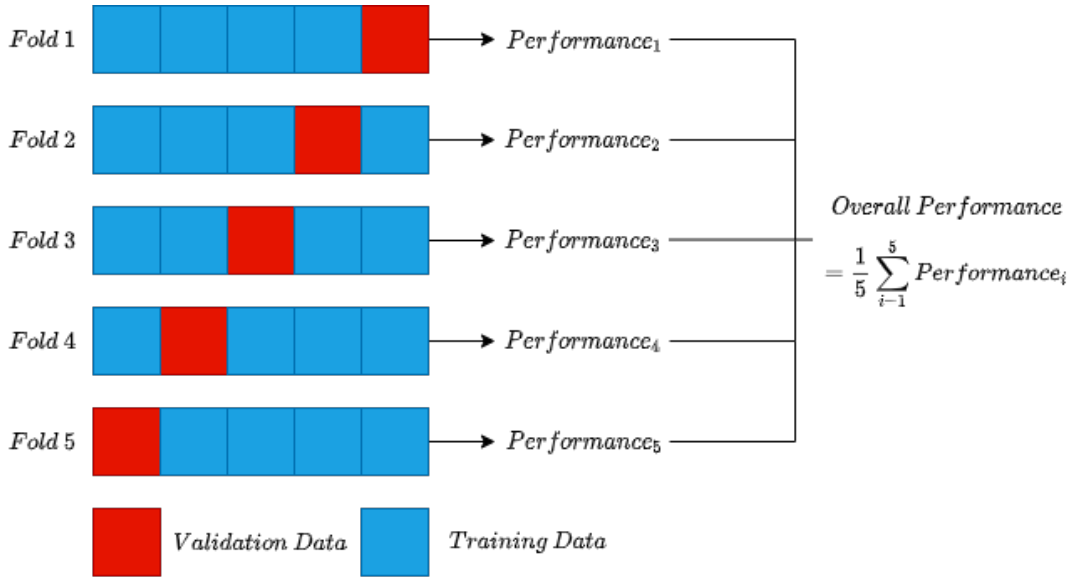

FIGURE 3.8: A visual representation of the k-fold cross validation procedure.

3.3.4 Post-processing

The overall model performance was determined before and after post-processing, using morphological operations, of the CNN predictions. Morphological operations use a structuring element that is rastered over the image to adjust the arrangement of features in an image. For this work, the chosen structuring element was a square, with the origin being at the center. Two morphological operations were used for post-processing of the binary images, erosion, and dilation. Erosion eliminates all pixels (reduces value from 1 to 0) within a structuring element except for the origin, where that structuring element fits within an object (all pixel values of the structuring element are 1). Dilation increases the dimensions of objects by changing the value of the origin of the structuring element from 0 to 1 if any part of the structuring element contacts a pixel with a value of 1 [546]. A visual depiction of erosion and dilution of an arbitrary object by a 3x3 square structuring element can be seen in Figure 3.9a and Figure 3.9b, respectively. Opening is erosion followed by dilation, which removes noisy patches and spurs from the image while maintaining the original shape and size of the objects. Closing is dilation followed by erosion which helps in filling small gaps found in the objects in the image[546]. The sequence of morphological operations that yielded the best results was: erosion, opening, closing, and erosion. All morphological transformations were performed using the python package OpenCV [488]. For each morphological

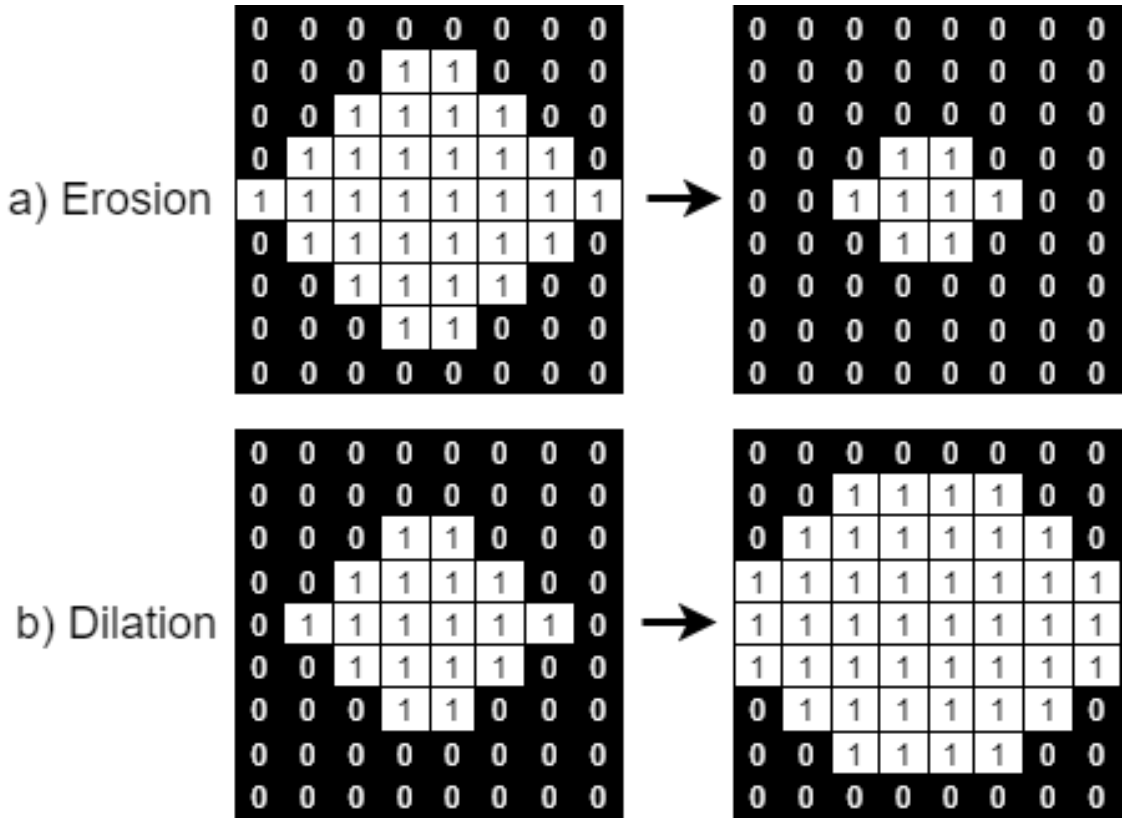

FIGURE 3.9: The a) erosion and b) dilation morphological transformations used in the post processing of the CNN output. For both processes the structuring element is a 3x3 square.

step, the structuring element size was iterated between 1x1 and 100x100, and the size that yielded the greatest improvement to the IOU for that particular image was chosen.

3.4 Results

3.4.1 Hyperparameter Optimization

The raw output from the top 5 hyperparameter configurations for the segmentation of WC in Ni-WC optical microscopy images using the vanilla U-Net CNN are shown in Table 3.3. The top model had an area under the ROC curve (AUC-ROC) of 0.944, a mean IOU of 0.87, and a mean dice coefficient of 0.929. Although the hyperparameter values listed in the table are similar in magnitude, the range in configurations between the models is significant. One hyperparameter that was consistent across the top 5 models was the SGD optimization

function. It is important to note that during the hyperparameter optimization, only vanilla SGD (i.e. no momentum) was tested. There is no conclusive evidence to show that one optimization function performs best across all types of data; however, for the samples analyzed in this paper, SGD had the best performance as shown in Table 3.3 [547]. Even exclusively using SGD as the optimizer, model architectures varied enormously, and resulted in large differences in performance. These differences in performance are expected since each model differs in the way it extracts features from the data [548]. Ultimately, it is the symphony of hyperparameters and model architecture that dictate the performance. SGD's positive performance is possibly due to the fact that it has been shown to generalize features better than adaptive optimization methods (e.g. Adam) [549, 550]. One known disadvantage of SGD is the potential to get stuck in local minima, due to the gradient being small in all directions. Using momentum, which incorporates a velocity vector of past gradients to SGD, can help propel backpropagation through problematic areas and towards the global minima [551]. To determine momentum's effect on the top model's performance, a second hyperparameter search was done with momentum ranging from 0 to 1, in 0.1 increments. Incorporating a momentum of 0.8 increased the mean IOU to 0.882 with a mean dice coefficient of 0.937.

The results for the hyperparameter optimization of the various backbones tested for both the U-Net and LinkNet are shown in Table 3.4; These values are the raw outputs from the models with no post-processing. No post-processing was done during the hyperparameter search to ensure efficient use of the computational resources provided by ISAIC. The best backbone for the U-Net used the mobilenet encoder achieving an AUC-ROC of 0.939, a mean IOU of 0.855, and a mean dice coefficient of 0.922, which is slightly worse than the original U-Net architecture (IOU of 0.882 and DC of 0.937). Comparatively, the top backbone for LinkNet was the resnet50 encoder, which had slightly better performance than the U-Net with an AUC-ROC of 0.945, a mean IOU of 0.879, and a mean dice coefficient of 0.935. The resnet50 encoder maintains the original residual block structure of the encoder of LinkNet, only slightly deeper [515]. All of the models utilized BCE as part of the loss function. BCE is a common loss function for binary classification as it mimics using maximum likelihood estimation to fit the model. It also pairs well with the sigmoid activation function during backpropagation since the sigmoid function outputs values between 0 and 1, which are the required range for $\hat{p}$ in equation 3.12[552].

The only instance where transfer learning outperformed training a model from scratch is

TABLE 3.3: The hyperparameters and their corresponding value for the top 5 vanilla U-net models trained during the hyperparameter optimization. Note that for SGD that momentum was set to the default of 0.

Hyperparameter	1	2	3	4	5
Batch Normalization	True	True	True	True	True
Batch Size	2	2	2	6	6
Learning Rate	0.01	0.001	0.01	0.001	0.1
Learning Rate Decay	0.5	0.75	0.25	0.25	0.75
Dropout Rate	0.8	0.5	0.5	0.2	0.1
L2 Regularization term	0	0	0.0001	0.01	0.001
Kernel Size	4	3	5	3	2
Number of Filters	16	16	16	32	16
Activation	elu	elu	elu	relu	elu
Loss Function	DL	BCE	BCE + DL	DL	BCE
Optimizer	SGD	SGD	SGD	SGD	SGD
AUC-ROC	**0.944**	0.942	0.942	0.936	0.935
Mean IOU	**0.870**	0.864	0.863	0.849	0.848
Mean DC	**0.929**	0.926	0.925	0.917	0.916

the U-net using the VGG16 encoder, Here the encoder weights from training the model on the ImageNet dataset [542] were unchanged during training. Thus, the model's learned ability to generalize and extract features was able to be transferred to the Ni-WC optical images used in this work. The success of transfer learning highlights the power of a large dataset (e.g. ImageNet [542]), and the models trained on it, to generalize to a variety of problems. Even though there is a stark difference between the features belonging to natural images compared to microstructures, the model was still able to achieve a mean IOU of 0.851. Due to time and resource constraints, fine-tuning the ImageNet weights was not able to be done; however, this could potentially increase the accuracy of the predictions.

TABLE 3.4: The hyperparameters and their corresponding value used for the training of the top performing model for each backbone and model architecture. Note that for SGD that momentum was set to the default of 0 and for Adam β_1 and β_2 were set to 0.9 and 0.999 respectively.

Hyperparameter	Model Architecture				
	Unet			LinkNet	
	mobilenet	renet50	vgg16	mobilenet	resnet50
Batch Normalization	True	True	True	True	False
Batch Size	2	4	4	2	4
Learning Rate	0.1	0.01	0.001	0.01	0.01
Learning Rate Decay	0.75	0.75	0.99	0.25	0.75
Decay Patience	5	5	10	20	30
Decoder Block Type	nn upsampling	transpose	nn upsampling	transpose	transpose
Encoder Weights	he normal	he normal	ImageNet	he normal	he normal
Freeze Encoder	False	False	True	False	False
Loss Function	BCE+DL	BCE	BCE+DL	BCE+DL	BCE
Optimizer	SGD	Adam	RMSprop	SGD	RMSprop
AUC-ROC	0.939	0.927	0.937	0.939	0.945
mean IOU	0.855	0.834	0.851	0.859	0.879
mean DC	0.922	0.903	0.918	0.923	0.935

3.4.2 K-fold Cross Validation

The results from the 5-fold cross-validation experiments on the test dataset are shown in Table 3.5. The values shown are after post-processing to illustrate the best performance that can be achieved with an automated pipeline. In the final column, the mean of the raw outputs are shown in brackets. The average increase in performance with post-processing is 0.02 - 0.07 across all metrics. When comparing the raw outputs from k-fold cross validation with the hyperparameter search, the generalization error increased for all models. A slight decrease in performance of the U-Net was achieved compared to the results of the top model

TABLE 3.5: The 5-fold cross validation performance of each model on the Ni-WC test dataset. The final column shows the mean performance across all of the folds, with the raw output values in brackets.

Model	Metric	Value for each for each fold					Mean
		1	2	3	4	5	
U-Net	AUC-ROC	0.968	0.962	0.964	0.967	0.966	**0.965** (0.935)
	Mean IOU	0.918	0.904	0.909	0.914	0.911	**0.911** (0.841)
	Mean DC	0.957	0.949	0.952	0.955	0.953	**0.953** (0.913)
U-Net/mobilenet	AUC-ROC	0.889	0.902	0.947	0.857	0.854	0.890 (0.871)
	Mean IOU	0.769	0.782	0.872	0.711	0.702	0.767 (0.741)
	Mean DC	0.868	0.876	0.829	0.932	0.824	0.866 (0.848)
U-Net/resnet50	AUC-ROC	0.926	0.925	0.941	0.926	0.936	0.931 (0.910)
	Mean IOU	0.831	0.829	0.864	0.833	0.854	0.843 (0.814)
	Mean DC	0.907	0.906	0.927	0.908	0.921	0.914 (0.896)
U-Net/VGG16	AUC-ROC	0.941	0.951	0.900	0.951	0.959	0.940 (0.913)
	Mean IOU	0.870	0.874	0.782	0.878	0.900	0.860 (0.808)
	Mean DC	0.930	0.932	0.876	0.935	0.945	0.924 (0.892)
LinkNet/mobilenet	AUC-ROC	0.955	0.947	0.946	0.952	0.947	0.950 (0.910)
	Mean IOU	0.890	0.871	0.894	0.881	0.869	0.876 (0.803)
	Mean DC	0.941	0.931	0.931	0.936	0.929	0.934 (0.889)
LinkNet/resnet50	AUC-ROC	0.945	0.937	0.937	0.935	0.938	0.939 (0.911)
	Mean IOU	0.867	0.861	0.855	0.850	0.855	0.858 (0.814)
	Mean DC	0.928	0.925	0.921	0.918	0.921	0.922 (0.898)

during the hyperparameter optimization shown in Table 3.3. Since the test set is unseen by the model it is used to showcase the model's classification ability; the minimal increase in error on the test set compared to the validation set during the hyperparameter search highlights the model's ability to perform on unseen data. Similar results were found when comparing the cross-validated and hyperparameter search results for the different model architectures of the U-Net and LinkNet, with the exception of the U-Net with a mobilenet encoder. This could be due to this model being biased towards the validation set during the hyperparameter search, giving a false sense of the model's ability to perform on unseen data.

The CNN struggled to properly classify the various defects that can be formed during

deposition. These problems were consistent across all models used in this work. Thus, to reduce redundancy, only the output of the U-Net will be explicitly discussed. One specific instance is cracking in the sample, which can be found at the bottom of the input image shown in Figure 3.10a. Although this crack is classified as part of the background, as seen in the ground truth in Figure 3.10b, the CNN falsely classified it as part of the carbide class, shown in Figure 3.10c. The type I error still remained after post-processing which can be seen in Figure 3.10d. Similar results were also found with pores in the carbides, where the model preferred to classify them as part of the carbide. This is expected given that both show similar pixel intensity values under optical microscopy. During the grinding and polishing stage of metallurgical sample perperation, the softer Ni matrix is preferentially worn, resulting in the WC particles being elevated in the sample. This is characterized by the dark outline that is found around each particle, that share a similar pixel distribution as the pores and cracks. During the ground truth labelling there were instances where the dark outline was included in the mask of the carbide. Therefore, the model was being trained to recognize the distribution of pixels that belong to the pores and cracks as belonging to the

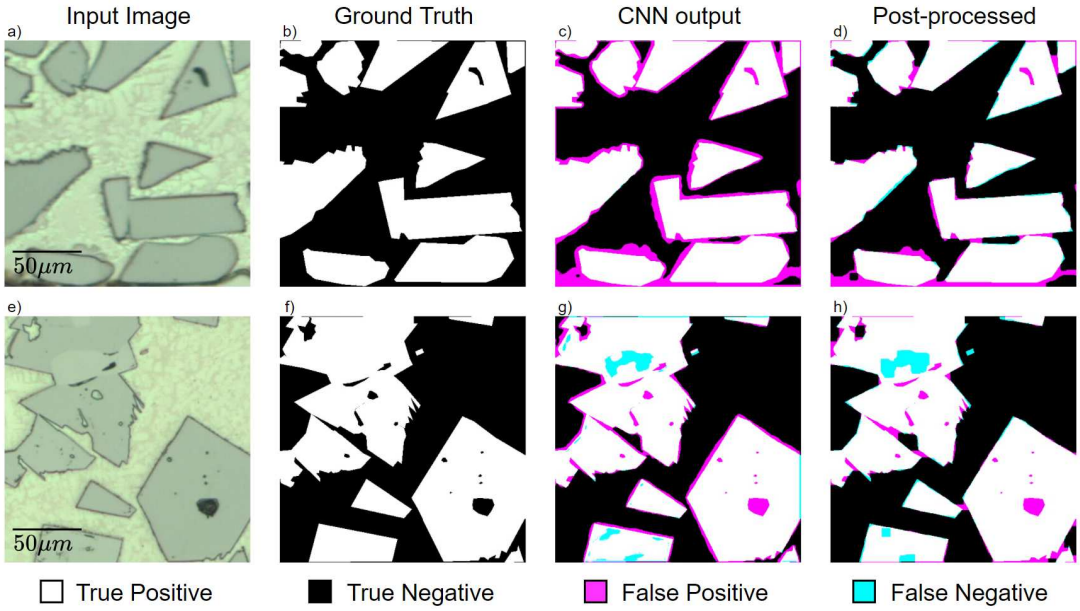

FIGURE 3.10: Visual depiction of the segmentation results where a) and e) show the input images into the CNN; b) and f) show the corresponding ground truth for images a) and e) respectively; c) and g) show the raw outputs of the CNN; d) and h) show the post-processed output. For all images the white pixels show the true positives, the black pixels show the true negatives, the magenta pixels show the false positives, and the teal pixels show the false negatives.

carbide particle, contributing to the type I errors found in the predictions.

Thermal degradation of the WC particles was another defect that was largely falsely classified by the CNN. Dissolution of WC in NiCrBSi has been shown to form W-Ni-Cr intermetallics along the particle boundary during PTA deposition [10]. A large dissolution zone can be seen at the bottom of Figure 3.10a that resulted in a false positive error due to the similarity in the pixel distributions between these regions and the WC particles, relative to the matrix. The model also performed poorly at accurately determining the edge of the WC particles, shown by the ring of type I errors surrounding the particles in Figure 3.10c and Figure 3.10g. Downsampling is important for CNNs to reduce the dimensionality of the image data, to reduce the chance of overfitting, and to allow the network to learn larger spatial context. The trade-off to this methodology is the model reduces its ability to distinguish high-frequency details, reducing the accuracy of classifying object boundaries[553]. Therefore, the coupling of the dissolution of W and C surrounding the WC particles, and the poor edge definition of the model's output, resulted in poor resolution when classifying WC particles exhibiting thermal degradation. In the development of the U-Net, Ronneberger *et al.* integrated an energy function into the loss function that increased the cost associated with the incorrect classification of border pixels around HeLa cells [500]. The additional cost forced the model to learn the boundaries around cells and could also be used to improve the boundary detection of WC particles. This may reduce the error caused by the poor classification of the thermal degradation of WC.

Similar to the inability to consistently characterize carbide that experience thermal degradation, the model also struggled to separate the carbides that had boundaries close together. Instead, the CNN tends to connect these areas reducing the individual particle count found in each image. This tends to be exacerbated by post-processing, as seen in the bottom right of Figure 3.10g and h, where type I errors are introduced after post-processing. The post-processing pipeline only accepts changes to the image that will result in an increase in the IOU of the image. Although new type I errors are introduced, the objective outcome does improve. Using simple non-local morphological transformations may not be the optimal choice for the post-processing of CNN output. Other post-processing methods such as conditional random fields [554], and localized adaptive methods [555] may improve the end results.

3.4.3 Model Uncertainty

For this work, the model's uncertainty was not quantified. Quantification of the carbide characteristics in Ni-WC microstructures in the context of PTA-AM will be used as a tool for maximizing the retention of WC during deposition. In a research context, the amount of data pertaining to a single sample is minimal, and the bottleneck for creating samples lies in the time required for sample preparation prior to optical microscopy. The size of the features is large enough to visually determine whether the model's prediction is correct, and the risk associated with uncertain predictions is low. Thus, the computational expense for quantifying the model's uncertainty outweighed the potential risk.

3.5 Calculating Carbide Percent and Mean Free Path

The carbide percent and the mean free path were determined for the entire test dataset and compared with the values from the ground truth images as seen in Table 3.6. The carbide percent and mean free path from the image shown in Figure 3.1a using both the CNN, and the image processing techniques [480, 489] are shown in Table 3.7. The CNN predictions were much closer to the actual measurements than those determined using image processing techniques. The carbide percent was calculated by determining the area of the white pixels over the total area of the image. Mean free path was quantified using two different methods. One of the methods uses equation 3.1, where N_L is determined by drawing 25 lines horizontally across the image, and counting the number of carbide intercepts, as described in ASTM STP 839 [478]. The location of these lines is randomly generated to try and mimic the manual calculation described in the ASTM standard. This process is repeated 15 times to have a valid statistical representation of the range of possible values for the mean free path. A problem with automating this process is that a carbide/matrix intercept of a binary image is when the pixels change from back to white or vise versa. The transition in pixel value is not always indicative of a carbide/matrix intercept. For example, the model tends to incorrectly classify pores and cracks as belonging to the carbide class, which would underestimate the mean free path. The second method used for calculating the mean free path was by simply scanning the image horizontally and counting the number of black pixels in between white pixels. This method operates under the assumption that all black pixels

belong to the matrix, which is not always correct. Pores, cracks, and false negatives incurred during the model's prediction are all cases that reject this assumption.

TABLE 3.6: The carbide percent and mean free path calculated over the entire testing dataset. The values stated are the mean ± the standard deviation for the test set. Mean free path (ASTM) refers to the methods described in ASTM STP 839 [478], and mean free path (CBP) refers to the method of counting the number of black pixels between areas of white pixels.

Measurement	Ground Truth	Model Prediction
Carbide Percent (Area %)	40 ± 11	41 ± 11
Mean Free Path (ASTM) (μm)	64.4 ± 30	79.9 ± 40
Mean Free Path (CBP) (μm)	89.7 ± 29.4	115 ± 35

TABLE 3.7: The carbide percent and mean free path calculated for the image shown in Figure 3.1a. The values stated are the mean ± the standard deviation for the test set. Mean free path (ASTM) refers to the methods described in ASTM STP 839 [478], and mean free path (CBP) refers to the method of counting the number of black pixels between areas of white pixels.

Measurement	Ground Truth	Model Prediction	Otsu's Method [480]	K-means Clustering [489]
Carbide Percent (Area %)	22	30	18	54
Mean Free Path (ASTM) (μm)	41.2 ± 7.8	37.3 ± 9.6	32.3 ± 26.6	16.3 ± 7.2
Mean Free Path (CBP) (μm)	52.8 ± 44	49.9 ± 42.8	48.6 ± 39.1	25.8 ± 26.1

A minor discrepancy can be seen between the values of the carbide percent for the ground truth images and the model's predictions, even though the model's predictions contain type I errors. During the post-processing step, the elimination of a large portion of type I errors also tend to incorporate more type II errors due to the global application of the morphological operations. The addition of type II errors offsets some of the type I errors in images that the model predicted poorer on, resulting in the carbide percentage being closer to that of the ground truth. Both the ground truth and the predictions had similar standard deviations in carbide percentages. These results empirically show that the carbide percent determined from the model's predictions are reflective of what is contained in the optical image.

The difference of mean free path values for the ground truth using the ASTM calculation and the counting black pixels (CBP) method are within 25 microns of the model's predictions. A difference of 25 microns in the mean free path could drastically effect the MMCs ability to resist abrasive wear depending on the size distribution on the abrasive [13]. One major

contributing factor to the large difference is including defects in the background class of the ground truth images, highlighted in Figure 3.10f. Since these areas are represented by small areas of black in the ground truth images, they will be falsely included in the quantification of the mean free path for the ground truth; this will drastically decrease the average value. The models predictions typically included defects as being part of the carbide class, thus not including them in the mean free path. Also, the intricate details of the carbides are smoothed out in the models predictions, omitting them from the mean free path calculation. Therefore, the lower value for mean free path from the ground truth images may be inaccurate, and the higher values from the models predictions may be a closer estimation of the mean free path.

Another important thing to note from Table 3.6 is the large standard deviation in the MFP values for both the models predictions and the ground truth. It is evident in Figure 3.3 that the physical phenomena of particle settling could be a large contributing factor, since there would be large discrepancy in the MFP depending on where the test image originated in the sample. The impact the depth where the image was taken from on the MFP is shown in Table 3.8, and a visual representation of the data for the CPB method can be seen in Figure 3.11. All points shown are from test images taken from the same sample, and the distance values reported are from the bottom of the sample. The mean free path tends to be smaller when comparing the bottom and the top of the sample; the middle contains a range of values. When the effects of particle settling are removed, the mean and standard deviation of the mean free path for the predictions and the ground truth, as well as the general trend of the values, are similar. The large overlap in the mean free path highlights the accuracy of the predictions. However, images that were taken at similar depths in the sample still display large deviations in the mean free path. Therefore, the stochastic nature of the particle settling that occurs during deposition creates local deviations in the mean free path, based on the particle shape, size, and orientation in the melt. The local differences in mean free path are also exacerbated by taking 256x256 pixel crops during the image acquisition process. Therefore, analyzing the mean free path from 256x256 crops of random portions of the image may not be representative of the entire image, and stitching the images together prior to determining the mean free path may help reduce the deviation. Image stitching could not be done in the current study, due to the sparseness of the crops used for the test set meaning a stitched image would not be metallurgically representative of the sample and result in a poor comparison.

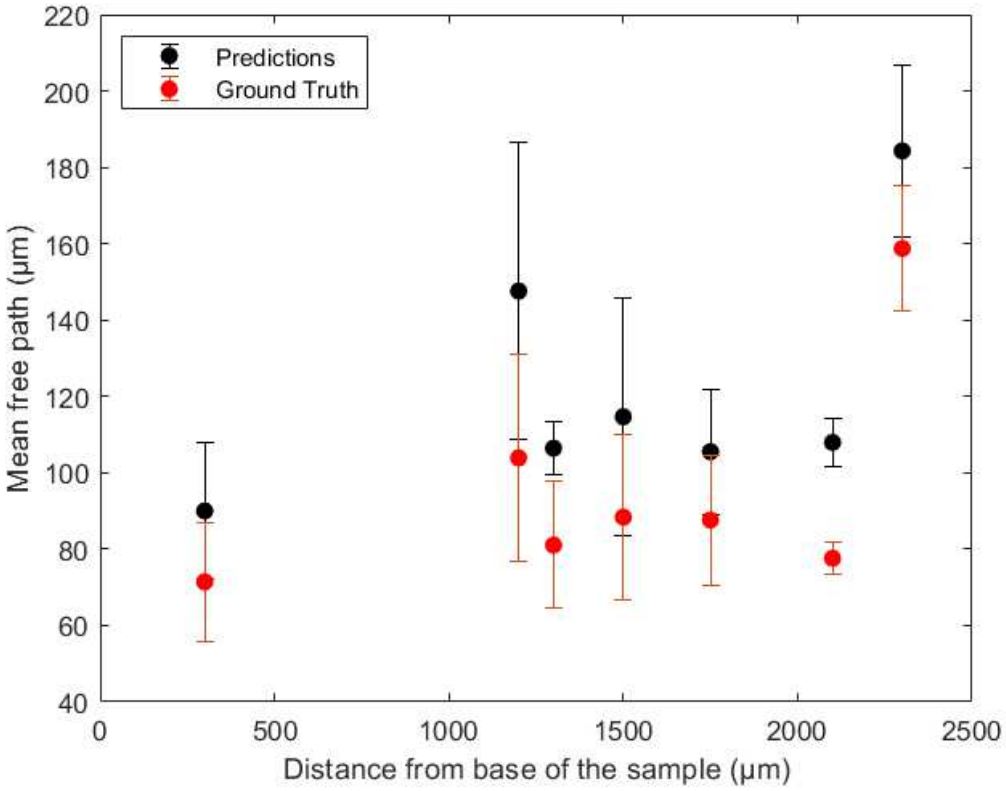

FIGURE 3.11: The mean free path as a function of depth in the sample. All points are the mean free path of test images that were taken from the same sample. The depth is measured from the bottom of the sample.

When comparing the ASTM and the CBP methods for determining the mean free path, the CBP method tends to have higher values for the predictions, and ground truth. The difference in the mean free path between the ground truth and the models predictions is also greater for the CPB method. A key distinction between the two methods is the representation of the mean free path. The ASTM method is an estimation of the average distance between the particles, since it uses multiple horizontal lines to sample the image to estimate the number of carbide particles per length. The CBP method is a direct quantification of the mean free path and accounts for all of the data provided by the image. In the context of digital images, counting the number of carbide intercepts is rudimentary compared to physically measuring the distance between particles over the entire image. Additionally, performing the physical measurements is computationally inexpensive. Therefore, for computationally determining MFP, the methods described in ASTM STP 839 may be outdated and may need to be improved to reflect the current state-of-the-art.

TABLE 3.8: The mean free path calculated at different depths in the sample. The values stated are the mean ± the standard deviation for the specific depth. Mean free path (ASTM) refers to the methods described in ASTM STP 839 [478], and mean free path (CBP) refers to the method of counting the number of black pixels between areas of white pixels. Note that depth is measured from the bottom of the sample.

Depth	Ground Truth (ASTM)	Model Prediction (ASTM)	Ground Truth (CBP)	Model Prediction (CBP)
300	46.9 ± 12.2	55.5 ± 12.4	71.4 ± 15.6	90 ± 17.8
1200	79.2 ± 30.6	106.2 ± 36.1	103.9 ± 27.2	147.6 ± 38.9
1300	69.3 ± 10.9	67.5 ± 7.6	81.1 ± 16.6	106.4 ± 6.8
1500	60.5 ± 16.8	76.8 ± 21.2	88.4 ± 21.8	114.7 ± 31
1750	60 ± 13.6	72.4 ± 12.3	87.6 ± 17.1	105.5 ± 16.3
2100	52 ± 4.9	65.4 ± 6.9	77.6 ± 4.1	108 ± 6.4
2300	140.9 ± 27	175.1 ± 49.3	158.7 ± 16.3	184.3 ± 22.5

3.5.1 Uncertainty of Measuring Carbide Characteristics

The uncertainty of measuring carbide percentage and the mean free path is an extension of the epistemic and aleatoric uncertainty from the model. This is due to the calculations of the carbide percent and mean free path being direct quantifications of models output. Therefore, without the quantification of the uncertainty of the model, the calculations of carbide percent and mean free path should be taken as qualitative evidence.

3.6 Discussion

3.6.1 Reduction in Processing Time

Although the predictions made by the model are not as accurate as those achieved by manually labeling the image, the average mean free path and carbide percent are within 25 μm and 1%, respectively. The largest difference between the two methods is in the processing time. Manually segmenting images from a sample that has a height of 30mm and a length of 100mm would take on the order of hours, whereas the model can semantically segment that sample in less than a minute. In the context of PTA-AM, the lower processing time could drastically reduce the time to optimize the deposition strategy to maximize the carbide percent and minimize the mean free path for the context of abrasive wear resistance.

3.6.2 CNN Transferability

As mentioned above, the training set only contained images of monocrystalline WC in a NiCrBSi matrix. Spherical eutectic WC is also used in industrial applications as they have been shown to have improved wear resistance under high-stress conditions compared to monocrystalline WC, warranted to the combination of high hardness and toughness [10]. Creating a ground truth for spherical WC has proven to be a difficult task, as many of the carbides undergo considerable dissolution during deposition. Degraded carbides have a fractured appearance, as seen in Figure 3.12a, making them challenging to accurately hand label. However, since spherical eutectic WC are still prevalent in the industry, it would be beneficial for the model to have the capability to segment them from optical images.

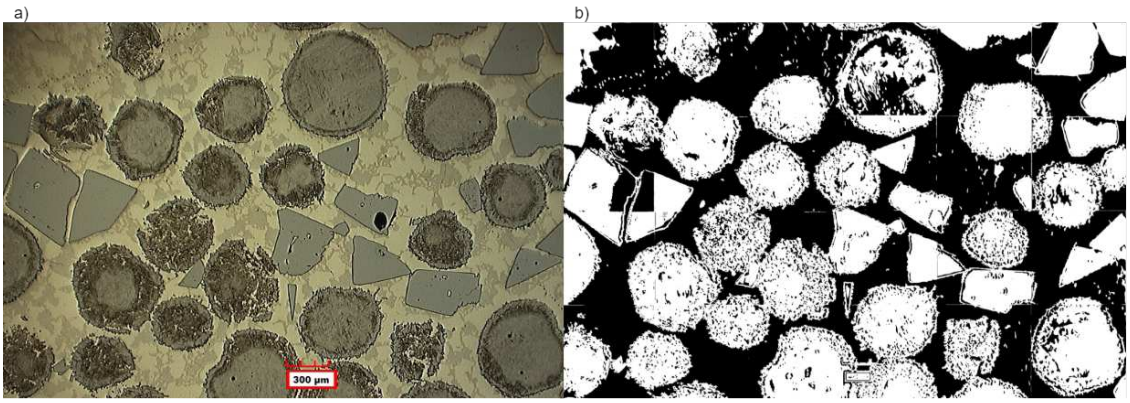

FIGURE 3.12: a) Image of a PTA-AM sample containing monocrystalline angular WC and spherical eutectic WC. The scale bar size is increased for reader clarity. b) The raw output from the U-Net on image a).

To test whether a U-Net only trained on angular monocrystalline WC has the robustness to also predict on spherical WC, the image shown in Figure 3.12a was cropped into 256x256 sections, totalling 48 images. The images were passed through the same post-processing pipeline prior to being passed through the model. Only the top fold from the original U-Net architecture was tested, and the classification threshold that performed best for the test set was also used for these images. No ground truths were made for these images due to the morphological complexity of the spherical carbides induced by the thermal degradation. No post-processing was done due to the inability to optimize the IOU against the ground truth. Manual application of morphological operations could have been used to improve the results, but the goal of this section was to show what is capable in an automated process that can be applied to any image. Additionally, no evaluation of the carbide percent or mean free path

was done since there was no ground truth images to compare the results to.

The raw predictions made by the model can be seen in Figure 3.12b. There are some sources of errors and uncertainty that became apparent during this experiment. One of those being bevelling of the corners of the sample, illustrated by the shadowing seen in the top left of Figure 3.12b, resulting in type I errors. Another source of error is artifacts left behind from polishing that resulted in additional type I errors. The model's predictions also tended to vary based on the other features contained within the cropped images that aren't representative of the sample as a whole; this was typically a source of type II errors in the prediction. An area where the U-Net seemed to improve on over images with just angular WC is the ability to correctly label the thermal degradation of the WC. The model was also better at separating particles that were close together. Even though it is apparent that many errors are present in the predictions, a visual comparison between the0 input image and the model predictions, the U-Net is capable of segmenting the spherical eutectic WC. It is speculated that significant improvement would be made if some data containing spherical eutectic carbides were added to the training dataset, and the model optimization process was repeated with the new dataset.

3.6.3 Machine Learning in Materials Science

The results of this study show that CNNs are capable of extracting the carbide percent and mean free path from optical images. Extrapolating these results to other materials systems, the equivalents of these measurements would be phase fraction and secondary dendrite arm spacing; both of which involve significant manual intervention to determine. Based on the ability of a U-Net trained only on angular WC to be able to also segment spherical WC, it can be speculated that if a dataset of optical microstructural images with the same intraclass feature variance as the ImageNet [542] dataset was developed, the model's ability to generalize features contained in microstructures would be able to be transferred to a multitude of metallic systems. The model's ability to extract information from images could be coupled with compositional data from energy-dispersive x-ray spectroscopy (EDX) and phase data from x-ray diffraction to create an automated phase-detection pipeline. This could reduce the need for using advanced characterization methods to extract microstructural information from material systems and allow for the same information to be gathered by using simpler,

more cost-effective methods. With the rapid advancement of new manufacturing technologies like additive manufacturing, reducing the need for advanced imaging techniques to properly characterize microstructures would decrease the time to optimize the deposition strategy for new materials. Compiling a dataset of this caliber would require significant collaboration across the materials science research community. However, such an effort would allow materials scientists to be able to fully exploit the capabilities of machine learning models, and revolutionize the way that materials research is done.

3.7 Conclusion

The effectiveness of semantically segmenting optical images of NiCrBSi-WC metal matrix composites using an automated convolutional neural network (CNN) pipeline has been demonstrated. The methodology described in this work is capable of more accurate segmentation of WC particles when compared with conventional image processing methods discussed in section 1. From the output of the U-Net CNN, the mean free path and carbide percent can be quantified as an effective empirical estimation of what is present in the sample. There is a significant reduction in the required user time to perform quantitative metallography on Ni-WC optical images. This may allow for better optimization of deposition strategies for maximum carbide retention and correlations between the carbide distribution and wear resistance that may not have been made previously. The robustness of the U-Net was also tested by applying the best-performing model to images that contained spherical eutectic WC that were not present in any of the training data. The model was able to segment the spherical WC with considerable accuracy. These results show that the applications of computer vision for materials science are not limited to complex imaging modalities and can be applied to more accessible methods like optical microscopy. Continued development of computer vision models will likely lead to CNNs replacing humans for the task of microstructure quantification.

3.8 Data Availability

The raw data required to reproduce these findings are available to download from DOI: 10.17632/2wmbc95xy9.1. The processed data required to reproduce these findings are available to download from DOI: 10.17632/2wmbc95xy9.1.

Chapter 4

Microstructural Characterization and Wear Resistance of 60 and 70wt% WC - NiCrBSi Thin Walls Deposited Using Plasma Transferred Arc Additive Manufacturing.

To be submitted as **Dylan Rose**, Tonya Wolfe, and Hani Henein, *Microstructural Characterization and Wear Resistance of 60 and 70wt% WC - NiCrBSi Thin Walls Deposited Using Plasma Transferred Arc Additive Manufacturing.*, JOM, 2023. The goal of this chapter is to address thesis objective 2 by changing the WC content from 60wt% to 70 and 80wt% WC in a NiCrBSi matrix.

4.1 Abstract

Plasma transferred arc additive manufacturing (PTA-AM) was used to deposit 60, 70, and 80wt% WC - NiCrBSi metal matrix composites. The 60 wt% samples had a homogeneous distribution of WC particles. At 70 and 80wt%, two defects were found in the microstructure: areas completely void of WC, termed denuded regions, and large pores. The microstructure

of the 60wt% sample consisted of blocky complex carbides ($(Ni_4W_2Cr_2Si)C_3$), γ-Ni cellular dendrites, a halo around the primary dendrites, and a lamellar eutectic of Ni_3Si/Ni_3B. There is increased thermal degradation of WC at 70wt% WC, causing a wider array of complex carbides, and higher W contents in the γ-Ni dendrites and the halo. Thermo-calc software was used to model the solidification of NiCrBSi and NiCrBSi with 10wt% W to determine the effect that W addition has on the solidification of the Ni alloy, and the results were compared to the 60 and 70wt% WC - NiCrBSi PTA-AM deposits. The abrasive wear resistance and the impact resistance of 60, 70, and 80wt% WC deposited with PTA-AM were comparable to a 60wt% WC - NiCrBSi PTA overlay.

4.2 Introduction

Industries ranging from agriculture [1–3] to pipelines [4–6] and mining [7–9] encounter abrasive wear provoking environments. The Canadian Energy Sector incurs losses in the billions of dollars annually due to the replacement of damaged components that have failed due to abrasive wear [10]. To mitigate the issue, traditional methods such as material substitution, surface treatments, and overlaying equipment with a hard metal or some form of metal matrix composite (MMC) are used. An MMC consists of a tough metal matrix with a homogenous distribution of a hard reinforcement phase, usually in the form of chromium (eg. Cr_3C_2) [556–558] or tungsten carbide (WC) [13, 41, 559]. Currently, NiCrBSi embedded with 65wt% WC overlayed using plasma transfer arc (PTA) offers the best wear resistance in mining applications with severe abrasion and impact wear [11, 559]. In PTA, a plasma arc is struck between a substrate and a tungsten electrode, and the material is mechanically fed into the arc and deposited onto the substrate material. Under conventional PTA conditions, the Ni matrix solidifies as primary γ-Ni dendrites, with Ni/Ni_3B eutectic [10, 11, 41]. The high heat input from conventional PTA causes convective mass transfer of W and C from the WC particles, reducing the erosion and corrosion resistance of the overlay [40–42]. The introduction of W and C into the matrix causes the formation of high W containing intermetallics throughout the Ni matrix, including Cr_3C_2, Cr_7C_3, and Ni_2W_4C or W_2C (β) polymorphs and α-WC [10, 11, 42, 43].

Plasma Transferred Arc Additive Manufacturing (PTA-AM) is an advanced metal additive manufacturing technology that uses a plasma arc as a heat source to deposit material in a

layer-by-layer fashion. It is a variant of the more commonly known method of PTA welding, but with the added capability of building up complex shapes in three dimensions. PTA-AM has been used for the deposition of Ni-based superalloys [26, 229], stainless steel [30, 560], tool steel [31], and titanium alloys [28, 561]. There has been limited research done on PTA-AM of WC-NiCrBSi MMCs. Mercado Rojas *et al.* [36] altered the operating parameters during PTA-AM of a 60wt%WC - NiCrBSi MMC, and found that the overall microstructure contained WC, γ-Ni, Ni_3Si, Ni_3B, and $Cr_{23}C_6$. The phases present in the microstructure do not suggest the degree of carbide dissolution that is experienced during PTA-AM; this could be attributed to the low heat input. However, no compositional analysis was done on the various phases of the microstructure to confirm the extent of the dissolved W in the matrix.

The present study aims to investigate how increasing the WC content from 60 to 70 and 80wt% in WC-Ni MMCs affects the distribution of carbides, formation of complex carbides, solidification structure of the matrix, and resistance to abrasive wear. The solidification of the MMC was modeled using Thermo-calc's Scheil solidification simulation, which was compared to the microstructure from the PTA-AM deposits. The effects of varying levels of W in the matrix on the solidification sequence of the microstructure is discussed. Additionally, the abrasive wear resistance and impact resistance of 60, 70, and 80wt% WC - NiCrBSi PTA-AM deposit are compared with a 60wt% WC - NiCrBSi PTA overlay.

4.3 Materials and Methods

4.3.1 Thermodynamics of WC-NiCrBSi

To understand the solidification sequence of the phases present in the microstructure of the PTA-AM of WC-NiCrBSi, Thermo-calc (v2022b, TCNI12 database) thermodynamic software was used. Thermo-calc results provide a framework for the thermodynamic and microstructural literature available for the WC-NiCrBSi system. The solidification simulations were done on the nominal composition of the Ni matrix (Table 4.1), and the Ni matrix with the addition of 10wt% W, to provide an understanding of how the addition of W affects the microstructure of the NiCrBSi matrix. It should be noted that the average overall W content

TABLE 4.1: Composition and size of the matrix material used in this work.

	Composition (wt%)						
Matrix Material	Ni	Cr	B	Si	C	Fe	Size Range (μm)
WOKA Durit 6030	Bal.	5.0 - 6.5	0.8 - 1.2	3.8 - 4.3	0.2 - 0.5	< 1.5	+63 -180

found in the Ni-matrix from the PTA-AM of 70wt% WC-NiCrBSi was ≈7.7wt% (≈2.0at%), and that no carbon was included in the thermodynamic calculations due to the low solubility (2.8 at%) of C in Ni [562]. Additionally, with the addition of C in the Scheil calculation Thermo-calc always forms WC. Removing C would force W to be in a solid solution with Ni, and the W in the matrix phases could be compared with PTA-AM. Scheil solidification was chosen as it is one of the limiting conditions in solidification. The concentration of the solute can be determined using Equation 4.1, where C_s is the concentration of the solid, k is the partition coefficient, V_s is the volume fraction of solid that has formed, and C is the nominal composition of the alloy.

$$C_s = kC(1 - V_s)^{(k-1)} \tag{4.1}$$

4.3.2 Plasma Transferred Arc Additive Manufacturing

The PTA-AM experiments were carried out using a Stellite Starweld 300M constant current power source with a Stellite Excalibur PTA torch. The PTA gantry system and torch can be seen in Figure 4.1. A 4.8 mm thoriated-tungsten electrode with a 4 mm setback was used, as recommended by the manufacturer. The electrode tip angle was maintained between 10 to 20 degrees. The operating parameters are shown in Table 4.2. For comparison, the operating parameters used for conventional PTA overlays are presented. It should be noted that the current is set based on the PTA controller dial, which is analog and was calibrated within the range of 100-200A. The values used in this experiment were lower than the calibrated region, and a linear extrapolation may not be valid. The energy density was calculated by dividing the power (current x voltage) by the powder feed rate. The contrast in the energy density (6.9 kJ/g for overlays and 1.6 kJ/g for AM) would create different thermodynamic conditions and resultant microstructure between the two methods. This reinforces the need for a complete microstructural analysis of the WC-Ni system under AM conditions. The

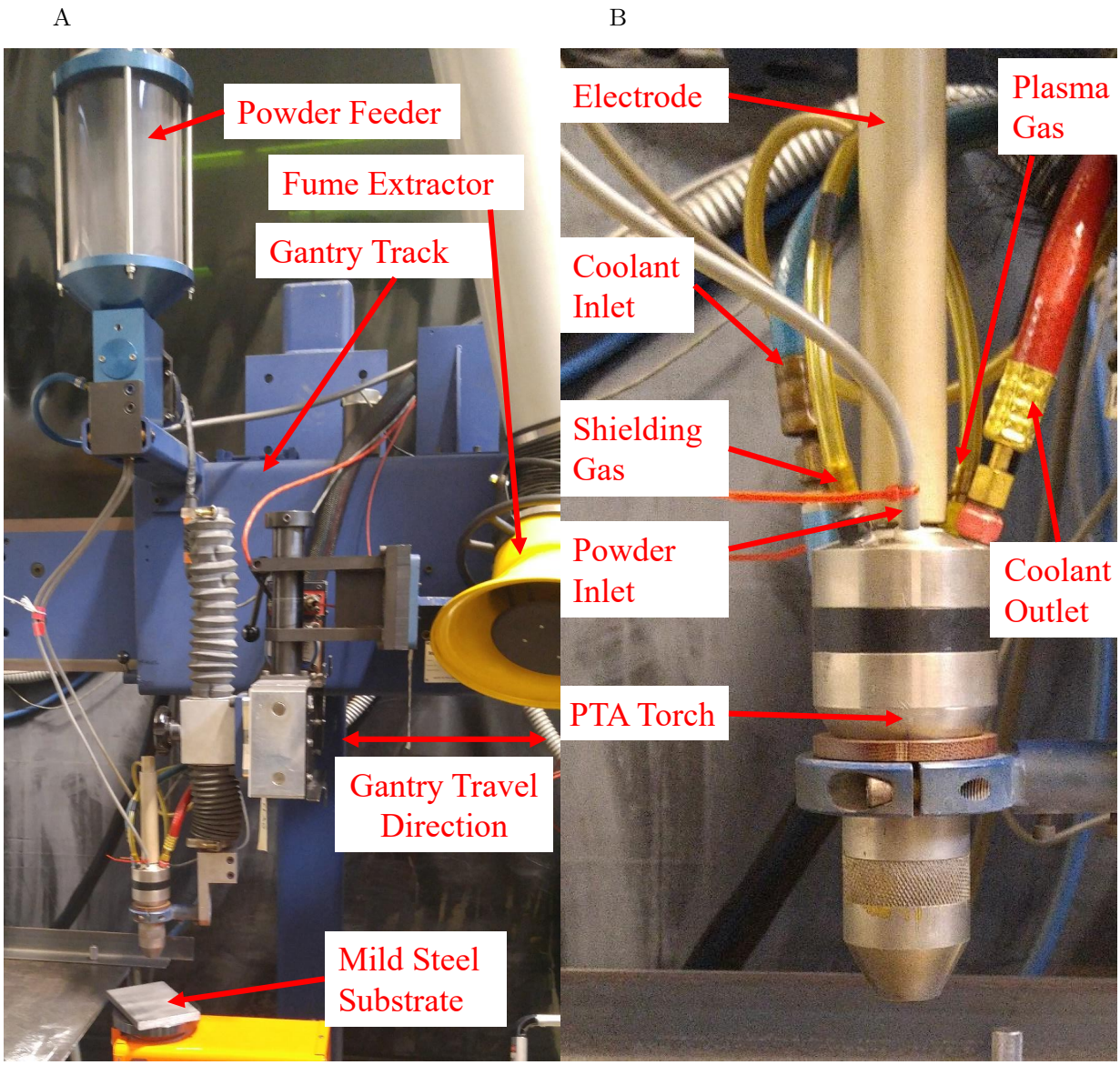

FIGURE 4.1: The PTA gantry system (A), and PTA torch (B) used for this work.

powder used for deposition was a blend of WOKA Durit 6030 and Kennametal SCNC070 monocrystalline WC, whose composition and size range is shown in Table 4.1 and Table 4.3, respectively. To build the single-track, multi-layer walls, the torch oscillated using the built-in gantry system with a width of 27mm, and the height was adjusted manually to maintain a constant voltage. At the end of each layer, a dwell time of 0.4s was used to ensure an even layer height. The Ni-WC MMC was deposited onto sand-blasted 12.7 mm (1/2") thick mild steel substrates with no pre-heat.

TABLE 4.2: The operating parameters used for the Stellite Starweld 300M PTA.

Operating Parameters	PTA-Conventional	PTA-AM
Current (A)	130	37
Voltage (V)	24	20
Travel Speed (mm/min)	230	600
Powder Feed Rate (g/min)	27	27
Energy Density (kJ/g)	6.9	1.6

TABLE 4.3: The composition and size WC powder used in this work.

		Composition (wt%)		
WC Powders	Powder Morphology	W	C	Size Range (μm)
Kennametal SCNC070 Monocrystalline	Angular	93.6	6.4	+63 -180

4.3.3 Infrared Imaging

A Mikron M7640 infrared camera was used to monitor the build's temperature to determine the effects of balling on the part's thermal history. The infrared camera has a temperature range of 0 to 2000°C, and is equipped with a 640x480 focal plane array microbolometer with a spectral bandwidth of 8-14 μm. The emissivity was not measured during the deposition, and during the experiment, the emissivity was set to 1. Therefore, the infrared results were used as qualitative observations to compare the heat build-up. LumaSpec™Offline Analyzer 5.0 software was used to set the range of temperatures recorded to be from 200-700°C to reduce the saturation of the images.

4.3.4 Characterization

An in-depth characterization of the microstructure of 60, 70, and 80wt% WC in a NiCrBSi matrix was conducted. The optical microscopy images were taken using an Olympus PMG3 optical microscope, and images were captured using an Olympus Q color 5 camera with Quartz PCI V5 software. Scanning electron microscopy was used to characterize the solidification structure of the PTA-AM deposits. The SEM used in this work was a Tescan Vega 3 equipped with a thermal emission source. The microstructure was imaged using an accelerating voltage of 20keV, and a working distance of 15mm. The SEM also contains an Oxford election dispersive spectroscopy system which was used to acquire semi-quantitative compositional data of all of the phases in the microstructure. All compositional data in this

section is an average of 10 data points. The phase distribution was determined using a Zeiss Sigma field emission SEM (FESEM) equipped with an AZtechSynergy electron backscatter diffraction detector.

4.3.5 Wear and Impact Testing

The abrasive wear, and impact resistance of the 60, 70, and 80wt% WC-NiCrBSi PTA-AM samples were tested and compared with a conventional overlay. Testing the performance was a means of determining if adding more WC would lead to superior properties. Wear performance was determined using a dry sand, rubber wheel abrasion test, following procedure A in the ASTM G65-16 standard. The sand in the Athabasca oil sands are generally angular quartz particles, 95% of which are less than 150µm [563]. The sand particles ranged from 50 to 70 mesh (297 to 210 μm), and the size of the test coupon was 25.4mm x 76.2mm x 12.7mm. Procedure A, which is a 6000-revolution test as outlined in the ASTM standard, was done twice per sample. The first test is to remove any of the softer surface matrix material and expose the carbides underneath. The second test is performed on the scar from the first test to mimic steady-state wear conditions. The impact test is a non-standardized test developed by Fisher *et al.* for testing the impact resistance of overlays for oilsands applications [564]. The test coupon is 25.4 x 69.9 x 12.7mm and is struck by an S2 tool steel hammer at 150rpm, creating an impact of approximately 8J. The test is run for 3-minute intervals, and the coupon is weighed before and after each interval, for 24 minutes or until failure. A rotary impact test was chosen to understand the material's resistance to repeated low-energy impacts and is a routine test for characterizing overlays in the oil sands mining sector.

4.4 Results

4.4.1 Thermodynamic Evaluation of WC-NiCrBSi

The Scheil solidification simulation done in Thermo-calc for the NiCrBSi matrix is shown in Figure 4.2, and the composition of the phases can be found in Table 4.4. The first phase to form is γ-Ni solid solution at just below 1300°C, containing high amounts of Si and Cr, with

TABLE 4.4: The composition of the different phases from the Scheil solidification of the NiCrBSi matrix shown in Figure 4.2 using Thermo-calc.

	at%				
Phase	Ni	Si	Cr	Fe	B
γ-Ni	85.8 - 80.2	7.4 - 14.1	6.0 - 5.3	0.7 - 0.2	0.1 - 0.2
Ni_3B	68.4 - 65.0	-	5.1 - 8.5	1.5	25.0
Ni_3Si	75.2 - 74.9	24.3 - 24.9	0.5 - 0.2	-	-

traces of Fe and B. The next phase to form is Ni_3B at ≈1050°C, with the highest amounts of Cr and Fe, while γ-Ni continues to form. As the primary phase grows the Si content increases, while the Cr content decreases. After solidification of γ-Ni ceases, a eutectic between Ni_3B and Ni_3Si is formed at ≈950°C. The Ni_3Si did not contain any other alloying elements.

A Scheil solidification simulation was also done for NiCrBSi matrix with 10 wt% W (Figure 4.3), and the composition of the different phases are found in Table 4.5. Primary solidification begins with γ-Ni solid solution at a slightly lower temperature (≈1220°C), containing W and higher levels of Si, Cr, and Fe than the matrix without W (Figure 4.2). Since the TCNI12 database only contains binary and ternary thermodynamic data, the decrease in the melting point could be due to error in the extrapolation to a 6-element system. The equilibrium partition coefficient for W, Cr, and Fe in the presence of Ni and Si are 2.0, 1.1, and 1.1, respectively [565]. The reduction in W, Cr, and Fe in γ-Ni as solidification progresses follows the values of the partition coefficients [565]. One major difference when adding W to the Scheil simulation is the formation of Ni_3Si instead of Ni_3B before the formation of the Ni_3Si/Ni_3B eutectic. The Ni_3Si phase had trace amounts of Cr and Fe, while the Ni_3B phase contained the highest amounts of Cr, Fe, and B. Additionally, there is the formation of WB during the solidification of Ni_3Si/Ni_3B, which was not present in the Sheil simulation with no W.

4.4.2 PTA-AM: Comparison between 60, 70, and 80wt% WC

The as-built samples for the 60, 70, and 80wt% monocrystalline WC are shown in Figure 4.4, and the sample dimensions are 90mm x 27mm x 6mm, 75mm x 27mm x 8mm, and 65mm x 27mm x 9mm for the height, length, and thickness, respectively. Comparing the builds in Figure 4.4, the higher loading of WC increased the surface roughness of the wall. The

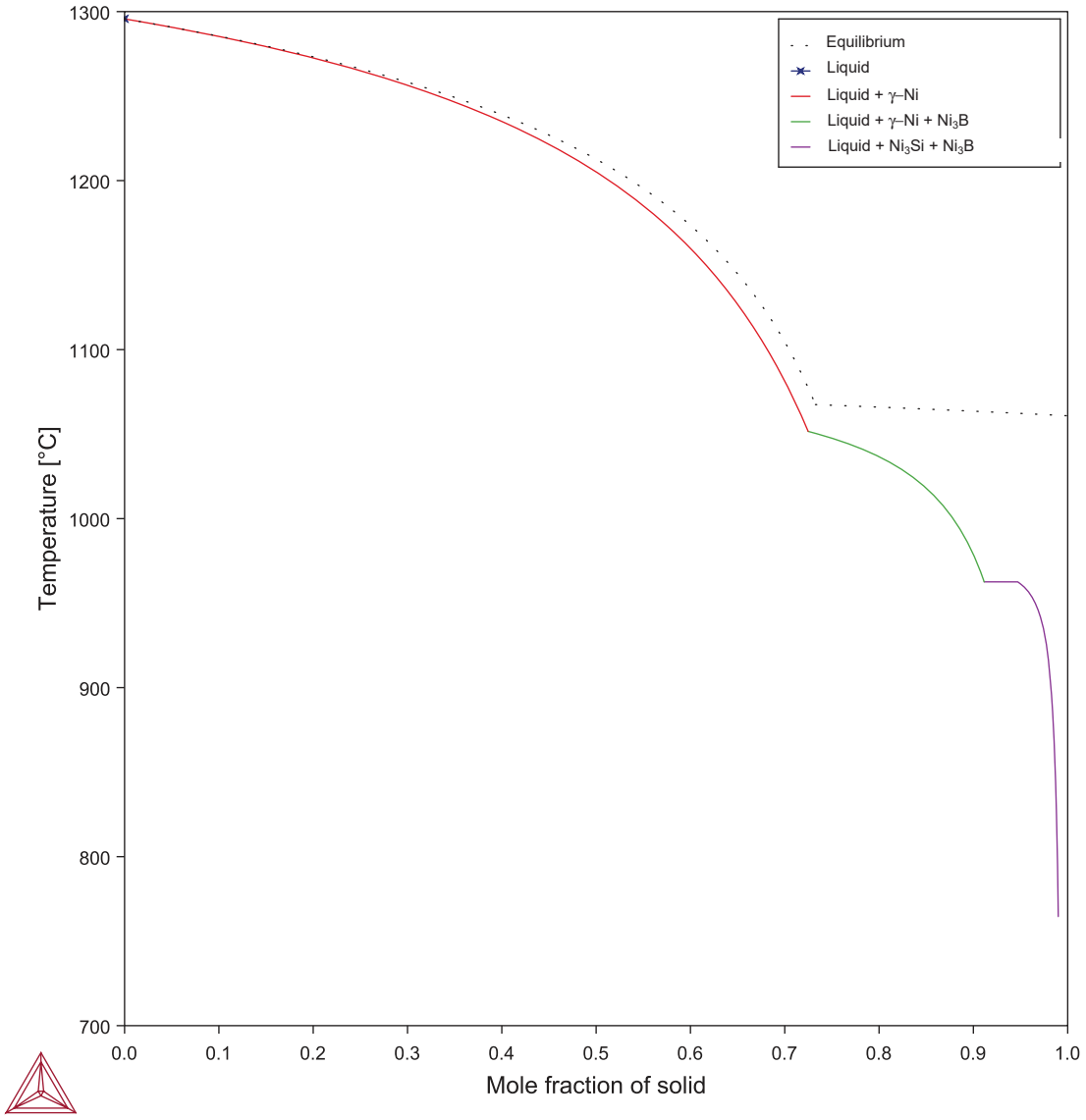

FIGURE 4.2: Scheil solidification simulation of Durit 6030 NiCrBSi matrix. The compositions for the different phases are provided in Table 4.4.

60 wt% WC wall had more slumping during the deposition, denoted by the inconsistent layer geometry (red arrows in Figure 4.4A). The red square at the bottom of the samples in Figure 4.4 shows that the first few layers have a slightly different texture and layer geometry. Instead of being a uniform stringer bead, the first layer was discontinuous balls; this is known as the "balling effect" and is a common defect in AM [566–568]. The balling effect is due to insufficient wetting [568–570] of the MMC with the substrate due to the lack of substrate pre-heat, and low heat input from the plasma. Once sufficient heat had been supplied, the MMC was uniformly deposited. The balling effect is exacerbated by the increased carbide

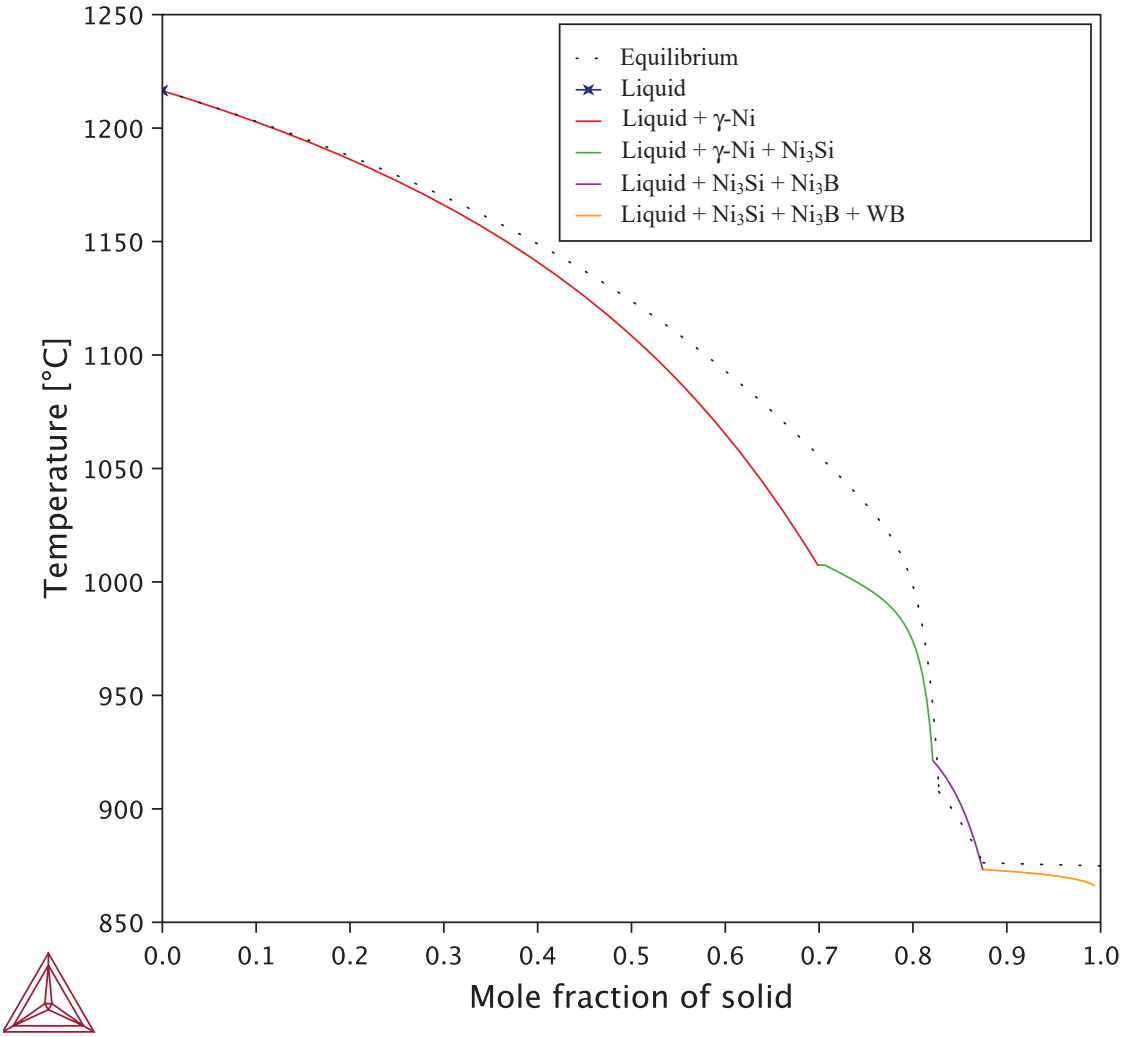

FIGURE 4.3: Scheil solidification simulation of Durit 6030 NiCrBSi matrix with 10wt% W. The compositions for the different phases are provided in Table 4.5.

content, which could be due to the reduced flowability of the melt [571], and an increase in the effective viscosity [572]. The balling effect can cause discontinuities in the build in each subsequent layer[36]. In some cases, the space between the balling is filled in by the liquid, but in others, the error cascades through the rest of the build. The observation of balling is also a sign of poor bonding with the substrate, which would decrease the heat transfer efficiency between the substrate and the part.

An infrared camera was used to monitor the heat accumulation during the PTA-AM build

TABLE 4.5: The composition of the different phases shown in Figure 4.3 using Thermo-calc. The range of values highlights the difference in composition as solidification progresses, where the first and last numbers are the composition at the beginning and end of solidification, respectively. If no range is given the composition was constant.

	at%					
Phase	Ni	W	Si	Cr	Fe	B
γ-Ni	81.5 - 80.2	1.4 - 0.5	10.0 - 13.0	6.3 - 5.7	0.8 - 0.6	-
Ni_3Si	75.4	-	23.5	0.9	0.2	-
Ni_3B	63.1 - 64.2	-	-	9.0 - 8.5	2.9 - 2.3	25.0
WB	-	51.8 - 55.7	-	-	-	48.2 - 44.3

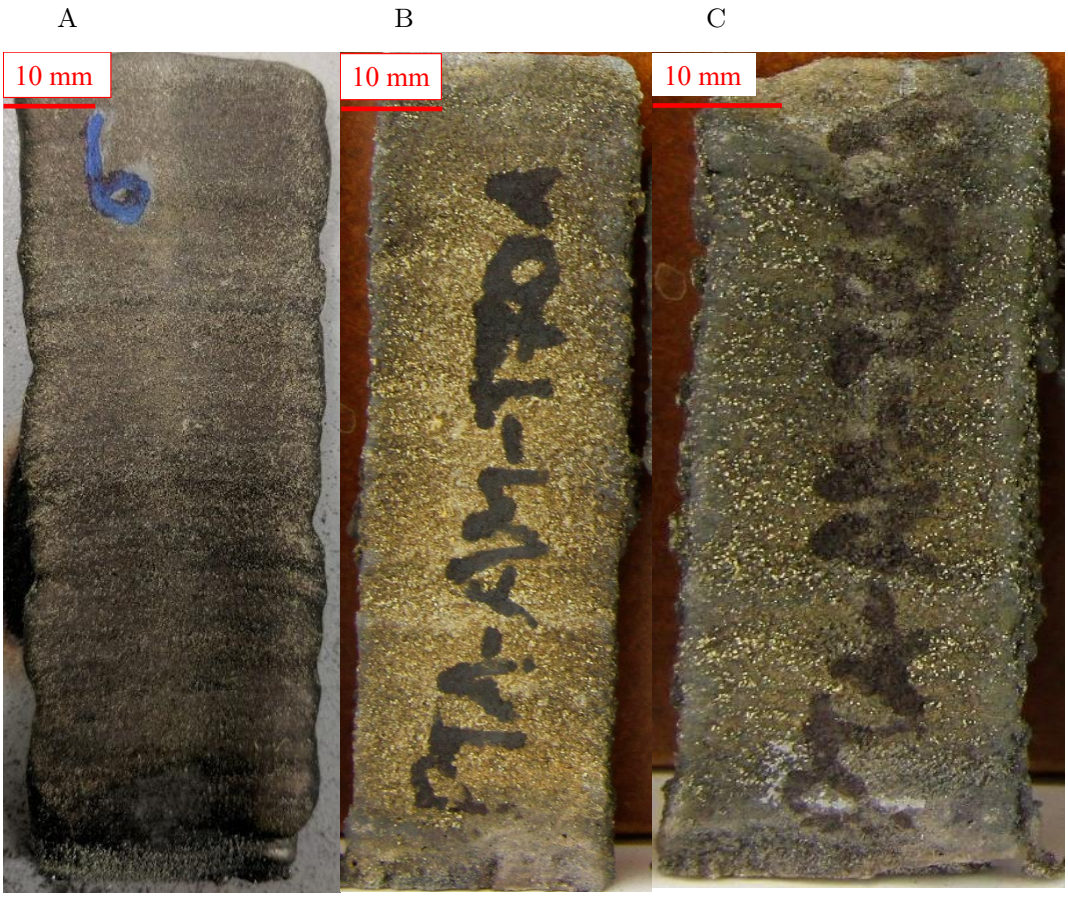

FIGURE 4.4: PTA-AM samples containing 60(A), 70(B), and 80(C) wt% monocrystalline WC in a Durit 6030 NiCrBSi matrix. The sample dimensions for A, B, and C are 90mm x 30mm x 6mm, 75mm x 27mm x 8mm, and 65mm x 27mm x 9mm, respectively

process, and are shown in Figure 4.5. Note that these walls differ from those shown in Figure 4.4. The samples shown in Figure 4.5A and Figure 4.5C use the same operating parameters shown in Table 4.2. Increasing the energy density has been previously shown to increase

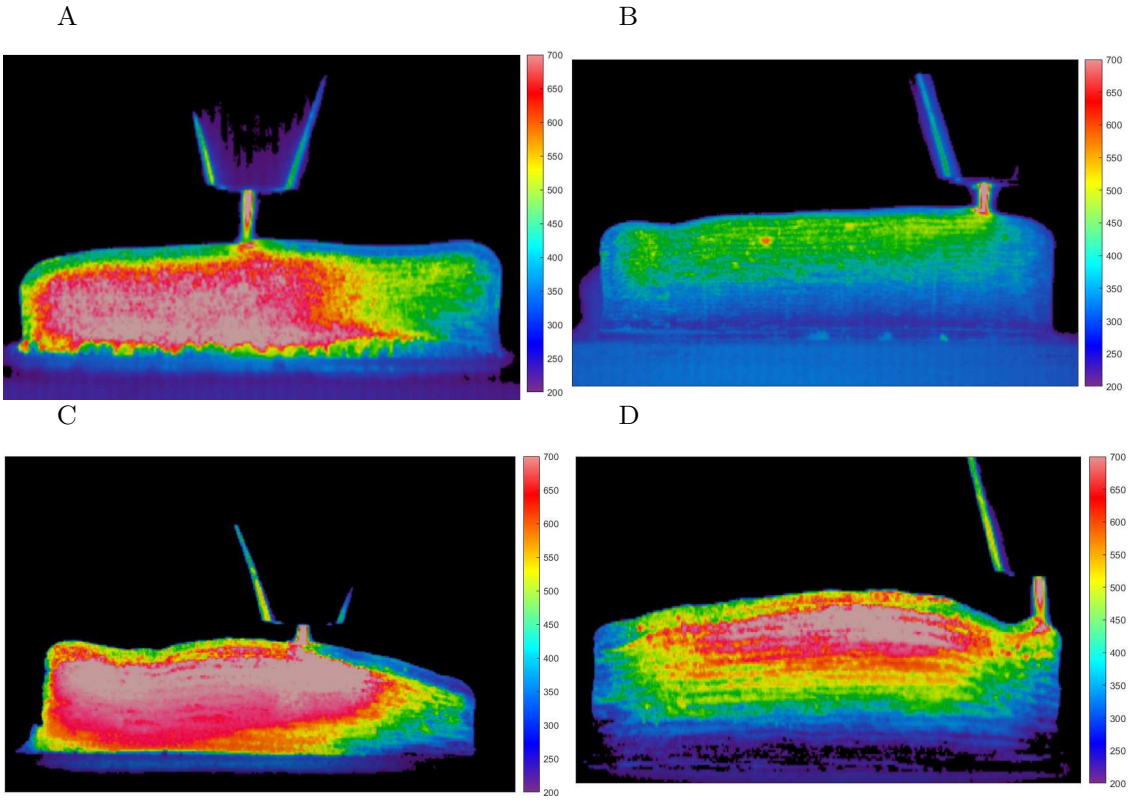

FIGURE 4.5: A) 60wt% WC with constant 37A current, B) 60wt% starting at 95A current, then dropping to 37A after 5 layers, C) 70wt% WC with constant 37A current, and D) 70wt% starting at 95A current, then dropping to 37A after 5 layers. The sample dimensions for A, B, C, and D, are 100 x 26mm, 100 x 25mm, 100 x 26mm, and 100 x 35mm, respectively. Note that the torch oscillates back and forth from left to right.

the wetting of the newly deposited material and decrease the balling effect [566, 573, 574]. For Figure 4.5B and Figure 4.5D, the current was increased to 95A for the first 5 layers, and then decreased to 37A. Samples A and C could be removed manually with ease, while the higher current samples were metallurgically bonded. Comparing the thermal profile from Figure 4.5A and Figure 4.5B, as well as Figure 4.5C and Figure 4.5D, it can be seen that the bonding with the substrate drastically changes the amount of heat that is retained during printing. For the 60wt% sample, the average temperature in the sample decreased, and significantly more heat was transferred to the substrate based on the increase in substrate temperature. The effects of adding 10wt% more WC on the thermal history is plainly shown when comparing Figure 4.5A and Figure 4.5B with Figure 4.5C and Figure 4.5D. The 70wt% samples had more heat accumulation than the 60wt% samples, which could be attributed to the difference in thermal properties between the two deposits. The heat capacity for Ni and WC at 200 - 700°C is 7.8 - 8.0 J/molK [575] and 27.6 - 36.0 J/molK [576], respectively.

Additionally, the thermal conductivity of Ni is 90 [577] and WC is 110 [578] W/mK. With the heat capacity and thermal conductivity of WC being higher than Ni, the more WC content in the sample, the more heat that will be accumulated in the sample. The significant amount of porosity in the sample (Figure 4.6) would lead to poor heat transfer through the wall, which could attribute to the higher amounts of heat accumulation.

4.4.3 Microstructural Characterization

4.4.3.1 Macrostructural Comparison of 60, 70, and 80wt% WC in NiCrBSi

The macrostructure of 60, 70, and 80 wt% WC in a NiCrBSi matrix are shown in Figure 4.6A, Figure 4.6B, and Figure 4.6C, respectively. The 60wt% sample had a homogeneous distribution of WC particles with very little porosity. With an additional 10 and 20 wt% WC, two defects dominate the macrostructure: areas void of WC, termed denuded regions [11] (labeled in Figure 4.6C), and large pores. Due to the undesirable microstructure obtained from both 70 and 80wt% WC, 80wt% WC was not considered for further analysis for this thesis work. The large pores were speculated to be a result of different mechanisms. The

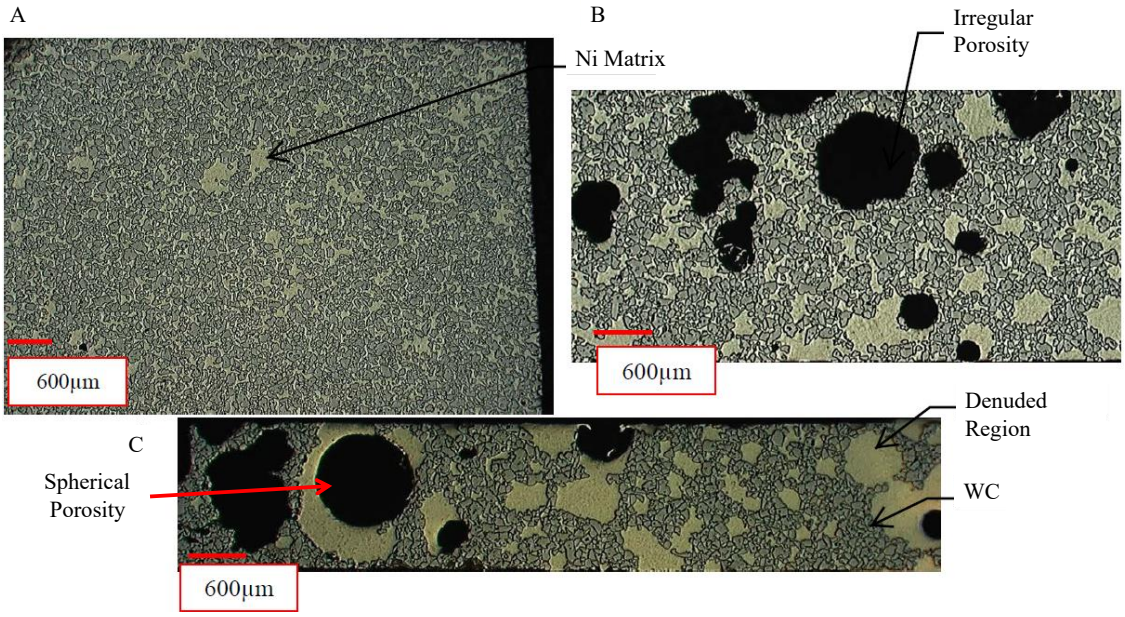

FIGURE 4.6: The microstructures from the samples shown in Figure 4.4, where A is 60wt% WC, B is 70wt% WC, and C is 80wt% WC. The light green is the Durit 6030 matrix, the dark green particles are WC, and the black regions within the sample are pores.

large irregular shaped pores could be manufacturing defects resulting from sub-optimal deposition parameters, and poor flowability of the melt pool from increased apparent viscosity [572]. There has not been any confirmed mechanism that causes denuded region formation. Sundaramoorthy *et al.* proposed that denuded regions could be from liquid Ni forming in the plasma not mixing with the remainder of the melt pool due to surface tension [10]. Wolfe *et al.* suggests that W vapor formed in the plasma may diffuse into Ni droplets and enter the pool as a mushy phase [11]. The mushy spheres would then retain their spherical shape during solidification. Denuded region formation is discussed more in Chapter 5.

4.4.3.2 Characterization of 60wt% WC in NiCrBSi

Backscatter SEM was used to observe the microstructure of 60wt% monocrystalline WC in NiCrBSi matrix, shown in Figure 4.7. Higher magnification images can be found in Figure 4.8 to Figure 4.10. The monocrystalline WC are the large white angular particles. There were three primary morphologies of secondary carbides that formed during solidification, which include blocky carbide (A), small blocky carbides (B), and ring carbides (C), shown in Figure 4.8. The Ni matrix formed a cellular dendritic structure (D), most of which contained a halo (E) surrounding the dendrite shown in Figure 4.9. The interdendritic region contains a lamellar eutectic (F). Previous literature states that the eutectic of 60wt% WC in NiCrBSi consists of γ-Ni and Ni_3B [10, 18, 43]. Using a laser heat source, the eutectic structure is lamellar [579, 580]. The red box in Figure 4.10 show instances where the eutectic structure may be too fine to be resolved with SEM. A phase with a ring-like morphology (G) can also be found throughout the microstructure, and based on the cracks seen as the black lines in the red square in Figure 4.11, this phase is likely brittle. The cracks form when the ring phase is in close proximity to a WC particle, and could be due to thermal residual stresses during solidification [581, 582].

The composition of the different phases are located in Table 4.6. Since no W is found in the matrix alloy, one of the mechanisms that could introduce W to the microstructure is convective mass transfer from the WC during the PTA-AM deposition process. Convective mass transfer from WC during PTA is a common phenomenon [10, 11, 13, 42, 43]. The brighter phases have a higher molecular weight, highlighting the distribution of W throughout the microstructure. Convective mass transfer of W and C resulted in three different morphologies of

secondary complex carbide particles (A, B, and C) containing varying amounts of alloying elements. The larger blocky carbides (A) had higher W, C, and Cr content ($(Ni_4W_2Cr_2Si)C_3$), while the smaller (B) ones had a higher Ni and Si content ($(Ni_3WCrSi)C_2$). The ring carbides (C) tend to have the highest Ni, and lowest W content ($(Ni_8W_4Cr_3Si_2)C_6$) out of all of the carbides.

The primary phase (D) is a Ni solid solution containing W, Si, Cr, and Fe. The halo

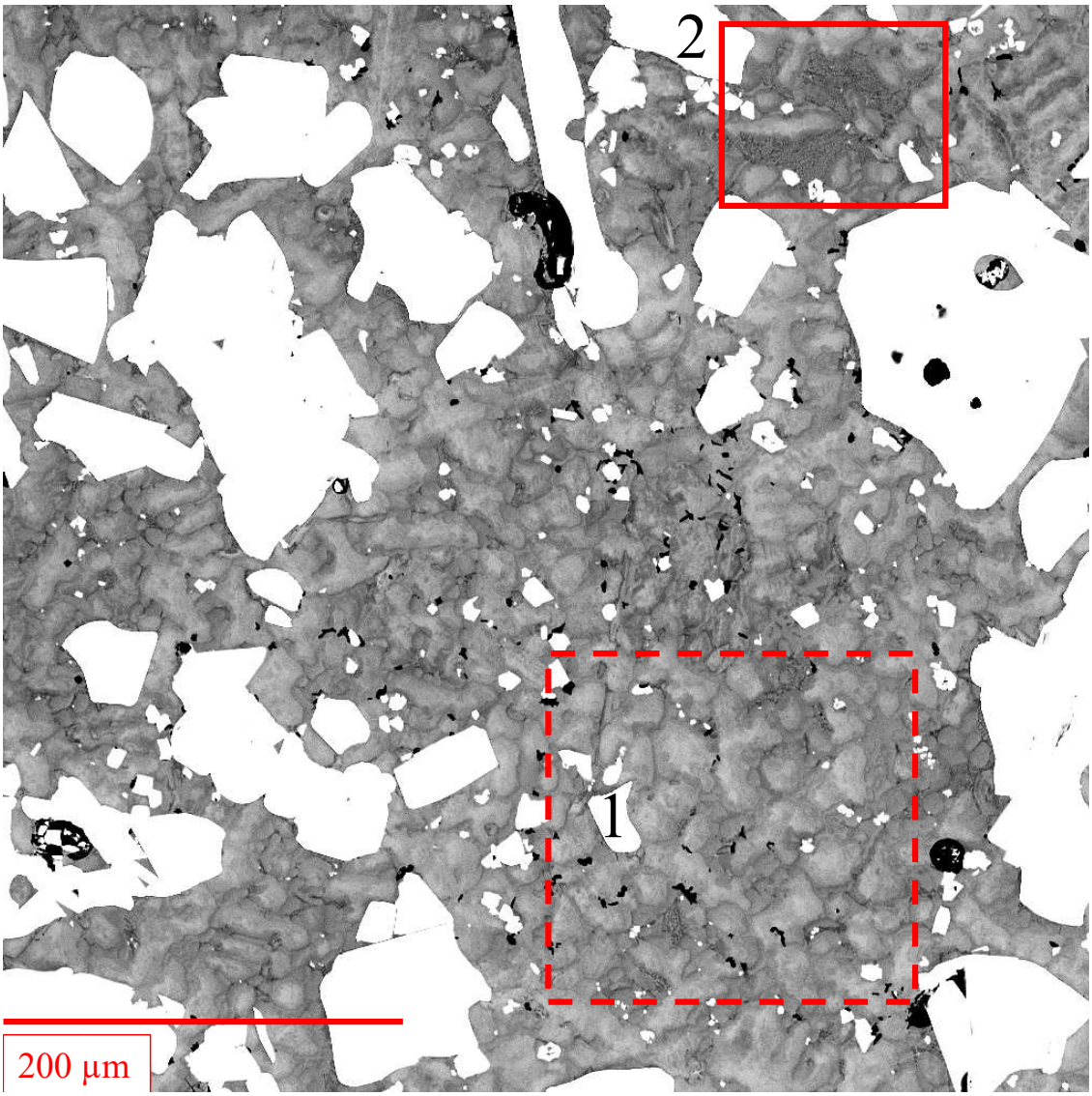

FIGURE 4.7: Backscatter SEM image of 60wt% WC. The heavier elements are shown as brighter, highlighting the distribution of W throughout the sample. The dashed red square (1) and the red square (2) is where Figure 4.8 and Figure 4.9 were taken respectively.

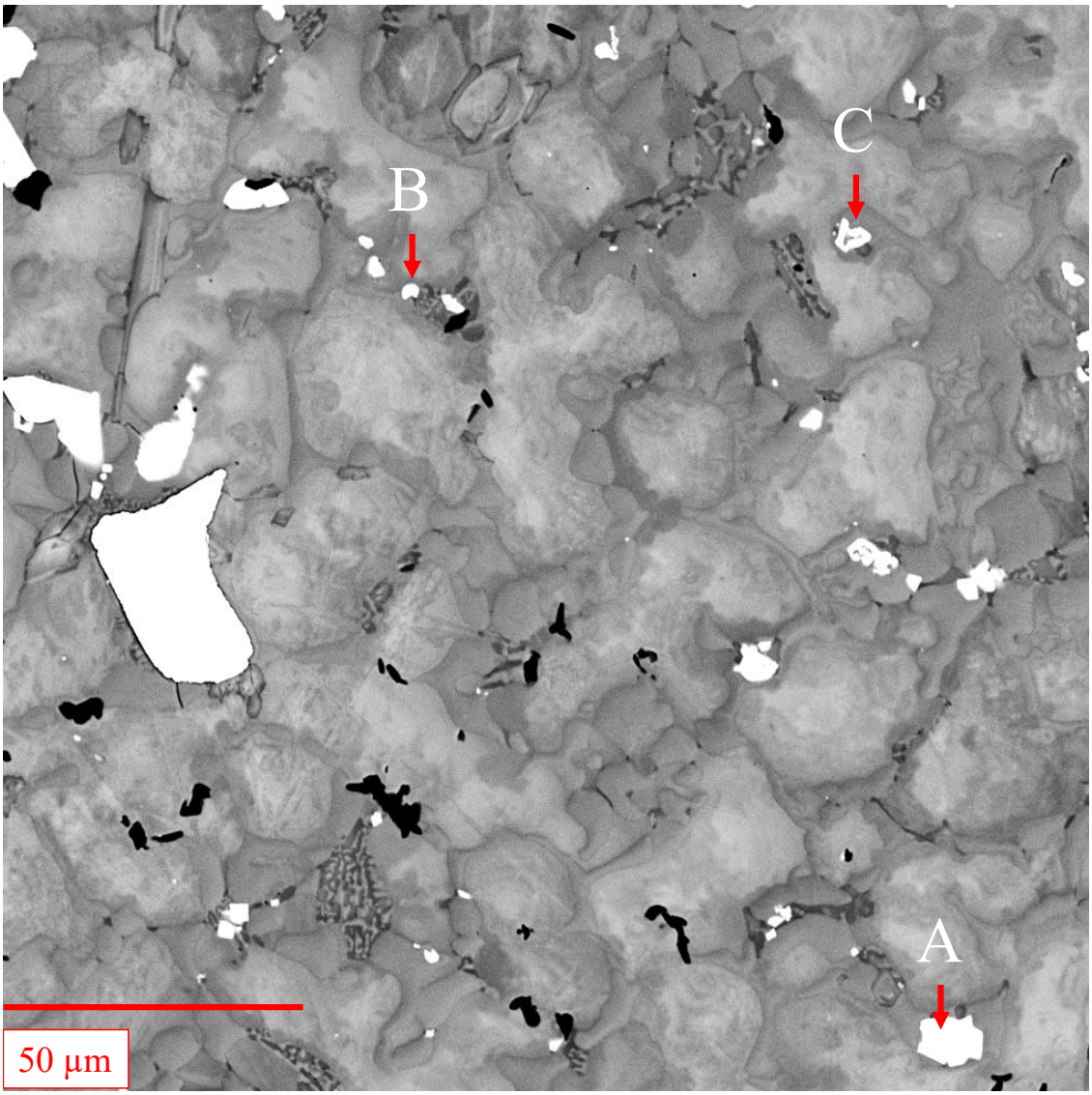

FIGURE 4.8: Backscatter SEM image from the dashed red square (1) in Figure 4.7 of 60wt% WC - NiCrBSi. The phases with a higher molecular weight are shown as brighter. The letters correspond to the compositions presented in Table4.6.

(E) around the primary phase contains no W, less Cr and Fe, and more Si. The equilibrium partition coefficient for W, Cr, and Fe in the presence of Ni and Si are 2.0, 1.1, and 1.1, respectively [565]. In contrast, the partition coefficient for Si is around 0.5. It should be noted that the equilibrium partition coefficient would be affected by the interaction between the alloying elements, and by the change in the solidification temperature caused by the alloying additions [565]. However, the distribution of the alloying elements in the Ni matrix is supported by the ternary equilibrium partition coefficients [565]. The primary phase that

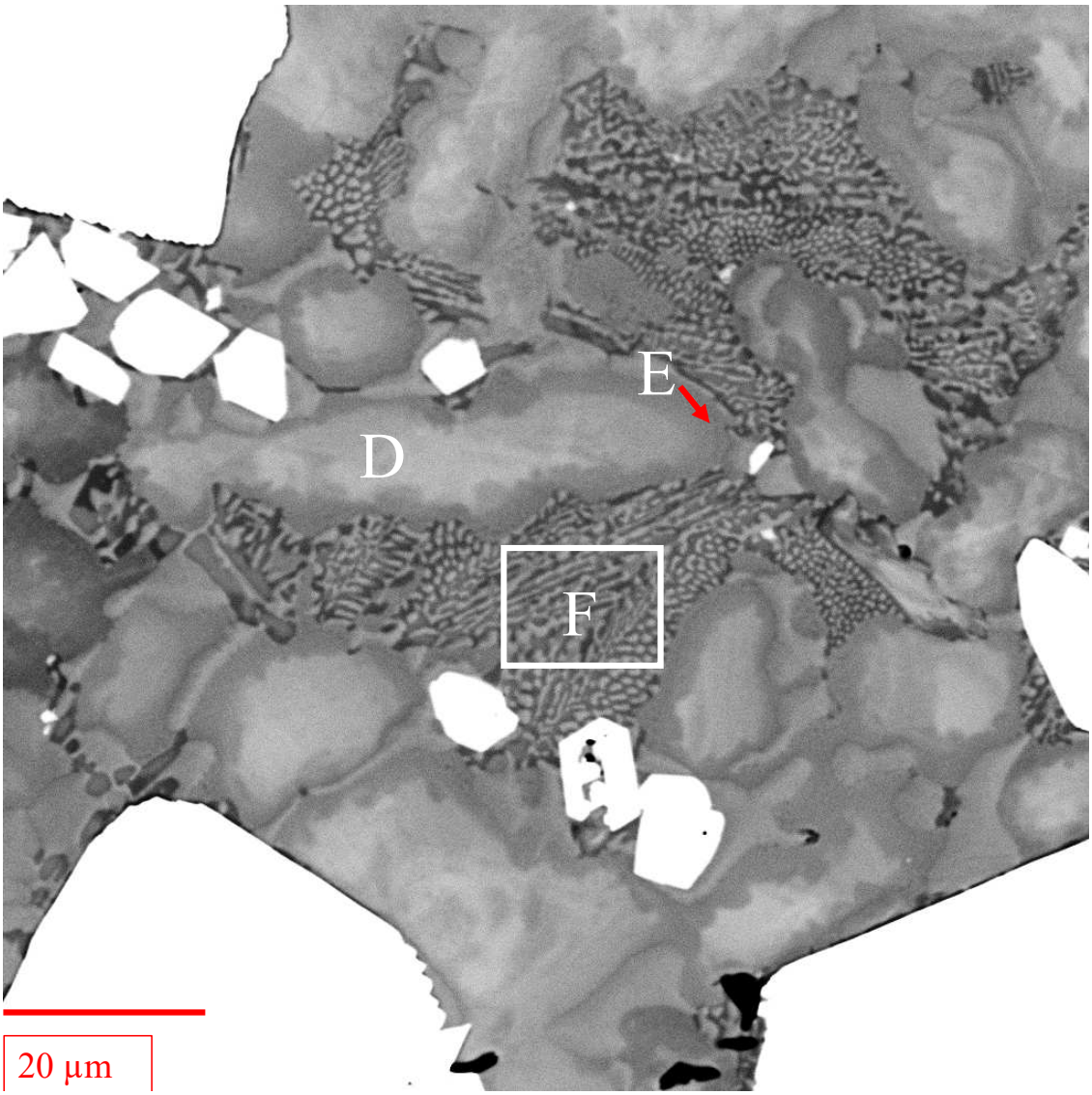

FIGURE 4.9: Backscatter SEM image from the red square (2) in Figure 4.7 of 60wt% WC - NiCrBSi. The phases with a higher molecular weight are shown as brighter. The letters correspond to the compositions presented in Table4.6.

solidifies first has higher concentrations of W, Cr, and Fe than phases that form later in the solidification process (from the remaining liquid after forming the primary phase). The light phase in the lamellar eutectic (F) has less Si, and slightly higher levels of Cr compared to the dark phase. The lamellar spacing is 1.04 μm, and the interaction volume for the emission of characteristic x-rays in iron is approximately $1\mu m^3$ [583]. Therefore, it is possible that some of the detected characteristic x-rays from the dark phase of the eutectic are included in the signal from the light phase of the eutectic, and vice versa. This would mean that the

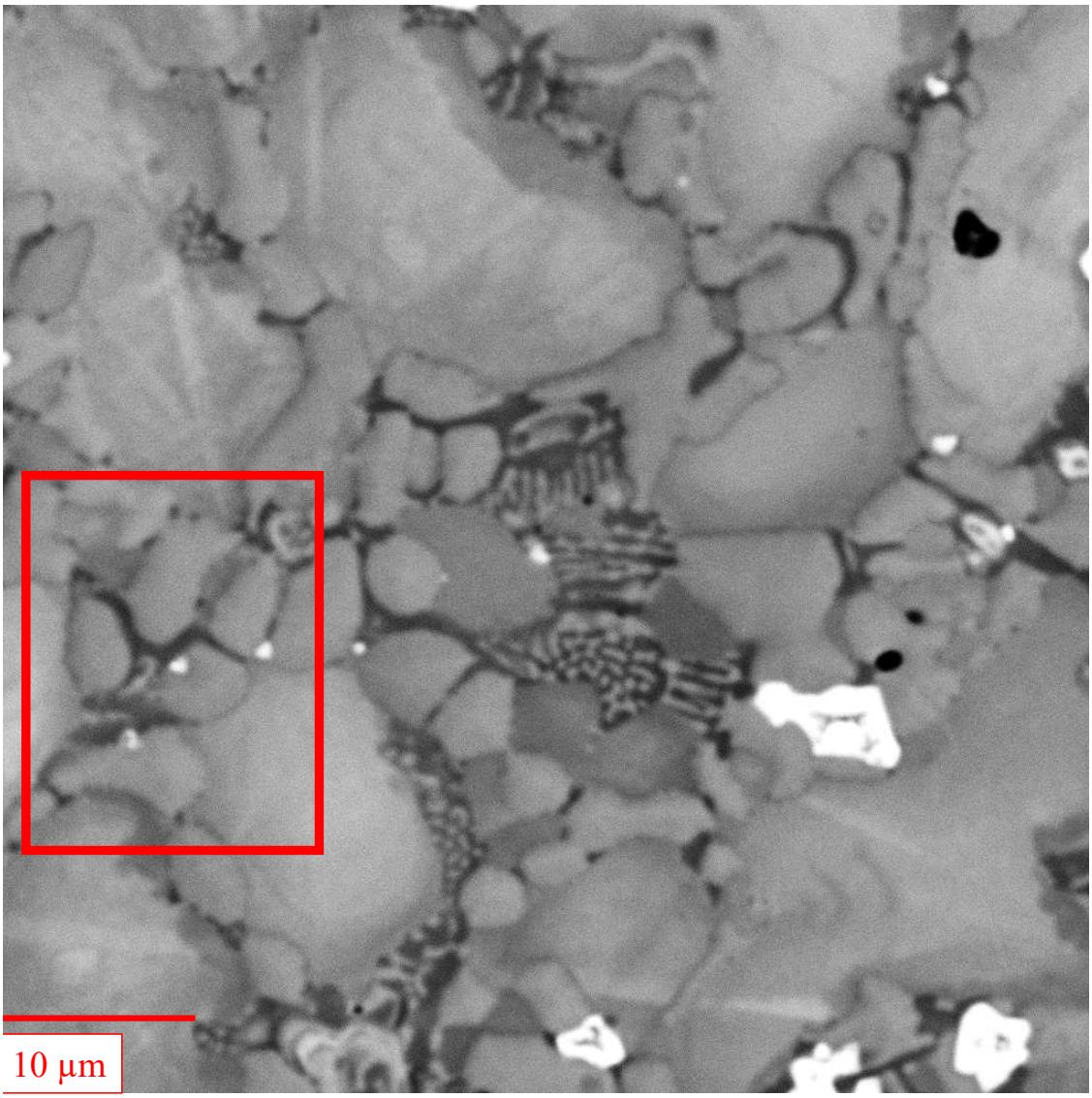

FIGURE 4.10: Backscatter SEM image of 60wt% WC - NiCrBSi. The phases with a higher molecular weight are shown as brighter. The letters correspond to the compositions presented in Table4.6.

Si content in the light phase, and the Cr content in the dark phase could be overestimated. The ring phase (G ($(Ni_4WCr_{13}Si)C_{10}$)) contained all of the alloying elements except for Fe.

4.4.3.3 Characterization of 70wt% WC in NiCrBSi

A low magnification backscatter SEM image mainly of a denuded region in a 70wt% angular monocrystalline WC in NiCrBSi is shown in Figure 4.12. Higher magnification images of the

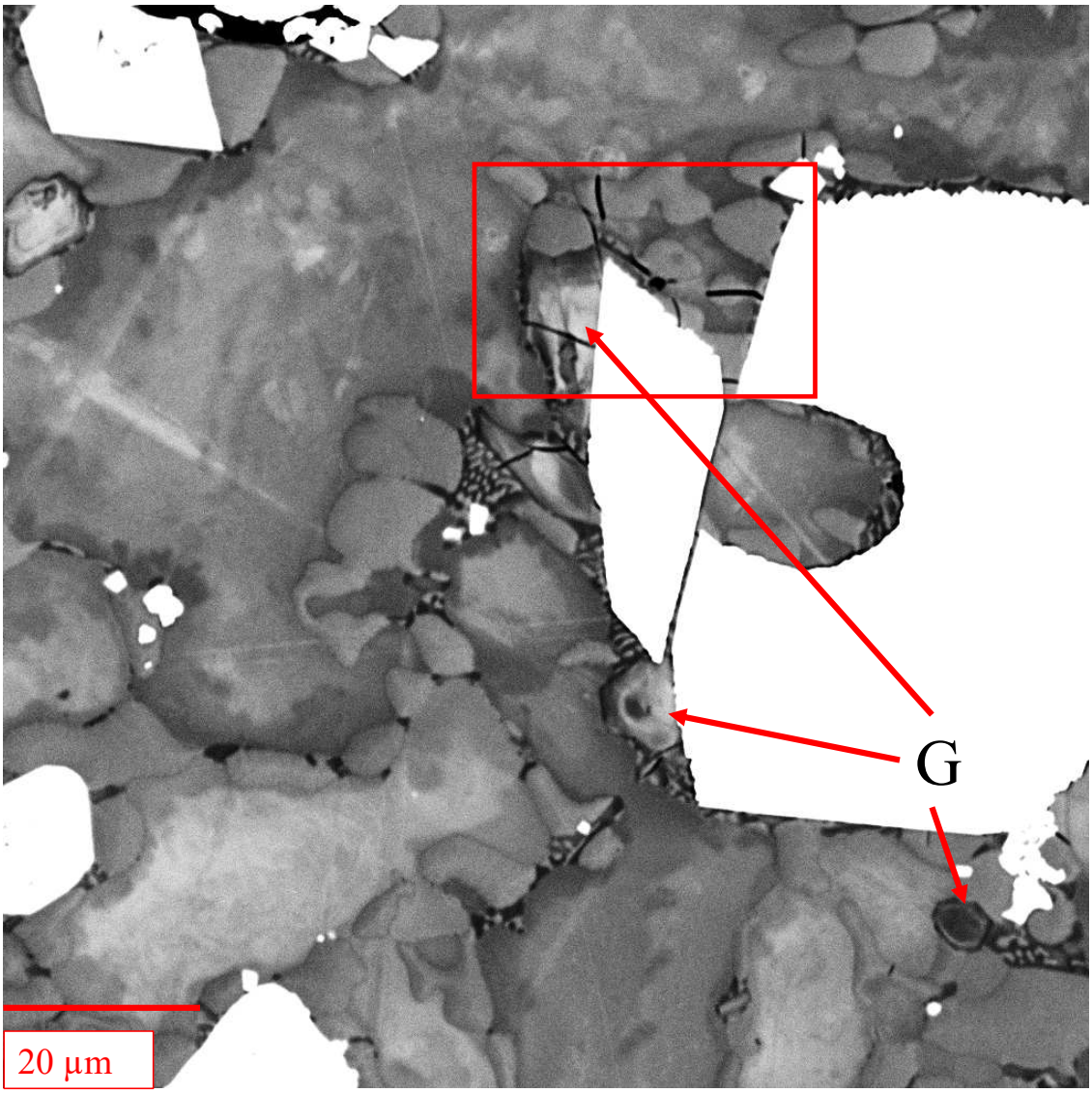

FIGURE 4.11: Backscatter SEM image of 60wt% WC - NiCrBSi. The phases with a higher molecular weight are shown as brighter. The letters correspond to the compositions presented in Table4.6.

microstructure are presented in Figures 4.13 to 4.17. The monocrystalline WC are the large white angular particles. The convective mass transfer of W and C from the WC is evident by the abundance of secondary W phases growing on the monocrystalline WC, shown in Figure 4.13 [18, 19, 584, 585]. The W and C dissolved in the Ni matrix resulted in different morphologies of secondary carbide phases, such as star carbides (A), needle carbides (B), and blocky carbides (C). The Ni matrix contains a primary dendritic phase (D), most with halos (E) around the primary phase, similar to what is found at 60wt% WC. The interdendritic

region contains a lighter grey phase (F), and a darker grey phase (G). There are regions where there is eutectic growth (H and I). Additionally, there is a ring-shaped carbide (J) found in the interdendritic regions.

The composition of the different phases are shown in Table 4.7. The secondary carbide phases all contained varying amounts of W, C, and Cr, with the star morphology (A) containing the most W ($(NiW_3Cr_6)C_6$), and the ring phase (J) having the most Cr ($(Ni_2WCr_9)C_9$). The blocky carbide phase (C) had small amounts of Si detected ($Ni_4W_2Cr_2Si)C_3$). The W

TABLE 4.6: The composition of the different phases shown in Figure 4.8 to Figure 4.10 using EDX. Note that the composition provided are averaged from multiple point, and may not sum to 100%.

		at%					
Letter	Description	Ni	W	Si	C	Cr	Fe
A	Blocky Carbide	31.2	17.7	8.2	22.3	20.6	-
B	Small Blocky Carbide	37.8	18.3	13.3	30.0	15.3	-
C	Ring Carbide	42.9	21.4	11.0	17.4	17.3	-
D	Primary Phase	82.1	2.4	6.7	-	6.2	2.6
E	Halo Around Primary Phase	85.5	-	10.2	-	4.2	2.1
F	Eutectic: Light Phase	85.7	-	9.9	-	3.0	1.3
	Eutectic: Dark Phase	80.7	-	16.8	-	2.0	1.2
G	Ring Phase	11.2	3.6	3.8	38.8	45.8	-

TABLE 4.7: The composition of the different phases shown in Figure 4.12 to Figure 4.17 using EDX. For the eutectic NL stands for non-lamellar and L stands for lamellar.

		at%					
Letter	Description	Ni	W	Si	C	Cr	Fe
A	Star Carbide	6.1	19.5	-	35.9	38.5	-
B	Needle Carbide	13.2	14.2	-	35.9	36.7	-
C	Blocky Carbide	31.0	18.8	7.9	22.7	19.6	-
D	Primary Phase	83.5	3.3	6.1	-	7.2	3.0
E	Halo Around Primary Phase	81.1	1.8	8.3	-	6.0	2.9
F	Eutectic: Light Phase (NL)	91.5	-	3.8	-	4.6	1.7
G	Eutectic: Dark Phase (NL)	77.7	-	17.8	-	3.1	1.3
H	Eutectic: Light Phase (L)	82.4	-	12.3	-	3.7	1.6
I	Eutectic: Dark Phase (L)	78.8	-	17.4	-	2.9	1.0
J	Ring Phase	7.8	4.8	-	44.3	43.1	-

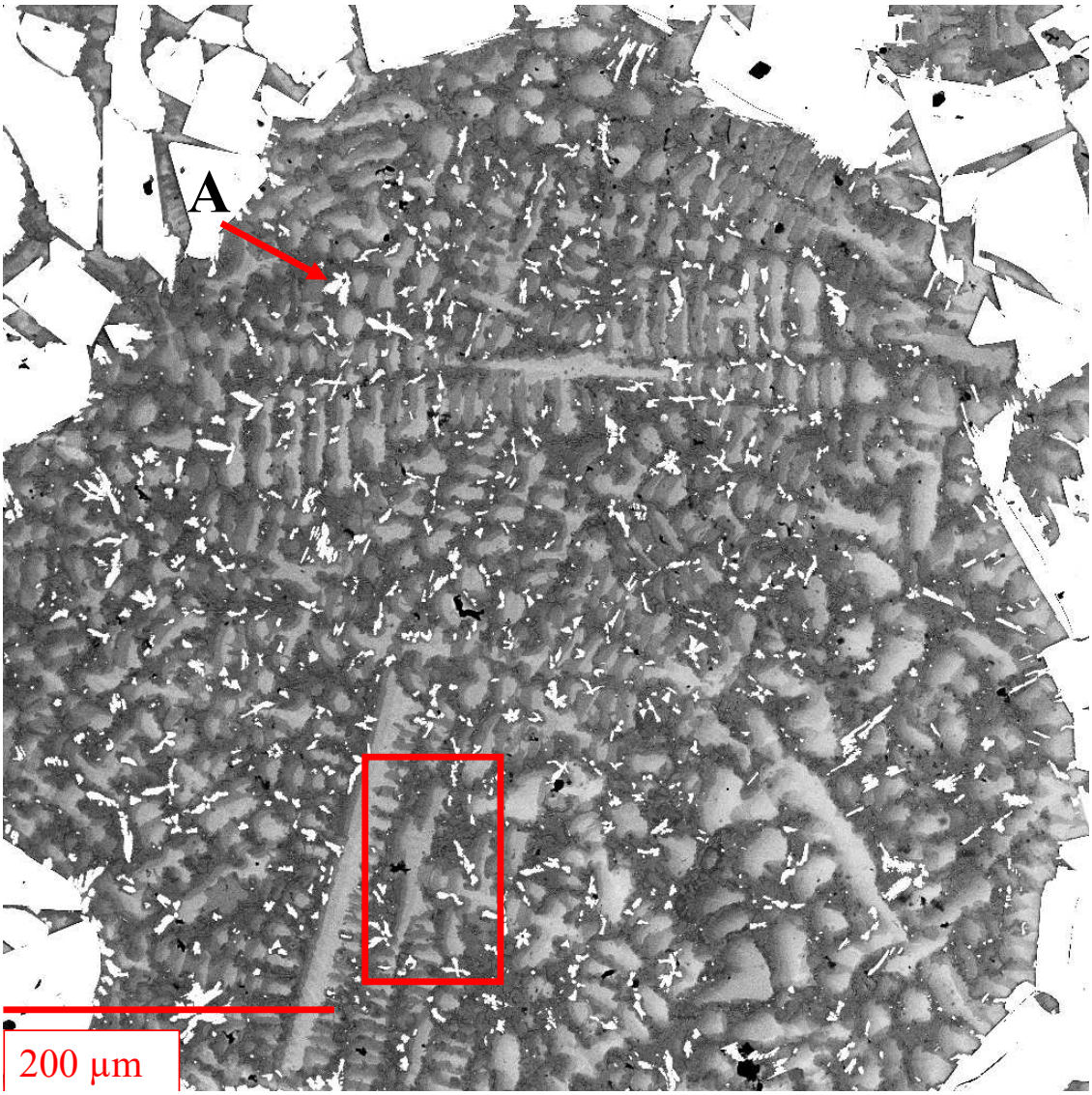

FIGURE 4.12: Backscatter SEM image of 70wt% WC. The heavier elements are shown as brighter highlighting the distribution of W throughout the sample. The letters correspond to the compositions presented in Table 4.7. The red square is where Figure 4.14 is taken.

primary M characteristic x-ray, and Si primary K_α have an energy of 1.774 and 1.739keV, respectively. The similar magnitude of characteristic x-rays makes them difficult to distinguish during EDX analysis, as seen in the EDX spectrum presented in Figure 4.18. In the presence of Si, W's L_α peak of 8.396 keV helps to distinguish between the two. Si only has the single L_α peak that is detectable with EDX; therefore, the Si content could be influenced by the presence of W. The primary phase (D) of the Ni matrix had a higher W and Cr content, but lower Si content than the halo (E) surrounding the primary phase. Having higher

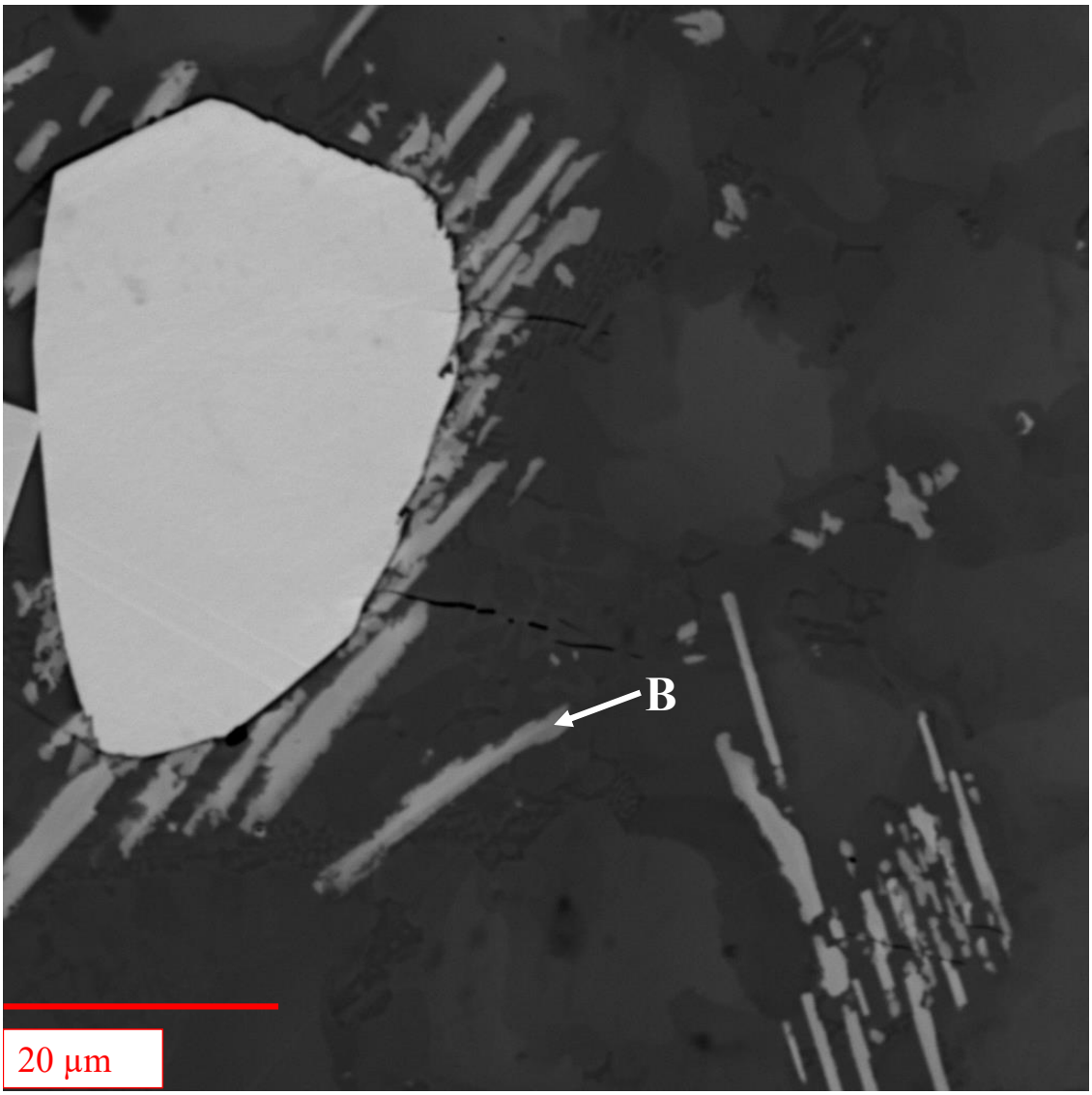

FIGURE 4.13: Backscatter SEM image of 70wt% WC. The heavier elements are shown as brighter highlighting the distribution of W throughout the sample. The letters correspond to the compositions presented in Table 4.7.

concentrations of Cr and W in the primary phase is supported by the equilibrium partition coefficient being greater than unity in the presence of Si[565]. In the interdendritic region, the phases contained higher levels of Si, and lower levels of Cr and Fe. The composition of the light interdendritic phase in the non-lamellar (F) and lamellar (H) structures are slightly different, due to the elevated Si content in the lamellar structure. The average lamellar spacing is 1.02 μm for 70wt% WC - NiCrBSi, and the interaction volume for the emission of characteristic x-rays in iron is approximately $1\mu m^3$ [583]. Therefore, it is possible that some

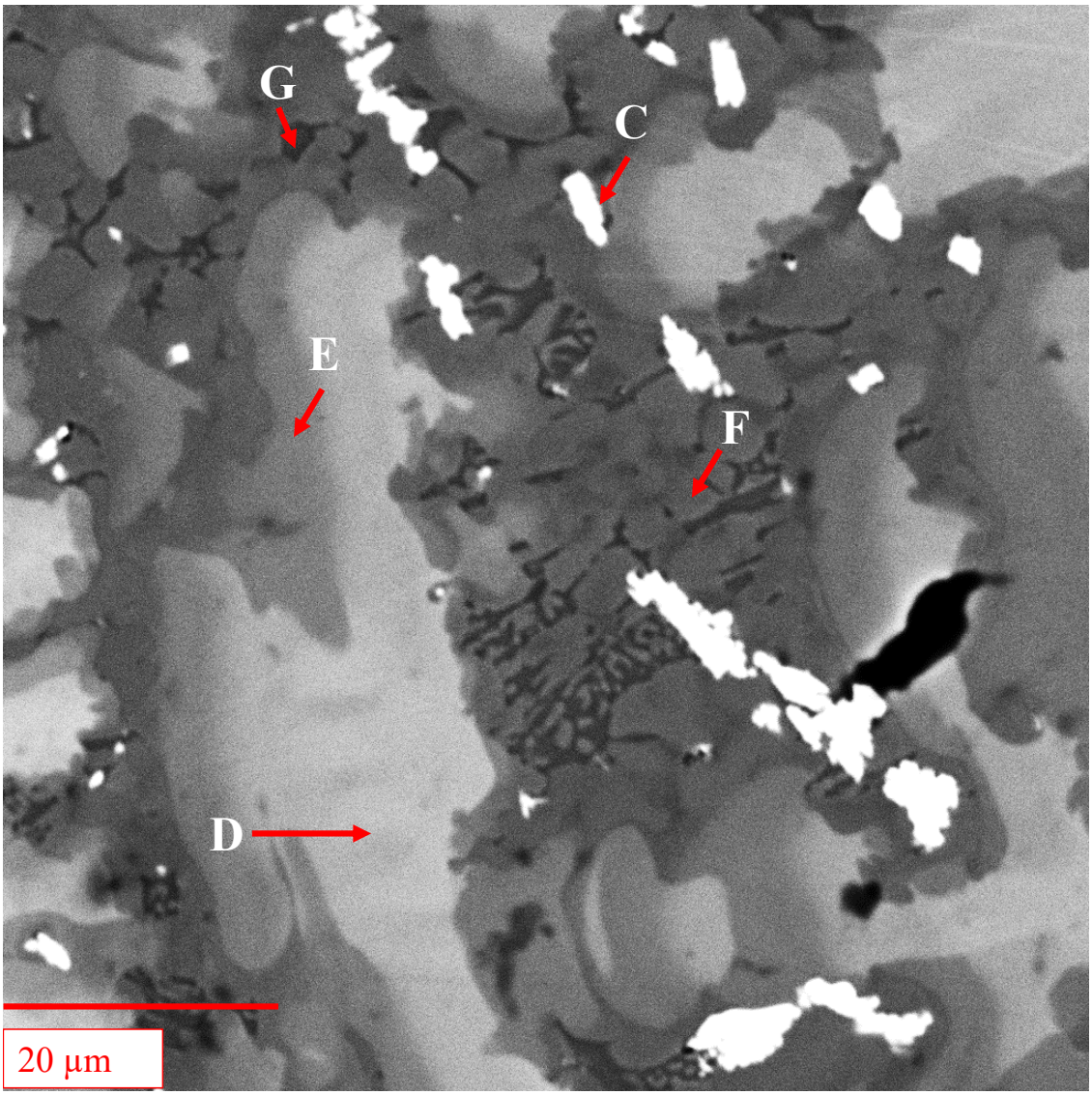

FIGURE 4.14: Backscatter SEM image of 70wt% WC. The heavier elements are shown as brighter highlighting the distribution of W throughout the sample. The letters correspond to the compositions presented in Table 4.7.

of the detected characteristic x-rays from phase I was included in the signal from phase H causing elevated levels of Si, and reduced levels of Cr and Fe. Based on the EDX compositional data, it is possible that the light (F and H) dark phases (G and I) are the same phase.

EBSD was used to determine the phase distribution in 70wt% monocrystalline WC in NiCrBSi, as seen in Figure 4.19. The image is 200x200 pixels with a step size of 1 μm. The blue phase is γ-Ni, the red phase is Ni_3B, the yellow phase is WC, and the teal phase is

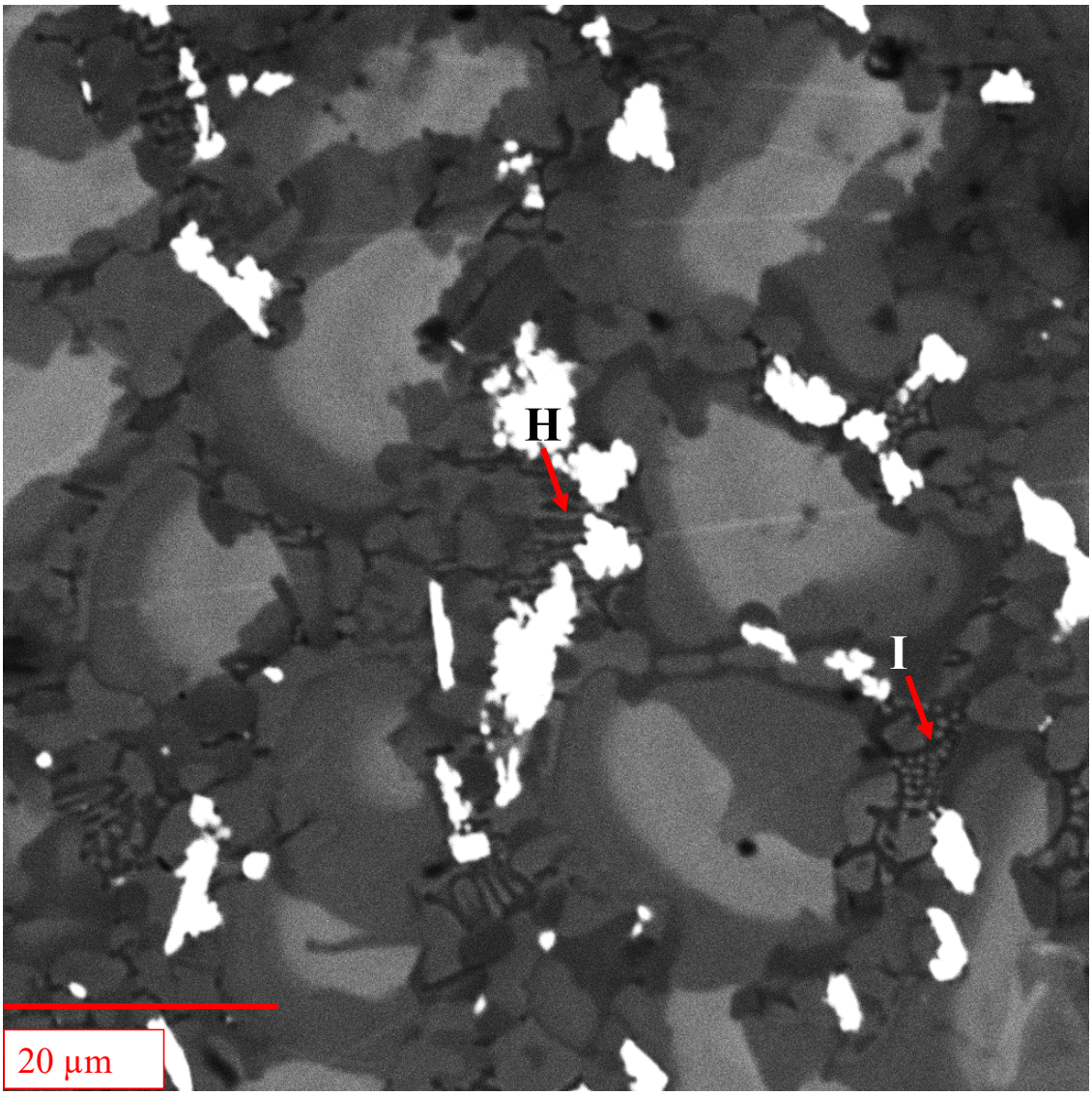

FIGURE 4.15: Backscatter SEM image of 70wt% WC. The heavier elements are shown as brighter highlighting the distribution of W throughout the sample. The letters correspond to the compositions presented in Table 4.7.

W_2C. All of the black pixels were unable to be classified. Ni_3W_3C was included in the phase database during data collection, but was not contained within the sample. Ni_3Si was also included, but due to the similarity in cell spacing between Ni (0.345 nm) and Ni_3Si (0.351 nm), Ni_3Si was unable to be distinguished from Ni. It was found that the halo around with primary phase was also γ-Ni. The interdendritic regions contained mostly Ni_3B, and γ-Ni. The large step size of 1 μm would not be able to resolve the eutectic, resulting in just γ-Ni or Ni_3B being detected. Additionally, the needle phase (B) was found to be W_2C, which

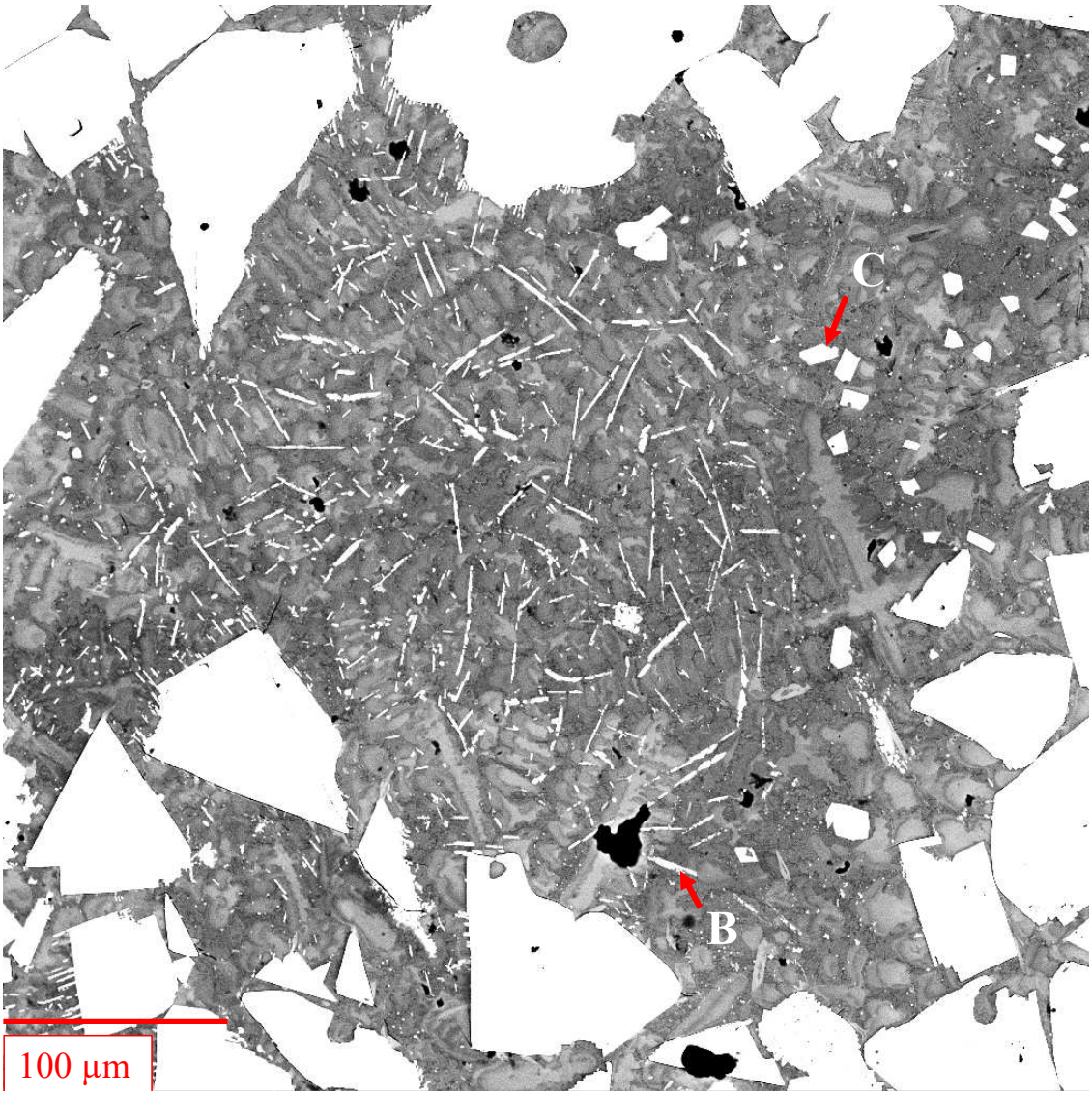

FIGURE 4.16: Backscatter SEM image of 70wt% WC. The heavier elements are shown as brighter highlighting the distribution of W throughout the sample. The letters correspond to the compositions presented in Table 4.7.

forms in the interdendritic regions and around the edge of the primary WC. Although the composition of the needle phase measured with EDX (B in Table 4.7) contains Cr, and Ni, the EBSD results are based on crystal structure, and not composition. Additionally, Cr has been shown to be substitutional with W in the W_2C crystal structure. [586]

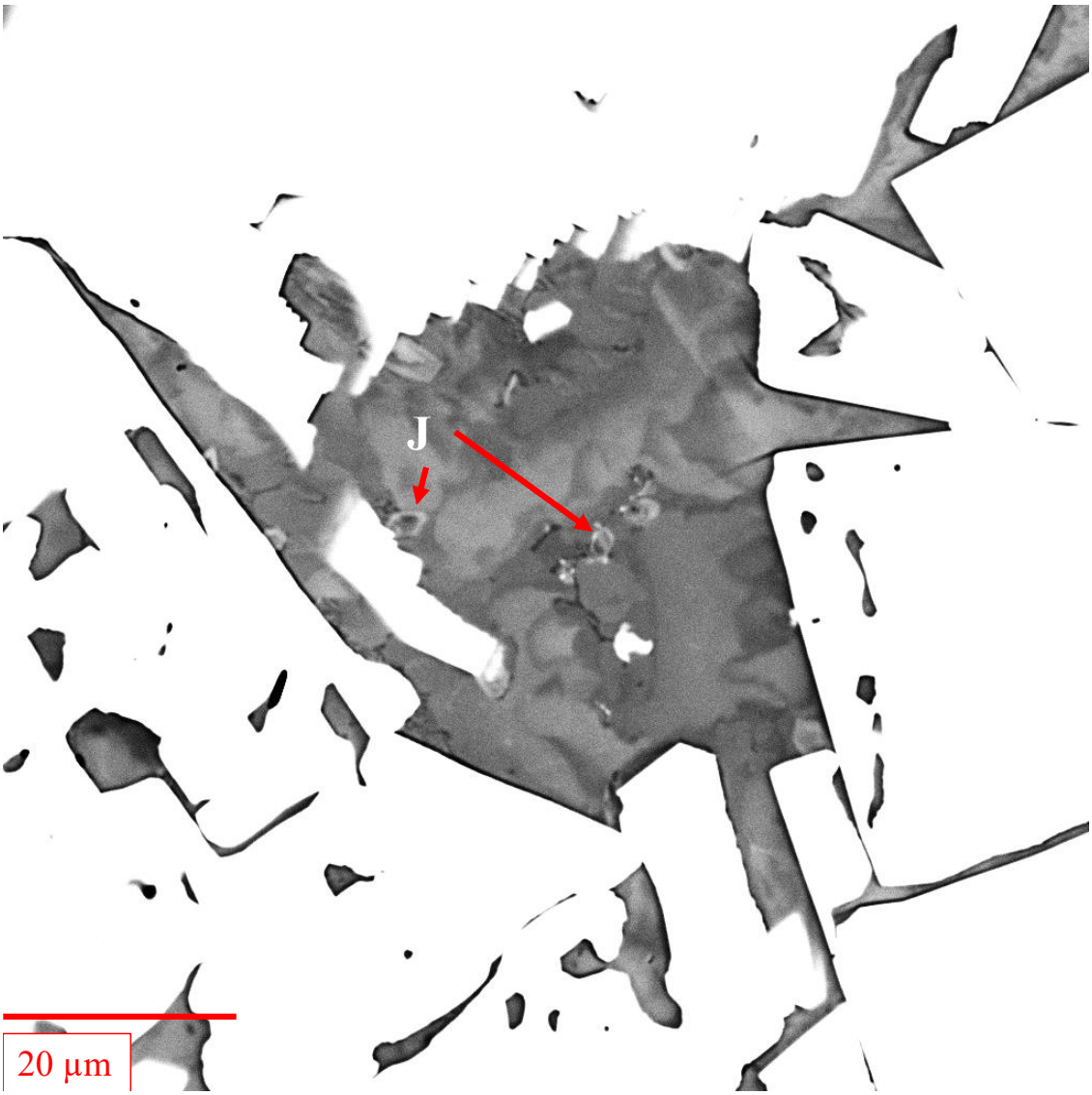

FIGURE 4.17: Backscatter SEM image of 70wt% WC. The heavier elements are shown as brighter highlighting the distribution of W throughout the sample. The letters correspond to the compositions presented in Table 4.7.

4.5 Discussion

4.5.1 Solidification of WC-NiCrBSi

4.5.1.1 60wt% WC-NiCrBSi

From the SEM images, the solidification sequence for 60wt% WC - NiCrBSi can be hypothesized. Due to their high W content, the first phases to form are likely the secondary carbide

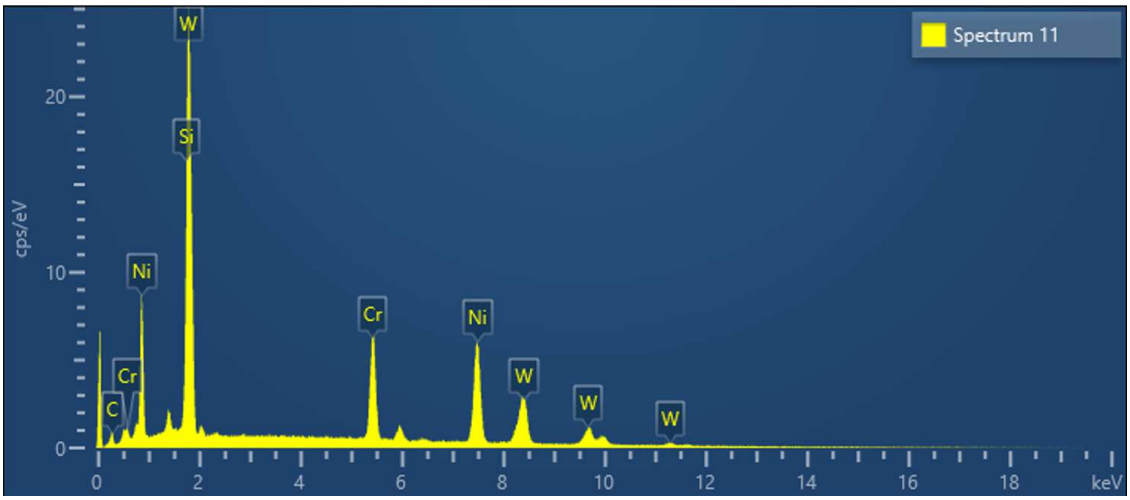

FIGURE 4.18: EDX spectrum from point F in Figure 4.16 highlighting the overlap of the primary Si and W peaks.

phases (Table 4.6 A-C). Additionally, CrC's (Table 4.6 G) found in the interdendritic regions likely form prior to γ-Ni since the melting point of Cr_3C_2 is 1900°C [587]. Following the formation of the high W phases, the primary γ-Ni phase (Table 4.6 D) forms. Dendrite coring could cause there to be microsegregation in the dendrites as they grow, resulting in a difference in composition during the primary solidification. The higher levels of W, Cr, and Fe in the primary phase are supported by the partition coefficients being higher than unity [565]. Therefore, it could be that the formation of the halo (D in Table 4.6) is due to dendrite coring. The continued growth of the primary phase would then bring the composition of the liquid to the eutectic composition, after which there is eutectic growth of Ni and Ni_3B (Table 4.6 F).

4.5.1.2 70wt% WC-NiCrBSi

The SEM, EDX, and EBSD data can be used to estimate the solidification sequence for 70wt% WC - NiCrBSi. Due to their high W content, the first phases to form are the different varieties of secondary carbide phases (Table 4.7 A-C) found in the microstructure. Based on the composition, it is difficult to determine the order the secondary carbides form due to their similarities in W content. The next phase that forms could be the CrC (Table 4.7 J) since the melting point of Cr_3C_2 is 1900°C [587]. After the carbides have formed, the first Ni phase to form would be the primary dendritic phase (Table 4.7 D). The halo surrounding the primary dendrites (Table 4.7 E) could be due to dendrite coring during

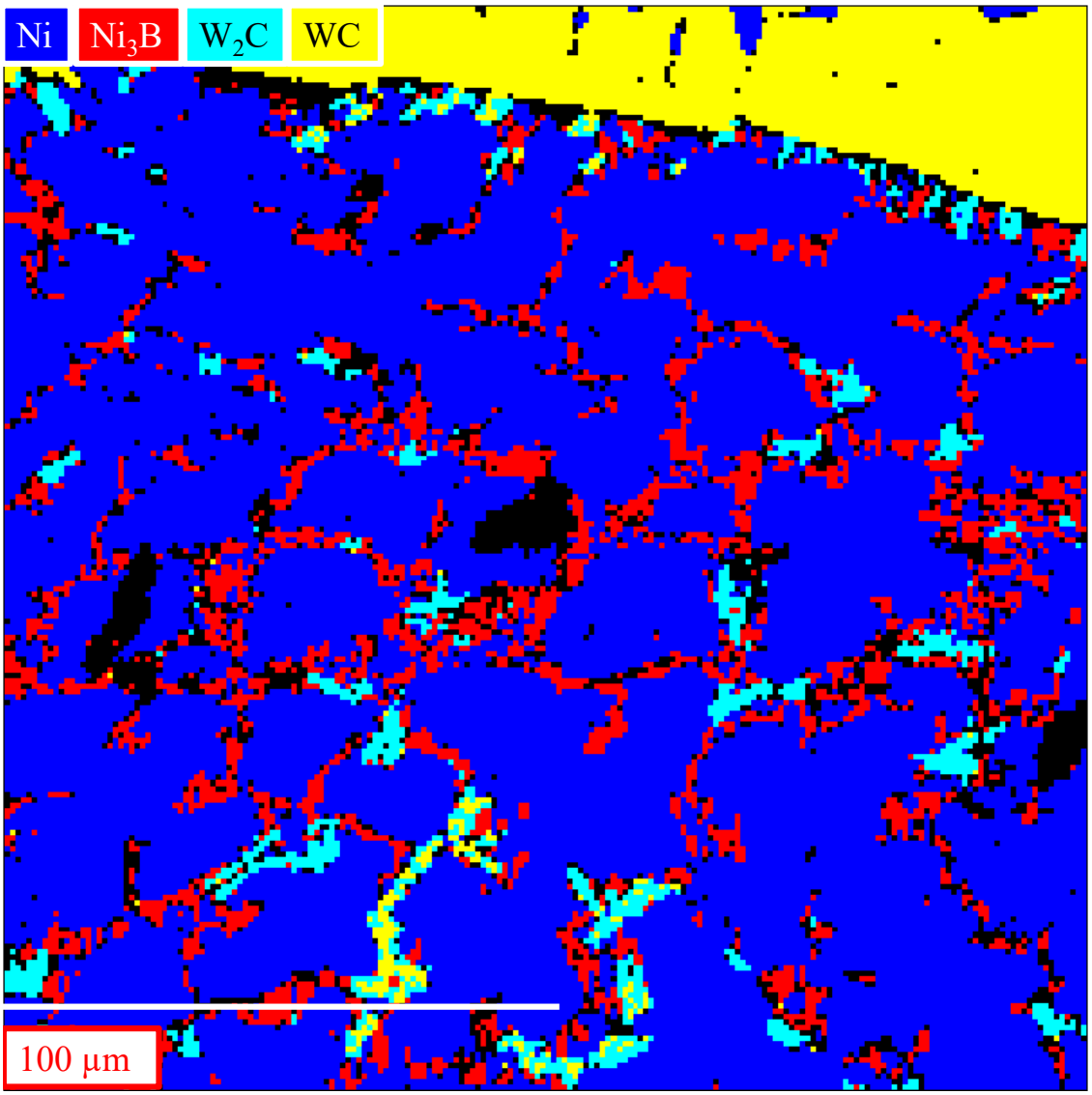

FIGURE 4.19: Phases detected using EBSD, where blue is Ni, red is Ni_3B, yellow is WC, and teal is W_2C. The grid is 200x200 pixels with a step size of 1 μm.

primary solidification. After the formation of the halo, the next phase to form is the eutectic solidification of Ni_3B, and a Ni-Si solid solution.

4.5.2 Comparing Thermo-calc to PTA-AM

A comparison of the compositions from the Thermo-calc (Figure 4.3) simulations and the PTA-AM of 60 (Figure 4.7) and 70wt% WC (Figure 4.12) are shown in Table 4.8. The solidification sequence proposed by the Sheil solidification simulation from Thermo-calc (Figure 4.3)

does have some resemblance to what is experienced during PTA-AM. In Thermo-calc and PTA-AM, the solidification of the matrix begins with the primary solidification of a γ-Ni solid solution. In the Scheil simulation, the composition of the alloying elements varies as solidification progresses. This doesn't happen in the PTA-AM samples, as the composition of the phases tends to have a constant composition during the entire solidification process. The composition of the alloying elements in the primary phase for the 60 and 70wt% WC samples under PTA-AM are outside of the compositional ranges simulated by Thermo-calc. The Cr, W, and Fe contents are higher, while the Si content is lower in PTA-AM compared to Scheil solidification.

Where Thermo-calc deviates from PTA-AM is not including the solidification of the halo. In the 60wt% (Figure 4.9) and 70wt% WC (Figure 4.14), there is generally a distinct line between the primary phase and the halo. It is likely that the halo is the continued growth of the primary phase at a different composition. In the Scheil solidification simulation, the formation of the halo should be a separate phase that is formed after γ-Ni solidification. The lack of halo formation would contribute to the compositional differences of the other phases between PTA-AM and Scheil (Table 4.8). The Ni_3Si formation prior to the formation of the eutectic is also not representative of PTA-AM. The solidification of the Ni_3Si/Ni_3B is in agreement with what is found in PTA-AM, although the compositions are different. The last phase to form is WB in the Scheil solidification, which could be the tiny white spherical spots in the eutectic in Figure 4.10 and Figure 4.14. TEM could be done on the eutectic to confirm whether the white points in the eutectic are WB. The Scheil solidification simulations are a good tool for attempting to understand the solidification sequence of the NiCrBSi matrix in PTA-AM, but the rapid solidification conditions of PTA-AM are different than Scheil resulting in major microstructural differences. Additionally, since the TCNI12 database only contains binary and ternary thermodynamic data, the extrapolations that are made to a 6 element system could be incorrect, and result in a difference in the composition of the predicted phases.

4.5.3 Microstructural Comparison Between 60 and 70wt% WC in NiCrBSi

From the compositional data gathered using EDX (Table 4.6 and Table 4.7), increasing the WC content from 60 to 70wt% appears to increase the amount of thermal degradation of WC. The secondary dendrite arm spacing (SDAS) was measured to estimate the cooling rate for 60 and 70wt% WC. It was found that the locations in the sample shown in Figure 4.7 (60wt%) and Figure 4.12 (70wt%) had a SDAS of 11.5 $\pm$ 2.0 and 12.7 $\pm$ 2.4 μm, respectively. With the significant overlap of the standard deviations, it was assumed that the cooling rates at these two locations were similar. The area fraction of secondary carbides were compared between Figure 4.7 and Figure 4.12, and it was found that the 60wt% sample had a secondary carbide area fraction of 2.9% while the 70wt% samples was 4.28%. Additionally, a comparison between the composition of the phases presented in Figure 4.7, and Figure 4.12 are presented in Table 4.8. The semi-quantitative EDX measurements show that there is more W in the primary phase of the 70wt% sample, and W present in the halo around the primary phase. No W exists in the halo around the primary phase in the 60wt% WC sample. Therefore, with a higher volume fraction of secondary carbide phases and higher levels of W in the Ni matrix, it is deduced that the 70wt% WC did have higher levels of convective mass transfer of W. Comparing the microstructure of 60 and 70wt% WC is thus determining the effect W has on the microstructure of rapidly solidified NiCrBSi.

Adding more dissolved W in the matrix causes significant changes to the overall microstructure. The 70wt% samples had a wider array of secondary carbides that formed, as opposed to the 60wt% samples that contained mainly the large blocky morphology ($(Ni_4W_2Cr_2Si)C_3$). The large blocky morphology ($(Ni_4W_2Cr_2Si)C_3$) was still present in the 70wt% sample, illustrated in Figure 4.16, with similar composition. However, the ring carbide (C ($(Ni_8W_4Cr_3Si_2)C_6$)) in Figure 4.8) was not found in the 70wt% sample. In the 70wt% samples, the secondary carbides are finer plates in a needle ($(NiWCr_3)C_3$) or star ($(NiW_3Cr_6)C_6$) morphology, with higher concentrations of Cr. The difference in the secondary carbide morphology may be attributed to the increase in the dissolved W and C in the Ni matrix from the increased convective mass transfer. Additionally, the carbides in the 70wt% samples tended to have more W, and Cr than those found in the 60wt% sample. Both samples formed a high Cr (CrC) ring phase that is typically found in close proximity to the WC particles. This could

be due to the convective mass transfer of C from the WC particles reacting with the Cr in the Ni solution to form the high Cr carbides.

One of the significant differences between the 60 and 70wt% WC samples was the structure of the Ni matrix. The 70wt% sample showed more obvious dendritic structure, than the 60wt% sample. The primary γ-Ni dendrites in the 70wt% sample had more dissolved W (9.9 wt%) than those found in the 60wt% sample (7.5 wt%). The difference in W content is due to the increased thermal degradation of WC in the 70wt% sample. The higher W content in Ni could result in a finer Ni structure. Both samples had halos that formed around the primary γ-Ni dendrites. The halo in 60wt% WC has no W, while the halo for 70wt% WC had 5.9 wt% W. The increased convective mass transfer of W caused W to be rejected from the primary phase into the liquid, which is then retained in the halo phase. Although in EDX, the W could be mistaken as Si for 60wt%, based on the EDX spectrum shown in Figure 4.20, none of the secondary W peaks (L_α = 8.396 keV) are present (as seen in the EDX spectrum for the halo in 70wt% in Figure 4.21). Additionally, the contrast of the halo compared to the primary dendrite in Figure 4.9 supports that W is likely not present in the halo in the 60wt% sample. The halo for the 70wt% sample has more Cr and Fe, and less Si. There have been no studies on the effect of W on the partitioning of Cr, and Fe in Ni. In ternary Ni-5Si-3W alloys, W does not affect the partition coefficient of Si compared to Ni-5Si [565]. However, this may change with higher W content. The halo formation in both the 60 and 70wt% samples is postulated to be from dendrite coring causing continued growth of the primary phase at a different composition.

TABLE 4.8: Comparison between the matrix phases in 60wt% WC - (Figure 4.7) and 70wt% WC (Figure 4.12) - NiCrBSi. Note that the composition provided are averaged from multiple point, and may not sum to 100%.

		PTA-AM (at%)						Thermo-calc 10wt%W (at%)					
WC Content	Description	Ni	W	Si	C	Cr	Fe	Ni	W	Si	Cr	Fe	B
60wt% WC	Primary Phase	82.1	2.4	6.4	-	6.5	2.6	81.5 - 80.2	1.4 - 0.5	10.0 - 13.0	6.3 - 5.7	0.8 - 0.6	-
	Halo	84.4	-	10.3	-	3.2	2.0	-	-	-	-	-	-
	Light Eutectic	87.0	-	9.7	-	2.3	1.0	63.1 - 64.2	-	-	9.0 - 8.5	2.9 - 2.3	25.0
	Dark Eutectic	80.4	-	18.2	-	1.4	-	75.4	-	23.5	0.9	0.2	-
70wt% WC	Primary Phase	84.0	3.5	5.8	-	7.2	3.0	81.5 - 80.2	1.4 - 0.5	10.0 - 13.0	6.3 - 5.7	0.8 - 0.6	-
	Halo	81.0	1.9	8.3	-	6.0	2.9	-	-	-	-	-	-
	Light Eutectic (NL)	92.9	-	1.3	-	4.8	1.6	63.1 - 64.2	-	-	9.0 - 8.5	2.9 - 2.3	25.0
	Dark Eutectic (NL)	75.0	-	22.4	-	1.8	0.7	75.4	-	23.5	0.9	0.2	-
	Light Eutectic(L)	80.4	-	15.6	-	2.9	1.1	63.1 - 64.2	-	-	9.0 - 8.5	2.9 - 2.3	25.0
	Dark Eutectic (L)	78.6	-	18.1	-	2.4	0.9	75.4	-	23.5	0.9	0.2	-

The interdendritic regions for 60wt% have a higher tendency to be a lamellar eutectic. In 70wt% WC, the increased W content appears to reduce the amount of lamellar eutectic found. However, drawing any conclusions from a 2-D cross-section of the microstructure is

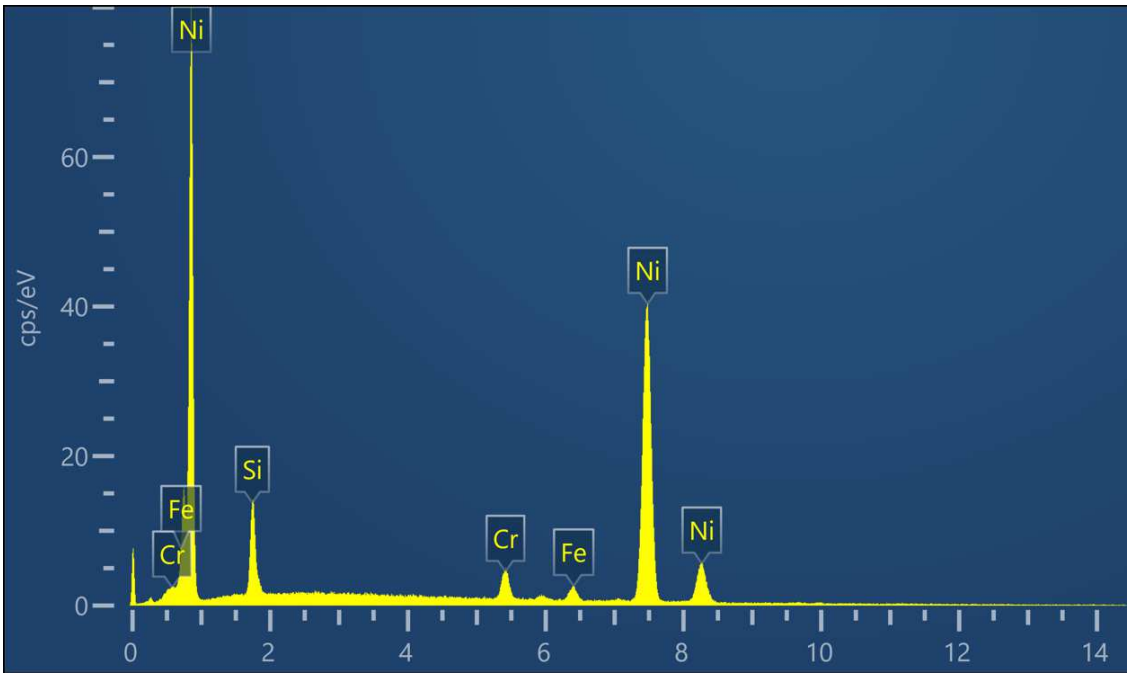

FIGURE 4.20: EDX spectrum of halo in 60wt% WC - NiCrBSi.

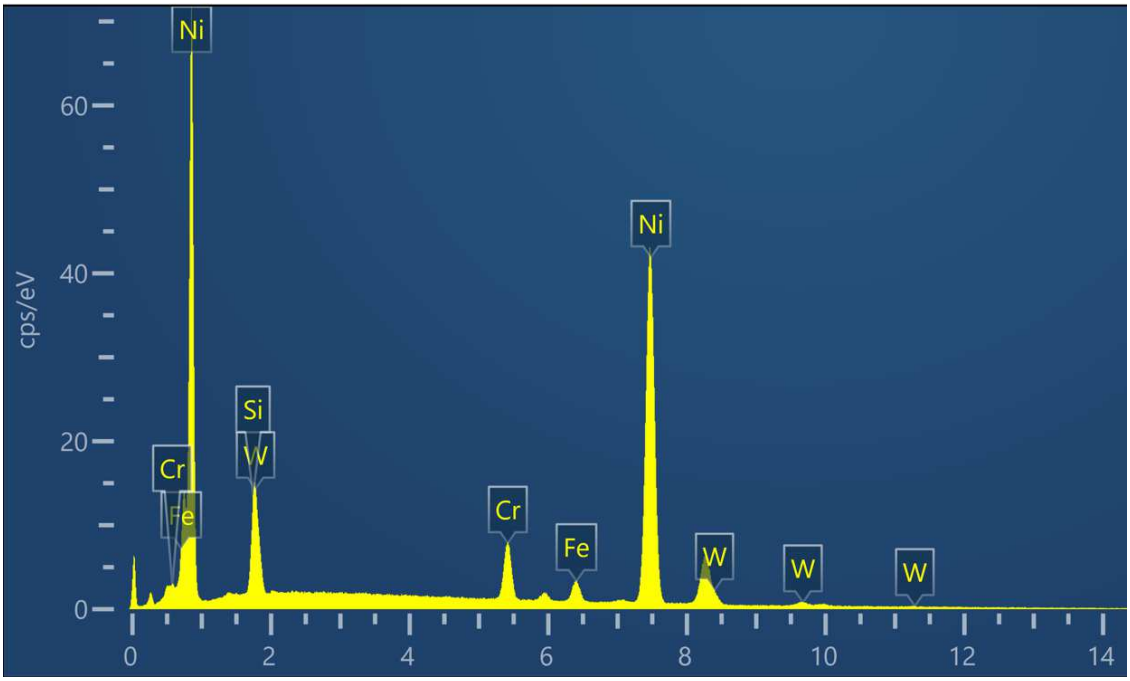

FIGURE 4.21: EDX spectrum of halo in 70wt% WC - NiCrBSi.

difficult. Additionally, the eutectic structure could be too fine to be resolved using SEM, and may require higher magnification techniques like TEM. A better understanding of the differences in the eutectic structure could be established using serial sectioning using a focused ion beam SEM (FIBSEM). Using FIBSEM, a 3-D rendering of the entire microstructure could be created, and a more thorough comparison of the microstructure between 60 and 70wt% WC could be conducted.

4.5.4 Wear and Impact Testing

The results from the ASTM G65 tests are shown in Figure 4.22A. The lower first scar mass loss from the higher WC samples is likely due to the higher amount of WC on the surface of the sample, shown by the rough surface in Figure 4.4. Based on the second scar mass loss, the AM samples had comparable abrasive wear resistance under the test conditions. Additionally, the AM samples performed slightly better in the repeated rotary impacts, as presented in Figure 4.22B. For the case of 70 and 80wt%, even with the manufacturing defects and denuded regions, the abrasive wear and impact resistance were similar to 60wt% overlays. This implies that with the removal of these defects, the performance may surpass conventional overlays. However, the displayed results are from a single sample, and more tests would be required to definitively compare the performance of AM and conventional WC-Ni MMCs.

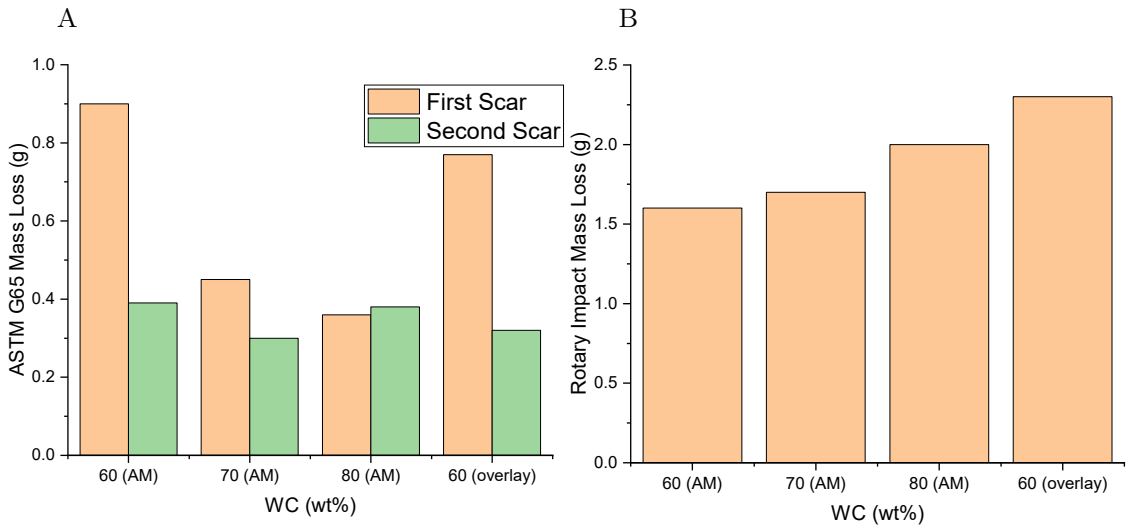

FIGURE 4.22: A) and B) The results comparing the samples shown in Figure 4.4 and a 60wt% overlay for ASTM G65 and rotary impact test, respectively.

4.6 Conclusion

PTA-AM was used to deposit thin walls of a 60, 70, and 80wt% WC - NiCrBSi metal matrix composite. Increasing the WC content from 60 to 70 wt% caused large irregular and spherical-shaped pores and denuded regions. The increased WC content also caused more thermal degradation of the WC, causing more W and C to be dissolved in the Ni matrix. Having more W dissolved in the Ni matrix caused precipitation of more complex carbides, higher levels of W in the Ni dendrites and halo. The Scheil solidification simulations did not include the solidification of the halo around the primary phase. The difference between the Scheil simulations and PTA-AM samples highlights the need for more thermodynamic and microstructural characterization data that need to be generated for the NiCrBSi-WC system. The abrasive and impact resistance are comparable between the 60, 70, and 80wt% PTA-AM samples, and the 60wt% overlay, showing that the superior abrasive wear resistance of WC-NiCrBSi overlays could be applied to additively manufactured parts.

Chapter 5

Microstructural Characterization of 70wt% WC-NiBSi Deposited by PTA-AM

To be submitted as **Rose, D**, Tonya Wolfe, and Hani Henein *Microstructural Characterization of 70wt% WC-NiBSi Deposited by PTA-AM*, Additive Manufacturing, 2023. This chapter satisfies thesis objective 3 by developing a relationship among the cooling rate during solidification, deposition height, degree of thermal degradation experienced by WC particles, and the resulting microstructure of 70wt% WC-NiBSi MMCs produced through the PTA-AM method. It should be noted that section 5.5.4 is not part of the to be published document.

5.1 Abstract

Plasma transferred arc additive manufacturing (PTA-AM) was used to deposit a cylinder composed of 70wt% WC - NiBSi metal matrix composites. Two defects dominated the microstructure: areas completely void of WC termed denuded regions and large pores. These defects reduced the overall carbide mass percent below 70wt%. Electromagnetic levitation (EML) was used to correlate the secondary dendrite arm spacing to the solidification cooling rate in order to estimate the solidification cooling rate of the PTA-AM sample throughout

the entire cylinder build. The solidification cooling rate differed by two orders of magnitude between the first and last layers of the sample, resulting in coarsening of the dendritic microstructure. An inverse correlation was found between the convective mass transfer of W and C from WC and the solidification cooling rate, where slower cooling rates resulted in upwards of 28wt% W within the γ-Ni dendrites. Thermo-calc software was used to model 70wt% WC - NiBSi under Scheil solidification conditions, and were compared with the rapidly solidified microstructure from PTA-AM. A possible mechanism for denuded regions is exceeding the maximum packing of angular WC (62wt%), causing localized pools of matrix material.

5.2 Introduction

Environmental conditions that induce abrasive wear on metallic components are common across a wide range of industrial processes, including agriculture [3], pipelines [588], and mining [43]. A common approach to prevent abrasive wear is the application of a metal matrix composite (MMC) coating to prolong the component's service life. Typical matrix materials are Ni alloys [10, 13], Co alloys [589–592], Fe alloys [593, 594] and Al alloys [595, 596], while reinforcement particles include B_4C [597, 598], SiC [599, 600], TiC [601, 602], and WC [603, 604]. Plasma transferred arc (PTA) is industrially used to deposit MMC composite coatings at loadings of 60-65wt% carbide. An illustration of the PTA process can be found in Figure 5.1. In PTA, an arc is struck between a tungsten electrode and a substrate, and powder is fed co-axially into the plasma, where it is melted and deposited onto the substrate. An MMC with optimal properties to combat abrasive wear environments is WC in a NiCrBSi matrix [605]. The microstructure of the matrix typically consists of γ-Ni dendrites, with a γ-Ni/Ni_3B eutectic [10]. Dissolution of the WC can cause the formation of brittle intermetallics such as Ni_2W_4C, Cr_2B, Cr_3C_2, and Cr_7C_3 [10, 43]. The inclusion of Cr in the matrix increases the dissolution of WC during the deposition process, which increases the mean free path between carbides and decreases the abrasive wear resistance [606]. Therefore, the NiBSi alloy could be an alternative matrix material that would reduce the dissolution of WC [13].

Direct energy deposition (DED) is an additive manufacturing (AM) technique that is compatible with a wide range of material compositions, including functionally graded materials

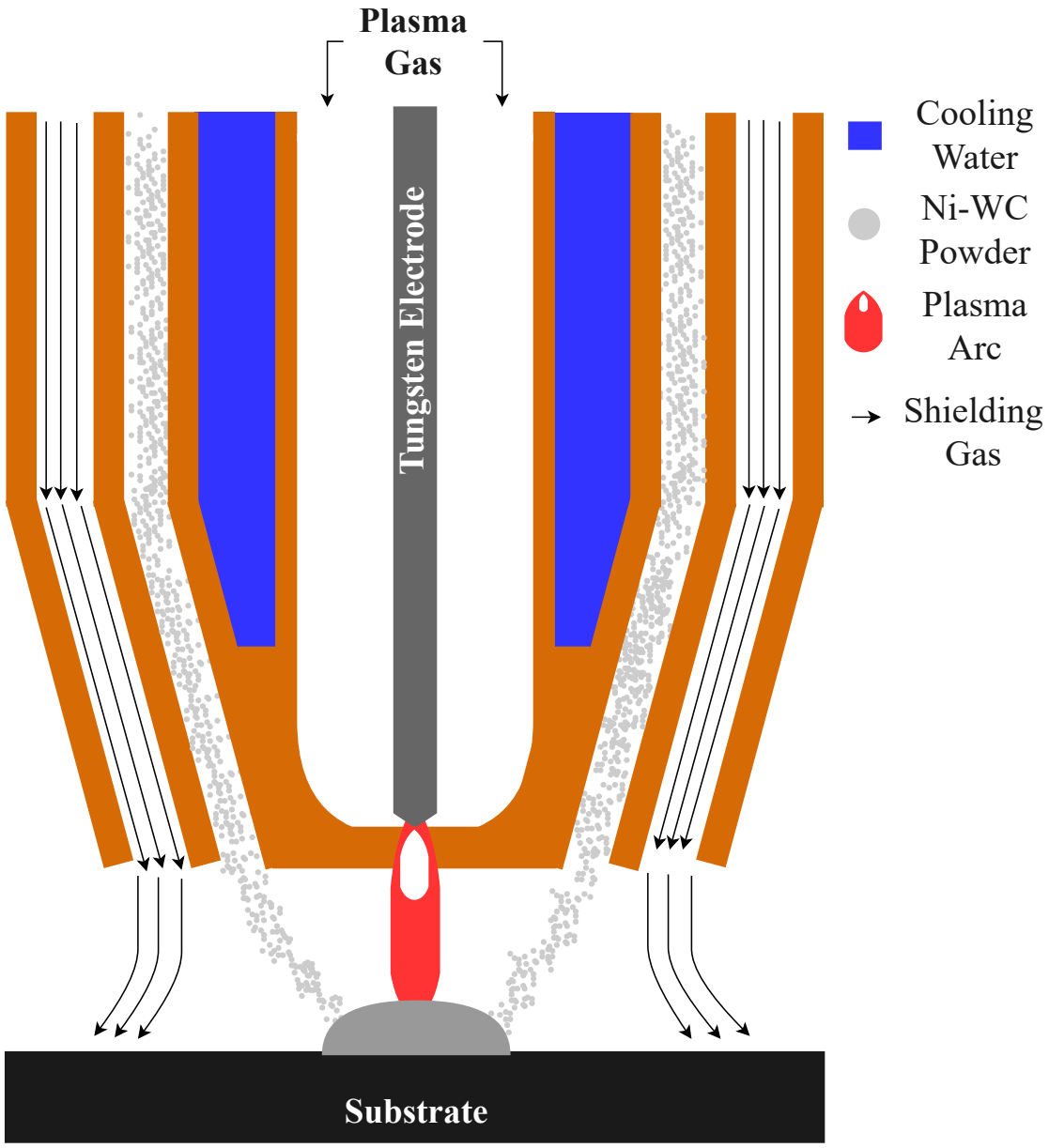

FIGURE 5.1: A cross-section of the water cooled copper PTA nozzle. A plasma arc is struck between a tungsten electrode and a substrate. WC-Ni powder is fed co-axially into the plasma where it is melted and deposited on to the substrate. The entire process is protected using an inert shielding gas.

[607] and metal matrix composites [608]. The feedstock is either powder or wire that is fed into the heat source, where it is melted and deposited onto the substrate material. The deposition modalities for DED include: wire and arc additive manufacturing (WAAM), laser-based DED, electron beam, and PTA [609]. Mercado Rojas *et al.* [36] performed a Taguchi L18 design of experiments (DOE) to determine the effects of different operating parameters on the build geometry when depositing NiCrBSi-WC MMCs using plasma transferred arc additive manufacturing (PTA-AM). Through x-ray diffraction (XRD), they found that the microstructure consisted of γ-Ni, Ni_3Si, Ni_3B, and $Cr_{23}C_6$. Liu *et al.* [190] used electron beam melting (EBM) to deposit 55 mm $\times$ 20 mm $\times$ 30 mm samples out of NiBSi - 65wt%WCp powder and found that the microstructure contained dendritic γ-Ni with precipitation of Ni_3B and Ni_3Si. The dissolution of WC during EBM caused the formation of secondary carbides throughout the matrix. Zhao *et. al.*[580] deposited a NiBSiFe - WC tubular wire using laser wire deposition and found that the dissolution of WC during deposition caused the microstructure to be composed of a (Ni, Fe) solid solution, Ni_3B, Ni_2W_4C, and Fe_3W_3C. Although these studies identify the phases present across the sample surface, no research has been done to understand how the microstructure and composition change through the entire height of the build. Understanding how the composition, more specifically W content, changes under different processing conditions will allow for the AM process to be optimized to maximize the retention of WC. One challenge when using PTA is obtaining an accurate thermal history of the deposit due to the emission of ultraviolet radiation and reflection from the arc on the deposit's surface[11]. Obtaining an accurate thermal history is critical to understand the microstructural evolution that occurs during PTA deposition.

Electromagnetic levitation (EML) is a containerless method for melting metallic samples. EML uses two coaxial coils with high-frequency alternating current in opposition that induces eddy currents in the same direction within the metal specimen resting between them. The interaction between the generated eddy currents and the nonuniform magnetic field from the coils generates a Lorentz force that can overcome the gravitational force acting on the metal sample, causing levitation [610]. The eddy currents also heat the sample through Joule heating beyond the liquidus temperature and induce convection in the melt to homogenize the sample composition [611, 612]. During the cooling stage, the current to the coils is reduced to only what is required for levitation, and the sample is cooled with jets of inert gas; the power remains active until complete solidification [613]. EML, coupled with

various diagnostic equipment such as a pyrometer and a high-speed camera, allows the solidification process to be analyzed under various thermal conditions. Some of the observable solidification characteristics that can be observed using EML are growth front velocity [614], macrosegregation [615], dendrite growth morphology [616], thermophysical properties [617–619], and liquid phase separation [620, 621].

The present study uses PTA-AM to deposit 70wt% WC in a NiBSi matrix. EML was used to analyze the evolution of the microstructure as a function of the thermal history. The challenges faced when performing EML on a WC-Ni MMC will be outlined, and overall phase distribution and composition will be compared with PTA-AM. The effects of heat input on carbide dissolution, the eutectic structure, and the mechanism behind denuded region formation will be discussed.

5.3 Materials and Methods

5.3.1 Thermodynamic Modelling

Thermo-calc software (version 2022b) equipped with the TCNI12 database was used to model the solidification and resulting microstructure of the matrix of 70wt%WC - NiBSi. To model the solidification a Scheil solidification simulation was done in Thermo-calc on two different compositions. One is the nominal matrix composition presented in Table 5.1, and the next is the average matrix composition found throughout the cross-section of the PTA-AM sample, shown in Table 5.2. The Scheil solidification experiments provide a foundation of what the current literature predicts the solidification of WC-NiBSi could be. Under Scheil, the concentration of the solute can be determined using Equation 5.1, where C_s is the concentration of the solid, k is the partition coefficient, V_s is the volume fraction of solid that has formed, and C is the nominal composition of the alloy.

$$C_s = kC(1 - V_s)^{(k-1)} \tag{5.1}$$

5.3.2 Plasma Transferred Arc - Additive Manufacturing

The PTA system used to deposit the WC-Ni MMCs was a Kennametal Stellite™ STAR-WELD 400A, with an Excaliber II torch. A 2% thoriated-tungsten electrode ground to an angle of 20° was placed 4mm above the edge of the plasma borehole in the nozzle. A mild steel substrate was placed on a Gullco GP-200 H-B automated welder positioner that rotates horizontally to give the desired cylindrical shape. Ar gas (99% purity) was used to protect the melt from oxidation, a carrier gas for the powder, and plasma ionization. The operating parameters for the system can be found in Table 5.3. It should be noted that for the current and voltage, a range of values was used during the experiment. The current and voltage started at 100A and 25V, respectively, to ensure adequate bonding with the substrate. After 5 layers, the current was decreased by 1 A/s until 65A was reached; at this point, the voltage was dropped to 23 V. The lower heat input was used to reduce the risk of slumping of material between layers and to reduce the amount of carbide dissolution. The voltage is maintained during the build using the arc length control (ALC) functionality of the PTA system.

The matrix material used for the PTA-AM experiments was Höganäs 1538-40 NiBSi powder, whose composition can be seen in Table 5.4. A backscatter scanning electron microscope

TABLE 5.1: The composition of NiBSi used for the Thermo-calc analysis.

Component	Mole Fraction	Mass Fraction
Ni	0.84	0.946
B	0.101	0.021
Si	0.056	0.03
Fe	0.003	0.003

TABLE 5.2: The average matrix composition used for the Thermo-calc analysis.

Component	Mole Fraction	Mass Fraction
Ni	0.785	0.864
B	0.104	0.021
Si	0.058	0.03
Fe	0.003	0.003
W	0.022	0.077
C	0.028	0.005

(SEM) image of the powder can be seen Figure 5.2A. The size range is +53 -180 µm, and it can be seen in Figure 5.2A the morphology of the powder is spherical. There is some evidence of satellites, non-spherical powder, and porosity in the powder, which are common defects found in gas atomized powder [622]. Defects in the powder feedstock have been shown to reduce the quality of PTA-AM deposits [623]. The reinforcement particles in the MMC are Oerlikon Metco WOKA 50115 monocrystalline WC. The monocrystalline WC has an angular morphology and a size range between +63 -180 µm. An SEM image of the monocrystalline WC powder is shown in Figure 5.2B. Prior to deposition, the powder is combined at a ratio of 30 wt% NiBSi, and 70wt% WC and is mechanically mixed for 1 hour to ensure a homogeneous blend of the materials.

5.3.3 Electromagentic Levitation

The electromagnetic levitation experiments were conducted at Institut für Materialphysik im Weltraum, Deutsches Zentrum für Luft-und Raumfahrt (DLR) in Köln, Germany. A schematic of the EML experiment can be seen in Figure 5.3 [624]. EML uses a radiofrequency magnetic field generated by water-cooled copper coils connected to a high-frequency generator that operates close to 400kHz. The coils are arranged in a conical shape, with 7 windings below the sample, and 4 counter windings above the sample, produces a strong electromagnetic field in opposition to the gravity vector. The sample size for EML is roughly 1g of material; these samples were made by sectioning already deposited PTA-AM samples with the composition shown in Table 5.4. The sample is placed in an alumina crucible and placed

TABLE 5.3: The operating parameters that were used for PTA-AM deposition. It should be noted that for current and voltage, a range is given. The current and voltage are higher at the beginning of the experiment, to achieve bonding with the substrate.

Operating Parameter	Parameter Value
Current	100 - 65A
Voltage	25 - 23V
Travel Speed	600 mm/min
Powder Flow Rate	27 g/min
Plasma Gas Flow Rate	1.5 SLM
Powder Gas Flow Rate	1.5 SLM
Shielding Gas Flow Rate	12 SLM

A

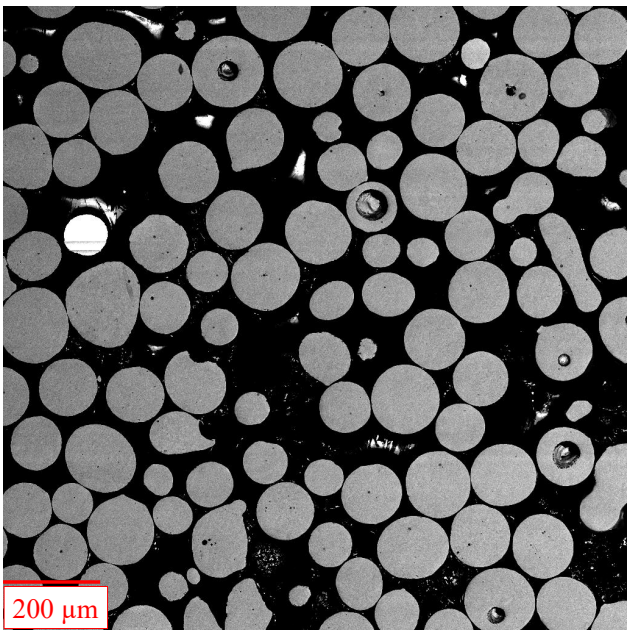

B

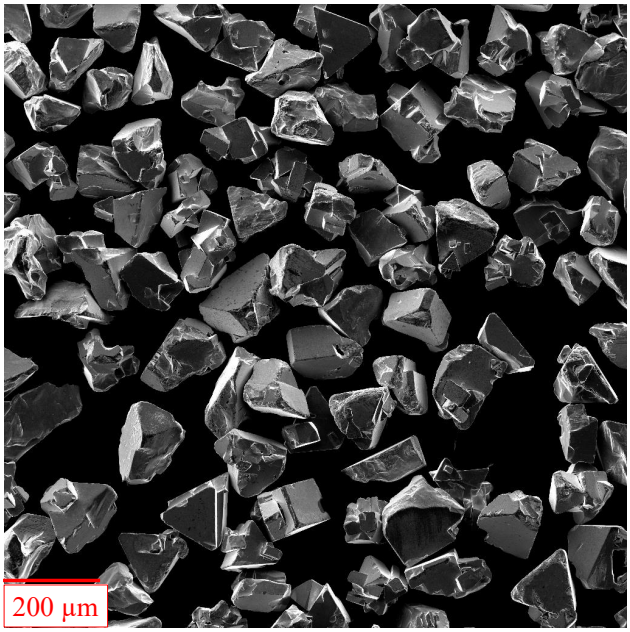

FIGURE 5.2: a) A backscatter electron SEM image of the Höganäs 1538-40 NiBSi powder feedstock; b) An SEM image of the angular monocrystalline WC powder used in this work.

TABLE 5.4: Composition of the powder feedstock used for PTA-AM deposition. The total material wt% refers to the proportion of that material that was placed in the powder feeder of the PTA.

	Composition (wt%)			Composition (wt%)			
Reinforcement Type	W	C	Matrix Type	Ni	B	Si	Fe
angular monocrystalline WC	93.8	6.2	NiBSi	Bal.	1.8 - 2.4	2.5 - 3.5	<0.5

within the coils. Oxidation is prevented by reducing the pressure in the chamber to 10^{-5} Pa and then backfilled with 99.9999% He to 50 kPa. The temperature of the experiments was monitored using an infrared pyrometer operating at 100Hz, with an emissivity set to 1. The generated temperature profiles were required to be calibrated with the transformation temperatures measured using differential scanning calorimetry (DSC). The experiment was captured using a high-speed camera recording at 75000 frames per second. Typically, the sample is cooled using a stream of He gas while the sample remains levitated, which allows for complete control over cooling rates. The high volume loading of WC in the samples required a higher magnetic field to maintain the levitation of the sample. Since the strength of the magnetic field is also responsible for heating the sample, the stream of He gas could not cool the sample below the liquidus temperature of the alloy (1055°C). To cool the sample, the power to the coils was terminated, and the sample was cooled through contact with the alumina crucible, which acts as a heterogeneous nucleation site for the onset of solidification.

5.3.4 Differential Scanning Calorimetry

The DSC was done using a Linseis HDSC PT1600 thermogravimetric analyzer. The samples were prepared by sectioning 40-50mg from the EML samples to ensure that the composition remained the same. The samples were processed at heating/cooling rates of 5 and 10 °C/min, and the liquidus temperature was reported as the offset of the endothermic peak upon heating. A linear interpolation to 0 °C/min was used to determine the liquidus temperature at equilibrium [625].

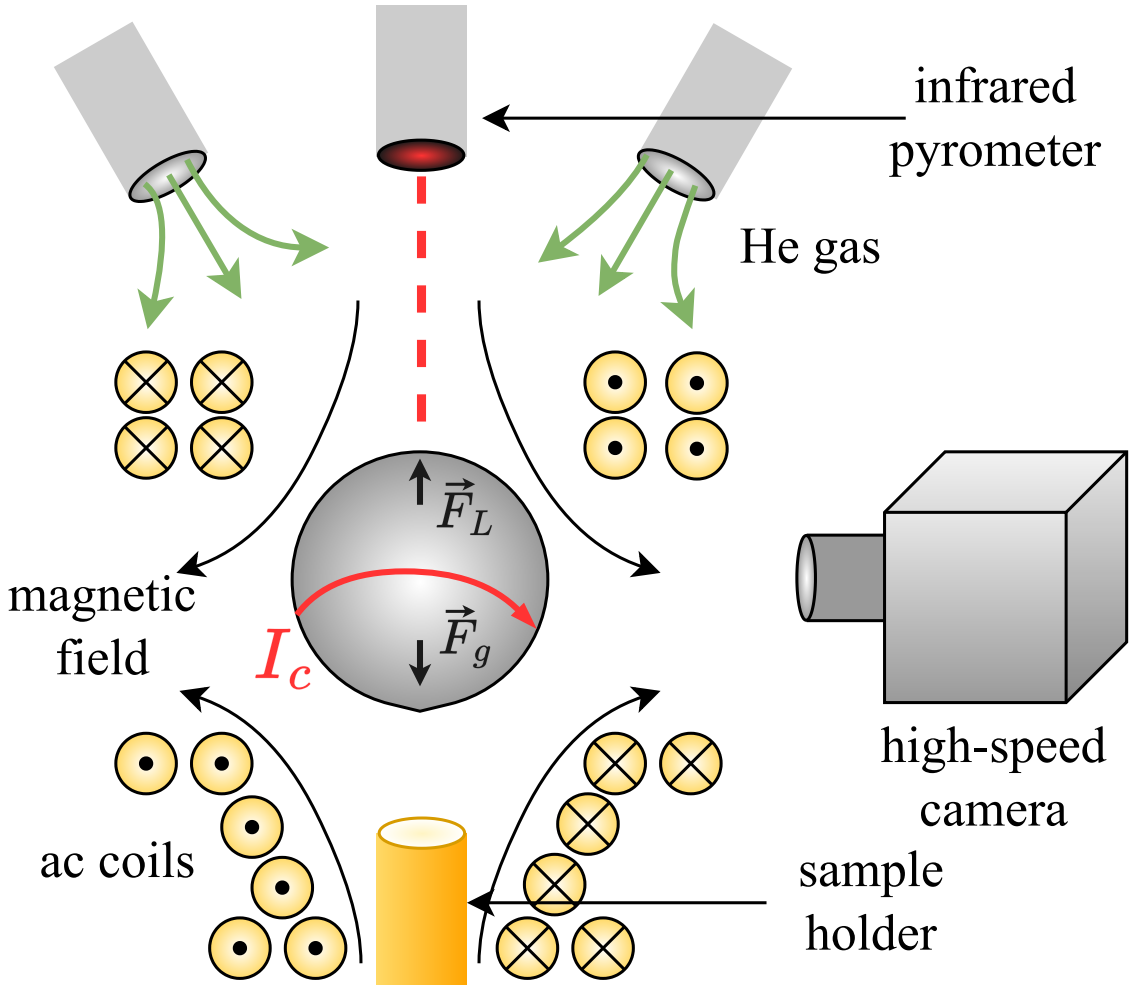

FIGURE 5.3: A schematic of the EML process at DLR. The black arrows show the direction of the magnetic field induced by the coils. I_c denotes the current that is generated from the coils magnetic field. F_L and F_g are the levitation force and gravitation force, respectively.

5.3.5 Advanced Imaging

The SEM used for this work was a Tescan Vega 3, which uses a thermal emission source. The images were taken at an accelerating voltage of 20keV, and a working distance of 15mm. Semi-quantitative compositional data was acquired using an Oxford electron dispersive spectroscopy (EDS) system, calibrated for 20 keV. Electron backscatter diffraction (EBSD) was done using a Zeiss Sigma field emission SEM (FESEM), equipped with an AZtechSynergy acquisition system.

5.4 Results

5.4.1 Thermodynamic Modelling

5.4.1.1 Scheil Solidification: Matrix Composition

The Scheil solidification plot for the nominal matrix composition (Table 5.1) is shown in Figure 5.4, and the composition of the different phases are shown in Table 5.5. Where a range of compositions is given, the first and last numbers represent the composition at the

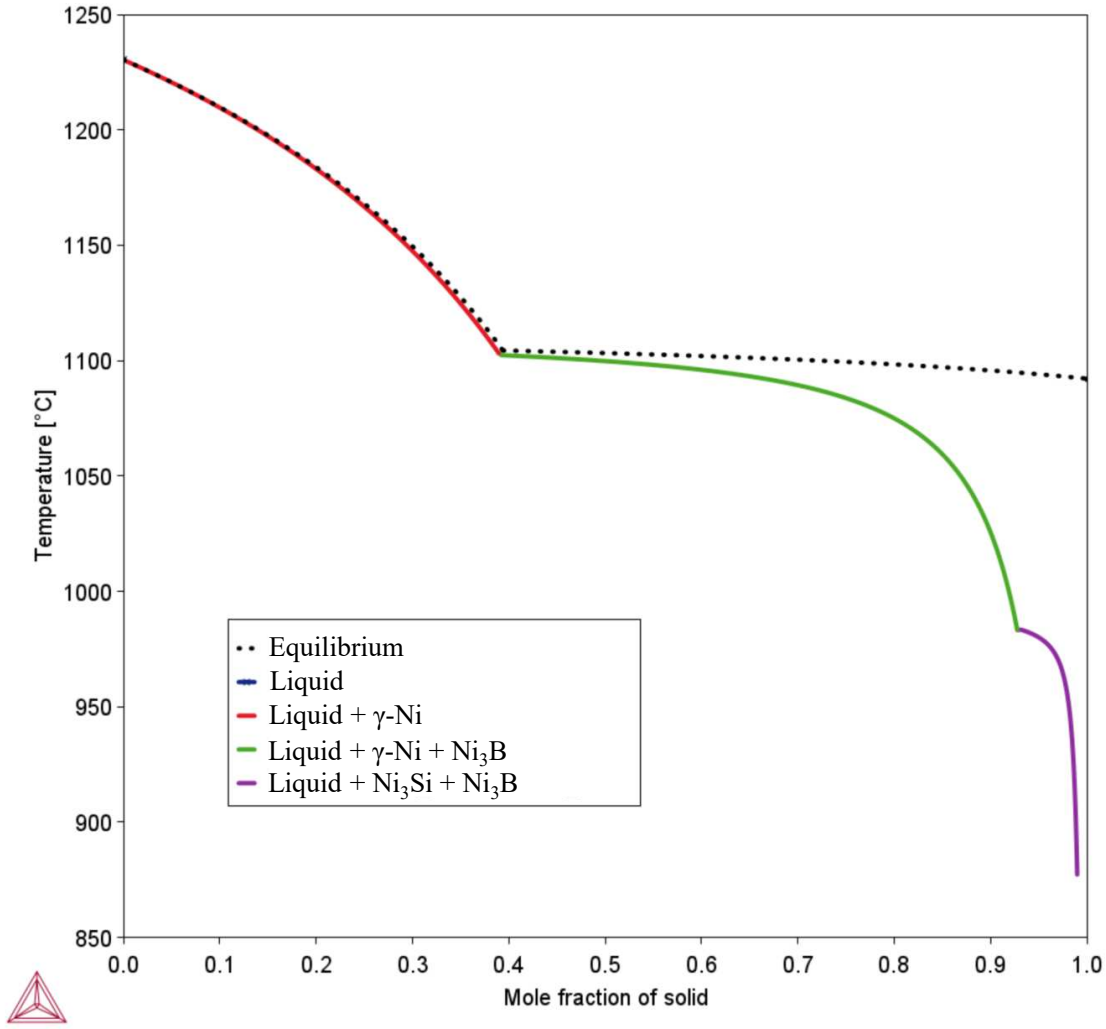

FIGURE 5.4: Scheil solidification diagram for the composition shown in Table 5.1. The average composition of the different phases are shown in Table 5.5.

TABLE 5.5: The composition of the different phases shown in Figure 5.4 using Thermo-calc. The range of values highlights the difference in composition as solidification progresses, where the first and last numbers are the composition at the beginning and end of solidification, respectively. If no range is given the composition was constant.

	at%			
Phase	Ni	Si	Fe	B
γ-Ni	92.4 - 85.6	7.2 - 14.1	0.2 - 0.1	0.2 - 0.3
Ni_3B	75.0	-	-	25.0
Ni_3Si	75.0	25.0	-	-

start and end of solidification, respectively. The first phase to form is γ-Ni solid solution at just above ≈1225°C. The γ-Ni phase consists mostly of Ni and Si, with some traces of B, and Fe. The rejection of Si to the liquid is similar to what is found for Ni-Si-W ternary alloys [565]. After forming primary Ni, Ni_3B forms just above 1100°C while continuing to form WC and γ-Ni. Just below 1000°C, a eutectic of Ni_3Si and Ni_3B forms.

5.4.1.2 Scheil Solidification: Matrix Composition with added W

To study the effect of adding W and C on the solidification sequence of the Ni matrix, a Scheil solidification simulation was done using the average matrix composition (Table 5.2) through the entire height of the build, which is shown in Figure 5.5. The composition of all the phases are found in Table 5.6. The solidification starts with γ-Ni solid solution at ≈1180°C containing low W, C, and Fe, and high Si content. A W_2FeB_2 phase forms at ≈1025°C containing high amounts of W and Fe, followed by the nucleation and growth of Ni_3B just above 1000°C. The Ni_3B phase is alloyed with small amounts of Fe. At ≈930°C an FCC phase of WC forms, which could be FCC γ-$WC_{(1-x)}$ since it is stable between 37.1 and 50 at% C. However, the starting temperature of the γ-$WC_{(1-x)}$ (930°C) is far below the stable temperature range for γ-$WC_{(1-x)}$ (2216-2755°C) [626, 627]. The next phase forms at just above 900°C and is Ni_3Si. Solidification continues from 900 to ≈700°C, with small amounts of the aforementioned phases solidifying. The last to form is $B_{19}C$, which forms at ≈750°C.

Adding W and C to the Ni matrix drastically changed the Scheil solidification simulation. For both compositions, the first phase to form was a γ-Ni solid solution with similar amounts of Si, Fe, and B. The solidification start temperature for γ-Ni was slightly lower with the

W and C addition. A majority of the W and C was used in forming W_2FeB_2, γ-$WC_{(1-x)}$, and $B_{19}C$. The solidification start temperature of Ni_3B and Ni_3Si were both lower with the added W and C, but the composition was not affected. The matrix with added W and C also solidified until ≈725°C, where just the matrix finishes solidifying at ≈875°C.

5.4.2 PTA-AM of 70wt%WC - NiBSi

A cylinder made from 70wt% WC - NiBSi is shown in Figure 5.6, with dimensions of 50x40x1.5mm for the height, diameter, and layer width, respectively. The average layer height was 1.67mm, totaling 30 layers for this build. A 1.67mm layer height is much larger

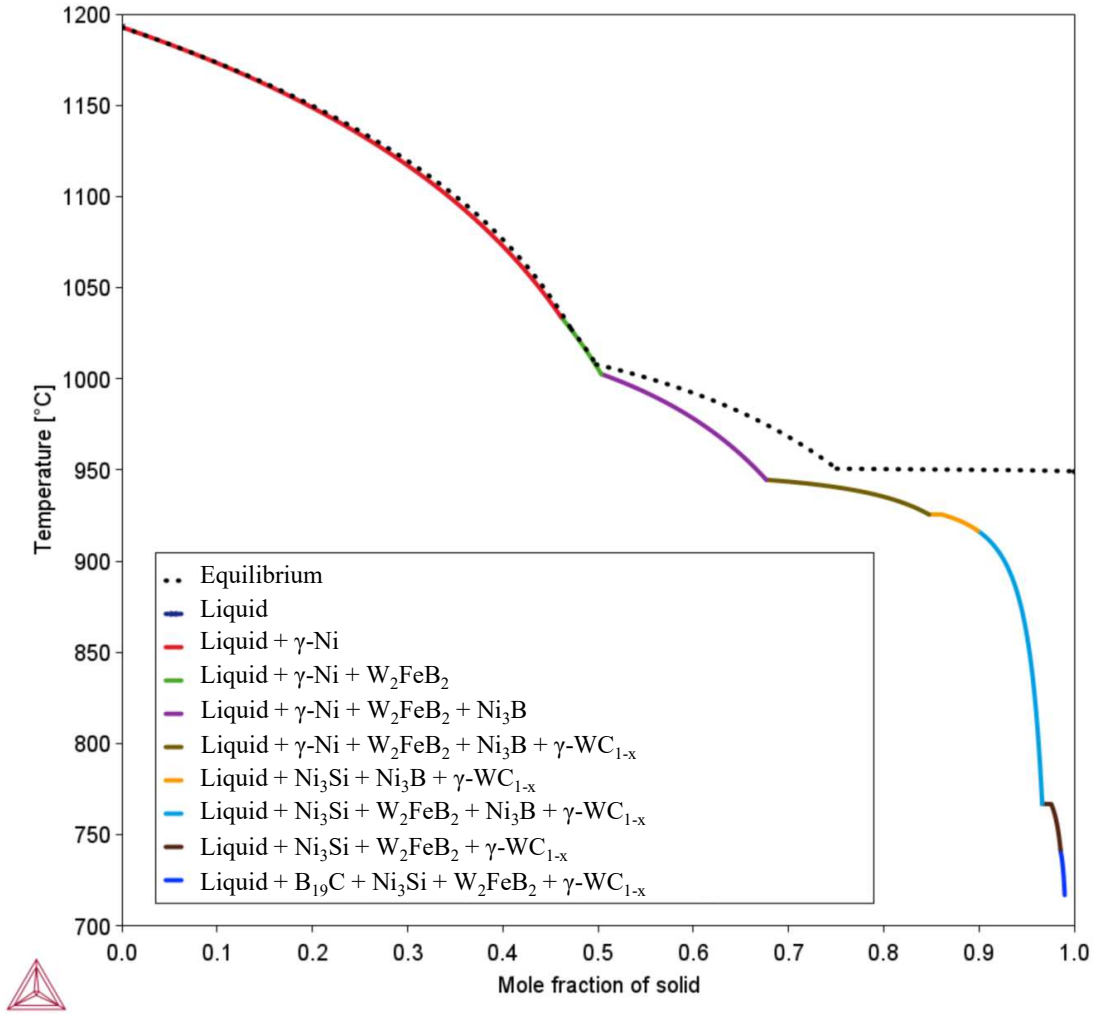

FIGURE 5.5: The Scheil solidification diagram from the composition shown in Table 5.2.

TABLE 5.6: The composition of the different phases shown in Figure 5.5 using Thermo-calc. The range of values highlights the difference in composition as solidification progresses, where the first and last numbers are the composition at the beginning and end of solidification, respectively. If no range is given the composition was constant.

	at%					
Phase	Ni	W	Si	C	Fe	B
γ-Ni	89.2 - 85.1	1.2 - 0.4	8.6 - 13.3	0.6 - 1.1	0.3 - 0.0	0.2
W_2FeB_2	1.8	38.2	-	-	20.0	40.0
Ni_3B	74.7 - 74.9	-	-	-	0.3 - 0.1	25.0
γ-WC_{1-x}	-	55.4	-	44.6	-	-
Ni_3Si	75.0	-	25.0	-	-	-
$B_{19}C$	-	-	-	5.0	-	95.0

than laser DED [628], slightly lower than wire and arc additive manufacturing (WAAM) [629], and is more than double PTA-AM of 60wt%WC - NiCrBSi[36]. There is a significant amount of surface roughness from the high loading of WC and not having sufficient matrix material to create a smooth finish. Although there is high surface roughness, the individual layers can not be observed on the profile of the cylinder, which is typical for large layer heights like those found in WAAM [118, 156, 628], and PTA-AM of 17-4 PH [623]. One significant perturbation on the surface can be seen near the bottom of the sample, likely caused by the gradient of operating parameters that occurs after the first 5 layers.

5.4.2.1 Defects in the Microstructure

Low magnification backscatter SEM images of the deposit shown in Figure 5.6 are shown in Figure 5.7, where the WC particles are shown in white, and the black holes within the sample are porosity. The left of Figure 5.7a shows the sample bonded to the steel substrate. The carbides are homogeneously distributed in the NiBSi matrix for the first layer, with very little porosity. Significant secondary WC phases are also present, illustrated by the abundance of brighter constituents in the matrix shown in Figure 5.8. No W is present in the matrix alloy prior to PTA-AM deposition. The formation of secondary phases containing high amounts of W is evidence that the WC undergoes some dissolution during the PTA-AM process. The dilution of the substrate in the first layer causes a surplus of Fe and C dissolved in the matrix, which bonds with the W and C from the dissolution of WC particles to form carbide phases. In subsequent layers, two defects dominate the microstructure; the first are areas void of WC, termed denuded regions [11], and the second is porosity. Denuded regions

FIGURE 5.6: An example of a PTA-AM build of 70wt% angular monocrystalline WC in a NiBSi matrix. The sample is 50mm tall, and has a diameter of 40mm.

are industrially recognized defects for the high loading of reinforcement particles in metal matrix composites across different deposition methods. The mechanism that causes denuded region formation is unreported.

The porosity that is found falls under two morphological categories, one being large irregular shapes and the other being spherical pores. The large irregular-shaped pores are likely manufacturing defects. For the PTA, the voltage is governed by the arc length or the distance from the tip of the electrode to the substrate. During the deposition, the arc length controller (ALC) attempts to maintain the stand-off distance to keep the voltage constant. However, there is a response time for the voltage sensor to communicate the voltage change and for the torch's height to be adjusted, resulting in instances where the voltage drops below 23V. A stand-off distance that is too low will result in two individual tracks of material being deposited, one from each of the co-axial nozzles. The decreased volume of the matrix material, and low heat input results in a weld pool with poor flowability. This would lead to regions of no WC as well as regions with no matrix leading to irregular pores. It is suggested that the two individual tracks could be one of the causes of the formation of the irregularly shaped pores. Another possible mechanism is increasing the carbide content beyond the packing limit of angular WC [630].

The formation of the spherical porosity could be due to the formation of CO/CO_2 gas during the deposition. The generation of CO/CO_2 has been reported previously in laser cladding of WC-Ni [631, 632]. Additionally, inadequate shielding has been observed to cause porosity in the PTA-AM of 17-4PH stainless steel[623]. The dissolution of WC results in dissolved carbon and inadequate shielding from the atmosphere, as well as the oxide layer on the surface of the powder results in dissolved oxygen. The dissolved carbon and oxygen react to form CO/CO_2, which is trapped due to rapid solidification. Note that this was observed through the microstructural characterization.

5.4.2.2 WC and Pore Area Percent

The carbide and porosity area percent were tracked through the entire height of the build from micrographs, shown in Figure 5.9. It is assumed that area% is equal to the volume% of WC. The black, red, and blue line correspond to the porosity, carbide, and theoretical area

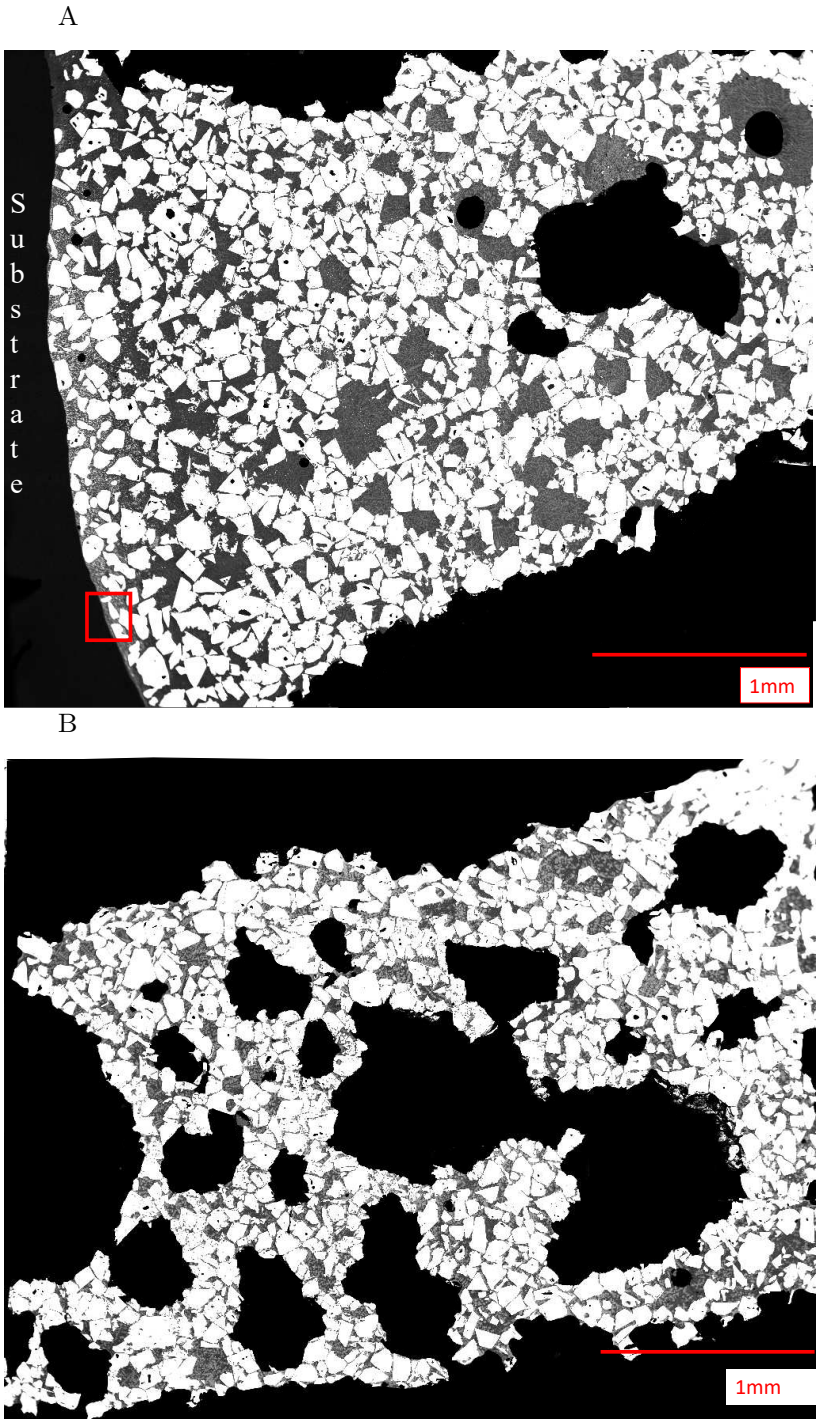

FIGURE 5.7: Low magnification Backscatter SEM of the bottom (a) and middle (b) of the PTA-AM build shown in Figure 5.6. The WC particles are shown in white. Two defects dominate the microstructure, large pores (black circles) and areas void of WC termed denuded regions. The white patches inside the pores and outside of the sample are artifacts from the SEM imaging. The red square represent where Figure 5.8 was taken.

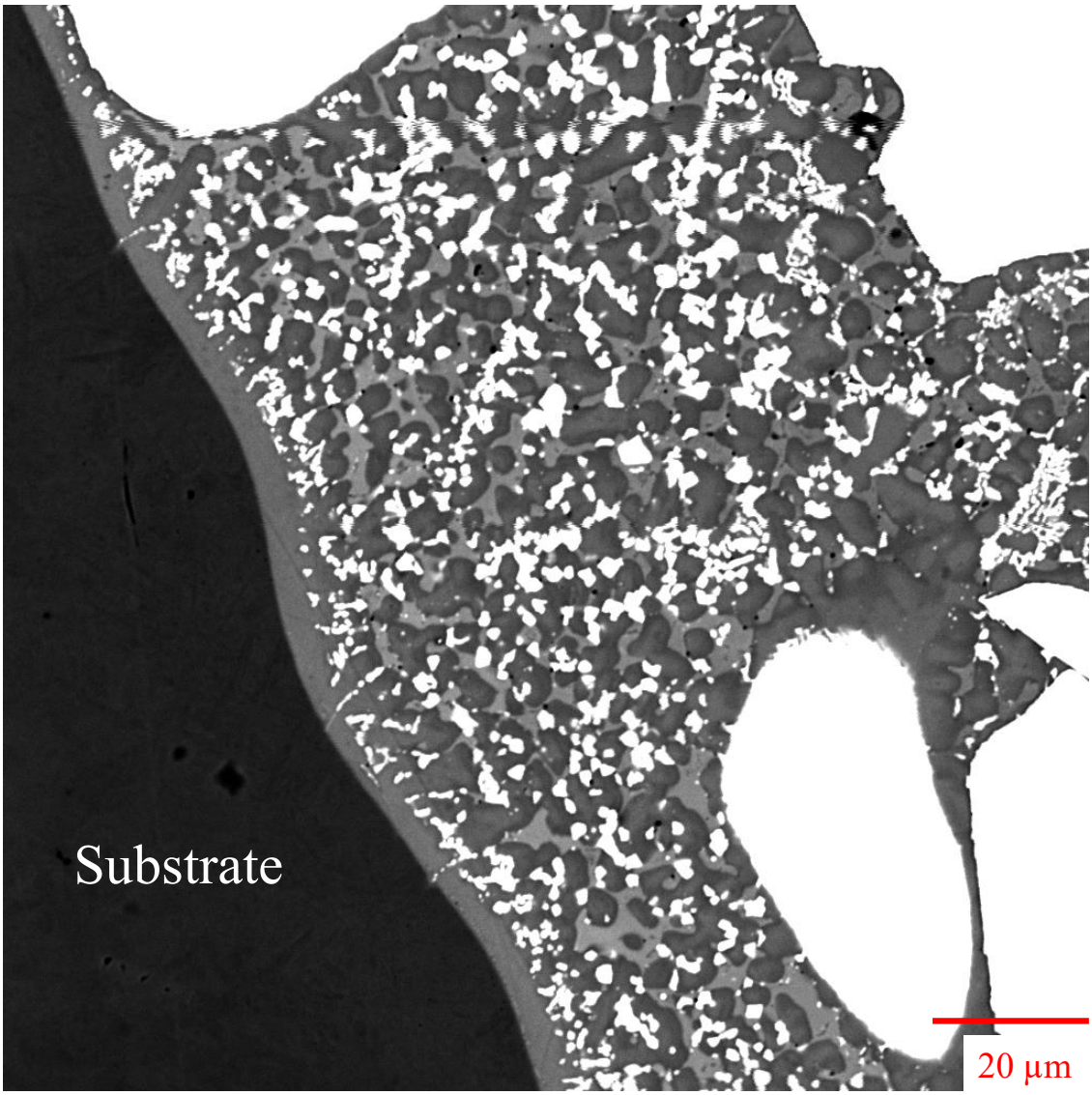

FIGURE 5.8: A 2000x backscatter SEM image showing the effects of substrate dilution on the microstructure.

percent for 70wt% WC (57 area%), respectively. It was also found that the maximum packing of angular WC with a d50 of 112μm is 47vol%, shown as the green line [630]. From the plot, it can be deduced that the porosity and carbide percent are inversely correlated. After 30mm, the fluctuations in the carbide area% decrease, which could point to the retention of WC reaching a steady state. Experiments, where the build height is higher than 48mm, would be required to confirm if the carbide area% reaches a steady state. At no point through the cross-section does the volume loading of WC in the sample reach the theoretical volume loading for 70wt% WC (57 area%). This is likely due 70wt% (57 area%) being higher than

the maximum packing of WC at the current size range (47 area% or 62wt%). However, with a small amount of porosity, the carbide retention falls to values closer to or exceeding the maximum packing (47 area%). Where the WC content surpasses the maximum packing of WC is likely due to the discrepancy between area and volume percent. The plot in Figure 5.9 highlights that adding more WC should theoretically increase the carbide retention in the sample; in practice, this is not the case. The reduction in matrix material to bind the WC particles together may not allow for higher retention of carbides, especially when the solidification rate is increased from the lower heat input.

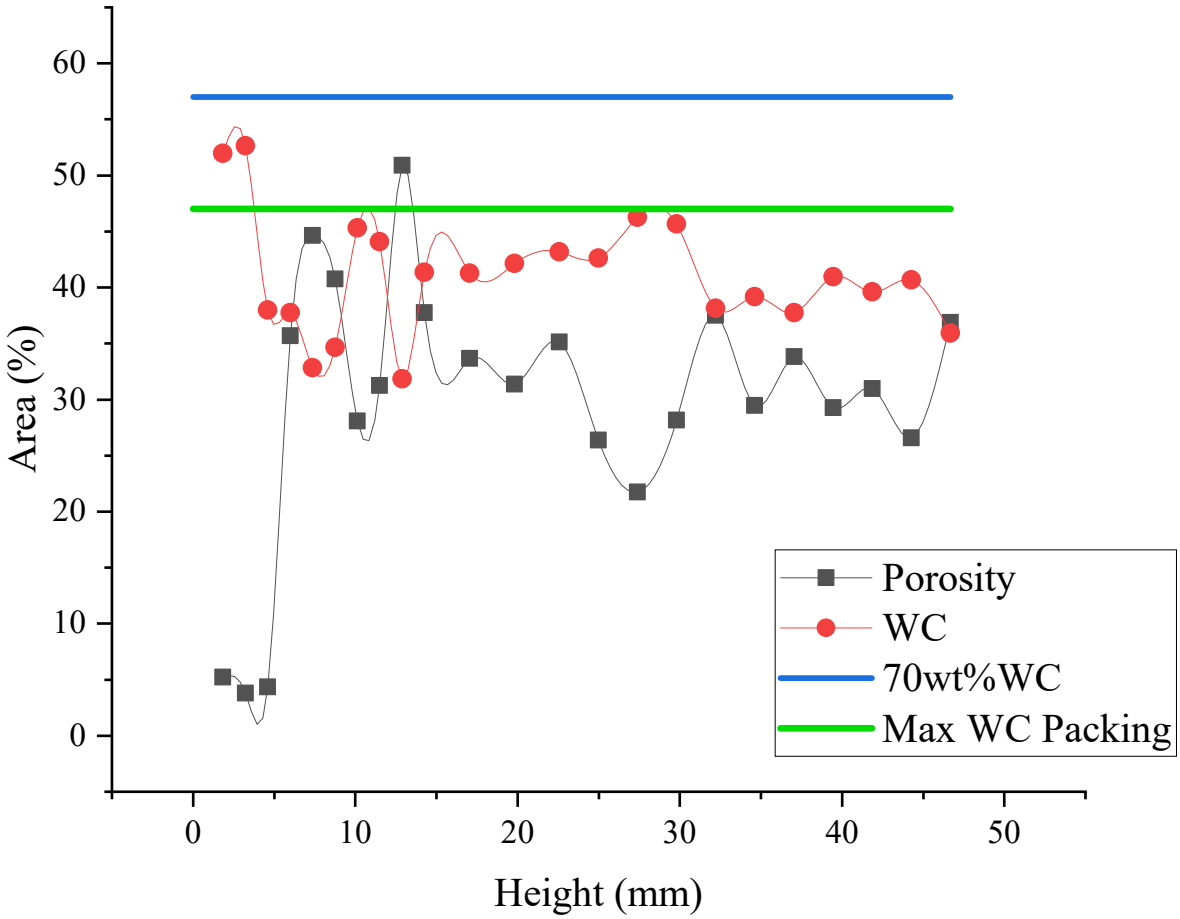

FIGURE 5.9: The carbide (red circles) and porosity (black squares) area percent as a function of height in the PTA-AM build shown in Figure 5.6. The blue line shows what the theoretical area percent is for 70wt% WC-NiBSi. The green line corresponds to the max packing of WC with a D50 of 112 μm [630].

5.4.2.3 Microstructural Comparison Between Interparticle and Denuded Regions

There has not been any confirmed mechanism explaining the presence of denuded regions. According to a study by Sundaramoorthy *et. al.*, denuded regions in the solidified microstructure of alloys may be caused by the formation of liquid nickel droplets in the plasma during PTA. These droplets may not completely mix with the surrounding melt pool due to surface tension. In contrast, Wolfe *et. al.* proposed an alternative explanation for denuded regions. They suggested that tungsten vapor formed in the plasma during PTA processing may diffuse into nickel droplets and enter the melt pool as a mushy phase, which is a mixture of solid and liquid phases. This mushy phase could then solidify to form the denuded regions. Both of the above mechanisms suggest a difference in the composition of the denuded regions compared to the interparticle regions. To test the proposed theories, the composition (Table 5.7) and microstructure (Figure 5.10) of the denuded and interparticle regions were compared. Looking at the microstructure, both regions contain small blocky W-rich phases (A). In both cases, the microstructure is dendritic with significant solubility of W in the primary phase (B). The dendrites are surrounded by a halo (C), and the interdendritic regions contain two phases: one of Ni (D), and another being a Ni solid solution of Si and

TABLE 5.7: The composition of the phases in the denuded region (D) and interparticle region (I). The letters correspond to the letters in Figure 5.10. Carbon was ignored for these measurements.

		at%			
Region	Description	Ni	W	Si	Fe
Interparticle	A	51.4	48.6	–	–
	B	89.8	10.2	–	–
	C	89.0	4.9	4.9	1.2
	D	100	–	–	–
	E	85.5	–	13.5	1.0
	Overall	89.0	2.4	8.0	0.9
Denuded	A	47.3	52.7	–	–
	B	89.7	10.3	–	–
	C	88.3	4.8	5.7	1.1
	D	100	–	–	–
	E	84.5	–	14.6	0.9
	Overall	90.5	2.3	6.6	0.6

Fe. The overall composition of the two regions is also similar. Based on the microstructural and compositional evidence, it is likely that the previously mentioned mechanisms of un-mixed or un-melted Ni are likely not the cause of denuded regions, and another mechanism is responsible for the formation of these defects. Therefore, the microstructure of only the denuded regions will be discussed, as it is representative of the microstructure of the entire sample at a given height.

5.4.2.4 Microstructure of a denuded region in PTA-AM 70wt%WC - NiBSi

The microstructure using backscatter mode on the SEM is shown in Figure 5.11. Each image corresponds to a different height in the sample, where Figure 5.11A is at the lowest location, and Figure 5.11D is at the highest location. The images are all denuded regions due to the large concentration of matrix material, and there is no WC to hinder the dendritic growth of the microstructure. From Figure 5.11, it can be seen that the microstructure in the denuded zones is dendritic at all heights in the build. The dendritic microstructure becomes coarser as the build progresses.

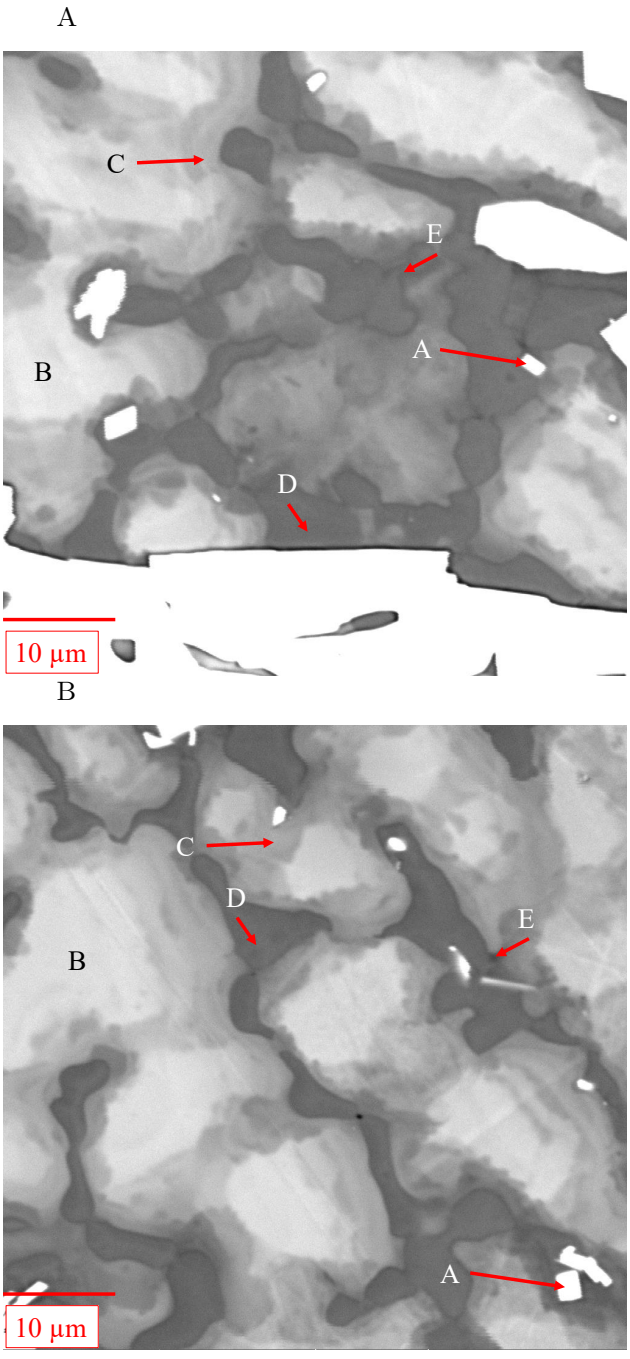

FIGURE 5.10: High magnificiation backscatter SEM images showing matrix microstructure of the interparticle regions (A) and the denuded regions (B). The labels correspond to the compositions shown in Table 5.7.

A

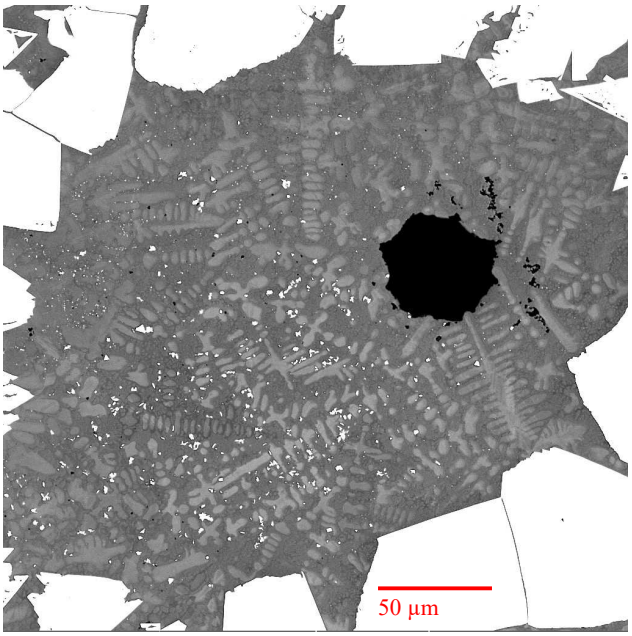

B

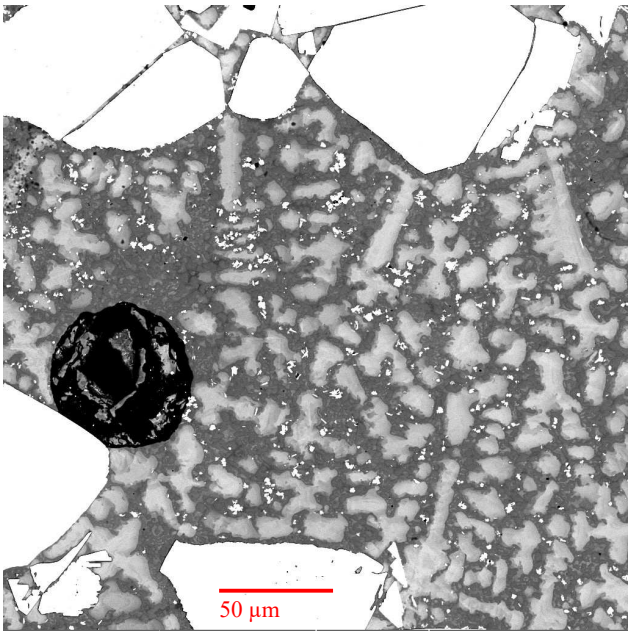

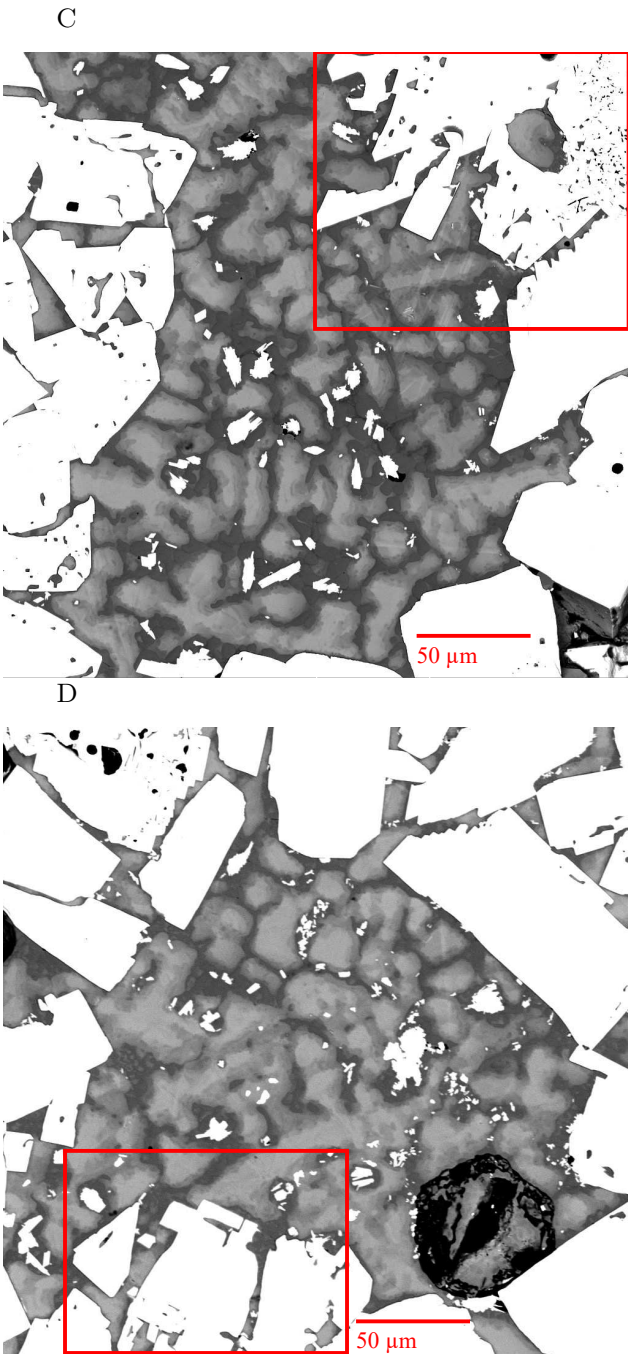

FIGURE 5.11: Backscatter SEM images of the PTA-AM build shown in Figure 5.6 taken at different heights; a) is taken at 0.924mm; b) is taken at 8.75mm; c) is taken at 19.81mm; d) is taken at 41.86mm.

Higher magnification SEM images are shown in Figure 5.12. All the images are taken at the same magnification to highlight the coarsening of the dendritic structure. Throughout the microstructure are small plate-like secondary W particles (A). The Ni microstructure consists of primary dendrites (B), most of which have a halo (C) surrounding the primary phase. At lower points in the sample, the halo around the primary phase is less prominent than at higher points. There are many instances throughout the sample where a phase with the same composition/contrast as the halo is found in the interdendritic regions, as seen in Figure 5.12B. The interdendritic regions are dominated by phase D, with seams of a slightly darker phase E. Phase E is found more frequently at lower points in the sample, and is almost completely eliminated halfway up the sample (19.81mm) as the dendritic structure coarsens.

To quantify the coarsening of the microstructure, the secondary dendrite arm spacing (SDAS) was measured at differing heights throughout the build, as shown in Figure 5.13. The coarsening of the microstructure and the increase in SDAS indicates that the solidification cooling rate of the sample decreases as the number of layers increases. In the beginning layers, the steel substrate acts as a heat sink causing much higher solidification rates, since there is no substrate pre-heat [633, 634]. At higher layers, the solidification cooling rate decreases due to heat accumulation in the sample [635, 636]. The higher amount of heat accumulation also appears to have coarsened the secondary carbide phase (A). The area fraction of secondary carbides is plotted as a function of height shown in Figure 5.14. As the height increases, the area fraction of secondary carbides increases. The first point on the plot is taken at the bottom of the sample, and dilution with the substrate caused a higher area fraction of secondary W phases (Figure 5.8).

A

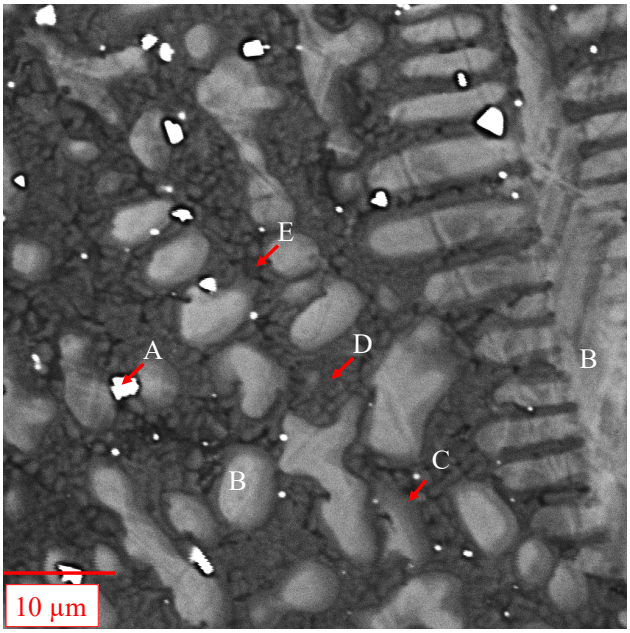

B

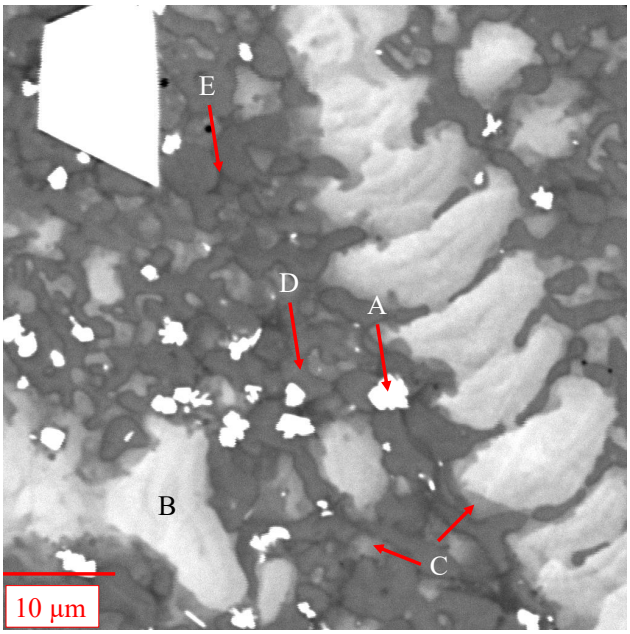

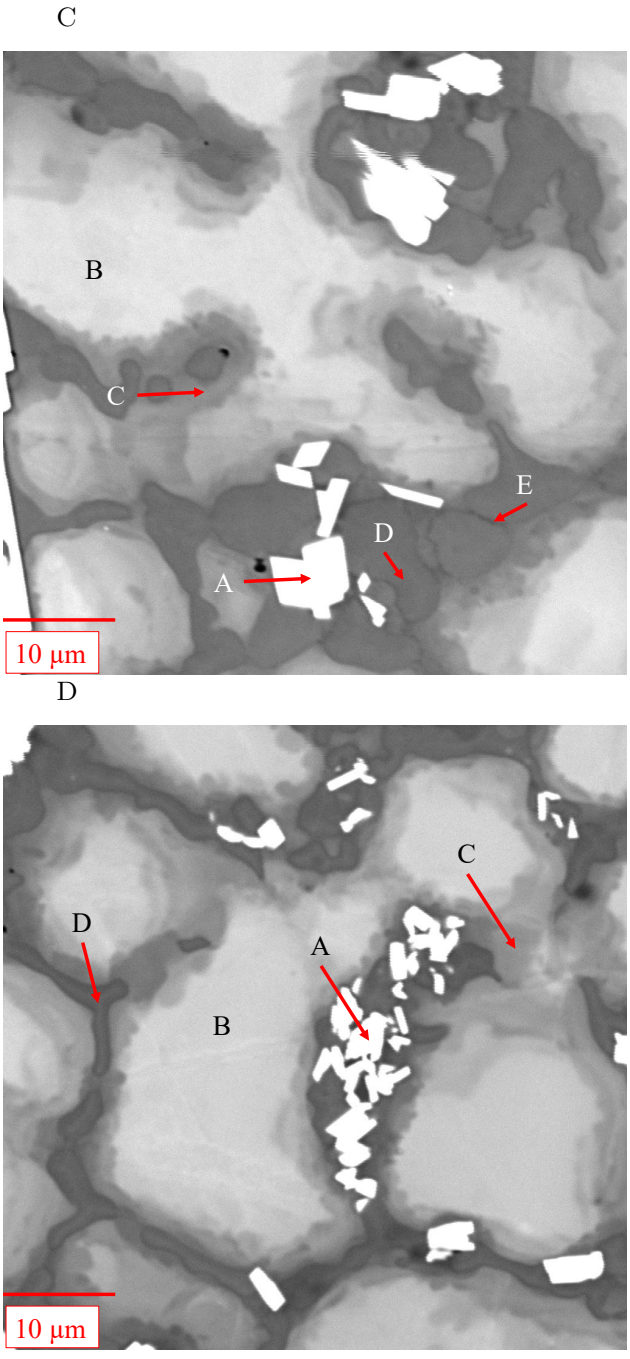

FIGURE 5.12: Backscatter SEM images of the PTA-AM build shown in Figure 5.6 taken at different heights; a) is taken at 0.924mm; b) is taken at 8.75mm; c) is taken at 19.81mm; d) is taken at 41.86mm.

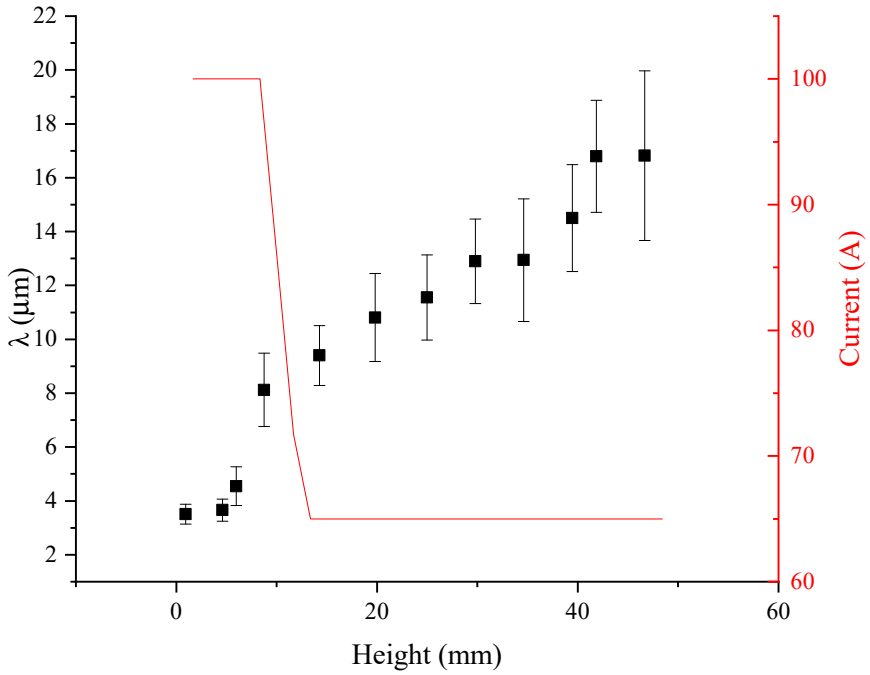

FIGURE 5.13: The change in secondary dendrite arm spacing as a function of height for the PTA-AM deposit.

The composition of the different phases of the microstructure at each height shown in Figure 5.11 are found in Table 5.8. Additionally, the composition of the primary phase (A) and the halo (B) around the Ni phase, as a function of height, are shown in Figure 5.15A and Figure 5.15B, respectively. The secondary WC phases present have an average composition of 75wt% W and 25wt% Ni; likely, carbon is also present but undetected with EDX. The composition of the primary phase (Figure 5.15A) faces greater fluctuations as the build progresses. The use of backscatter mode highlights the distribution of W from the dissolution of the WC particles, with the higher concentration being in the primary phase formed during solidification. The partition coefficient of W is larger than unity (2.0) in Ni [565, 637], meaning that during solidification, W tends to segregate in the dendritic core. There is slight solubility of Fe and Si in the primary phase in the beginning layers, but they are no longer present after 15mm. The high levels of Fe in the first layers are likely from dilution with the steel substrate. The primary characteristic x-ray for Si (Lα) is 1.739, and for W (M) is 1.774, as seen in Figure 5.16. Therefore, the Si content could be a measuring error from the EDX. As the height increases, the W content in the primary phase also increases, which signifies there could be more carbide dissolution as the build progresses. Referring back to the microstructures shown in Figure 5.11, it can be seen in the area marked by the red square

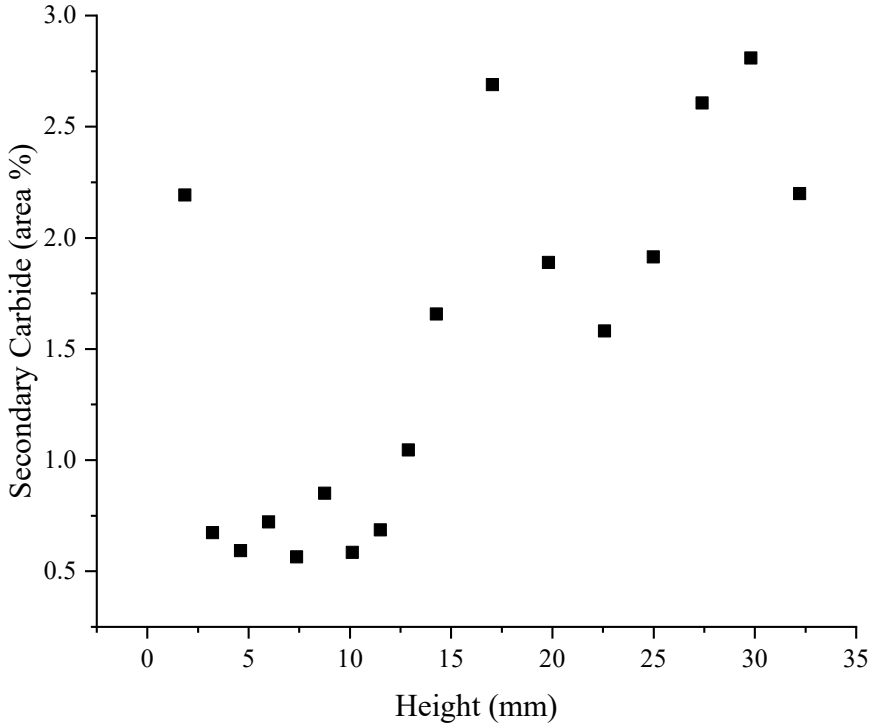

FIGURE 5.14: The area fraction of secondary carbides as a function of height.

that in Figure 5.11C and Figure 5.11D, there is more thermal degradation of the WC compared to Figure 5.11A and Figure 5.11B, leading to the increased W content in the matrix, and higher area fractions of secondary carbide phases (Figure 5.14). The first 3 data points, where the W content is the lowest, correspond to where the heat input and the solidification cooling rate are the highest. For conventional PTA, as the heat input increases, the cooling rate decreases, and the amount of carbide dissolution increases [11, 13, 471]. Therefore, for both conventional PTA and PTA-AM, the solidification cooling rate plays a significant role in dictating the amount of carbide dissolution.

The Ni halo had a fairly consistent composition, besides the introduction of W at around 10mm, which lines up with the W content in the primary phase surpassing 20wt%. According to the Ni-W phase diagram [638], 20wt% is lower than the solubility of W in Ni. Additionally, the high Fe and C content in the Ni halo in the first layer is due to the dilution of the steel substrate. It is interesting that the Fe was rejected more into the liquid and not retained in the primary phase since the partition coefficient of Fe in Ni-Si-Fe ternary alloys is above unity [565]. Fe being rejected into the liquid highlights the influence composition, and solidification cooling rate has on the partition coefficient of different elements.

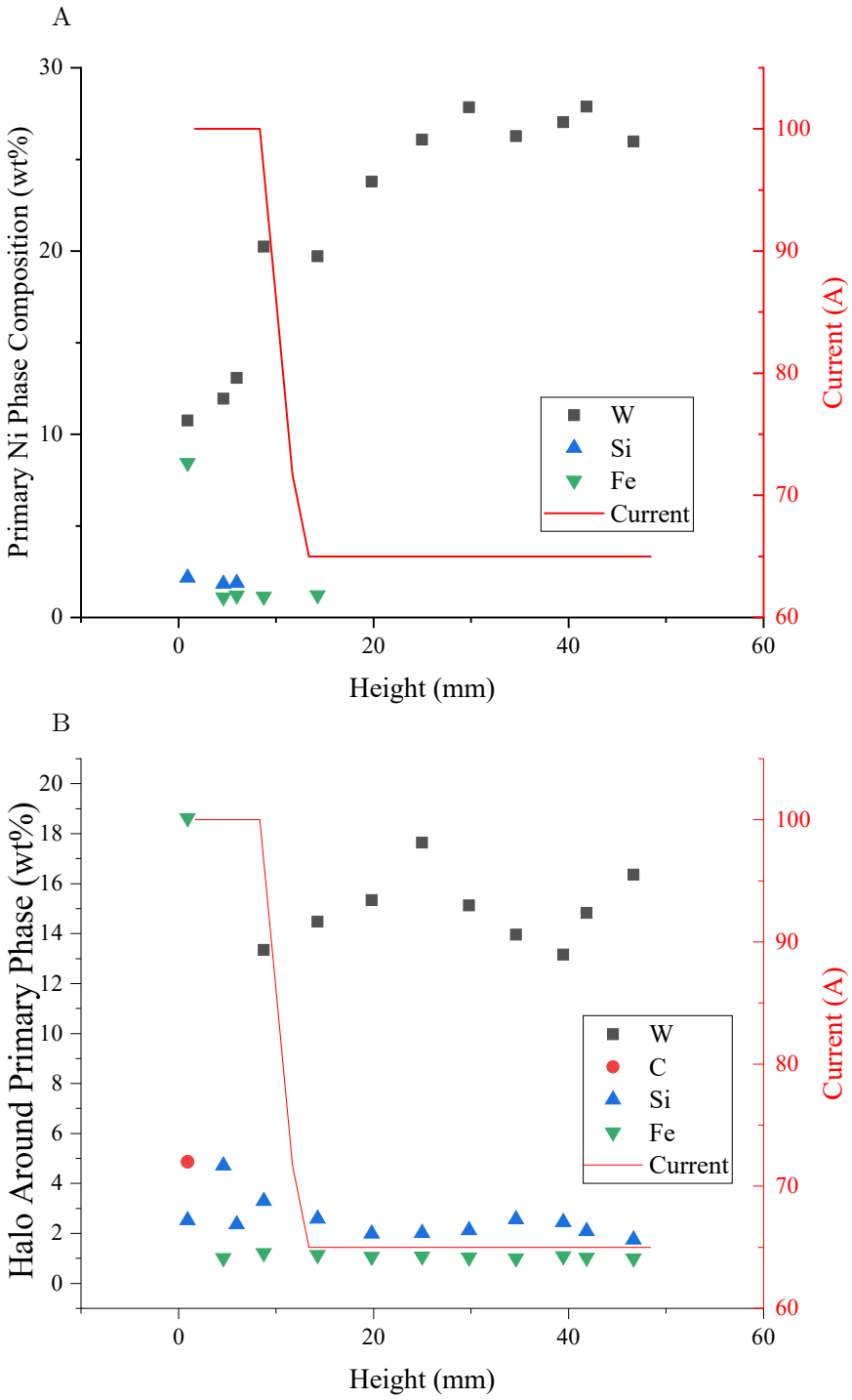

FIGURE 5.15: a) shows the composition of the primary phase as a function of height; b) shows the composition of the Ni halo around the primary phase as a function of height. It should be noted that the Ni content is the remainder of the composition and is not shown on the plot.

TABLE 5.8: The composition of the different phases shown in Figure 5.12 for the 70wt% WC - NiBSi PTA-AM sample. The average compositions from the Scheil simulations are provided for comparison.

		PTA-AM (at%)					Thermo-calc (at%)					
Phase	Height (mm)	Ni	W	Si	C	Fe	Ni	W	Si	C	Fe	B
A	0.924	54.3	45.7	–	–	–	2.0	38.0	–	–	20.0	40.0
	8.75	46.9	53.1	–	–	–						
	19.81	48.6	51.4	–	–	–						
	41.86	43.4	56.6	–	–	–						
B	0.924	83.9	2.7	4.7	–	8.8	87.2	0.7	11.0	0.8	0.1	0.2
	8.75	91.1	7.5	–	–	1.4						
	19.81	90.9	9.1	–	–	–						
	41.86	89.0	11.0	–	–	–						
C	0.924	60.4	–	4.3	19.3	16.0	–	–	–	–	–	–
	8.75	86.9	4.5	7.3	–	1.3						
	19.81	88.9	5.3	4.5	–	1.3						
	41.86	89.0	5.1	4.7	–	1.2						
D	0.924	100	–	–	–	–	74.8	–	–	–	0.2	25.0
	8.75	100	–	–	–	–						
	19.81	97.0	–	3.0	–	–						
	41.86	100	–	–	–	–						
E	0.924	78.9	–	15.1	–	6.0	75.0	–	25.0	–	–	–
	8.75	84.6	–	15.4	–	–						
	19.81	84.3	–	14.9	–	0.8						

In the interdendritic regions, phase D is typically 100% Ni. It could be that this phase is Ni_3B[10, 36, 190], since boron is undetectable using EDX. Phase E in the interdendritic regions had high Si content and some instances of dissolved Fe. The high Fe content in the first 1mm is likely from dilution with the substrate. Based on the atomic fraction of Ni to Si, it could be that this phase is Ni_3Si, which has been detected using x-ray diffraction on 60wt% WC - NiCrBSi deposited using PTA-AM [36]. The characteristic x-rays from phase E could contain signal from phase D since the interaction volume for characteristic x-rays in Fe is $1\mu m^3$. The small volumes of phase E (Figure 5.12C) could cause some of the Ni from phase D to be detected, reducing the detected Si content. The phase fraction of phase E tends to decrease as the height increases, and it is no longer found at the uppermost layers (Figure 5.12D).

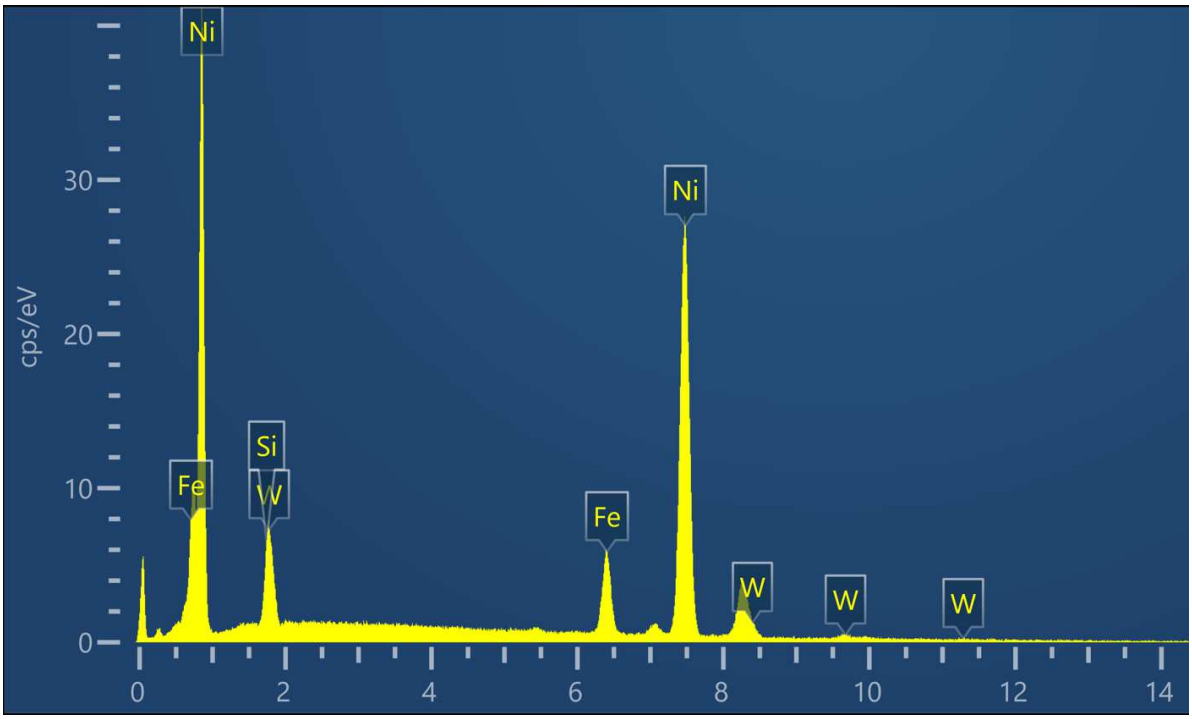

FIGURE 5.16: EDX spectrum from a primary dendrite in Figure 5.12A to highlight the overlapping EDX peaks of W and Si.

5.4.2.5 Comparing Thermo-calc with PTA-AM

The composition of the Scheil calculations for the average matrix composition (Figure 5.5) is compared with PTA-AM in Table 5.8. During the Scheil simulation, W_2FeB_2 formed instead of the NiW (A) phase that likely formed during PTA-AM. No W_2FeB_2 was found in the PTA-AM microstructure. The W content in the primary phase (B) was much higher (2-10x) than what was predicted by Scheil. The Scheil simulation also predicted much higher levels of Si in the primary phase than what was detected. The halo (C) was not formed during the Scheil simulation. Thermo-calc was able to predict the formation of Ni_3B, however, it forms in conjunction with the continued growth of γ-Ni, instead of after. After γ-Ni solidification, Ni_3Si formed, which is reflective of the PTA-AM build. No γ-WC_{1-x} or $B_{19}C$ likely formed during PTA-AM. The major discrepancies between Thermo-calc and PTA-AM highlights the need for more thermodynamic and microstructural data to be generated for the WC-NiBSi system.

5.4.3 EML of 70wt% WC - NiBSi

5.4.3.1 Temperature Calibration

The goal of the EML tests was to be able to track the thermal history of the composite powders and relate it to the microstructure of the solidified EML powders. The thermal history during the EML experiments was recorded using an infrared pyrometer. The DSC was used to calibrate the IR pyrometer data from the EML experiments. The heat flow (black line), and temperature (red line) profiles from the 5 °C/min run is shown in Figure 5.17. The rise in heat flow upon cooling corresponds to the exothermic reaction that occurs when transitioning from a liquid to a solid phase. The first exothermic peak likely corresponds to the solidification of the primary phase, while the second peak corresponds to the eutectic solidification. From the heat flow plot, the liquidus was taken as the onset of the first exothermic peak. For the 10 °C/min sample, the average liquidus was 1027°C, while at 5 °C/min, the liquidus was recorded to be 1041°C. Extrapolating the data to 0 °C/min, the

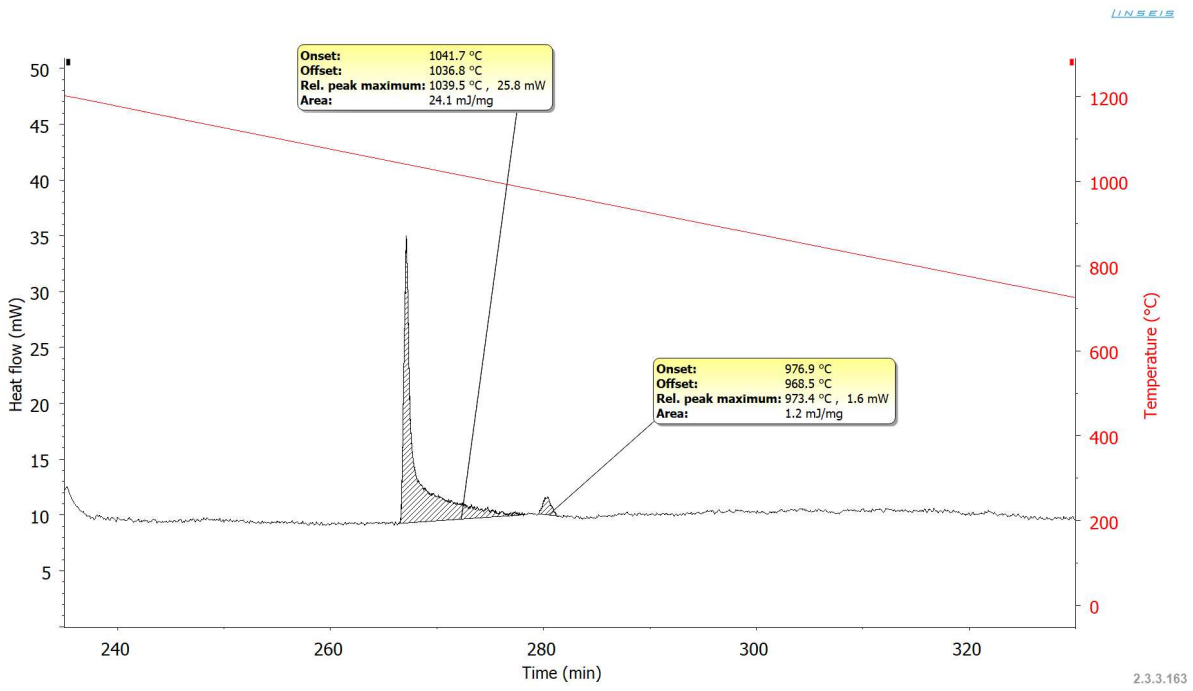

FIGURE 5.17: Heat flow, and temperature plot taken from the 5 °C/min DSC run of 70wt% WC in NiBSi. The first exothermic peak is likely the solidification of the primary phase, while the second peak corresponds to the eutectic. The black line corresponds to the heat flow and the red line is the temperature profile.

liquidus temperature at equilibrium was determined to be 1055°C. The eutectic temperature was calculated to be 976°C.

The temperatures recorded using the infrared pyrometer were adjusted using Equation 5.2, where T_{pyr} is the temperature recorded by the infrared pyrometer, T_e^{DSC} is the eutectic temperature measured by the DSC, and T_e^{pyr} is the eutectic temperature measured by the pyrometer.

$$T = \left(\frac{1}{T_{pyr}} + \frac{1}{T_e^{DSC}} - \frac{1}{T_e^{pyr}}\right)^{-1} \tag{5.2}$$

The calibrated thermal history is shown in Figure 5.18. The eutectic temperature was chosen due to an initial change in slope on cooling at point A, which is likely the onset of primary solidification. There is likely heterogeneous nucleation of the primary phase on WC. Each sample experienced some eutectic undercooling followed by recalescence. The temperature at the end of recalescence (C) is close to the equilibrium eutectic temperature [639]. The solidification cooling rate prior to eutectic nucleation (B) multiplied by the recalescence time was added to the recalescence temperature (C) to determine T_e^{pyr}, to offset any energy absorbed by the droplet [640].

5.4.3.2 EML Microstructure

A low magnification backscatter SEM image of one of the EML samples of 70 wt% WC in NiBSi is shown in Figure 5.19, and its corresponding thermal history was shown in Figure 5.18. All the EML samples had a significant amount of porosity. Since the EML samples were previously deposited PTA-AM samples, it is unknown whether the porosity was formed during EML or remained from the PTA-AM deposition. Significant care is taken to eliminate oxygen from the EML chamber, and the morphology of the pores is non-spherical. It is speculated that the porosity was likely retained from PTA-AM deposition or due to insufficient stirring of the liquid due to the high volume fraction of WC. Regardless of the thermal history, denuded regions are found in all EML samples.

Higher magnification backscatter SEM images of a denuded region's microstructure are shown in Figure 5.20. The microstructure for all EML samples is dendritic. Additionally, all of the EML samples contained varying degrees of a halo (B) around the primary dendrites. The interdendritic regions contains three phases. The phase that creates the halo (B) around

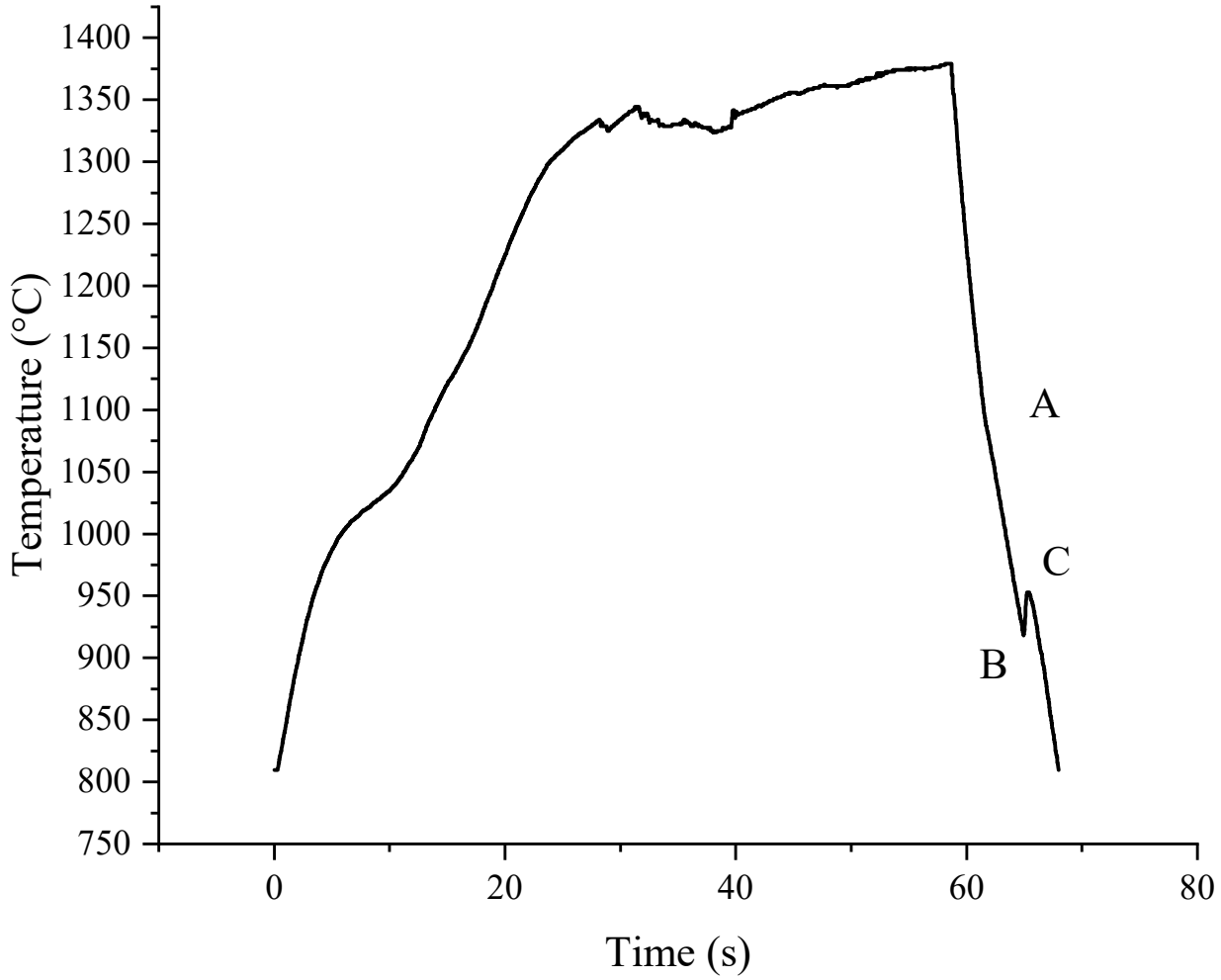

FIGURE 5.18: Thermal history from one of the EML samples.

the primary dendrite can also be found in the interdendritic regions, based on the composition of the lighter grey regions (Figure 5.20A). The majority of the interdendritic region is taken up by a phase with a slightly darker contrast (C) than that of phase B. Between some of the patches of phase C, is small pockets of a dark phase (D). Interdendritic porosity (also seen in Figure 5.11A) was found throughout the EML samples. During solidification, the material volumetrically contracts while the already formed dendritic network coarsens; this prevents liquid from filling in the pores left from the contracting material[641]. The result is solidification porosity as seen in the red square Figure 5.20B.

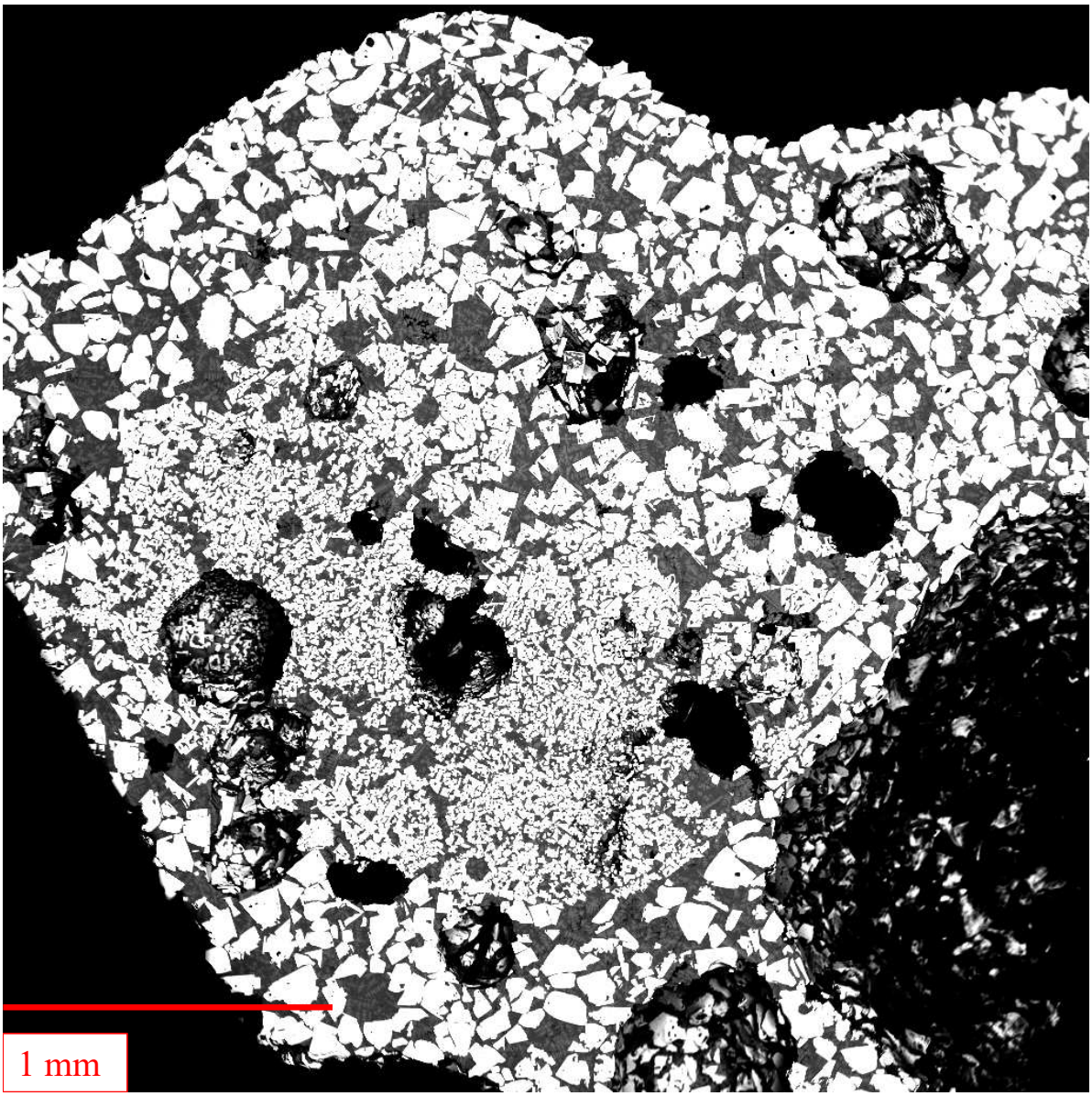

FIGURE 5.19: Low mag Backscatter SEM of the bottom of one of the EML samples with the composition show in Table 5.4, where the WC particles are shown in white, and pores in black;

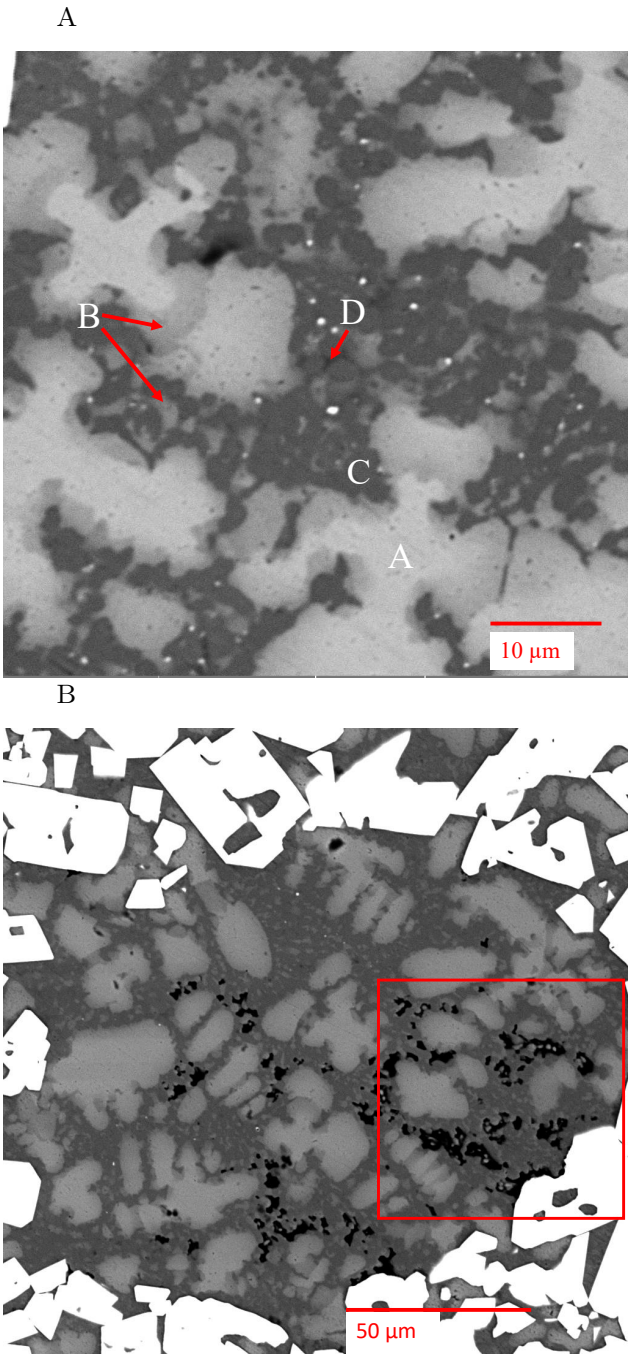

FIGURE 5.20: A) Backscatter image showing the different phases present in the microstructure in the EML samples; B) Backscatter SEM image showing an example of a microstructure of an EML sample

5.4.3.3 EML Secondary Dendrite Arm Spacing

The secondary dendrite arm spacing as a function of solidification cooling rate for the EML experiments was plotted, as seen in Figure 5.21. There does not appear to be much of a difference in the SDAS above 50°C/s. Only one sample could be cooled using the He gas streams, causing a slower solidification cooling rate. The relation between SDAS (λ_S) and solidification cooling rate is shown in Equation 5.3, where λ_o is a material constant, R is the solidification cooling rate, and n should be close to 0.33 [642].

$$\lambda_S = \lambda_o(R)^{-n} \tag{5.3}$$

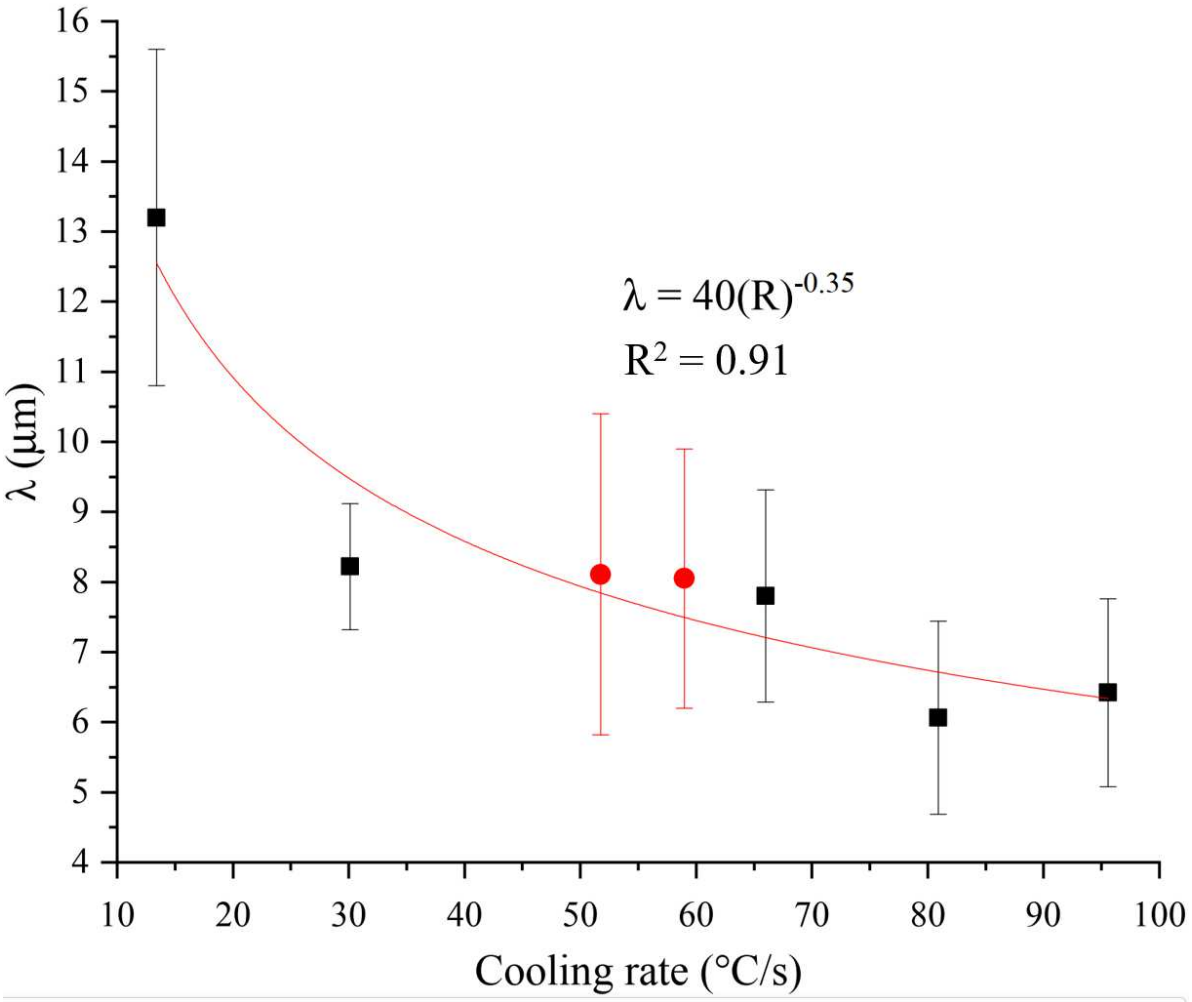

FIGURE 5.21: The SDAS from the 70wt% WC-Ni EML samples as a function of the solidification cooling rate. The red points are from 70wt% WC in NiBSi, and the black points are from 70wt% WC - NiCrBSi.

The developed correlation had an exponent of 0.35, and an R^2 of 0.91. The EML samples varied in compositions with respect to each other. The red and black points in the Figure 5.21 correspond to 70wt% WC in a NiBSi and NiCrBSi matrix, respectively. The difference in composition does not appear to have an impact on the relationship between SDAS and solidification cooling rate.

5.5 Discussion

5.5.1 Carbide Dissolution

When using PTA to deposit WC - Ni overlays, the higher heat input leads to more carbide dissolution [14–18]. It should be noted that there are limited studies done on Cr-free WC-Ni metal matrix composites. The higher heat input increases the peak temperature and reduces the cooling rate for single-pass welds and overlays. Higher peak temperatures and slower cooling rates create favorable conditions for convective mass transfer causing WC breakdown. The higher peak temperatures cause more breakdown of the WC, increasing the free W and C atoms for diffusion with NiBSi [643]. Additionally, slower cooling rates increase the time for diffusion. Convective mass transfer is often characterized by a reaction layer and heterogeneous microstructure around the WC particles [20, 585]. This is supported by the W-C phase diagram presented by Kurlov *et. al.* [626]. Although some secondary WC phases surround the primary carbides, there was no interaction layer or heterogeneous microstructure around the particles.

Additive manufacturing has drastically different thermal cycling than overlaying. The material was continuously deposited for the cylinder shown in Figure 5.6. Constantly re-heating the same results in a large amount of heat accumulation; this increases the amount of material that remelts and drastically reduces the cooling rate. Using the SDAS measurements found in Figure 5.13, and the relationship between SDAS and solidification cooling rate (Figure 5.21), the solidification cooling rate as a function of height for the PTA-AM samples can be estimated and is displayed in Figure 5.22A. It can be seen that the solidification cooling rate changes by 2 orders of magnitude when comparing the bottom to the top of the sample. Even though the heat input is higher for the first 6mm, the solidification cooling rate is also

higher due to the steel substrate acting as a heat sink. The effectiveness of the steel substrate acting as a heat sink decreases as the build progresses due to the entire system's temperature increasing and the newly deposited material's proximity to the substrate. The relationship between the solidification cooling rate and the amount of W in the primary phase can be seen in Figure 5.22B. The plot strongly suggests that the cooling rate of the PTA-AM deposit is directly correlated to the amount of W found in the Ni matrix. Additionally, the amount of W in the primary phase seems to plateau at 27wt% which is close to the low temperature solubility limit of W in Ni (26.5wt% at 500°C)[626]. From Figure 5.14, the amount of secondary carbide phases also increases with height (decreases with cooling rate). Therefore, it is likely that the amount of carbide dissolution increases as the cooling rate decreases for PTA-AM of WC - NiBSi deposits. Higher amounts of convective mass transfer would increase the mean free path between particles. This conclusion is also supported by Figure 3.11 in Chapter 3, where the mean free path between the WC particles also increased as the height increased.

5.5.2 Microstructure Evolution During Solidification

EBSD was done to understand the localized phase distribution and is shown in Figure 5.23. The primary phase detected was γ-Ni (A), and the eutectic phase was γ-Ni(B)/Ni_3B(C), which aligns with previous studies [10]. Ni_3Si was also included in the analysis and was not detected due to the similarity in the lattice parameters between γ-Ni (3.45 Å) and Ni_3Si (3.51 Å). It could be that the Ni found in the interdendritic regions is Ni_3Si based on the composition shown in Table 5.8.

For the solidification of the matrix of 70wt% WC - NiBSi, the first phase to solidify could be the secondary WC phases (phase A in Figure 5.12). The next phase to solidify would be the primary γ-Ni dendrites (phase B in Figure 5.12) with high solubility of W. The effect of the solidification cooling rate on the dendritic structure's coarseness can be seen in Figure 5.11. As the temperature decreases, the γ-Ni phase continues to grow around the dendrites (phase C in Figure 5.12), with lower W content than the dendrites. After the primary solidification (B and C), eutectic solidification begins forming phases Ni_3B (D) and (Ni,Si) solid solution(E). The eutectic structure also experiences significant coarsening as the solidification cooling rate decrease. With two dimensional cross-sections, and the limited resolution of the

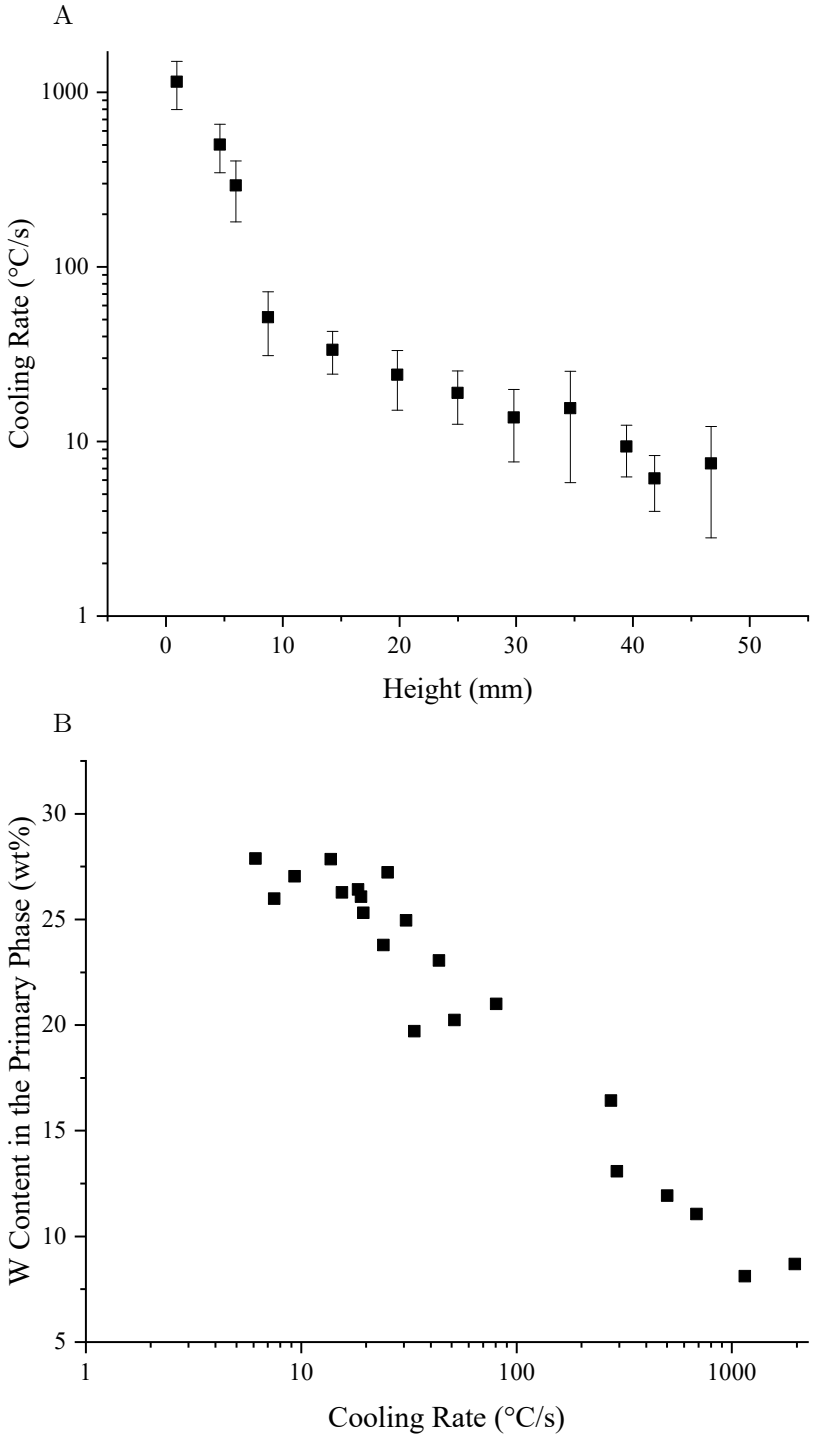

FIGURE 5.22: a) The estimated solidification cooling rates as a function of height for the PTA-AM b) shows the effect of the solidification cooling rate on the W content of the primary phase from the PTA-AM samples.

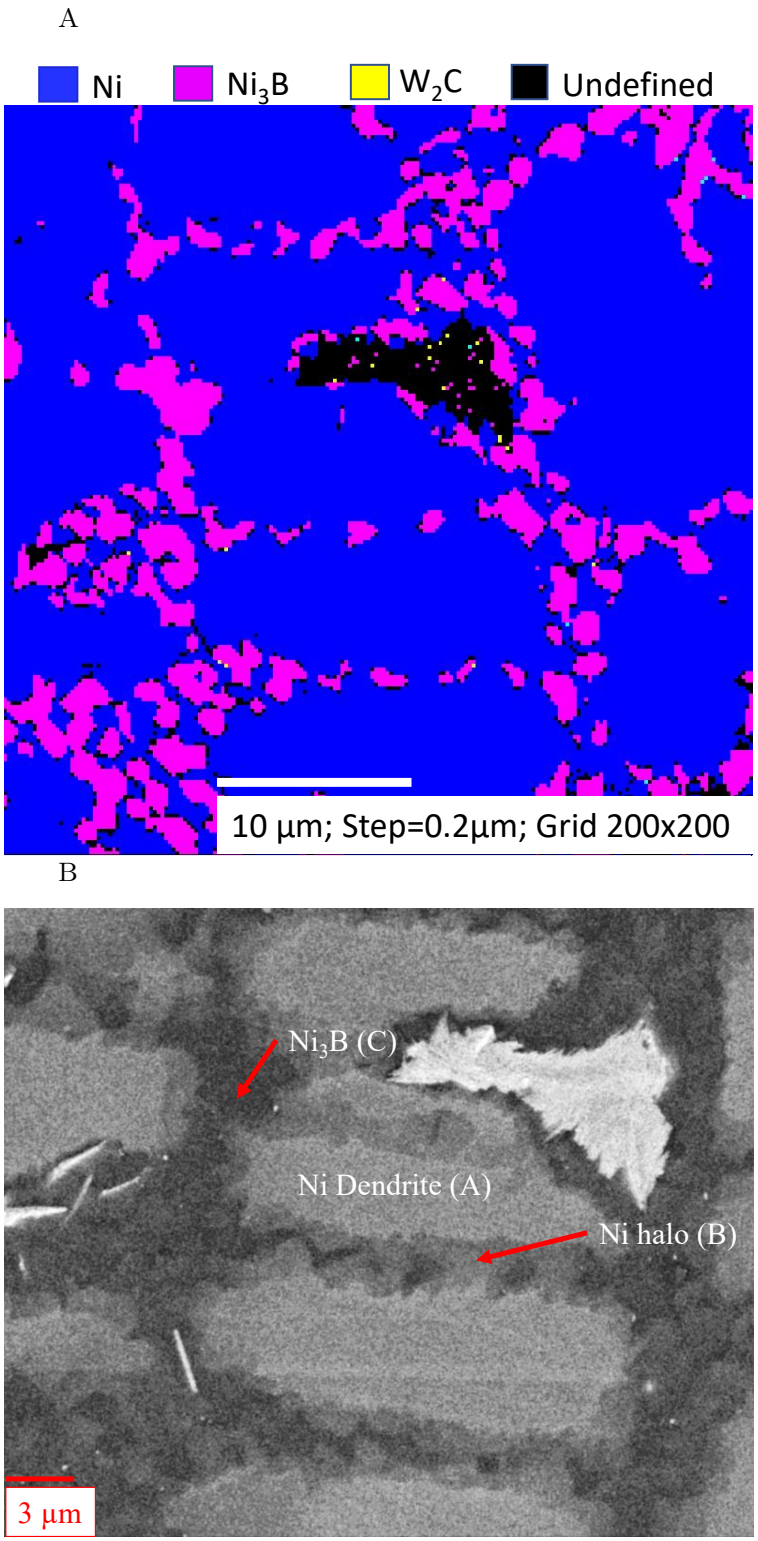

FIGURE 5.23: a) Phase map taken from the EBSD, with a step size of 0.2µm and a field of view of 40x40µm; b) FESEM image corresponding to the phase map shown in a).

SEM, the eutectic structure could not be resolved. Higher resolution characterization methods such as TEM could be used to resolve the eutectic structure. Additionally, Bridgman solidification experiments could offer controlled solidification experiments to determine how the eutectic structure changes with solidification cooling rate.

5.5.3 Denuded Regions

Previous literature [10, 11] suggests that denuded regions have a different composition than the surrounding material. In section 5.4.2.3 it was discovered that there is likely no difference in composition between the denuded and interparticle regions. A possible mechanism of denuded region formation could be due to surpassing the maximum packing of angular WC. With a D50 of 112μm, angular WC can achieve a maximum packing of 62wt% [630]. During the PTA-AM, the high loading of WC could cause particles to become interlocked, preventing the movement of WC in the meltpool. The interlocked particles could create localized pools of matrix material that solidify as denuded regions. The research to verify the above mechanism of denuded region formation is still ongoing.

5.5.4 Removing Cr from the matrix

This section compares the microstructure from the 70wt% WC - NiCrBSi samples from Chapter 4 with the 70wt% WC - NiBSi samples presented in this chapter. It is important to note the compositional differences between the matrix materials, seen in Table 5.9. Apart from Cr, the NiCrBSi sample has lower B and higher Si and Fe content than the NiBSi matrix material. In addition to differences in matrix composition, the solidification rate plays a significant role in the amount of WC dissolution (Figure 5.22B). To compare the composition (Table 5.8) of 70wt% WC - NiBSi (Figure 5.12) with 70 wt% WC - NiCrBSi (Table 4.7, Figure 4.12) similar solidification conditions should be compared. The average SDAS of 70wt%

TABLE 5.9: Composition of the matrix materials used in this work.

	Composition (wt%)						
Matrix Material	Ni	Cr	B	Si	C	Fe	Size Range (μm)
WOKA Durit 6030	Bal.	5.0 - 6.5	0.8 - 1.2	3.8 - 4.3	0.2 - 0.5	$<$ 1.5	+63 -180
Höganäs 1538-40	Bal.	-	1.8 - 2.4	2.5 - 3.5	-	$<$ 0.5	+53 -180

WC - NiCrBSi of the sample location presented in Chapter 4 was 11.2 μm. At 19.81mm in the 70wt% WC - NiBSi sample, the SDAS was measured to be 10.8 μm. Therefore, the composition data presented in Table 4.7 will be compared to the 19.81mm compositional data presented in Table 5.8. The compositions are listed again in Table 5.10 for easy comparison.

The star (A Figure 4.12) and needle (B Figure 4.13) carbide morphology were only found in the 70wt% WC - NiCrBSi, and not in the NiBSi sample. The blocky carbide in the 70wt% WC - NiCrBSi sample (C Figure 4.14) had more of a rounded morphology compared to those found in the 70wt% WC - NiBSi (A Figure 5.12) The composition of the blocky carbide differed significantly between the two. In the NiCrBSi sample, the blocky carbide composed of Ni, W, Si, C, and Cr ($(Ni_4W_2Cr_2Si)C_3$), while in NiBSi, it was just NiW.

The solidification structure of the matrix was similar between the NiCrBSi and NiBSi samples. Both samples contained dendritic γ-Ni with a halo surrounding the primary dendrite. After primary solidification, both samples formed a eutectic of γ-Ni (Ni, Si)/Ni_3B. There are some stark differences in the composition of the matrix phases between the NiBSi, and NiCrBSi samples. For the NiBSi sample, the γ-Ni dendrites only contained Ni and W, while the NiCrBSi sample had Ni, W, Si, Cr, and Fe. The difference in W content was quite drastic. The NiBSi primary dendrites had almost 3x the atomic fraction of W compared to the NiCrBSi. This could be attributed to the NiCrBSi matrix having a higher area fraction of high W containing complex carbides (4.28%) than the NiBSi sample (1.89%), leaving less W to be dissolved in the NiCrBSi matrix. The halo around the γ-Ni dendrite also had a higher atomic fraction of W and less Si and Fe. Ni_3B had a similar amount of Si, but no Fe was detected in the NiBSi sample. The high Ni and Si γ-Ni phase had slightly less Si and Fe in the NiBSi matrix.

Due to the differences in matrix composition (Table 5.9), it is challenging to compare the differences in Si and Fe. However, the W content can be roughly compared. The overall composition of the region shown in Figure 5.11C is compared to Figure 4.12, and is shown in Table 5.10. It should be noted that the NiBSi did not have any C detected, which is likely due to the poor measuring accuracy of C using EDX. However, C is likely present and may change the atomic ratios of the elements. The results show that the NiBSi (4.1at%) had more overall W than the NiCrBSi sample (2.1at%). This suggests that the NiBSi sample underwent higher degrees of WC dissolution than the NiCrBSi sample. For the comparison

TABLE 5.10: The composition of the different phases found in the 70wt% WC NiBSi compared with 70wt% WC - NiCrBSi

	NiBSi(at%)					NiCrBSi(at%)					
Description	Ni	W	Si	C	Fe	Ni	W	Si	C	Cr	Fe
Star Carbide	–	–	–	–	–	6.1	19.5	–	35.9	38.5	–
Needle Carbide	–	–	–	–	–	13.2	14.2	–	35.9	36.7	–
Blocky Carbide	48.6	51.4	–	–	–	31.0	18.8	7.9	22.7	19.6	–
γ-Ni	90.9	9.1	–	–	–	83.5	3.3	6.1	–	7.2	3.0
γ-Ni Halo	88.9	5.3	4.5	–	1.3	81.1	1.8	8.3	–	6.0	2.9
Ni_3B	97.0	–	3.0	–	–	91.5	–	3.8	–	4.6	1.7
γ-Ni (Ni,Si)	84.3	–	14.9	–	0.8	77.7	–	17.8	–	3.1	1.3
Overall	89.0	4.1	5.9	–	1.0	60.3	2.1	5.8	23.4	5.4	2.0

to hold merit, the same depth of analysis presented in this chapter should be conducted for the 70wt% WC - NiCrBSi.

5.6 Conclusions

Plasma-transferred arc additive manufacturing was used to deposit 70wt% WC - NiBSi metal matrix composites. Electromagnetic levitation was used to understand the effects of the solidification cooling rate on the secondary dendrite arm spacing. The carbide retention was far below 70wt% due to the formation of porosity, and denuded regions during the deposition. The thermal history of the EML samples was used to relate the cooling rate to the secondary dendrite arm spacing; this was used to estimate the solidification cooling rate for the PTA-AM samples. The dissolution of WC increased with height during the PTA-AM build due to decreasing cooling rate, as evident by higher levels of W in the primary dendrites and larger volume fraction of secondary carbides. The thermal history of the EML and PTA-AM experiments may have resulted in a divorced eutectic structure, however, higher magnification characterization methods such as TEM should be conducted to confirm the eutectic structure. Denuded regions were formed under all experimental conditions, and the composition was the same between the denuded regions and the interparticle regions. Denuded regions could be the result of exceeding the maximum packing of the WC particles during the PTA-AM process.

Chapter 6

Adding Different Ratios of Spherical Eutectic WC/W_2C to 70wt%WC-NiCrBSi

The following chapter will discuss the effects of replacing varying amounts of monocrystalline (MC) WC with spherical eutectic (SE) WC/W_2C in 70wt% WC - NiCrBSi PTA-AM deposits. Combining both spherical and angular WC may lead to denser packing, creating a more homogeneous distribution of WC[630]. The effect of powder quality will be tested by using spherical eutectic WC/W_2C from two different powder producers, SE1, and SE2. The different MMC compositions that were tested are (35wt% MC, 35wt% SE)WC -, (52.5 wt% MC, 17.5wt%SE)WC -, and (17.5 wt% MC, 52.5wt% SE) - NiCrBSi. The microstructure from the (35wt% MC, 35wt% SE)WC - NiCrBSi samples using the two different carbides will be compared and discussed. All samples were deposited using the same operating parameters of the PTA shown in Table 4.2.

6.1 Adding SE1 Spherical Eutectic WC/W_2C

To test the effect of different powder morphologies on the microstructure of the PTA-AM deposit, SE1 spherical eutectic WC/W_2C was added. SEM images of the SE1 spherical eutectic WC/W_2C feedstock can be seen in Figure 6.1. The SE1 WC/W_2C had surface defects on

most of the powder that was imaged. The composition of the matrix, and WC and WC/W_2C are shown in Table 6.1 and Table 6.2, respectively. From Table 6.2, it can be seen that SE1 has slightly higher C content than SE2. Cross sections of the PTA-AM deposits with different WC combinations are shown in Figure 6.2 to 6.4, where the bottom, middle, and top of each sample are shown. It should be noted that the entire cross-section of the sample is not shown for any of the samples found, but the bottom, middle, and top are organized to provide an idea of what the cross-section could look like. With the addition of 17.5 and 35wt% SE1 spherical carbides, the carbide distribution becomes more homogeneous with less porosity and denuded regions, compared to the purely monocrystalline samples shown in Figure 4.6. Denuded regions and large pores are still found in the samples. It appears that the more spherical eutectic WC/W_2C that is added, the higher the tendency to form pores and denuded regions. Adding over 50wt% spherical eutectic WC led to an increased occurrence of denuded regions and pores compared to lower spherical carbide contents, as seen in Figure 6.4. There is also thermal degradation of the WC/W_2C shown by the dark rings around the spherical carbides. Carbide degradation is a common phenomenon when using WC/W_2C deposited with PTA[11, 16, 18]. At the bottom of the samples, there does not appear to be any carbide degradation, but as the sample height increases, so does the propensity to have carbide breakdown. Thermal degradation of the WC/W_2C does tend to increase the occurrence of pores and denuded regions as seen in Figure 6.2. However, denuded regions will still form when there is no apparent thermal breakdown of the WC/W_2C, which can be seen at the bottom of Figure 6.4. The degree of carbide breakdown also increases as the amount of SE1 increases.

A backscatter SEM image showing the microstructure of a denuded region from a

TABLE 6.1: Composition of the matrix materials used in this work.

	Composition (wt%)						
Matrix Material	Ni	Cr	B	Si	C	Fe	Size Range (μm)
WOKA Durit 6040	Bal.	6.9 - 8.2	1.5 - 1.8	3.2 - 3.8	0.2 - 0.4	$<$ 1.5	+63 -180

TABLE 6.2: The different WC powders used in this work.

		Composition (wt%)		
WC Powders	Powder Morphology	W	C	Size Range (μm)
Kennametal SCNC070 Monocrystalline	Angular	93.6	6.4	+63 -180
SE1	Spherical	95.5	4.5	+125 -180
SE2	Spherical	96.0	4.0	+50 -180

A

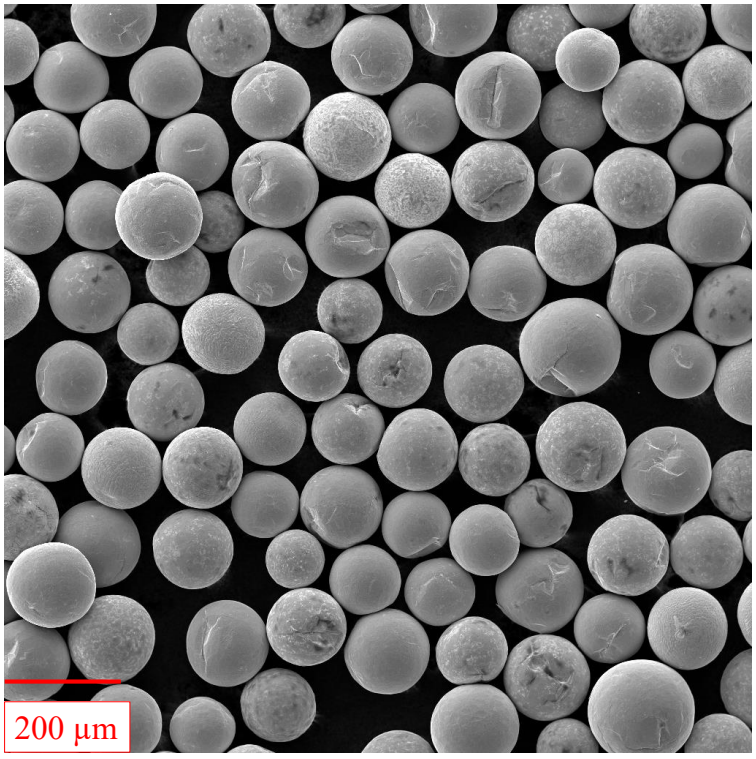

B

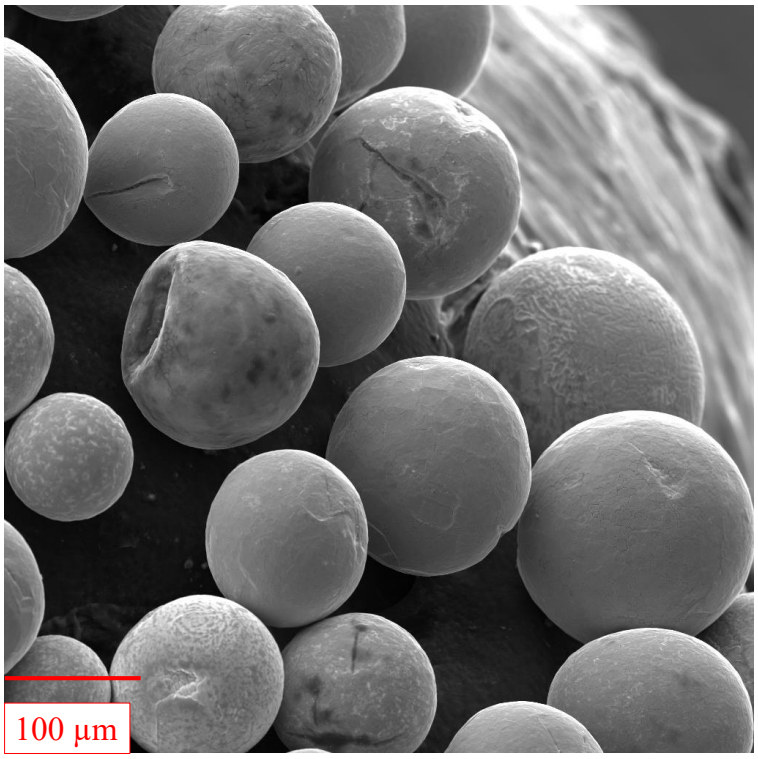

FIGURE 6.1: SEM images of the SE1 spherical eutectic WC/W_2C feedstock.

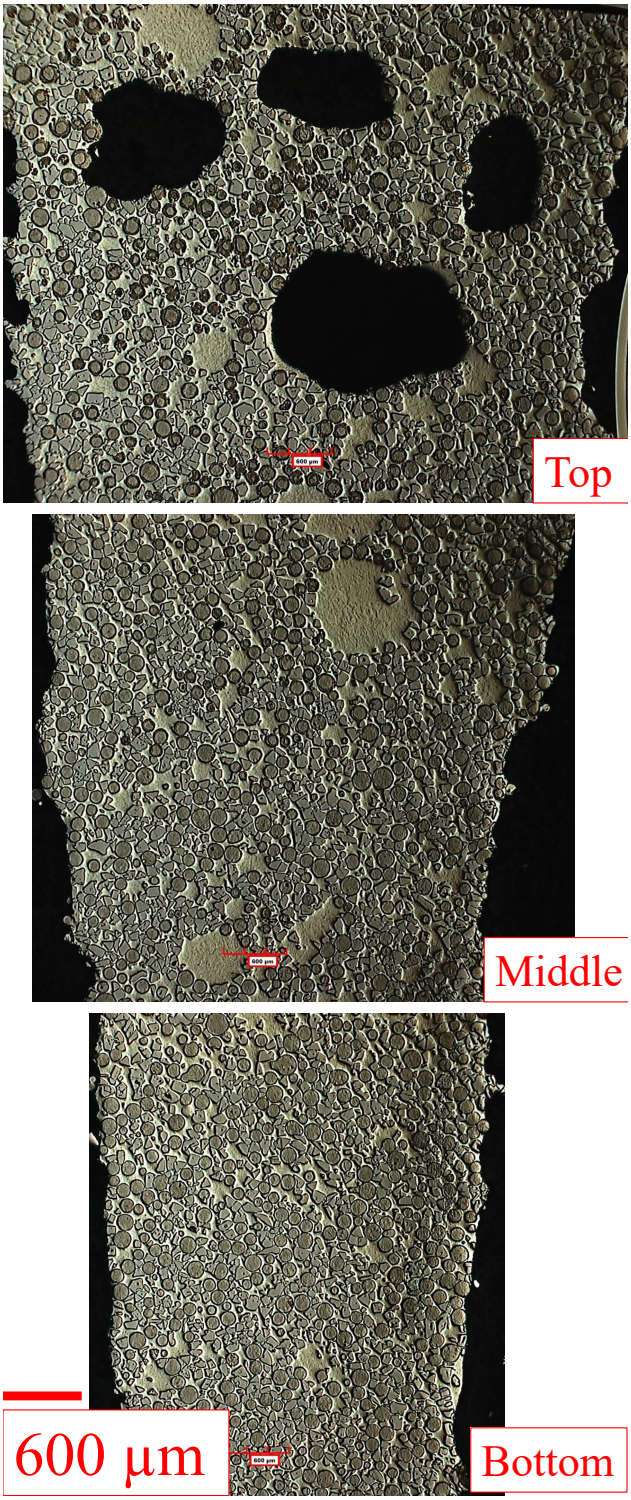

FIGURE 6.2: PTA-AM samples with: a) 35wt% SE1 spherical and 35wt% SCNC070 angular WC.

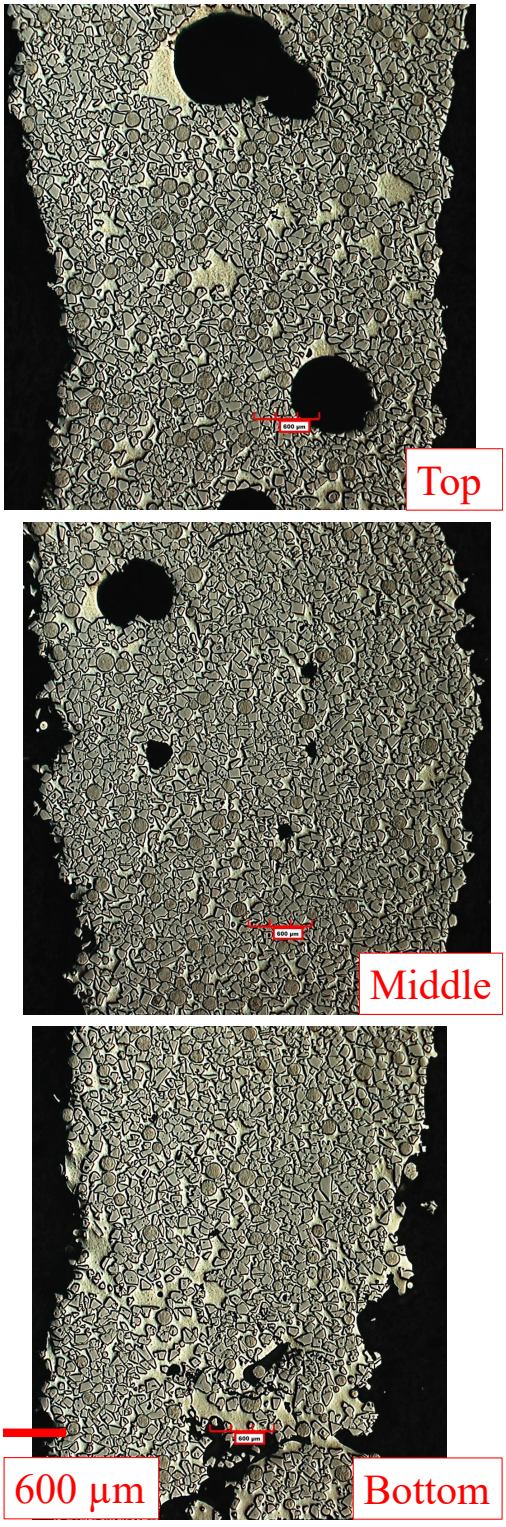

FIGURE 6.3: PTA-AM samples with: a) 17.5wt% SE1 spherical and 52.5wt% SCNC070 angular WC.

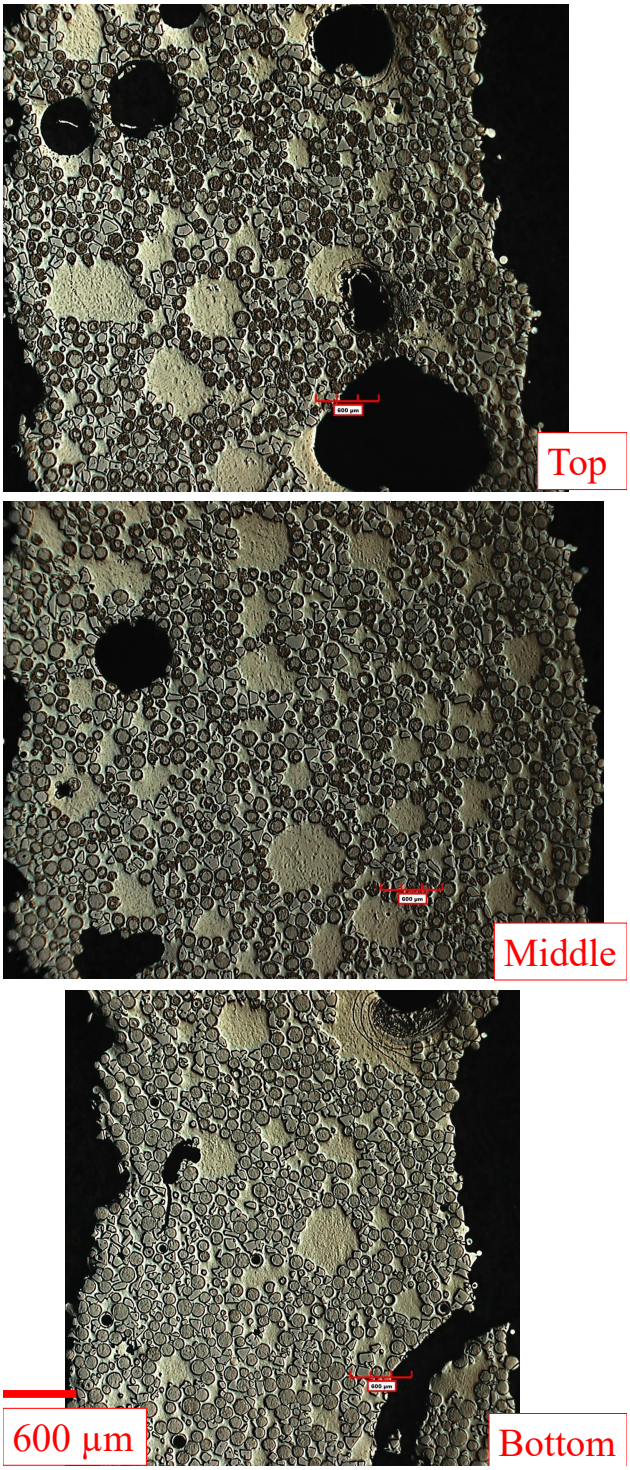

FIGURE 6.4: PTA-AM samples with: a) 52.5wt% SE1 spherical and 17.5wt% SCNC070 angular WC.

sample containing 35wt% SE1 spherical eutectic WC/W_2C and 35wt% angular monocrystalline WC in a Durit 6040 matrix is shown in Figure 6.5. The introduction of spherical WC drastically increases the amount of secondary W-rich carbides that form compared to monocrystalline (Figure 4.12). The spectrum of different carbide morphologies are shown in Figure 6.6 to Figure 6.10. Clusters of small blocky carbides (A) are found throughout the microstructure and emanating radially from the degraded SE1 particles (Figure 6.6). In some instances, these clusters are replaced with a single large blocky carbide (A in Figure 6.8). Where there is denser packing of just angular monocrystalline WC (Figure 6.10),

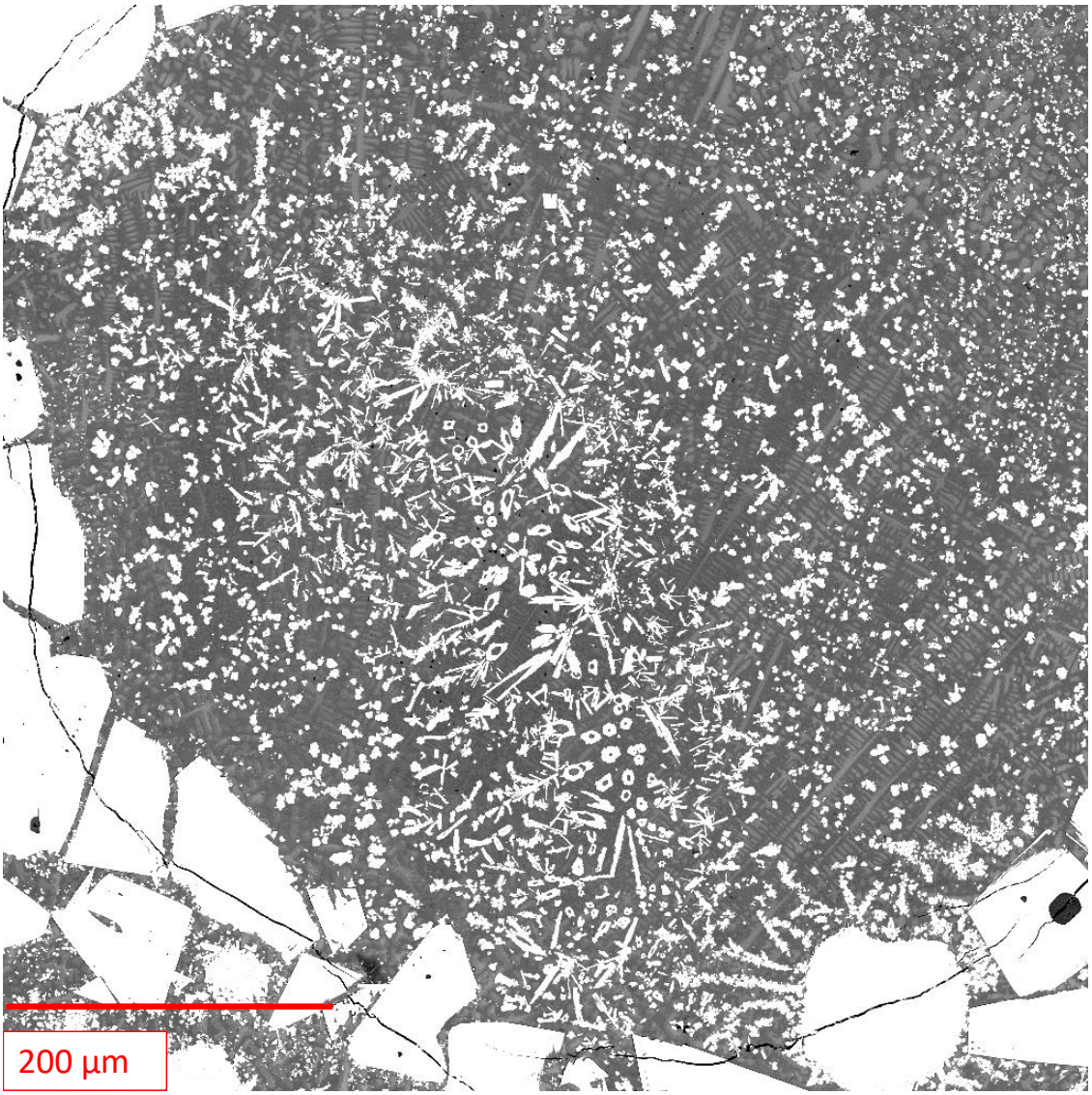

FIGURE 6.5: Backscatter SEM image of a denuded region from 35wt% spherical eutectic WC/W2C, and 35wt% angular monocrystalline WC in Durit 6030 matrix.

the microstructure mainly consists of the blocky type of carbide. The other carbides found in the microstructure have a ring (B) and an acicular (C) morphology. Around some of the acicular and ring-type carbides is a slightly darker high W carbide phase (D).

The composition of the various carbide morphologies taken with EDX are found in Table 6.3. The three main types of carbides all contain various amounts of Ni, W, C, and Cr. The atomic ratios for the blocky, ring, and rod/acicular carbides are $(Ni_3W_4Cr)C_6$, $(Ni_6W_2Cr)C_3$, and $(Ni_3W_4Cr)C_6$, respectively. The blocky and acicular carbides appear to have the same composition, while the ring-type carbides contain much higher levels of Ni and Cr. The carbides that form on the edge of the acicular carbides contain all of the alloying elements in the MMC.

Figure 6.11 and Figure 6.12 show the different phases of the NiCrBSi matrix. The microstructure consists of a dendritic primary phase (E), with a small amount of haloing (F) surrounding the primary phase. In Figure 6.11, it can be seen that this haloing (F) appears to be the continued growth of the primary phase (E). The interdendritic regions contains two phases: a lighter grey phase (G) and a dark grey phase (H). Most interdendritic regions are made up of the lighter phase G; however, there are instances of coupled eutectic growth seen in Figure 6.12.

The composition of the matrix phases are shown in Table 6.3. It should be noted that C was ignored when analyzing the matrix phases. The primary phase (E) contains higher

TABLE 6.3: The composition of the different phases shown in Figure 6.6 to Figure 6.12 using EDX.

		at%					
Letter	Description	Ni	W	Si	C	Cr	Fe
A	Blocky Carbide	20.6	30.0	-	41.6	6.9	-
B	Ring Carbide	47.1	14.7	-	26.6	8.6	1.6
C	Rod/acicular Carbide	19.4	30.3	-	42.9	7.4	-
D	Edge of rod/acicular Carbide	43.1	11.0	7.5	29.2	12.8	1.2
E	Primary Phase	80.3	3.4	5.2	-	6.9	3.7
F	Halo Around Primary Phase	81.3	1.8	9.3	-	5.8	3.1
G	Light Eutectic Phase	93.2	-	-	-	4.8	2.0
H	Dark Eutectic Phase	80.3	-	18.7	-	3.1	1.4

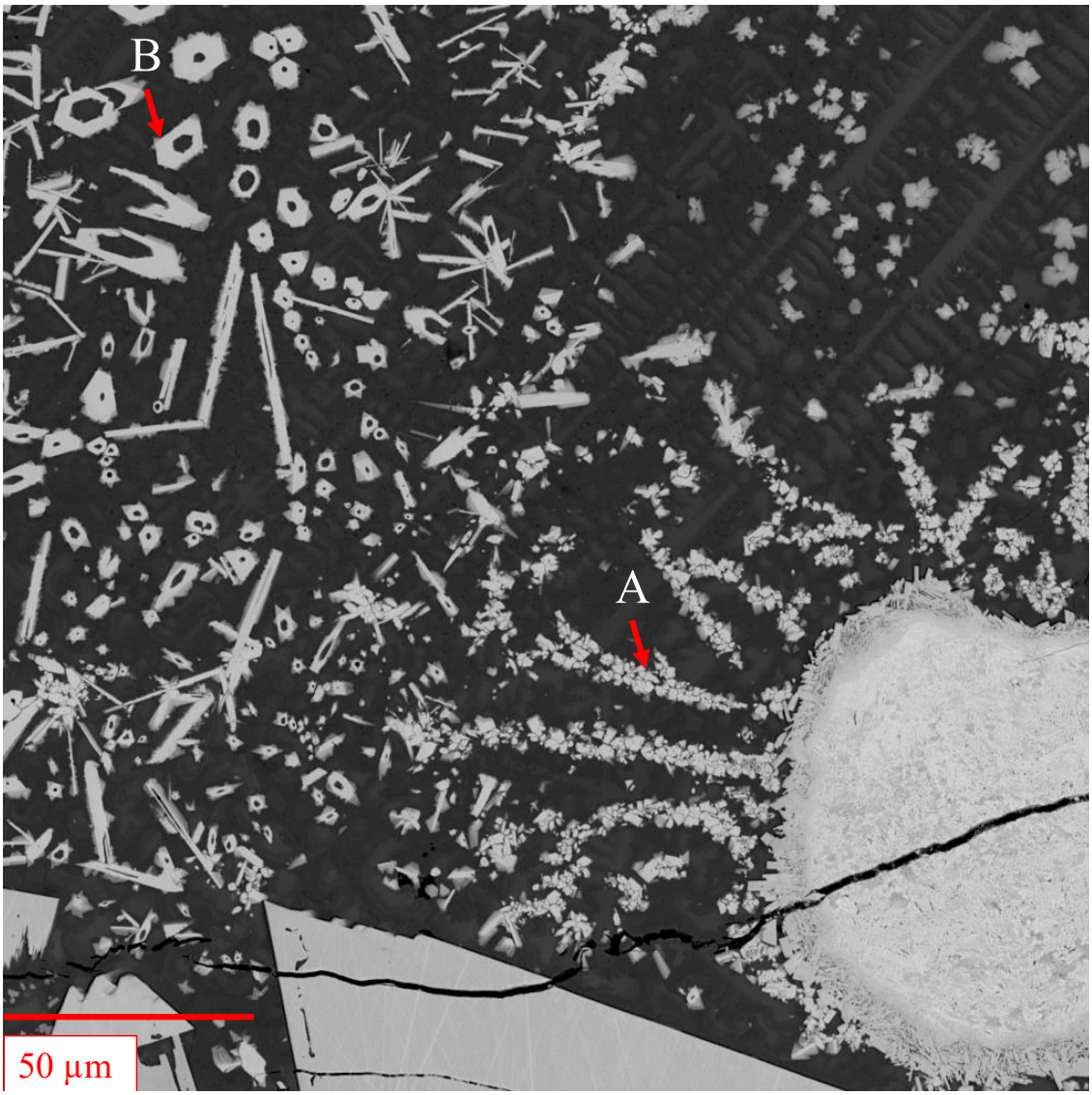

FIGURE 6.6: Backscatter SEM showing range of secondary carbide phases in the 35wt% SE1 sample.

W, Cr, and Fe levels, which aligns with the partitioning coefficients of those elements in Ni [565]. The halo (F) around the primary phase contains slightly lower levels of W but higher Si content. In the interdendritic region, the light phase (G) was a solid solution of Ni, Cr, and Fe, with no W or Si present. This phase is likely Ni_3B [13, 36, 43]. The dark phase (H) in the interdendritic region is a Ni-Si solid solution with Cr and Fe additions.

The solidification sequence for 35wt% SE1 spherical eutectic WC/W_2C, 35wt% angular monocrystalline WC, and 30wt% NiCrBSi is similar to what is described in Section 4.5.1.2

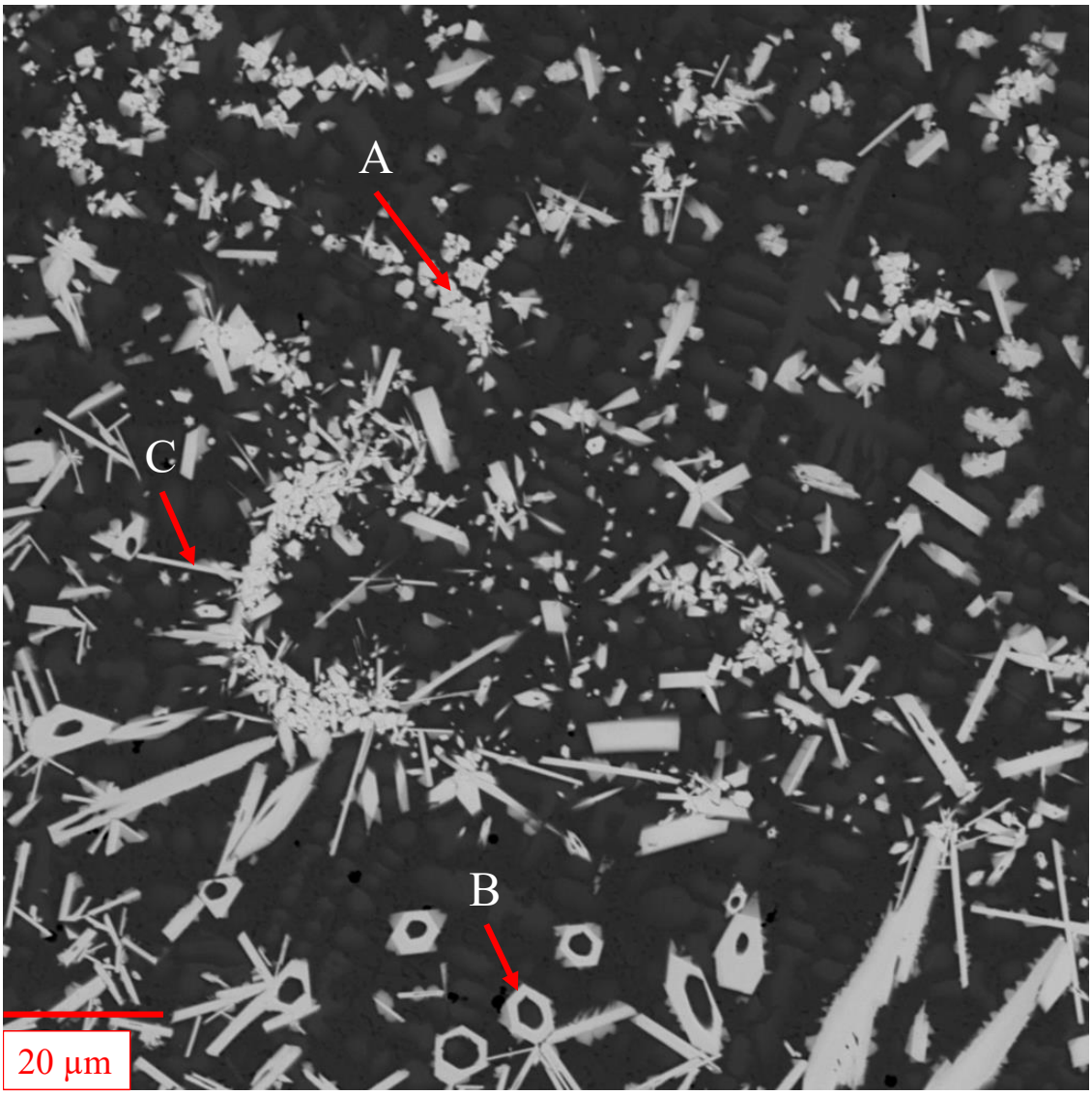

FIGURE 6.7: Backscatter SEM showing range of secondary carbide phases in the 35wt% SE1 sample.

for 70wt% monocrystalline WC - NiCrBSi. The first phases to solidify are likely the various high W-containing carbides (A-D). Upon matrix solidification, the primary phase (E) solidifies first, with the continued growth of the primary phase causing the halo (F) around the primary phase. After primary solidification, there is eutectic solidification of phases G and H. The breakdown of WC/W_2C is discussed more in Section 6.3.

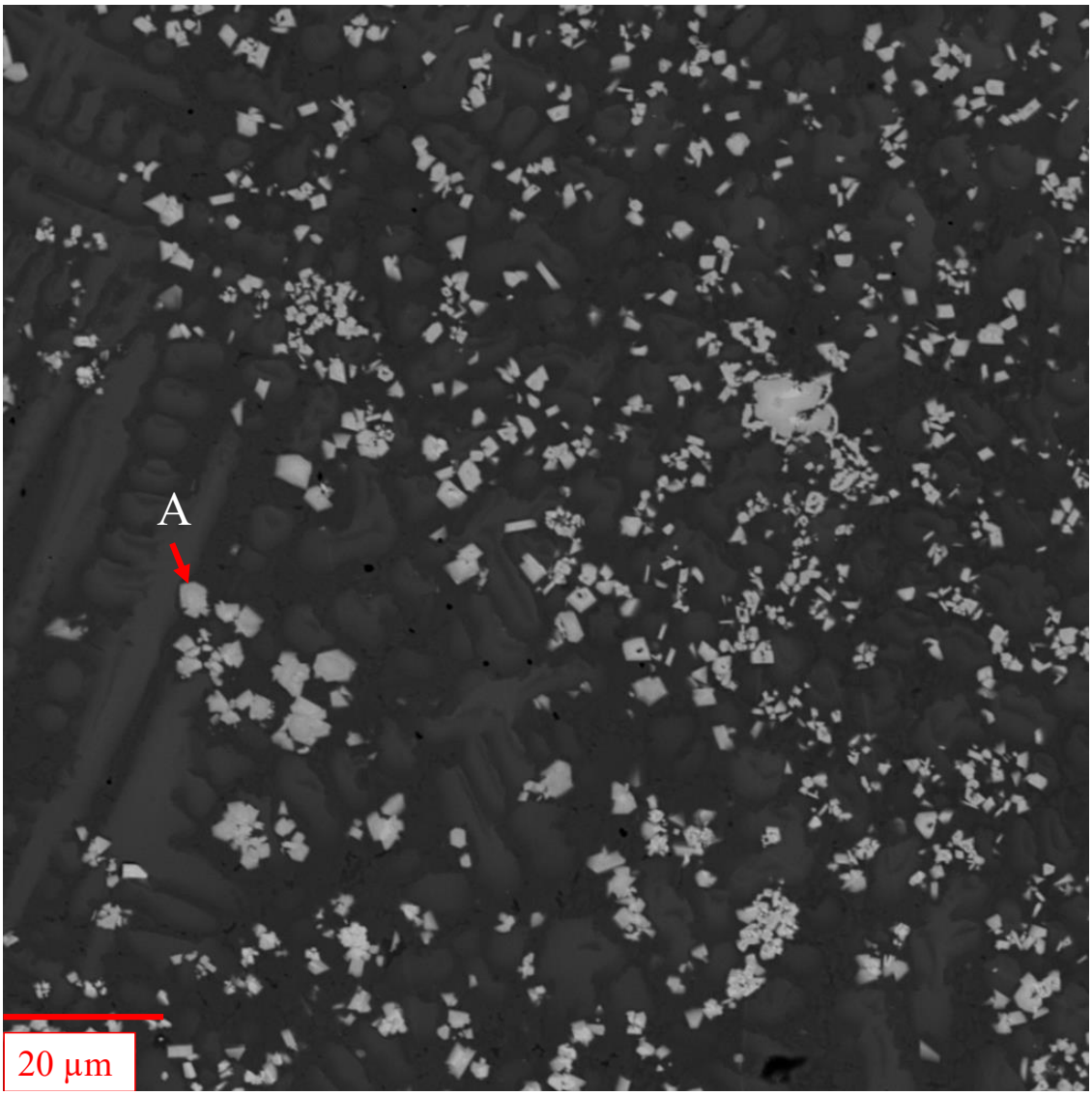

FIGURE 6.8: Backscatter SEM showing mostly blocky secondary carbides in the 35wt% SE1 sample.

6.2 Adding SE2 Spherical WC/W_2C

SE2 spherical WC/W_2C was also added with monocrystalline WC in 70wt% WC - NiCrBSi PTA-AM deposits to determine the effect that powder from different manufacturers has on the microstructure. The SE2 spherical WC/W_2C feedstock can be seen in Figure 6.13. When compared with the SE1 powder feedstock (Figure 6.1), it appears that the SE1 powder has more powder with surface flaws than the SE2 powder. The effect of adding 35, 17.5, and 52.5wt% SE2 spherical WC/W_2C on the macrostructure is shown in Figure 6.14, Figure 6.15,

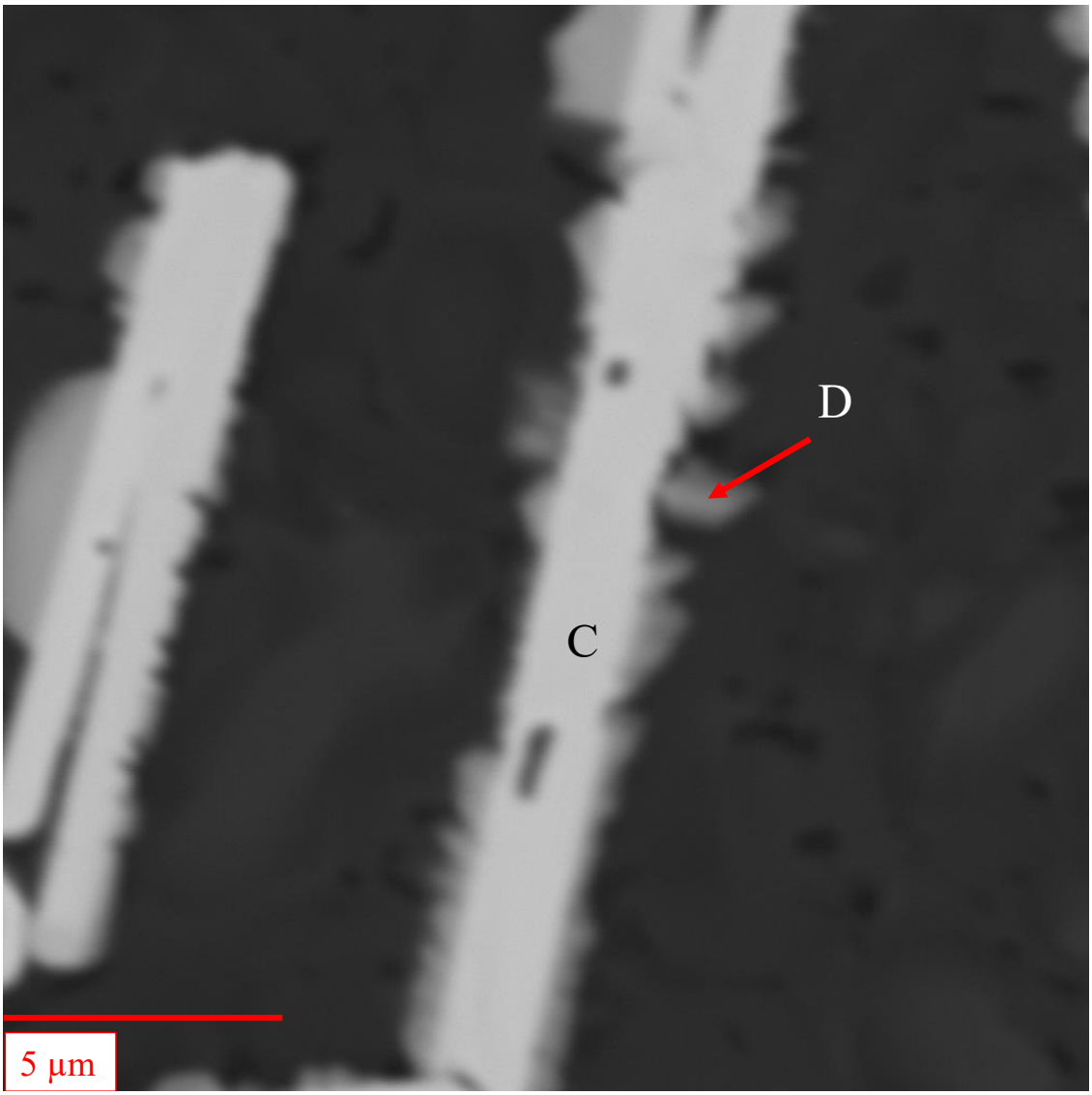

FIGURE 6.9: Backscatter SEM showing the acicular carbide in the 35wt% SE1 sample.

and Figure 6.16, respectively. The 35wt% SE2 spherical WC/W_2C sample had a homogeneous distribution of WC throughout the entire cross-section. At lower (17.5wt%) eutectic WC contents, the homogeneous distribution of WC remains until the upper portion of the sample. There was also limited WC/W_2C breakdown at low (17.5wt%) and mid (35wt%) contents of SE2 carbides. Higher levels (52.5wt%) of SE2 spherical WC/W_2C led to a poor distribution of carbides throughout the entire sample. As the height increased, there were more denuded regions and porosity, as well as carbide breakdown of the WC/W_2C. Denuded regions and porosity are also found in regions with limited carbide breakdown (Figure 6.15).

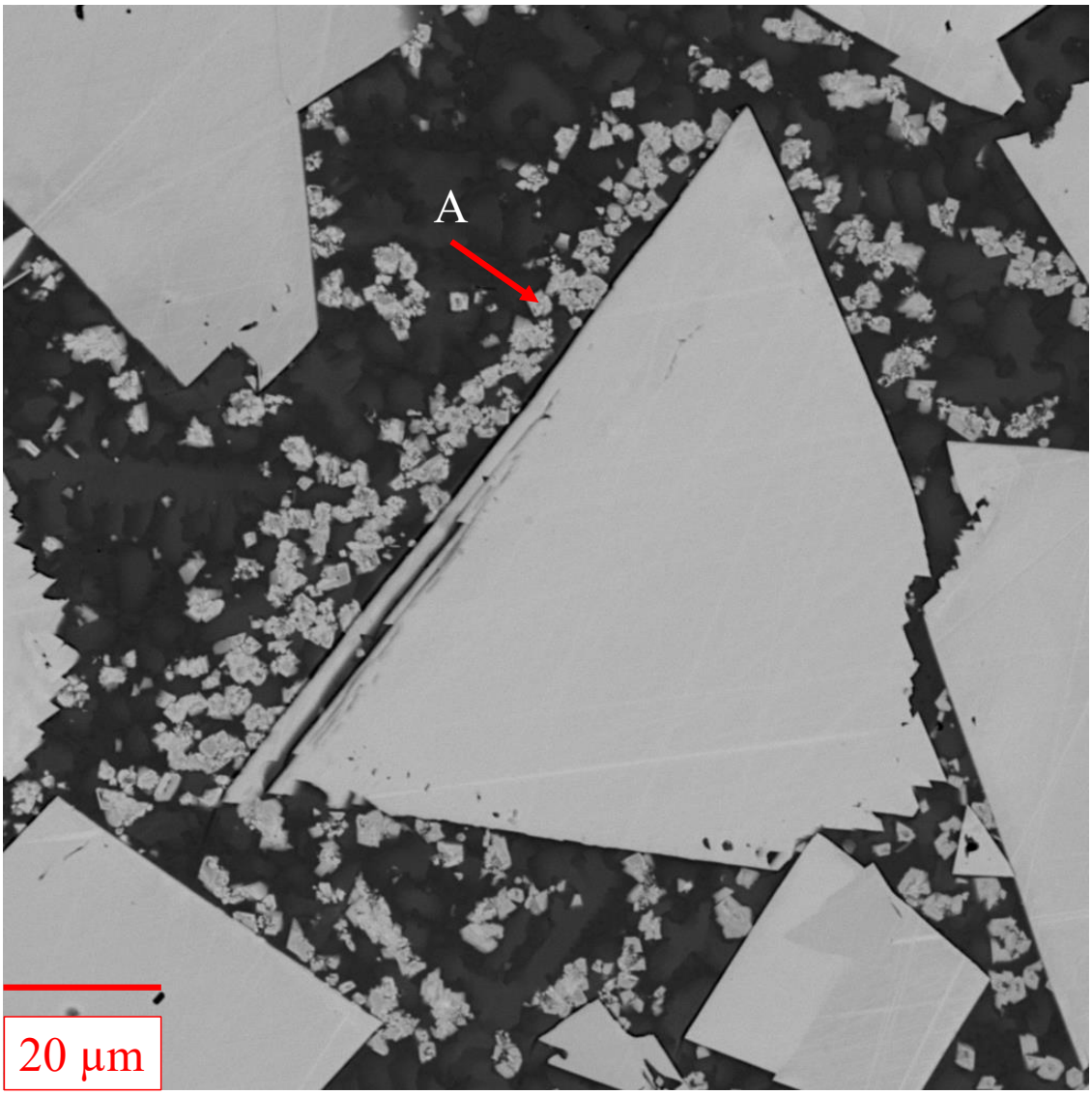

FIGURE 6.10: Backscatter SEM of monocrystalline WC in the 35wt% SE1 sample.

Backscatter SEM images showing the microstructure of the interparticle regions of 35wt% SE2 spherical eutectic WC/W_2C, 35wt% angular monocrystalline WC, and 40wt% Durit 6040 can be found in Figure 6.17 and Figure 6.18. Large blocky (A) secondary carbides formed in the microstructure and tended to be in close proximity to the retained WC particles. Cracks can also be found throughout the microstructure, especially where there are large blocky carbides or clusters of carbides bridging primary WC (red squares in Figure 6.17). The cracks could be due to thermal residual stresses, or solidification shrinkage during the deposition process. At higher magnification, the minor convective mass transfer of the SE2 spherical eutectic WC/W_2C is evident by the reaction layer (dark grey ring) around the

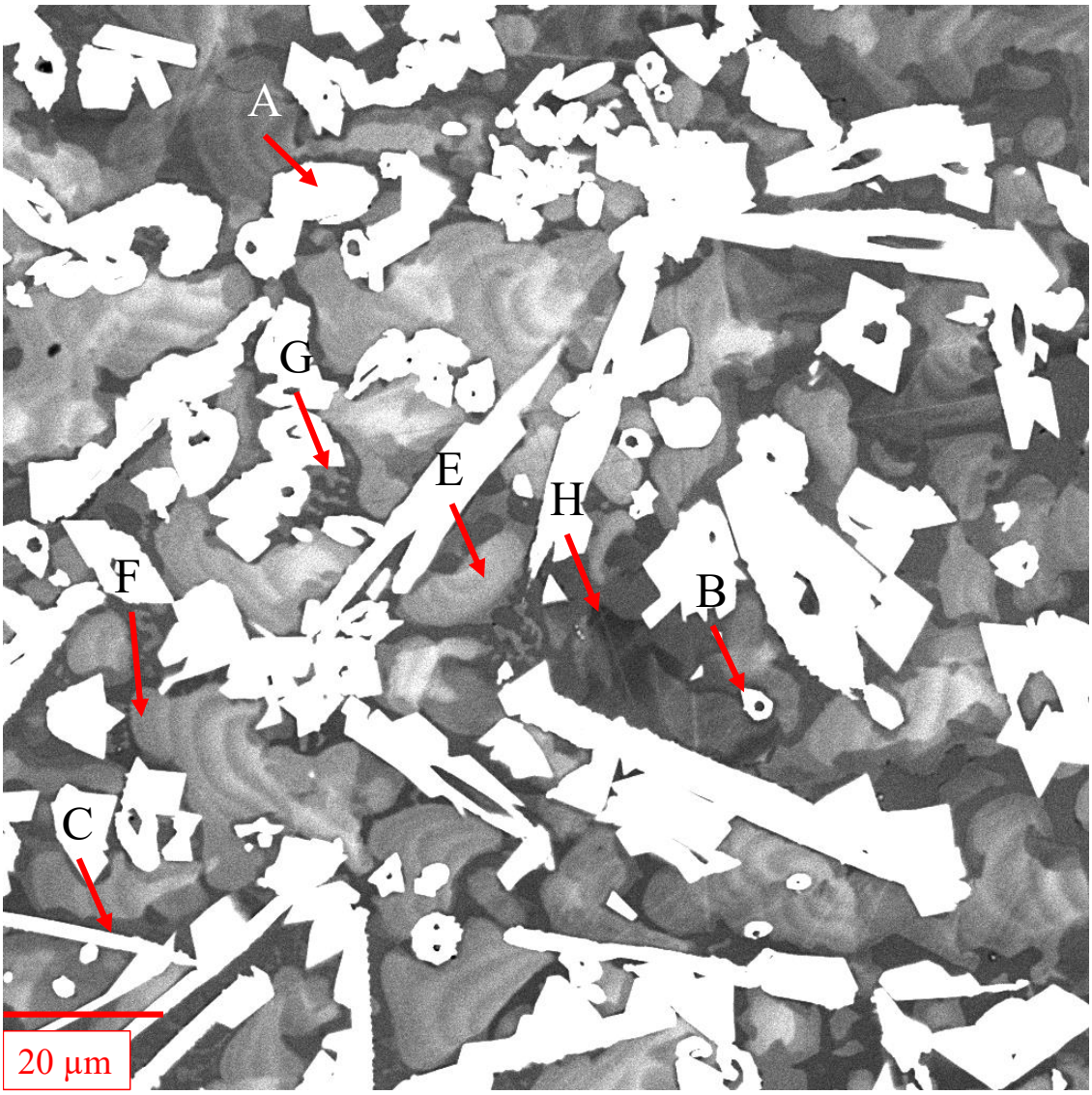

FIGURE 6.11: Backscatter SEM showing the phases of the matrix in the 35wt% SE1 sample.

spherical carbides [18]. The dark grey ring is due to the diffusion of Ni into the SE2 carbide.

Higher magnification images of the Durit 6040 NiCrBSi matrix can be found in Figure 6.19 and Figure 6.20. There is a small, high W-containing phase (B) in the interdendritic region, denoted by the high white contrast of the phase. The matrix contains a lighter primary phase (C), with a halo (D) around the primary phase. The interdendritic phases consist of a lighter grey phase (E), and a eutectic between a lighter phase (F), and a darker phase (G).

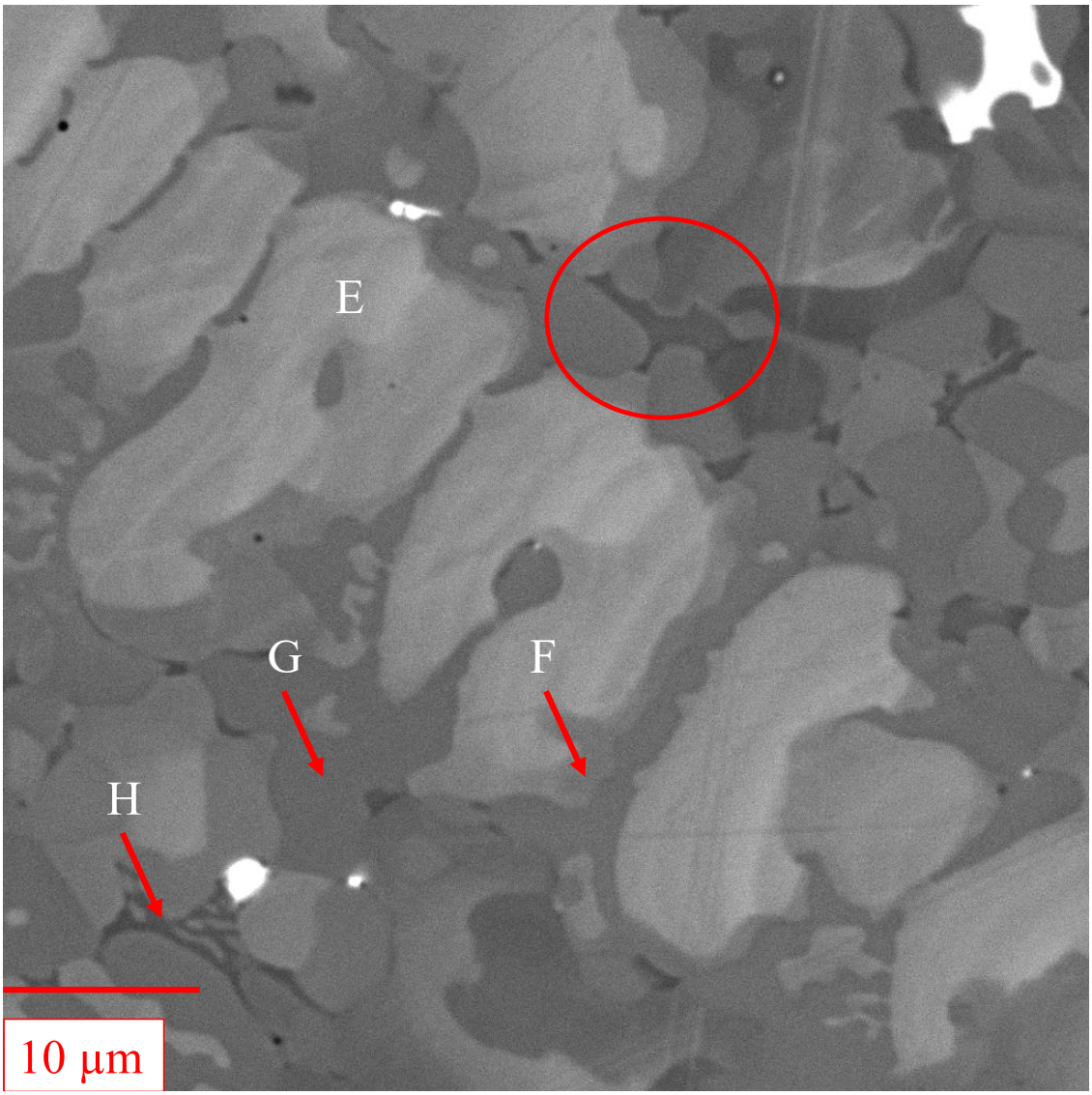

FIGURE 6.12: Backscatter SEM showing the phases of the matrix in the 35wt% SE1 sample.

The composition of the different phases found throughout the microstructure are shown in Table 6.4. The large blocky carbide (A) is a complex carbide containing Ni, W, Si, and Cr, in the atomic ratio's $(Ni_3W_3Cr_2Si)C_3$. The bright interdendritic phase (B) contains a high amount of Ni, Cr, Si, and W, with traces of Fe $(Ni_2WCr_3Si)C_3$). The primary phase (C) and the halo (D) is a Ni solid solution of W, Si, Cr, and Fe; however, the primary phase contains more W, Cr, and less Si than the halo. In the interdendritic region, the light phase (E) is a solid solution of Ni with some Cr and Fe detected. The light phase (F) of the eutectic has the same composition to phase E except with detected Si, and the darker phase (G) is Ni_3Si with small amounts of Cr and Fe. It is likely that phases E and F are the same. The

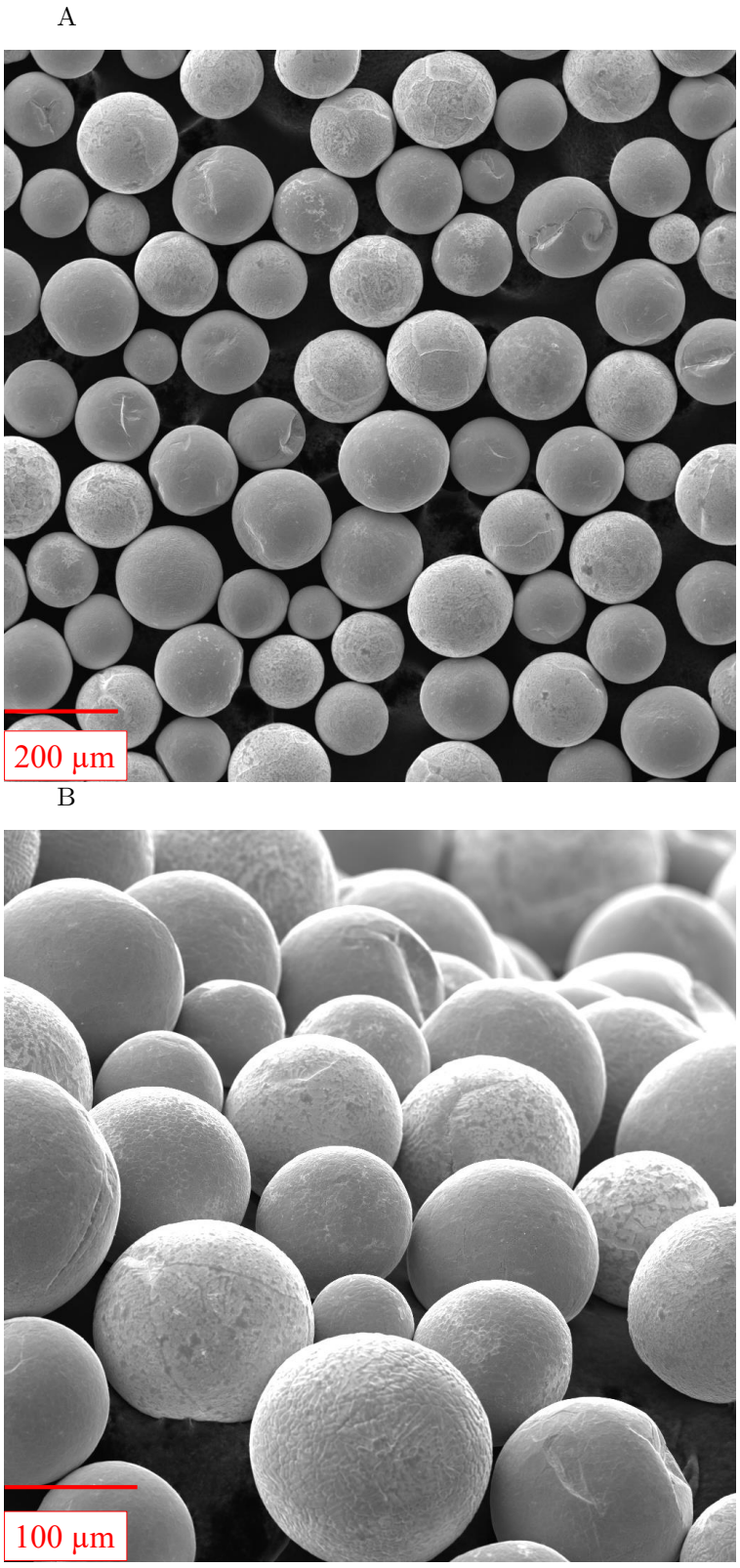

FIGURE 6.13: SEM images of the SE2 spherical eutectic WC/W_2C feedstock.

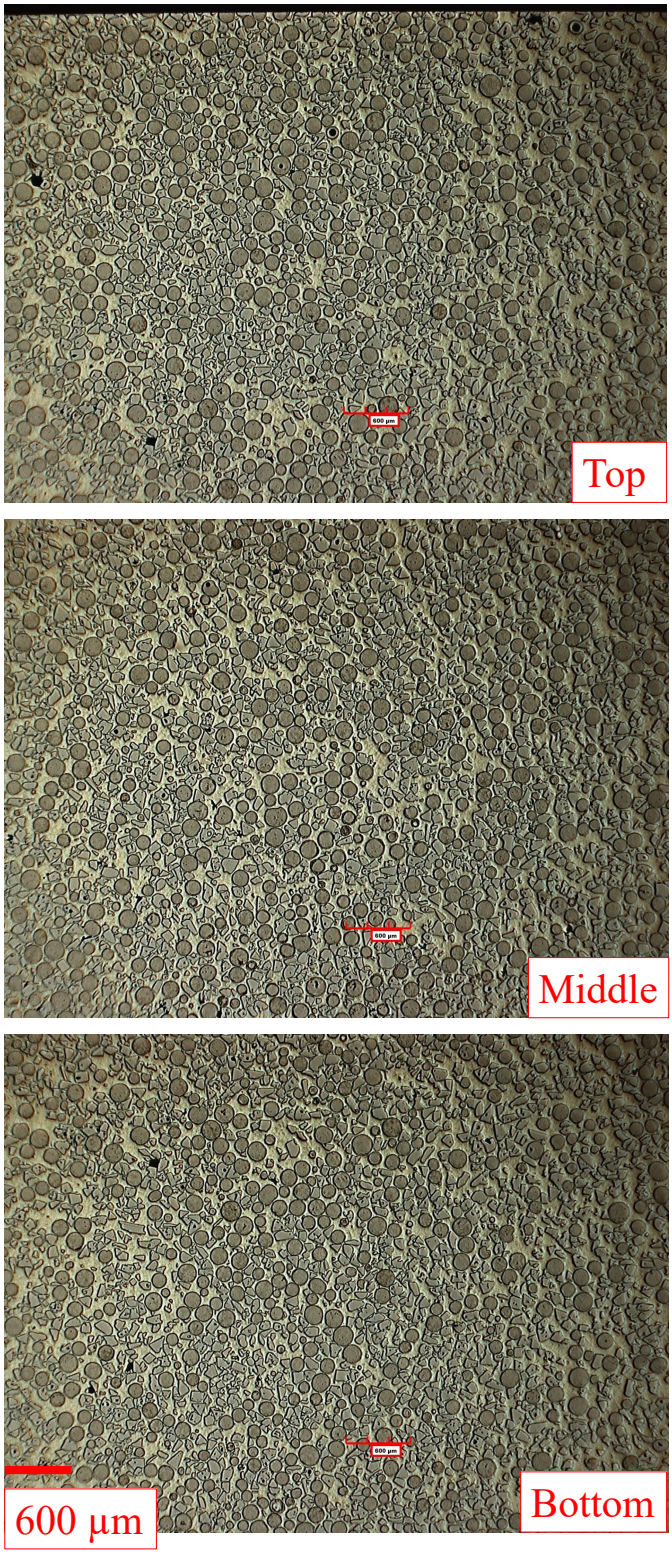

FIGURE 6.14: PTA-AM samples with: a) 35wt% SE2 spherical and 35wt% SCNC070 angular WC.

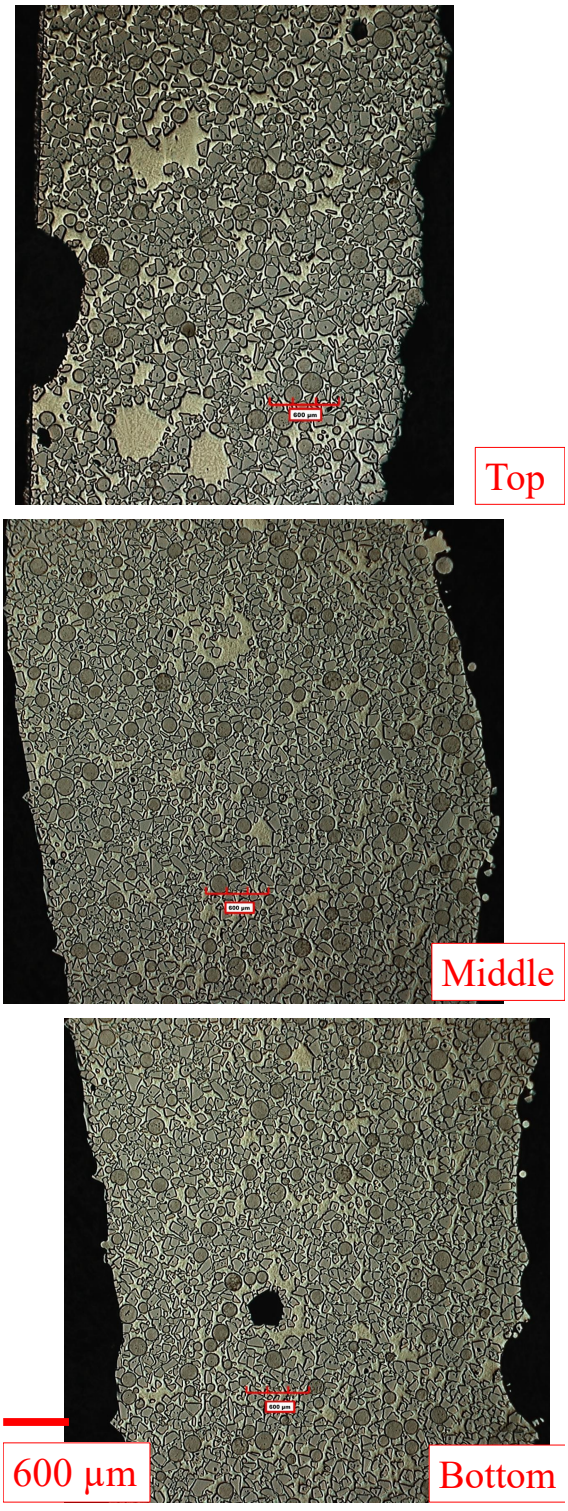

FIGURE 6.15: PTA-AM samples with: a) 17.5wt% SE2 spherical and 52.5wt% SCNC070 angular WC.

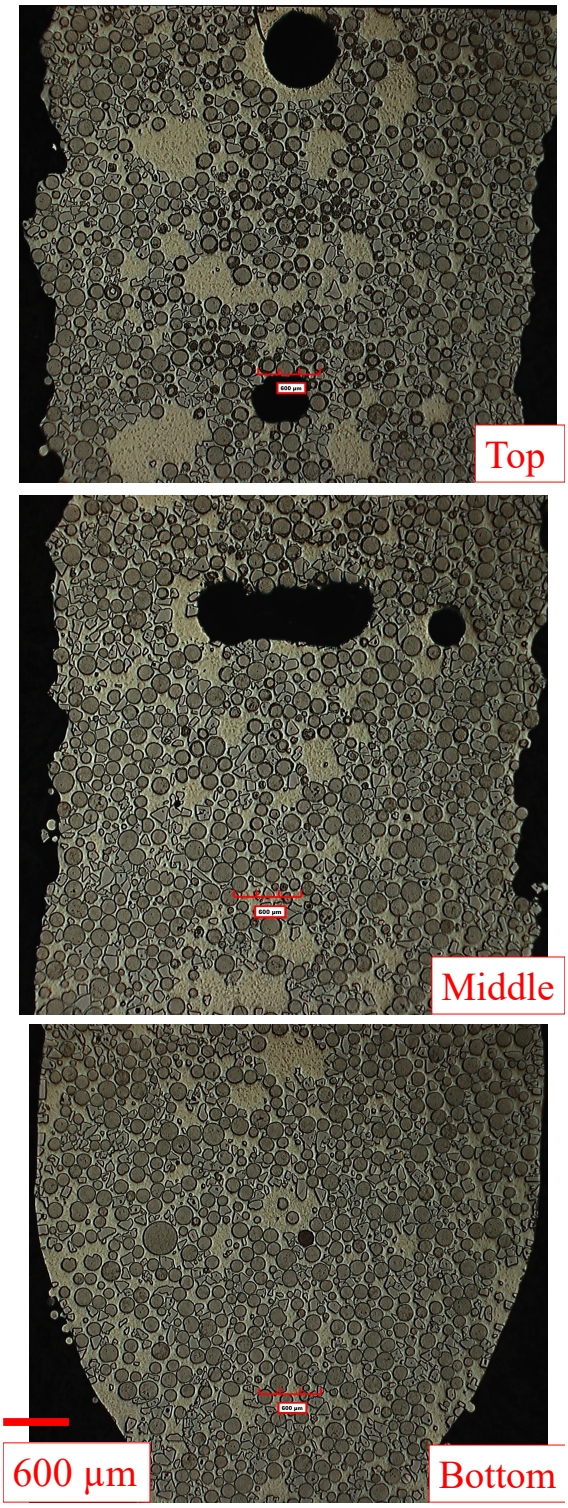

FIGURE 6.16: PTA-AM samples with: a) 52.5wt% SE2 spherical and 17.5wt% SCNC070 angular WC.

TABLE 6.4: The composition of the different phases shown in the 35wt% SE2 sample (Figure 6.17 to Figure 6.20) using EDX.

		at%					
Letter	Description	Ni	W	Si	C	Cr	Fe
A	Blocky Carbide	29.0	20.4	8.2	25.1	17.5	-
B	Bright Interdendritic Phase	20.6	10.4	10.4	29.2	34.1	1.1
C	Primary Phase	81.6	3.3	5.4	-	7.9	3.5
D	Halo Around Primary Phase	80.4	1.9	6.8	-	7.4	3.5
E	Light Eutectic Phase (non-lamellar)	93.0	-	-	-	4.9	1.9
F	Light Eutectic Phase (lamellar)	86.4	-	7.0	-	4.9	1.6
G	Dark Eutectic Phase	75.1	-	22.2	-	1.9	0.9

small lamellar spacing (1.1 μm) is similar to the size of the interaction volume ($\approx 1\mu m^3$ [583]) that releases characteristic x-rays. The signal from phase F could encompass some of phase G, changing the detected composition to include Si.

The solidification sequence is likely the same between the two samples. The high W (A and B) phases likely solidify first, followed by the primary phase (C). Similar to the halos found in the microstructures shown in Chapter 4 and Chapter 5, the halo (D) is likely extended growth of the primary phase at a different composition. After the halo formation, the remaining liquid undergoes eutectic solidification. In areas where it appears that only phase E or G is found (red circle in Figure 6.12), eutectic is likely found, but at much higher resolutions than can be resolved using SEM. TEM could be done on those areas to determine if a lamellar eutectic is found in those regions.

6.3 Microstructural Comparison between SE1 and SE2 Spherical Eutectic WC/W_2C

The 35wt% SE2 (Figure 6.14) spherical eutectic WC/W_2C sample had a homogeneous distribution of WC throughout the entire cross-section of the sample. In contrast, the 35wt% SE1 spherical (Figure 6.2) initially had a homogeneous distribution of WC, but developed pores and denuded regions as the build progressed. With both powders, the 17wt% samples (Figure 6.3, Figure 6.15) started with a homogenous distribution of WC, but developed pores

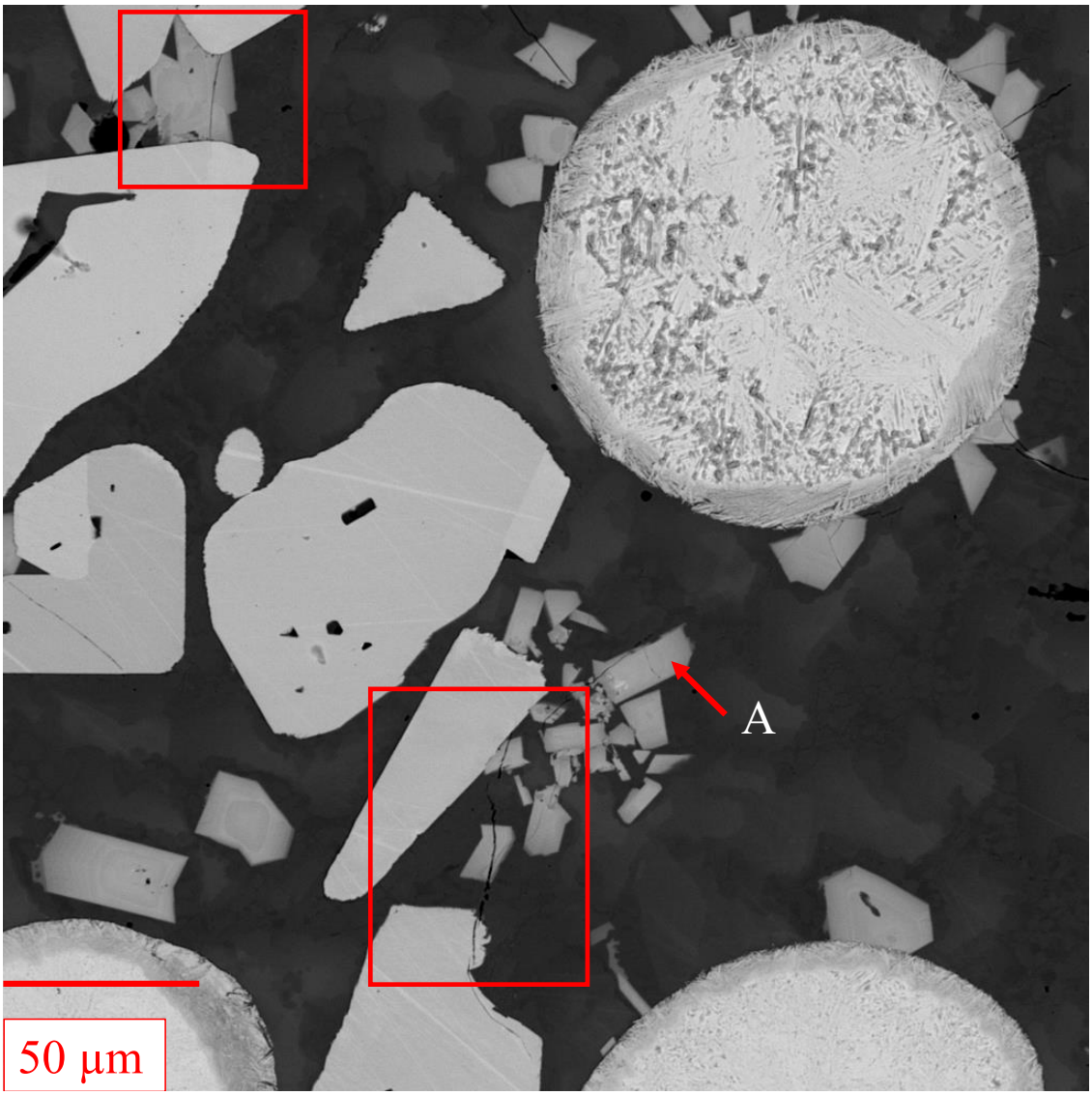

FIGURE 6.17: Backscatter SEM showing the breakdown of SE2 spherical WC/W_2C, and the distribution of secondary carbides.

and denuded regions at later portions of the build. The 52.5wt% (Figure 6.4, Figure 6.16) samples had denuded regions throughout the cross-section using both powders.

Comparing higher magnification images of the microstructure of the 35wt% SE1 (Figure 6.6,Figure 6.7) with the SE2 (Figure 6.17, Figure 6.19), the SE1 samples had higher degrees of degradation of the spherical WC/W_2C. A high magnification image of a degraded SE1 WC/W_2C particle is shown in Figure 6.21, and the composition of the phases present are shown in Table 6.5. The center (A) of the degraded carbide could be δ-WC based on

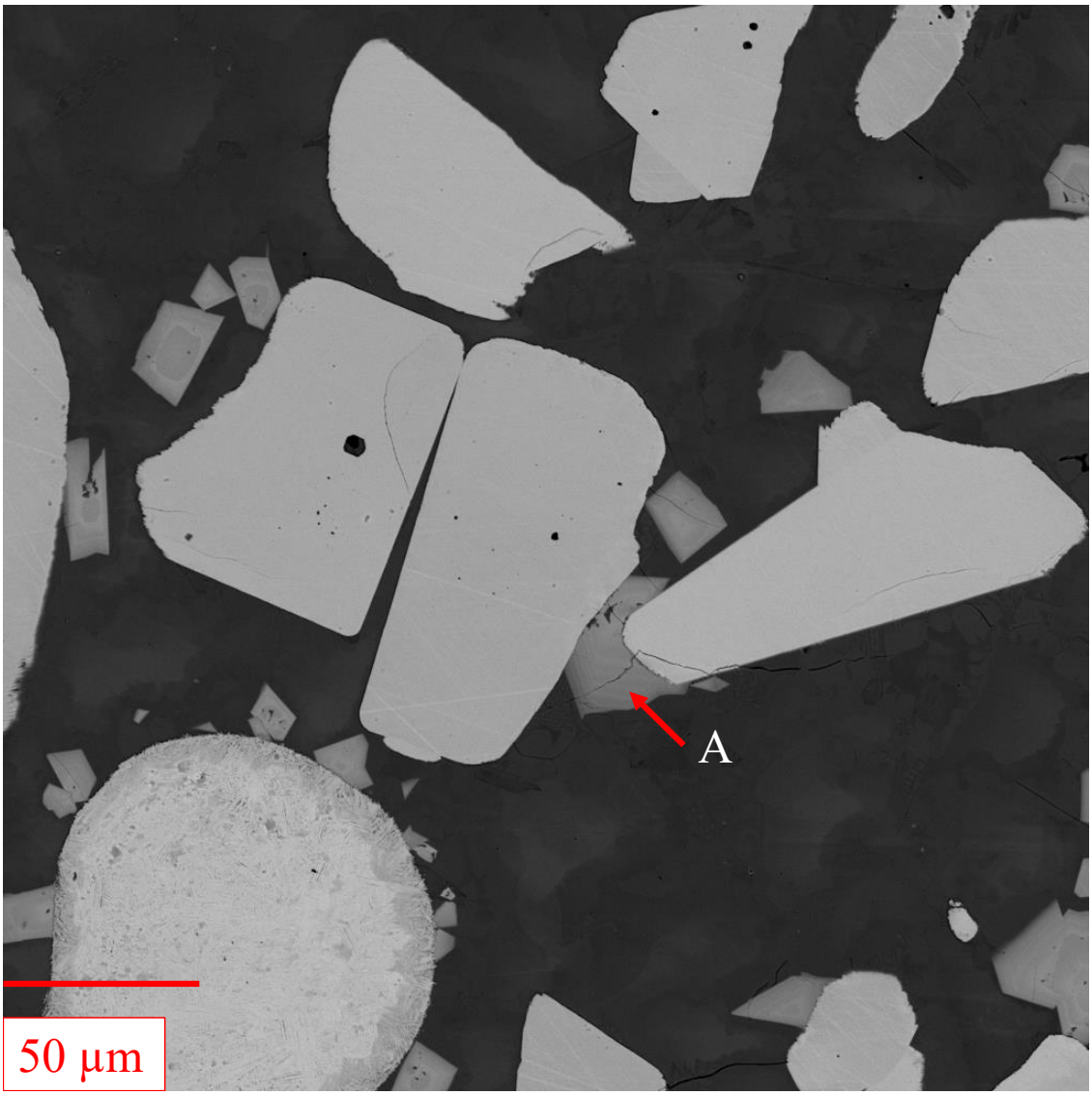

FIGURE 6.18: Backscatter SEM showing the breakdown of SE2 spherical WC/W_2C, and the distribution of secondary carbides.

W and C atomic fractions. However, carbon is below the detection limit of EDX, so other characterization methods, such as TEM, should be done to confirm the center of the carbide being δ-WC. The reaction layer (B) around the center of the particle contains Ni and small amounts of Cr ($Ni_3W_6Cr)C_9$), showing the reaction of the WC/W_2C with the NiCrBSi matrix. On the outer extremities of the degraded particle, two morphology of carbides are found: blocky (C) and rod/acicular (D). Both C and D have a similar composition, which is close to WC with traces of Ni. Carbide C has a similar morphology to the blocky carbide (A in Figure 6.8), while carbide D is similar in shape to the rod carbides (C in Figure 6.9).

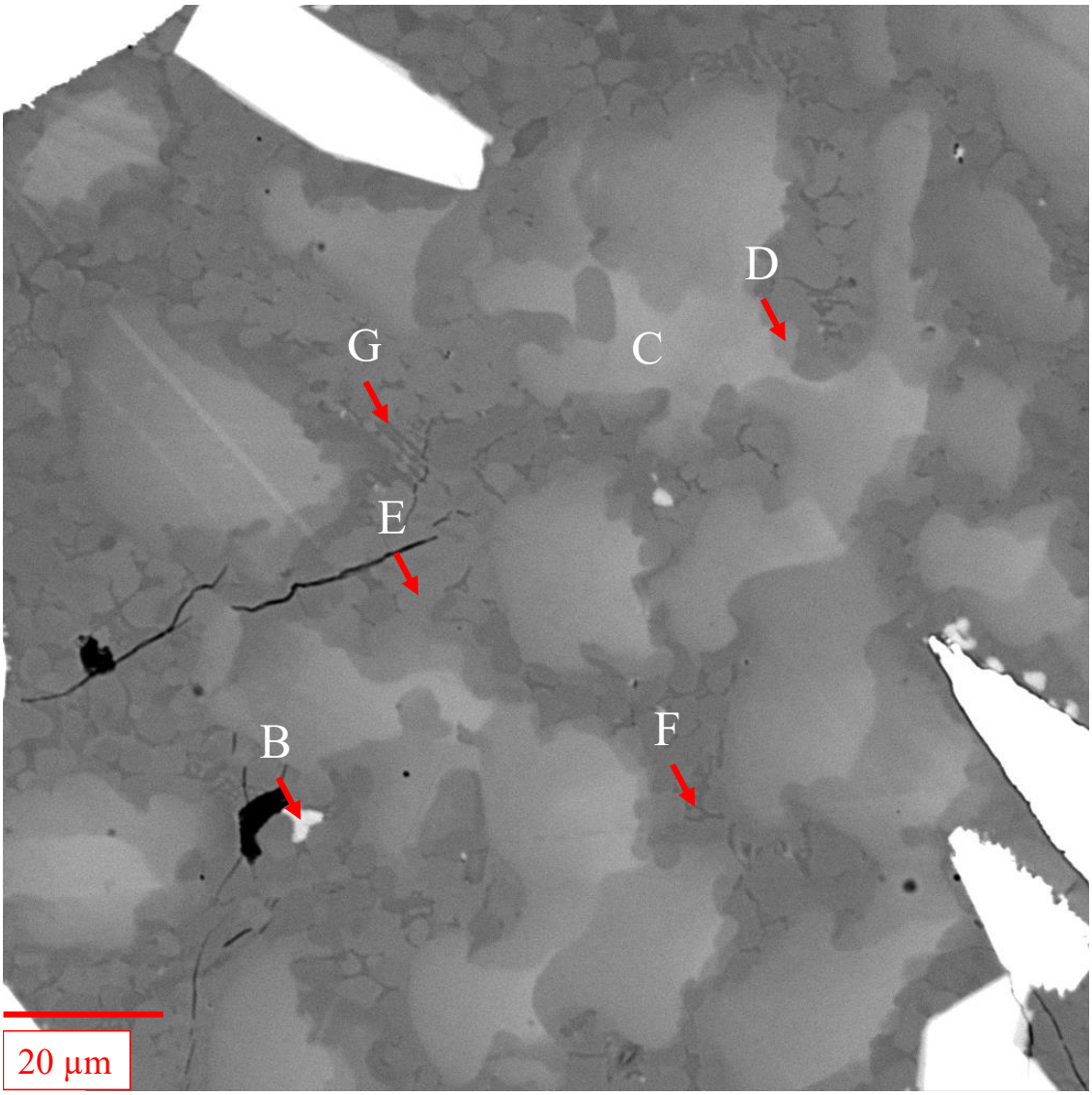

FIGURE 6.19: Backscatter SEM showing the phases of the Ni matrix. The letters correspond to the compositions provided in Table 6.4.

However, the blocky and rod carbides in the matrix (Figure 6.7) contain higher levels of Ni than those surrounding degraded carbides. There are also some slightly darker blocky carbides (E)($(Ni_{14}W_3Cr_3Si)C_8$) on the outer extremities. The dark phase (F) in the center of the particle is WO_2. The oxygen could be from improper shielding during deposition [30], or oxygen introduced during the powder-making process.

The blocky and rod/acicular carbides in the SE1 samples are likely remnants of spherical SE1 WC/W_2C that have undergone dissolution diffusion of the W_2C[17, 18, 644]. This

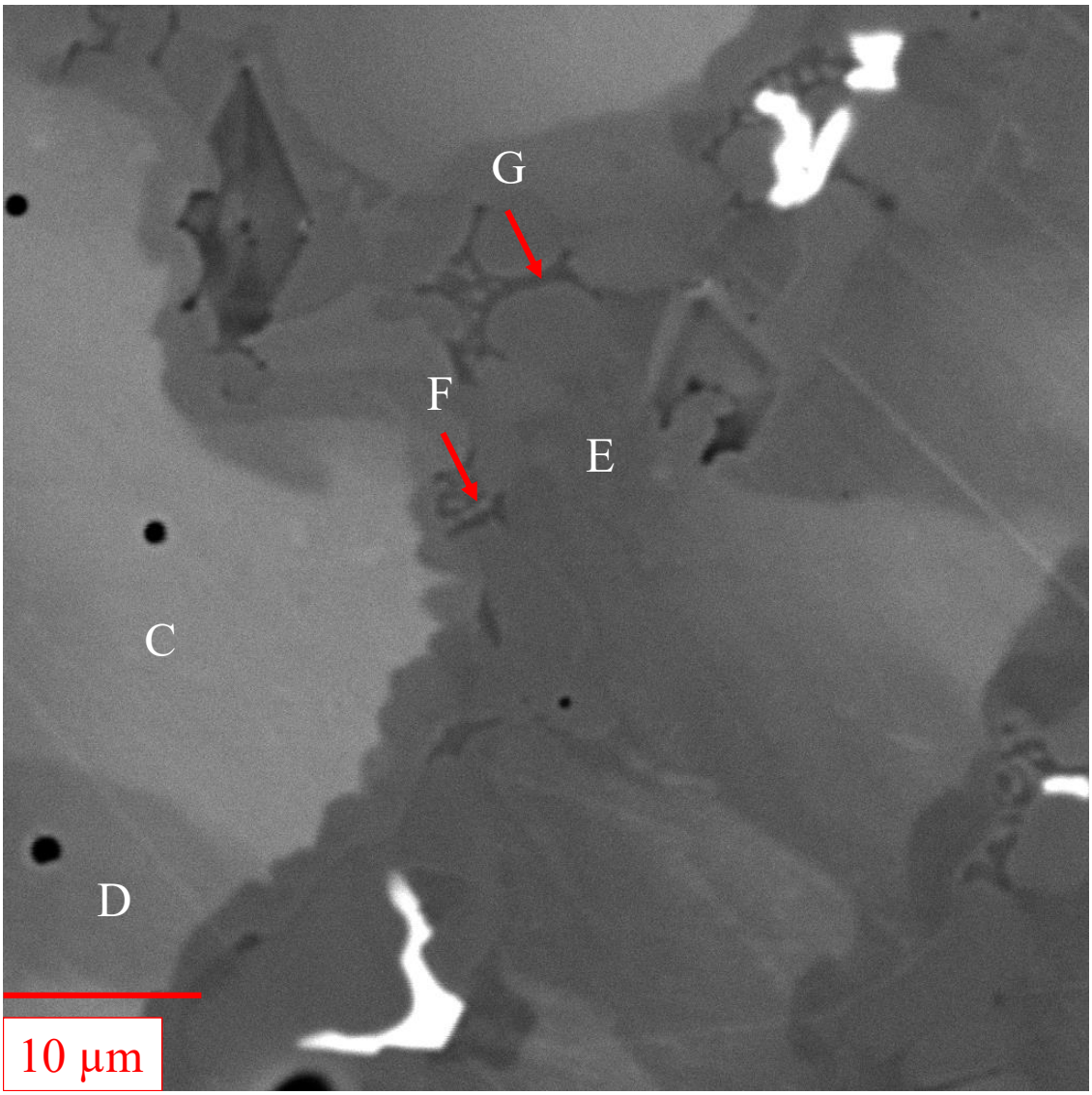

FIGURE 6.20: Backscatter SEM showing the phases of the Ni matrix. The letters correspond to the compositions provided in Table 6.4.

is supported by the W-C phase diagram (Figure 6.22). The two types of carbides in eutectic WC/W_2C are δ(WC) and $\beta(W_2C)$. Primary δ-WC is stable between 300K and 3030-3050K and will undergo phase transformations when exposed to nonstoichiometric carbon contents. W_2C has three polymorphs, β'', β', and β, which have been found to breakdown at 1250°C to δ-WC and W [11]. With low transformation temperatures, the W_2C is dissolved into the Ni matrix leaving behind the block- and rod/acicular-like morphology of WC. Some of the dissolved W reacts with the matrix elements to form the ring carbide E $(Ni_2W_4Cr)C_3$ in the SE1 samples (B Figure 6.21), and the blocky carbide phase $(Ni_3W_2Cr_2)C_3$. Likely,

the differing amount of convective mass transfer of the WC/W_2C between the SE1 and SE2 samples led to different morphologies and compositions of M_7C_3 (B in SE1, and A in SE2) carbides. The remnant WC can undergo further dissolution to form phase D in Figure 6.9 ($(Ni_3W_2Cr_2Si)C_4$) and phase E in Figure 6.21($(Ni_{14}W_3Cr_3Si)C_8$).

A high magnification image of a degraded SE2 particle is shown in Figure 6.23. The black in the center of the particle is porosity. The composition of the phases are shown in Table 6.6 The center (A) of the carbide could be δ-WC based on the atomic ratio of W and C. Again, TEM analysis should be done to confirm this. The reaction layer (B) surrounding the

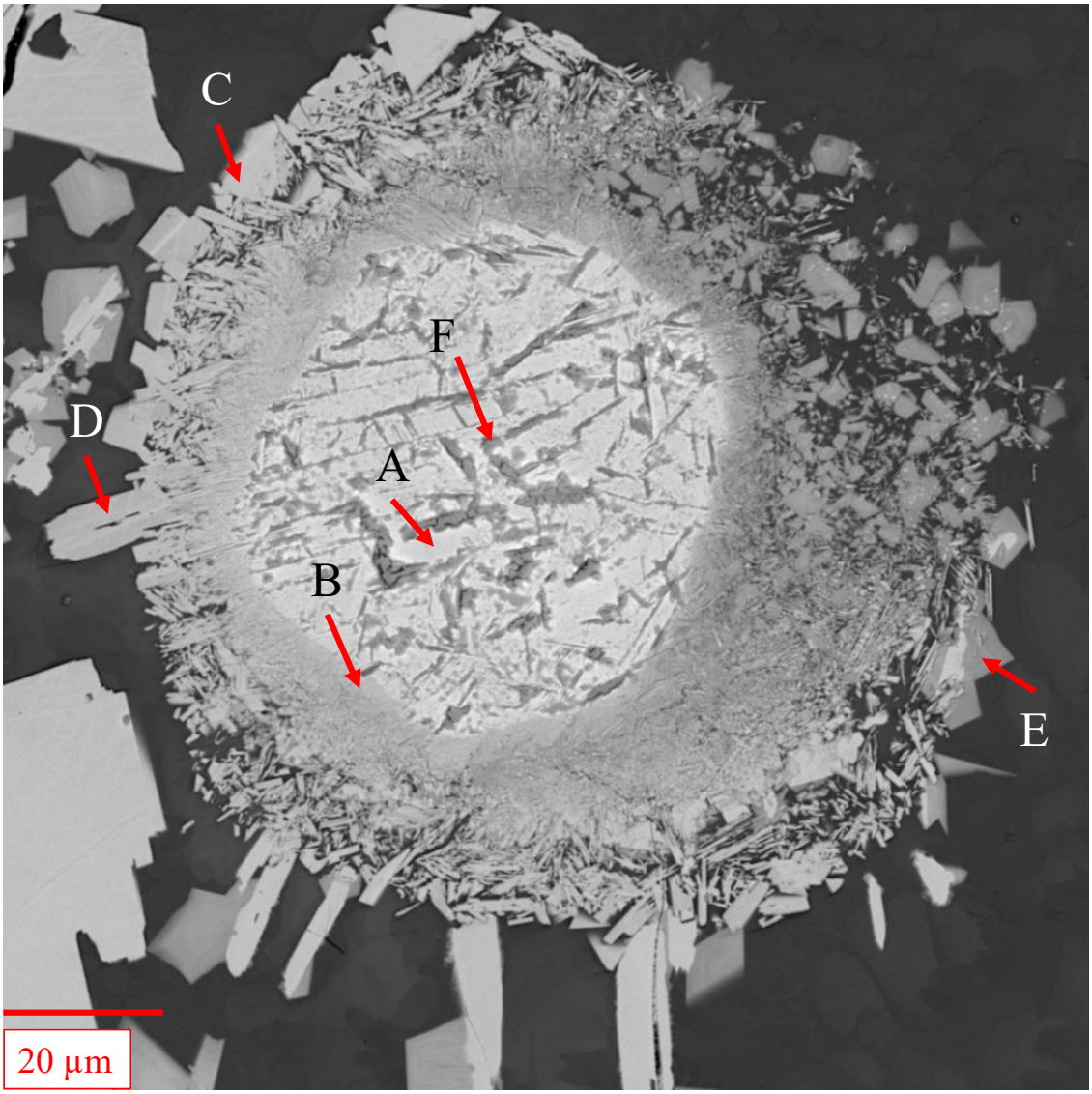

FIGURE 6.21: Backscatter SEM showing the breakdown of SE1 WC/W_2C particle.

SE2 particle contained mainly Ni, W, C, and Cr with some dissolved Si ($(Ni_4W_4Cr_2Si)C_4$). The blocky carbides (C) found around the particle has a similar composition to the reaction layer (B) ($(Ni_4W_4Cr_2Si)C_4$). The blocky carbides have a similar composition to those found throughout the NiCrBSi matrix (A in Figure 6.17), and could be one of the sources of their formation. There are instances where there are acicular carbides (D) that are mostly W and C, with small amounts of Ni and Cr ($(NiW_5)C_6$). However, the acicular carbides were not found throughout the microstructure. This could be some of the δ-WC from the WC/W_2C particles that has had a minor reaction with the NiCrBSi matrix. The darker (E) portion of the center of the particle is WO_2.

A common theme across all the samples was increased convective mass transfer of the WC/W_2C as the build height increased. As discussed in Chapter 5, the cooling rate of the sample drastically decreases as the build progresses. At lower portions of the build, the high cooling rate would decrease the amount of time for the breakdown of β-W_2C, which

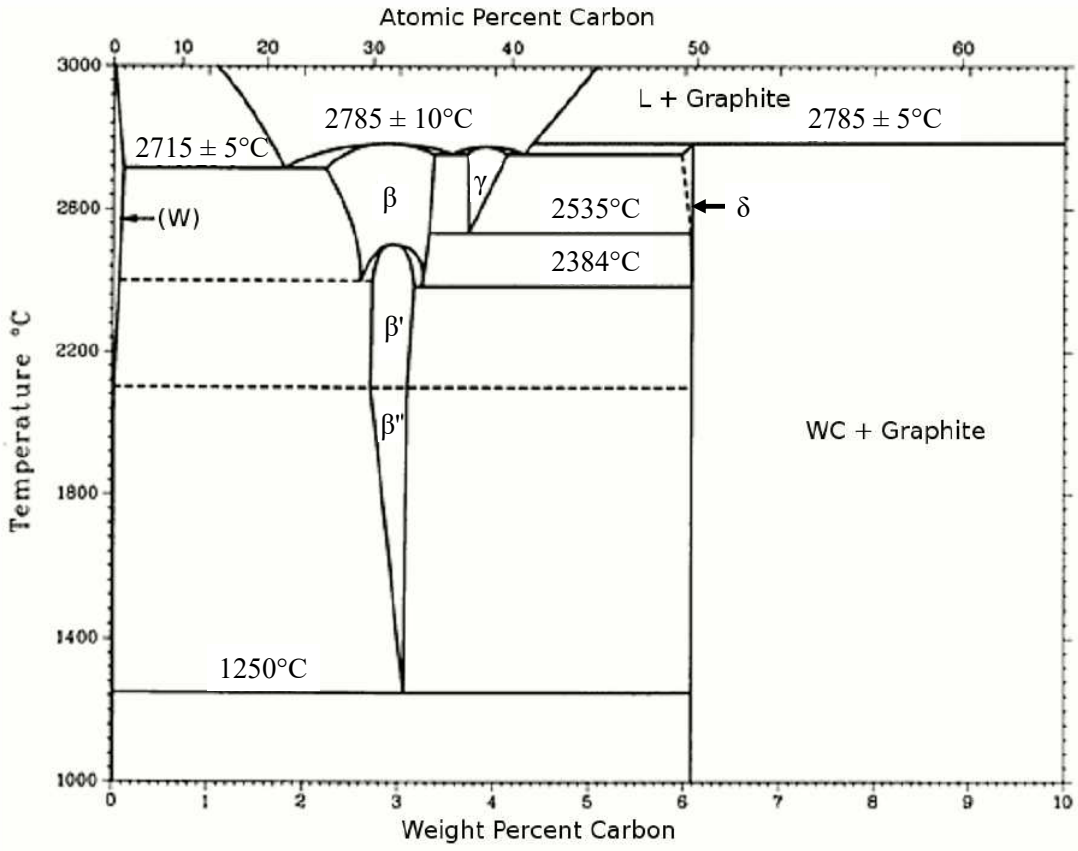

FIGURE 6.22: W-C phase diagram (reimaged from [11].)

happens at 1250°C. As the cooling rate decreases, the more time the carbide is exposed to temperatures below 1250°C, resulting in more WC/W_2C breakdown. More research needs to be done to determine the effect of WC/W_2C's exposure to liquid Ni, and how that affects the transformation temperature of WC/W_2C at 1250°C. The discrepancy in the extent of WC/W_2C breakdown between the two powders could be due to the quality of the two powders. The SE1 samples did appear to have more surface defects than the SE2 powder. The surface flaws could enhance the reaction between the liquid NiCrBSi and the WC/W_2C powder. There could be different ratios of WC and W_2C in the powders, and since W_2C is less stable than WC (Figure 6.22), it is more susceptible to thermal degradation. Further

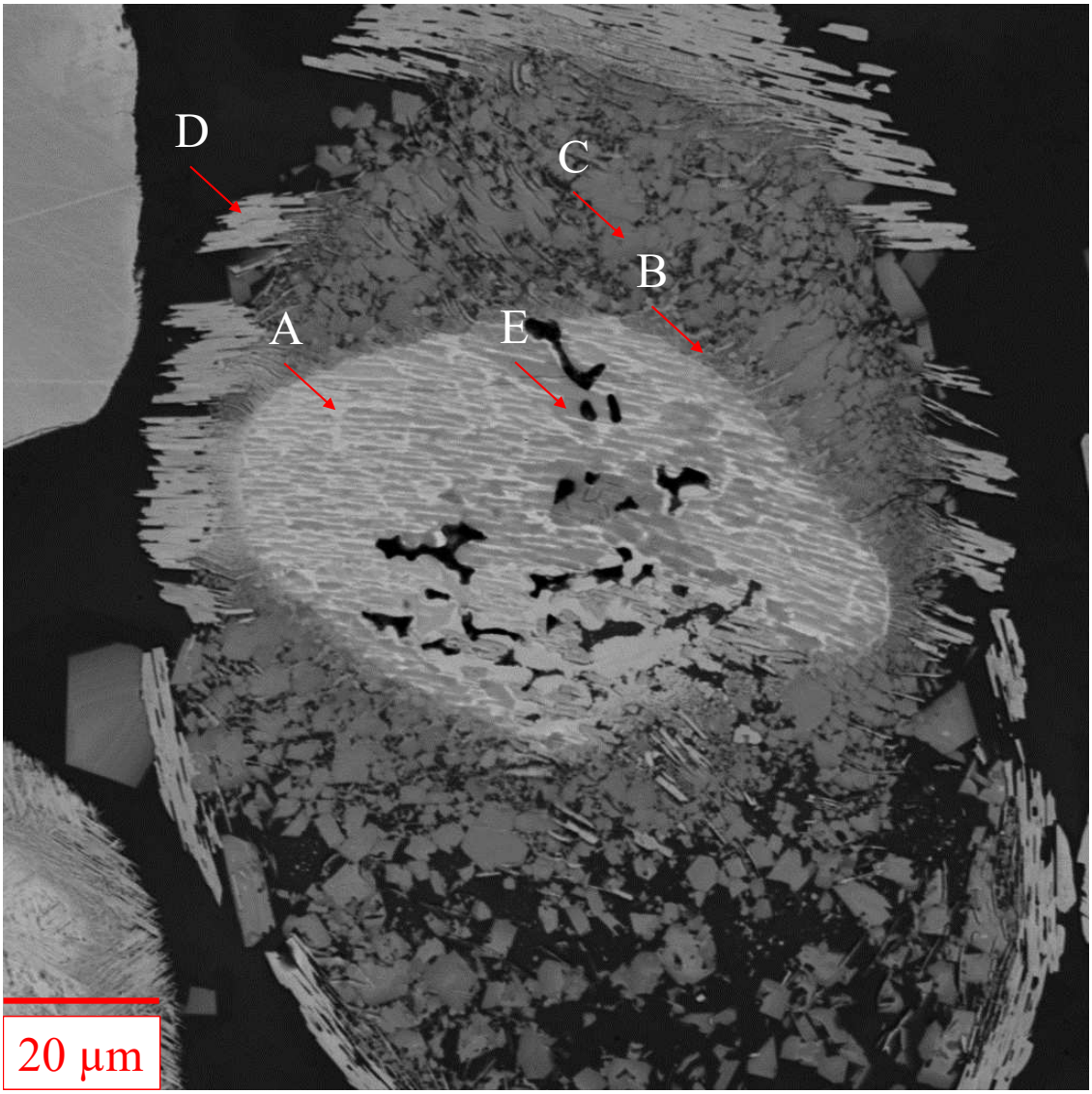

FIGURE 6.23: Backscatter SEM showing the breakdown of SE2 WC/W_2C particle.

TABLE 6.5: The composition of the different phases around the degraded SE1 carbide in Figure 6.21 using EDX. All the EDX compositions are the average of mulitple points across different degraded carbides.

	at%					
Letter	Ni	W	Si	C	Cr	O
A	-	49.7	-	50.3	-	-
B	15.1	27.0	-	53.4	4.6	-
C	2.8	39.8	-	57.3	-	-
D	8.0	39.9	-	52.1	-	-
E	27.4	16.5	8.5	31.3	16.3	-
F	-	30.0	-	-	-	70.0

TABLE 6.6: The composition of the different phases around the degraded SE2 carbide in Figure 6.23 using EDX. All the EDX compositions are the average of mulitple points across different degraded carbides.

	at%					
Letter	Ni	W	Si	C	Cr	O
A	-	54.9	-	45.12	-	-
B	27.2	27.8	6.3	27.2	11.6	-
C	27.3	24.6	7.3	27.9	12.9	-
D	8.0	39.7	-	49.0	3.3	-
E	-	33.5	-	-	-	64.0

analysis should be done to quantify the contact time required for the convective mass transfer of both SE carbides. These findings highlight the importance of the quality of feedstock material. Additionally, the significance of minimizing dwell times (i.e. maximizing cooling rate) in PTA-AM with spherical eutectic carbides to reduce the degree of thermal degradation of WC/W_2C.

6.4 Conclusion

This chapter explored the effect of adding spherical WC/W_2C from two manufacturers: SE1 and SE2. The total WC content in the samples was 70wt%. The different MMC compositions that were tested are (35wt% MC, 35wt% SE)WC -, (52.5 wt% MC, 17.5wt%SE)WC -, and (17.5 wt% MC, 52.5wt% SE) - NiCrBSi. For the SE1 samples, the 17.5wt% SE sample

had the best distribution of WC, with the fewest amount of denuded regions, porosity, and carbide breakdown. For SE2, the 35wt% sample had a homogeneous distribution of WC through the entire cross-section. The SE1 spherical showed much higher susceptibility to convective mass transfer and fracturing during the PTA-AM deposition process, resulting in a more comprehensive array of secondary carbide phases in the microstructure. It is likely that the blocky and rod/acicular-shaped carbides were remnant WC from the SE1 WC/W_2C powder and that the ring carbide formed in situ. The SE2 did not show any signs of fracturing and only underwent a small amount of convective mass transfer during the PTA-AM process. This resulted in a single blocky morphology of carbide that likely formed in situ during solidification. It is speculated that the difference in powder behavior is attributed to the amount of surface defects that formed during the powder manufacturing process, and highlights the need for quality feedstock for additive manufacturing processes.

Chapter 7

Concluding Remarks

7.1 Summary

The objective of this thesis is to investigate how the composition and solidification rate of metal matrix composites (MMCs) affect the thermal degradation of tungsten carbide (WC), as well as the resulting microstructure of WC-Ni MMCs fabricated using PTA-AM. This was achieved by studying the microstructure at various heights (solidification cooling rates) in a PTA-AM build, such as WC distribution (mean free path and carbide volume percent), complex carbide fraction and composition, and matrix solidification structure and composition. The composition of the MMC was altered by varying the carbide content (60, 70, and 80wt%), matrix composition (NiCrBSi, NiBSi), and carbide morphology and type (angular monocrystalline WC and spherical eutectic WC/W_2C). This thesis achieves its objective through the following work:

1. Convolutional neural networks were used to semantically segment WC particles from NiCrBSi-WC optical microscopy images. This work aimed to create an automated pipeline to quantify the carbide distribution of PTA-AM deposited 60wt%WC - NiCrBSi MMCs by determining the carbide volume percent and mean free path (thesis objective 1). The U-Net was chosen as the CNN based on its proficiency in segmenting images with similar features to WC-Ni microstructures, and its outstanding performance with small datasets. In addition to the vanilla architecture, the encoders from mobilenet, resnet50, and vgg16, as well as the LinkNet architecture with a mobilenet and resnet50

encoder, were tested. The evaluation metrics used were intersection over union, the dice coefficient, and the area under the receiver operating characteristic curve. A non-local means filter, mean shift, and image augmentation were used to preprocess the optical microscopy images prior to being passed through the model. A hyperparameter search was done to find the optimal values for batch normalization, batch size, learning rate, learning rate decay, dropout rate, L2 regularization, kernel size, number of filters, activation function, loss function, and optimizer. K-fold cross-validation was used to determine the final performance of the model. The vanilla U-net architecture performed best with a mean AUC-ROC, IOU, and dice coefficient of 0.965, 0.911, and 0.953 across the test dataset, respectively. From the segmented images, the mean free path was determined using ASTM STP 839 and a new proposed computational method, where the physical distance between the particles is determined by counting the pixels separating them. The carbide percent, mean free path (ASTM), and mean free path (CBP) were 40 $\pm$ 11, 64.4 $\pm$ 30, and 89.7 $\pm$ 29.4 for the ground truth images, and 41 $\pm$ 11, 79.9 $\pm$ 40, and 115 $\pm$ 35 for the model predictions, respectively. Spherical WC/W_2C could be segmented using the same model, even though no spherical WC/W_2C was found in the training data, highlighting the robustness of the models' segmentation abilities. The mean free path of the WC particles increases as the build height increases.

2. PTA-AM was used to investigate the impact of increasing WC content from 60 to 70 and 80 wt% on the distribution of WC, formation of complex carbides, solidification structure of the matrix, and resistance to abrasive wear in WC-Ni MMCs (thesis objective 2). PTA-AM deposits with 60wt% angular monocrystalline WC in NiCrBSi had a homogenous distribution of WC particles and little porosity throughout the entire build. The microstructure showed some carbide dissolution, evident by the formation of high W containing complex carbides and dissolved W in the γ-Ni dendrites. Halos of γ-Ni formed around the already formed dendrites with higher Si, Cr, and Fe contents; outside the ring experienced coupled growth of γ-Ni and Ni_3B. Increasing the WC content to 70wt% monocrystalline WC in NiCrBSi caused the microstructure to be dominated by defects in the form of denuded regions, and prominent irregular and spherical-shaped pores. The irregular pores are likely manufacturing defects from poor flowability of 70wt% WC-Ni MMCs. The spherical-shaped pores could be from the formation of CO/CO_2 gas during the manufacturing process. Higher WC content

resulted in slightly elevated levels of carbide dissolution, observable by the broader array of high W complex carbides, and increased W content in the γ-Ni dendrites and halo phase surrounding the dendrites. The interdendritic regions contained a eutectic of γ-Ni/Ni_3B. The microstructural results were compared to Scheil solidification simulations done using Thermo-calc thermodynamic software. The Scheil solidification simulations did not include the halo around the primary dendrites, and the levels of W found in the primary Ni phase were much lower than that of PTA-AM.

3. A microstructural analysis was done on a PTA-AM build of 70wt% monocrystalline WC in a NiBSi matrix. This work aimed to establish a relationship between the cooling rate during solidification, deposition height, level of thermal degradation of WC particles, and resulting microstructure of 70 wt% WC-NiBSi MMCs during the PTA-AM fabrication process (thesis objective 3). Electromagnetic levitation was done on the PTA-AM deposited material to understand the relation between cooling rate and secondary dendrite arm spacing. The carbide volume percent was determined as a function of height, and it was found that the retained WC never hit the theoretical value of 70wt%. The poor carbide retention was due to large pores and denuded regions. The pores were likely caused by a combination of manufacturing defects and CO/CO_2 gas formation during deposition. There was no difference in the microstructure or composition between the denuded, and interparticle regions. Evidence suggests that denuded regions could be from exceeding the maximum packing of WC (62wt%); experiments to prove this are ongoing. At all heights of the build, the microstructure was dendritic γ-Ni with halos around the primary phase. The W content in the γ-Ni dendrites increases from 2.7 to 11 at% when comparing 1mm to 42mm of build height. Additionally, the W in the halo increases from 0 to 4.5at% after 9mm of material is deposited. The increase in W content in the matrix suggests that the cooling rate may significantly influence the carbide dissolution. These findings support the conclusion made previously (Chapter 3) that the interparticle spacing increases with height. The microstructural results were compared to Scheil solidification simulations done using Thermo-calc thermodynamic software. Similar to the 70wt%WC-NiCrBSi, the Scheil solidification simulations did not include the halo around the primary dendrites, and the levels of W found in primary γ-Ni phase in the PTA-AM samples were 2-10x higher than the Scheil simulation.

4. The impact of incorporating spherical eutectic WC/W_2C particles from two manufacturers, SE1 and SE2, on the degree of thermal degradation of WC and its corresponding microstructure in 70 wt% WC-NiCrBSi deposited through PTA-AM was investigated. The total WC content in all samples was 70 wt%. Various MMC compositions were examined, including (35 wt% MC, 35 wt% SE)WC-, (52.5 wt% MC, 17.5 wt% SE)WC-, and (17.5 wt% MC, 52.5 wt% SE)WC-NiCrBSi. Adding 17.5 and 35wt% appeared to improve the distribution of WC; however, 52.5wt% contained large fractions of pores and denuded regions. During the PTA-AM deposition process, the SE1 spherical powder demonstrated a higher susceptibility to convective mass transfer and fracturing, resulting in a broader range of secondary carbide phases in the microstructure. This difference in the carbide powder behavior is hypothesized to be due to variations in the number of surface defects formed during powder production. The higher degree of degradation observed in SE1 compared to SE2 underscores the importance of utilizing high-quality feedstock for additive manufacturing processes.

7.2 Implications

This thesis provides a better understanding of the effects of composition, carbide type, and thermal history on the microstructure and carbide dissolution of WC-Ni MMCs deposited using PTA-AM. All of the experimental factors changed the distribution, and morphology of the phases present in the microstructure. Exploring the microstructure under differing thermal conditions is critical for assessing the evolution of the microstructure during additive manufacturing. The culmination of this work makes the following contributions:

1. Developing a comprehensive understanding of the microstructure of WC-Ni during PTA-AM for 60 and 70wt% WC under different experimental conditions; this work is critical for creating accurate thermodynamic and microstructural models for WC-Ni under differing solidification conditions. Understanding the feasibility of increasing the WC content in PTA-AM deposits and its effects on WC retention is essential for understanding the material limitations of the AM modality.

2. Creating a relationship between cooling rate and secondary dendrite arm spacing for 70wt% monocrystalline WC in NiBSi. Linking the thermal history, and the corresponding microstructure is essential for understanding the evolution of the microstructure during PTA-AM, especially when the physical measurement of the thermal history is difficult.

3. Developing an automated pipeline for quantifying the carbide distribution of WC-Ni optical microscopy images. The methods used can be transferred to similar material systems that require similar computations, and act as building blocks for using deep learning to analyze microstructural images. Additionally, the constructed pipeline reduces the processing time of WC-Ni optical microscopy images from hours to seconds.

4. Understanding how the processing influences carbide dissolution of WC in Ni during PTA-AM; this is important for the manufacturing of WC-Ni, and developing a preferential thermal history that should be maintained for minimizing loss of WC.

7.3 Recommendations

Based on the knowledge gained from this thesis work, prior to commercialization the PTA-AM process could be optimized for the deposition of WC-Ni MMCs in the following ways:

1. Ensuring that the maximum packing of WC is not exceeded. A Hall Flowmeter test should be conducted on the WC powder prior to deposition to determine the maximum packing of WC. The packing of WC could be improved by incorporating different size ranges and morphologies (angular and spherical)of WC. Not exceeding the maximum packing of WC should eliminate denuded regions from the deposit.

2. The highest possible, and consistent cooling rate should be maintained through the entire deposition of WC-Ni MMCs to minimize the thermal degradation of WC. This should maximize the retention of WC, and minimize the mean free path between particles. Additionally, a consistent cooling rate would eliminate the difference in the microstructure as the build progresses. A suggested method would be incorporating an inter-layer dwell time, and a water-cooled substrate to allow the previous layer to cool, prior to the deposition of the next layer.

7.4 Future Work

Based on an extensive literature review (Chapter 2), there have not been any studies of 70wt% WC deposited using PTA-AM, nor has there been any published literature on processing WC-Ni with EML. The information developed in this thesis informs thermodynamic modeling of the rapid solidification of WC-Ni MMCs. The future recommendations to build upon the presented work are as follows:

1. Conduct further PTA-AM deposition trials with 70wt% WC in NiBSi with the following conditions:
    i. Use higher heat inputs to promote the wetting of the WC-Ni MMC to reduce the concentration of irregularly shaped pores.
    ii. Introduce a water-cooled plate under the substrate to increase the solidification rate and reduce the amount of carbide dissolution experienced at later points in the build.
    iii. Introduce an inter-layer dwell time to reduce heat accumulation and the cooling rate during the deposition process [209].
    iv. Improve the shielding capabilities during PTA-AM to see if there is a change in the amount of porosity in 70wt% WC - NiBSi.
    v. Perform optical emission spectroscopy to analyze the spectrum and electron density of the plasma to determine if any metal vapor or CO/CO_2 is emitted during deposition [645, 646]. The aim of conducting these experiments is to identify whether any further gas ionization is occurring and to ascertain the reason behind the formation of the significant spherical pores.
    vi. Perform the same experimental process conducted in Chapter 5 with 17.5wt% and 35wt% spherical eutectic WC/W_2C to determine the resonance time required for WC/W_2C to begin degrading in Ni.
    vii. Try varying sizes of WC to improve the maximum packing of WC in an attempt to eliminate denuded regions.
2. A proposed analytical method is to perform focused ion beam scanning electron microscopy (FIB-SEM) to perform 3-D reconstruction of a WC-Ni sample containing

denuded regions [647, 648]. X-ray microscopy could not penetrate the WC particles to perform the 3-D reconstruction. A 3-D reconstruction of a denuded region would provide precious information on the morphological evolution of denuded regions and if there is a link between porosity and denuded region formation. A FIB-SEM analysis is now available at the NanoFab at the University of Alberta.

3. Perform Auger electron spectroscopy to better understand the distribution of boron and carbon in the microstructure since these elements cannot be detected using EDX. Determining the distribution of lighter elements would grant new insights into the partitioning of elements during solidification, and could be used to determine if there is segregation of boron and carbon that was not previously detected.

4. Perform TEM analysis to determine the eutectic structure of 70wt% WC - NiBSi. Additionally, determine the range of lamellar spacing for 70wt%WC - NiCrBSi.

5. Run electromagnetic levitation on 70wt% WC-NiBSi at differing cooling rates and W contents to create a better correlation between secondary dendrite arm spacing and the cooling rate. The relationship between SDAS and cooling rate would then have higher compositional accuracy to what is found in PTA-AM, and allow for a more accurate quantification of the cooling rates experienced during PTA-AM. If the peak temperature of PTA-AM can be accurately modeled, then coupling temperature, cooling rate, and resulting composition would be valuable inputs for thermodynamic software, such as Thermo-calc, to increase the accuracy of the microstructural modeling of NiBSi-WC metal matrix composites.

6. The abrasive wear performance under ASTM-G65 conditions should be determined for 70wt% WC - NiBSi to improve the feasibility of industrial implementation and whether there are performance increases when increasing the WC content. ASTM-G65 testing should be withheld until the cause of metallurgical defects is determined, and remedied to provide an accurate representation of increasing the WC content.

7. The improvements that can be made to the convolutional neural network are:

    i. Obtaining more data from various optical microscopes that use different light sources; this will make the WC and Ni matrix appear a different color other than shades of green. Having a broader spectrum of pixel intensities would make the

model more robust, and likely eliminate the need for the pixel mean shift pre-processing algorithm.

ii. Revise the training dataset to make the ground truth more accurate, and not contain any edge pixels or defects. Adding images with spherical carbides with varying amounts of breakdown to the training data would increase the ability of the model to segment spherical WC.

iii. Include data from various magnifications would allow for faster processing times, and increase the robustness of the model.

iv. Include a new loss function that has a higher penalty for type I errors across an area where there are significant gradients in the pixel intensity; this may help with having a better separation between WC particles.

v. Determine the aleatoric uncertainty in the model by using dropout before each layer in the model, and at the time of testing, over hundreds of iterations. The uncertainty of the model ensemble can be estimated by determining the variance in the model's predictions; this quantifies the potential for some inputs to have noisier outputs based on the nodes that are active.

7.5 Academic Contributions

Journal Publications:

This thesis has resulted in the following published journal manuscripts:

1. Lehmann,T; **Rose, D**; Ranjbar, E; Ghasri-Khouzani, M; Tavakoli, M; Henein, H; Wolfe, T; and Qureshi, AJ. *Large-scale metal additive manufacturing: a holistic review of the state of the art and challenges*, International Materials Reviews. Vol. 67(4), 2022.

2. **Rose, D**; Forth, J; Henein, H; Wolfe, T; and Qureshi, AJ. *Automated semantic segmentation of NiCrBSi-WC optical microscopy images using convolutional neural networks*, Computational Materials Science. Vol. 210, (2022).

3. **Rose, D**, Tonya Wolfe, and Hani Henein *Microstructural Characterization of 70wt% WC-NiBSi Deposited by PTA-AM.* to be submitted to the journal Additive Manufacturing, 2023.

4. **Dylan Rose**, Tonya Wolfe, and Hani Henein *Microstructural Characterization and Wear Resistance of 60 and 70wt% WC - NiCrBSi Thin Walls Deposited Using Plasma Transferred Arc Additive Manufacturing.* to be submitted to JOM, 2023.

Conferences:

This thesis also resulted in the following conference presentations:

1. **Rose, D**; Wolfe, T; and Henein, H; *Denuded region formation in NiBSi-WC metal matrix composites deposited by plasma transferred arc additive manufacturing*, Holistic Innovation in Additive Manufacturing Conference, June 21-22, 2022, **Conference presentation**.

2. **Rose, D**; Forth, J; Henein, H; Wolfe, T; and Qureshi, AJ. *Semantic Segmentation of NiBSi-WC optical microscopy images using a convolutional neural network* , Materials Science and Technology Conference, Oct. 17-20, 2021, **Conference presentation**.

3. **Rose, D**; Forth, J; Henein, H; Wolfe, T; and Qureshi, AJ. *Semantic Segmentation of NiBSi-WC optical microscopy images using a convolutional neural network* , Holistic Innovation in Additive Manufacturing Conference, June 1-2, 2021, **Conference poster**.

4. **Rose, D**; Wolfe, T; and Henein, H; *Major Defects in 70wt% WC-Ni deposits using Plasma Transferred Arc – Additive Manufacturing*, Holistic Innovation in Additive Manufacturing Conference, June 26-27, 2019, **Conference presentation**.

5. **Rose, D**; Wolfe, T; and Henein, H; *Formation of Denuded Region in Additive Manufactured Parts using Plasma Transferred Arc Welding*, CMSC: Canadian Materials Science Conference, June 19-22, 2018, **Conference presentation**.

Bibliography

[1] Abbas S. Alwan. Effect of quenching media on the mechanical properties and abrasive wear resistance of (34cr4) steel blade with soil texture used in agricultural equipments. *Engineering and Technology Journal*, 32(9):2205–2215, 2014. ISSN 1681-6900. URL https://etj.uotechnology.edu.iq/article_99975.html.

[2] Jiří Votava. Usage of abrasion-resistant materials in agriculture. *Journal of Central European Agriculture*, 15(2):119–128, jun 2014. ISSN 1332-9049. doi: 10.5513/JCEA.V15I2.2647. URL https://hrcak.srce.hr/ojs/index.php/jcea/article/view/2647.

[3] A H Jones and P Roffey. The improvement of hard facing coatings for ground engaging applications by the addition of tungsten carbide. *Wear*, 267(5):925–933, 2009. ISSN 0043-1648. doi: https://doi.org/10.1016/j.wear.2009.01.042. URL https://www.sciencedirect.com/science/article/pii/S0043164809002592.

[4] Md Aminul Islam and Zoheir N. Farhat. Effect of impact angle and velocity on erosion of API X42 pipeline steel under high abrasive feed rate. *Wear*, 311(1-2):180–190, mar 2014. ISSN 0043-1648. doi: 10.1016/J.WEAR.2014.01.005.

[5] Oluwaseun Ezekiel Adedeji, Lisheng Zhang, David E.S. Breakey, and R. Sean Sanders. Investigation of abrasive wear in contact load-dominated slurry flows using a Toroid Wear Tester. *Wear*, 477:203767, jul 2021. ISSN 0043-1648. doi: 10.1016/J.WEAR.2021.203767.

[6] Lei Ba, Qian Gao, Wang Cen, Jing Wang, and Zhenjiang Wen. The impact-abrasive wear behavior of high wear resistance filling pipeline with explosion treatment. *Vacuum*, 192:110427, oct 2021. ISSN 0042-207X. doi: 10.1016/J.VACUUM.2021.110427.

[7] A. I. Gusev, N. A. Kozyrev, A. A. Usoltsev, R. E. Kryukov, and A. R. Mikhno. Development of a flux-cored wire for surfacing mining equipment operating in the conditions of shock-abrasive wear. *IOP Conference Series: Earth and Environmental Science*, 206 (1):012034, nov 2018. ISSN 1755-1315. doi: 10.1088/1755-1315/206/1/012034. URL https://iopscience.iop.org/article/10.1088/1755-1315/206/1/012034https://iopscience.iop.org/article/10.1088/1755-1315/206/1/012034/meta.

[8] M. Petrica, E. Badisch, and T. Peinsitt. Abrasive wear mechanisms and their relation to rock properties. *Wear*, 308(1-2):86–94, nov 2013. ISSN 0043-1648. doi: 10.1016/J.WEAR.2013.10.005.

[9] Liqun Xu, Cathy Vose, and David StJohn. Abrasive wear study of selected white cast irons as liner materials for the mining industry. *Wear*, 162-164(PART B):820–832, apr 1993. ISSN 0043-1648. doi: 10.1016/0043-1648(93)90083-X.

[10] Ravikumar Sundaramoorthy, Shawn X Tong, Dipen Parekh, and Chinnia Subramanian. Effect of matrix chemistry and WC types on the performance of Ni-WC based MMC overlays deposited by plasma transferred arc (PTA) welding. *Wear*, 376-377:1720–1727, 2017. ISSN 0043-1648. doi: https://doi.org/10.1016/j.wear.2017.01.027. URL https://www.sciencedirect.com/science/article/pii/S0043164817300959.

[11] Tonya Wolfe. *Homogeneity of Metal Matrix Composites Deposited by Plamsa Transferred Arc Welding*. PhD thesis, University of Alberta, Edmonton, 2010.

[12] Patricio F Mendez, Nairn Barnes, Kurtis Bell, Steven D Borle, Satya S Gajapathi, Stuart D Guest, Hossein Izadi, Ata Kamyabi Gol, and Gentry Wood. Welding processes for wear resistant overlays. *Journal of Manufacturing Processes*, 16(1):4–25, 2014. ISSN 1526-6125. doi: https://doi.org/10.1016/j.jmapro.2013.06.011. URL https://www.sciencedirect.com/science/article/pii/S1526612513000807.

[13] T Liyanage, G Fisher, and A P Gerlich. Microstructures and abrasive wear performance of PTAW deposited Ni–WC overlays using different Ni-alloy chemistries. *Wear*, 274-275:345–354, 2012. ISSN 0043-1648. doi: https://doi.org/10.1016/j.wear.2011.10.001. URL https://www.sciencedirect.com/science/article/pii/S0043164811006090.

[14] Maurizio Fenech, Maurice Grech, and John C. Betts. The in-flight temperature variation and dissolution of WC powder particles producing an Fe–Cr–W–C system by direct laser deposition. *Surface and Coatings Technology*, 207:211–217, aug 2012. ISSN 0257-8972. doi: 10.1016/J.SURFCOAT.2012.06.063.

[15] G. Y. Wang, S. N. Gu, and S. Yang. Microstructure and properties of tungsten heavy alloys fabricated by laser direct deposition. *Materials Science and Technology (United Kingdom)*, 33(4):415–420, mar 2017. ISSN 17432847. doi: 10.1080/02670836.2016.1221492.

[16] T. E. Abioye, P. K. Farayibi, D. G. McCartney, and A. T. Clare. Effect of carbide dissolution on the corrosion performance of tungsten carbide reinforced Inconel 625 wire laser coating. *Journal of Materials Processing Technology*, 231:89–99, may 2016. ISSN 0924-0136. doi: 10.1016/J.JMATPROTEC.2015.12.023.

[17] Mujian Xia, Dongdong Gu, Chenglong Ma, Hongmei Zhang, Donghua Dai, Hongyu Chen, Changpeng Li, Zhongjiao Zhou, Guofeng Chen, and Ingomar Kelbassa. Fragmentation and refinement behavior and underlying thermodynamic mechanism of WC reinforcement during selective laser melting of Ni-based composites. *Journal of Alloys and Compounds*, 777:693–702, mar 2019. ISSN 0925-8388. doi: 10.1016/J.JALLCOM.2018.11.056.

[18] Shengbin Zhao, Chenpeng Jia, Yuxue Yuan, Lixin Wang, Yiming Huang, and Lijun Yang. Insights into microstructural evolution and dissolution characteristics of reinforced particles in tungsten carbide-nickel composite coatings prepared by laser hot-wire deposition. *International Journal of Refractory Metals and Hard Materials*, 103:105720, feb 2022. ISSN 0263-4368. doi: 10.1016/J.IJRMHM.2021.105720.

[19] S. Ilo, Ch Just, E. Badisch, J. Wosik, and H. Danninger. Effects of interface formation kinetics on the microstructural properties of wear-resistant metal–matrix composites. *Materials Science and Engineering: A*, 527(23):6378–6385, sep 2010. ISSN 0921-5093. doi: 10.1016/J.MSEA.2010.06.060.

[20] S. S. Babu, R. P. Martukanitz, K. D. Parks, and S. A. David. Toward prediction of microstructural evolution during laser surface alloying. *Metallurgical and Materials Transactions A 2002 33:4*, 33(4):1189–1200, 2002. ISSN 1543-1940. doi:

10.1007/S11661-002-0220-4. URL https://link.springer.com/article/10.1007/s11661-002-0220-4.

[21] ASTM International. Additive Manufacturing - ASTM International, 2017. URL https://www.astm.org/industry/additive-manufacturing-overview.html.

[22] Brett P. Conner, Guha P. Manogharan, Ashley N. Martof, Lauren M. Rodomsky, Caitlyn M. Rodomsky, Dakesha C. Jordan, and James W. Limperos. Making sense of 3-D printing: Creating a map of additive manufacturing products and services. *Additive Manufacturing*, 1:64–76, oct 2014. ISSN 22148604. doi: 10.1016/j.addma.2014.08.005.

[23] E Herderick. Additive manufacturing of metals: A review. *Materials Science and Technology Conference*, 2(176252):1413–1425, 2011.

[24] J. L. Prado-Cerqueira, J. L. Diéguez, and A. M. Camacho. Preliminary development of a Wire and Arc Additive Manufacturing system (WAAM). *Procedia Manufacturing*, 13:895–902, jan 2017. ISSN 23519789. doi: 10.1016/j.promfg.2017.09.154.

[25] T. Artaza, A. Alberdi, M. Murua, J. Gorrotxategi, J. Frías, G. Puertas, M. A. Melchor, D. Mugica, and A. Suárez. Design and integration of WAAM technology and in situ monitoring system in a gantry machine. *Procedia Manufacturing*, 13:778–785, jan 2017. ISSN 23519789. doi: 10.1016/j.promfg.2017.09.184.

[26] E. A. Alberti, B. M.P. Bueno, and A. S.C.M. D'Oliveira. Additive manufacturing using plasma transferred arc. *International Journal of Advanced Manufacturing Technology*, 83(9-12):1861–1871, apr 2016. ISSN 14333015. doi: 10.1007/s00170-015-7697-7.

[27] S. Mandal, S. Kumar, P. Bhargava, C. H. Premsingh, C. P. Paul, and L. M. Kukreja. An Experimental Investigation and Analysis of PTAW Process. *http://dx.doi.org/10.1080/10426914.2014.984227*, 30(9):1131–1137, sep 2015. ISSN 15322475. doi: 10.1080/10426914.2014.984227. URL https://www.tandfonline.com/doi/abs/10.1080/10426914.2014.984227.

[28] Kevin Hoefer and Peter Mayr. Additive manufacturing of titanium parts using 3d plasma metal deposition. *Materials Science Forum*, 941 MSF:2137–2141, 2018. ISSN 02555476. doi: 10.4028/www.scientific.net/MSF.941.2137.

[29] Kevin Hoefer, Alexander Nitsche, Kevin Gordon Abstoss, Goekan Ertugrul, Andre Haelsig, and Peter Mayr. Multi-material Additive Manufacturing by 3D Plasma Metal Deposition for Graded Structures of Super Duplex Alloy 1.4410 and the Austenitic Corrosion Resistant Alloy 1.4404. *Jom*, 71(4):1554–1559, apr 2019. ISSN 15431851. doi: 10.1007/s11837-019-03356-4.

[30] Sandy Moghazi, Tonya Wolfe, Douglas Ivey, and Hani Henein. Plasma Transfer Arc Additive Manufacturing of 17-4 PH: Assessment of Defects. *The International Journal of Advanced Manufacturing Technology*, In press, 2020.

[31] Sagar H. Nikam and Neelesh Kumar Jain. 3D-finite element simulation and image processing based prediction of width and height of single-layer deposition by micro-plasma-transferred arc process. *The International Journal of Advanced Manufacturing Technology 2017 95:9*, 95(9):3679–3691, dec 2017. ISSN 1433-3015. doi: 10.1007/S00170-017-1472-X. URL https://link.springer.com/article/10.1007/s00170-017-1472-x.

[32] J. J. Lin, Y. H. Lv, Y. X. Liu, B. S. Xu, Z. Sun, Z. G. Li, and Y. X. Wu. Microstructural evolution and mechanical properties of Ti-6Al-4V wall deposited by pulsed plasma arc additive manufacturing. *Materials and Design*, 102:30–40, jul 2016. ISSN 18734197. doi: 10.1016/j.matdes.2016.04.018.

[33] Jianjun Lin, Yaohui Lv, Yuxin Liu, Zhe Sun, Kaibo Wang, Zhuguo Li, Yixiong Wu, and Binshi Xu. Microstructural evolution and mechanical property of Ti-6Al-4V wall deposited by continuous plasma arc additive manufacturing without post heat treatment. *Journal of the Mechanical Behavior of Biomedical Materials*, 69:19–29, may 2017. ISSN 18780180. doi: 10.1016/j.jmbbm.2016.12.015.

[34] Fujia Xu, Yaohui Lv, Yuxin Liu, Fengyuan Shu, Peng He, and Binshi Xu. Microstructural Evolution and Mechanical Properties of Inconel 625 Alloy during Pulsed Plasma Arc Deposition Process. *Journal of Materials Science and Technology*, 29(5):480–488, may 2013. ISSN 10050302. doi: 10.1016/j.jmst.2013.02.010.

[35] J.G. Mercado Rojas, T. Wolfe, B.A. Fleck, and Ahmed Jawad Qureshi. Plasma transferred arc additive manufacturing of Nickel metal matrix composites. *Manufacturing Letters*, 18:31–34, oct 2018. doi: 10.1016/J.MFGLET.2018.10.001.

[36] Jose Guadalupe Mercado Rojas, Morteza Ghasri-Khouzani, Tonya Wolfe, Brian Fleck, Hani Henein, and Ahmed Jawad Qureshi. Preliminary geometrical and microstructural characterization of WC-reinforced NiCrBSi matrix composites fabricated by plasma transferred arc additive manufacturing through Taguchi-based experimentation. *The International Journal of Advanced Manufacturing Technology*, 113(5):1451–1468, 2021. ISSN 1433-3015. doi: 10.1007/s00170-020-06388-2. URL https://doi.org/10.1007/s00170-020-06388-2.

[37] P C Collins, D A Brice, P Samimi, I Ghamarian, and H L Fraser. Microstructural Control of Additively Manufactured Metallic Materials. *Annual Review of Materials Research*, 46(1):63–91, jul 2016. ISSN 1531-7331. doi: 10.1146/annurev-matsci-070115-031816. URL https://doi.org/10.1146/annurev-matsci-070115-031816.

[38] T. DebRoy, H. L. Wei, J. S. Zuback, T. Mukherjee, J. W. Elmer, J. O. Milewski, A. M. Beese, A. Wilson-Heid, A. De, and W. Zhang. Additive manufacturing of metallic components – Process, structure and properties. *Progress in Materials Science*, 92: 112–224, mar 2018. ISSN 0079-6425. doi: 10.1016/J.PMATSCI.2017.10.001.

[39] John J. Lewandowski and Mohsen Seifi. Metal Additive Manufacturing: A Review of Mechanical Properties. *Annual Review of Materials Research*, 46(1):151–186, 2016. ISSN 1531-7331. doi: 10.1146/annurev-matsci-070115-032024. URL http://www.annualreviews.org/doi/10.1146/annurev-matsci-070115-032024.

[40] Z Kamdi, P H Shipway, K T Voisey, and A J Sturgeon. Abrasive wear behaviour of conventional and large-particle tungsten carbide-based cermet coatings as a function of abrasive size and type. *Wear*, 271(9):1264–1272, 2011. ISSN 0043-1648. doi: https://doi.org/10.1016/j.wear.2010.12.060. URL https://www.sciencedirect.com/science/article/pii/S0043164811002353.

[41] A Neville, F Reza, S Chiovelli, and T Revega. Erosion–corrosion behaviour of WC-based MMCs in liquid–solid slurries. *Wear*, 259(1):181–195, 2005. ISSN 0043-1648. doi: https://doi.org/10.1016/j.wear.2005.02.037. URL https://www.sciencedirect.com/science/article/pii/S0043164805001201.

[42] Gary Fisher, Tonya Wolfe, and Kim Meszaros. The Effects of Carbide Characteristics on the Performance of Tungsten Carbide-Based Composite Overlays, Deposited by

Plasma-Transferred Arc Welding. *Journal of Thermal Spray Technology*, 22(5):764–771, 2013. ISSN 1544-1016. doi: 10.1007/s11666-012-9877-4. URL https://doi.org/10.1007/s11666-012-9877-4.

[43] T. Liyanage, G. Fisher, and A. P. Gerlich. Influence of alloy chemistry on microstructure and properties in NiCrBSi overlay coatings deposited by plasma transferred arc welding (PTAW). *Surface and Coatings Technology*, 205(3):759–765, 2010. ISSN 02578972. doi: 10.1016/j.surfcoat.2010.07.095. URL http://dx.doi.org/10.1016/j.surfcoat.2010.07.095.

[44] Tuan D. Ngo, Alireza Kashani, Gabriele Imbalzano, Kate T.Q. Nguyen, and David Hui. Additive manufacturing (3D printing): A review of materials, methods, applications and challenges. *Composites Part B: Engineering*, 143:172–196, jun 2018. ISSN 13598368. doi: 10.1016/j.compositesb.2018.02.012.

[45] Joshua Bard, Dana Cupkova, Newell Washburn, and Garth Zeglin. Robotic concrete surface finishing: a moldless approach to creating thermally tuned surface geometry for architectural building components using Profile-3D-Printing. *Construction Robotics*, 2 (1):53–65, 2018. ISSN 2509-8780. doi: 10.1007/s41693-018-0014-x.

[46] ISO 17296-2 - Additive manufacturing - General principles - Part 2: Overview of process categories and feedstock - First Edition, 2015.

[47] Aurora Labs, 2014. URL http://auroralabs3d.com/.

[48] Additive Manufacturing Machines & Materials | GE Additive. URL https://www.ge.com/additive/.

[49] Xact Metal: Accessible, High-Caliber 3D Metal Printing is Here. URL https://www.xactmetal.com/.

[50] Jérémie Dumas, Jean Hergel, and Sylvain Lefebvre. Bridging the gap: Automated steady scaffoldings for 3D printing. *ACM Transactions on Graphics*, 33(4):1–10, jul 2014. ISSN 15577333. doi: 10.1145/2601097.2601153.

[51] Kailun Hu, Shuo Jin, and Charlie C.L. Wang. Support slimming for single material based additive manufacturing. *CAD Computer Aided Design*, 65:1–10, aug 2015. ISSN 00104485. doi: 10.1016/j.cad.2015.03.001.

[52] Di Wang, Yongqiang Yang, Ruicheng Liu, Dongming Xiao, and Jianfeng Sun. Study on the designing rules and processability of porous structure based on selective laser melting (SLM). *Journal of Materials Processing Technology*, 213(10):1734–1742, oct 2013. ISSN 09240136. doi: 10.1016/j.jmatprotec.2013.05.001.

[53] Daniel Thomas, Hons Computer, and Aided Product. *The Development of Design Rules for Selective Laser Melting The Development of Design Rules for Selective Laser Melting*. Universiy of Wales Institute Cardiff, 2010.

[54] F. Calignano. Design optimization of supports for overhanging structures in aluminum and titanium alloys by selective laser melting. *Materials and Design*, 64:203–213, dec 2014. ISSN 18734197. doi: 10.1016/j.matdes.2014.07.043.

[55] Renishaw plc. Educational article - Design for metal AM - A beginner ' s guide, 2017. URL http://www.renishaw.com/en/design-for-metal-am-a-beginners-guide-feature--43333.

[56] Yaoyu Ding, Rajeev Dwivedi, and Radovan Kovacevic. Process planning for 8-axis robotized laser-based direct metal deposition system: A case on building revolved part. *Robotics and Computer-Integrated Manufacturing*, 44:67–76, apr 2017. ISSN 07365845. doi: 10.1016/j.rcim.2016.08.008.

[57] Prabhjot Singh and Debasish Dutta. Multi-direction slicing for layered manufacturing. *Journal of Computing and Information Science in Engineering*, 1(2):129–142, jun 2001. ISSN 15309827. doi: 10.1115/1.1375816.

[58] Rajeev Dwivedi and Radovan Kovacevic. An expert system for generation of machine inputs for laser-based multi-directional metal deposition. *International Journal of Machine Tools and Manufacture*, 46(14):1811–1822, nov 2006. ISSN 08906955. doi: 10.1016/j.ijmachtools.2005.11.008.

[59] Rajeev Dwivedi and Radovan Kovacevic. Automated torch path planning using polygon subdivision for solid freeform fabrication based on welding. *Journal of Manufacturing Systems*, 23(4):278–291, jan 2004. ISSN 02786125. doi: 10.1016/S0278-6125(04)80040-2.

[60] Jayaprakash Sharma Panchagnula and Suryakumar Simhambhatla. Additive manufacturing of complex shapes through weld-deposition and feature based slicing. In *ASME*

International Mechanical Engineering Congress and Exposition, Proceedings (IMECE), volume 2A-2015, page V02AT02A004. ASME, nov 2015. ISBN 9780791857359. doi: 10.1115/IMECE2015-51583.

[61] Jayaprakash Sharma Panchagnula and Suryakumar Simhambhatla. Manufacture of complex thin-walled metallic objects using weld-deposition based additive manufacturing. *Robotics and Computer-Integrated Manufacturing*, 49:194–203, feb 2018. ISSN 07365845. doi: 10.1016/j.rcim.2017.06.003.

[62] Pinar Urhal, Andrew Weightman, Carl Diver, and Paulo Bartolo. Robot assisted additive manufacturing: A review. *Robotics and Computer-Integrated Manufacturing*, 59:335–345, oct 2019. ISSN 07365845. doi: 10.1016/j.rcim.2019.05.005.

[63] Bert Lauwers, Fritz Klocke, Andreas Klink, A. Erman Tekkaya, Reimund Neugebauer, and Don McIntosh. Hybrid processes in manufacturing. *CIRP Annals - Manufacturing Technology*, 63(2):561–583, jan 2014. ISSN 17260604. doi: 10.1016/j.cirp.2014.05.003.

[64] Z. Zhu, V. G. Dhokia, A. Nassehi, and S. T. Newman. A review of hybrid manufacturing processes - State of the art and future perspectives. *International Journal of Computer Integrated Manufacturing*, 26(7):596–615, jul 2013. ISSN 13623052. doi: 10.1080/0951192X.2012.749530.

[65] Aydin Nassehi, Stephen Newman, Vimal Dhokia, Zicheng Zhu, and Reza Imani Asrai. Using formal methods to model hybrid manufacturing processes. In *Enabling Manufacturing Competitiveness and Economic Sustainability*, pages 52–56, Berlin, Heidelberg, 2012. Springer Berlin Heidelberg. doi: 10.1007/978-3-642-23860-4_8.

[66] Stephen T. Newman, Zicheng Zhu, Vimal Dhokia, and Alborz Shokrani. Process planning for additive and subtractive manufacturing technologies. *CIRP Annals - Manufacturing Technology*, 64(1):467–470, jan 2015. ISSN 17260604. doi: 10.1016/j.cirp.2015.04.109.

[67] K. P. Karunakaran, S. Suryakumar, Vishal Pushpa, and Sreenathbabu Akula. Low cost integration of additive and subtractive processes for hybrid layered manufacturing. *Robotics and Computer-Integrated Manufacturing*, 26(5):490–499, oct 2010. ISSN 07365845. doi: 10.1016/j.rcim.2010.03.008.

[68] Xinhong Xiong, Haiou Zhang, and Guilan Wang. Metal direct prototyping by using hybrid plasma deposition and milling. *Journal of Materials Processing Technology*, 209 (1):124–130, jan 2009. ISSN 09240136. doi: 10.1016/j.jmatprotec.2008.01.059.

[69] Lan Ren, Todd Sparks, Jianzhong Ruan, and Frank Liou. Integrated process planning for a multiaxis hybrid manufacturing system. *Journal of Manufacturing Science and Engineering, Transactions of the ASME*, 132(2):0210061–0210067, apr 2010. ISSN 10871357. doi: 10.1115/1.4001122.

[70] Zicheng Zhu, Vimal Dhokia, Stephen T. Newman, and Aydin Nassehi. Application of a hybrid process for high precision manufacture of difficult to machine prismatic parts. *International Journal of Advanced Manufacturing Technology*, 74(5-8):1115–1132, sep 2014. ISSN 14333015. doi: 10.1007/s00170-014-6053-7.

[71] Olivier Kerbrat, Pascal Mognol, and Jean Yves Hascoët. A new DFM approach to combine machining and additive manufacturing. *Computers in Industry*, 62(7):684–692, sep 2011. ISSN 01663615. doi: 10.1016/j.compind.2011.04.003.

[72] Bryce Salmi. The World's Largest 3D Metal Printer Is Churning Out Rockets, 2019. URL https://spectrum.ieee.org/aerospace/space-flight/the-worlds-largest-3d-metal-printer-is-churning-out-rockets.

[73] Joris Peels. MX3D Uses Robot Arm to Make 3D Printed Robot Arm, Installs It on Robot, 2020. URL https://3dprint.com/270122/mx3d-uses-robot-arm-to-3d-print-robot-arm-installs-it-on-robot-d/.

[74] Yaoyu Ding and Radovan Kovacevic. Feasibility Study on 3-D Printing of Metallic Structural Materials with Robotized Laser-Based Metal Additive Manufacturing. *Jom*, 68(7):1774–1779, jul 2016. ISSN 15431851. doi: 10.1007/s11837-016-1929-7.

[75] Yaoyu Ding, James Warton, and Radovan Kovacevic. Development of sensing and control system for robotized laser-based direct metal addition system. *Additive Manufacturing*, 10:24–35, apr 2016. ISSN 22148604. doi: 10.1016/j.addma.2016.01.002.

[76] Huadong Zheng, Ming Cong, Dong Liu, Yi Liu, and Yu Du. Automatic path and trajectory planning for laser cladding robot based on CAD. In *2016 IEEE International Conference on Mechatronics and Automation, IEEE ICMA 2016*, pages 1338–1343. IEEE, aug 2016. ISBN 9781509023943. doi: 10.1109/ICMA.2016.7558757.

[77] Guocai Ma, Gang Zhao, Zhihao Li, and Wenlei Xiao. A Path Planning Method for Robotic Wire and Arc Additive Manufacturing of Thin-Walled Structures with Varying Thickness. *IOP Conference Series: Materials Science and Engineering*, 470(1), 2019. ISSN 1757899X. doi: 10.1088/1757-899X/470/1/012018.

[78] Michael Sheetz. Relativity, a company 3D printing entire rockets, raises $140 million from venture firms Bond, Tribe, 2019. URL https://www.cnbc.com/2019/10/01/rocket-builder-relativity-raises-140-million-from-mary-meeker-others.html.

[79] MX3D, 2020. URL https://mx3d.com/.

[80] AML3D, 2020. URL https://aml3d.com/.

[81] AMFG. Thinking Big: 4 Impressive Applications of Large-Scale 3D Printing, 2019. URL https://amfg.ai/2019/04/02/thinking-big-4-impressive-applications-of-large-scale-3d-printing/.

[82] Ahmed H. Maamoun, Mohamed Elbestawi, Goulnara K. Dosbaeva, and Stephen C. Veldhuis. Thermal post-processing of AlSi10Mg parts produced by Selective Laser Melting using recycled powder. *Additive Manufacturing*, 21:234–247, may 2018. ISSN 22148604. doi: 10.1016/j.addma.2018.03.014.

[83] A M Paradowska, J W H Price, R Ibrahim, and T R Finlayson. The effect of heat input on residual stress distribution of steel welds measured by neutron diffraction. *Journal of Achievements in Materials and Manufacturing Engineering*, 17(1):385–388, 2006.

[84] Elham Mirkoohi, James R. Dobbs, and Steven Y. Liang. Analytical modeling of residual stress in direct metal deposition considering scan strategy. *International Journal of Advanced Manufacturing Technology*, 106(9-10):4105–4121, feb 2020. ISSN 14333015. doi: 10.1007/s00170-019-04919-0.

[85] Donghong Ding, Zengxi Pan, Dominic Cuiuri, and Huijun Li. A tool-path generation strategy for wire and arc additive manufacturing. *International Journal of Advanced Manufacturing Technology*, 73(1-4):173–183, jul 2014. ISSN 14333015. doi: 10.1007/s00170-014-5808-5.

[86] Donghong Ding, Zengxi Pan, Dominic Cuiuri, and Huijun Li. A practical path planning methodology for wire and arc additive manufacturing of thin-walled structures. *Robotics and Computer-Integrated Manufacturing*, 34:8–19, aug 2015. ISSN 07365845. doi: 10.1016/j.rcim.2015.01.003.

[87] Donghong Ding, Zengxi Pan, Dominic Cuiuri, Huijun Li, and Nathan Larkin. Adaptive path planning for wire-feed additive manufacturing using medial axis transformation. *Journal of Cleaner Production*, 133:942–952, oct 2016. ISSN 09596526. doi: 10.1016/j.jclepro.2016.06.036.

[88] Shuo Yin, Pasquale Cavaliere, Barry Aldwell, Richard Jenkins, Hanlin Liao, Wenya Li, and Rocco Lupoi. Cold spray additive manufacturing and repair: Fundamentals and applications. *Additive Manufacturing*, 21:628 – 650, 2018. ISSN 2214-8604. doi: https://doi.org/10.1016/j.addma.2018.04.017.

[89] Yannick Cormier, Philippe Dupuis, Aslan Farjam, Antoine Corbeil, and Bertrand Jodoin. Additive manufacturing of pyramidal pin fins: Height and fin density effects under forced convection. *International Journal of Heat and Mass Transfer*, 75:235 – 244, 2014. ISSN 0017-9310. doi: https://doi.org/10.1016/j.ijheatmasstransfer.2014.03.053.

[90] Philippe Dupuis, Yannick Cormier, Marianne Fenech, and Bertrand Jodoin. Heat transfer and flow structure characterization for pin fins produced by cold spray additive manufacturing. *International Journal of Heat and Mass Transfer*, 98:650 – 661, 2016. ISSN 0017-9310. doi: https://doi.org/10.1016/j.ijheatmasstransfer.2016.03.069.

[91] J. Dutta Majumdar, A. Pinkerton, Z. Liu, I. Manna, and L. Li. Microstructure characterisation and process optimization of laser assisted rapid fabrication of 316L stainless steel. *Applied Surface Science*, 247(1-4):320–327, jul 2005. ISSN 01694332. doi: 10.1016/j.apsusc.2005.01.039.

[92] A A Adeyemi, ET Akinlabi, R M Mahamood, K O Sanusi, S Pityana, and M Tlotleng. Influence of laser power on microstructure of laser metal deposited 17-4 ph stainless steel. *IOP Conference Series: Materials Science and Engineering*, 225:012028, aug 2017. ISSN 1757-8981. doi: 10.1088/1757-899x/225/1/012028.

[93] Sabina Luisa Campanelli, Andrea Angelastro, Carmine Gabriele Signorile, and Giuseppe Casalino. Investigation on direct laser powder deposition of 18 Ni (300)

marage steel using mathematical model and experimental characterisation. *International Journal of Advanced Manufacturing Technology*, 89(1-4):885–895, mar 2017. ISSN 14333015. doi: 10.1007/s00170-016-9135-x.

[94] Nancy Yang, J. Yee, B. Zheng, K. Gaiser, T. Reynolds, L. Clemon, W. Y. Lu, J. M. Schoenung, and E. J. Lavernia. Process-Structure-Property Relationships for 316L Stainless Steel Fabricated by Additive Manufacturing and Its Implication for Component Engineering. *Journal of Thermal Spray Technology*, 26(4):610–626, apr 2017. ISSN 10599630. doi: 10.1007/s11666-016-0480-y.

[95] Kai Zhang, Shijie Wang, Weijun Liu, and Xiaofeng Shang. Characterization of stainless steel parts by Laser Metal Deposition Shaping. *Materials and Design*, 55:104–119, mar 2014. ISSN 18734197. doi: 10.1016/j.matdes.2013.09.006.

[96] M. L. Griffith, M. T. Ensz, J. D. Puskar, C. V. Robino, J. A. Brooks, J. A. Philliber, J. E. Smugeresky, and W. H. Hofmeister. Understanding the microstructure and properties of components fabricated by Laser Engineered Net Shaping (LENS). *Materials Research Society Symposium - Proceedings*, 625(1):9–20, nov 2000. ISSN 02729172. doi: 10.1557/PROC-625-9.

[97] J. Yu, M. Rombouts, and G. Maes. Cracking behavior and mechanical properties of austenitic stainless steel parts produced by laser metal deposition. *Materials and Design*, 45:228–235, mar 2013. ISSN 18734197. doi: 10.1016/j.matdes.2012.08.078.

[98] Jin Yao, Tao Suo, Shuangyin Zhang, Feng Zhao, Hongtao Wang, Jiabin Liu, Yuzeng Chen, and Yulong Li. Influence of heat-treatment on the dynamic behavior of 3D laser-deposited Ti-6Al-4V alloy. *Materials Science and Engineering A*, 677:153–162, nov 2016. ISSN 09215093. doi: 10.1016/j.msea.2016.09.036.

[99] Amanda J. Sterling, Brian Torries, Nima Shamsaei, Scott M. Thompson, and Denver W. Seely. Fatigue behavior and failure mechanisms of direct laser deposited Ti-6Al-4V. *Materials Science and Engineering A*, 655:100–112, 2016. ISSN 09215093. doi: 10.1016/j.msea.2015.12.026.

[100] Y. Lu, H. B. Tang, Y. L. Fang, D. Liu, and H. M. Wang. Microstructure evolution of sub-critical annealed laser deposited Ti-6Al-4V alloy. *Materials and Design*, 37:56–63, 2012. ISSN 02641275. doi: 10.1016/j.matdes.2011.12.016.

[101] Shuangyin Zhang, Xin Lin, Jing Chen, and Weidong Huang. Heat-treated microstructure and mechanical properties of laser solid forming Ti-6Al-4V alloy. *Rare Metals*, 28 (6):537–544, dec 2009. ISSN 10010521. doi: 10.1007/s12598-009-0104-5.

[102] Peng Hui Li, Wei Guo Guo, Wei Dong Huang, Yu Su, Xin Lin, and Kang Bo Yuan. Thermomechanical response of 3D laser-deposited Ti-6Al-4V alloy over a wide range of strain rates and temperatures. *Materials Science and Engineering A*, 647:34–42, oct 2015. ISSN 09215093. doi: 10.1016/j.msea.2015.08.043.

[103] Beth E. Carroll, Todd A. Palmer, and Allison M. Beese. Anisotropic tensile behavior of Ti-6Al-4V components fabricated with directed energy deposition additive manufacturing. *Acta Materialia*, 87:309–320, apr 2015. ISSN 13596454. doi: 10.1016/j.actamat.2014.12.054.

[104] Chunlei Qiu, G. A. Ravi, Chris Dance, Andrew Ranson, Steve Dilworth, and Moataz M. Attallah. Fabrication of large Ti-6Al-4V structures by direct laser deposition. *Journal of Alloys and Compounds*, 629:351–361, apr 2015. ISSN 09258388. doi: 10.1016/j.jallcom.2014.12.234.

[105] Allen Bagheri, Nima Shamsaei, and Scott M. Thompson. Microstructure and mechanical properties of ti-6al-4v parts fabricated by laser engineered net shaping. In *ASME International Mechanical Engineering Congress and Exposition, Proceedings (IMECE)*, volume 2A-2015. American Society of Mechanical Engineers, nov 2015. ISBN 9780791857359. doi: 10.1115/IMECE2015-51698.

[106] Yuwei Zhai, Haize Galarraga, and Diana A. Lados. Microstructure, static properties, and fatigue crack growth mechanisms in Ti-6Al-4V fabricated by additive manufacturing: LENS and EBM. *Engineering Failure Analysis*, 69:3–14, nov 2016. ISSN 13506307. doi: 10.1016/j.engfailanal.2016.05.036.

[107] Yuwei Zhai, Diana A Lados, Eric J Brown, and Gregory N Vigilante. Understanding the microstructure and mechanical properties of Ti-6Al-4V and Inconel 718 alloys manufactured by Laser Engineered Net Shaping. *Additive Manufacturing*, 27:334–344, 2019. ISSN 2214-8604. doi: https://doi.org/10.1016/j.addma.2019.02.017.

[108] T. Wang, Y. Y. Zhu, S. Q. Zhang, H. B. Tang, and H. M. Wang. Grain morphology evolution behavior of titanium alloy components during laser melting deposition additive manufacturing. *Journal of Alloys and Compounds*, 632:505–513, may 2015. ISSN 09258388. doi: 10.1016/j.jallcom.2015.01.256.

[109] Fei Lv, Lida Shen, Huixin Liang, Deqiao Xie, Changjiang Wang, and Zongjun Tian. Mechanical properties of AlSi10Mg alloy fabricated by laser melting deposition and improvements via heat treatment. *Optik*, 179:8–18, feb 2019. ISSN 00304026. doi: 10.1016/j.ijleo.2018.10.112.

[110] Parnian Kiani, Alexander D Dupuy, Kaka Ma, and Julie M Schoenung. Directed energy deposition of AlSi10Mg: Single track nonscalability and bulk properties. *Materials & Design*, 194:108847, 2020. ISSN 0264-1275. doi: https://doi.org/10.1016/j.matdes.2020.108847.

[111] Fabrizia Caiazzo, Vittorio Alfieri, Paolo Argenio, and Vincenzo Sergi. Additive manufacturing by means of laser-aided directed metal deposition of 2024 aluminium powder: Investigation and optimization. *Advances in Mechanical Engineering*, 9(8):1–12, aug 2017. ISSN 16878140. doi: 10.1177/1687814017714982.

[112] Bo Chen, Yongzhen Yao, Xiaoguo Song, Caiwang Tan, Liang Cao, and Jicai Feng. Microstructure and mechanical properties of additive manufacturing AlSi10Mg alloy using direct metal deposition. *Ferroelectrics*, 523(1):153–166, jan 2018. ISSN 15635112. doi: 10.1080/00150193.2018.1392147.

[113] Yang Liu, Chao Liu, Wensheng Liu, Yunzhu Ma, Siwei Tang, Chaoping Liang, Qingshan Cai, and Cheng Zhang. Optimization of parameters in laser powder deposition AlSi10Mg alloy using Taguchi method. *Optics and Laser Technology*, 111(October 2018):470–480, 2019. ISSN 00303992. doi: 10.1016/j.optlastec.2018.10.030.

[114] Xian Wang, Liqun Li, Jingyu Qu, and Wang Tao. Microstructure and mechanical properties of laser metal deposited AlSi10Mg alloys. *Materials Science and Technology (United Kingdom)*, 35(18):2284–2293, dec 2019. ISSN 17432847. doi: 10.1080/02670836.2019.1674022.

[115] Tao Gu, Bo Chen, Caiwang Tan, and Jicai Feng. Microstructure evolution and mechanical properties of laser additive manufacturing of high strength Al-Cu-Mg alloy. *Optics and Laser Technology*, 112:140–150, apr 2019. ISSN 00303992. doi: 10.1016/j.optlastec.2018.11.008.

[116] P. Ganesh, R. Kaul, C. P. Paul, Pragya Tiwari, S. K. Rai, R. C. Prasad, and L. M. Kukreja. Fatigue and fracture toughness characteristics of laser rapid manufactured Inconel 625 structures. *Materials Science and Engineering A*, 527(29-30):7490–7497, nov 2010. ISSN 09215093. doi: 10.1016/j.msea.2010.08.034.

[117] Chongliang Zhong, Jochen Kittel, Andres Gasser, and Johannes Henrich Schleifenbaum. Study of nickel-based super-alloys Inconel 718 and Inconel 625 in high-deposition-rate laser metal deposition. *Optics and Laser Technology*, 109:352–360, jan 2019. ISSN 00303992. doi: 10.1016/j.optlastec.2018.08.003.

[118] Y L Hu, Y L Li, S Y Zhang, X Lin, Z H Wang, and W D Huang. Effect of solution temperature on static recrystallization and ductility of Inconel 625 superalloy fabricated by directed energy deposition. *Materials Science and Engineering: A*, 772:138711, 2020. ISSN 0921-5093. doi: https://doi.org/10.1016/j.msea.2019.138711.

[119] H. Qi, M. Azer, and A. Ritter. Studies of standard heat treatment effects on microstructure and mechanical properties of laser net shape manufactured INCONEL 718. *Metallurgical and Materials Transactions A: Physical Metallurgy and Materials Science*, 40(10):2410–2422, 2009. ISSN 10735623. doi: 10.1007/s11661-009-9949-3.

[120] Zuo Li, Jing Chen, Shang Sui, Chongliang Zhong, Xufei Lu, and Xin Lin. The microstructure evolution and tensile properties of Inconel 718 fabricated by high-deposition-rate laser directed energy deposition. *Additive Manufacturing*, 31:100941, 2020. ISSN 2214-8604. doi: https://doi.org/10.1016/j.addma.2019.100941.

[121] Mingming Ma, Zemin Wang, and Xiaoyan Zeng. Effect of energy input on microstructural evolution of direct laser fabricated IN718 alloy. *Materials Characterization*, 106: 420–427, jul 2015. ISSN 10445803. doi: 10.1016/j.matchar.2015.06.027.

[122] Xiaoming Zhao, Jing Chen, Xin Lin, and Weidong Huang. Study on microstructure and mechanical properties of laser rapid forming Inconel 718. *Materials Science and Engineering A*, 478(1-2):119–124, apr 2008. ISSN 09215093. doi: 10.1016/j.msea.2007.05.079.

[123] Chongliang Zhong, Andres Gasser, Jochen Kittel, Konrad Wissenbach, and Reinhart Poprawe. Improvement of material performance of Inconel 718 formed by high deposition-rate laser metal deposition. *Materials and Design*, 98:128–134, may 2016. ISSN 18734197. doi: 10.1016/j.matdes.2016.03.006.

[124] Yachao Wang and Jing Shi. Recrystallization behavior and tensile properties of laser metal deposited Inconel 718 upon in-situ ultrasonic impact peening and heat treatment. *Materials Science and Engineering: A*, 786:139434, 2020. ISSN 0921-5093. doi: https://doi.org/10.1016/j.msea.2020.139434.

[125] P D Nezhadfar, Alexander S Johnson, and Nima Shamsaei. Fatigue behavior and microstructural evolution of additively manufactured Inconel 718 under cyclic loading at elevated temperature. *International Journal of Fatigue*, 136:105598, 2020. ISSN 0142-1123. doi: https://doi.org/10.1016/j.ijfatigue.2020.105598.

[126] Kellen D. Traxel and Amit Bandyopadhyay. First Demonstration of Additive Manufacturing of Cutting Tools using Directed Energy Deposition System: Stellite™-Based Cutting Tools. *Additive Manufacturing*, 25:460–468, jan 2019. ISSN 22148604. doi: 10.1016/j.addma.2018.11.019.

[127] Kedar Mallik Mantrala, Mitun Das, Vamsi Krishna Balla, Ch. Srinivasa Rao, and V. V. S. Kesava Rao. Additive Manufacturing of Co-Cr-Mo Alloy: Influence of Heat Treatment on Microstructure, Tribological, and Electrochemical Properties. *Frontiers in Mechanical Engineering*, 1, mar 2015. ISSN 2297-3079. doi: 10.3389/fmech.2015.00002.

[128] Ziyad Smoqi, Joshua Toddy, Harold (Scott) Halliday, Jeffrey E. Shield, and Prahalada Rao. Process-structure relationship in the directed energy deposition of cobalt-chromium alloy (Stellite 21) coatings. *Materials and Design*, 197:109229, 2021. ISSN 18734197. doi: 10.1016/j.matdes.2020.109229.

[129] G. D. Janaki Ram, C. K. Esplin, and B. E. Stucker. Microstructure and wear properties of LENS® deposited medical grade CoCrMo. *Journal of Materials Science: Materials in Medicine*, 19(5):2105–2111, may 2008. ISSN 09574530. doi: 10.1007/s10856-007-3078-6.

[130] Minlin Zhong, Wenjin Liu, Guoqing Ning, Lin Yang, and Yanxia Chen. Laser direct manufacturing of tungsten nickel collimation component. *Journal of Materials Processing Technology*, 147(2):167–173, apr 2004. ISSN 09240136. doi: 10.1016/j.jmatprotec.2003.12.009.

[131] N. Chekir, Y. Tian, J. J. Sixsmith, and M. Brochu. Effect of travel speed and sub-β transus post deposition heat treatments on thin Ti-6Al-4V laser wire deposits. *Materials Science and Engineering A*, 724:376–384, may 2018. ISSN 09215093. doi: 10.1016/j.msea.2018.03.100.

[132] Bernd Baufeld, Erhard Brandl, and Omer Van Der Biest. Wire based additive layer manufacturing: Comparison of microstructure and mechanical properties of Ti-6Al-4V components fabricated by laser-beam deposition and shaped metal deposition. *Journal of Materials Processing Technology*, 211(6):1146–1158, 2011. ISSN 09240136. doi: 10.1016/j.jmatprotec.2011.01.018.

[133] Erhard Brandl, Frank Palm, Vesselin Michailov, Bernd Viehweger, and Christoph Leyens. Mechanical properties of additive manufactured titanium (Ti-6Al-4V) blocks deposited by a solid-state laser and wire. *Materials and Design*, 32(10):4665–4675, 2011. ISSN 02641275. doi: 10.1016/j.matdes.2011.06.062.

[134] N. Chekir, Y. Tian, R. Gauvin, N. Brodusch, J. J. Sixsmith, and M. Brochu. Laser Wire Deposition of Thick Ti-6Al-4V Buildups: Heat Transfer Model, Microstructure, and Mechanical Properties Evaluations. *Metallurgical and Materials Transactions A: Physical Metallurgy and Materials Science*, 49(12):6490–6508, dec 2018. ISSN 10735623. doi: 10.1007/s11661-018-4927-2.

[135] Y. N. Zhang, X. Cao, P. Wanjara, and M. Medraj. Oxide films in laser additive manufactured Inconel 718. *Acta Materialia*, 61(17):6562–6576, oct 2013. ISSN 13596454. doi: 10.1016/j.actamat.2013.07.039.

[136] C. V. Haden, G. Zeng, F. M. Carter, C. Ruhl, B. A. Krick, and D. G. Harlow. Wire and arc additive manufactured steel: Tensile and wear properties. *Additive Manufacturing*, 16:115–123, aug 2017. ISSN 22148604. doi: 10.1016/j.addma.2017.05.010.

[137] Vittoria Laghi, Michele Palermo, Lavinia Tonelli, Giada Gasparini, Lorella Ceschini, and Tomaso Trombetti. Tensile properties and microstructural features of 304L

austenitic stainless steel produced by wire-and-arc additive manufacturing. *International Journal of Advanced Manufacturing Technology*, 106(9-10):3693–3705, feb 2020. ISSN 14333015. doi: 10.1007/s00170-019-04868-8.

[138] Mehran Rafieazad, Mahya Ghaffari, Alireza Vahedi Nemani, and Ali Nasiri. Microstructural evolution and mechanical properties of a low-carbon low-alloy steel produced by wire arc additive manufacturing. *International Journal of Advanced Manufacturing Technology*, 105(5-6):2121–2134, dec 2019. ISSN 14333015. doi: 10.1007/s00170-019-04393-8.

[139] Mariacira Liberini, Antonello Astarita, Gianni Campatelli, Antonio Scippa, Filippo Montevecchi, Giuseppe Venturini, Massimo Durante, Luca Boccarusso, Fabrizio Memola Capece Minutolo, and A. Squillace. Selection of Optimal Process Parameters for Wire Arc Additive Manufacturing. In *Procedia CIRP*, volume 62, pages 470–474. Elsevier B.V., jan 2017. doi: 10.1016/j.procir.2016.06.124.

[140] Van Thao Le and Dinh Si Mai. Microstructural and mechanical characteristics of 308L stainless steel manufactured by gas metal arc welding-based additive manufacturing. *Materials Letters*, 271:127791, jul 2020. ISSN 18734979. doi: 10.1016/j.matlet.2020.127791.

[141] John W. Elmer and Gordon Gibbs. The effect of atmosphere on the composition of wire arc additive manufactured metal components. *Science and Technology of Welding and Joining*, 24(5):367–374, jul 2019. ISSN 17432936. doi: 10.1080/13621718.2019.1605473.

[142] Jonas Lunde, Mostafa Kazemipour, Salar Salahi, and Ali Nasiri. Microstructure and Mechanical Properties of AISI 420 Stainless Steel Produced by Wire Arc Additive Manufacturing. In *Minerals, Metals and Materials Series*, pages 413–424. Springer, 2020. ISBN 9783030362959. doi: 10.1007/978-3-030-36296-6_39.

[143] Leilei Wang, Jiaxiang Xue, and Qiang Wang. Correlation between arc mode, microstructure, and mechanical properties during wire arc additive manufacturing of 316L stainless steel. *Materials Science and Engineering A*, 751:183–190, mar 2019. ISSN 09215093. doi: 10.1016/j.msea.2019.02.078.

[144] Armando Caballero, Jialuo Ding, Supriyo Ganguly, and Stewart Williams. Wire + Arc Additive Manufacture of 17-4 PH stainless steel: Effect of different processing

conditions on microstructure, hardness, and tensile strength. *Journal of Materials Processing Technology*, 268:54–62, jun 2019. ISSN 09240136. doi: 10.1016/j.jmatprotec.2019.01.007.

[145] Wei Wu, Jiaxiang Xue, Leilei Wang, Zhanhui Zhang, Yu Hu, and Changwen Dong. Forming Process, Microstructure, and Mechanical Properties of Thin-Walled 316L Stainless Steel Using Speed-Cold-Welding Additive Manufacturing. *Metals*, 9(1):109, jan 2019. ISSN 2075-4701. doi: 10.3390/met9010109.

[146] Tingting Wang, Yuanbin Zhang, Zhihong Wu, and Chuanwei Shi. Microstructure and properties of die steel fabricated by WAAM using H13 wire. *Vacuum*, 149:185–189, mar 2018. ISSN 0042207X. doi: 10.1016/j.vacuum.2017.12.034.

[147] Xiaohui Chen, Jia Li, Xu Cheng, Bei He, Huaming Wang, and Zheng Huang. Microstructure and mechanical properties of the austenitic stainless steel 316L fabricated by gas metal arc additive manufacturing. *Materials Science and Engineering A*, 703: 567–577, aug 2017. ISSN 09215093. doi: 10.1016/j.msea.2017.05.024.

[148] Bintao Wu, Zengxi Pan, Donghong Ding, Dominic Cuiuri, Huijun Li, and Zhenyu Fei. The effects of forced interpass cooling on the material properties of wire arc additively manufactured Ti6Al4V alloy. *Journal of Materials Processing Technology*, 258:97–105, aug 2018. ISSN 09240136. doi: 10.1016/j.jmatprotec.2018.03.024.

[149] P. M. Sequeira Almeida and S. Williams. Innovative process model of Ti-6Al-4V additive layer manufacturing using cold metal transfer (CMT). In *21st Annual International Solid Freeform Fabrication Symposium - An Additive Manufacturing Conference, SFF 2010*, pages 25–36, 2010.

[150] J. R. Hönnige, P. A. Colegrove, B. Ahmad, M. E. Fitzpatrick, S. Ganguly, T. L. Lee, and S. W. Williams. Residual stress and texture control in Ti-6Al-4V wire + arc additively manufactured intersections by stress relief and rolling. *Materials and Design*, 150:193–205, jul 2018. ISSN 18734197. doi: 10.1016/j.matdes.2018.03.065.

[151] Jian Gou, Junqi Shen, Shengsun Hu, Yinbao Tian, and Ying Liang. Microstructure and mechanical properties of as-built and heat-treated Ti-6Al-4V alloy prepared by cold metal transfer additive manufacturing. *Journal of Manufacturing Processes*, 42: 41–50, jun 2019. ISSN 15266125. doi: 10.1016/j.jmapro.2019.04.012.

[152] Yinbao Tian, Junqi Shen, Shengsun Hu, Zhijiang Wang, and Jian Gou. Microstructure and mechanical properties of wire and arc additive manufactured Ti-6Al-4V and AlSi5 dissimilar alloys using cold metal transfer welding. *Journal of Manufacturing Processes*, 46:337–344, oct 2019. ISSN 15266125. doi: 10.1016/j.jmapro.2019.09.006.

[153] Chen Zhang, Yufei Li, Ming Gao, and Xiaoyan Zeng. Wire arc additive manufacturing of Al-6Mg alloy using variable polarity cold metal transfer arc as power source. *Materials Science and Engineering A*, 711(August 2017):415–423, jan 2018. ISSN 09215093. doi: 10.1016/j.msea.2017.11.084.

[154] A. Horgar, H. Fostervoll, B. Nyhus, X. Ren, M. Eriksson, and O. M. Akselsen. Additive manufacturing using WAAM with AA5183 wire. *Journal of Materials Processing Technology*, 259:68–74, sep 2018. ISSN 09240136. doi: 10.1016/j.jmatprotec.2018.04.014.

[155] Baoqiang Cong, Jialuo Ding, and Stewart Williams. Effect of arc mode in cold metal transfer process on porosity of additively manufactured Al-6.3%Cu alloy. *International Journal of Advanced Manufacturing Technology*, 76(9-12):1593–1606, feb 2015. ISSN 14333015. doi: 10.1007/s00170-014-6346-x.

[156] Xiangfang Xu, Jialuo Ding, Supriyo Ganguly, and Stewart Williams. Investigation of process factors affecting mechanical properties of INCONEL 718 superalloy in wire + arc additive manufacture process. *Journal of Materials Processing Technology*, 265: 201–209, mar 2019. ISSN 09240136. doi: 10.1016/j.jmatprotec.2018.10.023.

[157] D. Clark, M. R. Bache, and M. T. Whittaker. Shaped metal deposition of a nickel alloy for aero engine applications. *Journal of Materials Processing Technology*, 203 (1-3):439–448, jul 2008. ISSN 09240136. doi: 10.1016/j.jmatprotec.2007.10.051.

[158] Cui E. Seow, Harry E. Coules, Guiyi Wu, Raja H.U. Khan, Xiangfang Xu, and Stewart Williams. Wire + Arc Additively Manufactured Inconel 718: Effect of post-deposition heat treatments on microstructure and tensile properties. *Materials and Design*, 183: 108157, dec 2019. ISSN 18734197. doi: 10.1016/j.matdes.2019.108157.

[159] Ivan Jurić, Ivica Garašić, Matija Bušić, and Zoran Kožuh. Influence of Shielding Gas Composition on Structure and Mechanical Properties of Wire and Arc Additive Manufactured Inconel 625. *Jom*, 71(2):703–708, feb 2019. ISSN 15431851. doi: 10.1007/s11837-018-3151-2.

[160] Wang Yangfan, Chen Xizhang, and Su Chuanchu. Microstructure and mechanical properties of Inconel 625 fabricated by wire-arc additive manufacturing. *Surface and Coatings Technology*, 374:116–123, sep 2019. ISSN 02578972. doi: 10.1016/j.surfcoat.2019.05.079.

[161] Hisataka Takagi, Hiroyuki Sasahara, Takeyuki Abe, Hiroki Sannomiya, Shinichiro Nishiyama, Shuichiro Ohta, and Kunimitsu Nakamura. Material-property evaluation of magnesium alloys fabricated using wire-and-arc-based additive manufacturing. *Additive Manufacturing*, 24:498–507, dec 2018. ISSN 22148604. doi: 10.1016/j.addma.2018.10.026.

[162] Thomas Klein, Aurel Arnoldt, Martin Schnall, and Stefan Gneiger. Microstructure Formation and Mechanical Properties of a Wire-Arc Additive Manufactured Magnesium Alloy. *JOM*, 73(4):1126–1134, 2021. ISSN 1543-1851. doi: 10.1007/s11837-021-04567-4.

[163] Ji Bi, Junqi Shen, Shengsun Hu, Yahui Zhen, Fengliang Yin, and Xianzheng Bu. Microstructure and mechanical properties of AZ91 Mg alloy fabricated by cold metal transfer additive manufacturing. *Materials Letters*, 276:10–13, 2020. ISSN 18734979. doi: 10.1016/j.matlet.2020.128185.

[164] Donghong Ding, Zengxi Pan, Stephen van Duin, Huijun Li, and Chen Shen. Fabricating superior NiAl bronze components through wire arc additive manufacturing. *Materials*, 9(8), aug 2016. ISSN 19961944. doi: 10.3390/ma9080652.

[165] Chen Shen, Zengxi Pan, Donghong Ding, Lei Yuan, Ning Nie, Ying Wang, Dongzhi Luo, Dominic Cuiuri, Stephen van Duin, and Huijun Li. The influence of post-production heat treatment on the multi-directional properties of nickel-aluminum bronze alloy fabricated using wire-arc additive manufacturing process. *Additive Manufacturing*, 23:411–421, oct 2018. ISSN 22148604. doi: 10.1016/j.addma.2018.08.008.

[166] G. P. Rajeev, M. R. Rahul, M. Kamaraj, and Srinivasa R. Bakshi. Microstructure and high temperature mechanical properties of wire arc additively deposited Stellite 6 alloy. *Materialia*, 12(January):100724, 2020. ISSN 25891529. doi: 10.1016/j.mtla.2020.100724.

[167] Lei Ji, Jiping Lu, Changmeng Liu, Chenchen Jing, Hongli Fan, and Shuyuan Ma. Microstructure and mechanical properties of 304L steel fabricated by arc additive manufacturing. *MATEC Web of Conferences*, 128:03006, oct 2017. ISSN 2261-236X. doi: 10.1051/matecconf/201712803006.

[168] Oguzhan Yilmaz and Adnan A. Ugla. Microstructure characterization of SS308LSi components manufactured by GTAW-based additive manufacturing: shaped metal deposition using pulsed current arc. *International Journal of Advanced Manufacturing Technology*, 89(1-4):13–25, mar 2017. ISSN 14333015. doi: 10.1007/s00170-016-9053-y.

[169] Bishal Silwal and Michalel Santangelo. Effect of vibration and hot-wire gas tungsten arc (GTA) on the geometric shape. *Journal of Materials Processing Technology*, 251: 138–145, jan 2018. ISSN 09240136. doi: 10.1016/j.jmatprotec.2017.08.010.

[170] Fude Wang, Stewart Williams, and Matthew Rush. Morphology investigation on direct current pulsed gas tungsten arc welded additive layer manufactured Ti6Al4V alloy. *International Journal of Advanced Manufacturing Technology*, 57(5-8):597–603, nov 2011. ISSN 02683768. doi: 10.1007/s00170-011-3299-1.

[171] Bernd Baufeld, Omer Van der Biest, and Rosemary Gault. Additive manufacturing of Ti-6Al-4V components by shaped metal deposition: Microstructure and mechanical properties. *Materials and Design*, 31(SUPPL. 1):S106–S111, jun 2010. ISSN 02641275. doi: 10.1016/j.matdes.2009.11.032.

[172] Jian Wang, Xin Lin, Jiaqiang Li, Aitang Xue, Fenggang Liu, Weidong Huang, and Enquan Liang. A study on obtaining equiaxed prior-β grains of wire and arc additive manufactured Ti-6Al-4V. *Materials Science and Engineering A*, 772:138703, jan 2020. ISSN 09215093. doi: 10.1016/j.msea.2019.138703.

[173] J. Donoghue, A. A. Antonysamy, F. Martina, P. A. Colegrove, S. W. Williams, and P. B. Prangnell. The effectiveness of combining rolling deformation with Wire-Arc Additive Manufacture on β-grain refinement and texture modification in Ti-6Al-4V. *Materials Characterization*, 114:103–114, apr 2016. ISSN 10445803. doi: 10.1016/j.matchar.2016.02.001.

[174] Filomeno Martina, Paul A. Colegrove, Stewart W. Williams, and Jonathan Meyer. Microstructure of Interpass Rolled Wire + Arc Additive Manufacturing Ti-6Al-4V

Components. *Metallurgical and Materials Transactions A: Physical Metallurgy and Materials Science*, 46(12):6103–6118, oct 2015. ISSN 10735623. doi: 10.1007/s11661-015-3172-1.

[175] J. Y. Bai, C. L. Fan, Sb Lin, C. L. Yang, and B. L. Dong. Effects of thermal cycles on microstructure evolution of 2219-Al during GTA-additive manufacturing. *International Journal of Advanced Manufacturing Technology*, 87(9-12):2615–2623, dec 2016. ISSN 14333015. doi: 10.1007/s00170-016-8633-1.

[176] J H Ouyang, H Wang, and R Kovacevic. Rapid prototyping of 5356-aluminum alloy based on variable polarity gas tungsten arc welding: process control and microstructure. *Materials and Manufacturing Processes*, 17(1):103–124, apr 2002. ISSN 1042-6914. doi: 10.1081/AMP-120002801.

[177] Bernd Baufeld. Mechanical properties of INCONEL 718 parts manufactured by shaped metal deposition (SMD). *Journal of Materials Engineering and Performance*, 21(7):1416–1421, jul 2012. ISSN 10599495. doi: 10.1007/s11665-011-0009-y.

[178] Daniel Clark, Martin R. Bache, and Mark T. Whittaker. Microstructural characterization of a polycrystalline nickel-based superalloy processed via tungsten-intert-gas-shaped metal deposition. *Metallurgical and Materials Transactions B: Process Metallurgy and Materials Processing Science*, 41(6):1346–1353, jul 2010. ISSN 10735615. doi: 10.1007/s11663-010-9410-4.

[179] Yanming Guo, Yu Liu, Ard Oerlemans, Songyang Lao, Song Wu, and Michael S Lew. Deep learning for visual understanding: A review. *Neurocomputing*, 187:27–48, 2016. ISSN 0925-2312. doi: https://doi.org/10.1016/j.neucom.2015.09.116. URL https://www.sciencedirect.com/science/article/pii/S0925231215017634.

[180] Yangyang Guo, Houhong Pan, Lingbao Ren, and Gaofeng Quan. Microstructure and mechanical properties of wire arc additively manufactured AZ80M magnesium alloy. *Materials Letters*, 247:4–6, jul 2019. ISSN 18734979. doi: 10.1016/j.matlet.2019.03.063.

[181] Yangyang Guo, Gaofeng Quan, Yinglong Jiang, Lingbao Ren, Lingling Fan, and Houhong Pan. Formability, microstructure evolution and mechanical properties of wire arc additively manufactured AZ80M magnesium alloy using gas tungsten arc welding. *Journal of Magnesium and Alloys*, 9(1):192–201, 2021. ISSN 22139567. doi: 10.1016/j.jma.2020.01.003.

[182] Bosheng Dong, Zengxi Pan, Chen Shen, Yan Ma, and Huijun Li. Fabrication of Copper-Rich Cu-Al Alloy Using the Wire-Arc Additive Manufacturing Process. *Metallurgical and Materials Transactions B: Process Metallurgy and Materials Processing Science*, 48(6):3143–3151, dec 2017. ISSN 10735615. doi: 10.1007/s11663-017-1071-0.

[183] Zixiang Li, Yinan Cui, Jie Wang, Changmeng Liu, Jiachen Wang, Tianqiu Xu, Tao Lu, Haorui Zhang, Jiping Lu, Shuyuan Ma, Hongli Fan, and Shuiyuan Tang. Characterization of microstructure and mechanical properties of stellite 6 part fabricated by wire arc additive manufacturing. *Metals*, 9(4):474, apr 2019. ISSN 20754701. doi: 10.3390/met9040474.

[184] G. Marinelli, F. Martina, S. Ganguly, and S. Williams. Development of Wire + Arc additive manufacture for the production of large-scale unalloyed tungsten components. *International Journal of Refractory Metals and Hard Materials*, 82:329–335, aug 2019. ISSN 22133917. doi: 10.1016/j.ijrmhm.2019.05.009.

[185] Suyog Jhavar, N. K. Jain, and C. P. Paul. Development of micro-plasma transferred arc (μ-PTA) wire deposition process for additive layer manufacturing applications. *Journal of Materials Processing Technology*, 214(5):1102–1110, may 2014. ISSN 09240136. doi: 10.1016/j.jmatprotec.2013.12.016.

[186] Xianghui Ren, Chen Yu, and Wenjie Zhang. The Microstructure and Mechanical Properties of 308L Alloy Fabricated by Micro-plasma Arc Additive Manufacturing. *Journal of Physics: Conference Series*, 1347:12070, 2019. ISSN 1742-6588. doi: 10.1088/1742-6596/1347/1/012070.

[187] Yuehai Feng, Bin Zhan, Jie He, and Kehong Wang. The double-wire feed and plasma arc additive manufacturing process for deposition in Cr-Ni stainless steel. *Journal of Materials Processing Technology*, 259:206–215, sep 2018. ISSN 09240136. doi: 10.1016/j.jmatprotec.2018.04.040.

[188] Joy Gockel, Jack Beuth, and Karen Taminger. Integrated control of solidification microstructure and melt pool dimensions in electron beam wire feed additive manufacturing of ti-6al-4v. *Additive Manufacturing*, 1:119–126, 2014. ISSN 22148604. doi: 10.1016/j.addma.2014.09.004.

[189] Hongbo Suo, Zheyuan Chen, Jianrong Liu, Shuili Gong, and Jianzhong Xiao. Microstructure and Mechanical Properties of Ti-6Al-4V by Electron Beam Rapid Manufacturing. *Rare Metal Materials and Engineering*, 43(4):780–785, 2014. ISSN 1875-5372. doi: https://doi.org/10.1016/S1875-5372(14)60083-7.

[190] Z. Liu, Z. B. Zhao, J. R. Liu, L. Wang, S. X. Zhu, G. Yang, S. L. Gong, Q. J. Wang, and R. Yang. Deformation behaviors of as-built and hot isostatically pressed Ti-6Al-4V alloys fabricated via electron beam rapid manufacturing. *Journal of Materials Science and Technology*, 35(11):2552–2558, 2019. ISSN 10050302. doi: 10.1016/j.jmst.2019.04.032.

[191] Zheng Liu, Zibo Zhao, Jianrong Liu, Lei Wang, Guang Yang, Shuili Gong, Qingjiang Wang, and Rui Yang. Effect of α texture on the tensile deformation behavior of Ti–6Al–4V alloy produced via electron beam rapid manufacturing. *Materials Science and Engineering A*, 742(September 2018):508–516, 2019. ISSN 09215093. doi: 10.1016/j.msea.2018.11.012.

[192] Zheng Liu, Zibo Zhao, Jianrong Liu, Qingjiang Wang, Zhenghua Guo, Zemin Liu, Yida Zeng, Guang Yang, and Shuili Gong. Effects of solution-aging treatments on microstructure features, mechanical properties and damage behaviors of additive manufactured Ti–6Al–4V alloy. *Materials Science and Engineering: A*, 800:140380, 2021. ISSN 0921-5093. doi: https://doi.org/10.1016/j.msea.2020.140380.

[193] Xuewei Tao, Zhengjun Yao, Shasha Zhang, Zhong Li, and Yi Xu. Correlation Between Heat-Treated Microstructure and Mechanical and Fretting Wear Behavior of Electron Beam Freeform-Fabricated Ti6Al4V Alloy. *JOM*, 71(7):2313–2320, jul 2019. ISSN 15431851. doi: 10.1007/s11837-019-03469-w.

[194] Qun Tang, Shengyong Pang, Binbin Chen, Hongbo Suo, and Jianxin Zhou. A three dimensional transient model for heat transfer and fluid flow of weld pool during electron beam freeform fabrication of Ti-6-Al-4-V alloy. *International Journal of Heat and Mass Transfer*, 78:203–215, 2014. ISSN 0017-9310. doi: https://doi.org/10.1016/j.ijheatmasstransfer.2014.06.048.

[195] A Manjunath, V Anandakrishnan, S Ramachandra, and K Parthiban. Experimental investigations on the effect of pre-positioned wire electron beam additive manufacturing process parameters on the layer geometry of titanium 6Al4V. *Materials Today:*

Proceedings, 21:766–772, 2020. ISSN 2214-7853. doi: https://doi.org/10.1016/j.matpr.2019.06.755.

[196] Florian Pixner, Fernando Warchomicka, Patrick Peter, Axel Steuwer, Magnus Hörnqvist Colliander, Robert Pederson, and Norbert Enzinger. Wire-based additive manufacturing of ti-6al-4v using electron beam technique. *Materials*, 13(15), 2020. ISSN 1996-1944. doi: 10.3390/ma13153310.

[197] F Pixner, R Buzolin, S Schönfelder, D Theuermann, F Warchomicka, and N Enzinger. Contactless temperature measurement in wire-based electron beam additive manufacturing Ti-6Al-4V. *Welding in the World*, 2021. ISSN 1878-6669. doi: 10.1007/s40194-021-01097-0.

[198] K N Kalashnikov, V E Rubtsov, N L Savchenko, T A Kalashnikova, K S Osipovich, A A Eliseev, and A V Chumaevskii. The effect of wire feed geometry on electron beam freeform 3D printing of complex-shaped samples from Ti-6Al-4V alloy. *The International Journal of Advanced Manufacturing Technology*, 105(7):3147–3156, 2019. ISSN 1433-3015. doi: 10.1007/s00170-019-04589-y.

[199] Brian J. Hayes, Brian W. Martin, Brian Welk, Samuel J. Kuhr, Thomas K. Ales, David A. Brice, Iman Ghamarian, Andrew H. Baker, Christina V. Haden, D. Gary Harlow, Hamish L. Fraser, and Peter C. Collins. Predicting tensile properties of Ti-6Al-4V produced via directed energy deposition. *Acta Materialia*, 133:120–133, jul 2017. ISSN 13596454. doi: 10.1016/j.actamat.2017.05.025.

[200] R. W. Bush and C. A. Brice. Elevated temperature characterization of electron beam freeform fabricated Ti-6Al-4V and dispersion strengthened Ti-8Al-1Er. *Materials Science and Engineering A*, 554:12–21, 2012. ISSN 09215093. doi: 10.1016/j.msea.2012.05.083.

[201] Dongheng Xu, Han Wang, Xuewei Tao, Zhengjun Yao, Shasha Zhang, and Moliar Oleksander. Investigation on Microstructure, Hardness and Wear Resistance of Electron Beam Wire-Feeding Deposited Inconel 718 Alloy Coatings. *Metals and Materials International*, 2019. ISSN 2005-4149. doi: 10.1007/s12540-019-00494-x.

[202] M. A. Wahab. Manual Metal Arc Welding and Gas Metal Arc Welding. In *Comprehensive Materials Processing*, volume 6, pages 49–76. Elsevier Ltd, may 2014. ISBN 9780080965338. doi: 10.1016/B978-0-08-096532-1.00610-5.

[203] S. W. Williams, F. Martina, A. C. Addison, J. Ding, G. Pardal, and P. Colegrove. Wire + Arc additive manufacturing. *Materials Science and Technology (United Kingdom)*, 32(7):641–647, may 2016. ISSN 17432847. doi: 10.1179/1743284715Y.0000000073.

[204] Filomeno Martina, Jialuo Ding, Stewart Williams, Armando Caballero, Gonçalo Pardal, and Luisa Quintino. Tandem metal inert gas process for high productivity wire arc additive manufacturing in stainless steel. *Additive Manufacturing*, 25:545–550, jan 2019. ISSN 22148604. doi: 10.1016/j.addma.2018.11.022.

[205] Ramesh Singh. Welding and Joining Processes. In Ramesh Singh, editor, *American Society of Mechanical Engineers, Production Engineering Division (Publication) PED*, volume 51, pages 163–195. Butterworth-Heinemann, 2 edition, 1991. ISBN 0791808521. doi: 10.1016/b978-0-12-804176-5.00015-3.

[206] Jicai Feng, Hongtao Zhang, and Peng He. The CMT short-circuiting metal transfer process and its use in thin aluminium sheets welding. *Materials and Design*, 30(5): 1850–1852, may 2009. ISSN 02641275. doi: 10.1016/j.matdes.2008.07.015.

[207] C. G. Pickin and K. Young. Evaluation of cold metal transfer (CMT) process for welding aluminium alloy. *Science and Technology of Welding and Joining*, 11(5):583–585, sep 2006. ISSN 13621718. doi: 10.1179/174329306X120886.

[208] Jianglong Gu, Jialuo Ding, Stewart W. Williams, Huimin Gu, Jing Bai, Yuchun Zhai, and Peihua Ma. The strengthening effect of inter-layer cold working and post-deposition heat treatment on the additively manufactured Al-6.3Cu alloy. *Materials Science and Engineering A*, 651:18–26, jan 2016. ISSN 09215093. doi: 10.1016/j.msea.2015.10.101.

[209] Thomas Lehmann, Akshay Jain, Yash Jain, Henriette Stainer, Tonya Wolfe, Hani Henein, and Ahmed Jawad Qureshi. Concurrent Geometry- and Material-based Process Identification and Optimization for Robotic CMT-based Wire Arc Additive Manufacturing. *Materials & Design*, In press, 2020.

[210] Kohei Oyama, Spyros Diplas, Mohammed M'hamdi, Anette E. Gunnæs, and Amin S. Azar. Heat source management in wire-arc additive manufacturing process for Al-Mg and Al-Si alloys. *Additive Manufacturing*, 26:180–192, mar 2019. ISSN 22148604. doi: 10.1016/j.addma.2019.01.007.

[211] Davoud Jafari, Tom H J Vaneker, and Ian Gibson. Wire and arc additive manufacturing: Opportunities and challenges to control the quality and accuracy of manufactured parts. *Materials & Design*, 202:109471, 2021. ISSN 0264-1275. doi: https://doi.org/10.1016/j.matdes.2021.109471.

[212] P. M. Dickens, M. S. Pridham, R. C. Cobb, I. Gibson, and G. Dixon. Rapid prototyping using 3-D welding. In *Solid Freeform Fabrication Proceedings*, pages 280–290, 1992.

[213] Ramesh Singh. Chapter 3 - Welding and Joining Processes BT - Applied Welding Engineering. In Ramesh Singh, editor, *Applied Welding Engineering*, pages 147–170. Butterworth-Heinemann, Boston, 2012. ISBN 978-0-12-391916-8. doi: http://dx.doi.org/10.1016/B978-0-12-391916-8.00015-7.

[214] Fangda Xu, Vimal Dhokia, Paul Colegrove, Anthony McAndrew, Stewart Williams, Andrew Henstridge, and Stephen T. Newman. Realisation of a multi-sensor framework for process monitoring of the wire arc additive manufacturing in producing Ti-6Al-4V parts. *International Journal of Computer Integrated Manufacturing*, 31(8):785–798, 2018. ISSN 13623052. doi: 10.1080/0951192X.2018.1466395.

[215] Zengxi Pan, Donghong Ding, Bintao Wu, Dominic Cuiuri, Huijun Li, and John Norrish. Arc Welding Processes for Additive Manufacturing: A Review. In *Transactions on Intelligent Welding Manufacturing*, pages 3–24. Springer, Singapore, 2018. doi: 10.1007/978-981-10-5355-9_1.

[216] Yan Ma, Dominic Cuiuri, Nicholas Hoye, Huijun Li, and Zengxi Pan. The effect of location on the microstructure and mechanical properties of titanium aluminides produced by additive layer manufacturing using in-situ alloying and gas tungsten arc welding. *Materials Science and Engineering A*, 631:230–240, apr 2015. ISSN 09215093. doi: 10.1016/j.msea.2015.02.051.

[217] Chen Shen, Zengxi Pan, Dominic Cuiuri, Jon Roberts, and Huijun Li. Fabrication of Fe-FeAl Functionally Graded Material Using the Wire-Arc Additive Manufacturing Process. *Metallurgical and Materials Transactions B: Process Metallurgy and Materials Processing Science*, 47(1):763–772, feb 2016. ISSN 10735615. doi: 10.1007/s11663-015-0509-5.

[218] Chen Shen, Zengxi Pan, Yan Ma, Dominic Cuiuri, and Huijun Li. Fabrication of iron-rich Fe-Al intermetallics using the wire-arc additive manufacturing process. *Additive Manufacturing*, 7:20–26, jul 2015. ISSN 22148604. doi: 10.1016/j.addma.2015.06.001.

[219] Fude Wang, Stewart Williams, Paul Colegrove, and Alphons A. Antonysamy. Microstructure and mechanical properties of wire and arc additive manufactured Ti-6Al-4V. *Metallurgical and Materials Transactions A: Physical Metallurgy and Materials Science*, 44(2):968–977, feb 2013. ISSN 10735623. doi: 10.1007/s11661-012-1444-6.

[220] E. Brandl, B. Baufeld, C. Leyens, and R. Gault. Additive manufactured Ti-6A1-4V using welding wire: Comparison of laser and arc beam deposition and evaluation with respect to aerospace material specifications. In *Physics Procedia*, volume 5, pages 595–606. Elsevier B.V., jan 2010. doi: 10.1016/j.phpro.2010.08.087.

[221] A. K. Lakshminarayanan, V. Balasubramanian, and K. Elangovan. Effect of welding processes on tensile properties of AA6061 aluminium alloy joints. *International Journal of Advanced Manufacturing Technology*, 40(3-4):286–296, jan 2009. ISSN 02683768. doi: 10.1007/s00170-007-1325-0.

[222] J. F. Wang, Q. J. Sun, H. Wang, J. P. Liu, and J. C. Feng. Effect of location on microstructure and mechanical properties of additive layer manufactured Inconel 625 using gas tungsten arc welding. *Materials Science and Engineering A*, 676:395–405, oct 2016. ISSN 09215093. doi: 10.1016/j.msea.2016.09.015.

[223] Donghong Ding, Zengxi Pan, Dominic Cuiuri, and Huijun Li. Wire-feed additive manufacturing of metal components: technologies, developments and future interests. *International Journal of Advanced Manufacturing Technology*, 81(1-4):465–481, oct 2015. ISSN 14333015. doi: 10.1007/s00170-015-7077-3.

[224] Zhili Feng. *Processes and Mechanisms of Welding Residual Stress and Distortion*. Elsevier Ltd., oct 2005. ISBN 9781855737716. doi: 10.1533/9781845690939.

[225] F. Martina, J. Mehnen, S. W. Williams, P. Colegrove, and F. Wang. Investigation of the benefits of plasma deposition for the additive layer manufacture of Ti-6Al-4V. *Journal of Materials Processing Technology*, 212(6):1377–1386, jun 2012. ISSN 09240136. doi: 10.1016/j.jmatprotec.2012.02.002.

[226] MAR Yarmuch. *Effect of Welding Parameters on the Plasma Transferred Arc Welding (PTAW) Process for Autogenous Beads and 410SS-WC Overlays*. University of Alberta, 2006.

[227] Eduardo André Alberti, Bruno Machado Pereira Bueno, and Ana Sofia C.M. D'Oliveira. Processamento de ligas de níquel com técnica de manufatura aditiva utilizando plasma por arco transferido. *Soldagem e Inspecao*, 20(2):137–147, 2015. ISSN 19806973. doi: 10.1590/0104-9224/SI2002.02.

[228] Eloisa Pereira Cardozo, Sergio Ríos, Supriyo Ganguly, and Ana Sofia C.M. D'Oliveira. Assessment of the effect of different forms of Inconel 625 alloy feedstock in Plasma Transferred Arc (PTA) additive manufacturing. *International Journal of Advanced Manufacturing Technology*, 98(5-8):1695–1705, sep 2018. ISSN 14333015. doi: 10.1007/s00170-018-2340-z.

[229] Eva M. Perez-Soriano, Enrique Ariza, Cristina Arevalo, Isabel Montealegre-Melendez, Michael Kitzmantel, and Erich Neubauer. Processing by additive manufacturing based on plasma transferred arc of hastelloy in air and argon atmosphere. *Metals*, 10(2):200, jan 2020. ISSN 20754701. doi: 10.3390/met10020200.

[230] K. Hoefer, J. Rodriguez, A. Haelsig, K. G. Abstoss, and P. Mayr. Fabrication of SS316L to Ni80Cr20 graded structures by 3D plasma metal deposition. *Welding in the World*, pages 1–5, mar 2020. ISSN 18786669. doi: 10.1007/s40194-020-00870-x.

[231] Johnnatan Rodriguez, Kevin Hoefer, Andre Haelsig, and Peter Mayr. Functionally graded SS 316l to ni-based structures produced by 3D plasma metal deposition. *Metals*, 9(6):620, may 2019. ISSN 20754701. doi: 10.3390/met9060620.

[232] K. Hoefer, A. Haelsig, and P. Mayr. Arc-based additive manufacturing of steel components–comparison of wire- and powder-based variants. *Welding in the World*, 62 (2):243–247, mar 2018. ISSN 00432288. doi: 10.1007/s40194-017-0527-9.

[233] Robert P. Mudge and Nicholas R. Wald. Laser engineered net shaping advances additive manufacturing and repair. *Welding Journal (Miami, Fla)*, 86(1):44–48, 2007. ISSN 00432296.

[234] Abdollah Saboori, Alberta Aversa, Giulio Marchese, Sara Biamino, Mariangela Lombardi, and Paolo Fino. Application of directed energy deposition-based additive manufacturing in repair. *Applied Sciences (Switzerland)*, 9(16):3316, aug 2019. ISSN 20763417. doi: 10.3390/app9163316.

[235] R. Liu, Z. Wang, T. Sparks, F. Liou, and J. Newkirk. 13 - aerospace applications of laser additive manufacturing. In Milan Brandt, editor, *Laser Additive Manufacturing*, Woodhead Publishing Series in Electronic and Optical Materials, pages 351 – 371. Woodhead Publishing, 2017. ISBN 978-0-08-100433-3. doi: https://doi.org/10.1016/B978-0-08-100433-3.00013-0.

[236] Yong Feng Lu and Yoshinobu Aoyagi. Temperature rise and heat flux induced by laser beam with double-gaussian intensity distribution. *Japanese Journal of Applied Physics*, 34(7R):3759–3763, 1995. ISSN 13474065. doi: 10.1143/JJAP.34.3759.

[237] Wiesława Piekarska and Marcin Kubiak. Theoretical investigations into heat transfer in laser-welded steel sheets. In *Journal of Thermal Analysis and Calorimetry*, volume 110, pages 159–166. Springer, oct 2012. doi: 10.1007/s10973-012-2486-0.

[238] A. Marmołowski and W. Kiełczyński. Modelling of the heat flux density distribution for laser beam welding. In *Solid State Phenomena*, volume 183 of *Solid State Phenomena*, pages 241–248. Trans Tech Publications Ltd, 2012. ISBN 9783037853207. doi: 10.4028/www.scientific.net/SSP.183.241.

[239] Agustin M. Fudolig, Hiroshi Nogami, and Jun Ichiro Yagi. Numerical analysis of the flow characteristics and temperature distribution in metal beads subjected to transferred arc plasma impingement. *ISIJ International*, 37(6):630–636, jun 1997. ISSN 09151559. doi: 10.2355/isijinternational.37.630.

[240] Jun Wang, Zengxi Pan, Dominic Cuiuri, and Huijun Li. Phase constituent control and correlated properties of titanium aluminide intermetallic alloys through dual-wire arc additive manufacturing. *Materials Letters*, 242:111–114, may 2019. ISSN 18734979. doi: 10.1016/j.matlet.2019.01.112.

[241] T. E. Abioye, P. K. Farayibi, and A. T. Clare. A comparative study of Inconel 625 laser cladding by wire and powder feedstock. *Materials and Manufacturing Processes*, 32(14):1653–1659, oct 2017. ISSN 15322475. doi: 10.1080/10426914.2017.1317787.

[242] A. Simchi. The role of particle size on the laser sintering of iron powder. *Metallurgical and Materials Transactions B: Process Metallurgy and Materials Processing Science*, 35(5):937–948, oct 2004. ISSN 10735615. doi: 10.1007/s11663-004-0088-3.

[243] V.I. Murav'ev, R.F. Krupskii, R.A. Fizulakov, and P.G. Demyshev. Effect of the quality of filler wire on the formation of pores in welding of titanium alloys. *Welding International*, 22(12):853–858, 2008. doi: 10.1080/09507110802650610.

[244] Geir Langelandsvik, Mathieu Grandcolas, Kristian G. Skorpen, Trond Furu, Odd M. Akselsen, and Hans Jørgen Roven. Development of al-tic wire feedstock for additive manufacturing by metal screw extrusion. *Metals*, 10(11), 2020. ISSN 2075-4701. doi: 10.3390/met10111485.

[245] E.M. Ryan, T.J. Sabin, J.F. Watts, and M.J. Whiting. The influence of build parameters and wire batch on porosity of wire and arc additive manufactured aluminium alloy 2319. *Journal of Materials Processing Technology*, 262:577–584, 2018. ISSN 0924-0136. doi: https://doi.org/10.1016/j.jmatprotec.2018.07.030.

[246] Jiang Long Gu, Jia Luo Ding, Bao Qiang Cong, Jing Bai, Hui Min Gu, Stewart W. Williams, and Yu Chun Zhai. The influence of wire properties on the quality and performance of wire+arc additive manufactured aluminium parts. In *Materials Science and Advanced Technologies in Manufacturing II*, volume 1081 of *Advanced Materials Research*, pages 210–214. Trans Tech Publications Ltd, 2 2015. doi: 10.4028/www.scientific.net/AMR.1081.210.

[247] Nikita V. Muravyev, Konstantin A. Monogarov, Uwe Schaller, Igor V. Fomenkov, and Alla N. Pivkina. Progress in Additive Manufacturing of Energetic Materials: Creating the Reactive Microstructures with High Potential of Applications. *Propellants, Explosives, Pyrotechnics*, 44(8):941–969, aug 2019. ISSN 0721-3115. doi: 10.1002/prep.201900060.

[248] Filippo Montevecchi, Giuseppe Venturini, Niccolò Grossi, Antonio Scippa, and Gianni Campatelli. Heat accumulation prevention in Wire-Arc-Additive-Manufacturing using air jet impingement. *Manufacturing Letters*, 17:14–18, aug 2018. ISSN 22138463. doi: 10.1016/j.mfglet.2018.06.004.

[249] J. V. Gordon, C. V. Haden, H. F. Nied, R. P. Vinci, and D. G. Harlow. Fatigue crack growth anisotropy, texture and residual stress in austenitic steel made by wire and

arc additive manufacturing. *Materials Science and Engineering A*, 724:431–438, may 2018. ISSN 09215093. doi: 10.1016/j.msea.2018.03.075.

[250] Aref Yadollahi, Nima Shamsaei, Scott M. Thompson, Alaa Elwany, and Linkan Bian. Mechanical and microstructural properties of selective laser melted 17-4 ph stainless steel. In *ASME International Mechanical Engineering Congress and Exposition, Proceedings (IMECE)*, volume 2A-2015. American Society of Mechanical Engineers (ASME), mar 2015. ISBN 9780791857359. doi: 10.1115/IMECE2015-52362.

[251] R. Rashid, S. H. Masood, D. Ruan, S. Palanisamy, R. A. Rahman Rashid, and M. Brandt. Effect of scan strategy on density and metallurgical properties of 17-4PH parts printed by Selective Laser Melting (SLM). *Journal of Materials Processing Technology*, 249:502–511, nov 2017. ISSN 09240136. doi: 10.1016/j.jmatprotec.2017.06.023.

[252] Zhiheng Hu, Haihong Zhu, Hu Zhang, and Xiaoyan Zeng. Experimental investigation on selective laser melting of 17-4PH stainless steel. *Optics and Laser Technology*, 87: 17–25, jan 2017. ISSN 00303992. doi: 10.1016/j.optlastec.2016.07.012.

[253] Somayeh Pasebani, Milad Ghayoor, Sunil Badwe, Harish Irrinki, and Sundar V. Atre. Effects of atomizing media and post processing on mechanical properties of 17-4 PH stainless steel manufactured via selective laser melting. *Additive Manufacturing*, 22: 127–137, aug 2018. ISSN 22148604. doi: 10.1016/j.addma.2018.05.011.

[254] S. D. Meredith, J. S. Zuback, J. S. Keist, and T. A. Palmer. Impact of composition on the heat treatment response of additively manufactured 17–4 PH grade stainless steel. *Materials Science and Engineering A*, 738:44–56, dec 2018. ISSN 09215093. doi: 10.1016/j.msea.2018.09.066.

[255] Bradley C. Salzbrenner, Jeffrey M. Rodelas, Jonathan D. Madison, Bradley H. Jared, Laura P. Swiler, Yu Lin Shen, and Brad L. Boyce. High-throughput stochastic tensile performance of additively manufactured stainless steel. *Journal of Materials Processing Technology*, 241:1–12, mar 2017. ISSN 09240136. doi: 10.1016/j.jmatprotec.2016.10.023.

[256] Abiodun Bayode, Sisa Pityana, Esther Titilayo Akinlabi, and Mxolisi Brendon Shongwe. Effect of scanning speed on laser deposited 17-4PH stainless steel. In *Proceedings of 2017 8th International Conference on Mechanical and Intelligent Manufacturing*

Technologies, ICMIMT 2017, pages 1–5. Institute of Electrical and Electronics Engineers Inc., may 2017. ISBN 9781538603772. doi: 10.1109/ICMIMT.2017.7917404.

[257] I. Mathoho, E. T. Akinlabi, N. Arthur, M. Tlotleng, and B. Masina. Metallurgical Characteristics of Laser Peened 17-4 PH SS Processed by LENS Technique. In *Minerals, Metals and Materials Series*, pages 279–285. Springer International Publishing, 2019. ISBN 9783030058609. doi: 10.1007/978-3-030-05861-6_25.

[258] Youheng Fu, Haiou Zhang, Guilan Wang, and Huafeng Wang. Investigation of mechanical properties for hybrid deposition and micro-rolling of bainite steel. *Journal of Materials Processing Technology*, 250:220–227, dec 2017. ISSN 09240136. doi: 10.1016/j.jmatprotec.2017.07.023.

[259] Eckart Uhlmann, Robert Kersting, Tiago Borsoi Klein, Marcio Fernando Cruz, and Anderson Vicente Borille. Additive Manufacturing of Titanium Alloy for Aircraft Components. In *Procedia CIRP*, volume 35, pages 55–60. Elsevier B.V., jan 2015. doi: 10.1016/j.procir.2015.08.061.

[260] Dipankar Banerjee and J. C. Williams. Perspectives on titanium science and technology. *Acta Materialia*, 61(3):844–879, feb 2013. ISSN 13596454. doi: 10.1016/j.actamat.2012.10.043.

[261] Masafumi Kikuchi. The use of cutting temperature to evaluate the machinability of titanium alloys. *Acta Biomaterialia*, 5(2):770–775, feb 2009. ISSN 17427061. doi: 10.1016/j.actbio.2008.08.016.

[262] Yanyan Zhu, Xiangjun Tian, Jia Li, and Huaming Wang. The anisotropy of laser melting deposition additive manufacturing Ti-6.5Al-3.5Mo-1.5Zr-0.3Si titanium alloy. *Materials and Design*, 67:538–542, feb 2015. ISSN 18734197. doi: 10.1016/j.matdes.2014.11.001.

[263] Qiang Zhang, Jing Chen, Zhuang Zhao, Hua Tan, Xin Lin, and Weidong Huang. Microstructure and anisotropic tensile behavior of laser additive manufactured TC21 titanium alloy. *Materials Science and Engineering A*, 673:204–212, 2016. ISSN 09215093. doi: 10.1016/j.msea.2016.07.040.

[264] J. Alcisto, A. Enriquez, H. Garcia, S. Hinkson, T. Steelman, E. Silverman, P. Valdovino, H. Gigerenzer, J. Foyos, J. Ogren, J. Dorey, K. Karg, T. McDonald, and O. S.

Es-Said. Tensile properties and microstructures of laser-formed Ti-6Al-4V. *Journal of Materials Engineering and Performance*, 20(2):203–212, 2011. ISSN 10599495. doi: 10.1007/s11665-010-9670-9.

[265] Qiang Zhang, Jing Chen, Lilin Wang, Hua Tan, Xin Lin, and Weidong Huang. Solidification Microstructure of Laser Additive Manufactured Ti-6Al-2Zr-2Sn-3Mo-1.5Cr-2Nb Titanium Alloy. *Journal of Materials Science and Technology*, 32(4):381–386, 2016. ISSN 10050302. doi: 10.1016/j.jmst.2015.11.019.

[266] Muhammad Rizwan, Junxia Lu, Fei Chen, Ruxia Chai, Rafi Ullah, Yuefei Zhang, and Ze Zhang. Microstructure Evolution and Mechanical Behavior of Laser Melting Deposited TA15 Alloy at 500 °C under In-Situ Tension in SEM. *Acta Metallurgica Sinica (English Letters)*, pages 1–12, mar 2021. ISSN 21941289. doi: 10.1007/s40195-021-01214-4.

[267] M. J. Bermingham, D. H. StJohn, J. Krynen, S. Tedman-Jones, and M. S. Dargusch. Promoting the columnar to equiaxed transition and grain refinement of titanium alloys during additive manufacturing. *Acta Materialia*, 168:261–274, apr 2019. ISSN 13596454. doi: 10.1016/j.actamat.2019.02.020.

[268] Q. Zhang, J. Chen, X. Lin, H. Tan, and W. D. Huang. Grain morphology control and texture characterization of laser solid formed Ti6Al2Sn2Zr3Mo1.5Cr2Nb titanium alloy. *Journal of Materials Processing Technology*, 238:202–211, dec 2016. ISSN 09240136. doi: 10.1016/j.jmatprotec.2016.07.011.

[269] Erhard Brandl and Daniel Greitemeier. Microstructure of additive layer manufactured Ti-6Al-4V after exceptional post heat treatments. *Materials Letters*, 81:84–87, 2012. ISSN 0167577X. doi: 10.1016/j.matlet.2012.04.116.

[270] Vittorio Alfieri, Fabrizia Caiazzo, and Vincenzo Sergi. Autogenous laser welding of AA 2024 aluminium alloy: Process issues and bead features. In *Procedia CIRP*, volume 33, pages 406–411. Elsevier B.V., jan 2015. doi: 10.1016/j.procir.2015.06.094.

[271] A. Haboudou, P. Peyre, A. B. Vannes, and G. Peix. Reduction of porosity content generated during Nd: YAG laser welding of A356 and AA5083 aluminium alloys. *Materials Science and Engineering A*, 363(1-2):40–52, dec 2003. ISSN 09215093. doi: 10.1016/S0921-5093(03)00637-3.

[272] Rongshi Xiao and Xinyi Zhang. Problems and issues in laser beam welding of aluminum-lithium alloys, apr 2014. ISSN 15266125.

[273] C. Borsellino, G. Di Bella, and V. F. Ruisi. Adhesive joining of aluminium AA6082: The effects of resin and surface treatment. *International Journal of Adhesion and Adhesives*, 29(1):36–44, jan 2009. ISSN 01437496. doi: 10.1016/j.ijadhadh.2008.01.002.

[274] Shivraman Thapliyal. Challenges associated with the wire arc additive manufacturing (WAAM) of aluminum alloys. *Materials Research Express*, 6(11):112006, 2019. ISSN 2053-1591. doi: 10.1088/2053-1591/ab4dd4.

[275] J Hatch. *Aluminum: Properties and Physical Metallurgy (Livre numérique Google)*, volume 1984. American Society for Metals, 1984. ISBN 1615031693.

[276] Martin Kristoffersen, Miguel Costas, Tim Koenis, Vegard Brøtan, Christian O. Paulsen, and Tore Børvik. On the ballistic perforation resistance of additive manufactured AlSi10Mg aluminium plates. *International Journal of Impact Engineering*, 137:103476, mar 2020. ISSN 0734743X. doi: 10.1016/j.ijimpeng.2019.103476.

[277] M. Javidani, J. Arreguin-Zavala, J. Danovitch, Y. Tian, and M. Brochu. Additive Manufacturing of AlSi10Mg Alloy Using Direct Energy Deposition: Microstructure and Hardness Characterization. *Journal of Thermal Spray Technology*, 26(4):587–597, apr 2017. ISSN 10599630. doi: 10.1007/s11666-016-0495-4.

[278] Sen Li, Lin Jie Zhang, Jie Ning, Xiang Wang, Gui Feng Zhang, Jian Xun Zhang, Suck Joo Na, and Bodaghi Fatemeh. Comparative study on the microstructures and properties of wire+arc additively manufactured 5356 aluminium alloy with argon and nitrogen as the shielding gas. *Additive Manufacturing*, 34:101206, aug 2020. ISSN 22148604. doi: 10.1016/j.addma.2020.101206.

[279] Markus Köhler, Sierk Fiebig, Jonas Hensel, and Klaus Dilger. Wire and Arc Additive Manufacturing of Aluminum Components. *Metals*, 9(5):608, may 2019. ISSN 2075-4701. doi: 10.3390/met9050608.

[280] Lobna Wahsh, M. Azzam, Mohamed Turky, H. Salem, F. Hamdy, A. Mansour, and A. ElShater. Parameter selection for wire arc additive manufacturing (waam) process. pages 78–85, 01 2018. doi: 10.7449/2018mst/2018/mst_2018_78_85.

[281] Liwei Wang, Yingchao Suo, Zhimin Liang, Dianlong Wang, and Qian Wang. Effect of titanium powder on microstructure and mechanical properties of wire + arc additively manufactured Al-Mg alloy. *Materials Letters*, 241:231–234, apr 2019. ISSN 18734979. doi: 10.1016/j.matlet.2019.01.117.

[282] Huijun Wang, Wenhui Jiang, Jiahu Ouyang, and Radovan Kovacevic. Rapid prototyping of 4043 Al-alloy parts by VP-GTAW. *Journal of Materials Processing Technology*, 148(1):93–102, may 2004. ISSN 09240136. doi: 10.1016/j.jmatprotec.2004.01.058.

[283] Yunpeng Nie, Peilei Zhang, Xi Wu, Guojin Li, Hua Yan, and Zhishui Yu. Rapid prototyping of 4043 Al-alloy parts by cold metal transfer. *Science and Technology of Welding and Joining*, 23(6):527–535, aug 2018. ISSN 17432936. doi: 10.1080/13621718.2018.1438236.

[284] Arturo Gomez Ortega, Luis Corona Galvan, Mehdi Salem, Kamel Moussaoui, Stephane Segonds, Sébastien Rouquette, and Frédéric Deschaux-Beaume. Characterisation of 4043 aluminium alloy deposits obtained by wire and arc additive manufacturing using a Cold Metal Transfer process. *Science and Technology of Welding and Joining*, 24(6): 538–547, aug 2019. ISSN 1362-1718. doi: 10.1080/13621718.2018.1564986.

[285] Qiuyu Miao, Dongjiang Wu, Dongsheng Chai, Yu Zhan, Guijun Bi, Fangyong Niu, and Guangyi Ma. Comparative study of microstructure evaluation and mechanical properties of 4043 aluminum alloy fabricated by wire-based additive manufacturing. *Materials and Design*, 186:108205, jan 2020. ISSN 18734197. doi: 10.1016/j.matdes.2019.108205.

[286] C. H. Cáceres, C. J. Davidson, and J. R. Griffiths. The deformation and fracture behaviour of an AlSiMg casting alloy. *Materials Science and Engineering A*, 197(2): 171–179, jul 1995. ISSN 09215093. doi: 10.1016/0921-5093(94)09775-5.

[287] C. H. Cáceres and Q. G. Wang. Dendrite cell size and ductility of Al-Si-Mg casting alloys: Spear and Gardner revisited, 1996. ISSN 13640461.

[288] C. H. Caceres, C. J. Davidson, J. R. Griffiths, and Q. G. Wang. The effect of Mg on the microstructure and mechanical behavior of Al-Si-Mg casting alloys. *Metallurgical and Materials Transactions A: Physical Metallurgy and Materials Science*, 30(10):2611–2618, oct 1999. ISSN 10735623. doi: 10.1007/s11661-999-0301-8.

[289] Gouri D. Bhasale, Aarush Sood, Shashi R. Singh, Amit Pandey, and Amber Shrivastava. High Temperature Corrosion of Additively Manufactured Inconel 625. In *Minerals, Metals and Materials Series*, pages 1329–1338. Springer, 2020. ISBN 9783030362959. doi: 10.1007/978-3-030-36296-6_123.

[290] Beata Dubiel and Jan Sieniawski. Precipitates in additively manufactured inconel 625 superalloy. *Materials*, 12(7):1144, apr 2019. ISSN 19961944. doi: 10.3390/ma12071144.

[291] L. C.M. Valle, A. I.C. Santana, M. C. Rezende, J. Dille, O. R. Mattos, and L. H. de Almeida. The influence of heat treatments on the corrosion behaviour of nickel-based alloy 718. *Journal of Alloys and Compounds*, 809:151781, nov 2019. ISSN 09258388. doi: 10.1016/j.jallcom.2019.151781.

[292] C. V. Mikler, V. Chaudhary, T. Borkar, V. Soni, D. Choudhuri, R. V. Ramanujan, and R. Banerjee. Laser additive processing of Ni-Fe-V and Ni-Fe-Mo Permalloys: Microstructure and magnetic properties. *Materials Letters*, 192:9–11, apr 2017. ISSN 18734979. doi: 10.1016/j.matlet.2017.01.059.

[293] C. V. Mikler, V. Chaudhary, T. Borkar, V. Soni, D. Jaeger, X. Chen, R. Contieri, R. V. Ramanujan, and R. Banerjee. Laser Additive Manufacturing of Magnetic Materials. *Jom*, 69(3):532–543, mar 2017. ISSN 15431851. doi: 10.1007/s11837-017-2257-2.

[294] G. L. Makar and J. Kruger. Corrosion of magnesium. *International Materials Reviews*, 38(3):138–153, 1993. ISSN 17432804. doi: 10.1179/imr.1993.38.3.138.

[295] Yizao Wan, Guangyao Xiong, Honglin Luo, Fang He, Yuan Huang, and Xiaoshong Zhou. Preparation and characterization of a new biomedical magnesium-calcium alloy. *Materials and Design*, 29(10):2034–2037, dec 2008. ISSN 02641275. doi: 10.1016/j.matdes.2008.04.017.

[296] Matthew Murphy, Mark Turski, William Warfield, and Paul Lyon. The effect of changes in hydraulic fracking fluid chemistries on the dissolution rate of dissolvable magnesium frack plug components. In *Proceedings - SPE Annual Technical Conference and Exhibition*, volume 2019-Septe. Society of Petroleum Engineers, sep 2019. ISBN 9781613996638. doi: 10.2118/195987-ms.

[297] Y. Cai, L. Wan, Z. H. Guo, C. Y. Sun, D. J. Yang, Q. D. Zhang, and Y. L. Li. Hot deformation characteristics of AZ80 magnesium alloy: Work hardening effect and

processing parameter sensitivities. *Materials Science and Engineering A*, 687:113–122, feb 2017. ISSN 09215093. doi: 10.1016/j.msea.2017.01.057.

[298] P. Frigola, R. Agustsson, S. Boucher, a. Murokh, H. Badakov, a. Fukasawa, P. Musumeci, J. Rosenzweig, G. Travish, L. Faillace, Roma La, D. Cormier, and T. Mahale. Development of Solid Freeform Fabrication (Sff) for the Production of Rf Photoinjectors Ebm Fabrication Process. In *Proceedings of the 23rd Particle Accelerator Conference*, pages 2015–2017, 2009.

[299] Arne Röttger, Karina Geenen, Matthias Windmann, Florian Binner, and Werner Theisen. Comparison of microstructure and mechanical properties of 316 L austenitic steel processed by selective laser melting with hot-isostatic pressed and cast material. *Materials Science and Engineering A*, 678:365–376, dec 2016. ISSN 09215093. doi: 10.1016/j.msea.2016.10.012.

[300] Z. Xu, J. W. Murray, C. J. Hyde, and A. T. Clare. Effect of post processing on the creep performance of laser powder bed fused Inconel 718. *Additive Manufacturing*, 24: 486–497, dec 2018. ISSN 22148604. doi: 10.1016/j.addma.2018.10.027.

[301] M. E. Aydinöz, F. Brenne, M. Schaper, C. Schaak, W. Tillmann, J. Nellesen, and T. Niendorf. On the microstructural and mechanical properties of post-treated additively manufactured Inconel 718 superalloy under quasi-static and cyclic loading. *Materials Science and Engineering A*, 669:246–258, jul 2016. ISSN 09215093. doi: 10.1016/j.msea.2016.05.089.

[302] Yinbao Tian, Junqi Shen, Shengsun Hu, Jian Han, Qian Wang, and Yangchuan Cai. Effects of ultrasonic peening treatment layer by layer on microstructure of components fabricated by wire and arc additive manufacturing. *Materials Letters*, 284:128917, 2021. ISSN 18734979. doi: 10.1016/j.matlet.2020.128917.

[303] Behzad Parvaresh, Reza Salehan, and Reza Miresmaeili. Investigating Isotropy of Mechanical and Wear Properties in As-Deposited and Inter-Layer Cold Worked Specimens Manufactured by Wire Arc Additive Manufacturing. *Metals and Materials International*, 27(1):92–105, 2021. ISSN 2005-4149. doi: 10.1007/s12540-020-00793-8.

[304] I. Tabernero, A. Calleja, A. Lamikiz, and L. N. López De Lacalle. Optimal parameters for 5-axis Laser cladding. *Procedia Engineering*, 63:45–52, jan 2013. ISSN 18777058. doi: 10.1016/j.proeng.2013.08.229.

[305] A. Calleja, I. Tabernero, A. Fernández, A. Celaya, A. Lamikiz, and L. N. López De Lacalle. Improvement of strategies and parameters for multi-axis laser cladding operations. *Optics and Lasers in Engineering*, 56:113–120, may 2014. ISSN 01438166. doi: 10.1016/j.optlaseng.2013.12.017.

[306] Yamazaki Mazak Corporation. INTEGREX i-400AM. URL https://www.mazakusa.com/machines/integrex-i-400am/.

[307] Uk.dmgmori.com. LASERTEC 65 3D hybrid - ADDITIVE MANUFACTURING Machines by DMG MORI, 2018. URL https://uk.dmgmori.com/products/machines/advanced-technology/additive-manufacturing/powder-nozzle/lasertec-65-3d-hybrid.

[308] Gerald C. Anzalone, Chenlong Zhang, Bas Wijnen, Paul G. Sanders, and Joshua M. Pearce. A low-cost open-source metal 3-D printer. *IEEE Access*, 1:803–810, 2013. ISSN 21693536. doi: 10.1109/ACCESS.2013.2293018.

[309] Yuenyong Nilsiam, Amberlee Haselhuhn, Bas Wijnen, Paul Sanders, and Joshua M. Pearce. Integrated voltage-current monitoring and control of gas metal arc weld magnetic ball-jointed open source 3-D printer. *Machines*, 3(4):339–351, nov 2015. ISSN 20751702. doi: 10.3390/machines3040339.

[310] X. Lu, Y. F. Zhou, X. L. Xing, L. Y. Shao, Q. X. Yang, and S. Y. Gao. Open-source wire and arc additive manufacturing system: formability, microstructures, and mechanical properties. *International Journal of Advanced Manufacturing Technology*, 93(5-8):2145–2154, nov 2017. ISSN 14333015. doi: 10.1007/s00170-017-0636-z.

[311] Chenming Wu, Chengkai Dai, Guoxin Fang, Yong Jin Liu, and Charlie C.L. Wang. RoboFDM: A robotic system for support-free fabrication using FDM. In *Proceedings - IEEE International Conference on Robotics and Automation*, pages 1175–1180. IEEE, may 2017. ISBN 9781509046331. doi: 10.1109/ICRA.2017.7989140.

[312] Chengkai Dai, Charlie C.L. Wang, Chenming Wu, Sylvain Lefebvre, Guoxin Fang, and Yong Jin Liu. Support-free volume printing by multi-axis motion. *ACM Transactions on Graphics*, 37(4):1–14, jul 2018. ISSN 15577368. doi: 10.1145/3197517.3201342.

[313] Fang Li, Shujun Chen, Zhaoyang Wu, and Zhihong Yan. Adaptive process control of wire and arc additive manufacturing for fabricating complex-shaped components.

International Journal of Advanced Manufacturing Technology, 96(1-4):871–879, apr 2018. ISSN 14333015. doi: 10.1007/s00170-018-1590-0.

[314] Xu Zhang, Mingyang Li, Jian Hui Lim, Yiwei Weng, Yi Wei Daniel Tay, Hung Pham, and Quang Cuong Pham. Large-scale 3D printing by a team of mobile robots. *Automation in Construction*, 95:98–106, nov 2018. ISSN 09265805. doi: 10.1016/j.autcon.2018.08.004.

[315] Musa K. Jouaneh, Zhixiao Wang, and David A. Dornfeld. Trajectory Planning for Coordinated Motion of a Robot and a Positioning Table: Part 1—Path Specification. *IEEE Transactions on Robotics and Automation*, 6(6):735–745, 1990. ISSN 1042296X. doi: 10.1109/70.63274.

[316] Maxime Chalvin, Sébastien Campocasso, Thomas Baizeau, and Vincent Hugel. Automatic multi-axis path planning for thinwall tubing through robotized wire deposition. *Procedia CIRP*, 79:89–94, jan 2019. ISSN 22128271. doi: 10.1016/j.procir.2019.02.017.

[317] Donghong Ding, Zengxi Pan, Dominic Cuiuri, Huijun Li, Nathan Larkin, and Stephen Van Duin. Automatic multi-direction slicing algorithms for wire based additive manufacturing. *Robotics and Computer-Integrated Manufacturing*, 37:139–150, feb 2016. ISSN 07365845. doi: 10.1016/j.rcim.2015.09.002.

[318] Lan Ren, Todd Sparks, Jianzhong Ruan, and Frank Liou. Process planning strategies for solid freeform fabrication of metal parts. *Journal of Manufacturing Systems*, 27(4): 158–165, oct 2008. ISSN 02786125. doi: 10.1016/j.jmsy.2009.02.002.

[319] Jianzhong Ruan, Todd E. Sparks, Ajay Panackal, F. W. Liou, Kunnayut Eiamsa-Ard, Kevin Slattery, Hsin Nan Chou, and Mary Kinsella. Automated slicing for a multiaxis metal deposition system. *Journal of Manufacturing Science and Engineering, Transactions of the ASME*, 129(2):303–310, apr 2007. ISSN 10871357. doi: 10.1115/1.2673492.

[320] Rajeev Dwivedi, Srdja Zekovic, and Radovan Kovacevic. A novel approach to fabricate uni-directional and branching slender structures using laser-based direct metal deposition. *International Journal of Machine Tools and Manufacture*, 47(7-8):1246–1256, jun 2007. doi: 10.1016/J.IJMACHTOOLS.2006.08.012.

[321] Tiago A. Rodrigues, V. Duarte, R. M. Miranda, Telmo G. Santos, and J. P. Oliveira. Current status and perspectives on wire and arc additive manufacturing (WAAM). *Materials*, 12(7):1121, apr 2019. ISSN 19961944. doi: 10.3390/ma12071121.

[322] Yu Ming Zhang, Yiwei Chen, Pengjiu Li, and Alan T. Male. Weld deposition-based rapid prototyping: A preliminary study. *Journal of Materials Processing Technology*, 135(2-3 SPEC.):347–357, apr 2003. ISSN 09240136. doi: 10.1016/S0924-0136(02)00867-1.

[323] Donghong Ding, Zengxi Pan, Dominic Cuiuri, Huijun Li, Stephen Van Duin, and Nathan Larkin. Bead modelling and implementation of adaptive MAT path in wire and arc additive manufacturing. *Robotics and Computer-Integrated Manufacturing*, 39:32–42, jun 2016. ISSN 07365845. doi: 10.1016/j.rcim.2015.12.004.

[324] Haisen Zhao, Fanglin Gu, Qi Xing Huang, Jorge Garcia, Yong Chen, Changhe Tu, Bedrich Benes, Hao Zhang, Daniel Cohen-Or, and Baoquan Chen. Connected fermat spirals for layered fabrication. In *ACM Transactions on Graphics*, volume 35, pages 1–10. Association for Computing Machinery, jul 2016. ISBN 9781450342797. doi: 10.1145/2897824.2925958.

[325] Fei Ren, Yuwen Sun, and Dongming Guo. Combined reparameterization-based spiral toolpath generation for five-axis sculptured surface machining. *International Journal of Advanced Manufacturing Technology*, 40(7-8):760–768, feb 2009. ISSN 02683768. doi: 10.1007/s00170-008-1385-9.

[326] M. Bertoldi, M Yardimci, C. M Pistor, and S. I. Guceri. Domain Decomposition and Space Filling Curves in Toolpath Planning and Generation. In *1998 International Solid Freeform Fabrication Symposium*, pages 267–276, Austin, Texas, 1998. The University of Texas at Austin. doi: 10.26153/tsw/608.

[327] W. K. Chiu, Y. C. Yeung, and K. M. Yu. Toolpath generation for layer manufacturing of fractal objects. *Rapid Prototyping Journal*, 12(4):214–221, 2006. ISSN 13552546. doi: 10.1108/13552540610682723.

[328] Tobias Wasser, Anshu Dhar Jayal, and Christoph Pistor. Implementation and Evaluation of Novel Buildstyles in Fused Deposition Modeling (FDM). In *1999 International Solid Freeform Fabrication Symposium*, pages 95–102, Austin, Texas, 1999. The University of Texas at Austin. doi: 10.26153/tsw/722.

[329] Prabhjot Singh and Debasish Dutta. Offset slices for multidirection layered deposition. *Journal of Manufacturing Science and Engineering, Transactions of the ASME*, 130 (1), feb 2008. ISSN 10871357. doi: 10.1115/1.2783217.

[330] Lior Shapira, Ariel Shamir, and Daniel Cohen-Or. Consistent mesh partitioning and skeletonisation using the shape diameter function. *Visual Computer*, 24(4):249–259, apr 2008. ISSN 01782789. doi: 10.1007/s00371-007-0197-5.

[331] Michael R. Dunlavey. Efficient Polygon-Filling Algorithms for Raster Displays. *ACM Transactions on Graphics (TOG)*, 2(4):264–273, jan 1983. ISSN 15577368. doi: 10.1145/245.248.

[332] S. C. Park and B. K. Choi. Tool-path planning for direction-parallel area milling. *CAD Computer Aided Design*, 32(1):17–25, jan 2000. ISSN 00104485. doi: 10.1016/S0010-4485(99)00080-9.

[333] V. T. Rajan, Vijay Srinivasan, and Konstantinos A. Tarabanis. The optimal zigzag direction for filling a two-dimensional region. *Rapid Prototyping Journal*, 7(5):231–241, dec 2001. ISSN 13552546. doi: 10.1108/13552540110410431.

[334] H. Li, Z. Dong, and G. W. Vickers. Optimal toolpath pattern identification for single island, sculptured part rough machining using fuzzy pattern analysis. *Computer-Aided Design*, 26(11):787–795, nov 1994. ISSN 00104485. doi: 10.1016/0010-4485(94)90092-2.

[335] R. T. Farouki, T. Koenig, K. A. Tarabanis, J. U. Korein, and J. S. Batchelder. Path planning with offset curves for layered fabrication processes. *Journal of Manufacturing Systems*, 14(5):355–368, jan 1995. ISSN 02786125. doi: 10.1016/0278-6125(95)98872-4.

[336] Y. Yang, H. T. Loh, J. Y.H. Fuh, and Y. G. Wang. Equidistant path generation for improving scanning efficiency in layered manufacturing. *Rapid Prototyping Journal*, 8 (1):30–37, 2002. ISSN 13552546. doi: 10.1108/13552540210413284.

[337] Hongcheng Wang, Peter Jang, and James A. Stori. A metric-based approach to two-dimensional (2D) tool-path optimization for high-speed machining. *Journal of Manufacturing Science and Engineering, Transactions of the ASME*, 127(1):33–48, feb 2005. ISSN 10871357. doi: 10.1115/1.1830492.

[338] Prashant Kulkarni, Anne Marsan, and Debasish Dutta. Review of process planning techniques in layered manufacturing. *Rapid Prototyping Journal*, 6(1):18–35, 2000. ISSN 13552546. doi: 10.1108/13552540010309859.

[339] Harry Blum. A Transformation for Extracting New Descriptors of Shape. In Weiant Wathen-Dunn, editor, *Models for the Perception of Speech and Visual Form*, pages 362–380. MIT Press, Cambridge, 1967.

[340] Eric Berger, Ken Conley, Josh Faust, Tully Foote, Brian Gerkey, Jeremy Leibs, Morgan Quigley, and Rob Wheeler. ROS - Introduction. URL https://wiki.ros.org/ROS/Introduction.

[341] Shaun Edwards, Jorge Nicho, and Jonathan Meyer. The Descartes Planning Library for Semi-constrained Cartesian Trajectories, 2015. URL https://wiki.ros.org/descartes.

[342] Levi Armstrong. Optimization Motion Planning with Tesseract and TrajOpt for Industrial Applications, 2018. URL https://rosindustrial.org/news/2018/7/5/optimization-motion-planning-with-tesseract-and-trajopt-for-industrial-applications

[343] Victor Lamoine. ROS Additive Manufacturing, 2017. URL https://rosindustrial.org/news/2017/9/12/ros-additive-manufacturing.

[344] Carosena Meola, Simone Boccardi, and Giovanni maria Carlomagno. Chapter 3 - Infrared Thermography Basics. pages 57–83. Woodhead Publishing, 2017. ISBN 978-1-78242-171-9. doi: https://doi.org/10.1016/B978-1-78242-171-9.00003-6.

[345] Gustavo Tapia and Alaa Elwany. A Review on Process Monitoring and Control in Metal-Based Additive Manufacturing. *Journal of Manufacturing Science and Engineering*, 136(6):060801, oct 2014. doi: 10.1115/1.4028540.

[346] Tuomas Purtonen, Anne Kalliosaari, and Antti Salminen. Monitoring and adaptive control of laser processes. *Physics Procedia*, 56(C):1218–1231, jan 2014. ISSN 18753892. doi: 10.1016/j.phpro.2014.08.038.

[347] Sarah K. Everton, Matthias Hirsch, Petros I. Stavroulakis, Richard K. Leach, and Adam T. Clare. Review of in-situ process monitoring and in-situ metrology for metal additive manufacturing. *Materials and Design*, 95:431–445, apr 2016. ISSN 18734197. doi: 10.1016/j.matdes.2016.01.099.

[348] Charalabos Doumanidis and Yong Min Kwak. Geometry modeling and control by infrared and laser sensing in thermal manufacturing with material deposition. *Journal of Manufacturing Science and Engineering, Transactions of the ASME*, 123(1):45–52, feb 2001. ISSN 15288935. doi: 10.1115/1.1344898.

[349] Mehrdad Iravani-Tabrizipour and Ehsan Toyserkani. An image-based feature tracking algorithm for real-time measurement of clad height. *Machine Vision and Applications*, 18(6):343–354, nov 2007. ISSN 09328092. doi: 10.1007/s00138-006-0066-7.

[350] Jun Xiong, Guangjun Zhang, Zhilong Qiu, and Yongzhe Li. Vision-sensing and bead width control of a single-bead multi-layer part: Material and energy savings in GMAW-based rapid manufacturing. *Journal of Cleaner Production*, 41:82–88, feb 2013. ISSN 09596526. doi: 10.1016/j.jclepro.2012.10.009.

[351] Jun Xiong and Guangjun Zhang. Adaptive control of deposited height in GMAW-based layer additive manufacturing. *Journal of Materials Processing Technology*, 214 (4):962–968, apr 2014. ISSN 09240136. doi: 10.1016/j.jmatprotec.2013.11.014.

[352] Jun Xiong, Ziqiu Yin, and Weihua Zhang. Closed-loop control of variable layer width for thin-walled parts in wire and arc additive manufacturing. *Journal of Materials Processing Technology*, 233:100–106, jul 2016. doi: 10.1016/J.JMATPROTEC.2016.02.021.

[353] Sukhomay Pal, Surjya K. Pal, and Arun K. Samantaray. Sensor based weld bead geometry prediction in pulsed metal inert gas welding process through artificial neural networks. *International Journal of Knowledge-Based and Intelligent Engineering Systems*, 12(2):101–114, 2008. ISSN 18758827. doi: 10.3233/KES-2008-12202.

[354] Nuri Akkas, Durmuş Karayel, Sinan Serdar Ozkan, Ahmet Oğur, and Bayram Topal. Modeling and analysis of the weld bead geometry in submerged arc welding by using adaptive neurofuzzy inference system. *Mathematical Problems in Engineering*, 2013: 1–10, oct 2013. ISSN 1024123X. doi: 10.1155/2013/473495.

[355] Yongzhe Li, Yunfei Sun, Qinglin Han, Guangjun Zhang, and Imre Horváth. Enhanced beads overlapping model for wire and arc additive manufacturing of multi-layer multi-bead metallic parts. *Journal of Materials Processing Technology*, 252:838–848, feb 2018. ISSN 09240136. doi: 10.1016/j.jmatprotec.2017.10.017.

[356] Dongming Hu and Radovan Kovacevic. Sensing, modeling and control for laser-based additive manufacturing. *International Journal of Machine Tools and Manufacture*, 43 (1):51–60, jan 2003. ISSN 08906955. doi: 10.1016/S0890-6955(02)00163-3.

[357] Guijun Bi, Andres Gasser, Konrad Wissenbach, Alexander Drenker, and Reinhart Poprawe. Identification and qualification of temperature signal for monitoring and control in laser cladding. *Optics and Lasers in Engineering*, 44(12):1348–1359, dec 2006. ISSN 01438166. doi: 10.1016/j.optlaseng.2006.01.009.

[358] Guijun Bi, Andres Gasser, Konrad Wissenbach, Alexander Drenker, and Reinhart Poprawe. Characterization of the process control for the direct laser metallic powder deposition. *Surface and Coatings Technology*, 201(6):2676–2683, 2006. ISSN 02578972. doi: 10.1016/j.surfcoat.2006.05.006.

[359] Guijun Bi, Bert Schürmann, Andres Gasser, Konrad Wissenbach, and Reinhart Poprawe. Development and qualification of a novel laser-cladding head with integrated sensors. *International Journal of Machine Tools and Manufacture*, 47(3-4): 555–561, mar 2007. ISSN 08906955. doi: 10.1016/j.ijmachtools.2006.05.010.

[360] Lie Tang and Robert G. Landers. Melt pool temperature control for laser metal deposition processes-part I: Online temperature control. *Journal of Manufacturing Science and Engineering, Transactions of the ASME*, 132(1):0110101–0110109, feb 2010. ISSN 10871357. doi: 10.1115/1.4000882.

[361] G. Bi, C. N. Sun, and A. Gasser. Study on influential factors for process monitoring and control in laser aided additive manufacturing. *Journal of Materials Processing Technology*, 213(3):463–468, mar 2013. ISSN 09240136. doi: 10.1016/j.jmatprotec.2012.10.006.

[362] Mohammad H. Farshidianfar, Amir Khajepour, and Adrian Gerlich. Real-time control of microstructure in laser additive manufacturing. *International Journal of Advanced Manufacturing Technology*, 82(5-8):1173–1186, feb 2016. ISSN 14333015. doi: 10.1007/s00170-015-7423-5.

[363] CC Doumanidis and DE Hardt. Simultaneous in-process control of heat affected zone and cooling rate during arc welding. *Welding Journal*, 69(5):186s–196s, may 1990.

[364] C. S. Wu, J. Q. Gao, X. F. Liu, and Y. H. Zhao. Vision-based measurement of weld pool geometry in constant-current gas tungsten arc welding. *Proceedings of the Institution of Mechanical Engineers, Part B: Journal of Engineering Manufacture*, 217(6):879–882, jun 2003. ISSN 09544054. doi: 10.1243/09544050360673279.

[365] Yanling Xu, Gu Fang, Na Lv, Shanben Chen, and Ju Jia Zou. Computer vision technology for seam tracking in robotic GTAW and GMAW. *Robotics and Computer-Integrated Manufacturing*, 32:25–36, apr 2015. ISSN 07365845. doi: 10.1016/j.rcim.2014.09.002.

[366] A. S. Babkin and E. A. Gladkov. Identification of welding parameters for quality welds in GMAW. *Welding Journal*, 95(1):37s–46s, 2016. ISSN 00432296.

[367] Zhili Feng, Jian Chen, and Zongyao Chen. Monitoring weld pool surface and penetration using reversed electrode images. *Welding Journal*, 96(10):367s–375s, 2017.

[368] Sergio Ríos, Paul A. Colegrove, Filomeno Martina, and Stewart W. Williams. Analytical process model for wire + arc additive manufacturing. *Additive Manufacturing*, 21:651–657, may 2018. doi: 10.1016/J.ADDMA.2018.04.003.

[369] Almir Heralić, Anna Karin Christiansson, and Bengt Lennartson. Height control of laser metal-wire deposition based on iterative learning control and 3D scanning. *Optics and Lasers in Engineering*, 50(9):1230–1241, sep 2012. ISSN 01438166. doi: 10.1016/j.optlaseng.2012.03.016.

[370] Abdalla R. Nassar, Jayme S. Keist, Edward W. Reutzel, and Todd J. Spurgeon. Intra-layer closed-loop control of build plan during directed energy additive manufacturing of Ti-6Al-4V. *Additive Manufacturing*, 6:39–52, apr 2015. doi: 10.1016/J.ADDMA.2015.03.005.

[371] Donghong Ding, Chen Shen, Zengxi Pan, Dominic Cuiuri, Huijun Li, Nathan Larkin, and Stephen Van Duin. Towards an automated robotic arc-welding-based additive manufacturing system from CAD to finished part. *CAD Computer Aided Design*, 73:66–75, apr 2016. ISSN 00104485. doi: 10.1016/j.cad.2015.12.003.

[372] Marc Preissler, Chen Zhang, Maik Rosenberger, and Gunther Notni. Platform for 3D inline process control in additive manufacturing. In Peter Lehmann, Wolfgang Osten, and Armando Albertazzi Gonçalves, editors, *Optical Measurement Systems for*

Industrial Inspection X, volume 10329, page 103290R. International Society for Optics and Photonics, jun 2017. ISBN 9781510611030. doi: 10.1117/12.2270493.

[373] Marc Preissler, Chen Zhang, Maik Rosenberger, and Gunther Notni. Approach for Process Control in Additive Manufacturing Through Layer-Wise Analysis with 3-Dimensional Pointcloud Information. In *2018 International Conference on Digital Image Computing: Techniques and Applications, DICTA 2018*, pages 1–6. IEEE, dec 2019. ISBN 9781538666029. doi: 10.1109/DICTA.2018.8615803.

[374] Yuan Li, You Fu Li, Qing Lin Wang, De Xu, and Min Tan. Measurement and defect detection of the weld bead based on online vision inspection. *IEEE Transactions on Instrumentation and Measurement*, 59(7):1841–1849, jul 2010. ISSN 00189456. doi: 10.1109/TIM.2009.2028222.

[375] Wei Huang and Radovan Kovacevic. Development of a real-time laser-based machine vision system to monitor and control welding processes. *International Journal of Advanced Manufacturing Technology*, 63(1-4):235–248, nov 2012. ISSN 02683768. doi: 10.1007/s00170-012-3902-0.

[376] Jun Xiong and Guangjun Zhang. Online measurement of bead geometry in GMAW-based additive manufacturing using passive vision. *Measurement Science and Technology*, 24(11):115103, nov 2013. ISSN 13616501. doi: 10.1088/0957-0233/24/11/115103.

[377] Fenglin Lü, Huabin Chen, Chongjian Fan, and Shanben Chen. A novel control algorithm for weld pool control. *Industrial Robot*, 37(1):89–96, jan 2010. ISSN 0143991X. doi: 10.1108/01439911011009993.

[378] SICK Ltd. Profiler 2 SHORT RANGE DISTANCE SENSOR OPERATING INSTRUCTIONS, 2019.

[379] Scott M. Thompson, Linkan Bian, Nima Shamsaei, and Aref Yadollahi. An overview of Direct Laser Deposition for additive manufacturing; Part I: Transport phenomena, modeling and diagnostics. *Additive Manufacturing*, 8:36–62, 2015. ISSN 22148604. doi: 10.1016/j.addma.2015.07.001.

[380] C. Li, Z. Y. Liu, X. Y. Fang, and Y. B. Guo. Residual Stress in Metal Additive Manufacturing. In *Procedia CIRP*, volume 71, pages 348–353. Elsevier B.V., jan 2018. doi: 10.1016/j.procir.2018.05.039.

[381] Fencheng Liu, Xin Lin, Gaolin Yang, Menghua Song, Jing Chen, and Weidong Huang. Recrystallization and its influence on microstructures and mechanical properties of laser solid formed nickel base superalloy Inconel 718. *Rare Metals*, 30(SUPPL.1):433–438, mar 2011. ISSN 10010521. doi: 10.1007/s12598-011-0319-0.

[382] William D. Callister and David G. Rethwisch. *Materials science and engineering : an introduction*. Wiley, 10 edition, 2018. ISBN 9781119321590.

[383] Q. Zhang, J. Chen, H. Tan, X. Lin, and W. D. Huang. Influence of solution treatment on microstructure evolution of TC21 titanium alloy with near equiaxed β grains fabricated by laser additive manufacture. *Journal of Alloys and Compounds*, 666:380–386, 2016. ISSN 09258388. doi: 10.1016/j.jallcom.2016.01.065.

[384] L. Zhuo, L. Changmeng, L. Dong, and W. Huaming. Effect of heat treatment on microstructure and tensile properties of laser deposited titanium alloy TC21. *Materials Research Innovations*, 18(sup4):S4929–S4932, jul 2014. ISSN 1433075X. doi: 10.1179/1432891714Z.000000000812.

[385] Qiang Zhang, Jing Chen, Zhongliang Qi, Xin Lin, Hua Tan, and Weidong Huang. A Processing Route for Achieving Isotropic Tensile Properties in Laser Solid Formed α+β Titanium Alloy. *Metallurgical and Materials Transactions A: Physical Metallurgy and Materials Science*, 49(8):3651–3662, 2018. ISSN 10735623. doi: 10.1007/s11661-018-4695-z.

[386] C. M. Liu, H. M. Wang, X. J. Tian, H. B. Tang, and D. Liu. Microstructure and tensile properties of laser melting deposited Ti-5Al-5Mo-5V-1Cr-1Fe near β titanium alloy. *Materials Science and Engineering A*, 586:323–329, 2013. ISSN 09215093. doi: 10.1016/j.msea.2013.08.032.

[387] X Wu, R Sharman, J Mei, and W Voice. Microstructure and properties of a laser fabricated burn-resistant Ti alloy. *Materials & Design*, 25(2):103–109, 2004. ISSN 0261-3069. doi: https://doi.org/10.1016/j.matdes.2003.10.004.

[388] P L Blackwell and A Wisbey. Laser-aided manufacturing technologies; their application to the near-net shape forming of a high-strength titanium alloy. *Journal of Materials Processing Technology*, 170(1):268–276, 2005. ISSN 0924-0136. doi: https://doi.org/10.1016/j.jmatprotec.2005.05.014.

[389] Hao Deng, Longqing Chen, Wenbin Qiu, Zhou Zheng, Yi Tang, Zhendong Hu, Yongqiang Wei, Zuxi Xia, Guomin Le, Jun Tang, and Xudong Cui. Microstructure and mechanical properties of as-deposited and heat treated Ti-5Al-5Mo-5V-3Cr-1Zr (Ti-55531) alloy fabricated by laser melting deposition. *Journal of Alloys and Compounds*, 810:151792, 2019. ISSN 0925-8388. doi: https://doi.org/10.1016/j.jallcom.2019.151792.

[390] Ali Zhang, Dong Liu, Xinhua Wu, and Huaming Wang. Effect of heat treatment on microstructure and mechanical properties of laser deposited Ti60A alloy. *Journal of Alloys and Compounds*, 585:220–228, 2014. ISSN 0925-8388. doi: https://doi.org/10.1016/j.jallcom.2013.09.149.

[391] Charles Carson. Heat Treating of Titanium and Titanium Alloys. In *Heat Treating of Nonferrous Alloys*. ASM International, 2016. ISBN 978-1-62708-169-6. doi: 10.31399/asm.hb.v04e.a0006283.

[392] F F Schmidt and R A Wood. Heat treatment of titanium and titanium alloys. Technical report, NASA Marshall Space Flight Center, Huntsville, AL, United States, 1996.

[393] Rodney R. Boyer. Titanium and Its Alloys: Metallurgy, Heat Treatment and Alloy Characteristics. In *Encyclopedia of Aerospace Engineering*. John Wiley & Sons, Ltd, Chichester, UK, dec 2010. doi: 10.1002/9780470686652.eae198.

[394] Amanda Sterling, Nima Shamsaei, Brian Torries, and Scott M. Thompson. Fatigue Behaviour of Additively Manufactured Ti-6Al-4 v. In *Procedia Engineering*, volume 133, pages 576–589. Elsevier Ltd, jan 2015. doi: 10.1016/j.proeng.2015.12.632.

[395] S. Leuders, M. Thöne, A. Riemer, T. Niendorf, T. Tröster, H. A. Richard, and H. J. Maier. On the mechanical behaviour of titanium alloy TiAl6V4 manufactured by selective laser melting: Fatigue resistance and crack growth performance. *International Journal of Fatigue*, 48:300–307, mar 2013. ISSN 01421123. doi: 10.1016/j.ijfatigue.2012.11.011.

[396] Peng Hui Li, Wei Guo Guo, Kang Bo Yuan, Yu Su, Jian Jun Wang, Xin Lin, and Yan Ping Li. Effects of processing defects on the dynamic tensile mechanical behavior of laser-solid-formed Ti-6Al-4 V. *Materials Characterization*, 140:15–29, jun 2018. ISSN 10445803. doi: 10.1016/j.matchar.2018.03.032.

[397] N Chekir, J J Sixsmith, R Tollett, and M Brochu. Laser wire deposition of a large Ti-6AI-4V space component the methodology for creating a functional Ti-6Al-4V satellite part using LWD additive manufacturing is detailed. *Welding Journal*, 98(6):172S–180S, 2019. doi: 10.29391/2019.98.014.

[398] *Nickel Alloy, Corrosion and Heat Resistant, Investment Castings 52.5Ni - 19Cr - 3.0Mo - 5.1(Cb+Ta) - 0.90Ti - 0.60Al - 18Fe Vacuum Melted Homogenization and Solution Heat Treated*, sep 2000.

[399] *Nickel Alloy, Corrosion and Heat-Resistant, Bars, Forgings, and Rings 52.5Ni - 19Cr - 3.0Mo - 5.1Cb (Nb) - 0.90Ti - 0.50Al - 18Fe Consumable Electrode or Vacuum Induction Melted 1775 F (968 C) Solution Heat Treated, Precipitation-Hardenable*, jun 2009.

[400] D F Paulonis and J J Schirra. Alloy 718 at Pratt & Whitney: Historical Perspective and Future Challenges. In *Superalloys 718, 625, 706 and Various Derivatives (2001)*, pages 13–23, 2001. ISBN 0-87339-510-7. doi: 10.7449/2001/Superalloys_2001_13_23.

[401] Robert Schafrik, Douglas Ward, and Jon Groh. Application of Alloy 718 in GE Aircraft Engines: Past, Present and Next Five Years. In *Superalloys 718, 625, 706 and Various Derivatives (2001)*, pages 1–11, 2001. doi: 10.7449/2001/Superalloys_2001_1_11.

[402] J F Radavich. The Physical Metallurgy of Cast and Wrought Alloy 718. In *Superalloys 718 Metallurgy and Applications (1989)*, pages 229–240, 1989. ISBN 0-87339-097-0. doi: 10.7449/1989/Superalloys_1989_229_240.

[403] G. D. Janaki Ram, A. Venugopal Reddy, K. Prasad Rao, G. M. Reddy, and J. K. Sarin Sundar. Microstructure and tensile properties of Inconel 718 pulsed Nd-YAG laser welds. *Journal of Materials Processing Technology*, 167(1):73–82, aug 2005. ISSN 09240136. doi: 10.1016/j.jmatprotec.2004.09.081.

[404] Jon Lambarri, Josu Leunda, Virginia García Navas, Carlos Soriano, and Carmen Sanz. Microstructural and tensile characterization of Inconel 718 laser coatings for aeronautic components. *Optics and Lasers in Engineering*, 51(7):813–821, jul 2013. ISSN 01438166. doi: 10.1016/j.optlaseng.2013.01.011.

[405] P. L. Blackwell. The mechanical and microstructural characteristics of laser-deposited IN718. *Journal of Materials Processing Technology*, 170(1-2):240–246, dec 2005. ISSN 09240136. doi: 10.1016/j.jmatprotec.2005.05.005.

[406] Markus Bambach and Irina Sizova. Hot working behavior of selective laser melted and laser metal deposited Inconel 718. In *AIP Conference Proceedings*, volume 1960, page 170001. American Institute of Physics Inc., may 2018. ISBN 9780735416635. doi: 10.1063/1.5035058.

[407] Yaocheng Zhang, Li Yang, Tingyi Chen, Weihui Zhang, Xiwang Huang, and Jun Dai. Investigation on the optimized heat treatment procedure for laser fabricated IN718 alloy. *Optics and Laser Technology*, 97:172–179, dec 2017. ISSN 00303992. doi: 10.1016/j.optlastec.2017.06.027.

[408] Xiaogang You, Yi Tan, Shuang Shi, Jenn Ming Yang, Yinong Wang, Jiayan Li, and Qifan You. Effect of solution heat treatment on the precipitation behavior and strengthening mechanisms of electron beam smelted Inconel 718 superalloy. *Materials Science and Engineering A*, 689:257–268, mar 2017. ISSN 09215093. doi: 10.1016/j.msea.2017.01.093.

[409] E. Hosseini and V. A. Popovich. A review of mechanical properties of additively manufactured Inconel 718, dec 2019. ISSN 22148604.

[410] Frederick Lia, Joshua Z. Park, Jayme S. Keist, Sanjay Joshi, and Richard P. Martukanitz. Thermal and microstructural analysis of laser-based directed energy deposition for Ti-6Al-4V and Inconel 625 deposits. *Materials Science and Engineering A*, 717:1–10, feb 2018. ISSN 09215093. doi: 10.1016/j.msea.2018.01.060.

[411] G. P. Dinda, A. K. Dasgupta, and J. Mazumder. Laser aided direct metal deposition of Inconel 625 superalloy: Microstructural evolution and thermal stability. *Materials Science and Engineering A*, 509(1-2):98–104, may 2009. ISSN 09215093. doi: 10.1016/j.msea.2009.01.009.

[412] Y. L. Hu, X. Lin, S. Y. Zhang, Y. M. Jiang, X. F. Lu, H. O. Yang, and W. D. Huang. Effect of solution heat treatment on the microstructure and mechanical properties of Inconel 625 superalloy fabricated by laser solid forming. *Journal of Alloys and Compounds*, 767:330–344, oct 2018. ISSN 09258388. doi: 10.1016/j.jallcom.2018.07.087.

[413] Y. L. Hu, X. Lin, X. B. Yu, J. J. Xu, M. Lei, and W. D. Huang. Effect of Ti addition on cracking and microhardness of Inconel 625 during the laser solid forming processing. *Journal of Alloys and Compounds*, 711:267–277, jul 2017. ISSN 09258388. doi: 10.1016/j.jallcom.2017.03.355.

[414] Marleen Rombouts, Gert Maes, Myrjam Mertens, and Willy Hendrix. Laser metal deposition of Inconel 625: Microstructure and mechanical properties. *Journal of Laser Applications*, 24(5):052007, nov 2012. ISSN 1042-346X. doi: 10.2351/1.4757717.

[415] F. J. Xu, Y. H. Lv, B. S. Xu, Y. X. Liu, F. Y. Shu, and P. He. Effect of deposition strategy on the microstructure and mechanical properties of Inconel 625 superalloy fabricated by pulsed plasma arc deposition. *Materials and Design*, 45:446–455, mar 2013. ISSN 18734197. doi: 10.1016/j.matdes.2012.07.013.

[416] Alberta Aversa, Abdollah Saboori, Erica Librera, Michele de Chirico, Sara Biamino, Mariangela Lombardi, and Paolo Fino. The role of Directed Energy Deposition atmosphere mode on the microstructure and mechanical properties of 316L samples. *Additive Manufacturing*, 34(February):101274, 2020. ISSN 22148604. doi: 10.1016/j.addma.2020.101274.

[417] K. Benarji, Y. Ravi Kumar, A. N. Jinoop, C. P. Paul, and K. S. Bindra. Effect of Heat-Treatment on the Microstructure, Mechanical Properties and Corrosion Behaviour of SS 316 Structures Built by Laser Directed Energy Deposition Based Additive Manufacturing. *Metals and Materials International*, 27(3):488–499, 2021. ISSN 20054149. doi: 10.1007/s12540-020-00838-y.

[418] K. Saeidi, X. Gao, Y. Zhong, and Z. J. Shen. Hardened austenite steel with columnar sub-grain structure formed by laser melting. *Materials Science and Engineering A*, 625:221–229, feb 2015. ISSN 09215093. doi: 10.1016/j.msea.2014.12.018.

[419] Aref Yadollahi, Nima Shamsaei, Scott M. Thompson, and Denver W. Seely. Effects of process time interval and heat treatment on the mechanical and microstructural properties of direct laser deposited 316L stainless steel. *Materials Science and Engineering A*, 644:171–183, sep 2015. ISSN 09215093. doi: 10.1016/j.msea.2015.07.056.

[420] Du-Rim Eo, Sun-Hong Park, and Jung-Wook Cho. Inclusion evolution in additive manufactured 316L stainless steel by laser metal deposition process. *Materials &*

Design, 155:212–219, 2018. ISSN 0264-1275. doi: https://doi.org/10.1016/j.matdes.2018.06.001.

[421] K. Saeidi, X. Gao, F. Lofaj, L. Kvetková, and Z. J. Shen. Transformation of austenite to duplex austenite-ferrite assembly in annealed stainless steel 316L consolidated by laser melting. *Journal of Alloys and Compounds*, 633:463–469, jun 2015. ISSN 09258388. doi: 10.1016/j.jallcom.2015.01.249.

[422] Michał Ziętala, Tomasz Durejko, Marek Polański, Izabela Kunce, Tomasz Płociński, Witold Zieliński, Magdalena Łazińska, Wojciech Stępniowski, Tomasz Czujko, Krzysztof J. Kurzydłowski, and Zbigniew Bojar. The microstructure, mechanical properties and corrosion resistance of 316 L stainless steel fabricated using laser engineered net shaping. *Materials Science and Engineering A*, 677:1–10, nov 2016. ISSN 09215093. doi: 10.1016/j.msea.2016.09.028.

[423] Xiaohui Chen, Jia Li, Xu Cheng, Huaming Wang, and Zheng Huang. Effect of heat treatment on microstructure, mechanical and corrosion properties of austenitic stainless steel 316L using arc additive manufacturing. *Materials Science and Engineering A*, 715:307–314, feb 2018. ISSN 09215093. doi: 10.1016/j.msea.2017.10.002.

[424] Chengcheng Wang, Xipeng Tan, Erjia Liu, and Shu Beng Tor. Process parameter optimization and mechanical properties for additively manufactured stainless steel 316L parts by selective electron beam melting. *Materials and Design*, 147:157–166, jun 2018. ISSN 18734197. doi: 10.1016/j.matdes.2018.03.035.

[425] T. P.S. Gill, V. Shankar, M. G. Pujar, and P. Rodriguez. Effect of composition on the transformation of δ-ferrite TO σ in type 316 stainless steel weld metals. *Scripta Metallurgica et Materiala*, 32(10):1595–1600, may 1995. ISSN 0956716X. doi: 10.1016/0956-716X(95)00242-N.

[426] M. Schwind, J. Källqvist, J. O. Nilsson, J. Ågren, and H. O. Andrén. σ-phase precipitation in stabilized austenitic stainless steels. *Acta Materialia*, 48(10):2473–2481, jun 2000. ISSN 13596454. doi: 10.1016/S1359-6454(00)00069-0.

[427] R A Lula. *Stainless steel*. 1985.

[428] ASTM A564 / A564M - 19A, Standard Specification for Hot-Rolled and Cold-Finished Age-Hardening Stainless Steel Bars and Shapes, 2019. URL https://www.astm.org/Standards/A564.htm.

[429] H. Nakagawa and T. Miyazaki. Effect of retained austenite on the microstructure and mechanical properties of martensitic precipitation hardening stainless steel. *Journal of Materials Science*, 34(16):3901–3908, 1999. ISSN 00222461. doi: 10.1023/A:1004626907367.

[430] Tyler LeBrun, Takayuki Nakamoto, Keitaro Horikawa, and Hidetoshi Kobayashi. Effect of retained austenite on subsequent thermal processing and resultant mechanical properties of selective laser melted 17-4 PH stainless steel. *Materials and Design*, 81:44–53, sep 2015. ISSN 18734197. doi: 10.1016/j.matdes.2015.05.026.

[431] C. N. Hsiao, C. S. Chiou, and J. R. Yang. Aging reactions in a 17-4 PH stainless steel. *Materials Chemistry and Physics*, 74(2):134–142, mar 2002. ISSN 02540584. doi: 10.1016/S0254-0584(01)00460-6.

[432] M. Murayama, Y. Katayama, and K. Hono. Microstructural evolution in a 17-4 PH stainless steel after aging at 400 C. *Metallurgical and Materials Transactions A: Physical Metallurgy and Materials Science*, 30(2):345–353, 1999. ISSN 10735623. doi: 10.1007/s11661-999-0323-2.

[433] Kuei Chang Hsu and Chih Kuang Lin. High-temperature fatigue crack growth behavior of 17-4 PH stainless steels. *Metallurgical and Materials Transactions A: Physical Metallurgy and Materials Science*, 35 A(9):3018–3024, 2004. ISSN 10735623. doi: 10.1007/s11661-004-0044-5.

[434] C. Fahir Arisoy, Gokhan Basman, and M. Kelami Sesen. Failure of a 17-4 PH stainless steel sailboat propeller shaft. *Engineering Failure Analysis*, 10(6):711–717, dec 2003. ISSN 13506307. doi: 10.1016/S1350-6307(03)00041-4.

[435] Jun Wang, Hong Zou, Cong Li, Ruling Zuo, Shaoyu Qiu, and Baoluo Shen. Relationship of microstructure transformation and hardening behavior of type 17-4 PH stainless steel. *Journal of University of Science and Technology Beijing: Mineral Metallurgy Materials (Eng Ed)*, 13(3):235–239, jun 2006. ISSN 10058850. doi: 10.1016/S1005-8850(06)60050-9.

[436] Yu Sun, Rainer J. Hebert, and Mark Aindow. Effect of heat treatments on microstructural evolution of additively manufactured and wrought 17-4PH stainless steel. *Materials and Design*, 156:429–440, oct 2018. ISSN 18734197. doi: 10.1016/j.matdes.2018.07.015.

[437] D. Wang, C. T. Chi, W. Q. Wang, Y. L. Li, M. S. Wang, X. G. Chen, Z. H. Chen, X. P. Cheng, and Y. J. Xie. The effects of fabrication atmosphere condition on the microstructural and mechanical properties of laser direct manufactured stainless steel 17-4 PH. *Journal of Materials Science and Technology*, 35(7):1315–1322, jul 2019. ISSN 10050302. doi: 10.1016/j.jmst.2019.03.009.

[438] Setsuo Takaki, Kazuhiro Fukunaga, Junaidi Syarif, and Toshihiro Tsuchiyama. Effect of Grain Refinement on Thermal Stability of Metastable Austenitic Steel. *MATERIALS TRANSACTIONS*, 45(7):2245–2251, 2004. ISSN 1345-9678. doi: 10.2320/matertrans.45.2245.

[439] Jun Wang, Hong Zou, Cong Li, Shao yu Qiu, and Bao luo Shen. The effect of microstructural evolution on hardening behavior of type 17-4PH stainless steel in long-term aging at 350 C. *Materials Characterization*, 57(4-5):274–280, dec 2006. ISSN 10445803. doi: 10.1016/j.matchar.2006.02.004.

[440] ASM Handbook Committee. *ASM Handbook Volume 2: Properties and Selection: Nonferrous Alloys and Special-Purpose Materials*, volume 2. ASM International, dec 1990. doi: 10.31399/asm.hb.v02.9781627081627.

[441] Emma Sjölander and Salem Seifeddine. The heat treatment of Al-Si-Cu-Mg casting alloys, jul 2010. ISSN 09240136.

[442] E. Sjölander and S. Seifeddine. Artificial ageing of Al-Si-Cu-Mg casting alloys. *Materials Science and Engineering A*, 528(24):7402–7409, sep 2011. ISSN 09215093. doi: 10.1016/j.msea.2011.06.036.

[443] F Alghamdi and M Haghshenas. Microstructural and small-scale characterization of additive manufactured AlSi10Mg alloy. *SN Applied Sciences*, 1(3):255, 2019. ISSN 2523-3971. doi: 10.1007/s42452-019-0270-5.

[444] Martin Eden Glicksman. *Principles of solidification: An introduction to modern casting and crystal growth concepts*. Springer New York, 2011. ISBN 9781441973436. doi: 10.1007/978-1-4419-7344-3.

[445] ASTM F75-18, Standard Specification for Cobalt-28 Chromium-6 Molybdenum Alloy Castings and Casting Alloy for Surgical Implants (UNS R30075), 2018. URL http://www.astm.org/cgi-bin/resolver.cgi?F75-18.

[446] T. Kilner, R. M. Pilliar, G. C. Weatherly, and C. Allibert. Phase identification and incipient melting in a cast Co-Cr surgical implant alloy. *Journal of Biomedical Materials Research*, 16(1):63–79, jan 1982. ISSN 0021-9304. doi: 10.1002/jbm.820160109.

[447] Shingo Mineta, Shigenobu Namba, Takashi Yoneda, Kyosuke Ueda, and Takayuki Narushima. Carbide formation and dissolution in biomedical CO-CR-MO alloys with different carbon contents during solution treatment. *Metallurgical and Materials Transactions A: Physical Metallurgy and Materials Science*, 41(8):2129–2138, aug 2010. ISSN 10735623. doi: 10.1007/s11661-010-0227-1.

[448] H. S. Dobbs and J. L.M. Robertson. Heat treatment of cast Co-Cr-Mo for orthopaedic implant use. *Journal of Materials Science*, 18(2):391–401, feb 1983. ISSN 00222461. doi: 10.1007/BF00560627.

[449] J. Cohen, R. M. Rose, and J. Wulff. Recommended heat treatment and alloy additions for cast Co-Cr surgical implants. *Journal of Biomedical Materials Research*, 12(6): 935–937, nov 1978. ISSN 0021-9304. doi: 10.1002/jbm.820120613.

[450] M. Caudillo, M. Herrera-Trejo, M. R. Castro, E. Ramírez, C. R. González, and J. I. Juárez. On carbide dissolution in an as-cast ASTM F-75 alloy. *Journal of Biomedical Materials Research*, 59(2):378–385, feb 2002. ISSN 00219304. doi: 10.1002/jbm.10001.

[451] M. Herrera, A. Espinoza, J. Méndez, M. Castro, J. López, and J. Rendón. Effect of C content on the mechanical properties of solution treated as-cast ASTM F-75 alloys. *Journal of Materials Science: Materials in Medicine*, 16(7):607–611, jul 2005. ISSN 09574530. doi: 10.1007/s10856-005-2530-8.

[452] H. R. Lashgari, Sh Zangeneh, and M. Ketabchi. Isothermal aging effect on the microstructure and dry sliding wear behavior of Co-28Cr-5Mo-0.3C alloy. *Journal*

of Materials Science, 46(22):7262–7274, nov 2011. ISSN 00222461. doi: 10.1007/s10853-011-5686-2.

[453] Mantrala Kedar Mallik, Ch Srinivasa Rao, and V. V.S. Kesava Rao. Effect of heat treatment on hardness of Co-Cr-Mo alloy deposited with laser engineered net shaping. In *Procedia Engineering*, volume 97, pages 1718–1723. Elsevier Ltd, jan 2014. doi: 10.1016/j.proeng.2014.12.323.

[454] Félix A. España, Vamsi Krishna Balla, Susmita Bose, and Amit Bandyopadhyay. Design and fabrication of CoCrMo alloy based novel structures for load bearing implants using laser engineered net shaping. *Materials Science and Engineering C*, 30(1):50–57, jan 2010. ISSN 09284931. doi: 10.1016/j.msec.2009.08.006.

[455] Mallik Mantrala, Ch.Srinivasa Rao, and Vaddi Rao. Influence of heat Treatment on Tensile Properties of LENS Deposited Co-Cr-Mo alloy. In *6th International & 27th All India Manufacturing Technology, Design and Research Conference (AIMTDR-2016)*, pages 52–54, 2016.

[456] Chalasani Dharmendra, Amir Hadadzadeh, Babak Shalchi Amirkhiz, and Mohsen Mohammadi. The Morphology, Crystallography, and Chemistry of Phases in Wire-Arc Additively Manufactured Nickel Aluminum Bronze. In *Minerals, Metals and Materials Series*, pages 443–453. Springer International Publishing, 2019. ISBN 9783030058609. doi: 10.1007/978-3-030-05861-6_41.

[457] C. Dharmendra, A. Hadadzadeh, B. S. Amirkhiz, G. D. Janaki Ram, and M. Mohammadi. Microstructural evolution and mechanical behavior of nickel aluminum bronze Cu-9Al-4Fe-4Ni-1Mn fabricated through wire-arc additive manufacturing. *Additive Manufacturing*, 30:100872, dec 2019. ISSN 22148604. doi: 10.1016/j.addma.2019.100872.

[458] Chen Shen, Gang Mu, Xueming Hua, Fang Li, Dongzhi Luo, Xiangru Ji, and Chi Zhang. Influences of postproduction heat treatments on the material anisotropy of nickel-aluminum bronze fabricated using wire-arc additive manufacturing process. *International Journal of Advanced Manufacturing Technology*, 103(5-8):3199–3209, aug 2019. ISSN 14333015. doi: 10.1007/s00170-019-03700-7.

[459] Wonjong Jeong, Young Sam Kwon, and Dongsik Kim. Three-dimensional printing of tungsten structures by directed energy deposition. *Materials and Manufacturing Processes*, 34(9):986–992, jul 2019. ISSN 15322475. doi: 10.1080/10426914.2019.1594253.

[460] Chun Li, Shiyu Ma, Xue Liu, Jinfeng Li, and Guomin Le. Microstructures and properties of 80W-20Fe alloys prepared using laser melting deposition process. *International Journal of Refractory Metals and Hard Materials*, 77:113–119, dec 2018. ISSN 22133917. doi: 10.1016/j.ijrmhm.2018.08.005.

[461] Duncan Stewart. 3D printing growth accelerates again. URL https://www2.deloitte.com/us/en/insights/industry/technology/technology-media-and-telecom-predictions/3d-printing-market.html.

[462] Neng Li, Shuai Huang, Guodong Zhang, Renyao Qin, Wei Liu, Huaping Xiong, Gongqi Shi, and Jon Blackburn. Progress in additive manufacturing on new materials: A review, feb 2019. ISSN 10050302.

[463] M. A. Easton, M. Qian, A. Prasad, and D. H. StJohn. Recent advances in grain refinement of light metals and alloys. *Current Opinion in Solid State and Materials Science*, 20(1):13–24, feb 2016. ISSN 13590286. doi: 10.1016/j.cossms.2015.10.001.

[464] M. J. Bermingham, D. Kent, H. Zhan, D. H. Stjohn, and M. S. Dargusch. Controlling the microstructure and properties of wire arc additive manufactured Ti-6Al-4V with trace boron additions. *Acta Materialia*, 91:289–303, jun 2015. ISSN 13596454. doi: 10.1016/j.actamat.2015.03.035.

[465] S. Mereddy, M. J. Bermingham, D. Kent, A. Dehghan-Manshadi, D. H. StJohn, and M. S. Dargusch. Trace Carbon Addition to Refine Microstructure and Enhance Properties of Additive-Manufactured Ti-6Al-4V. *JOM*, 70(9):1670–1676, sep 2018. ISSN 15431851. doi: 10.1007/s11837-018-2994-x.

[466] Nesma T. Aboulkhair, Ian Maskery, Chris Tuck, Ian Ashcroft, and Nicola M. Everitt. The microstructure and mechanical properties of selectively laser melted AlSi10Mg: The effect of a conventional T6-like heat treatment. *Materials Science and Engineering A*, 667:139–146, jun 2016. ISSN 09215093. doi: 10.1016/j.msea.2016.04.092.

[467] National Research Council of Canada. Associate Committee on Tribology. A strategy for tribology in Canada: enhancing reliability and efficiency through the reduction of wear and friction. Technical report, 1986.

[468] Hui Wang, Weiming Xia, and Yuansheng Jin. A study on abrasive resistance of Ni-based coatings with a WC hard phase. *Wear*, 195(1):47–52, 1996. ISSN 0043-1648. doi: https://doi.org/10.1016/0043-1648(95)06762-0. URL https://www.sciencedirect.com/science/article/pii/0043164895067620.

[469] N M Melendez, V V Narulkar, G A Fisher, and A G McDonald. Effect of reinforcing particles on the wear rate of low-pressure cold-sprayed WC-based MMC coatings. *Wear*, 306(1):185–195, 2013. ISSN 0043-1648. doi: https://doi.org/10.1016/j.wear.2013.08.006. URL https://www.sciencedirect.com/science/article/pii/S0043164813004596.

[470] Sima A Alidokht and Richard R Chromik. Sliding wear behavior of cold-sprayed NI-WC composite coatings: Influence OF WC content. *Wear*, page 203792, 2021. ISSN 0043-1648. doi: https://doi.org/10.1016/j.wear.2021.203792. URL https://www.sciencedirect.com/science/article/pii/S0043164821001812.

[471] E Badisch and M Kirchgaßner. Influence of welding parameters on microstructure and wear behaviour of a typical NiCrBSi hardfacing alloy reinforced with tungsten carbide. *Surface and Coatings Technology*, 202(24):6016–6022, 2008. ISSN 0257-8972. doi: https://doi.org/10.1016/j.surfcoat.2008.06.185. URL https://www.sciencedirect.com/science/article/pii/S025789720800621X.

[472] T W Clyne and P J Withers. *An Introduction to Metal Matrix Composites*. Cambridge University Press, Cambridge, 1993. ISBN 9780521483575. doi: DOI:10.1017/CBO9780511623080. URL https://www.cambridge.org/core/books/an-introduction-to-metal-matrix-composites/1F8F6103DBF4CE7E48EAE95EAA56CBA4.

[473] Š Houdková, F Zahálka, M Kašparová, and L M. Berger. Comparative Study of Thermally Sprayed Coatings Under Different Types of Wear Conditions for Hard Chromium Replacement. *Tribology Letters*, 43(2):139–154, 2011. ISSN 1573-2711. doi: 10.1007/s11249-011-9791-9. URL https://doi.org/10.1007/s11249-011-9791-9.

[474] Y Pan, D Y Li, and H Zhang. Enhancing the wear resistance of sintered WC–Co composite by adding pseudo-elastic TiNi constituent. *Wear*, 271(9):1916–1921, 2011. ISSN 0043-1648. doi: https://doi.org/10.1016/j.wear.2011.01.052. URL https://www.sciencedirect.com/science/article/pii/S0043164811001451.

[475] M. Anderson, Chiovelli, S, and R Llewellyn. The Use of Tungsten Carbide Materials for Oilsand Wear Applications. *Thermal Spray 2003 : Advancing the Science and Applying the Technology*, 1:509–518, 2003.

[476] Hiroyuki Saito, Akira Iwabuchi, and Tomoharu Shimizu. Effects of Co content and WC grain size on wear of WC cemented carbide. *Wear*, 261(2):126–132, 2006. ISSN 0043-1648. doi: https://doi.org/10.1016/j.wear.2005.09.034. URL https://www.sciencedirect.com/science/article/pii/S0043164805004588.

[477] J Y Sheikh-Ahmad and J A Bailey. The wear characteristics of some cemented tungsten carbides in machining particleboard. *Wear*, 225-229:256–266, 1999. ISSN 0043-1648. doi: https://doi.org/10.1016/S0043-1648(98)00361-5. URL https://www.sciencedirect.com/science/article/pii/S0043164898003615.

[478] J H Steele and J L McCall, editors. *Application of Quantitative Microscopy to Cemented Carbides*. ASTM International, West Conshohocken, PA, jan 1984. ISBN 978-0-8031-4905-2. doi: 10.1520/STP839-EB. URL https://www.astm.org/DIGITAL{_}LIBRARY/STP/SOURCE{_}PAGES/STP839.htm.

[479] K Van Acker, D Vanhoyweghen, R Persoons, and J Vangrunderbeek. Influence of tungsten carbide particle size and distribution on the wear resistance of laser clad WC/Ni coatings. *Wear*, 258(1):194–202, 2005. ISSN 0043-1648. doi: https://doi.org/10.1016/j.wear.2004.09.041. URL https://www.sciencedirect.com/science/article/pii/S0043164804002662.

[480] N Otsu. A Threshold Selection Method from Gray-Level Histograms. *IEEE Transactions on Systems, Man, and Cybernetics*, 9(1):62–66, 1979. ISSN 0018-9472 VO - 9. doi: 10.1109/TSMC.1979.4310076.

[481] J Canny. A Computational Approach to Edge Detection. *IEEE Transactions on Pattern Analysis and Machine Intelligence*, PAMI-8(6):679–698, 1986. ISSN 1939-3539 VO - PAMI-8. doi: 10.1109/TPAMI.1986.4767851.

[482] J. Macqueen. Some methods for classification and analysis of multivariate observations. In *In 5-th Berkeley Symposium on Mathematical Statistics and Probability*, pages 281–297, 1967.

[483] P.J. Evennett and C. Hammond. Microscopy | overview. In Paul Worsfold, Alan Townshend, and Colin Poole, editors, *Encyclopedia of Analytical Science (Second Edition)*, pages 32–41. Elsevier, Oxford, second edition edition, 2005. ISBN 978-0-12-369397-6. doi: https://doi.org/10.1016/B0-12-369397-7/00376-9. URL https://www.sciencedirect.com/science/article/pii/B0123693977003769.

[484] Almambet Iskakov and Surya R Kalidindi. A Framework for the Systematic Design of Segmentation Workflows. *Integrating Materials and Manufacturing Innovation*, 9 (1):70–88, 2020. ISSN 2193-9772. doi: 10.1007/s40192-019-00166-z. URL https://doi.org/10.1007/s40192-019-00166-z.

[485] H Peregrina-Barreto, I R Terol-Villalobos, J J Rangel-Magdaleno, A M Herrera-Navarro, L A Morales-Hernández, and F Manríquez-Guerrero. Automatic grain size determination in microstructures using image processing. *Measurement*, 46(1):249–258, 2013. ISSN 0263-2241. doi: https://doi.org/10.1016/j.measurement.2012.06.012. URL https://www.sciencedirect.com/science/article/pii/S0263224112002539.

[486] Andrew Campbell, Paul Murray, Evgenia Yakushina, Stephen Marshall, and William Ion. New methods for automatic quantification of microstructural features using digital image processing. *Materials & Design*, 141:395–406, 2018. ISSN 0264-1275. doi: https://doi.org/10.1016/j.matdes.2017.12.049. URL https://www.sciencedirect.com/science/article/pii/S0264127517311620.

[487] Stéfan van der Walt, Johannes L. Schönberger, Juan Nunez-Iglesias, François Boulogne, Joshua D. Warner, Neil Yager, Emmanuelle Gouillart, Tony Yu, and the scikit-image contributors. scikit-image: image processing in Python. *PeerJ*, 2:e453, 6 2014. ISSN 2167-8359. doi: 10.7717/peerj.453. URL https://doi.org/10.7717/peerj.453.

[488] G. Bradski. The OpenCV Library. *Dr. Dobb's Journal of Software Tools*, 2000.

[489] David Arthur and Sergei Vassilvitskii. K-means++: The advantages of careful seeding. volume 8, pages 1027–1035, 01 2007. doi: 10.1145/1283383.1283494.

[490] Afsaneh Jalalian, Syamsiah B T Mashohor, Hajjah Rozi Mahmud, M Iqbal B Saripan, Abdul Rahman B Ramli, and Babak Karasfi. Computer-aided detection/diagnosis of breast cancer in mammography and ultrasound: a review. *Clinical Imaging*, 37(3):420–426, 2013. ISSN 0899-7071. doi: https://doi.org/10.1016/j.clinimag.2012.09.024. URL https://www.sciencedirect.com/science/article/pii/S0899707112002938.

[491] Alex Krizhevsky, Ilya Sutskever, and Geoffrey E. Hinton. Imagenet classification with deep convolutional neural networks. In *Proceedings of the 25th International Conference on Neural Information Processing Systems - Volume 1*, NIPS'12, page 1097–1105, Red Hook, NY, USA, 2012. Curran Associates Inc.

[492] Karen Simonyan and Andrew Zisserman. Very deep convolutional networks for large-scale image recognition, 2015.

[493] Ian Goodfellow, Yoshua Bengio, and Aaron Courville. Deep Feedforward Networks. In *Deep Learning*, chapter 6, pages 165–166. MIT Press, 2016. URL http://www.deeplearningbook.org.

[494] Zhou and Chellappa. Computation of optical flow using a neural network. In *IEEE 1988 International Conference on Neural Networks*, pages 71–78 vol.2, 1988. ISBN VO -. doi: 10.1109/ICNN.1988.23914.

[495] Jürgen Schmidhuber. Deep learning in neural networks: An overview. *Neural Networks*, 61:85–117, 2015. ISSN 0893-6080. doi: https://doi.org/10.1016/j.neunet.2014.09.003. URL https://www.sciencedirect.com/science/article/pii/S0893608014002135.

[496] Vijay Badrinarayanan, Alex Kendall, and Roberto Cipolla. Segnet: A deep convolutional encoder-decoder architecture for image segmentation, 2016.

[497] Liang-Chieh Chen, George Papandreou, Iasonas Kokkinos, Kevin Murphy, and Alan L. Yuille. Deeplab: Semantic image segmentation with deep convolutional nets, atrous convolution, and fully connected crfs, 2017.

[498] Mohamed Omran, Christoph Lassner, Gerard Pons-Moll, Peter V. Gehler, and Bernt Schiele. Neural body fitting: Unifying deep learning and model-based human pose and shape estimation, 2018.

[499] Christian Szegedy, Wei Liu, Yangqing Jia, Pierre Sermanet, Scott Reed, Dragomir Anguelov, Dumitru Erhan, Vincent Vanhoucke, and Andrew Rabinovich. Going deeper with convolutions, 2014.

[500] Olaf Ronneberger, Philipp Fischer, and Thomas Brox. U-net: Convolutional networks for biomedical image segmentation, 2015.

[501] C. Shashank Kaira, Xiaogang Yang, Vincent De Andrade, Francesco De Carlo, William Scullin, Doga Gursoy, and Nikhilesh Chawla. Automated correlative segmentation of large Transmission X-ray Microscopy (TXM) tomograms using deep learning. *Materials Characterization*, 142(May):203–210, 2018. ISSN 10445803. doi: 10.1016/j.matchar.2018.05.053. URL https://doi.org/10.1016/j.matchar.2018.05.053.

[502] Dmitry S. Bulgarevich, Susumu Tsukamoto, Tadashi Kasuya, Masahiko Demura, and Makoto Watanabe. Pattern recognition with machine learning on optical microscopy images of typical metallurgical microstructures. *Scientific Reports*, 8(1):3–9, 2018. ISSN 20452322. doi: 10.1038/s41598-018-20438-6. URL http://dx.doi.org/10.1038/s41598-018-20438-6.

[503] Ossama Abouelatta. Classification of Copper Alloys Microstructure Using Image Processing and Neural Network. *Journal of American Science*, 9:213–223, jun 2013.

[504] Aritra Chowdhury, Elizabeth Kautz, Bülent Yener, and Daniel Lewis. Image driven machine learning methods for microstructure recognition. *Computational Materials Science*, 123:176–187, 2016. ISSN 09270256. doi: 10.1016/j.commatsci.2016.05.034. URL http://dx.doi.org/10.1016/j.commatsci.2016.05.034.

[505] Seyed Majid Azimi, Dominik Britz, Michael Engstler, Mario Fritz, and Frank Mücklich. Advanced steel microstructural classification by deep learning methods. *Scientific Reports*, 8(1):1–14, 2018. ISSN 20452322. doi: 10.1038/s41598-018-20037-5.

[506] Tiberiu Stan, Zachary T. Thompson, and Peter W. Voorhees. Optimizing convolutional neural networks to perform semantic segmentation on large materials imaging datasets: X-ray tomography and serial sectioning. *Materials Characterization*, 160(January): 110119, 2020. ISSN 10445803. doi: 10.1016/j.matchar.2020.110119. URL https://doi.org/10.1016/j.matchar.2020.110119.

[507] Adam Paszke, Sam Gross, Francisco Massa, Adam Lerer, James Bradbury, Gregory Chanan, Trevor Killeen, Zeming Lin, Natalia Gimelshein, Luca Antiga, Alban Desmaison, Andreas Köpf, Edward Yang, Zach DeVito, Martin Raison, Alykhan Tejani, Sasank Chilamkurthy, Benoit Steiner, Lu Fang, Junjie Bai, and Soumith Chintala. Pytorch: An imperative style, high-performance deep learning library, 2019.

[508] Martin Abadi, Paul Barham, Jianmin Chen, Zhifeng Chen, Andy Davis, Jeffrey Dean, Matthieu Devin, Sanjay Ghemawat, Geoffrey Irving, Michael Isard, Manjunath Kudlur, Josh Levenberg, Rajat Monga, Sherry Moore, Derek G. Murray, Benoit Steiner, Paul Tucker, Vijay Vasudevan, Pete Warden, Martin Wicke, Yuan Yu, and Xiaoqiang Zheng. Tensorflow: A system for large-scale machine learning. In *12th USENIX Symposium on Operating Systems Design and Implementation (OSDI 16)*, pages 265–283, 2016. URL https://www.usenix.org/system/files/conference/osdi16/osdi16-abadi.pdf.

[509] Kentaro Wada. labelme: Image Polygonal Annotation with Python. https://github.com/wkentaro/labelme, 2016.

[510] Antoni Buades, Bartomeu Coll, and Jean-Michel Morel. Non-Local Means Denoising. *Image Processing On Line*, 1:208–212, 2011. https://doi.org/10.5201/ipol.2011.bcm_nlm.

[511] Ian Goodfellow, Yoshua Bengio, and Aaron Courville. Applications. In *Deep Learning*, pages 448–449. MIT Press, 2016. URL https://www.deeplearningbook.org/contents/applications.html.

[512] Connor Shorten and Taghi M. Khoshgoftaar. A survey on Image Data Augmentation for Deep Learning. *Journal of Big Data*, 6(1):60, 2019. ISSN 21961115. doi: 10.1186/s40537-019-0197-0. URL https://doi.org/10.1186/s40537-019-0197-0.

[513] Robail Yasrab, Naijie Gu, and Xiaoci Zhang. An encoder-decoder based convolution neural network (cnn) for future advanced driver assistance system (adas). *Applied Sciences*, 7(4), 2017. ISSN 2076-3417. doi: 10.3390/app7040312. URL https://www.mdpi.com/2076-3417/7/4/312.

[514] Vinod Nair and Geoffrey E. Hinton. Rectified linear units improve restricted boltzmann machines. In *Proceedings of the 27th International Conference on International*

Conference on Machine Learning, ICML'10, page 807–814, Madison, WI, USA, 2010. Omnipress. ISBN 9781605589077.

[515] Abhishek Chaurasia and Eugenio Culurciello. Linknet: Exploiting encoder representations for efficient semantic segmentation. *CoRR*, abs/1707.03718, 2017. URL http://arxiv.org/abs/1707.03718.

[516] Sergey Ioffe and Christian Szegedy. Batch normalization: Accelerating deep network training by reducing internal covariate shift. *CoRR*, abs/1502.03167, 2015. URL http://arxiv.org/abs/1502.03167.

[517] Kaiming He, Xiangyu Zhang, Shaoqing Ren, and Jian Sun. Deep residual learning for image recognition. *CoRR*, abs/1512.03385, 2015. URL http://arxiv.org/abs/1512.03385.

[518] Andrew G. Howard, Menglong Zhu, Bo Chen, Dmitry Kalenichenko, Weijun Wang, Tobias Weyand, Marco Andreetto, and Hartwig Adam. Mobilenets: Efficient convolutional neural networks for mobile vision applications. *CoRR*, abs/1704.04861, 2017. URL http://arxiv.org/abs/1704.04861.

[519] Chigozie Nwankpa, Winifred Ijomah, Anthony Gachagan, and Stephen Marshall. Activation functions: Comparison of trends in practice and research for deep learning, 2018.

[520] François Chollet et al. Keras. https://keras.io, 2015.

[521] Pavel Yakubovskiy. Segmentation models. https://github.com/qubvel/segmentation_models, 2019.

[522] Paul Jaccard. The distribution of the flora in the alpine zone.1. *New Phytologist*, 11(2): 37–50, 1912. doi: https://doi.org/10.1111/j.1469-8137.1912.tb05611.x. URL https://nph.onlinelibrary.wiley.com/doi/abs/10.1111/j.1469-8137.1912.tb05611.x.

[523] Lee R Dice. Measures of the Amount of Ecologic Association Between Species. *Ecology*, 26(3):297–302, apr 1945. ISSN 00129658, 19399170. doi: 10.2307/1932409. URL http://www.jstor.org/stable/1932409.

[524] W. R. Crum, O. Camara, and D. L. G. Hill. Generalized overlap measures for evaluation and validation in medical image analysis. *IEEE Transactions on Medical Imaging*, 25 (11):1451–1461, 2006. doi: 10.1109/TMI.2006.880587.

[525] Diederik P. Kingma and Jimmy Ba. Adam: A method for stochastic optimization, 2017.

[526] Djork-Arné Clevert, Thomas Unterthiner, and Sepp Hochreiter. Fast and accurate deep network learning by exponential linear units (elus), 2016.

[527] Ma Yi-de, Liu Qing, and Qian Zhi-bai. Automated image segmentation using improved pcnn model based on cross-entropy. In *Proceedings of 2004 International Symposium on Intelligent Multimedia, Video and Speech Processing, 2004.*, pages 743–746, Oct 2004. doi: 10.1109/ISIMP.2004.1434171.

[528] Carole H. Sudre, Wenqi Li, Tom Vercauteren, Sebastien Ourselin, and M. Jorge Cardoso. Generalised dice overlap as a deep learning loss function for highly unbalanced segmentations. *Lecture Notes in Computer Science*, page 240–248, 2017. ISSN 1611-3349. doi: 10.1007/978-3-319-67558-9_28. URL http://dx.doi.org/10.1007/978-3-319-67558-9_28.

[529] Saeid Asgari Taghanaki, Yefeng Zheng, S. Kevin Zhou, Bogdan Georgescu, Puneet Sharma, Daguang Xu, Dorin Comaniciu, and Ghassan Hamarneh. Combo loss: Handling input and output imbalance in multi-organ segmentation, 2018.

[530] Herbert Robbins and Sutton Monro. A Stochastic Approximation Method. *The Annals of Mathematical Statistics*, 22(3):400 – 407, 1951. doi: 10.1214/aoms/1177729586. URL https://doi.org/10.1214/aoms/1177729586.

[531] Léon Bottou, Frank E. Curtis, and Jorge Nocedal. Optimization methods for large-scale machine learning, 2018.

[532] T. Tieleman and G. Hinton. Lecture 6.5—RmsProp: Divide the gradient by a running average of its recent magnitude. COURSERA: Neural Networks for Machine Learning, 2012.

[533] Dominic Masters and Carlo Luschi. Revisiting small batch training for deep neural networks, 2018.

[534] D.Randall Wilson and Tony R Martinez. The general inefficiency of batch training for gradient descent learning. *Neural Networks*, 16(10):1429–1451, 2003. ISSN 0893-6080. doi: https://doi.org/10.1016/S0893-6080(03)00138-2. URL https://www.sciencedirect.com/science/article/pii/S0893608003001382.

[535] Yann A LeCun, Léon Bottou, Genevieve B Orr, and Klaus-Robert Müller. Efficient BackProp BT - Neural Networks: Tricks of the Trade: Second Edition. pages 9–48. Springer Berlin Heidelberg, Berlin, Heidelberg, 2012. ISBN 978-3-642-35289-8. doi: 10.1007/978-3-642-35289-8_3. URL https://doi.org/10.1007/978-3-642-35289-8_3.

[536] Nitish Shirish Keskar, Jorge Nocedal, Ping Tak Peter Tang, Dheevatsa Mudigere, and Mikhail Smelyanskiy. On large-batch training for deep learning: Generalization gap and sharp minima. *5th International Conference on Learning Representations, ICLR 2017 - Conference Track Proceedings*, pages 1–16, 2017.

[537] Leslie N. Smith. Cyclical learning rates for training neural networks, 2017.

[538] Kaichao You, Mingsheng Long, Jianmin Wang, and Michael I. Jordan. How does learning rate decay help modern neural networks?, 2019.

[539] Nitish Srivastava, Geoffrey Hinton, Alex Krizhevsky, Ilya Sutskever, and Ruslan Salakhutdinov. Dropout: A simple way to prevent neural networks from overfitting. *Journal of Machine Learning Research*, 15(56):1929–1958, 2014. URL http://jmlr.org/papers/v15/srivastava14a.html.

[540] Kaiming He, Xiangyu Zhang, Shaoqing Ren, and Jian Sun. Delving deep into rectifiers: Surpassing human-level performance on imagenet classification. In *Proceedings of the IEEE International Conference on Computer Vision (ICCV)*, December 2015.

[541] Stevo Bozinovski. Reminder of the first paper on transfer learning in neural networks, 1976. *Informatica*, 44, 09 2020. doi: 10.31449/inf.v44i3.2828.

[542] Jia Deng, Wei Dong, Richard Socher, Li-Jia Li, Kai Li, and Li Fei-Fei. Imagenet: A large-scale hierarchical image database. In *2009 IEEE conference on computer vision and pattern recognition*, pages 248–255. Ieee, 2009.

[543] Mikko Kotila. Autonomio Talos, 2019. URL http://github.com/autonomio/talos.

[544] Sebastian Raschka. Model evaluation, model selection, and algorithm selection in machine learning, 2020.

[545] Gareth James, Daniela Witten, Trevor Hastie, and Tibshirani Robert. Resampling Methods. In *An Introduction to Statistical Learning with Applications in R*, chapter 5, pages 177–205. Springer US, 2 edition, 2013. ISBN 978-1-0716-1417-4.

[546] King N. Ngan, Thomas Meier, and Douglas Chai. Chapter 4 - model-based coding. In King N. Ngan, Thomas Meier, and Douglas Chai, editors, *Advanced Video Coding: Principles and Techniques*, volume 7 of *Advances in Image Communication*, pages 183–249. Elsevier, 1999. doi: https://doi.org/10.1016/S0928-1479(99)80006-0. URL https://www.sciencedirect.com/science/article/pii/S0928147999800060.

[547] Ian Goodfellow, Yoshua Bengio, and Aaron Courville. Optimization for Training Deep Models. In *Deep Learning*, chapter 8, pages 271–325. MIT Press, 2016. URL http://www.deeplearningbook.org.

[548] Ibrahem Kandel, Mauro Castelli, and Aleš Popovič. Comparative study of first order optimizers for image classification using convolutional neural networks on histopathology images. *Journal of Imaging*, 6(9), 2020. ISSN 2313-433X. doi: 10.3390/jimaging6090092. URL https://www.mdpi.com/2313-433X/6/9/92.

[549] Nitish Shirish Keskar and Richard Socher. Improving generalization performance by switching from adam to sgd, 2017.

[550] Ashia C. Wilson, Rebecca Roelofs, Mitchell Stern, Nathan Srebro, and Benjamin Recht. The marginal value of adaptive gradient methods in machine learning, 2018.

[551] B.T. Polyak. Some methods of speeding up the convergence of iteration methods. *USSR Computational Mathematics and Mathematical Physics*, 4(5):1–17, 1964. ISSN 0041-5553. doi: https://doi.org/10.1016/0041-5553(64)90137-5. URL https://www.sciencedirect.com/science/article/pii/0041555364901375.

[552] Ian Goodfellow, Yoshua Bengio, and Aaron Courville. Probability and Information Theory. In *Deep Learning*, chapter 3, pages 65–66. MIT Press, 2016. URL http://www.deeplearningbook.org.

[553] D. Marmanis, K. Schindler, J.D. Wegner, S. Galliani, M. Datcu, and U. Stilla. Classification with an edge: Improving semantic image segmentation with boundary detection. *ISPRS Journal of Photogrammetry and Remote Sensing*, 135:158–172, 2018. ISSN 0924-2716. doi: https://doi.org/10.1016/j.isprsjprs.2017.11.009. URL https://www.sciencedirect.com/science/article/pii/S092427161630572X.

[554] Aashish Dhawan, Pankaj Bodani, and Vishal Garg. Post processing of image segmentation using conditional random fields. In *2019 6th International Conference on Computing for Sustainable Global Development (INDIACom)*, pages 729–734, 2019.

[555] Xin Pan, Jian Zhao, and Jun Xu. An end-to-end and localized post-processing method for correcting high-resolution remote sensing classification result images. *Remote Sensing*, 12(5), 2020. ISSN 2072-4292. doi: 10.3390/rs12050852. URL https://www.mdpi.com/2072-4292/12/5/852.

[556] M C Carvalho, Y Wang, J A S Souza, E M Braga, and L Li. Characterization of phases and defects in chromium carbide overlays deposited by SAW process. *Engineering Failure Analysis*, 60:374–382, 2016. ISSN 1350-6307. doi: https://doi.org/10.1016/j.engfailanal.2015.11.058. URL https://www.sciencedirect.com/science/article/pii/S1350630715301801.

[557] L. Ma, C. Huang, J. Jiang, R Hui, Y. Xie, and Z.S. Liu. Cracks formation and residual stress in chromium carbide overlays. *Engineering Failure Analysis*, 31:320–337, 2013. ISSN 1350-6307. doi: https://doi.org/10.1016/j.engfailanal.2013.01.050. URL https://www.sciencedirect.com/science/article/pii/S1350630713000629.

[558] N. Barnes, S. Borle, and P. F Mendez. Large anomalous features in the microstructure of chromium carbide weld overlays. *Science and Technology of Welding and Joining*, 22(7):595–600, oct 2017. ISSN 1362-1718. doi: 10.1080/13621718.2017.1278831. URL https://doi.org/10.1080/13621718.2017.1278831.

[559] M Jones and U Waag. The influence of carbide dissolution on the erosion–corrosion properties of cast tungsten carbide/Ni-based PTAW overlays. *Wear*, 271(9):1314–1324, 2011. ISSN 0043-1648. doi: https://doi.org/10.1016/j.wear.2011.01.046. URL https://www.sciencedirect.com/science/article/pii/S0043164811001220.

[560] M Dalaee, F Cheaitani, A Arabi-Hashemi, C Rohrer, B Weisse, C Leinenbach, and K Wegener. Feasibility study in combined direct metal deposition (DMD) and plasma

transfer arc welding (PTA) additive manufacturing. *The International Journal of Advanced Manufacturing Technology*, 106(9):4375–4389, 2020. ISSN 1433-3015. doi: 10.1007/s00170-019-04917-2. URL https://doi.org/10.1007/s00170-019-04917-2.

[561] S. Ríos, P. A. Colegrove, and S. W. Williams. Metal transfer modes in plasma Wire + Arc additive manufacture. *Journal of Materials Processing Technology*, 264:45–54, 2019. ISSN 0924-0136. doi: https://doi.org/10.1016/j.jmatprotec.2018.08.043. URL https://www.sciencedirect.com/science/article/pii/S0924013618303856.

[562] M Singleton and P Nash. The C-Ni (Carbon-Nickel) system. *Bulletin of Alloy Phase Diagrams*, 10(2):121–126, 1989. ISSN 0197-0216. doi: 10.1007/BF02881419. URL https://doi.org/10.1007/BF02881419.

[563] Peter Bayliss and A. A. Levinson. MINERALOGICAL REVIEW OF THE ALBERTA OIL SAND DEPOSITS (LOWER CRETACEOUS, MANNVILLE GROUP). *Bulletin of Canadian Petroleum Geology*, 24(2):211–224, jun 1976. ISSN 0007-4802. doi: 10.35767/GSCPGBULL.24.2.211.

[564] Gary Fisher, David Crick, John Wolodko, Duane Kichton, and Leo Parent. Impact Testing Of Materials For Oil Sands Processing Applications, mar 2007.

[565] A. Kagawa, M. Hirata, and Y. Sakamoto. Solute partitioning on solidification of nickel-base ternary alloys. *Journal of Materials Science 1990 25:12*, 25(12):5063–5069, dec 1990. ISSN 1573-4803. doi: 10.1007/BF00580130. URL https://link.springer.com/article/10.1007/BF00580130.

[566] J. P. Kruth, L. Froyen, J. Van Vaerenbergh, P. Mercelis, M. Rombouts, and B. Lauwers. Selective laser melting of iron-based powder. *Journal of Materials Processing Technology*, 149(1-3):616–622, jun 2004. ISSN 0924-0136. doi: 10.1016/J.JMATPROTEC.2003.11.051.

[567] Dongdong Gu and Yifu Shen. Balling phenomena in direct laser sintering of stainless steel powder: Metallurgical mechanisms and control methods. *Materials & Design*, 30(8):2903–2910, sep 2009. ISSN 0261-3069. doi: 10.1016/J.MATDES.2009.01.013.

[568] Ruidi Li, Jinhui Liu, Yusheng Shi, Li Wang, and Wei Jiang. Balling behavior of stainless steel and nickel powder during selective laser melting process. *The International Journal of Advanced Manufacturing Technology 2011 59:9*, 59(9):1025–1035, aug 2011. ISSN 1433-3015. doi: 10.1007/S00170-011-3566-1. URL https://link-springer-com.login.ezproxy.library.ualberta.ca/article/10.1007/s00170-011-3566-1.

[569] Saad A. Khairallah, Andrew T. Anderson, Alexander Rubenchik, and Wayne E. King. Laser powder-bed fusion additive manufacturing: Physics of complex melt flow and formation mechanisms of pores, spatter, and denudation zones. *Acta Materialia*, 108: 36–45, apr 2016. ISSN 1359-6454. doi: 10.1016/J.ACTAMAT.2016.02.014.

[570] Dongdong Gu, Hongqiao Wang, and Guoquan Zhang. Selective laser melting additive manufacturing of Ti-based nanocomposites: The role of nanopowder. *Metallurgical and Materials Transactions A: Physical Metallurgy and Materials Science*, 45 (1):464–476, jan 2014. ISSN 10735623. doi: 10.1007/S11661-013-1968-4/FIGURES/12. URL https://link-springer-com.login.ezproxy.library.ualberta.ca/article/10.1007/s11661-013-1968-4.

[571] A Kolsgaard and S Brusethaug. Fluidity of aluminium alloy AlSi7Mg–SiC particulate composite melts. *Materials Science and Technology*, 10(6):545–551, jun 1994. ISSN 0267-0836. doi: 10.1179/mst.1994.10.6.545. URL https://doi.org/10.1179/mst.1994.10.6.545.

[572] Nian Sheng Cheng and Adrian Wing Keung Law. Exponential formula for computing effective viscosity. *Powder Technology*, 129(1-3):156–160, jan 2003. ISSN 0032-5910. doi: 10.1016/S0032-5910(02)00274-7.

[573] Dongdong Gu and Yifu Shen. Processing conditions and microstructural features of porous 316L stainless steel components by DMLS. *Applied Surface Science*, 255(5, Part 1):1880–1887, 2008. ISSN 0169-4332. doi: https://doi.org/10.1016/j.apsusc.2008.06.118. URL https://www.sciencedirect.com/science/article/pii/S0169433208015456.

[574] Ruidi Li, Jinhui Liu, Yusheng Shi, Li Wang, and Wei Jiang. Balling behavior of stainless steel and nickel powder during selective laser melting process. *The International Journal of Advanced Manufacturing Technology*, 59(9):1025–1035, 2012.

ISSN 1433-3015. doi: 10.1007/s00170-011-3566-1. URL https://doi.org/10.1007/s00170-011-3566-1.

[575] . URL https://app.knovel.com/hotlink/itble/id:kt00XRAJY1/table-3-specific-heat/table-3-specific-heat.

[576] Carl L. Yaws. Knovel, 2009. URL https://app.knovel.com/hotlink/itble/id:kpYHTPHC09/yaws-handbook-thermodynamic/yaws-handbook-thermodynamic.

[577] . URL https://app.knovel.com/hotlink/itble/id:kt00XRDAC1/table-2-5-thermal-conductivities/table-2-5-thermal-conductivities.

[578] URL https://app.knovel.com/hotlink/itble/id:kt012140T6/table-10-19-properties/table-10-19-properties.

[579] Q. Li, T. C. Lei, and W. Z. Chen. Microstructural characterization of WCp reinforced Ni–Cr–B–Si–C composite coatings. *Surface and Coatings Technology*, 114(2-3):285–291, may 1999. ISSN 0257-8972. doi: 10.1016/S0257-8972(99)00056-0.

[580] Shengbin Zhao, Lijun Yang, Yiming Huang, and Sai Xu. A novel method to fabricate Ni/WC composite coatings by laser wire deposition: Processing characteristics, microstructural evolution and mechanical properties under different wire transfer modes. *Additive Manufacturing*, 38:101738, feb 2021. ISSN 2214-8604. doi: 10.1016/J.ADDMA.2020.101738.

[581] R. J. Arsenault and M. Taya. Thermal residual stress in metal matrix composite. *Acta Metallurgica*, 35(3):651–659, mar 1987. ISSN 0001-6160. doi: 10.1016/0001-6160(87)90188-X.

[582] S. Ho and E. J. Lavernia. Thermal residual stresses in metal matrix composites: A review. *Applied Composite Materials: An International Journal for the Science and Application of Composite Materials*, 2(1):1–30, 1995. ISSN 15734897. doi: 10.1007/BF00567374/METRICS. URL https://link.springer.com/article/10.1007/BF00567374.

[583] Yoosuf N Picard. Scanning Electron Microscopy, dec 2019. URL https://doi.org/10.31399/asm.hb.v10.a0006668.

[584] P. Q. Xu, J. W. Ren, P. L. Zhang, H. Y. Gong, and S. L. Yang. Analysis of formation and interfacial WC dissolution behavior of WC-Co/invar laser-TIG welded joints. *Journal of Materials Engineering and Performance*, 22(2):613–623, feb 2013. ISSN 15441024. doi: 10.1007/S11665-012-0279-Z/FIGURES/11. URL https://link.springer.com/article/10.1007/s11665-012-0279-z.

[585] Qian Wang, Qian Li, Liang Zhang, Dong Xu Chen, Hui Jin, Ji Dong Li, Jun Wei Zhang, and Chun Yan Ban. Microstructure and properties of Ni-WC gradient composite coating prepared by laser cladding. *Ceramics International*, 48(6):7905–7917, mar 2022. ISSN 0272-8842. doi: 10.1016/J.CERAMINT.2021.11.338.

[586] 50 mol.% cr2c in w2c (cr0.5w0.5c0.5 ht2) crystal structure: Datasheet from "pauling file multinaries edition – 2022" in springermaterials (https://materials.springer.com/isp/crystallographic/docs/sd_1253216). URL https://materials.springer.com/isp/crystallographic/docs/sd_1253216. Copyright 2016 Springer-Verlag Berlin Heidelberg & Material Phases Data System (MPDS), Switzerland & National Institute for Materials Science (NIMS), Japan.

[587] URL https://app.knovel.com/hotlink/itble/id:kt0091J1V3/table-6-melting-points/table-6-melting-points.

[588] S. Lata Sinha, S. Kumar Dewangan, and A. Sharma. Particulate Science and Technology An International Journal A review on particulate slurry erosive wear of industrial materials: In context with pipeline transportation of mineral-slurry A review on particulate slurry erosive wear of industrial materials: In context with pipeline transportation of mineral-slurry. *PARTICULATE SCIENCE AND TECHNOLOGY*, 35(1):103–118, 2017. ISSN 1548-0046. doi: 10.1080/02726351.2015.1131792. URL https://www.tandfonline.com/action/journalInformation?journalCode=upst20http://dx.

[589] J. Chen, X. Y. Li, T. Bell, and H. Dong. Improving the wear properties of Stellite 21 alloy by plasma surface alloying with carbon and nitrogen. *Wear*, 264(3-4):157–165, feb 2008. ISSN 0043-1648. doi: 10.1016/J.WEAR.2006.12.012.

[590] Artur Czupryński. Microstructure and abrasivewear resistance of metal matrix composite coatings deposited on steel grade AISI 4715 by powder plasma transferred arc welding part 1. Mechanical and structural properties of a cobalt-based alloy surface layer reinforced with pa. *Materials*, 14(9), 2021. ISSN 19961944. doi: 10.3390/ma14092382.

[591] Mayur S. Sawant and N. K. Jain. Investigations on wear characteristics of Stellite coating by micro-plasma transferred arc powder deposition process. *Wear*, 378-379: 155–164, 2017. ISSN 00431648. doi: 10.1016/j.wear.2017.02.041.

[592] Qing Yu Hou, J. S. Gao, and F. Zhou. Microstructure and wear characteristics of cobalt-based alloy deposited by plasma transferred arc weld surfacing. *Surface and Coatings Technology*, 194(2-3):238–243, may 2005. ISSN 0257-8972. doi: 10.1016/J.SURFCOAT.2004.07.065.

[593] B Song, Z. Wang, Q. Yan, Y. Zhang, J. Zhang, C. Cai, Q. Wei, and Y. Shi. Integral method of preparation and fabrication of metal matrix composite: Selective laser melting of in-situ nano/submicro-sized carbides reinforced iron matrix composites. *Materials Science and Engineering: A*, 707:478–487, nov 2017. ISSN 0921-5093. doi: 10.1016/J.MSEA.2017.09.092.

[594] Z. Zhang and R. Kovacevic. Laser cladding of iron-based erosion resistant metal matrix composites. *Journal of Manufacturing Processes*, 38:63–75, feb 2019. ISSN 1526-6125. doi: 10.1016/J.JMAPRO.2019.01.001.

[595] S V Prasad and R Asthana. Aluminum Metal-Matrix Composites for Automotive Applications: Tribological Considerations. *Tribology Letters*, 17(3):445–453, 2004. ISSN 1573-2711. doi: 10.1023/B:TRIL.0000044492.91991.f3. URL https://doi.org/10.1023/B:TRIL.0000044492.91991.f3.

[596] P. Samal, P. R. Vundavilli, A. Meher, and M. M. Mahapatra. Recent progress in aluminum metal matrix composites: A review on processing, mechanical and wear properties. *Journal of Manufacturing Processes*, 59:131–152, nov 2020. ISSN 1526-6125. doi: 10.1016/J.JMAPRO.2020.09.010.

[597] K A Sandy, H Henein, and K M Jaansalu. On the Contact of Liquid Nickel with Tungsten Carbide or Boron Carbide. *Canadian Metallurgical Quarterly*, 48(2):133–143, jun 2009. ISSN 0008-4433. doi: 10.1179/cmq.2009.48.2.133. URL https://doi.org/10.1179/cmq.2009.48.2.133.

[598] A R Kennedy. The microstructure and mechanical properties of Al-Si-B4C metal matrix composites. *Journal of Materials Science*, 37(2):317–323, 2002. ISSN 1573-4803. doi: 10.1023/A:1013600328599. URL https://doi.org/10.1023/A:1013600328599.

[599] S V Nair, J K Tien, and R C Bates. SiC-reinforced aluminium metal matrix composites. *International Metals Reviews*, 30(1):275–290, jan 1985. ISSN 0308-4590. doi: 10.1179/imtr.1985.30.1.275. URL https://doi.org/10.1179/imtr.1985.30.1.275.

[600] A. Riquelme, P. Rodrigo, M. D. Escalera-Rodríguez, and J. Rams. Characterisation and mechanical properties of Al/SiC metal matrix composite coatings formed on ZE41 magnesium alloys by laser cladding. *Results in Physics*, 13:102160, jun 2019. ISSN 2211-3797. doi: 10.1016/J.RINP.2019.102160.

[601] A. Perminov, M. Jurisch, G. Bartzsch, H. Biermann, T. Weißgärber, and O. Volkova. Manufacturing Fe–TiC metal matrix composite by Electron Beam Powder Bed Fusion from pre-alloyed gas atomized powder. *Materials Science and Engineering: A*, 813:141130, may 2021. ISSN 0921-5093. doi: 10.1016/J.MSEA.2021.141130.

[602] G. Muvvala, S. Mullick, and Ashish K. Nath. Development of process maps based on molten pool thermal history during laser cladding of Inconel 718/TiC metal matrix composite coatings. *Surface and Coatings Technology*, 399:126100, oct 2020. ISSN 0257-8972. doi: 10.1016/J.SURFCOAT.2020.126100.

[603] X. Yang, L. Wang, Z. Gao, Q. Wang, M. Du, and X. Zhan. WC distribution, microstructure evolution mechanism and microhardness of a developed Ti-6Al-4 V/WC MMC coating fabricated by laser cladding. *Optics Laser Technology*, 153:108232, sep 2022. ISSN 0030-3992. doi: 10.1016/J.OPTLASTEC.2022.108232.

[604] M. Ostolaza, J. I. Arrizubieta, M. Cortina, and A. Lamikiz. Study of the reinforcement phase dilution into the metal matrix in functionally graded Stellite 6 and WC metal matrix composite by Laser Metal Deposition. *Procedia CIRP*, 94:330–335, jan 2020. ISSN 2212-8271. doi: 10.1016/J.PROCIR.2020.09.062.

[605] G Fisher, T Wolfe, and K Meszaros. The Effects of Carbide Characteristics on the Performance of Tungsten Carbide-Based Composite Overlays, Deposited by Plasma-Transferred Arc Welding. *Journal of Thermal Spray Technology*, 22:764–771, 2013. doi: 10.1007/s11666-012-9877-4.

[606] D. Rose, J. Forth, H. Henein, T. Wolfe, and A.J. Qureshi. Automated semantic segmentation of NiCrBSi-WC optical microscopy images using convolutional neural networks. *Computational Materials Science*, 210:111391, jul 2022. ISSN 0927-0256. doi: 10.1016/J.COMMATSCI.2022.111391.

[607] H. Hotz, M. Zimmermann, S. Greco, B. Kirsch, and J. C. Aurich. Additive manufacturing of functionally graded Ti-Al structures by laser-based direct energy deposition. *Journal of Manufacturing Processes*, 68:1524–1534, aug 2021. ISSN 1526-6125. doi: 10.1016/J.JMAPRO.2021.06.068.

[608] A. Choudhary, A. Sadhu, S. Sarkar, and G. Nath, A. K.and Muvvala. Laser surface polishing of NiCrSiBC – 60WC ceramic-metal matrix composite deposited by laser directed energy deposition process. *Surface and Coatings Technology*, 404:126480, dec 2020. ISSN 0257-8972. doi: 10.1016/J.SURFCOAT.2020.126480.

[609] T. Lehmann, D. Rose, E. Ranjbar, M. Ghasri-Khouzani, M. Tavakoli, H. Henein, T. Wolfe, and A. Jawad Qureshi. Large-scale metal additive manufacturing: a holistic review of the state of the art and challenges. *International Materials Reviews*, 67 (4):410–459, may 2022. ISSN 0950-6608. doi: 10.1080/09506608.2021.1971427. URL https://doi.org/10.1080/09506608.2021.1971427.

[610] G. Lohöfer. Theory of an Electromagnetically Levitated Metal Sphere I: Absorbed Power. *SIAM Journal on Applied Mathematics*, 49(2):567–581, 1989. ISSN 0036-1399. doi: 10.1137/0149032.

[611] M. G Frohberg. Thirty years of levitation melting calorimetry – a balance. *Thermochimica Acta*, 337(1):7–17, 1999. ISSN 0040-6031. doi: https://doi.org/10.1016/S0040-6031(99)00159-8. URL https://www.sciencedirect.com/science/article/pii/S0040603199001598.

[612] H. Lv, Q.and Jiang, X. Jiao, J. Liu, J. Liu, and Z. Yang. Simulation analysis and experimental study of the temperature characteristics of electromagnetic levitation. *AIP Advances*, 8(10), 2018. ISSN 21583226. doi: 10.1063/1.5055678. URL http://dx.doi.org/10.1063/1.5055678.

[613] Ch.-A. Gandin, D Tourret, T Volkmann, D M Herlach, A Ilbagi, and H Henein. Solidification Modeling: From Electromagnetic Levitation to Atomization Processing, aug 2012. URL https://doi.org/10.1002/9783527647903.ch19.

[614] J. E. Rodriguez, C. Kreischer, T. Volkmann, and D. M. Matson. Solidification velocity of undercooled Fe-Co alloys. *Acta Materialia*, 122:431–437, 2017. ISSN 13596454. doi: 10.1016/j.actamat.2016.09.047.

[615] A. Saud, C. Gandin, M. Bellet, T. Volkmann, and D. Herlach. Simulation of shrinkage-induced macrosegregation in a multicomponent alloy during reduced-gravity solidification BT - TMS 2016 145th Annual Meeting Exhibition. pages 35–42, Cham, 2016. Springer International Publishing. ISBN 978-3-319-48254-5.

[616] C Karrasch, T Volkmann, J Valloton, M Kolbe, and D M Herlach. Bent dendrite growth in undercooled Fe-B alloy melts. *IOP Conference Series: Materials Science and Engineering*, 117:12015, 2016. ISSN 1757-8981. doi: 10.1088/1757-899x/117/1/012015. URL http://dx.doi.org/10.1088/1757-899X/117/1/012015.

[617] M. Mohr, R. K. Wunderlich, K. Zweiacker, S. Prades-Rödel, R. Sauget, A. Blatter, R. Logé, A. Dommann, A. Neels, W. L. Johnson, and H. J. Fecht. Surface tension and viscosity of liquid Pd43Cu27Ni10P20 measured in a levitation device under microgravity. *npj Microgravity*, 5(1), 2019. ISSN 23738065. doi: 10.1038/s41526-019-0065-4. URL http://dx.doi.org/10.1038/s41526-019-0065-4.

[618] H.J. Fecht and R. K. Wunderlich. Fundamentals of Liquid Processing in Low Earth Orbit: From Thermophysical Properties to Microstructure Formation in Metallic Alloys. *Jom*, 69(8):1261–1268, 2017. ISSN 15431851. doi: 10.1007/s11837-017-2417-4.

[619] R. K Wunderlich, M. Mohr, Y. Dong, U. Hecht, D. M. Matson, R. Hyers, G. Bracker, J. Lee, S. Schneider, X. Xiao, and H. J. Fecht. Thermophysical properties of the TiAl-2Cr-2Nb alloy in the liquid phase measured with an electromagnetic levitation device on board the International Space Station, ISS-EML. *International Journal of Materials Research*, 112(10):770–781, 2021. doi: doi:10.1515/ijmr-2021-8266. URL https://doi.org/10.1515/ijmr-2021-8266.

[620] C D Cao, T Letzig, G P Görler, and D M Herlach. Liquid phase separation in undercooled Co–Cu alloys processed by electromagnetic levitation and differential thermal analysis. *Journal of Alloys and Compounds*, 325(1):113–117, 2001. ISSN 0925-8388. doi: https://doi.org/10.1016/S0925-8388(01)01276-2. URL https://www.sciencedirect.com/science/article/pii/S0925838801012762.

[621] Y K Zhang, J Gao, L L Wei, M Kolbe, T Volkmann, and D Herlach. Novel insight into microstructural evolution of phase-separated Cu–Co alloys under influence of forced convection. *Journal of Materials Science*, 46(20):6603–6608, 2011. ISSN 1573-4803. doi: 10.1007/s10853-011-5609-2. URL https://doi.org/10.1007/s10853-011-5609-2.

[622] S. Luo, H. Wang, Z. Gao, Y. Wu, and H. Wang. Interaction between high-velocity gas and liquid in gas atomization revealed by a new coupled simulation model. *Materials Design*, 212:110264, dec 2021. ISSN 0264-1275. doi: 10.1016/J.MATDES.2021.110264.

[623] S. N El Moghazi, T. Wolfe, D. G Ivey, and H. Henein. Plasma transfer arc additive manufacturing of 17-4 PH: assessment of defects. *The International Journal of Advanced Manufacturing Technology*, 108(7):2301–2313, 2020. ISSN 1433-3015. doi: 10.1007/s00170-020-05540-2. URL https://doi.org/10.1007/s00170-020-05540-2.

[624] D. M Herlach. Non-Equilibrium Solidification of Undercooled Metallic Melts. *Metals*, 4(2):196–234, 2014. ISSN 2075-4701. doi: 10.3390/met4020196. URL http://www.mdpi.com/2075-4701/4/2/196.

[625] Eduardo Bellini Ferreira, Moysés L Lima, and Edgar D Zanotto. DSC Method for Determining the Liquidus Temperature of Glass-Forming Systems. *Journal of the American Ceramic Society*, 93(11):3757–3763, nov 2010. ISSN 0002-7820. doi: https://doi.org/10.1111/j.1551-2916.2010.03976.x. URL https://doi.org/10.1111/j.1551-2916.2010.03976.x.

[626] A. S. Kurlov and A. I. Gusev. Tungsten carbides and W-C phase diagram. *Inorganic Materials 2006 42:2*, 42(2):121–127, jan 2006. ISSN 1608-3172. doi: 10.1134/S0020168506020051. URL https://link.springer.com/article/10.1134/S0020168506020051.

[627] R. V. SARA. Phase Equilibria in the System Tungsten—Carbon. *Journal of the American Ceramic Society*, 48(5):251–257, may 1965. ISSN 1551-2916. doi: 10.1111/J.1151-2916.1965.TB14731.X. URL https://onlinelibrary.wiley.com/doi/full/10.1111/j.1151-2916.1965.tb14731.xhttps://onlinelibrary.wiley.com/doi/abs/10.1111/j.1151-2916.1965.tb14731.xhttps://ceramics.onlinelibrary.wiley.com/doi/10.1111/j.1151-2916.1965.tb14731.x.

[628] D.S. Shim, G.Y. Baek, J.S. Seo, G.Y. Shin, K.P. Kim, and K.Y. Lee. Effect of layer thickness setting on deposition characteristics in direct energy deposition (DED) process. *Optics Laser Technology*, 86:69–78, dec 2016. ISSN 0030-3992. doi: 10.1016/J.OPTLASTEC.2016.07.001.

[629] Aljaž Ščetinec, Damjan Klobčar, and Drago Bračun. In-process path replanning and online layer height control through deposition arc current for gas metal arc based

additive manufacturing. *Journal of Manufacturing Processes*, 64:1169–1179, apr 2021. ISSN 1526-6125. doi: 10.1016/J.JMAPRO.2021.02.038.

[630] Nancy Bhardwaj. *Fused Filament Fabrication of Metal-Ceramic High-Density Polyethylene Composites*. Master's of science, University of Alberta, 2022.

[631] S. Zhou, X. Zeng, Q. Hu, and Y. Huang. Analysis of crack behavior for Ni-based WC composite coatings by laser cladding and crack-free realization. *Applied Surface Science*, 255(5):1646–1653, dec 2008. ISSN 0169-4332. doi: 10.1016/J.APSUSC.2008.04.003.

[632] A. Weng, Z.and Wang, X. Wu, Y. Wang, and Z. Yang. Wear resistance of diode laser-clad Ni/WC composite coatings at different temperatures. *Surface and Coatings Technology*, 304:283–292, oct 2016. ISSN 0257-8972. doi: 10.1016/J.SURFCOAT.2016.06.081.

[633] Silja-Katharina Rittinghaus and Jonas Zielinski. Influence of Process Conditions on the Local Solidification and Microstructure During Laser Metal Deposition of an Intermetallic TiAl Alloy (GE4822). *Metallurgical and Materials Transactions A*, 52:1106–1116, 2021. doi: 10.1007/s11661-021-06139-2. URL https://doi.org/10.1007/s11661-021-06139-2.

[634] Abhijit Sadhu, Amit Choudhary, Sagar Sarkar, Amal M Nair, Pravanjan Nayak, Sagar Dadasahed Pawar, Gopinath Muvvala, Surjya K Pal, and Ashish Kumar Nath. A study on the influence of substrate pre-heating on mitigation of cracks in direct metal laser deposition of NiCrSiBC-60%WC ceramic coating on Inconel 718. *Surface and Coatings Technology*, 389:125646, 2020. ISSN 0257-8972. doi: https://doi.org/10.1016/j.surfcoat.2020.125646. URL https://www.sciencedirect.com/science/article/pii/S0257897220303157.

[635] Nathan A. Kistler, David J. Corbin, Abdalla R. Nassar, Edward W. Reutzel, and Allison M. Beese. Effect of processing conditions on the microstructure, porosity, and mechanical properties of Ti-6Al-4V repair fabricated by directed energy deposition. *Journal of Materials Processing Technology*, 264:172–181, feb 2019. ISSN 0924-0136. doi: 10.1016/J.JMATPROTEC.2018.08.041.

[636] Garrett J. Marshall, W. Joseph Young, Scott M. Thompson, Nima Shamsaei, Steve R. Daniewicz, and Shuai Shao. Understanding the Microstructure Formation of Ti-6Al-4V During Direct Laser Deposition via In-Situ Thermal Monitoring. *JOM*, 68(3): 778–790, mar 2016. ISSN 15431851. doi: 10.1007/S11837-015-1767-Z/FIGURES/11. URL https://link.springer.com/article/10.1007/s11837-015-1767-z.

[637] N. El-Bagoury and A. Nofal. Microstructure of an experimental Ni base superalloy under various casting conditions. *Materials Science and Engineering: A*, 527(29-30): 7793–7800, nov 2010. ISSN 0921-5093. doi: 10.1016/J.MSEA.2010.08.050.

[638] Masao Morishita, Koichiro Koyama, Kouichi Maeda, and Guofeng Zhang. Calculated phase diagram of the ni-w-b ternary system. *Materials Transactions, JIM*, 40(7):600–605, 1999. doi: 10.2320/matertrans1989.40.600.

[639] J. Xu, T. Yang, Z. Li, X. Wang, and Z. Xiao, Y.and Jian. The recalescence rate of cooling curve for undercooled solidification. *Scientific Reports 2020 10:1*, 10(1):1–5, jan 2020. ISSN 2045-2322. doi: 10.1038/s41598-019-56079-6. URL https://www.nature.com/articles/s41598-019-56079-6.

[640] Deutsches Zentrum für Luft-und Raumfahrt. Unpublished Work. 2023.

[641] L. Elmquist and A. Diószegi. Shrinkage porosity and its relation to solidification structure of grey cast iron parts. *http://dx.doi.org.login.ezproxy.library.ualberta.ca/10.1179/174313309X436664*, 23 (1):44–50, feb 2013. ISSN 13640461. doi: 10.1179/174313309X436664. URL https://www-tandfonline-com.login.ezproxy.library.ualberta.ca/doi/abs/10.1179/174313309X436664.

[642] W. Kruz and David J. Fisher. *Fundamentals of Solidification*. CRC Press, 4th edition, 1998. ISBN 978-0878498048.

[643] T. Rong, D. Gu, Q. Shi, S. Cao, and M. Xia. Effects of tailored gradient interface on wear properties of WC/Inconel 718 composites using selective laser melting. *Surface and Coatings Technology*, 307:418–427, dec 2016. ISSN 0257-8972. doi: 10.1016/J.SURFCOAT.2016.09.011.

[644] Xiaoyin Wang, Shengfeng Zhou, Xiaoqin Dai, Jianbo Lei, Jinbo Guo, Zhenjie Gu, and Tao Wang. Evaluation and mechanisms on heat damage of WC particles in Ni60/WC

composite coatings by laser induction hybrid cladding. *International Journal of Refractory Metals and Hard Materials*, 64:234–241, apr 2017. ISSN 0263-4368. doi: 10.1016/J.IJRMHM.2016.11.001.

[645] M. Schnick, U. Fuessel, M. Hertel, M. Haessler, A. Spille-Kohoff, and A. B. Murphy. Modelling of gas–metal arc welding taking into account metal vapour. *Journal of Physics D: Applied Physics*, 43(43):434008, nov 2010. ISSN 0022-3727. doi: 10.1088/0022-3727/43/43/434008. URL https://iopscience.iop.org/article/10.1088/0022-3727/43/43/434008https://iopscience.iop.org/article/10.1088/0022-3727/43/43/434008/meta.

[646] S. Zielińska, K. Musioł, K. Dzierga, S. Pellerin, F. Valensi, Ch De Izarra, and F. Briand. Investigations of GMAW plasma by optical emission spectroscopy. *Plasma Sources Science and Technology*, 16(4):832, oct 2007. ISSN 0963-0252. doi: 10.1088/0963-0252/16/4/019. URL https://iopscience.iop.org/article/10.1088/0963-0252/16/4/019https://iopscience.iop.org/article/10.1088/0963-0252/16/4/019/meta.

[647] Nan Nan, Jingxin Wang, and Anita Andicsová Eckstein. FIB-SEM Three-Dimensional Tomography for Characterization of Carbon-Based Materials. *Advances in Materials Science and Engineering*, 2019, 2019. ISSN 16878442. doi: 10.1155/2019/8680715.

[648] Carles Bosch, Albert Martínez, Nuria Masachs, Cátia M. Teixeira, Isabel Fernaud, Fausto Ulloa, Esther Pérez-Martínez, Carlos Lois, Joan X. Comella, Javier De-Felipe, Eduardo Soriano, and Eduardo Soriano. FIB/SEM technology and high-throughput 3D reconstruction of dendritic spines and synapses in GFP-labeled adult-generated neurons. *Frontiers in Neuroanatomy*, 9(MAY):60, may 2015. ISSN 16625129. doi: 10.3389/FNANA.2015.00060/ABSTRACT.